Collective Movement in Dictyostelium discoideum and Other Species. Modeling, Analysis and Simulations

Mete Demircigil

N°d'ordre NNT :2022LYSE1113

THESE de DOCTORAT DE L'UNIVERSITE DE LYON
opérée au sein de
l'Université Claude Bernard Lyon 1

Ecole Doctorale N° 512
Informatique et Mathématiques de Lyon (InfoMaths)

Spécialité de doctorat : Mathématiques appliquées
Discipline : Mathématiques

Soutenue publiquement le 26/08/2022, par :
Mete Demircigil

Mouvement collectif chez *Dictyostelium discoideum* et autres espèces. Modélisation, analyse et simulations.

Devant le jury composé de :

Hamel, François	Professeur des Universités	Université d'Aix-Marseille	Rapporteur
Vauchelet, Nicolas	Professeur des Universités	Université Sorbonne Paris Nord	Rapporteur
Doumic, Marie	Directrice de Recherche	Sorbonne Université	Examinatrice
Nadin, Grégoire	Directeur de Recherche	Sorbonne Université	Examinateur
Ribot, Magali	Professeure des Universités	Université d'Orléans	Examinatrice
Rivière, Charlotte	Professeure des Universités	Université Claude Bernard Lyon 1	Examinatrice
Tang, Min	Professeure Associée	Université Jiao Tong Shanghai	Examinatrice
Calvez, Vincent	Directeur de Recherche	Université Claude Bernard Lyon 1	Directeur de thèse
Rieu, Jean-Paul	Professeur des Universités	Université Claude Bernard Lyon 1	Invité

Abstract

Collective Movement in *Dictyostelium discoideum* and Other Species. Modeling, Analysis and Simulations.

This thesis is concerned with the modeling of collective cell movement and the analysis of spreading phenomena arising in these models.

The starting point of the thesis is the mathematical modeling of an experiment, where a colony of *Dictyostelium discoideum* is able to escape hypoxia through a remarkable collective behavior. It is shown that oxygen consumption leads to self-generated oxygen gradients, which serve as directional cues and trigger a collective movement towards higher oxygen regions. This movement is sustained over large scales by the perpetual consumption of oxygen by the cells. Through an elementary PDE model, the so-called Go or Grow model, we show that the combination of cell division and aerotaxis plays a key role in this collective behavior. In particular, this approach leads to an explicit formula for the propagation speed.

We carry out a thorough mathematical analysis of the Go or Grow model, including a result of existence and uniqueness locally in time of the model, an analysis of the inside dynamics of the propagating population, as well as a weak characterization of the asymptotic spreading behavior.

Following the aforementioned investigation, we address the question under which circumstance a cell population may propagate, by generating their own signaling gradients. We do a survey on existing results in the literature and discuss various modeling scenarios, which lead to this type of propagation phenomena.

Then, we propose an approach to design well-balanced numerical schemes for traveling waves in kinetic and parabolic models. The approach combines an estimate of the instantaneous spreading speed with techniques taken from the literature to design well-balanced schemes.

Finally, we study a stochastic individual-based Go or Grow model, which is based on a simple Go or Grow rule. We conjecture the large population limit, which can be seen as an alternative Go or Grow model, and investigate numerically the ancestral lineages of particles. This leads to an alternative viewpoint on the inside dynamics. The alternative Go or Grow model is analyzed and we give preliminary results estimating the asymptotic behavior of the spreading.

Keywords: Mathematical Biology, Chemotaxis, Modeling, Propagation Phenomena, Parabolic Equations, Kinetic Equations, Well-Balanced Schemes, Stochastic Processes.

Résumé

Cette thèse s'inscrit dans le domaine de la modélisation du mouvement cellulaire collectif et de l'analyse de phénomènes de propagation dans ces modèles.

Le point de départ de cette thèse est la modélisation mathématique d'une expérience, où une colonie de *Dictyostelium discoideum* parvient à échapper l'hypoxie grâce à un remarquable comportement collectif. Il est montré que la consommation d'oxygène conduit à des gradients d'oxygène auto-générés, qui servent d'indicateurs de navigation aux cellules et déclenchent un mouvement collectif vers des zones de teneur en oxygène plus élevée. Le mouvement se maintient sur des larges échelles à travers la consommation permanente d'oxygène par les cellules. Par un modèle élémentaire EDP, que nous désignons par modèle "Se déplacer ou Se diviser" (*Go or Grow* en anglais), nous montrons que la combinaison de la division cellulaire et de l'aérotactisme joue un rôle crucial dans ce comportement collectif. En particulier, cette approche conduit à une formule explicite de la vitesse de propagation.

Nous conduisons ensuite une analyse mathématique du modèle "Se déplacer ou Se diviser", qui inclut notamment un résultat d'existence et d'unicité du modèle localement en temps, une analyse de la dynamique intérieure de la population en propagation, ainsi qu'une caractérisation faible du comportement de propagation asymptotique.

Suite à ce travail, nous nous interrogeons sur les conditions sous lesquelles une population cellulaire peut se propager, en générant leur propre gradient de signalisation. Nous mentionnons des résultats antérieurs dans la littérature et discutons de divers scénarios de modélisation, qui conduisent à ce type de phénomènes de propagation.

Ensuite, nous proposons une approche pour concevoir des schémas numériques bien équilibrés pour des ondes progressives dans des modèles cinétiques et paraboliques. Cette approche combine une estimation de la vitesse de propagation instantanée, ainsi que des techniques documentées dans la littérature pour concevoir des schémas bien équilibrés.

Enfin, nous étudions un modèle "Se déplacer ou Se diviser" stochastique et individu-centré, qui se fonde sur une simple règle "Se déplacer ou Se diviser". Nous conjecturons une limite en large population, qui peut être vu comme un modèle "Se déplacer ou Se diviser" alernatif, et étudions numériquement les lignées ancestrales des particules. Ainsi, nous proposons un point de vue parallèle sur les dynamiques intérieures. Le modèle "Se déplacer ou Se diviser" alternatif est analysée et nous donnons des résultats préliminaires sur le comportement asymptotique de la propagation.

Mots-clés: Biologie mathématique, Chimiotactisme, Modélisation, Phénomènes de propagation, Equations paraboliques, Equations cinétiques, Schémas bien-équilibrés, Processus stochastique.

Résumé substantiel en français

Cette thèse s'inscrit dans le domaine de la modélisation du mouvement cellulaire collectif. De nombreux organismes unicellulaires ont la capacité de réagir à des changements de leur environnement en se déplaçant. Ces phénomènes sont généralement regroupés sous le terme de tactisme (par exemple chimiotactisme, aérotactisme, phototactisme, *etc...*) et sont étudiés notamment en tant que mécanisme d'adaptation.

Le premier chapitre est consituté d'un article [48] sur lequel nous avons collaboré en contribuant à la modélisation mathématique de l'expérience étudiée. A travers un dispositif expérimental, il est montré que lorsqu'une colonie de cellules *Dictyostelium discoideum*, un amibe de taille 50µm, est confinée verticalement entre deux plaques, sa consommation d'oxygène l'expose à de l'hypoxie. De plus, cette consommation d'oxygène conduit à des gradients d'oxygène, dits auto-générés. Ces gradients auto-générées déclenchent alors par aérotactisme un mouvement collectif vers l'extérieur, qui se fait sous forme d'un anneau. Cet anneau croît à vitesse constante et présente un profil constant sur des longues échelles de temps.

Dans un premier temps, ce phénomène est simulé numériquement par un modèle cellulaire Potts, qui inclut de la division cellulaire et une modulation d'aérotactisme. Dans un second temps, nous avons contributé à proposer un modèle EDP en champ moyen, qui se fonde sur le précédent modèle cellulaire Potts. Suite à la difficulté de mener à bien une analyse de ce modèle EDP, nous proposons une hypothèse de modélisation, dont le but est de montrer que les ingrédients susmentionnés sont suffisants pour expliquer un tel phénomène de propagation. Nous dénommons ce modèle "Se déplacer ou Se diviser" (*Go or Grow* en anglais). Il présente l'avantage de conduire à trouver des solutions explicites sous forme d'onde progressive et une formule explicite de la vitesse de propagation. De plus, il permet d'analyser les dynamiques intérieures, démontrant que dans le cas d'un aérotactisme fort, l'onde est de nature poussée, alors que dans le cas d'un aérotactisme faible, l'onde est de nature tirée. Enfin, en proposant des variations de ce modèle "Se déplacer ou Se diviser", nous testons la validité des conclusions tirées de ce modèle élémentaire.

Le deuxième chapitre est constituté d'un article [54], qui a été soumis au *Journal de l'École polytechnique — Mathématiques*. Nous y proposons une analyse mathématique du modèle "Se déplacer ou Se diviser", qui sert de complément au travail du chapitre précédent.

$\rho(t,x)$ dénotant la densité cellulaire et $N(t,x)$ la concentration en oxygène, le modèle "Se déplacer ou Se diviser" consiste alors en un système d'équations de réaction-diffusion-advection. Pour $(t,x) \in \mathbb{R}_+ \times \mathbb{R}$:

$$\begin{cases} \partial_t \rho - \partial_{xx}\rho + \partial_x \left(\chi \mathbb{1}_{N<N_{\text{th}}} \text{sign}(\partial_x N)\rho\right) = \mathbb{1}_{N>N_{\text{th}}}\rho \\ \partial_t N - D\partial_{xx}N = -\rho N, \end{cases}$$

où χ est la vitesse d'advection aérotactique, D la constante de diffusion de l'oxygène et N_{th} un seuil en dessous duquel la population est en régime "Se déplacer", et au-dessus duquel elle est en régime "Se diviser".

A cause du terme d'advection discontinu, le problème de Cauchy doit être traité avec soin. Nous établissons donc dans un premier temps un résultat d'existence et d'unicité de ce système, en réduisant le problème à une EDO, sous une condition de monotonicité de N. Ensuite, nous effectuons une analyse asymptotique du système. Toutes les solutions positives et bornées sous forme d'onde progressive sont calculées et une formule explicite de la vitesse minimale de propagation en est déduite. Une analyse de la dynamique intérieure des ondes progressives est proposée, qui étend notamment des résultats de [152] à des modèles de réaction-diffusion-advection. Puis, nous identifions la vitesse minimale σ^* comme la vitesse biologiquement pertinente dans un sens faible: si, nous introduisons la position du seuil $\bar{x}(t)$, tel que $N(t, \bar{x}(t)) = N_{\text{th}}$, alors sous certaines hypothèses, nous avons:

$$\begin{cases} \liminf\limits_{t\to+\infty} \dot{\bar{x}}(t) \leq \sigma^*, \\ \limsup\limits_{t\to+\infty} \dot{\bar{x}}(t) \geq \sigma^*. \end{cases}$$

Enfin, nous étendons cette étude à un modèle hyperbolique à deux vitesses avec persistence.

Le troisième chapitre a été publié comme article [36] dans l'ouvrage collectif [18]. Il a été écrit en collaboration avec Vincent Calvez et Roxana Sublet, notamment lors d'un stage de cette dernière encadré par les deux autres auteurs.

Nous partons du constat que les gradients auto-générés ont attiré une grande attention dans la littérature biologique récente. Ils sont proposés comme modèles de navigation et de déplacements collectifs et sont considérés comme constituant une stratégie robuste pour qu'une population cellulaire puisse naviguer dans son environnement. Le chapitre s'attache à discuter différents scénarios de modélisation pour modéliser une propagation de cellules, qui consomment en permanence son signal chimique et crée ainsi leur propre gradient de signalisation lors de leur propagation.

Nous commençons avec un célèbre modèle proposé par Keller et Segel [114] pour du chimiotactisme dans des bactéries. Après une présentation du modèle, nous construisons les solutions d'onde progressive de ce modèle. Nous discutons les limitations de cette approche et passons en revue quelques travaux qui mettent en lumière des problèmes de stabilité de ce modèle.

Dans un second temps, nous proposons deux extensions pertinentes de ce modèle, qui sont soutenues par des considérations biologiques. Les deux extensions donnent lieu à des solutions d'ondes progressives avec une valeur explicite pour la vitesse de l'onde. Nous concluons en mentionnant certains problèmes ouverts et des perspectives, en particulier un mécanisme remarquable de sélection de la vitesse, ayant lieu à l'arrière de l'onde.

Tous les résultats dans cette étude sont illustrés par des simulations numériques.

Le quatrième chapitre a été écrit en collaboration avec Benoit Fabrèges, qui a mené à bien la partie parabolique de ce chapitre. Avant de soumettre l'article, nous souhaitons davantage étudier si nous pouvons proposer une amélioration du schéma dans le cas cinétique.

Nous proposons une méthodologie pour concevoir des schémas numériques bien équilibrés afin d'étudier des solutions d'ondes progressives dans des modèles cinétiques et paraboliques, provenant de la biologie mathématique. Nous combinons des techniques de schémas bien équilibrés avec la formule, dite de LeVeque-Yee, qui estime de manière dynamique la

vitesse de propagation. Cette dernière formule est utilisée afin de considérer le problème d'évolution dans le référentiel en mouvement à cette vitesse. Dans ce référentiel les équations admettent une solution stationnaire. Les techniques de schémas bien équilibrés se prêtent particulièrement bien à l'étude de ces solutions stationnaires. Ensuite, nous procédons à une translation de la solution calculée de retour vers le référentiel stationnaire. Cette translation est effectuée de manière bien équilibrée. Nous illustrons cette méthodologie sur deux cas d'application: le premier est le modèle cinétique "Se déplacer ou Se diviser" mentionné brièvement dans le premier chapitre; le second est la célèbre équation parabolique de Fisher/Kolmogorov-Petrovsky-Piskunov (F/KPP). Dans les deux cas, nous montrons que le schéma numérique rend compte de manière cohérente simultanément de la vitesse de propagation et du profile d'onde à l'avant du front. De plus, nous montrons que pour l'équation F/KPP, le schéma est capable jusqu'à un certain degrés de correctement calculer le décalage, dit de Bramson.

Le cinquième chapitre est une présentation préliminaire de résultats, qui sont le fruit d'une collaboration avec Vincent Calvez et Milica Tomašević. La présentation est volontairement informelle et des affirmations non-rigoureuses sont soutenues par des simulations numériques.

Nous proposons un modèle stochastique "Se déplacer ou Se diviser" individu-centré: les K premières particules (comptées à partir de la droite) sont dans le régime "Se diviser" et les autres particules sont dans le régime "Se déplacer". Le modèle consiste alors en un système d'EDS décrivant un mouvement brownien avec advection (à vitesse χ dans le régime "Se déplacer" et vitesse nulle dans le régime "Se diviser), qui est combiné avec un processus poissonien de naissance pour les K premières particules. Nous commençons par donner une construction algorithmique du processus. Cette approche est complétée par une EDS qui décrit l'évolution de la mesure ponctuelle associée à la population.

Ensuite, nous conjecturons la limite dans le régime de large population quand $K \to +\infty$ sous une renormalisation appropriée. L'équation limite correspond alors à une EDP, qui peut être vue comme un modèle alternatif "Se déplacer ou Se diviser". Nous donnons des arguments numériques indiquant que dans la limite $K \to +\infty$ le modèle stochastique converge vers les ondes progressives solutions de cette EDP.

Enfin, nous étudions la lignée ancestrale des particules, en suivant une méthodologie proposée récemment dans [38, 74]. Numériquement, nous montrons que deux régimes différents existent, qui correspondent exactement les régimes de faible et fort aérotactisme du deuxième chapitre. Ce point de vue donne lieu à une interprétation alternative pour la dichotomie entre onde tirée et onde poussée.

Ce chapitre est une présentation préliminaire de résultats, fruits d'une collaboration avec Christopher Henderson.

Nous étudions le modèle EDP alternatif "Se déplacer ou Se diviser", que nous avons précédemment conjecturé comme équation limite du modèle stochastique "Se déplacer ou Se diviser" individu-centré. Nous montrons un résultat d'existence et d'unicité localement en temps pour ce modèle, qui est une adaptation du résultat analogue dans le deuxième chapitre.

Ensuite, nous proposons une conjecture sur le comportement asymptotique de la posi-

tion du seuil $\bar{x}(t)$:

$$\bar{x}(t) = \begin{cases} 2t - \frac{3}{2}\log(t) + O(1) & \text{if } \chi < 1 \\ 2t - \frac{1}{2}\log(t) + O(1) & \text{if } \chi = 1 \\ \left(\chi + \frac{1}{\chi}\right) + O(1) & \text{if } \chi > 1 \end{cases}.$$

Nous montrons les résultats intermédiaires suivants:

$$\begin{cases} \bar{x}(t) \leq 2t - \frac{3}{2}\log(t) + O(1) & \text{, if } \chi < 1 \\ 2t - \frac{1}{2}\log(t) + O(1) \leq \bar{x}(t) \leq 2t + O(1) & \text{, if } \chi = 1 \\ \bar{x}(t) \leq \left(\chi + \frac{1}{\chi}\right) + O(1) & \text{, if } \chi > 1 \end{cases}$$

Enfin, nous concluons le chapitre en montrant un résultat de stabilité asymptotique de l'onde progressive de vitesse minimale dans le cas d'un large biais aérotactique. Cette preuve se fonde sur une méthode d'énergie L^2.

Remerciements

Ce manuscrit est l'aboutissement d'un long voyage, dont il m'est difficile de dater le départ. J'aimerais ici exprimer ma gratitude infinie à l'ensemble des personnes, qui ont rendu possible ce voyage en me nourrissant, intellectuellement, matériellement et spirituellement. Si ce n'est chose déjà faite, j'espère un jour pouvoir leur rendre la pareille. J'en profite pour mentionner en particulier celleux-là, pour qui j'ai une pensée particulière, en écrivant ces lignes.

Tout d'abord, je pense à Vincent Calvez, qui a dirigé mes recherches dans le domaine des mathématiques appliquées à la biologie. Vincent a été une grande source d'inspiration tout le long de ce parcours: son enthousiasme, ainsi que sa large palette de connaissances m'étonneront toujours. Ce fut décidemment un immense plaisir et honneur de pouvoir travailler avec lui. De plus, sa douceur, son écoute et son attention pour les autres sont des qualités, que j'espère pouvoir cultiver.

Je remercie François Hamel et Nicolas Vauchelet, qui ont accepté de rapporter cette thèse. Leurs commentaires ont été une source de grand encouragement. C'est un plaisir que Grégoire Nadin participe à mon jury de thèse. Pendant mon comité de suivi, ses remarques étaient très pertinentes et bienveillantes et je l'en remercie. Given my experience at SJTU and my attachment to this institution, it is also a great honour to count Min Tang among my PhD thesis jury members, after she had already been member of my Master's thesis jury. Je remercie Charlotte Rivière d'accepter de faire partie du jury d'une thèse de mathématiques. Ce décloisonnement disciplinaire contribue au sens de la démarche scientifique de ces travaux, ce qui me réjouit beaucoup. Enfin, un grand merci à Marie Doumic et Magali Ribot d'avoir accepté de faire partie de mon jury de thèse.

Je souhaite aussi exprimer mon énorme gratitude à Christophe Anjard, Olivier Cochet-Escartin et Jean-Paul Rieu. La collaboration avec eux, qui a donné lieu à une pierre angulaire de cette thèse, a été scientifiquement et humainement très riche. Leur rigueur et leur exigence ont été très formatrices. En particulier, je les remercie de la confiance, qu'ils m'ont accordée, et de leur écoute vis-à-vis des idées de Vincent et de moi.

Merci également à Milica Tomašević, dont l'enthousiasme communicatif et les qualités pédagogiques ont été source de grande motivation. Je garderai un souvenir très particulier d'un dîner convivial avec au menu des délicieuses spécialités des Pouilles.

I am extremely grateful to Chris Henderson, whose invitation to Tucson has been a delightful experience. He has taught me a lot of very beautiful mathematics, and his perseverance when it comes to doing computations on black boards is certainly unmatched: thanks to him, I now tend to shy away less from long and formidable computations. It has also been a great pleasure to meet his family, Frances, Flor and Nell, with whom we have spent lovely moments, be it in Tucson or in Lyon. Moreover, I wish to acknowledge that the University of Arizona, who has honored me by hosting me, is on the land and territories of Indigenous peoples. Today, Arizona is home to 22 federally recognized tribes, with Tucson being home to the O'odham and the Yaqui. I also wish to express my gratitude to Lise-

Marie Imbert-Gérard and Tonatiuh Sánchez-Vizuet, who were kind enough to host me and to introduce me to Tajin seasoning, which has quickly become an essential ingredient in my kitchen! Furthermore, I would like to thank all the other wonderful people in Tucson, I had the honour to encounter, with a special thought to Bo for driving me around and showing me ways.

I also wish to thank Lenya Ryzhik, who I did not have the chance to meet in person, because of Covid restrictions, but who was willing to invite me to Stanford University. Hopefully, other occasions will make up for this missed opportunity.

C'était un formdiable plaisir de pouvoir travailler avec Benoit Fabrèges, dans un premier temps sur la modélisation du Covid, dans des conditions mémorables, puis sur des schémas numériques présentés dans cette thèse.

Une petite pensée aussi à Roxana Sublet, qui lors de son stage a fait preuve d'inventivité et d'une grande force de compréhension. Je lui souhaite une bonne continuation pour la suite.

Je souhaite également remercier des personnes avec qui j'ai eu le plaisir de parler de mathématiques appliquées à la biologie et qui ont toujours été très encourageante pour que je poursuive dans cette voie: Benoît Perthame à travers son cours ou ses livres a été une grande influence. Je le remercie également de m'avoir permis de visiter par deux reprises la Chine. Many thanks to Hu Dan, my supervisor at SJTU, who has welcomed me in his team. Jean Clairambault, dont l'enthousiasme et les encouragements sont inégalés. La jovialité de Thomas Lepoutre, ainsi que sa disponibilité resteront des souvenirs très chers. Ce fut toujours un plaisir de discuter avec Léo Girardin, qui m'a volontiers partagé ses connaissances sur les équations de réaction-diffusion. De même un grand merci à Jimmy Garnier, qui a toujours répondu avec beaucoup de clairvoyance à mes questions.

J'ai également une petite pensée pour mes adelphes de thèse, Léonard, Jean-Baptiste, Léna et Vianney, avec qui ce fut toujours très agréable de discuter. J'espère que la suite leur offrira les succès, qu'iels méritent, et plénitude.

Je remercie l'ensemble des membres du laboratoire de l'ICJ. Evidemment, parmi elleux, la formidable équipe Dracula, composée entre autres d'Olivier, Laurent, Léon, Mostafa, Samuel, Olivier, Thibault et Vitaly, qui ont toujours su me poser des questions intrigantes et ont toujours été disponibles lorsque j'avais des questions. Un grand merci aussi à Aymeric, Alexandre, Christian, Filippo, Francesco, Frédéric, Louis et Pierre-Damien. Tuna hocam, sizinle tanışmak büyük bir onurdu. İstanbul'a seyahatim sizin de sayenizdedir. Mücadelerinizde başarılar dilerim. A de nombreuses reprises sans l'aide Lydia Barlerin, Vincent Farget, Céline Laurent ou Christine Lesueur, j'aurais frôlé la galère et je souhaite leur témoigner toute ma réconnaissance. Ce fut aussi un immense plaisir de coorganiser le séminaires des doctorant-es avec Annette, Antoine, Gabriele, Gauthier et Sébastien. Merci aussi à David, Havva et Raphael. Merci à Léa, Hadi, David, Marion et Priscilla, ainsi que toustes les autres membres du labo, dont une liste exhaustive serait certainement trop longue.

Evidemment, je pense aussi à Kyriaki, que j'ai rencontrée lors de mon premier jour de thèse à Samos, et avec qui tout le long nous nous sommes serré les coudes. Nos ballades sur le campus et nos commentaires sur le bâtiment moche seront certainement parmi les choses, qui me manqueront le plus pour la suite.

Je n'aurais certainement pas réussi à aller au bout de cette thèse, sans mes copaines de lutte. Je ne les nomme pas et iels en connaissent les raisons, mais je sais que je peux compter sur vous le jour, où nous mangerons le coing (comme l'on dit en turc). Merci pour ce que vous faites et pour le sens que vous donnez à ma vie.

De très chaleureuses pensées aussi à: la fameuse team des razmokets, Arnaud, Con-

stantin, Dimitri, Etienne, Félix, Hugo et Lucie; mes ancien-nes colocs, Marion, Maxime et William; Antonin, Célien, Elisabeth et Noé; İdil; Pia; mon frère Kaya et ma soon-to-be belle-sœur Kim; et enfin mon père.

Fir meng zwee Schutzengelen,

Babama,

Contents

Chapter 0

Introduction

0.1 Biological Motivations: Collective Cell Movement

0.1.1 *Taxis* Phenomena: Cell Navigation in Heterogeneous Environments

Collective Cell Movement as an Adaptation Mechanism

This thesis is very broadly concerned with the question of collective cell movement in motile cells, *i.e.* which can move spatially: this could for example be bacteria with flagella swimming through a liquid phase [22], or amoeboids crawling via protrusions of lamellipodia [133]. In many cases, these cells can react to changes in their environment through displacement. These remarkable cellular responses to envionmental signals have been designated under the concept of *taxis* (pl. *taxes*), which comes from the Ancient Greek word τάξις for arrangement or order. Taxes are classified according to the nature of the signal, to which cells are exposed to: *aerotaxis* in the case of oxygen, *chemotaxis* in the case of another chemical, *phototaxis* in the case of stimulation by light, *thigmotaxis* in the case of a mechanical contact, *etc...* Of note, since oxygen can be viewed as a chemical, when we refer to chemotaxis in this manuscript, it may implicitly include aerotaxis, but we will use the term aerotaxis, when we specifically consider oxygen. Furthermore, taxis can describe the individual cell response to a signal, but in this thesis we will use the term to describe the collective behavior, which emerges from individual cell responses.

The scientific investigation of taxis phenomena dates back to the 1880's, where a series of discoveries has evidenced different types of taxes. To the best of our knowledge, the first description of a taxis phenomenon was a population of bacteria undergoing aerotaxis: in [63], when bacteria under a coverslip are exposed to low oxygen concentrations, they move to regions with higher oxygen concentrations such as the edges of the coverslip. This was interpretated as an adapatation mechanism, since oxygen is required in the cell metabolism, in particular as has been established later on for the production of adenosine triphosphate (ATP), which provides energy for many processes in living cells. Later on, the same author was able to show evidence for phototaxis [64] by concentrating light onto a small spot of the coverslip and noticing that bacteria would accumulate at the light spot. Finally, chemotaxis has been put into evidence in sperm cells [146] and in bacteria [147]. Of note, in the case of chemotaxis, there exist essentially two flavors: a signaling chemical can be a chemoattractant, which tends to attract cells, or a chemorepellant, which tends to repel cells.

As noted in [2, 10], although the studies [63, 64, 146, 147] have already postulated that these phenomena may play an important role as adaptation mechanisms in cells, for a

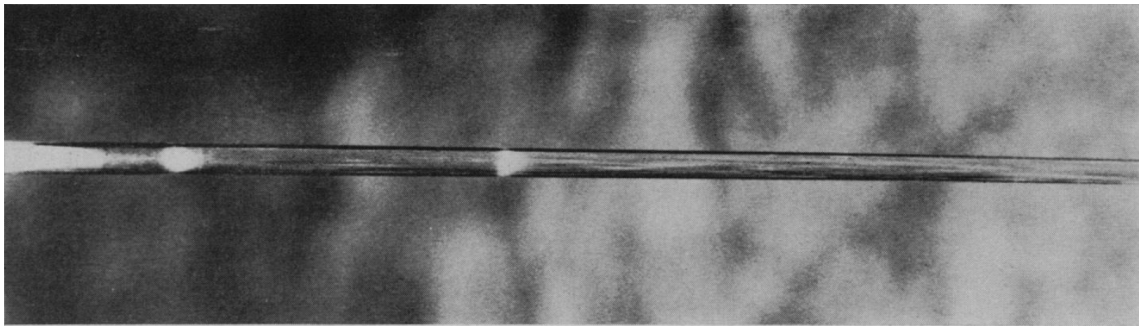

Figure 1: Photograph, taken from [5], showing bands of *E.coli* in a capillary tube traveling from the left to the right.

relatively long period of time the efforts to investigate these mechanism were rather scarce. Only in the 1960's, interest in these phenomena, in particular chemotaxis in bacteria, notably rose again, especially through the works [3–5]. From there on, studies on different taxes, considered as a large framework for adaptation mechanisms in cells, have risen again. An exhaustive survey of these studies clearly extends the scope of this manuscript, but in the following lines, we give some examples:

Chemotactic Traveling Bands in *Escherichia coli*. *Escherichia coli* (*E. coli* in short) is a bacterium of an average size of 1µm, which can swim in liquid phases via its flagella. In the seminal article [5], the author proposes an experimental setup to evidence chemotaxis in *E.coli*: approximately a million *E. coli* cells are placed at the end of a capillary. The capillary contains galactose, an energy source for *E. coli*, and oxygen, which is needed in order to oxydize the galactose. After a short time, a band of *E. coli* starts to propagate from their initial position to the other extremity of the capillary, whereas other cells are left behind (see Figure 1). In fact, a second slower band is also observed, but we will not discuss it here. By measuring the concentration of oxygen and galactose in each segment of the capillary, it is shown that the cells consume the entirety of galactose or oxygen (depending on which is the limited ressource) leading to chemical gradients directed towards the other extremity of the capillary. Via chemotaxis (or aerotaxis) the cells then move upwards this gradient, leading to the macroscopic propagation of the band. Furthermore, the study also excludes heterogeneity in cells by repeating the experiment with cells from different positions of the capillary and obtaining the same result. This shows that the emerging collective bheavior is not reliant on a diversity in individual behaviors.

Chemotaxis in *Dictyostelium discoideum*. *Dictyostelium discoideum* (*Dd* cells in short hereafter), sometimes also referred to as slime mold, is an amoeba with an average size of 50µm. *Dd* cells are the main living organism studied in this manuscript. These eukaryots can undergo two different development stages [189]. In normal circumstances, *Dd* cells live as single cells in soil, undergo cell division and feed on bacteria. However, in starvation conditions, cells produce cyclic adenaosine monophosphate (cAMP), which acts as a chemoattractant: this leads to an aggregation of up to several hundred thousand neighboring cells to form a multicellular structure, called slug (see Figure 2b). Cells regrouped in spores of the slug are then exposed to air and can escape the hostile environment, by being borne by the wind. This enables the start of a new life cycle for part of the cell population in a different environment. It has been demonstrated that chemotaxis

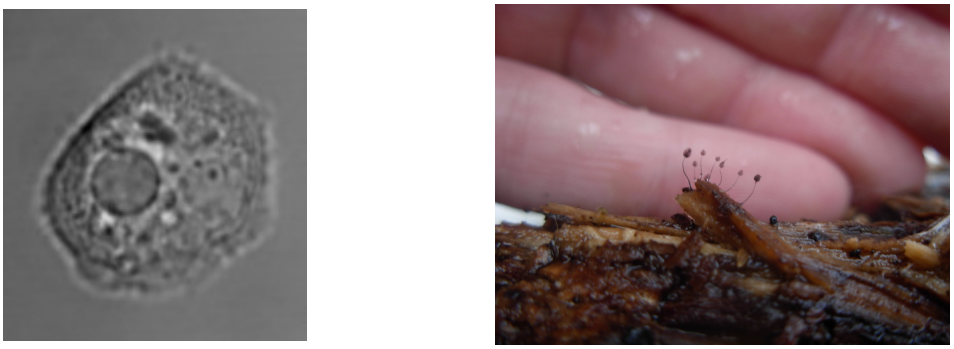

(a) (b)

Figure 2: (a): A *Dd* cell under a microscope, taken from [129]. (b): Photograph representing the slugs that *Dd* cells form. *Dictyostelium discoideum* by Chris Wagner in 2007, taken from CalPhotos Photo Database and licensed under CC BY-ND 3.0.

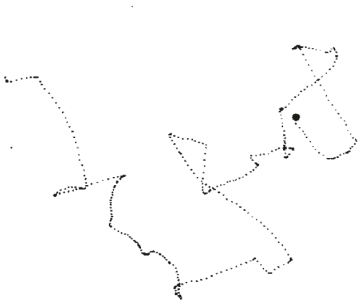

Figure 3: Representation of a typical Run and Tumble trajectory in a single *E. coli* cell, taken from [22]. The runs correspond to the relatively straight lines, which are interupted during a tumble leading to a reorientation of the cell's trajectory.

plays a crucial role in the formation of the slug [73, 189].

Emergence of Collective Movement: from Individual Cell Trajectories to Taxis

In the seminal paper [22], the authors have, through an elaborate experimental tracking of *E. coli*, unveiled the microscopic features of its movement: trajectories of an individual bacterium consists in a series of approximately straight lines (called *runs*), where the cell moves approximately with velocity $20\mu\text{m}\cdot\text{s}^{-1}$ for a duration following a Poisson distribution of mean 1s. The runs are interrupted by brief pauses (called *twiddles*, or *tumbles* later on in the litterature) of approximately 0.1s, where the cell reorients itself in a seemingly random direction (see Figure 3). This characteristic movement is now commonly referred to as Run and Tumble movement.

Furthermore, it is shown that when *E. coli* is exposed to a gradient of a chemoattractant a modulation of the tumbling frequency occurs: when cells move the gradient upward, the runs are longer, whereas they are shorter, when cells move the gradient downward. Theses biases in the cell trajectories lead then in average to a net displacement upward the gradient. Later on, the study on the chemotactic traveling bands [160] proposed an

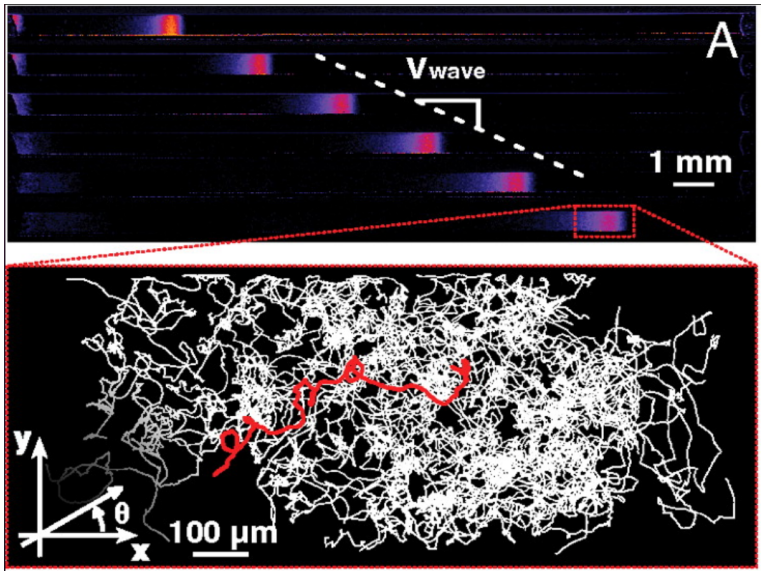

Figure 4: Experiment of chemotactic traveling waves of *E. coli* in a PDMS microchannel [160]. The upper figure represents successive snapshots of the same channel (500s between each frame). The lower figure represents the trajectories of single cells, where in red a single trajectory has been highlighted.

illustration of the emergence of chemotaxis as the consequence of an averaging in small biases in trajectories (see Figure 4).

In addition, the fact, that the law of reorientations is the same independently of whether cells move the gradient downward or upward, indicates that cells do not possess the ability to locally sense a spatial gradient: the authors in [22] argue that cells rather sense temporal variations in the surrounding concentration, which enables the modulation of the tumbling frequency. This fact may also be conforted by the observation that *E. coli* cells are very small, meaning that different parts of the cell are exposed to extremely small and indetectible variations in concentration: in fact at the scale of the cell size the chemical concentration may even be prone to local microscopic fluctations. These conclusions were later on supported by investigations on the signal transduction [16].

Although the Run and Tumble movement in *E. coli* is a very elegant account of how the individual cell movement can lead to macroscopic collective behavior, it is by far not the only one. For instance the trajectories of *Dd* cells may be much more diverse, including among others linear, spiral or directional reversal movements [60]. However, not unlike *E. coli*, the movement of *Dd* cells features a high directional persistence, which is the key ingredient to explain the emergence of chemotaxis [120]. Yet, the sensing mechanisms of the gradient drastically differ in both cells: because of its relatively large size, *Dd* cells can sense the spatial direction of the signal and thus orient their movement [120], whereas the law of change in directions with respect to the incoming direction in *E. coli* does not depend on the gradient, as pointed out above.

Intra-cellular Mechanisms

Taxis as a model of collective movement is certainly appealing in its way of proposing an elegant framework encompassing very different phenomena. However, the question of the microscopic movement of cells has already shown that this unified framework accounts for

different behaviors. If we further zoom in on the scale and investigate how the individual cell movement is governed by intra-cellular mechanisms, the diversity of biological phenomena decuples. For example, aerotaxis in *E. coli* can be explained through the signal transduction via the receptor Aer, which differs from the four receptors Tsr, Tar, Trg, and Tap involved in chemotaxis [173]. In contrast, the transduction of oxygen sensing in *Dd* cells remain unknown [48]. However, the difficulty of these questions falls beyond the scope of this thesis, as well as the understanding of its author. Hence, in this thesis we are not going to deal with the scale of intra-cellular mechanisms, but it certainly is worthwile remembering the diversity, which hides below the term taxis.

Let us conclude this Subsection by observing that, despite the great research interest that taxis phenomena have attracted, it still constitues a very active field of research and many questions remain to be answered. This is true for the intra-cellular mechanism described just above, but also for other aspects. For instance, eukaryotic cells can respond to chemotaxis by forming pseudopods, but the exact underlying physical process is still under investigation [104]. As another example: it is reasonable to suppose that aerotaxis plays an important role in eukaryotic cells, as a mechanism to increase the oxygen supply and thus the cell's ability to produce ATP. But as noted in [48, 56], the studies that bring evidence of aerotaxis in eukaryots are rather scarce.

0.1.2 Self-Generated Signaling Gradients: an Effective Navigation Strategy

The ability of cells to navigate through signaling gradients naturally raises the question of the emergence of signaling gradients. A widely considered hypothesis stipulates the existence of imposed external gradients: via a certain, possibly unknown, biological phenomenon emerges a signaling gradient, which offers signaling cues to a cell population, and the cell population responds in turn to this external gradient. However, only very few cases of such imposed external gradients are known in physiological situations [181]. An alternative model of navigation through signaling gradients is the model of self-generated signaling gradients (SGG in short from here on): the cells are in presence of a chemoattractant, which may for example be uniformly distributed in space. Then, the cell population acts as a sink by removing the chemoattractant, through degradation or consumption for instance. This induces the emergence of a signaling gradient. The cells via taxis follow this gradient and in turn continue its removal, leading to the propagation of the signaling gradient. Thus, it is the cells themselves that generate and propagate the signaling gradient, which constitutes in turn their navigation cues. On the scale of the experimental observation, SGG thus stand in contrast with preimposed gradients, via the emergence of a local dynamic gradient, rather than a global gradient. The model of navigation through SGG is in particular interesting, as it frees collective migration from the condition of an externally pre-imposed gradients [59].

We stress that in the case of SGG, there exists hence a feedback loop between the environment and the collective cell movement. This feedback loop plays a crucial role from a theoretical, experimental and modeling point of view as it drastically differs from the case of an imposed external gradient. Questions concerning for instance the navigation strategy and its effectiveness thus depend not only on the cellular mechanisms by which cells undergo taxis, but also on the way cells impact their environment. Hence, for example the investigation of how cells degrade the chemoattractant [135] plays an important role to understand their collective motion.

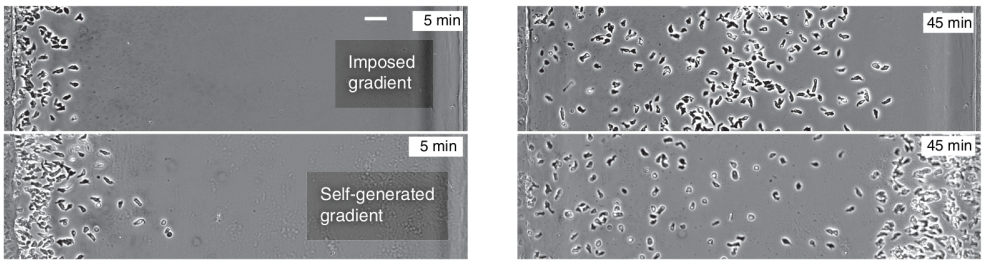

Figure 5: *Dd* cells exposed to imposed gradients (upper frames) and SGG (lower frames) in [182]. *Dd* cells perform better in SGG than in imposed gradients. The scale bar represents 50µm.

SGG: Advantages in Navigation Strategy

The model of SGG has attracted in the last decade much interest as it constitues an effective navigation strategy for cells in environments that may be very complex. First, SGG enable cells to navigate over long ranges. Contrary to externally imposed gradients, where a trade-off between the steepness of the gradient and the range of the gradient exists, in theory there exists no limit on the range of navigation through SGG [179, 180]. As a corollary, SGG also leads to a good exploration of space by enhancing range expansion, meaning that cells tend to displace faster and over longer distances (see Figure 5), as has been pointed out in [49, 179, 181]. The works of [139, 181, 182] have also pointed out that navigation through SGG constitutes an extremely robust navigation strategy, which may lead to important biological advantages in certain systems. Finally, SGG may serve as directional cues in complex environments. To illustrate this point, the authors of [182] have designed complex mazes and shown that a population of *Dd* cells is capable of navigating with a remarkable effectiveness through different mazes (see Figure 6 as an example of such a maze).

Examples of SGG

The first quantitative experimental evidence for SGG known to us is the already mentioned experiment of chemotactic traveling bands of *E. coli* in [5], although the author does not explicitly mention the concept of SGG, which seems to have become prevalent only in the past decade. However of note, as has shown the study [160], it seems that the contribution of the second chemoattractant secreted by the cells plays an important role in order for the cells to remain aggregated. Whereas the nutrient (*i.e.* galactose or oxygen) suits the framework of SGG, this second chemoattractant does not enter the framework of SGG, since rather than inducing a collective displacement, it leads to cell aggregation.

Furthermore, the features of SGG, such as robust navigation cues over long distances and not being constrained to an imposed signaling gradient, seem to be of particular interest in developmental biology [179, 180]. The first occurence *in vivo* has been evidenced in the embryogenesis of the zebrafish, where SGG play a key role during the initiation of the posterior lateral line in zebrafish [59, 185]. There, a population of approximately one hundred cells generate local signaling gradients through consumption over the whole posterior lateral line. Recently, a study [73] has evidenced that SGG cAMP gradients in *Dd* cells during the slug stage in combination with a spiral tip motion can explain surprising spiral waves of *Dd* cells inside the slug.

In parallel, SGG may also be involved in cancer invasion and metastasis. In the study

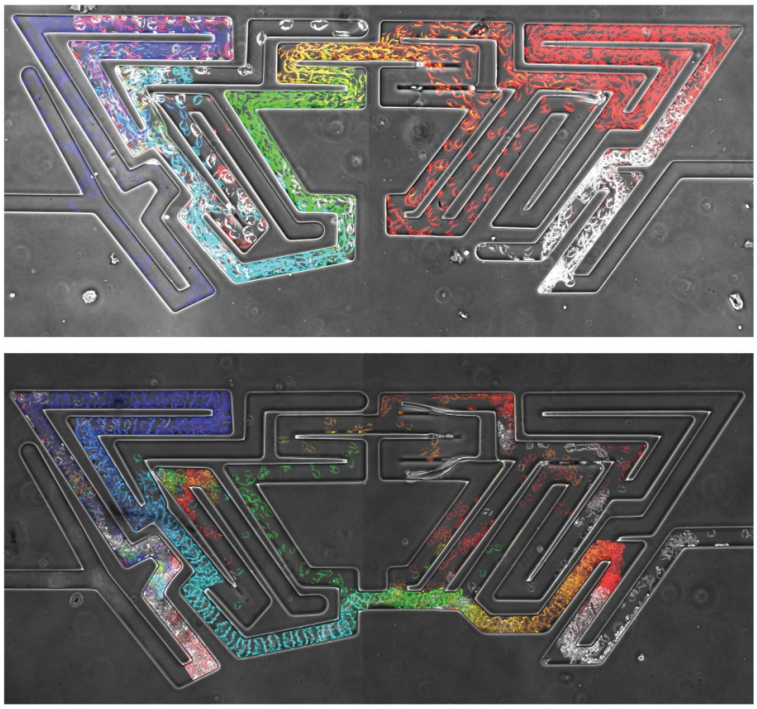

Figure 6: *Dd* cells solve a maze. Cells enter from the left and exit to the right. Time is represented by cell color, where blue shows earlier times and red later times. In the bottom figure, cells successfully senses a shortcut and chose the minimal route.

[162], authors have shown that cancer epithelial cells have the ability through self-generated epidermal growth factors (EGF) gradients to navigate in a microfluidic maze. These findings stand in stark contrast with the original belief that epithelial cells could not navigate without a preexisting chemical gradient. Later on, the study [56] has shown that cancer epithelial cells can also undergo migration through self-generated oxygen gradients, which has triggered the interest for the main experimental study, which we will consider in this thesis.

Many of the aforementioned studies postulate the ubiquity of SGG in cell systems. However, much investigation still needs to be undertaken to understand the biology in real life systems. In particular, the experimental study of SGG especially *in vivo* is complicated by the difficulty to prove through an experimental setup the existence of such dynamic SGG and the resulting navigation strategies [59].

0.2 On the Mathematical Modeling of Propagation Phenomena in Biology

0.2.1 The Modeling of Chemotaxis: three different Scales of Modeling

Many of the experiments, whose modeling we consider in this Subsection, take place on a short-time scale, where cell division plays a negligible role. For now, we leave the question of cell division and its induced propagation phenomena to the next Subsection, where we survey reaction-diffusion models.

Parabolic Models and the Macroscopic scale

One of the groundworks in the mathematical modeling of chemotaxis has been the celebrated Patlak-Keller-Segel (PKS) model, proposed independently in [145] and in [112, 114]. Although many variations on the model exists, in its essential form it is constituted of a system of parabolic equations describing the evolution of possibly several cell populations and chemotatic signals. For the sake of concision, we restrict ourselves here to a single cell population and a single chemoattractant. The cell population is modeled through a density in space and time $\rho(t,x)$, constituting what we call here the macroscopic scale, and so is the chemoattractant $c(t,x)$. The cells ρ undergo diffusion and are transported according to an advection field $\boldsymbol{\chi}[c]$, which can be seen as a chemotactic response function to the chemoattractant c. In parallel, the chemoattractant c is subject to a reaction-diffusion equation, where, depending on the specific modeling needs, the chemoattractant can for instance degrade over time, or be secreted or consumed by the cells:

$$\begin{cases} \partial_t \rho = \underbrace{D_\rho \Delta \rho}_{\text{diffusion}} \quad \underbrace{-\operatorname{div}(\rho \boldsymbol{\chi}[c])}_{\text{chemotactic transport}} & \text{(0.2.1a)} \\ \alpha \partial_t c = \underbrace{D_c \Delta c}_{\text{diffusion}} \quad \underbrace{-\beta c}_{\text{degradation}} \quad \underbrace{+\gamma \rho}_{\text{secretion by cells}} \quad \underbrace{-\delta \rho c}_{\text{consumption by cells}} . & \text{(0.2.1b)} \end{cases}$$

The chemotactic response function $\boldsymbol{\chi}[c]$ may take different shapes: common choices are a linear gradient sensing mechanism with $\boldsymbol{\chi}[c] = \chi \nabla c$, as well as a logarithmic gradient sensing mechanism with $\boldsymbol{\chi}[c] = \chi \frac{\nabla c}{c}$. The latter seems to be of great interest as it offers a scale-free response ability, which has been observed in different organisms, for instance [110]. Moreover, let us mention that when the time-dynamics of the chemoattractant is much faster than the time-dynamics of the cells, one can consider System (0.2.1) with $\alpha = 0$, leading to the so-called parabolic-elliptic PKS model.

System (0.2.1) has attracted much attention as it may lead to a critical mass phenomenon. Consider System (0.2.1) in $\mathbb{R}^2$, with $\alpha, \beta, \delta = 0$ and $\chi(c, \nabla c) = \chi \nabla c$ and suppose that the initial datum ρ^0 satisfies $\rho^0 \left(|\log(\rho^0)| + 1 + |x|^2 \right) \in L^1(\mathbb{R}^2)$. Let $M := \int_{\mathbb{R}^2} \rho^0$ the total mass of cells (which is conserved over time). Then if $M < \frac{8\pi}{\chi}$, the solution is global in time, whereas if $M > \frac{8\pi}{\chi}$, the solution blows-up in finite time [25, 58]. From a modeling perspective this can be interpretated as a condition under which a cell population forms a dense chemotactic aggregate.

Kinetic Transport Models and the Mesoscopic Scale

The discovery of the Run and Tumble movement in the seminal paper [22] (see the discussion in Section 0.1.1) gave rise to an approach that consists in describing the evolution of the cell density on a mesoscopic scale, *i.e.* the cell density is considered in time, space and the velocity, at which cells move [6, 7, 141]: the Othmer-Dunbar-Alt model consists then in the following kinetic evolution equation:

$$\partial_t f(t,x,v) + v \cdot \nabla_x f(t,x,v) = \int_V T[c](v',v) f(t,x,v') dv' - \int_V T[c](v,v') f(t,x,v) dv', \tag{0.2.2}$$

with $(t,x,v) \in \mathbb{R}_+ \times \mathbb{R}^d \times V$, where $V \subset \mathbb{R}^d$, that we suppose to be compact and isotropic, *i.e.* invariant under the action of the special orthonormal group $SO(d)$. Furthermore, we suppose without loss of generality that $|V| = 1$. Equation (0.2.2) expresses the fact that

cells move with velocity v (which corresponds to the aforementioned runs) and cells reorient themselves according to a law that is encoded through the tumbling kernel $T[c](v', v)$: at (t, x), $T[c](v', v)f(t, x, v')$ cells switch from velocity v' to velocity v. In fact Equation (0.2.2) can be seen as a mass-balance equation, where the left hand-side describes the movement according to the free-transport operator and the right hand-side keeps track of how many cells change velocity. Moreover, Equation (0.2.2) can be supplemented by the description of the evolution of the chemotactic field c such as in Equation (0.2.1b), with $\rho(t, x) := \int_V f(t, x, v)dv$.

Of note, although the Othmer-Dunbar-Alt model has been introduced with an explicit reference to the Run and Tumble motion in *E. coli*, the model is suited as well to describe other types of persistent cell motion, *i.e.* when locally in time a direction of movement in individual cells can be determined.

The kinetic model and the parabolic PKS are connected through the diffusive (or parabolic) scaling limit [46, 142, 143]. Suppose there exists a small parameter $\varepsilon > 0$, that corresponds to the ratio of the length of a run and its duration. Suppose that after the scaling $(\tilde{t}, \tilde{x}, v) = (\varepsilon^2 t, \varepsilon x, v)$, the tumbling kernel is under the shape $T_\varepsilon[c](v, v') = T_0[c] + \varepsilon T_1[c](v, v') + \mathcal{O}(\varepsilon^2)$, which encapsulates the fact that the modulation of the tumbling rate is of order ε. Then, one obtains:

$$\varepsilon^2 \partial_t f(t, x, v) + \varepsilon v \cdot \nabla_x f(t, x, v) = \int_V T_\varepsilon[c](v', v) f(t, x, v')dv' - \int_V T_\varepsilon[c](v, v') f(t, x, v)dv', \tag{0.2.3}$$

Set $j_\varepsilon(t, x) := \frac{1}{\varepsilon} \int_V v f(t, x, v)dv$ and integrating over V, we obtain the following mass conservation law:

$$\partial_t \rho_\varepsilon + \nabla \cdot j_\varepsilon = 0. \tag{0.2.4}$$

Now, suppose that in the limit $\varepsilon \to 0$, we have $f_\varepsilon = \rho_0 + \mathcal{O}(\varepsilon)$ and $\varepsilon^2 \partial_t j_\varepsilon = \mathcal{O}(\varepsilon)$. Multiplying Equation (0.2.3) with v and integrating over V yields:

$$\int_V v \otimes v dv \nabla \rho_0 = \int_V v T_1[c](v', v)dv \rho_0 - T_0[c] j_\varepsilon + \mathcal{O}(\varepsilon). \tag{0.2.5}$$

Hence combining Equations (0.2.4) and (0.2.5) and taking the limit leads to:

$$\partial_t \rho_0 + \nabla \cdot \left(D[c] \nabla \rho_0 - \boldsymbol{\chi}[c] \rho_0 \right) = 0, \tag{0.2.6}$$

with $D[c] = \frac{1}{T_0[c]} \int_V v \otimes v dv$ and $\boldsymbol{\chi}[c] = \frac{1}{T_0[c]} \int_V v T_1[c](v', v)dvdv'$. Thus the diffusive limit consists (formally) in Equation (0.2.6), which is of a slightly more general type than Equation (0.2.1a). We refer to [46] for a rigorous derivation of this limit.

The diffusive scaling limit naturally raises the question whether the obtained limit equation may accurately describe the evolution of the cell population. In the study [160], the authors have shown that depending on the cell population, the limit may be relevant, just as it may not be as well. An important criterion is the bias of the mean value of the velocity distribution. In fact, since the diffusive scaling limit averages the distribution of velocities, it assumes that $f(t, x, v) \approx \rho(t, x)$. Nevertheless as the authors [160] have pointed out, this approximation may not be valid: in that case, there is *a priori* no reason that the diffusive limit should be insightful. Hence, although the reduction to a parabolic model seems tempting, we should be invited to verify the validity of the underlying assumptions.

Finally, we briefly mention that there exist other scaling limits for Equation (0.2.2): in the studies [57, 71] a so-called hydrodynamic scaling limit has been considered, *i.e.* when

space scales as time. These other scaling limits clearly lead to other limit equations. Here again, the question to the modeler is whether these scaling limits are then insightful. In this thesis, we have not investigated such a hydrodynamic scaling limit.

Stochastic Individual-based Models and the Microscopic Scale

Both the macroscopic and the microscopic scale describe the evolution of the system as a density of cells. The underlying assumption is that there is a large number of cells and that the random fluctuations for instance in cell positions can be averaged and described through the cell density. However, one can also zoom in to the scale of an individual cell and describe their law of motion, which involves stochasticity. We discuss here very briefly these stochastic individual-based models.

First, one can describe the law of motion of each single cell of the population via its position $(\boldsymbol{X}_t)$. Given a static chemotactic field c, the position of the i-th cell evolves according to the following stochastic differential equation (in Itô's sense):

$$d\boldsymbol{X}_t^i = \boldsymbol{\chi}[c]\left(\boldsymbol{X}_t^i\right) dt + \sqrt{2D_\rho} d\boldsymbol{W}_t^i, \tag{0.2.7}$$

with $\boldsymbol{W}_t^i$ a d-dimensional Brownian movement. Via Itô's Lemma, one shows then that the cell distribution ρ, *i.e.* the probability distribution up to normalization of the stochastic process, satisfies Equation (0.2.1a).

In a second step, the System of SDEs (0.2.7) can be complemented with an evolution equation on the chemotactic concentration, such as Equation (0.2.1b). However, this makes the analysis considerably more complex. In the case of the parabolic-elliptic PKS case, *i.e.* when $\alpha = \beta = \delta = 0$ in Equation (0.2.1b), the chemical concentration becomes a convolution with the cell distribution (see [43, 75, 97]). We also refer to the parabolic-parabolic case, *i.e.* when $\beta = \delta = 0$ in Equation (0.2.1b), which has been considered in [105, 176].

Finally, other approaches for stochastic individual-based models exist. We briefly mention the work presented in [171], where the author proposes a stochastic process on the position and the velocity of the individual cell, mimicking the Run and Tumble movement and called velocity-jump process. Interestingly in that case, for a fixed concentration field, the probability distribution satisfies Equation (0.2.1a).

0.2.2 Reaction-Diffusion Equations and Spreading Phenomena in Biology

Reaction-diffusion equations have been a cornerstone in mathematical biology for the modeling of spatial spreading in populations. It is used to describe a wide variety of biological problems, such as for instance the introduction of rodents in a new geographic area [167] or a colony of bacteria expanding on a Petri dish. Although reaction-diffusion equations constitute a larger class of mathematical problems than what we describe in the following lines, in its essence they combine two ingredients to describe the evolution of a homogeneous population $\rho(t,x)$: (i) unbiased motion, modeled through a diffusion operator; (ii) a reaction term $f(\rho)$ depending (here exclusively) on the local population density, which can represent either growth of the population, when $f(\rho) > 0$, or decay of the population, when $f(\rho) < 0$:

$$\partial_t \rho - \Delta \rho = f(\rho), \tag{0.2.8}$$

where we have rescaled the Equation to obtain a diffusion constant equal to 1 and $f(1) = 0$. A prototype is the celebrated Fisher/Kolmogorov-Petrovsky-Piskunov (F/KPP) Equation

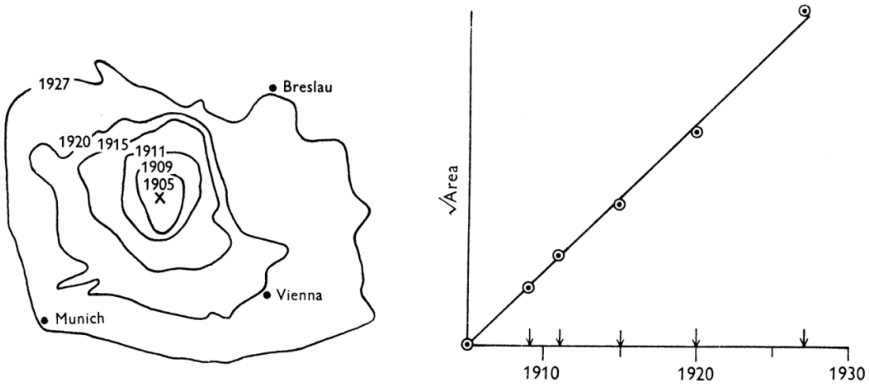

Figure 7: Representation, taken from [167], of the spread of muskrat in central Europe. It illustrates the linear spreading, *i.e.* at constant speed, and motivates the use of the F/KPP Equation as a model.

[72, 115], where $f(\rho) = \rho(1-\rho)$. It describes a competition among the individuals (*e.g.* for ressources): the higher the density ρ is, the lower is the per capita growth rate $\frac{f(\rho)}{\rho}$, with a saturation when the population reaches the maximal density $\rho = 1$. Many other shapes for f have been investigated according to the modeling needs for each precise problem. Noticeably, different shapes of f may lead to very different behaviors. The following (non-exhaustive) categorization for the shapes of f is very common:

- When f is non-negative and admits exactly 0 and 1 as zeros, then f is referred to as *monostable*. Example: $f(\rho) = \rho(1-\rho)(1+a\rho)$ with $a \geq 0$.
- When in addition, f satisfies the following inequality $f'(0)\rho \geq f(\rho)$ for $\rho \in [0,1]$, then f is referred to as of the *F/KPP type*. Example: $f(\rho) = \rho(1-\rho)(1+a\rho)$ with $a \in [0,2]$. Note that $a = 0$ yields exactly the F/KPP reaction term.
- When f admits exactly three zeros, that are $0, \theta, 1$ with $\theta \in (0,1)$ and $f'(0) < 0, f'(\theta) > 0, f'(1) < 0$. Then f is referred to as *bistable*. Example: $f(\rho) = \rho(\rho - \theta)(1-\rho)$.
- When $f \equiv 0$ on the interval $[0,\theta]$ with $\theta \in (0,1)$, $f > 0$ on the interval $(\theta,1)$ and $f(1) = 0$, then f is referred to as of the *ignition type*. Example $f(\rho) = \begin{cases} 0 & \text{if } \rho \leq \theta \\ (\rho-\theta)(1-\rho) & \text{else} \end{cases}$

For the rest of the manuscript, we will exclusively be interested by the monostable case.

Traveling Wave Solutions

Reaction-diffusion equations can give rise to a (linear) spreading phenomenon. Mathematically, this is reflectd by the existence of traveling wave solutions to Equation (0.2.8). Here, we treat exclusively the one-dimensional case (*i.e.* $x \in \mathbb{R}$). A traveling wave solution $(\tilde{\rho}, \sigma)$ is then constitued of a profile $\tilde{\rho} : \mathbb{R} \to [0,1]$ and a corresponding wave speed σ, such that $\rho(t,x) = \tilde{\rho}(x - \sigma t)$ is a solution of Equation (0.2.8). Plugging $\rho(t,x) = \tilde{\rho}(x-\sigma t)$ into Equation (0.2.8) leads to the following ODE for $\zeta \in \mathbb{R}$:

$$-\sigma\tilde{\rho}'(\zeta) - \tilde{\rho}''(\zeta) = f(\tilde{\rho}(\zeta)) \tag{0.2.9}$$

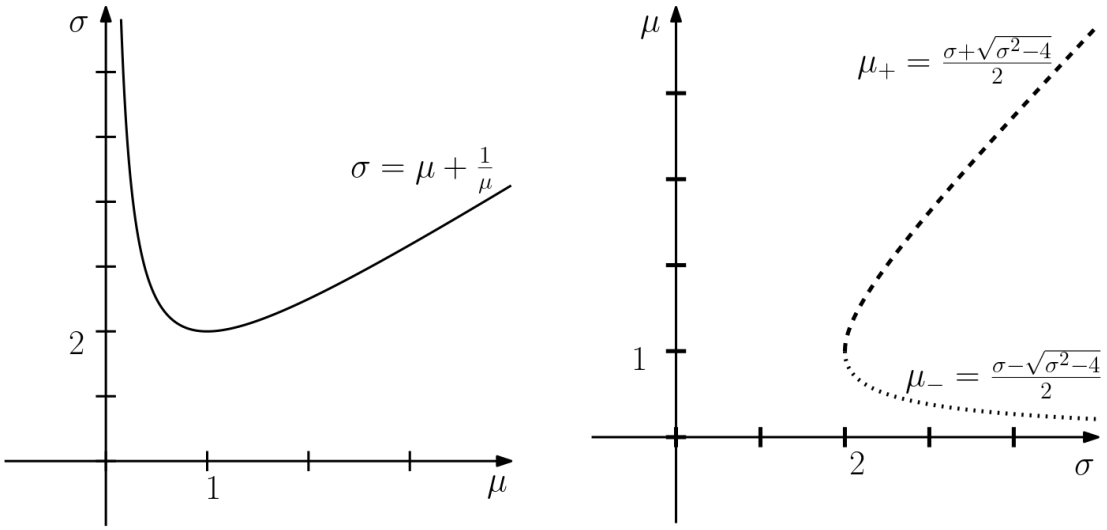

Figure 8: Graphic representations of the dispersion relation (0.2.11): $\mu^2 - \sigma\mu + 1 = 0$. The graphic on the left represents σ as a function of μ, with a minimum at $(\mu, \sigma) = (1, 2)$. The graphic on the right represents μ as a function of σ. Two branches $\mu_\pm$ exist in that case, which satisfy $\mu_- \leq 1 \leq \mu_+$ and start from the common point $(\sigma, \mu) = (2, 1)$.

Here we will consider solutions, such that $\sigma > 0$, *i.e.* the wave travels from the left side to the right side. Furthermore, we suppose that $\tilde{\rho}(-\infty) = 1$ and $\tilde{\rho}(+\infty) = 0$: one says that the (stable) state $\rho = 1$ invades the (unstable) state $\rho = 0$.

The works [11, 70, 72, 94, 115] have shown that in particular in the monostable case nonnegative traveling wave solutions exist. A way of proving their existence is by considering the phase portrait of ODE (0.2.9). Furthermore, it is important to keep in mind that the behavior around the state $\rho = 0$ is very instructive. Indeed, let us linearize the ODE (0.2.9) around the state $\rho = 0$. By a rescaling we can suppose that $f'(0) = 1$ and obtain:

$$-\sigma\tilde{\rho}' - \tilde{\rho}'' = \tilde{\rho} \tag{0.2.10}$$

Notice that the F/KPP condition $f(\rho) \leq \rho$ (as we assume that $f'(0) = 1$) implies that the solution of Equation (0.2.10) is in fact a supersolution of Equation (0.2.9). Furthermore, the characteristic polynomial of the ODE (0.2.10) is $X^2 + \sigma X + 1$ with discriminant $\sigma^2 - 4$. However, since we are looking for a nonnegative solution, any oscillating behavior that would arise from a complex root is prohibited. Hence $\sigma \geq 2$. Therefore we expect the behavior at $\zeta = +\infty$ of $\tilde{\rho}$ to be close to a decaying exponential $e^{-\mu\zeta}$, where:

$$\mu^2 - \sigma\mu + 1 = 0 \tag{0.2.11}$$

We refer to Equation (0.2.11) as the *dispersion relation*: it binds the wave speed σ with the exponential decay rate μ in $\zeta = +\infty$. Given σ, we have that $\mu_\pm = \frac{\sigma \pm \sqrt{\sigma^2-4}}{2} > 0$; and given μ, we have that $\sigma = \mu + \frac{1}{\mu} \geq 2$ (see Figure 8 for a graphic illustration). Hence, we wish to stress that the exact shape of the traveling wave is very instructive.

The works [11, 72, 94, 115] have also shown that in the monostable case the traveling wave solutions have the following structure: there exists a minimal wave speed $\sigma^* \geq 2$, such that for every wave speed $\sigma \geq \sigma^*$, there exists a corresponding traveling wave profile. Moreover, for f of the F/KPP type, we have in fact $\sigma^* = 2$. However, for instance when

$f(\rho) = \rho(1-\rho)(1+a\rho)$, with $a > 2$ [94], we have $\sigma^* > 2$. In addition, the traveling wave corresponding to the minimal wave speed does not decay in the F/KPP type slower than $\zeta e^{-\zeta}$, whereas every wave for $\sigma > \sigma^* = 2$ decays like $e^{-\mu_- \zeta}$, with $\mu_-(\sigma) = \frac{\sigma - \sqrt{\sigma^2-4}}{2} < 1$. In the case, where $\sigma^* > 2$, the minimal wave speed profile decays like $e^{-\mu_+ \zeta}$, with $\mu_+(\sigma^*) = \frac{\sigma^* + \sqrt{\sigma^{*2}-4}}{2} > 1$, and every profile for $\sigma > \sigma^*$ decays like $e^{-\mu_+(\sigma)\zeta}$. In other words, the wave corresponding to the minimal wave speed is also the wave that has the fastest exponential decay.

Interestingly, the minimal wave speed is also the wave speed, which is biologically relevant: given an inital datum ρ^0, which decreases fast enough, *i.e.* faster than the corresponding wave profile, ρ will converge to a traveling wave in a certain sense. The first such result dates back to [115], and we mention the result in [11]: for ρ^0 with support bounded above and for f of monostable or bistable type (when it admits a positive minimal velocity $\sigma^* > 0$), one has:

$$\lim_{t\to+\infty} \inf_{x\in[0,\sigma t]} \rho(t,x) = 1, \text{ for } \sigma < \sigma^* \text{ and } \lim_{t\to+\infty} \inf_{x\geq\sigma t} \rho(t,x) = 0, \text{ for } \sigma > \sigma^* \qquad (0.2.12)$$

Later on, more precise results have been obtained (see [154, 169] for the monostable non-F/KPP type and [29, 96] for the F/KPP type, as well as [184] for a general discussion on these results). Another way of framing it by the preceding observation, is to say that ρ converges to the wave profile with fastest decay. Although, the aforementioned studies prove this result in the corresponding specific cases, we are not aware of a general mathematical argument, which proves such a result, but it will be helpful through this manuscript to keep this general principle in mind.

Pulled and *Pushed* Waves

In [169], the author observes a qualitative difference in traveling wave solutions of reaction-diffusion equations. When $\sigma^* = 2$, the wave is called *pulled*: qualitatively, a pulled wave is driven by growth and diffusion of the population at the edge of the front with negligible contribution from the overall population. In fact the dynamics is dictated by the linear dynamics around the state $\rho = 0$. However, when $\sigma^* > 2$, the wave is *pushed*: qualitatively, a pushed wave is subject to a significant contribution from the overall population to the net propagation. These concepts have attracted interest especially in the field of evolution, since as noted in [152], pushed waves promote genetic diversity inside the propagation population, whereas pulled waves tend to select only the phenotypes at the leading edge of the invasion.

The exact definitions of pulled and pushed waves can vary in the literature. The historical definition as proposed in [169] (see also [154, 184]) is based on the criterion whether the minimal speed σ^* is equal to the speed of the linearized front around the steady state 0 (pulled), or greater than this speed (pushed). An alternative way of defining *pulled* waves may be the existence of the so-called Bramson shift (see [28, 29, 96, 183] or recently in critical cases [9, 83]), *i.e.* a logarithmic correction term in the propagation of level sets: $\rho(t,x) \to \tilde{\rho}(x - \sigma t - r\ln(t) - c)$, with $r = \frac{3}{2}$, or in specific critical cases $r = \frac{1}{2}$ [83]. On the contrary *pushed* waves merely have a constant correction term in the convergence rate of level sets [9, 70, 154, 169]: $\rho(t,x) \to \tilde{\rho}(x - \sigma t - c)$.

In [82, 152], the authors have proposed a new definition that is based on the study of the inside dynamics of the traveling waves. To do so, the authors introduce the formalism of neutral fractions: the traveling wave is decomposed in subparts and each subpart is marked with a neutral label, *i.e.* which does not interfer with the overall dynamics of

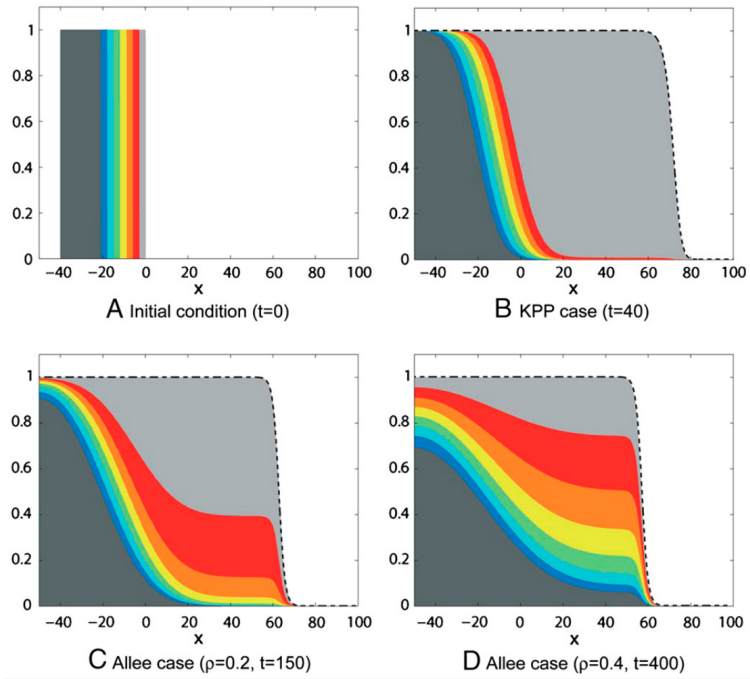

Figure 9: Figure taken from [152], which illustrates the evolution of neutral fractions in three cases. A: Depiction of the initial condition, which is the same for each case. B: Evolution of neutral fractions in a pulled case, with the F/KPP reaction term $f(\rho) = \rho(1-\rho)$. C& D: Evolution of neutral fractions in a pushed case, with a bistable reaction term $f(\rho) = \rho(1-\rho)(\rho-\theta)$ (with $\theta = 0.2$ for C and $\theta = 0.4$ for D). In each case, the dashed black curve corresponds to the traveling wave profile.

the traveling wave. The authors then move on to describe the evolution over time of the distribution of these labels. In the pushed case, after some time the traveling wave is composed of a perfect mixture homogeneous in space (at least on compact sets around the bulk of the wave) of each neutral fraction (see Figure 9 C and D): this shows that in fact every subpart of the wave contributes to the propagation of the wave. On the contrary, in the pulled case, after some time the traveling wave is almost exclusively composed of the neutral fraction, which constituted the leading edge, and all the other neutral fractions go extinct in the traveling wave (see Figure 9 B): hence in the pulled case, only the leading edge contributes to the propagation of the wave.

Finally, let us briefly mention a novel point of view on pushed waves, such as it has been point out in [74] (see also [38]). Instead of considering neutral fractions and their evolution (forward) in time, the authors of [74] consider the ancestral distribution of an individual particle inside the traveling wave: for each individual particle in the wave at time t, they study the backward in time stochastic process of the position of its ancestor $X_{s,t}$ at a time $t-s$ for $s \geq 0$. They show that this stochastic process has in the moving frame a stationary distribution when $s \to +\infty$, which is independent of the position X_t of the particle at time t. Hence, this backward stationary distribution can be interpretated as a quantification of how much each subpart of the wave contributes to the propagation.

0.2.3 The Interplay between Cell Division and Chemotaxis

As mentioned above, cell division and chemotaxis may take place on different time scales, which is why experimentally they have often been studied separately. Our presentation has until now followed the lines of this separation. However, cells that undergo chemotaxis may very well continue dividing, and by the preceding discussion on reaction-diffusion equations, we know that cell division combined with diffusion leads to an expansion phenomena, in parallel to chemotaxis. Hence, this raises naturally question how these two propagation phenomena combine. One of the main points of view of this manuscript is to shed light precisely on the intersection between chemotaxis and expansion by division-diffusion.

First, let us mention the studies [30, 33, 34], where the authors have inoculated a colony of *E. coli* on a Petri dish. They observe an expansion under the form of concentric rings followed by stationary symmetric patterns of spots or stripes (see Figure 10). The proposed explanation is that: (i) the colony expands first through division-diffusion, similarily to the dynamics described by the F/KPP equation. (ii) The cells trailing, *i.e.* the ones, which are not in the leading section of the expanding front, excrete a chemoattractant, which in turn leads to chemotactic aggregation, such as described by the PKS model: this chemotactic aggregation translates into the observed stationary patterns. Nevertheless in these studies, it is not entirely clear whether in the expanding front cell division really combines with chemotaxis, or whether the two phenomena merely happen to be simply juxtaposed, without a true interaction.

In parallel, many studies on SGG neglect cell division. However, in [172], the author emits the hypothesis that cell division is an important feature of SGG: in order to induce a sufficiently steep local gradient, the local cell population should reach a sufficient size, which is made possible through cell division. In turn, this will induce chemotaxis and the propagation through SGG. Nevertheless, here the hypothesis stipulates the necessity of cell division, but neglects the possible expansion induced by division-diffusion.

In contrast, the study [49] has investigated carefully the dynamics of a population of *E. coli*, whose propagation is induced through a SGG. By comparing *in vitro* and *in silico* experiments, the expansion to a mere division-diffusion driven expansion, such as the F/KPP dynamics, the authors show that chemotaxis enhances the range expansion and postulate that this feature may give a fitness advantage to the population. Nevertheless, the study does not compare the expansion to an expansion driven merely by chemotaxis without division.

Finally, on the mathematical side, the combination of division and chemotaxis has attracted in recent years much interest, especially since the introduction of the PKS system with Fisher growth term [137]. This Keller-Segel model with growth term has been the subject of numerous investigations in recent years, among which the works [27, 121, 137, 157, 158]. These types of models combine chemotaxis and cell division and exhibit traveling waves under some conditions on the parameters. Nevertheless, chemotactic self-aggregation (in the aformentioned studies) differs from the case of SGG, since both lead to chemotactic biases in opposite directions at the edge of expansion front. Recently, in the works [95, 99], the authors have investigated the case of *negative chemotaxis*, where the bias induced by chemotaxis is in the same direction than the propagation induced by division-diffusion and thus bears more similarity in spirit with the case of SGG.

0.2.4 Well-balanced Numerical Schemes

In Subsection 0.2.2 on reaction-diffusion equations, we have stressed the relevance of getting insight on the exact traveling wave profile. This was best illustrated through the dispersion

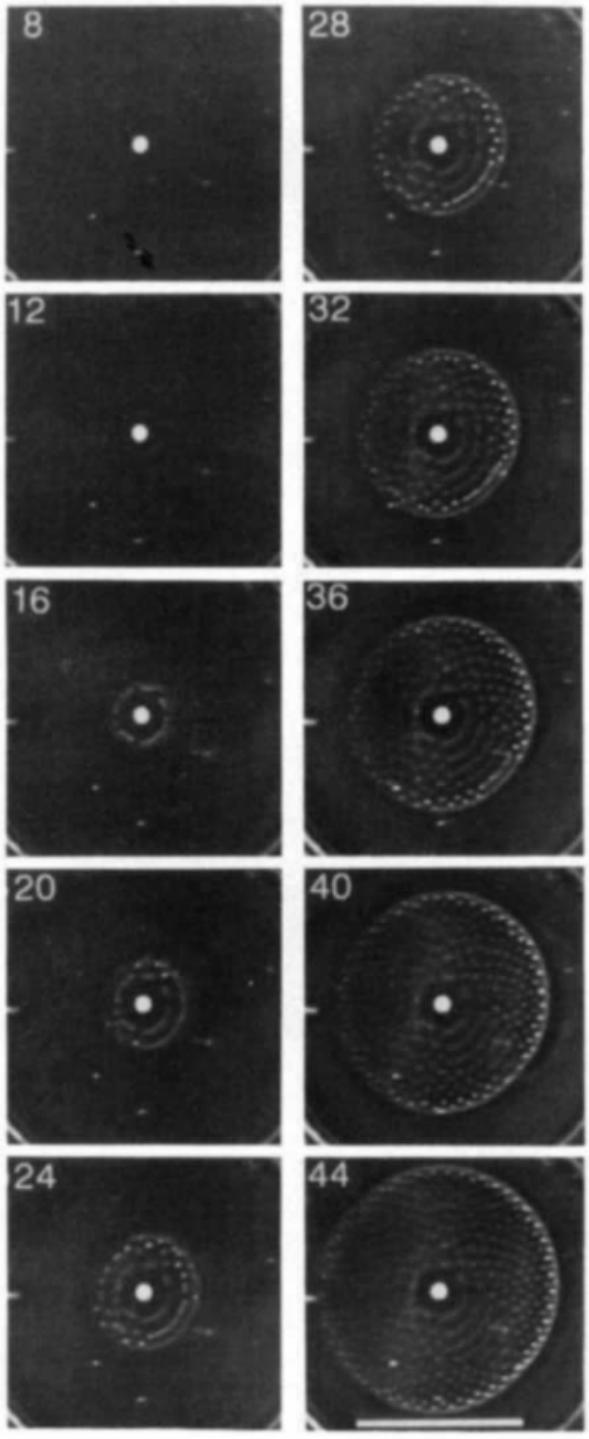

Figure 10: Figure, taken from [33], representing the expansion of an *E. coli* colony leading inside the ring to a stationary sunflower-like array. The images correspond to successive snapshots with interval 4h and the scale bar represents 4cm.

relation (0.2.11). Nevertheless, it may not always be possible to compute analytically the exact explicit wave profile. In that case, a natural alternative consists in investigating these questions numerically. In essence, a numerical scheme consists in the discretization of the problem on a finite mesh, which should lead to a fairly good approximation of the continuous problem. Thus, we may be interested in finding a suitable numerical scheme, in order to approximate well the traveling wave. Yet, it is a difficult problem to capture these traveling waves numerically, in particular since it asks for an accurate numerical computation over long times and large domains.

The philosophy of well-balanced (WB from here on) schemes consists in designing numerical schemes, which will be exact on the steady states (*e.g.* a stationary state or a traveling wave). More precisely, the discretization and the steady state commute: the (discretized) numerical scheme admits as steady state exactly the discretization of the steady state of the continuous problem. Hence, WB numerical schemes are especially well-suited for the numerical investigation of steady states. Furthermore as is shown in the monograph [8], WB schemes are efficient at reducing numerical errors and their growth over time, which is another of their advantages for traveling wave problems. In [87], the author shows also how WB numerical schemes may be adapted to parabolic problems. In [37], the authors have introduced a WB numerical scheme to compute traveling waves in kinetic models. Yet, this approach suffers from a drawback, as the numerical scheme is *stricto sensu* only WB in the case of a stationary wave and does not propose a scheme that is WB for waves with nonzero velocity.

0.3 Results obtained in this Thesis

We here give an overview of the results obtained in this thesis. The overview follows the order of the subsequent chapters. Of note in each Subsection, the notations may vary slightly in order to be consistent with the notations in the corresponding chapter: for instance σ or c for the wave speed, C, N or S for the chemoattractant and $\boldsymbol{\chi}$[1],$\boldsymbol{a}$ for the chemotactic advection field (we use the boldface print to indicate the vector field nature of the advection field, even in the one-dimensional case).

0.3.1 Hypoxia triggers Collective Migration in *Dictyostelium discoideum*

The starting point of this thesis has been the collaboration with a team from Institute for Light and Matter in Lyon, composed of Christophe Anjard, Olivier Cochet-Escartin and Jean-Paul Rieu. Through an experimental setup, they have investigated the collective behavior of *Dd* cells undergoing aerotaxis induced by self-generated oxygen gradients and cell division. We start by describing briefly the lines of the work published in the article [48], which we have reproduced in this manuscript in its integral form, before developping on our contribution with Vincent Calvez and the aforementioned team to this work.

Experimentally, the following emerging behavior of *Dd* cells in hypoxic conditions has been observed: when a colony of *Dd* cells is confined between two narrowly spaced plates, *Dd* cells form a dense ring moving outwards. After a brief transitory phase, the ring of cells moves at constant speed and constant density over the time course of the experiment (see Figure 11). It has been shown that the quick consumption of oxygen by *Dd* cells exposes them to hypoxia, *i.e.* a lack of oxygen, and in turn induces *aerotaxis* leading to a

[1]Here $\boldsymbol{\chi}$ denotes the chemotactic advection field, whereas later on χ denotes a constant chemotactic speed.

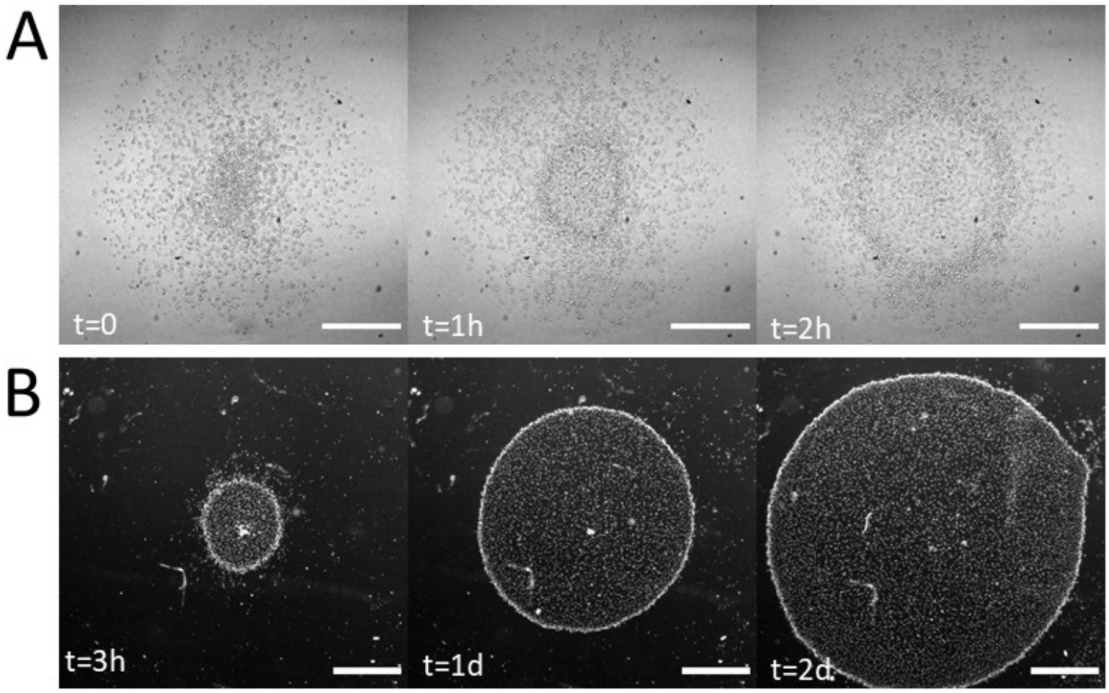

Figure 11: Formation and evolution of a dense ring of *Dd* cells after vertical confinement. A: Snapshots of early formation. The scale bar represents 500µm. B: Snapshots at longer times imaged under a binocular. The scale bar represents 1mm.

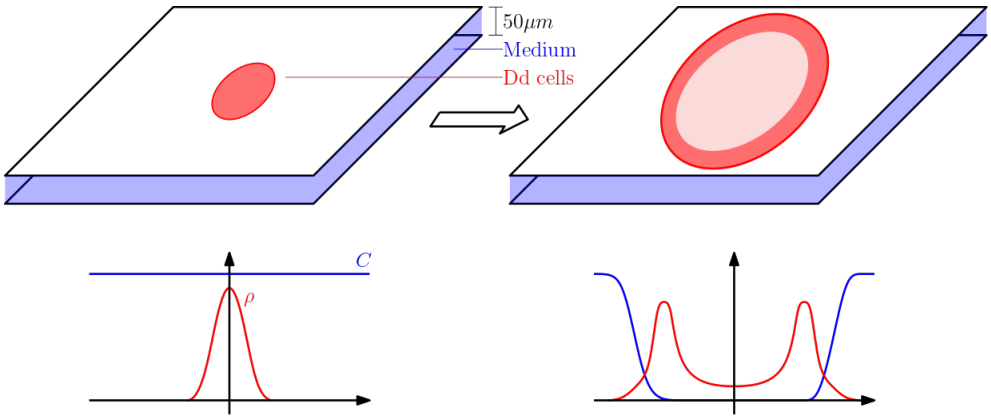

Figure 12: A schematic representation of the experiment presented in Figure 11. Cells are confined between two narrowly spaced plates and quickly consume available oxygen, so that the colony experiences self-induced hypoxic conditions. This, in turn, triggers outward migration of the colony under the form of a ring expanding at constant speed over long periods of time.

macroscopic outward motion (see Figure 12). Through cell tracking, it has been established that the cell behavior differs according to their position relative to the ring: (i) in the outer region of the ring, cells have a low persistent and unbiased motion; (ii) in the ring itself, cells have a persistent and biased motion towards higher oxygen regions; (iii) in the inner region of the ring, cells have a strongly persistent but unbiased motion. Of note, in the inner region, the cell population is less dense, but not negligible, meaning that a substantial part of the cells are left behind by the ring. In parallel, experiments in controlled oxygen gradients have led to a better characterization of the aerotactic response. Furthermore, it has been shown that the contribution of cell division is not negligible over the time-scale of the experiment, leading to an overall increase of the cell population, which is necessary to sustain the propagation to compensate for the cell leakage behind the ring.

Then, through a cellular Potts model, *i.e.* an individual-based cell algorithm, the collective behavior of the cell population was reproduced *in silico* by merely including a modulation of aerotaxis and cell divison depending on the level and the variations of oxygen. This shows that the combination of these two ingredients are sufficient to explain the emergence of a ring-shaped propagataion.

From there on, in collaboration with Vincent Calvez and the aforementioned team, we have first proposed a parabolic mean-field model mimicking the cellular Potts model, where ρ represents the cell density and C the oxygen concentration:

$$\begin{cases} \partial_t \rho = D\Delta\rho - \nabla \cdot (a(C, \nabla C)\rho) + r(C)\rho & \text{(0.3.1a)} \\ \partial_t C = D_{\text{oxy}}\Delta C - b(C)\rho, & \text{(0.3.1b)} \end{cases}$$

with $a(C, \nabla C) = a(C, \partial_r C) = \lambda_{\text{aero}}(C)\partial_r C$, assuming radial symmetry, λ_{aero} a decreasing function, which has been calibrated with the experimental data, $r(C) = r_0 \mathbb{1}_{C>C_0}$, C_0 a threshold value and $b(C)$ the oxygen consumption rate per cell. Numerical simulations of Equation (0.3.1) have shown similar results to the Potts model. Furthermore, assuming 1D planar system, neglecting curvature effects, we have shown that the wave profile with speed σ, $\rho(t, x) = \rho(x - \sigma t)$, satisfies the following simple relation:

$$\sigma\rho(-\infty) = \int_{\mathbb{R}} r(C(z))\rho(z)dz. \tag{0.3.2}$$

By roughly approximating the right hand-side with experimental data, we were able to obtain an estimate of the wave speed merely based on the shape of the cell density profile and the spatial cell division profile. However, a more thorough analysis of the mean-field model (0.3.1) seemed out of reach.

Hence, we have proposed as an alternative model the *Go or Grow* model. Cells have two disctinct behaviors: either, cells have a biased motion towards high oxygen regions, but do not divide (the *Go* behavior); or, cells have an unbiased motion, but do divide (the *Grow* behavior). The switch between both behaviors is induced when the ambient oxygen level crosses a threshold value C_0. Hence:

$$a(C, \partial_x C) = a_0 \mathbb{1}_{C<C_0} \text{sign}(\partial_x C) \text{ and } r(C) = r_0 \mathbb{1}_{C>C_0} \tag{0.3.3}$$

The aim of the Go or Grow model is to show that its ingredients are sufficient to trigger propagation via SGG and to determine the relative contribution of cell division and aerotaxis on the speed of the ring. Its relevance lies in the fact that through its simplicity, one can investigate analytically its traveling wave solutions. In particular, we stress that in that case Equation (0.3.1a) has piecewise constant coefficients, which is reminiscent

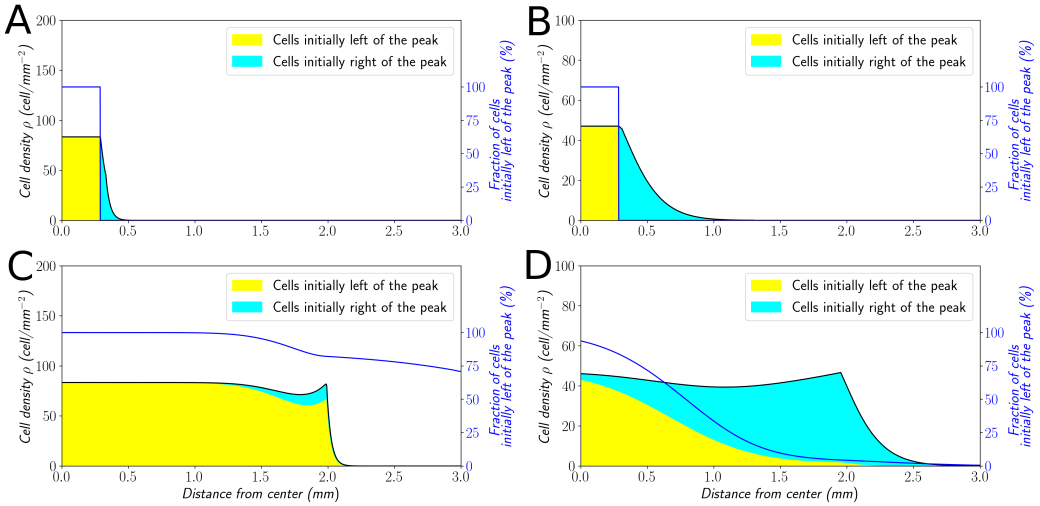

Figure 13: Classification of the inside dynamics in the Go or Grow model. Cells initially on the left-hand side or right-hand side of the peak get labeled differently (A and B). The labeling is neutral and does not change the dynamics of the cells. We let evolve the two colored population for some time and observe the mixing of the colors (C and D). In both cases $\sqrt{r_0 D} = 0.2\mu\text{m} \cdot \text{min}^{-1}$. (A and C) With $a_0 = 1\mu\text{m} \cdot \text{min}^{-1}$, the wave is pushed wave and after some time the front undergoes a spatially uniform mixing. (B and D) With $a_0 = 0.1\mu\text{m} \cdot \text{min}^{-1}$, the wave is pulled and only the fraction initially in the front is conserved in the front.

of a modeling hypothesis in [160]. In fact, we have shown numerically and in Chapter 2 mathematically that cells will propagate in a weak sense after a transient phase with speed:

$$\sigma^* = \begin{cases} a_0 + \dfrac{r_0 D}{a_0} & \text{if } a_0 > \sqrt{r_0 D} \\ 2\sqrt{r_0 D} & \text{if } a_0 \leq \sqrt{r_0 D} \end{cases} \tag{0.3.4}$$

Then, in order to quantify the relative contribution of cell division and diffusion to the overall wave speed, we introduce the fraction:

$$\varphi = \frac{\sigma_{\text{F/KPP}}}{\sigma^*} = \frac{2\sqrt{r_0 D}}{\sigma^*} \tag{0.3.5}$$

The relevance of quantity φ resides in its applicability to other experiments, which would involve SGG and division-diffusion. Here, we have that $\varphi = 40\%$, which shows that the dominant ingredient in setting the wave speed is aerotaxis.

Furthermore, we show that the dichotomy in Formula (0.3.4) translates into a dichotomy on the inside dynamics, by following the formalism of neutral fractions proposed in [152] (see Figure 13[2]). When aerotaxis is low, *i.e.* $a_0 \leq \sqrt{r_0 D}$, the wave is *pulled*, whereas when aerotaxis is high, *i.e.* $a_0 > \sqrt{r_0 D}$, the wave is *pushed*. This has been shown numerically and investigated mathematically in Chapter 2. Moreover, the same dynamics is observed in the Potts model.

Finally, through variations on the Go or Grow hypothesis, despite its simplicity, we show that the conclusions of the elementary Go or Grow model (0.3.3) seem to be valid for

[2]This Figure can be seen as an adaptation of Figure 9 to the present model.

more general models. We do so, first by introducting a second threshold C_0', below which aerotaxis stops:

$$a(C, \partial_x C) = a_0 \mathbb{1}_{C_0' < C < C_0} \mathrm{sign}(\partial_x C)$$

Numerically and to some extent analytically, we show that Formula (0.3.4) is a good approximation of the propagation speed (at most 15% relative error). In a second step, we consider more involved aerotactic responses and illustrate their qualitative influences via numerical simulations.

0.3.2 When SGG interact with Expansion by Cell Division and Diffusion. Analysis of a Minimal Model.

The work presented just above has shown the relevance of the Go or Grow model, as a minimal model to explain cell propagation induced by SGG and where cell division plays a role. In this Chapter, we carry out a thorough mathematical analysis of the Go or Grow model[3]:

$$\begin{cases} \partial_t \rho - \partial_{xx} \rho + \partial_x \left(\chi \mathbb{1}_{N < N_{\mathrm{th}}} \mathrm{sign}(\partial_x N) \rho \right) = \mathbb{1}_{N > N_{\mathrm{th}}} \rho & \text{(0.3.6a)} \\ \partial_t N - D \partial_{xx} N = -\rho N, & \text{(0.3.6b)} \end{cases}$$

where we have rescaled the Equation and swapped the label of the oxygen field for N (nutrient). This analysis consists (i) in a short-time analysis of the existence and uniqueness of the Cauchy problem; (ii) in the study of the long-time dynamics of System (0.3.6).

Because of the discontinous advection term $\partial_x(\chi \mathbb{1}_{N<N_{\mathrm{th}}} \mathrm{sign}(\partial_x N)\rho)$, the question of the well-posedness of System (0.3.6) turns out to be rather complicated. In order to circumvent this issue, we consider the problem in the framework, where N is increasing. Thus, there exist a unique position $\bar{x}(t)$ of the threshold (*i.e.* $N(t, \bar{x}(t)) = N_{\mathrm{th}}$). The strategy then consists in applying Banach's Fixed Point Theorem to the curve $\bar{x}(\,\cdot\,)$, which establishes existence and uniqueness locally in time of the solution. We here stress two subtleties of the strategy of proof. First, $\bar{x}(\,\cdot\,)$ is given by an ODE, but contrary to the standard ODE theory, the fixed point on $\bar{x}(\,\cdot\,)$ is applied in a $W^{1,p}$ space for $p \in (4, +\infty)$. Second, the strategy relies on a subtle endpoint parabolic regularity estimate on N. For the sake of concision and since the framework involves many notations, we do not state explicitly the obtained Theorem and refer to Chapter 2. The strategy of reducing the Cauchy problem for the PDE to the Cauchy problem of the scalar function in time $t \mapsto \bar{x}(t)$ (which implicitly depends on the PDE) is reminiscent of studies in one-dimensional free boundary problems (see, *e.g.* Chapter 3 in [67] on the Stefan problem, [117] in the context of front propagation, or [132] in the context of mutation-selection dynamics in evolutionary biology).

Then, we move on to describe all traveling waves (ρ^σ, N^σ) with speed $\sigma > 0$ and give a description of their exponential decay to the right side of the threshold:

Theorem 0.3.1. *There exists a minimal speed $\sigma^* > 0$, such that there exists a bounded and nonnegative traveling wave profile $(\rho^\sigma(z), N^\sigma(z))$ if and only if $\sigma \geq \sigma^*$. Given $\sigma \geq \sigma^*$, the traveling wave profile $(\rho^\sigma(z), N^\sigma(z))$ is unique. Moreover, the exact value of σ^* is given by*[4]*:*

$$\sigma^* = \begin{cases} \chi + \dfrac{1}{\chi} & \text{if } \chi > 1 \\ 2 & \text{if } \chi \leq 1 \end{cases} \tag{0.3.7}$$

[3] Here, we have changed the notations as well as normalized some constants. N represents the oxygen, $D = 1$, $r_0 = 1$, $a_0 = \chi$, $b(C) = -C$ and $D_{\mathrm{oxy}} = D$.

[4] This Formula is the same than Formula (0.3.4). We just have changed notations and normalized some constants.

Furthermore, the functions ρ^σ satisfy the following properties for $z \geq 0$ with $C^\sigma, D^\sigma > 0$:

- *for $\sigma > \sigma^*, \rho^\sigma(z) = A^\sigma e^{-\mu_-(\sigma)z} + B^\sigma e^{-\mu_+(\sigma)z}$, with $\mu_\pm(\sigma) = \frac{\sigma \pm \sqrt{\sigma^2-4}}{2}$*
- *for $\chi > 1$, $\sigma = \sigma^* = \chi + \frac{1}{\chi}, \rho^{\sigma^*}(z) = A^{\sigma^*} e^{-\mu_+(\sigma^*)z}$ and $\mu_+(\sigma^*) = \chi$*
- *for $\chi \leq 1, \sigma = \sigma_{F/KPP}, \rho^{\sigma_{F/KPP}}(z) = A^{\sigma_{F/KPP}}((1-\chi)z+1)e^{-z}$*

Next, we apply the methodology of neutral fractions introduced in [82, 152] to describe the inside dynamics of the waves, extending thereby their work to a reaction-diffusion-advection equation. We prove that:

- if $\chi > 1$ and $\sigma = \sigma^* = \chi + \frac{1}{\chi}$, then the wave is pushed.
- if $\sigma = 2$ or $\sigma > \sigma^*$, then the wave is pulled.

As we have mentioned before, we expect the biologically relevant spreading speed to be the minimal wave speed σ^*, or equivalently the wave speed, whose profile has the steepest decrease. To support this claim, we give a weak characterization of the asymptotic behavior of the instantaneous spreading speed $\dot{\tilde{x}}(t)$ under the restrictive (but rather reasonable) assumption that $\dot{\tilde{x}} \in L^\infty(\mathbb{R}_+)$.

Theorem 0.3.2. *Suppose that $\dot{\tilde{x}} \in L^\infty(\mathbb{R}_+)$ and that:*

$$\frac{\rho^0}{\rho^{\sigma^*}} \in L^\infty.$$

Then:

$$\liminf_{t \to +\infty} \dot{\tilde{x}}(t) \leq \sigma^*.$$

Theorem 0.3.3. *Suppose that $\dot{\tilde{x}} \in L^\infty(\mathbb{R}_+)$ and that $\rho^0 \in L^\infty$. Then, we have that:*

$$\limsup_{t \to +\infty} \dot{\tilde{x}}(t) \geq \sigma^*.$$

Notice in Theorem 0.3.2 that the initial datum ρ^0 cannot decrease slower than ρ^{σ^*}. These results show that for a biologically relevant initial datum ρ^0, which is expected to decay fast, the only reasonable candidate for convergence to a traveling wave profile is the one associated with the minimal wave speed. Nevertheless, convergence in a stronger sense is still an open question.

Finally, we propose a kinetic model as an alternative description on a mesoscopic scale. This model is still currently under investigation, but we briefly study the corresponding two-velocity model:

$$\begin{cases} \partial_t f^\pm \pm \varepsilon^{-1} \partial_x f^\pm = \varepsilon^{-2} \left(M(\pm\varepsilon^{-1}; N, \partial_x N)\rho - f^\pm \right) + \mathbb{1}_{N > N_{\text{th}}} \rho & \text{(0.3.8a)} \\ \partial_t N - D \partial_{xx} N = -\rho N, & \text{(0.3.8b)} \end{cases}$$

where $\rho := \frac{f^+ + f^-}{2}$ and,

$$M(\pm\varepsilon^{-1}; N, \partial_x N) = \begin{cases} 1 & \text{if } N > N_{\text{th}} \\ 1 \pm \varepsilon\chi & \text{if } N \leq N_{\text{th}} \text{ and } \partial_x N \geq 0 \\ 1 \mp \varepsilon\chi & \text{if } N \leq N_{\text{th}} \text{ and } \partial_x N < 0 \end{cases},$$

with $\chi < \varepsilon^{-1}$. We establish an equivalent to Theorem 0.3.1 for subsonic (*i.e.* $|\sigma| < \varepsilon^{-1}$) traveling wave solutions of System (0.3.8). For the sake of concision, we do not state the exponential decay properties here and refer to Chapter 2 Section 2.6.

Theorem 0.3.4. *In the parabolic regime $\varepsilon^{-2} > 1$ (see [26] for the terminology), there exists a minimal speed $\sigma^* \in (1, \varepsilon^{-1})$, such that for any $\sigma \in [\sigma^*, \varepsilon^{-1})$, there exists a corresponding bounded and nonnegative traveling wave profile $(f^{+,\sigma}, f^{-,\sigma}, N^\sigma)$. In addition, for $\sigma \in [\sigma^*, \varepsilon^{-1})$ fixed, the traveling wave profile $(f^{+,\sigma}(z), f^{-,\sigma}(z), N^\sigma(z))$ is unique. For $\sigma \in [0, \sigma^*)$, there does not exist a traveling wave profile. The expression of σ^* is given by:*

$$\sigma^* = \begin{cases} \dfrac{\chi + \frac{1}{\chi}}{1+\varepsilon^2} & \text{if } \chi > 1 \\ \dfrac{2}{1+\varepsilon^2} & \text{if } \chi \leq 1 \end{cases} \tag{0.3.9}$$

In the hyperbolic regime $\varepsilon^{-2} < 1$ (see [26]), there does not exist any subsonic traveling wave profile, i.e a wave traveling with speed $\sigma < \varepsilon^{-1}$.

In addition, the traveling wave solutions given by Theorem 0.3.4 correspond exactly to the traveling wave solutions given by Theorem 0.3.1 in the diffusive limit when $\varepsilon \to 0$.

0.3.3 Mathematical Modeling of Cell Collective Motion triggered by SGG

This Chapter has been written in collaboration with Vincent Calvez and Roxana Sublet, a graduate student, who did an internship supervized by Vincent Calvez and myself. The aim of the Chapter is to discuss broadly some of the mathematical questions that arise in models of SGG. Although most of the content discusses results from the literature, at the end we present a novel result.

We start by a discussion of the seminal paper [114], which proposes a model[5] for the movement of bacteria in a 1D capillary tube, such as in the experiment by Adler [5]:

$$\begin{cases} \partial_t \rho + \partial_x \left(-d \partial_x \rho + \chi \rho \partial_x \log(S) \right) = 0 & \text{(0.3.10a)} \\ \partial_t S = D \partial_{xx} S - k\rho, & \text{(0.3.10b)} \end{cases}$$

where ρ describes the cell density, χ a chemotactic strength[6] and S the signaling molecule, which satisfies $\lim_{x \to +\infty} S^0(x) = S_{\text{init}}$. Notice that Equation (0.3.10a) is under conservative form and hence mass is conserved $M := \int_{\mathbb{R}} \rho(t,x)dx$. The following result was established:

Theorem 0.3.5 (Keller and Segel [114])**.** *Assume $D = 0$ and $\chi > d$. Then, there exists a speed $c > 0$* [7] *(depending on M, k and S_{init}, but not on χ, nor d) and a stationary solution of System (0.3.10) in the moving frame $(\rho(x-ct), S(x-ct))$, such that ρ is positive and integrable, $\int_{\mathbb{R}} \rho(z)dz = M$, and S is increasing between the following limiting values*

$$\begin{cases} \lim_{z \to -\infty} S(z) = 0 \\ \lim_{z \to +\infty} S(z) = S_{init} \end{cases}$$

Strikingly the wave speed does not depend on χ and d, which stands in contrast with results that we will present below.

Nevertheless, System (0.3.10) suffers from two major drawbacks. First, via numerical simulation we show that the Cauchy problem does not guarantee positivity. Second, we

[5] This model has previously been discussed in Subsection 0.2.1.

[6] Note here that χ does not have the units of a speed, but that of a diffusion constant.

[7] In this Section, we denote the traveling wave speed by c, rather than σ, which has been the case until now.

do a brief survey of works indicating that the obtained wave in Theorem 0.3.5 is unstable. In order to remedy these two issues, we discuss two relevant extensions of the preceding model:

Scenario 1: Strongest advection at the back. We discuss the study of [160], where a second chemoattractant secreted by the bacteria is added:

$$\begin{cases} \partial_t \rho + \partial_x \left(-d\partial_x \rho + \rho \left(\chi_S \text{sign}(\partial_x S) + \chi_A \text{sign}(\partial_x A) \right) \right) = 0 & \text{(0.3.11a)} \\ \partial_t S = D_S \partial_{xx} S - k(S, \rho) & \text{(0.3.11b)} \\ \partial_t A = D_A \partial_{xx} A + \beta \rho - \alpha A, & \text{(0.3.11c)} \end{cases}$$

Note again that mass is conserved and bacteria are assumed to respond to the gradients in a binary way. In addition, the advection induced is merely the sum of the responses to each gradient. This leads to the following Theorem:

Theorem 0.3.6 (Saragosti *et al.* [160])**.** *There exists a speed $c > 0$, and a positive limit value $S_- < S_{init}$, such that System (0.3.11) admits a stationary solution in the moving frame $(\rho(x-ct), S(x-ct), A(x-ct))$, such that ρ is positive and integrable, $\int_{\mathbb{R}} \rho(z)dz = M$, A decays to zero on both sides, and S is increasing between the following limiting values*

$$\begin{cases} \lim_{z \to -\infty} S(z) = S_- \\ \lim_{z \to +\infty} S(z) = S_{init} \end{cases}$$

Moreover the speed $c > 0$ is determined by the following implicit relation,

$$\chi_S - c = \chi_A \frac{c}{\sqrt{c^2 + 4\alpha D_A}}$$

Since A is increasing, then decreasing, in the back of the wave there is a stronger advection than in the front of the wave. Interestingly, we note that here the signaling molecule is not entirely consumed, contrary to the case presented in Theorem 0.3.5.

Scenario 2: Cell compensated by growth. Then, we summarize the work on the Go or Grow model, presented in the first two Chapters. We argue that growth, *i.e.* cell division, can be an essential ingredient for propagation of cells under a single SGG.

Finally, we extend the Go or Grow hypothesis to include a logarithmic sensitivity to the gradient[8], such as was initially proposed by Keller and Segel [114]:

$$\begin{cases} \partial_t \rho + \partial_x \left(-d\partial_x \rho + \rho \chi \mathbb{1}_{S<S_0} \partial_x \log(S) \right) = r \mathbb{1}_{S>S_0} \rho & \text{(0.3.12a)} \\ \partial_t S = D\partial_{xx} S - k(S, \rho). & \text{(0.3.12b)} \end{cases}$$

This leads to the following new preliminary result:

Theorem 0.3.7. *Assume $D = 0$ and $k(S, \rho) = \kappa \rho S$ for some $\kappa > 0$. There exists a speed $c > 0$, and a positive limit value $\rho_- > 0$, such that System (0.3.12) admits a stationary solution in the moving frame $(\rho(x - ct), S(x - ct))$, such that ρ and S have the following limiting values*

$$\begin{cases} \lim_{z \to -\infty} \rho(z) = \rho_- \\ \lim_{z \to +\infty} \rho(z) = 0 \end{cases} \quad \textit{and} \quad \begin{cases} \lim_{z \to -\infty} S(z) = 0 \\ \lim_{z \to +\infty} S(z) = S_{init} \end{cases}$$

Moreover the speed $c > 0$ is given by the following dichotomy,

$$c = 2\sqrt{r \max\left\{ d, \chi \log\left(\frac{S_{init}}{S_0} \right) \right\}} \qquad \text{(0.3.13)}$$

[8]Here again, we stress that the parameter χ denotes a chemotactic strength as for System (0.3.10) and has the units of a diffusion constant.

Interestingly, the condition that $c \geq 2\sqrt{r\chi \log\left(\frac{S_{\text{init}}}{S_0}\right)}$ is imposed by the dynamics at the back of the wave, which stands in strong opposition to the more standard F/KPP case, where the wave speed selection is imposed by the dynamics at the very front of the wave. Finally, through numerical simulations, we give evidence that the Cauchy problem converges to the traveling wave propagating with speed c given by Formula (0.3.13). Of note, in the proof we show here again that c given by Formula (0.3.13) is in fact the minimal wave speed.

0.3.4 A Paradigm for Well-balanced Schemes for Traveling Waves emerging in Biological Models

In this Chapter, we expose a work in collaboration with Benoit Frabrèges. This Chapter is expected to be soon submitted as an article, but before we wish to improve some aspects of this work, such as possibly improving one of the schemes.

As we have already stressed, numerical investigation for models of SGG are extremely useful. Yet, this requires good numerical schemes, in order to capture for instance the correct exponential decay of the profiles. The works on WB schemes for kinetic models (see [37]) or parabolic models (see [87]) are in this respect very insightful. However, as we have pointed out, in order to design a WB scheme for traveling waves, one requires the knowledge of the spreading speed σ, which in many cases is not known *a priori*. In order to remedy here, we propose the use of LeVeque-Yee's formula [118, 131]: a traveling wave $\phi(x - \sigma t)$ satisfies the following advection equation:

$$\partial_t \phi + \sigma \partial_x \phi = 0$$

Integrating over $\mathbb{R}$, we find that:

$$\sigma = -\frac{\int_{\mathbb{R}} \partial_t \phi dx}{\phi(+\infty) - \phi(-\infty)} \tag{0.3.14}$$

The LeVeque-Yee speed estimator is then the discretized version of Formula (0.3.14) for a density, which may not necessarily be a traveling wave profile. Combining the LeVeque-Yee speed estimator with the methodology of WB schemes then leads to a seemingly new type of numerical schemes, which are particularly well suited for the numerical investigation of traveling wave phenomena. We illustrate this methodology on two models: the first is a kinetic Go or Grow model, which we have originally proposed in Chapter 2. This model has been the starting point of the present work. Then, in a second step, we illustrate the methodology on the F/KPP equation, which has been done in collaboration with Benoit Fabrèges.

A Well-balanced Numerical Scheme for a Kinetic Go or Grow Model

We consider the following system:

$$\begin{cases} \partial_t f + v\partial_x = \alpha^2 \left(M(v; N, \partial_x N)\rho - f\right) + \mathbb{1}_{N > N_{\text{th}}}\rho & \text{(0.3.15a)} \\ \partial_t N - D\partial_{xx} N = -\rho N, & \text{(0.3.15b)} \end{cases}$$

where $v \in V := \alpha V_0$, $\rho(t,x) := \frac{1}{|V|}\int_V f(t,x,v')dv'$, $\alpha > 1$ and M has as a zero first order moment when $N > N_{\text{th}}$, and $\text{sign}(\partial_x N)\chi$, when $N \leq N_{\text{th}}$. The dependency in α here as been chosen such that at least in a formal sense, when $\alpha \to +\infty$, System (0.3.15) converges

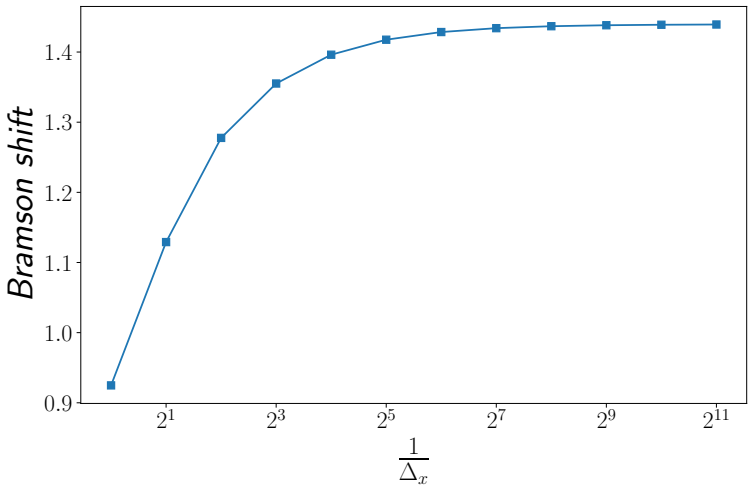

Figure 14: Fitting of the coefficient $r = 3/2$ of the Bramson shift (see Equation (0.3.19) with the WB scheme.

to the parabolic Go or Grow System (0.3.6) (see Chapter 2 or the discussion in Subsection 0.2.1). However, we will not investigate numerically this limit $\alpha \to +\infty$.

We discretize $f(t^n, x_i, v_j) = f^n_{i,j}$ on a grid and for notation purposes introduce a parallel grid with $z_i = x_i$. System (0.3.15) is then treated via the following time-splitting approach:

1. The Equation on N is treated via a standard Crank-Nicholson scheme.

2. a) We use the LeVeque-Yee speed estimator on N to obtain $\hat{\sigma}^n$.
   b) We compute a numerical approximation of $\tilde{f}(t, z, v) = f(t, x - \hat{\sigma}^n t, v)$ on the time interval (t^n, t^{n+1}) via a WB scheme, such as presented in [37].
   c) Then we transport the solution back to the stationary frame $f(t^{n+1}, x, v) = \tilde{f}(t^{n+1}, z + \hat{\sigma}^n \Delta t, v)$. To do so we compute the stationary solution of the following problem, for i, j and $z \in (z_i, z_{i+1})$:

$$\begin{cases} (v_j - \hat{\sigma}^n)\partial_z \hat{f} = \alpha^2 \left(M(v_j; N, \partial_z N)\hat{r} - \hat{f} \right) + \mathbb{1}_{N > N_{\text{th}}} \hat{\rho} \\ \hat{f}(z_i, v_j) = \tilde{f}(t^{n+1}, z_i, v_j), \text{ for } v_j > \hat{\sigma}^n \\ \hat{f}(z_{i+1}, v_j) = \tilde{f}(t^{n+1}, z_{i+1}, v_j), \text{ for } v_j < \hat{\sigma}^n \end{cases}$$

   Finally, we project on the given stationary solution $\hat{f}$, *i.e.* $f^{n+1}_{i,j} = \hat{f}(z_i + \hat{\sigma}^n \Delta t, v_j)$.

We compare the performance of the scheme with other numerical schemes. Although, numerically this WB scheme may perform poorer at capturing the speed wave compared to high-order schemes, such as a WENO scheme, it is the only scheme, which captures in a consistent way simultaneously the wave speed and the exponential decay rate at the leading edge of the profile: by this we mean that the numerical decay rate is extremely close to the theoretical decay rate associated with speed $\sigma = \sigma_{\text{num}}$, where σ_{num} is the numerical wave speed.

A Well-balanced Numerical Scheme for the F/KPP Equation

We consider the one-dimensional F/KPP Equation[9]:

$$\partial_t u - \partial_{xx} u = u(1-u) \tag{0.3.16}$$

In [87], the author has proposed a well-balanced approach for parabolic equations, which relies on an explicit Euler time integration. Here, we combine this methodology with the LeVeque-Yee speed estimator. Yet, numerically we observe that the explicit Euler time integration seems to only be stable under a parabolic CFL condition. Therefore, we propose as an alternative an implicit Euler time integration, which numerically appears to be stable under an hyperbolic CFL condition.

We discretize $u = (t^n, x_i) = u_i^n$ on a grid and for notation purposes introduce a parallel grid with $z_i = x_i$. The procedure of the numerical scheme can be summarized as follows:

1. We use LeVeque-Yee speed estimator on the profile u in order to obtain an estimate $\hat{\sigma}^n$ of the propagation speed.

2. Given $\hat{\sigma}^n$, on the time interval (t^n, t^{n+1}) we consider u in the moving frame $(t, z) = (t, x - \hat{\sigma}^n(t - t^n))$ and denote it by $\bar{u}$, which leads to Equation:

$$\partial_t \bar{u} - \hat{\sigma}^n \partial_z \bar{u} - \partial_{zz} \bar{u} = \bar{u}(1-\bar{u}) \tag{0.3.17}$$

   In order to deal with the nonlinear term in the right hand-side of Equation (0.3.17), we freeze the non-linear contribution to the term on each mesh $(t^n, t^{n+1}) \times (z_i, z_{i+1})$ by considering that $\bar{u}(1-\bar{u}) \approx \bar{u}\left(1 - \bar{u}^n_{i+\frac{1}{2}}\right)$, where $\bar{u}^n_{i+\frac{1}{2}} = \frac{\bar{u}^n_i + \bar{u}^n_{i+1}}{2}$. We then apply the methodology proposed in [87] to solve Equation (0.3.17), but we use an implicit Euler time integration, instead of the explicit Euler method.

3. It remains to shift back to the stationnary frame (t, x). Just as in the case of System (0.3.15), we use the values $\bar{u}_i^{n+1}$, which approximate $\bar{u}(t^{n+1}, z_i)$ in order to extrapolate a value for $u(t^{n+1}, x_i)$, *i.e.* $\bar{u}(t^{n+1}, z_i + \hat{\sigma}^n \Delta t^n)$. To do so we consider the stationnary solution $\hat{u}$ of Equation (0.3.17) in the cell (z_i, z_{i+1}):

$$\begin{cases} -\hat{\sigma}^n \partial_z \hat{u} - \partial_{zz} \hat{u} = \hat{u}(1 - \bar{u}^n_{i+\frac{1}{2}}), \text{ for } z \in \bar{C}_{i+\frac{1}{2}} \\ \hat{u}(z_i) = \bar{u}_i^{n+1} \text{ and } \hat{u}(z_{i+1}) = \bar{u}_{i+1}^{n+1}, \end{cases} \tag{0.3.18}$$

   with $\bar{u}^n_{i+\frac{1}{2}} = \frac{\bar{u}^n_i + \bar{u}^n_{i+1}}{2}$. Finally, we set $u_i^{n+1} := \hat{u}(z_i + \hat{\sigma}^n \Delta t^n)$.

The performances of the scheme are compared to other numerical schemes: a standard operator splitting approach, where the heat equation is treated with a Crank-Nicolson scheme, and the same approach as above, but where we set the fixed $\hat{\sigma}^n = 0$, which we refer to as the "0-wave" scheme. Interestingly, the WB scheme captures strikingly well the spreading speed, even for an extremely coarse mesh size. In particular the WB scheme performs here much better than the other schemes. Then, we investigate to which extend the scheme is able to capture the Bramson shift, which we briefly recall (see Subsection 0.2.2). We denote by $x_{\frac{1}{2}}(t)$, the level set $u\left(t, x_{\frac{1}{2}}(t)\right) = \frac{1}{2}$. Asymptotically:

$$x_{\frac{1}{2}}(t) = 2t - r\ln(t) + o(\ln(t)), \tag{0.3.19}$$

[9]This equation corresponds to Equation (0.2.8) with the reaction term $f(u) = u(1-u)$.

with $r = \frac{3}{2}$. Here we fit r for the numerical curve of $x_{\frac{1}{2}}(t)$ (see Figure 14) and find that, the finer mesh, the closer r gets to $\frac{3}{2}$. However, it seems that r converges to a value slightly lower than $\frac{3}{2}$.

0.3.5 A Stochastic Individual-based Go or Grow Model and its Preliminary Analysis

In this Chapter, we expose preliminary results of an ongoing collaboration with Vincent Calvez and Milica Tomašević.

The aim is to investigate a stochastic individual-based model of the Go or Grow System (0.3.6). Nevertheless, the rule determining the switch between the Go and the Grow behavior, that we have used until now ($N \leq N_{\text{th}}$: Go behavior, $N > N_{\text{th}}$ Grow behavior) leads to a stochastic model, which appears to be hardly tractable in a theoretical analysis. In fact following the work [105] on a parabolic-parabolic PKS model, we could replace ρ with a distribution of Dirac functions. But the non-linear term in Equation (0.3.6b) makes it analytically much less tractable, compared to the study in [105], where ρ merely intervenes as a source term. Furthermore, the well-posedness analysis of the Cauchy problem in Chapter 2 shows that it heavily relies on an endpoint regularity estimate of N. A distribution of Dirac functions being less regular, it points to the fact that in that case the well-posedness might not be guaranteed.

Hence, we define a new Go or Grow rule: the position of the threshold is set by the position of the K-th particle. In a sense, we consider that the first K particles consume enough oxygen for the oxygen concentration to drop below the threshold. This leads then to the following algorithmic construction of a stochastic process:

1. We consider a birth process through an exponential random variable with rate K. Once this clock rings, among the K first particles is chosen a particle uniformly at random, which will divide, *i.e.* be duplicated.

2. In between two birth times, the particles undergo the following SDE:

$$dX_t^i = \chi \mathbb{1}_{(\sum_j \mathcal{H}(X_t^j - X_t^i) > K)} dt + \sqrt{2} dW_t^i, \tag{0.3.20}$$

   with $\mathcal{H}$ the Heaviside function. $\sum_j \mathcal{H}(X_t^j - X_t^i)$ then denotes the rank of the particle. If this rank is above K, then the particles undergo an additional drift. Otherwise, they merely undergo Brownian motion.

Then, we give an SDE description of the point measure $Z_t = \sum_i \delta_{X_t^i}$. We start by introducing some notations: $H^i(Z_t)$ denotes the position of particle with rank i at time t, $\{W^i, i \in \mathbb{N}^*\}$ a family of independent standard one-dimensional Brownian motions and $\mathcal{N}(ds, di, d\theta)$ a Poisson point measure on $\mathbb{R}_+ \times \mathbb{N}^* \times [0,1]$ with intensity $ds \times \left(\sum_{j \geq 1} \delta_j(di)\right) \times d\theta$. Moreover, we denote:

$$b(x, Z_t) := \mathbb{1}_{\{\langle Z_t, \mathcal{H}(\,\cdot - x)\rangle \leq K\}},$$

which has value 1 if the number of particles to the right of x is not higher than K and

value 0, otherwise. Then, for $f \in C_b^2(\mathbb{R})$ we have:

$$\langle Z_t, f\rangle = \langle Z_0, f\rangle + \chi \int_0^t \sum_{i=1}^{\langle Z_s^-,1\rangle} f'(H^i(Z_s))(1 - b(H^i(Z_s), Z_s))ds$$
$$+ \sqrt{2}\int_0^t \sum_{i=1}^{\langle Z_s^-,1\rangle} f'(H^i(Z_s))dW_s^i + \int_0^t \sum_{i=1}^{\langle Z_s^-,1\rangle} f''(H^i(Z_s))ds$$
$$+ \int_0^t \int_{\mathbb{N}^*} \int_0^1 \mathbb{1}_{\{i\leq\langle Z_{s^-},1\rangle\}} \mathbb{1}_{\{\theta\leq b(H^i(Z_{s^-}),Z_{s^-})\}} f(H^i(Z_{s^-}))\mathcal{N}(ds, di, d\theta). \tag{0.3.21}$$

Next, we postulate that in the large population limit $K \to +\infty$, $\frac{1}{K}Z_t$ converges to the solution of the following PDE:

$$\begin{cases} \partial_t\rho - \partial_{xx}\rho + \partial_x\left(\chi\mathbb{1}_{x\leq\bar{x}(t)}\rho\right) = \mathbb{1}_{x>\bar{x}(t)}\rho \\ \int_{\bar{x}(t)}^{+\infty} \rho(t,x)dx = 1 \end{cases} \tag{0.3.22}$$

Interestingly, Theorem 0.3.1 remains valid for Equation (0.3.22). Although the rigorous derivation of this large population limit is postponed to future investigations, we investigate the stochastic process numerically and show that in the large population limit, when $K \to +\infty$, the spreading speed is given by Formula (0.3.7).

Finally, we apply the methodology of the works in [38, 74] on the ancestral distribution to this model. This discussion is rather informal, as rigorous results are still under investigation. But we support the claims with numerical simulations. We consider the stochastic process in the moving frame $(t, z) = (t, x - \sigma^* t)$ and suppose that it is close to the stationary distribution in this frame. For K fixed we then define the ancestral distribution $Y_{s,t}^i$: for $s \geq 0$, $Y_{s,t}^i$ is the position at time $t - s$ of the ancestor of the particle whose position at time t is X_t^i. We then conjecture that in the large population limit $K \to +\infty$, the ancestral distribution converges to a stochastic process, which satisfies the following SDE:

$$dY_s = \beta(Y_s)ds + \sqrt{2}dW_s, \tag{0.3.23}$$

where $\beta(z) = \sigma^* - \chi\mathbb{1}_{z\leq 0} + 2\frac{\partial_z\rho^{\sigma^*}}{\rho^{\sigma^*}}$. Moreover its probability distribution v satisfies the following PDE:

$$\partial_s v + \mathcal{L}v = 0, \tag{0.3.24}$$

where $\mathcal{L} := -\partial_{zz} + \partial_z(\beta\,\cdot)$. To conclude, we show that the dynamics of the ancestral distribution drastically differ when $\chi > 1$ or $\chi \leq 1$, which can be seen as an alternative interpretation to pushed or pulled waves. In fact, when $\chi > 1$, then the probability distribution v converges exponentially to a stationary distribution, which quantifies in a sense the contribution of each subpart of the wave. But, when $\chi \leq 1$ (the case $\chi = 1$ being slightly special), the probability distribution spreads towards $z = +\infty$: in a sense, in a pulled wave the ancestors come from the extreme leading edge of the wave.

0.3.6 An Alternative Go or Grow PDE Model and its Preliminary Analysis

The line of reasoning in the preceding Chapter naturally leads to the question of the investigation of Equation (0.3.22), which in many ways lends itself to a better analysis than

the initial Go or Grow System (0.3.6). In this Chapter, we present some preliminary results, which have emerged from an ongoing collaboration with Christopher Henderson.

The main question, we wish to investigate in this Chapter is the characterization of the asymptotic behavior of $\bar{x}(t)$. In fact, we conjecture that:

$$x(t) = \begin{cases} 2t - \frac{3}{2}\log(t) + O(1) & \text{if } \chi < 1 \\ 2t - \frac{1}{2}\log(t) + O(1) & \text{if } \chi = 1 \\ \left(\chi + \frac{1}{\chi}\right) + O(1) & \text{if } \chi > 1 \end{cases}. \tag{0.3.25}$$

In the case $\chi < 1$, this means that we would obtain for the asymptotics a (standard) Bramson shift, which has been well studied in the case of the F/KPP Equation (see [29, 96] for instance). In the case $\chi = 1$, the asymptotics undergo a similar Bramson shift, but with a different coefficient, which has recently been observed on the Burgers-F/KPP Equation [9] and a reaction-diffusion equation with a cubic monostable reaction term [83]. The case $\chi > 1$ corresponds to the pushed case, where the result is in accordance with many results on standard reaction-diffusion equations (*e.g.* [70, 154, 169]). Moreover this conjecture is in accordance with results presented on a free boundary problem in [20]. There, the authors have through formal computations determined the asymptotic behavior of the spreading, which depends merely on the traveling wave profile and how fast the initial datum decreases. Interestingly, the traveling wave profiles for this free boundary problem are exactly the same than the traveling wave solutions of Equation (0.3.22). Of note, the asymptotics (0.3.25) complement Theorems 0.3.2 and 0.3.3, whose proof applies *mutatis mutandis* to Equation (0.3.22).

First, we start by proving an existence and uniqueness result for ρ the solution to Equation (0.3.22) locally in time. The proof is very similar to the analogous result in Chapter 2 and is based on a fixed point theorem on the curve $\bar{x}(\,\cdot\,)$. Just as in Chapter 2, we need an enpoint regularity estimate, which we achieve by a careful hangdling of the singularity at the interface.

In a second step, we prove three intermediary results to Conjecture (0.3.25):

Proposition 0.3.8. *Suppose that:*

$$\int_{\mathbb{R}} e^{\min\left\{1,\frac{1}{\chi}\right\}x} \rho^0(x)dx < +\infty \tag{0.3.26}$$

Then, there exists a constant $C \in \mathbb{R}$, such that:

$$\bar{x}(t) \leq \sigma^* t + C, \tag{0.3.27}$$

where we recall that $\sigma^* = 2$, when $\chi \leq 1$, or $\sigma^* = \chi + \frac{1}{\chi}$, when $\chi > 1$.

Note that Condition (0.3.26) requires that the initial datum ρ^0 decreases fast enough, not unlike the condition that $\frac{\rho^0}{\rho^\sigma} \in L^\infty(\mathbb{R})$ presented in Theorem 0.3.2.

For the next two results, we start by considering $P(t,x) := \int_x^{+\infty} \rho(t,y)dy$, which satisfies:

$$\partial_t P - \partial_{xx} P + \chi \mathbb{1}_{P \geq 1} \partial_x P = \min\{1, P\} \tag{0.3.28}$$

In contrast with Equation (0.3.22), Equation (0.3.28) admits a certain comparison principle, which enables us to construct sub- and supersolutions. This then leads to the two following results:

Proposition 0.3.9. *Suppose that $\chi = 1$ and that:*

1. *There exists $t_0 > e^{\frac{1}{e}}$ and $A > 0$, such that for every $x \geq A$:*

$$e^{-\frac{x^2}{4t_0}} \leq P(0,x)$$

2. *There exists $B > 0$ and $\beta \in \mathbb{R}$, such that for every $x \leq -B$:*

$$-x + \alpha \leq P(0,x)$$

Then, there exists a constant $K \in \mathbb{R}$, such that:

$$\bar{x}(t) \geq 2t - \frac{\ln(t)}{2} - K$$

Proposition 0.3.10. *Suppose that $\chi < 1$ and that:*

1. *There exists $t_0 > 0$ and $A > 0$, such that for every $x \geq A$:*

$$P(0,x) \leq e^{-\frac{x^2}{4t_0}}$$

2. *There exists $B > 0$ and $\beta > 0$, such that for every $x \leq -B$:*

$$P(0,x) \leq \frac{-x}{2-\chi} + \beta$$

Then, there exists a constant $K \in \mathbb{R}$, such that:

$$\bar{x}(t) \leq 2t - \frac{3\ln(t)}{2} + K$$

Finally, for the case $\chi > 1$, we give an asymptotic stability result of the minimal traveling wave solution. We consider Equation (0.3.22) in the moving frame $(t,z) = (t, x - \bar{x}(t))$. Let $V = \beta'$, with $\beta = \frac{1}{\chi} - \chi \mathbb{1}_{z>0}$, $\rho_\infty(z) = \chi \varepsilon^{-\chi \mathbb{1}_{z>0} z}$ and $\gamma := \left(\frac{1}{2}\min\left\{\frac{1}{\chi}, \chi - \frac{1}{\chi}\right\}\right)^2$. Then we have the following theorem:

Theorem 0.3.11. *There exist $\theta, \phi \in \left[0, \frac{\pi}{2}\right)$ such that for $\eta \in \left(0, 2\cos^2(\phi)\gamma\right)$, there exists $\delta > 0$, such that if:*

$$\left\| \partial_z \left(\frac{\rho(0,\,\cdot\,)}{\rho_\infty} \right) \right\|^2_{L^2(e^V dz)} < \delta$$

Then, we have:

$$\left\| \frac{\rho(t,\,\cdot\,)}{\rho_\infty} - 1 \right\|^2_{L^2(e^V dz)} \leq \frac{\delta^2}{2\gamma\cos^2(\theta)} e^{-\eta t}$$

The proof, which is reminiscent of a line of reasoning presented in [39], is based on an energy method and uses a Poincaré inequality, which is deduced from the analysis of the spectral properties of the linearized operator in $L^2(e^V dz)$.

0.4 Future Investigations

We give here a brief overview of work that is currently under investigation, as well as a list of broad open questions, which have been raised by the work presented in this thesis and which may lead to interesting mathematical work.

0.4.1 On the Alternative Go or Grow PDE Models

In Chapter 6, we are mainly concerned with the investigation of Equation (0.3.22). However, we briefly mention yet another alternative Go or Grow Models:

$$\partial_t \rho - \partial_{xx}\rho + \partial_x \left(\chi \psi(\rho)\rho\right) = (1 - \psi(\rho))\rho, \tag{0.4.1}$$

where $\psi(s) = \mathbb{1}_{s\geq 1}$. Interestingly, Equation (0.4.1) for a general function ψ includes the Burgers-F/KPP Equation [9], with $\psi(s) = s$. In many ways, the Burgers-F/KPP Equation behaves very similarily to the different Go or Grow models. Jing An, Christopher Henderson and Lenya Rhyzik are currently working on the generalization for Burgers-F/KPP to Equation (0.4.1) for ψ convex and have obtained results on the asymptotic behavior of the level sets propagation. In turn, inspired by that methodology, we are currently working with Christopher Henderson on the case with $\psi(s) = \mathbb{1}_{s\geq 1}$, in order to obtain the same asymptotics than (0.3.25).

Furthermore, these Go or Grow models resemble also greatly a free boundary problem proposed in [20]:

$$\begin{cases} \partial_t u - \partial_{xx} u = u, \text{ for } x > \mu_t \\ u(t, \mu_t) = \alpha \text{ and } \partial_x u(t, \mu_t) = \beta \end{cases}, \tag{0.4.2}$$

with $\alpha, \beta \in \mathbb{R}$. In particular, when $\alpha > 0$ and $\beta = -\chi\alpha$, we recover a very similar dynamic to the Go or Grow models. In [20], through an elegant, yet non-rigorous argument, the authors have conjectured the same asymptotics than (0.3.25). We are not aware of any rigorous proof of these results. But we believe that the work on Equation (0.4.1) could lead to such a proof, thus contributing to a unified picture of the Go or Grow models, the Burgers-F/KPP Equation, Equation (0.4.1) with a general ψ and the free boundary problem (0.4.2).

Finally, these investigations also raise the question whether the asymptotics (0.3.25) are also valid for the initial Go or Grow model involving the chemical field N (0.3.6). The argument of [20] presented in Chapter 6 points to this conjecture. However, it is not at all clear how the dynamics of N interfere. In addition, if the results are true, then a natural open question is: why does the dynamics of N almost not contribute to the propagation of the cells?

0.4.2 On the Stochastic Go or Grow Model

We briefly summarize the questions, which we are currently working on with Vincent Calvez and Milica Tomašević.

First, we wish to give a rigorous proof of the large population limit when $K \to +\infty$ and show that in that case the measure $\frac{1}{K}\sum \delta_{X_i}$ converge in fact to the solution ρ of Equation (0.3.22). The study [52] on the N-Branching Brownian motion has shown that its limit when $N \to +\infty$ satisfies a free boundary problem of the form (0.4.2). This makes us believe that the proof of such a large population limit may well be in reach.

Then, following the work on ancestral distributions [38, 74], we wish to further investigate the link between the stochastic ancestral dynamics and prove rigorously the informal statements concerning the limit SDE (0.3.23) for $Y_{s,t}$ and its propability distribution v given by PDE (0.3.24). In particular, as already mentioned in [74], this may lead to an alternative interpretation of pulled and pushed waves.

0.4.3 Further Open Questions on SGG

Traveling Waves for the Kinetic Go or Grow Model

In this thesis we have investigated the question of traveling wave solutions for the kinetic Go or Grow model (0.3.15) in the special two-velocity case (see Chapter 2). For the general case, the question remains however open. In [35], the existence of traveling waves for a kinetic model in bacterial chemotaxis has been shown. We believe that the (rather long) argument also applies to the case of the kinetic Go or Grow model (0.3.15). However, we wish to proceed differently, by first studying the K-veloctiy case (for $K < +\infty$) and then using a compactness argument. This might lead to a better understanding of the traveling wave speed σ.

A General Parabolic Model for Cell Division and SGG

We can propose the following system to model a cell population undergoing taxis induced by a single SGG and cell division:

$$\begin{cases} \partial_t \rho - \partial_{xx}\rho + \partial_x \left(\boldsymbol{\chi}(N, \partial_x N)\rho\right) = r(N)\rho & \text{(0.4.3a)} \\ \partial_t N - D\partial_{xx} N = -\beta(N)\rho, & \text{(0.4.3b)} \end{cases}$$

where we suppose that the advection field and division field admit finite fixed values:

$$\lim_{x\to\pm\infty} \boldsymbol{\chi}(N, \partial_x N)|_{(t,x)} = \chi_\pm, \lim_{x\to-\infty} r(N)|_{(t,x)} = 0 \text{ and } \lim_{x\to-\infty} r(N)|_{(t,x)} = 1 \qquad (0.4.4)$$

We wish to investigate the existence of traveling wave solutions $(\rho(t,x), N(t,x)) = (\rho(x - \sigma t), N(x - \sigma t))$ for System (0.4.3). Currently, we are working on an existence result for such a traveling wave, which satisfies the property that ρ does not decrease slower than the F/KPP traveling wave, *i.e.* not slower than xe^{-x}. The key observation is that for a fixed profile N, and thus a fixed advection and division field, the elliptic problem for the traveling wave profile (σ, ρ) becomes:

$$-\sigma\rho' - \rho'' + (\chi(z)\rho)' = r(z)\rho \qquad (0.4.5)$$

But because of Condition (0.4.4) and as long as we can bound in a compact set the possible values of σ, the dependency of N on the elliptic problem induces merely a compact perturbation. In fact $\partial_z\left(\alpha(z)\cdot\right) + \beta(z)\cdot$ with $\alpha(\pm\infty) = \beta(\pm\infty) = 0$ is a compact perturbation of the Laplacian operator. Hence, we believe that the application of a fixed point theorem seems in reach. Nevertheless, for now we still have to work on technicalities.

If the proposed strategy were to succeed, the next natural question is then, whether this traveling wave is unique. Notice that until now in every result of this thesis, the condition that ρ does not decrease slower than the F/KPP traveling wave was sufficient to ensure uniqueness. However, in this case the questions remains completely unsolved. Furthermore, if uniqueness is not guaranteed, the arising question is then: which traveling wave does the Cauchy problem select, if it selects any at all? From the work here, a natural supposition would be the selection of the profile with minimal wave speed. Yet, it could even be that there exist more than one traveling wave profile associated to the minimal wave speed.

In Chapters 3 and 6, we have briefly discussed the question of the stability of the traveling wave profiles. Although, this question is different than the preceding one, a better understanding of the stability properties of the waves may give us insight into the preceding wave selection problem.

Chapter 1

Hypoxia triggers Collective Aerotactic Migration in *Dictyostelium discoideum*

This Chapter consists of an article [48], which has been published in the journal *eLife*.
It is shown that when a cell colony of *Dictyostelium discoideum* is covered, triggered by a quick consumption of the available oxygen, a dense ring of cells forms and moves outwards at constant speed and density.
Although our contribution to this article consitutes merely a subpart of the article, we have reproduced the article in its entirety. Our contribution consists in the mathematical modeling of the experiment and is the result of a collaboration between Christophe Anjard, Vincent Calvez, Olivier Cochet-Escard, M.D. and Jean-Paul Rieu: first, we propose a parabolic mean-field model to describe the phenomenon. Then, we propose an elementary Go or Grow model, which accounts for division, aerotaxis and diffusion of cells. Through the analysis of this model, we quantify the contribution of division and aerotaxis to the propagation speed. Moreover, a study of the inside dynamics is carried out. Finally, through variations of the Go or Grow model, we test the validity of its conclusions.
In Appendix A, we have included the figures and figure supplements of the article.
Moreover, in Appendix B, we have included a commentary [150] to the work in [23], which considers a very similar experiment to the one presented in this Chapter, but where the conclusions of the authors differ slightly from ours.

RESEARCH ARTICLE

Hypoxia triggers collective aerotactic migration in *Dictyostelium discoideum*

Olivier Cochet-Escartin[1†*], Mete Demircigil[2†], Satomi Hirose[3,4], Blandine Allais[1], Philippe Gonzalo[5,6], Ivan Mikaelian[5], Kenichi Funamoto[3,4,7], Christophe Anjard[1], Vincent Calvez[2†*], Jean-Paul Rieu[1†*]

[1]Institut Lumière Matière, UMR5306, Université Lyon 1-CNRS, Université de Lyon, Villeurbanne, France; [2]Institut Camille Jordan, UMR5208, Université Lyon 1-CNRS, Université de Lyon, Villeurbanne, France; [3]Graduate School of Biomedical Engineering, Tohoku University, Sendai, Japan; [4]Institute of Fluid Science, Tohoku University, Sendai, Japan; [5]Centre Léon Bérard, Centre de recherche en cancérologie de Lyon, INSERM 1052, CNRS 5286, Université Lyon 1, Université de Lyon, Lyon, France; [6]Laboratoire de Biochimie et Pharmacologie, Faculté de médecine de Saint-Etienne, CHU de Saint-Etienne, Saint-Etienne, France; [7]Graduate School of Engineering, Tohoku University, Sendai, Japan

Abstract Using a self-generated hypoxic assay, we show that the amoeba *Dictyostelium discoideum* displays a remarkable collective aerotactic behavior. When a cell colony is covered, cells quickly consume the available oxygen (O_2) and form a dense ring moving outwards at constant speed and density. To decipher this collective process, we combined two technological developments: porphyrin-based O_2 -sensing films and microfluidic O_2 gradient generators. We showed that *Dictyostelium* cells exhibit aerotactic and aerokinetic response in a low range of O_2 concentration indicative of a very efficient detection mechanism. Cell behaviors under self-generated or imposed O_2 gradients were modeled using an in silico cellular Potts model built on experimental observations. This computational model was complemented with a parsimonious 'Go or Grow' partial differential equation (PDE) model. In both models, we found that the collective migration of a dense ring can be explained by the interplay between cell division and the modulation of aerotaxis.

***For correspondence:**
olivier.cochet-escartin@univ-lyon1.fr (OC-E);
Vincent.Calvez@math.cnrs.fr (VC);
jean-paul.rieu@univ-lyon1.fr (J-PR)

†These authors contributed equally to this work

Competing interests: The authors declare that no competing interests exist.

Funding: See page 30

Preprinted: 18 August 2020
Received: 09 November 2020
Accepted: 30 July 2021
Published: 20 August 2021

Reviewing editor: Tatjana Piotrowski, Stowers Institute for Medical Research, United States

Introduction

Oxygen is the main electron acceptor for aerobic organism to allow efficient ATP synthesis. This high-energy metabolic pathway has contributed to the emergence and diversification of multicellular organism (***Chen et al., 2015***). While high O_2 availability in the environment seems a given, its rapid local consumption can generate spatial and temporal gradients in many places, including within multicellular organism. Oxygen level and gradients are increasingly recognized as a central parameter in various physiopathological processes (***Tonon et al., 2019***), cancer and development. The well-known HIF (hypoxia-inducible factor) pathway allows cells to regulate their behavior when exposed to hypoxia. At low O_2 levels, cells accumulate HIFα leading to the expression of genes that support cell functions appropriate to hypoxia (***Pugh and Ratcliffe, 2017***).

Another strategy used by organisms facing severe oxygen conditions is to move away from hypoxic regions, a mechanism called aerotaxis and first described in bacteria (***Engelmann, 1881***; ***Winn et al., 2013***). Aerotaxis will occur at the interface between environments with different oxygen content, such as soil/air, water/air or even within eukaryotic multicellular organisms between different tissues (***Lyons et al., 2014***). In such organisms, oxygen was proposed to be a morphogen as in placentation (***Genbacev et al., 1997***) or a chemoattractant during sarcoma cell invasion

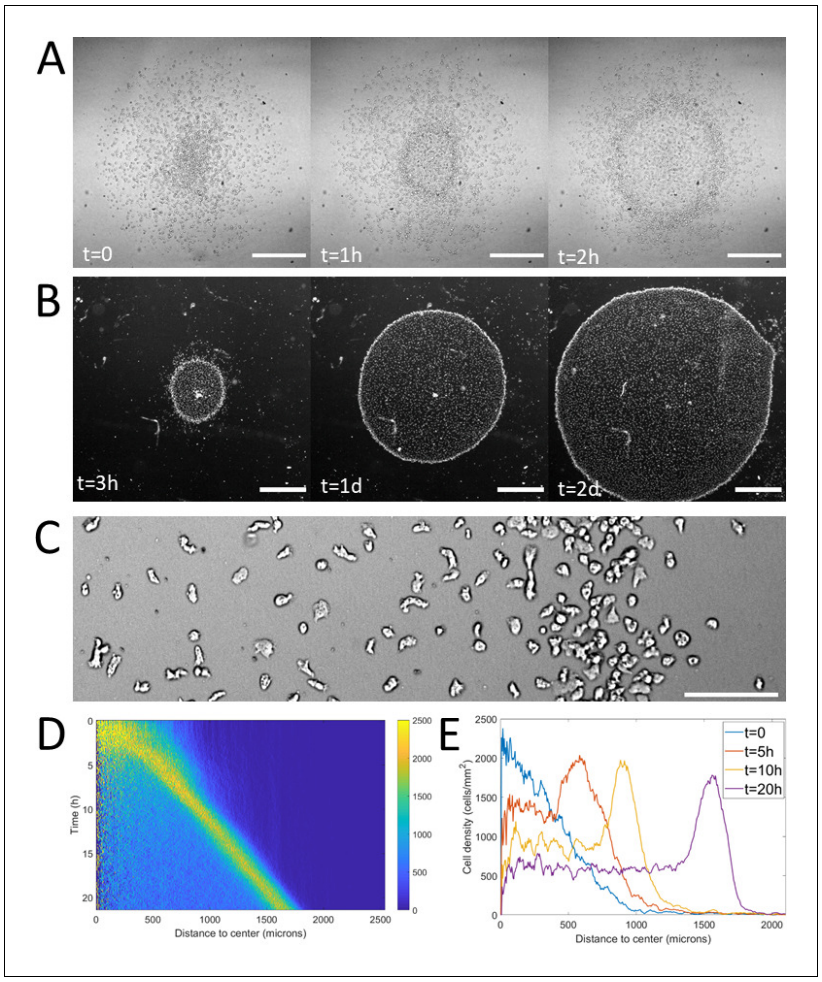

Figure 1. Formation and dynamics of a dense ring of cells after vertical confinement. (**A**) Snapshots of early formation, scale bars: 500 µm. (**B**) Snapshots at longer times imaged under a binocular, scale bars: 1 mm. (**C**) Close up on a ring (band with a higher density on the right hand side) already formed moving rightward and showing different cellular shapes in the ring and behind it, scale bar: 100 µm. (**D**) Kymograph of cell density over 20 hr showing the formation and migration of the highly dense ring. (**E**) Cell density profiles in the radial direction at selected time points.

The online version of this article includes the following source data and figure supplement(s) for figure 1:

Source data 1. Raw data for ***Figure 1***.
Figure supplement 1. Measurement of the confinement height 105 min after covering a cell colony with ~1000 cells plated on plastic with a coverglass using.
Figure supplement 2. Ring formation time decreases with cell number.
Figure supplement 2—source data 1. Raw data for ***Figure 1—figure supplement 2***.
Figure supplement 3. Morphological properties of a propagating ring.
Figure supplement 3—source data 1. Raw data for ***Figure 1—figure supplement 3***.
Figure supplement 4. Effective cell diffusion constant and instantaneous speeds as a function of distance to the center.
Figure supplement 4—source data 1. Raw data for ***Figure 1—figure supplement 4***.
Figure supplement 5. Cell velocity bias in the spot assay as a function of distance to the center.
Figure supplement 5—source data 1. Raw data for ***Figure 1—figure supplement 5***.

(***Lewis et al., 2016***). Aerotaxis may also play a role in morphogenesis. The notion that gradients of O_2 and energy metabolism govern spatial patterning in various embryos dates back to the classic work of ***Child, 1941***. Such notions have mostly been abandoned due to the inability to visualize such a gradient or clarify whether they are the result or the cause of developmental patterning

(*Coffman and Denegre, 2007*). Even at the single-cell level, *in vitro* experimental studies on aerotaxis are rare. One reason might be technical: gradient control and live monitoring of oxygen concentrations at the cellular level are difficult. More recently, Chang et al. found an asymmetric distribution of hypoxia-inducible factor regulating dorsoventral axis establishment in the early sea urchin embryo (*Chang et al., 2017*). Interestingly, they also found evidence for an intrinsic hypoxia gradient in embryos, which may be a forerunner to dorsoventral patterning.

Self-generated chemoattractant gradients have been reported to trigger the dispersion of melanoma cells (*Muinonen-Martin et al., 2014*; *Stuelten, 2017*), *Dictyostelium* cells (*Tweedy et al., 2016*) or the migration of the zebrafish lateral line primordium (*Donà et al., 2013*; *Venkiteswaran et al., 2013*). The mechanism is simple and very robust: the cell colony acts as a sink for the chemoattractant, removes it by degradation or uptake creating a gradient that, in turn, attracts the cells as long as the chemoattractant is present in the environment. Physiologically speaking, self-generated gradients have been demonstrated to increase the range of expansion of cell colonies (*Cremer et al., 2019*; *Tweedy and Insall, 2020*) and to serve as directional cues to help various cell types navigate complex environments, including mazes (*Tweedy et al., 2020*). Recently, it was demonstrated that after covering an epithelial cell colony by a coverglass non permeable to O_2, peripheral cells exhibit a strong outward directional migration to escape hypoxia from the center of the colony (*Deygas et al., 2018*). This is a striking example of a collective response to a self-generated oxygen gradient by eukaryotic cells. Oxygen self-generated gradients could therefore play important roles in a variety of contexts, such as development, cancer progression, or even environmental navigation in the soil.

Dictyostelium discoideum (*Dd*) is an excellent model system to study the fairly virgin field of aerotaxis and of self-generated gradients. *Dd* is an obligatory aerobic organism that requires at least 5% O_2 to grow at optimal exponential rate (*Cotter and Raper, 1968*; *Sandonà et al., 1995*) while slower growth can occur at 2% O_2. However, its ecological niche in the soil and around large amount of bacteria can result in reduced O_2 availability. During its multicellular motile stage, high oxygen level is one of the signal used to trigger culmination of the migrating slug (*Xu et al., 2012*). For many years, *Dd* has been a classical organism to study chemotaxis and has emulated the development of many models of emergent and collective behavior since the seminal work of Keller and Segel (*Hillen and Painter, 2009*; *Keller and Segel, 1970*). An integrated approach combining biological methods (mutants), technological progress, and mathematical modeling is very valuable to tackle the issue of aerotaxis.

In this article, we study the influence of O_2 self-generated gradients on *Dd* cells. Using a simple confinement assay, microfluidic tools, original oxygen sensors and theoretical approaches, we show that oxygen self-generated gradients can direct a seemingly collective migration of a cell colony. Our results confirm the remarkable robustness and long-lasting effect of self-generated gradients in collective migration. This case where oxygen is the key driver also suggests that self-generated gradients are widespread and a possible important feature in multicellular morphogenesis.

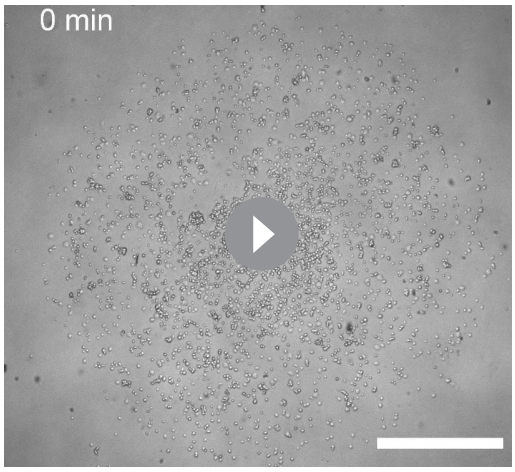

Video 1. Initial phase (0–4 hr) of ring formation and migration. Scale bar: 500 μm.
https://elifesciences.org/articles/64731#video1

Results

Confinement triggers formation and propagation of a self-sustained cell ring

To trigger hypoxia on a colony of *Dd* cells, we used a vertical confinement strategy (*Deygas et al., 2018*). A spot of cells with a radius of about 1 mm was deposited and covered by a larger glass coverslip with a radius of 9 mm. We measured the vertical confinement through confocal microscopy and found the

height between the bottom of the plate and the coverslip to be 50 µm (***Figure 1—figure supplement 1***).

Using spots containing around 2000 cells (initial density around 10^3 cells/mm^2), the formation of a dense ring of cells moving outwards was observed as quickly as 30 min after initiation of the confinement (***Figure 1A*** and ***Video 1***). This formation time however depended non-linearly on initial cell density (the denser, the faster, ***Figure 1—figure supplement 2***). Once triggered, this collective migration was self-maintained for tens of hours, even days and the ring could, at these points, span centimeters (***Figure 1B***).

Notably, as the ring expanded outwards, it left a trail of cells behind. This led to the formation of a central zone populated by cells which did not contribute directly to the migration of the ring (***Figure 1B***) but were still alive and moving albeit a clear elongated phenotype resembling pre-aggregative *Dd* cells (***Figure 1C*** and ***Video 2***). In comparison, cells in the ring or outside the colony were rounder, as usual vegetative cells (***Delanoë-Ayari et al., 2008***).

To study the properties of the ring, we computed density profiles using radial coordinates from the center of the colony to study cell density as a function of time and distance to the center (***Figure 1D–E***). We found that after a transitory period corresponding to the ring passing through the initial spot, the density in the ring, its width and its speed all remained constant over long time scales (***Figure 1—figure supplement 3***). The speed and density of the ring were found to be 1.2 ± 0.3 µm/min (mean ± std, N=9 independent experiments) and 1.9 10^3 ± 0.3 10^3 cells/mm^2 (mean ± std, N=4 independent experiments, that is fourfold higher than behind it, ***Figure 1E***) respectively. The density of cells left behind the ring was also found to remain constant after a transient regime (***Figure 1D***). As the diameter of the ring increased over time, the absence of changes in morphology implies an increase of the number of cells and thus an important role of cell division.

Overall, this self-sustained ring propagation is very robust and a long lasting collective phenotype that can easily be triggered experimentally. This shows that the spot assay is an excellent experimental system to study the response of a variety of cell types to vertical confinement and its physiological consequences (***Deygas et al., 2018***).

Cell dynamics in different regions

Following the reported shape differences, we questioned how cells behaved dynamically in different regions. To do so, we performed higher resolution, higher frame rate experiments to allow cell tracking over times on the order of tens of minutes. Both the cell diffusion constant and instantaneous cell speeds were fairly constant throughout the entire colony (***Figure 1—figure supplement 4***). Cell diffusion was 28.2 ± 1.4 µm^2/min (N=3 independent experiments, each containing at least 2000 cells), comparable to our measurement of activity at very low oxygen level in the microfluidic device (see below). To test the influence of motion bias, we projected cell displacements on the radial direction and computed mean speeds in this direction as a function of distance to the center. Random motion, either persistent or not, would lead to a null mean radial displacement whereas biased migration would be revealed by positive (outward motion) or negative (inward motion) values. Here, we found that significantly non-zero biases were observed only in a region spanning the entire ring and a few tens of microns behind and in front of it with the strongest positive biases found in the ring (***Figure 1—figure supplement 5***).

Overall, our results show that the different regions defined by the ring and its dynamics can be characterized in terms of cell behavior: (i) behind the ring in the hypoxic region: elongated

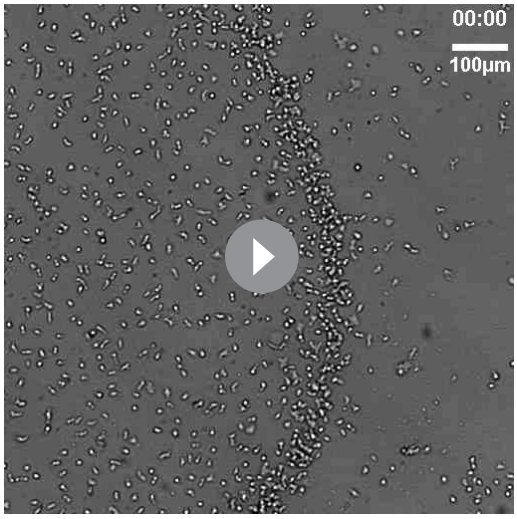

Video 2. High framerate, high-resolution imaging of cell dynamics in and behind the ring over 15 min. Time is in min:s and the scale bar represents 100 µm.
https://elifesciences.org/articles/64731#video2

shape, normal speeds, and low bias; (ii) in the ring: round shape, normal speeds and high bias.

Response of *Dd* cells to controlled oxygen gradients

The spot assay is experimentally simple but is not ideally suited to decipher the response of *Dd* cells to hypoxia since local concentrations and gradients of oxygen are coupled to cell dynamics and thus very difficult to manipulate. We hence designed a new double-layer PDMS microfluidic device allowing to quickly generate oxygen gradients in a continuous, controlled manner (***Figure 2A***). Briefly, cells were seeded homogenously within a media channel positioned 500 µm below two gas channels continuously perfused with pure nitrogen on one side and air on the other. As PDMS is permeable to these gases, the gas flows imposed hypoxic conditions on one side of the media channel while the other was kept at atmospheric oxygen concentration. Of note, the distance between the two gas channels, thereafter called the gap, varied from 0.5 mm to 2 mm in order to modify the steepness of the gradients in the median region of the media channels (***Figure 2A*** and Materials and methods).

To make sure that the gas flows were sufficient to maintain a constant O_2 distribution against leakages and against small variation in the fabrication process, we also developed O_2-sensing films to be able to experimentally measure O_2 profiles both in the microfluidic devices and in the spot assay. These films consisted of porphyrin based O_2 sensors embedded in a layer of PDMS. As O_2 gets depleted, the luminescence quenching of the porphyrin complex is reduced leading to an increase in fluorescence intensity (***Ungerböck et al., 2013***). Quantitative oxygen measurements were then extracted from this fluorescent signal using a Stern-Volmer equation (see Materials and methods and ***Figure 2—figure supplements 1–4*** for details).

Within 15 min, we observed the formation of a stable O_2 gradient in the devices closely resembling numerical predictions with or without cells (***Figure 2B*** and ***Figure 2—figure supplements 5–7***).

We then turned our attention to the reaction of the cells to this external gradient. We first noticed that depending on local O_2 concentrations, cell motility was remarkably different. Using cell tracking, we found that cell trajectories seemed much longer and more biased in hypoxic regions (***Figure 2C***). These aerokinetic (large increase in cell activity) and aerotactic responses were confirmed by quantifying the mean absolute distance travelled by cells (***Figure 2D*** top), or the mean distance projected along the gradient direction (***Figure 2D*** bottom) in a given time as a function of position in the device (***Figure 2D***). Since cells in the microfluidic devices were also experiencing oxygen gradients, we further tested if the observed was true aerokinesis. To do so, we compared cell motility in homogenous environments of either 20.95% or 0.4% O_2. We found cell diffusion constant to be D=40.2±9.6 μm^2/min (mean ± std) at 0.4% (***Figure 2—figure supplement 8***), comparable to our measurements in the center of the spot (***Figure 1—figure supplement 4***). At atmospheric oxygen concentrations though, this effective diffusion was clearly reduced as we measured it to be D=19.2±8.8 μm^2/min (***Figure 2—figure supplement 8***). The very significant difference ($p<0.0001$) demonstrates that *Dd* cells show an aerokinetic positive response to low oxygen, even in the absence of gradients. The second important observation stemming from the microfluidic experiments is an accumulation of cells at some midpoint within the cell channel (***Figure 2E***). Naively, one could have expected cells to follow the O_2 gradient over its entire span leading to an accumulation of all cells on the O_2 rich side of the channel. This did not happen and, instead, cells seemed to stop responding to the gradient at a certain point. Similarly, we observed a strong positive bias in hypoxic regions but the bias quickly fell to 0 as cells moved to oxygen levels higher than about 2% (***Figure 2D***), confirming that the observed cell accumulation was a result of differential migration and not, for example, differential cell division. In addition, if we inverted the gas channels halfway through the experiment, we observed that the cells responded in around 15 min (which is also the time needed to re-establish the gradient, see ***Figure 2—figure supplement 6***) and showed the same behavior, albeit in reverse positions. We measured the bias for the different gaps and for the situation of reversed gradient and obtained a value of 1.1 ± 0.4 µm/min (N=6, three independent experiments and for each, both directions of the gradient, each value stemming from a few hundred cells).

Of note, the position at which cells accumulated and stopped responding to the gradient was still in the region were the gradient was constantly increasing. This led to the hypothesis that, in addition

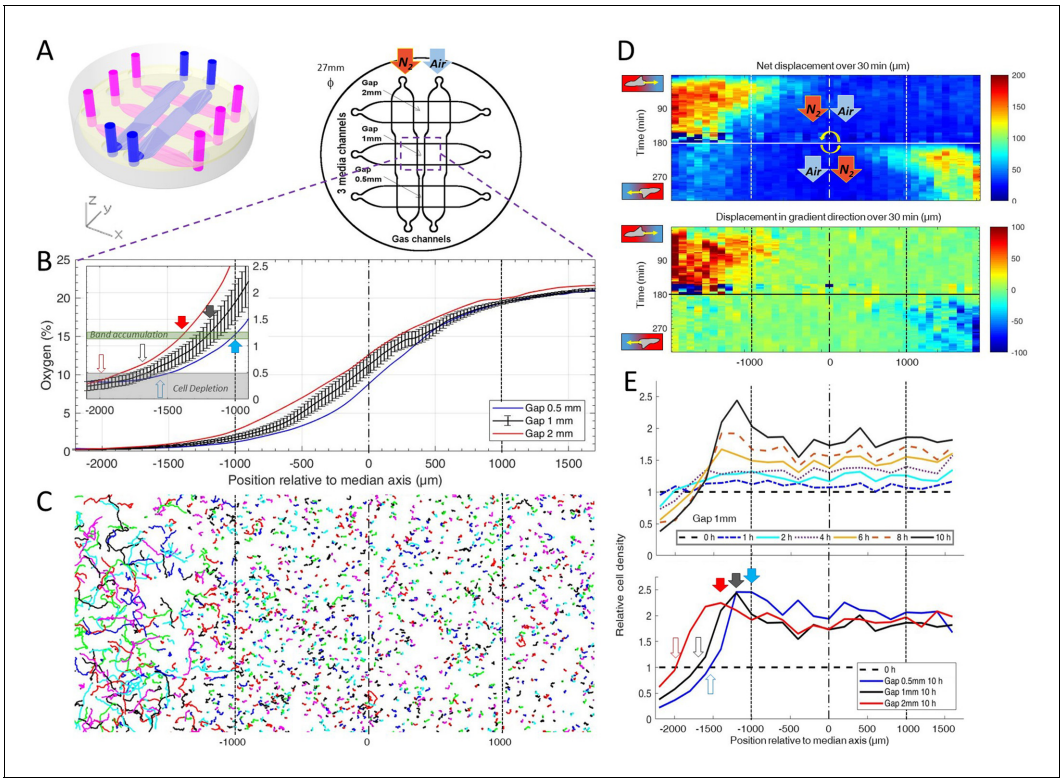

Figure 2. *Dictyostelium* single cells are attracted by an external O_2 gradient when O_2 level drops below 2%. (**A**) Schemes of the new double-layer PDMS microfluidic device allowing the control of the O_2 gradient by the separation distance (gap) between two gas channels located 0.5 mm above the three media channels and filled with pure nitrogen, and air (21% O_2). (**B**) Measured O_2 concentration profiles 30 min after N_2-Air injection to the left and right channels respectively (0–21% gradient) as a function of the position along the media channel for the three gaps. Error bars (see Methods) are reported only for gap 1 mm for clarity. The inset shows the 0–2.5% region under the nitrogen gas channel (arrows, see E). (**C**) Trajectories lasting 1 hr between 3 hr and 4 hr after establishment of a 0–21% gradient. Cells are fast and directed toward the air side in the region beyond the −1000 µm limit (O_2<2%). (**D**) Cell net displacement over 30 min (end to end distance, top kymograph) and 30 min displacement projected along gradient direction (bottom kymograph). Cells are fast and directed toward O_2, where O_2<2%, within 15 min after 0–21% gradient establishment at t=0. At t=180 min, the gradient is reversed to 21–0% by permuting gas entries. Cells within 15 min again respond in the 0–2% region. (**E**) Relative cell density histogram (normalized to t=0 cell density) as a function of the position along media channel. Top panel: long term cell depletion for positions beyond −1600 µm (O_2<0.5%, see inset of B) and resulting accumulation at about −1200 µm for gap 1 mm channel. The overall relative cell density increase is due to cell divisions. Bottom panel: cell depletion and accumulation at 10 hr for the three gaps. The empty and filled arrows pointing the limit of the depletion region, and max cell accumulation respectively are reported in the inset of B.

The online version of this article includes the following source data and figure supplement(s) for figure 2:

Source data 1. Raw data for ***Figure 2***.

Figure supplement 1. Oxygen profile measurements inside the microfluidic gradient generator device with a sensing film mounted on the bottom of the media channel.

Figure supplement 1—source data 1. Raw data for ***Figure 2—figure supplement 1***.

Figure supplement 2. Typical calibration data of sensing films mounted on a microfluidic device.

Figure supplement 2—source data 1. Raw data for ***Figure 2—figure supplement 2***.

Figure supplement 3. Typical calibration data and oxygen profile measurement with covered sensing films for the spot assay.

Figure supplement 3—source data 1. Raw data for ***Figure 2—figure supplement 3***.

Figure supplement 4. Image analysis pipeline to quantify oxygen map from O_2 sensitive sensing films.

Figure supplement 5. Numerical simulations of oxygen profiles.

Figure supplement 5—source data 1. Raw data for ***Figure 2—figure supplement 5***.

Figure supplement 6. Experimental oxygen gradient establishment in the microfluidic device (gap 0.5 mm).

Figure supplement 6—source data 1. Raw data for ***Figure 2—figure supplement 6***.

Figure supplement 7. Influence of plated cells on the steady oxygen tension in the microfluidic device (Computational results).

Figure supplement 7—source data 1. Raw data for ***Figure 2—figure supplement 7***.

Figure supplement 8. Aerokinesis of *Dd* cells in homogenous environments.

Figure supplement 8—source data 1. Raw data for ***Figure 2—figure supplement 8***.

to gradient strength, O_2 levels also play an important role in setting the strength of aerotaxis displayed by *Dd* cells.

Furthermore, when we compared experiments performed with different gaps, we found that the position of cell accumulation varied from one channel to another (***Figure 2E***). However, our O_2 sensors indicated that the accumulation occurred at a similar O_2 concentration of about 1% in all three channels (inset of ***Figure 2B***) thus strongly hinting that the parameter controlling the aerotactic response was O_2 levels.

Overall, these experiments in controlled environments demonstrated two main features of the response of *Dd* cells to hypoxia: a strong aerokinetic response and a positive aerotactic response, both modulated by local O_2 levels regardless of the local gradient. These results reveal a subtle cross talk between O_2 concentrations and gradients in defining cell properties and it would be very informative, in the future, to study in details the reaction of *Dd* cells to various, well defined hypoxic environments where O_2 concentrations and gradients can be independently varied.

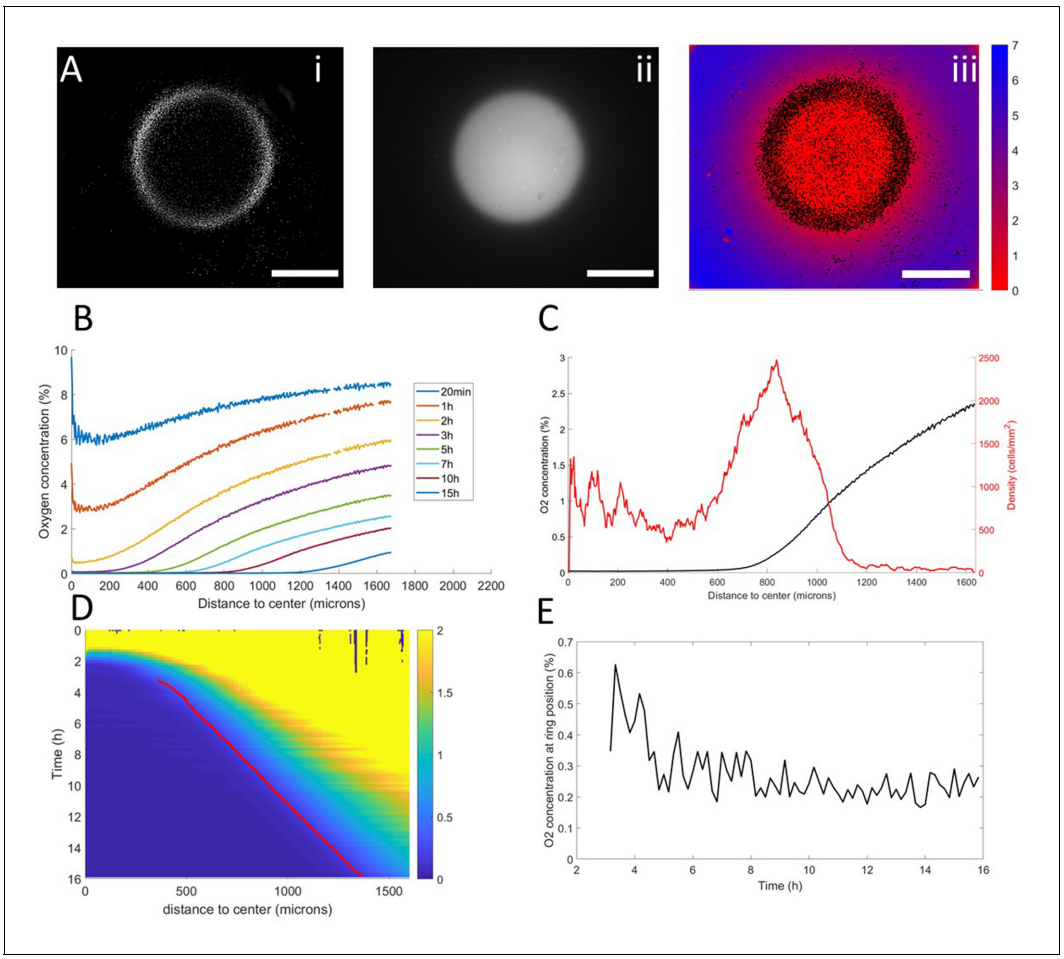

Figure 3. Interplay between ring dynamics and O_2 profiles. (**A**) (i) Treated image showing cell distribution at t=10h, (ii) raw fluorescent signal indicative of strong O_2 depletion, (iii) reconstructed image showing the center of mass of all detected cells and quantitative O_2 profiles (colorbar, in % of O_2), scale bars: 1 mm. (**B**) O_2 profiles averaged over all angles and shown at different times. (**C**) Radial profile of cell density and O_2 concentration at t=10h showing the position of the ring relative to the O_2 profile. (**D**) Kymograph of O_2 concentration (colorbar in %) with the position of the ring represented as a red line. The colormap is limited to the 0–2% range for readability but earlier time points show concentrations higher than the 2% limit. (**E**) O_2 concentration as measured at the position of the ring as a function of time showing that the ring is indeed following a constant concentration after a transitory period.

The online version of this article includes the following source data for figure 3:

Source data 1. Raw data for ***Figure 3***.

Coupled dynamics between oxygen profiles and collective motion

Thanks to these results, we turned our attention back to the collective migration of a ring of cells and asked whether similar aerotactic behaviors were observed under self-generated gradients. To do so, we performed spot experiments on the O_2-sensing films described above which allowed us to image, in parallel, cell behavior and O_2 distribution (***Figure 3A***, ***Figure 2—figure supplement 3*** and ***Video 3***).

In a first phase, preceding the formation of the ring, cell motion was limited and the structure of the colony remained mostly unchanged. As O_2 was consumed by cells, depletion started in the center and sharp gradients appeared at the edges of the colony (***Figure 3B–C***).

Then, the ring formed and started moving outwards, O_2 depletion continued and the region of high O_2 gradients naturally started moving outwards (***Figure 3B***). At this point, coupled dynamics between the cells and the O_2 distribution appeared and we observed that the position of the ring closely followed the dynamics of the O_2 field (***Figure 3D***), that is it followed a constant concentration of oxygen of 0.25% (***Figure 3C***).

In the process, three distinct regions were created. Behind the ring, O_2 was completely depleted and thus no gradient was visible. In front of the ring, the O_2 concentration remained high with high gradients. Finally, in the ring region, O_2 was low (<1%) and the gradients were strong. Based on our results in externally imposed gradients, we would thus expect cells to present a positive aerotactic bias mostly in the ring region which is indeed what we observed (***Figure 1—figure supplement 5***).

Minimal cellular Potts model

Based on these experimental results, we then asked whether this subtle response of *Dd* cells to complex oxygen environments was sufficient to explain the emergence of a highly stable, self-maintained collective phenomenon. To do so, we developed cellular Potts models based on experimental observations and tested whether they could reproduce the observed cell dynamics. Briefly, the ingredient underlying the model are as follows (details can be found in the Materials and methods section). First, all cells consume the oxygen that is locally available at a known rate (***Torija et al., 2006***). Cell activity increases at low O_2. Cells respond positively to O_2 gradients with a modulation of the strength of this aerotaxis based on local O_2 concentrations, as observed in our microfluidic experiments. Finally, all cells can divide as long as they sit in a high enough O_2 concentration (chosen at 0.7%) since it was demonstrated that cell division slows down in hypoxic conditions (***Schiavo and Bisson, 1989***; ***West et al., 2007***). Of note, all parameters were scaled so that both time and length scales in the Potts models are linked to experimental times and lengths (see Materials and methods).

Although this model is based on experimental evidence, some of its parameters are not directly related to easily measurable biological properties. Therefore, we decided to fit our parameters to reproduce as faithfully as possible the results of our microfluidic experiments. Through a trial and error procedure, we managed to reproduce these results qualitatively and quantitatively (***Video 4***) in terms of collective behavior, cell accumulation, and individual cell behavior (***Figure 4—figure supplement 1***).

We then applied this model and added O_2 consumption by cells, with initial conditions mimicking our spot assay and other ingredients mimicking the vertical confinement. We observed the rapid formation and migration of a ring (***Figure 4A–B***, ***Video 5***). This ring was remarkably similar to that observed in experiments. In particular, we found its speed to be constant after an initial transitory period (***Figure 4C***,

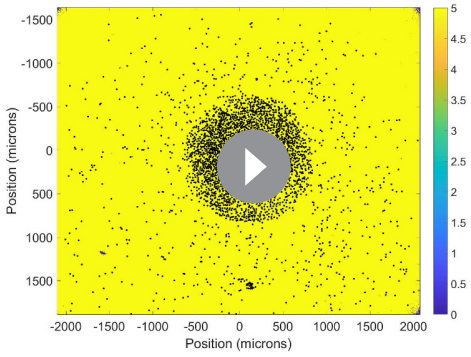

Video 3. Reconstruction of cell and oxygen dynamics from a spot experiment on an oxygen sensor. Cell positions are shown as black dots, oxygen in colors (scale bar in %). The entire movie spans 15 hr of experiment.
https://elifesciences.org/articles/64731#video3

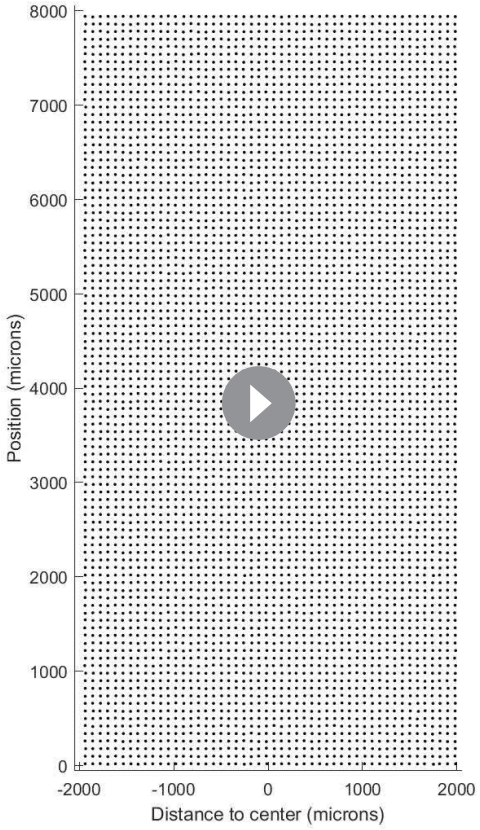

Video 4. Dynamics of the Potts model reproducing microfluidic experiments. Low oxygen regions are on the left and high oxygen on the right. Cell positions are shown as black dots and the entire movie represents the equivalent of 10 hr of experiments.
https://elifesciences.org/articles/64731#video4

Figure 4—figure supplement 2). This speed was also comparable to experimental ones. Similarly, the morphology of these simulated rings was constant over time with a fixed cell density and width (***Figure 4—figure supplement 2***). Finally, cell behavior was qualitatively well reproduced by this model (***Figure 4—figure supplement 3***).

In terms of coupled dynamics between cell density and O_2 profiles, we found here too that the driving force behind this collective phenomenon was the fact that the ring followed a constant O_2 concentration (***Figure 4D–E***).

We then asked what were the key ingredients in the model to trigger this phenomenon, a question we explored by tuning our original Potts model. We started by dividing cell consumption of oxygen by a factor of 3 (***Figure 5A***) and found that it did not significantly change the ring speed but could change the aspect of cell density in the central region. We then turned our attention to other key elements in the model.

If we turned off cell division in our models, the formation of the ring was mostly unchanged but after a short time, the ring started slowing down and even stopped as cell density was no longer sufficient to reach highly hypoxic conditions (comparing ***Figure 5A and B***). Second, we asked whether the observed and modeled aerokinesis was necessary to reproduce the collective migration. We found that it wasn't as models ran at different effective temperatures applied to all cells regardless of local O_2 concentrations all showed qualitatively similar behavior (see for example ***Figure 5C***). Of note though, lower effective temperatures led to less dense rings as fewer cells were able to start in the ring (***Figure 5—figure supplement 1***). Finally, we found that modulation of aerotaxis by local O_2 concentrations was essential. Indeed, as we increased the range of O_2 concentration at which aerotaxis is at play (***Figure 5G–H***), we found that forming rings became wider and less dense (***Figure 5D–E***) to the point where no actual ring could be distinguished if aerotaxis was kept constant for all cells (***Figure 5I***).

These numerical simulations based on cellular Potts models provide a good intuition of the phenomenon and reveal that cell division and aerotactic modulation are the two key ingredients to reproduce the ring of cells. Because of their versatility, they can also be used to make some predictions on the observed phenomenon. Experimentally, we tested two such predictions to demonstrate the relevance of the underlying assumptions.

First, we show in ***Figure 5B*** the effect of turning cell division off in the simulated spot. A similar result can be achieved by placing cells in a phosphate buffer medium, lacking nutrients and thus blocking cell division (***Kelly et al., 2021***). In this situation, at short time scales, a ring of cells started forming and expanding outwards in a similar fashion as in nutritive medium (***Figure 5—figure supplement 2***). After a few hours, however, the ring started slowing down until it completely stopped and cells started dispersing again. This is in complete agreement with the predictions of the Cellular Potts Model, as one can see by comparing the density kymographs (***Figure 5A*** and ***Figure 5—figure***

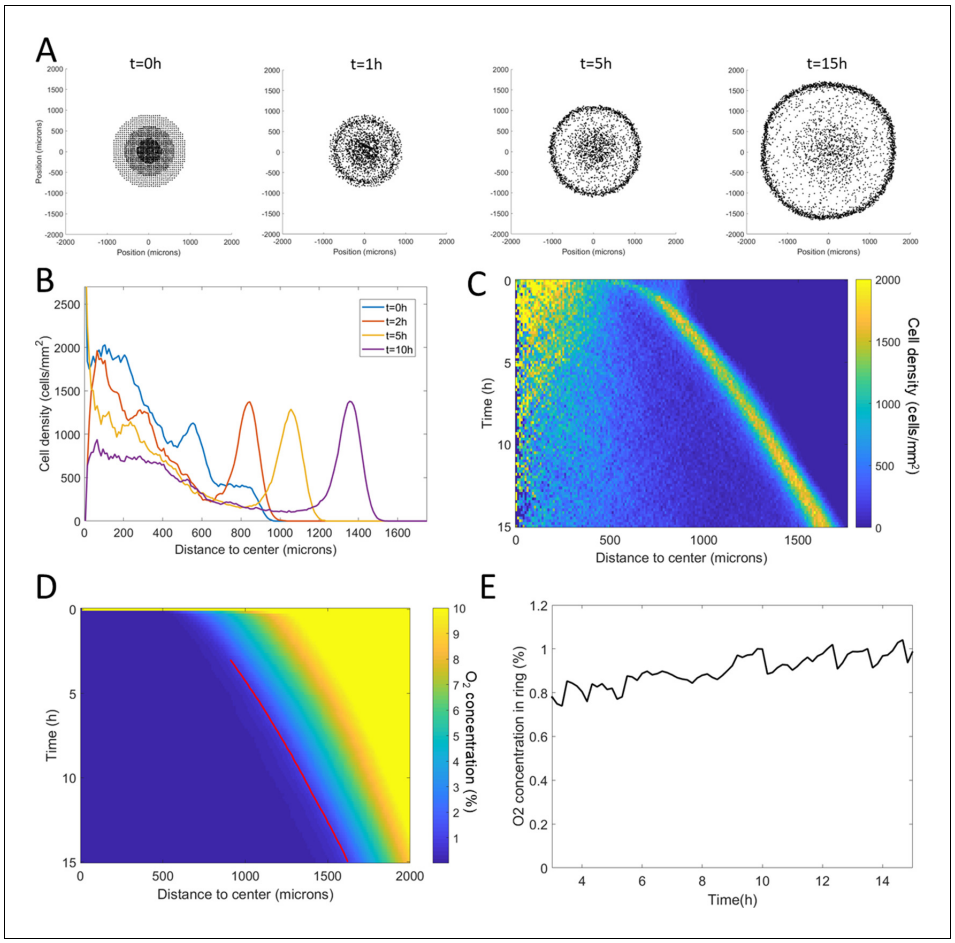

Figure 4. Minimal Potts model of ring formation and migration. (**A**) Snapshots of a simulated colony of cells showing the formation of highly dense ring of cells. (**B**) Cell density profiles averaged over all angles for four different times. (**C**) Corresponding kymograph of cell density (colorbar in cells/mm^2) as a function of time and distance to the center. Quantification in terms of microns and hours is described in the Materials and methods section. (**D**) Kymograph of O_2 concentration (colorbar in %) with the position of the ring represented as a red line. The colormap is limited to the 0–10% range for readability but earlier time points show concentrations higher than the 10% limit. (**E**) O_2 concentration at the ring position as a function of time showing that, here too, the ring follows a constant O_2 concentration.

The online version of this article includes the following source data and figure supplement(s) for figure 4:

Source data 1. Raw data for ***Figure 4***.

Figure supplement 1. Adjusting Potts model (right) to microfluidic experiments (left).

Figure supplement 1—source data 1. Raw data for ***Figure 4—figure supplement 1***, experiments corresponding to the left column.

Figure supplement 1—source data 2. Raw data for ***Figure 4—figure supplement 1***, simulations corresponding to the right column.

Figure supplement 2. Potts model ring features with parameters adjusted from the microfluidic experiments (***Figure 4—figure supplement 1***).

Figure supplement 2—source data 1. Raw data for ***Figure 4—figure supplement 2***.

Figure supplement 3. Comparison of cell behavior in spot experiments (left) and Potts models (right).

Figure supplement 3—source data 1. Raw data for ***Figure 4—figure supplement 3***, experiments corresponding to the left column.

Figure supplement 3—source data 2. Raw data for ***Figure 4—figure supplement 3***, simulations corresponding to the right column.

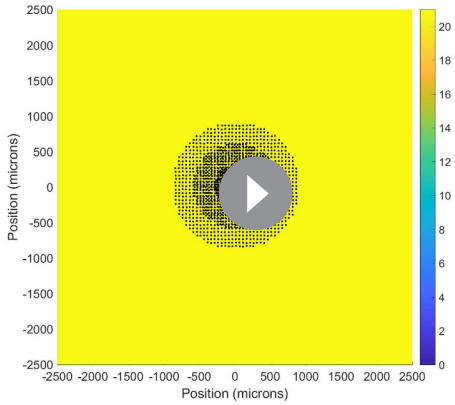

Video 5. Dynamics of the Potts model reproducing the spot experiments. Cell positions are shown as black dots and the oxygen is in colors (in %).
https://elifesciences.org/articles/64731#video5

supplement 2) and firmly demonstrates the importance of cell division in this behavior. At longer time scales though (t>10h), Dd cells started forming aggregates and entering a developmental phase (***Video 6***). This aggregation is presumably due to the concomitant expression of cell adhesion molecules and, apparition of self-organizing secreted cAMP pulses whose timing agrees with the one reported in classical free cell spot aggregation assays (***Gregor et al., 2010***). Cell-cell adhesion and cAMP signaling are not included in our models or numerical simulations that hence cannot predict the long times in ***Video 6***. However, the timing is well separated from the end of the ring expansion period (t<3.5h). This still demonstrates that the phenomenon observed here is relevant for both the single cell and collective stages of *Dd* life cycle.

Second, we used these numerical simulations to predict the behavior of cells in more complex environments. One can see the expansion of the ring as a way for each cell to optimize its own resources. This begs the question of what happens when more than one colony is present in the environment, a problem more directly relevant for real life situations. Can the different colonies sense their respective presence and adapt accordingly by migrating preferably away from one another or, on the other hand, will the depletion of oxygen induced by a neighboring colony increase hypoxia on this side and therefore accelerate migration? In this case, what would happen when two rings come in contact? We started exploring this question by simulating two colonies put in close proximity. These simulations predict that the formed rings do not repel each other, instead they tend to rush toward one another and, when they meet, they fuse together to make an elliptical front which then relaxes towards a more circular shape (***Video 7***). We then performed the corresponding experiment and found very similar behavior (***Video 7***).

Overall, these results show that the cellular Potts model indeed recapitulates all the major experimental observations with only two key ingredients (cell division and aerotactic modulation). However, they fall short of giving an in-depth quantitative description because they rely on many parameters and are not amenable to theoretical analysis per se.

'Go or Grow' hypothesis: a Mean-field approach

In order to complement the methodology of the cellular Potts model, we developed a mean-field approximation of the latter: the cell density ρ is subject to a reaction-advection-diffusion partial differential equation (PDE):

$$\frac{\partial \rho}{\partial t} = D\nabla \cdot (\nabla \rho) - \nabla \cdot (a(C, \nabla C)\rho) + r(C)\rho \tag{1}$$

C is the oxygen concentration, $a(C, \nabla C)$ corresponds to the aerotactic advection speed and $r(C)$ to the cell division rate. By assuming radial symmetry in agreement with the experiments, we propose $a(C, \nabla C) = a(C, \partial_r C) = \lambda_{aero}(C)\partial_r C$, where $\lambda_{aero}(C)$ is the already mentioned aerotactic strength fitting the microfluidic experiments with an upper O_2 concentration threshold C_0=0.7% (***Figure 5G*** and Material and Methods) and $r(C) = \begin{cases} r_0, if\ C>C_0 \\ 0, if\ C<C_0 \end{cases}$ is the division rate. When not specified, we use the same threshold C_0 for cell division and aerotaxis as for the cellular Potts model. Below, this assumption is coined as the 'Go or Grow' hypothesis. We thereby revisited the 'Go or Grow' model for glioma cells (***Hatzikirou et al., 2012***) with the transition between division and directional motion being mediated by oxygen levels rather than cell density in the mentionned

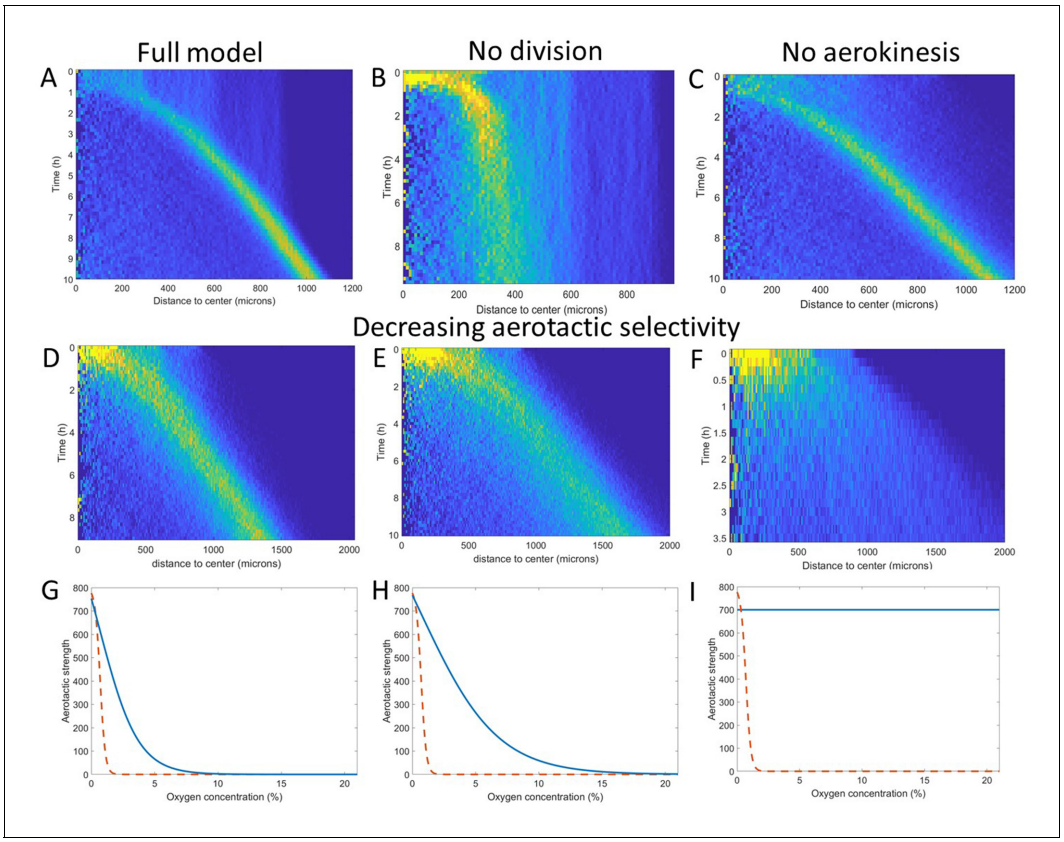

Figure 5. Key ingredients of the Potts model by density kymograph (DK) evaluation. (**A**) DK for the full model with reduced oxygen consumption as a basis for comparison. (**B**) DK in the absence of cell division, note the difference in length scale showing a clear limitation of motion in that case. (**C**) DK in the absence of aerokinesis (cell activity is not modulated by local oxygen concentrations). (**D**) DK with a modulation of aerotactic strength as shown in (**G**), note the wider ring. (**E**) DK with a modulation of aerotactic strength as shown in (**H**). (**F**) DK with a modulation of aerotactic strength as shown in (**I**), no ring appears and cells quickly migrate outwards as shown by the difference in time scales. (**G–I**) Three different aerotactic modulations, in blue, compared to the one used in the full model, shown in (**A**), drawn here as a red dashed line.
The online version of this article includes the following source data and figure supplement(s) for figure 5:

Source data 1. Raw data for ***Figure 5***.
Figure supplement 1. Effect of temperature on ring migration in Potts models.
Figure supplement 1—source data 1. Raw data for ***Figure 5—figure supplement 1***.
Figure supplement 2. Ring formation in a phosphate buffer.
Figure supplement 2—source data 1. Raw data for ***Figure 5—figure supplement 2***.

study. Congestion effects such as they may arise in the cellular Potts model or in experiments have been ignored.

Oxygen is subject to a simple diffusion-consumption equation, with $b(C)$ the consumption rate of oxygen per cell (see Materials and methods):

$$\frac{\partial C}{\partial t} = D_{oxy}\nabla\cdot(\nabla C) - b(C)\rho \tag{2}$$

The results obtained by numerical simulation of this mean-field model are comparable to the ones already obtained by the cellular Potts model: emergence of a high cell density area traveling at constant speed $\sigma \approx 1.0$ µm/min, leaving behind a trail of cells (***Figure 6A-B***).

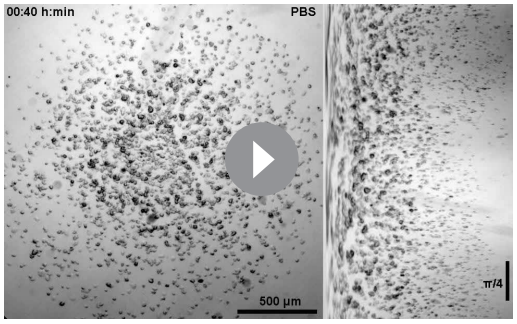

Video 6. Spot assay in phosphate buffer. Left: cell dynamics show the formation and migration of a ring of cells up to 4 hr at which point it started disintegrating and aggregates started forming around 10 hr. Right: polar visualization of cell dynamics with angles shown vertically and distance to the center horizontally. This visualization clearly shows the early propagation of a ring of cells.
https://elifesciences.org/articles/64731#video6

try $(\rho = \rho(t,r), C = C(t,r))$, neglecting thereby any curvature effects. We were interested in the study of a single front moving from left to right. Introducing the front speed σ, the front corresponds to a stationary solution in the moving frame $z = x - \sigma t$, that is, a traveling wave profile, satisfying:

$$-\sigma\frac{\partial\rho}{\partial z} = D\frac{\partial^2\rho}{\partial z^2} - \frac{\partial}{\partial z}(a(C,\partial_z C)\rho) + r(C)\rho \qquad (3)$$

In the general case, the theoretical analysis of such profiles and the determination of the front speeds σ seem out of reach due to the coupling with the reaction-diffusion equation on the O_2 concentration. Nonetheless, it is possible to derive simple relations between the shape of the wave and the speed of propagation. By integrating (***Equation 3***) over the line, we obtain:

$$\begin{aligned}(\sigma - a(C(-\infty),\partial_z C(-\infty)))\rho(-\infty)\\ = \int r(C(z))\rho(z)dz\end{aligned} \qquad (4)$$

This equation balances the net flux of cells to the far left-hand with the amount of mass created by heterogeneous (oxygen-dependent) cell division. We illustrated this relationship with the experimental data from ***Figure 1E***. In order to approximate the term $\int r(C(z))\rho(z)dz$, we used an observation that we made through numerical simulations: cell division stops roughly at half of the peak, meaning that cells left to the peak do not divide, while cells right to the peak continue dividing (see ***Figure 4E*** and ***Figure 6— figure supplement 1***). Therefore, we approximated by

A general framework for traveling waves in cells undergoing aerotaxis and division

From there onwards, we propose a mathematical framework that investigates general conditions under which collective behavior of cells undergoing cell division and aerotaxis is triggered. The aim was to confirm conclusions already obtained experimentally or through the cellular Potts model and to decipher the contribution of cell division to the collective behavior, while also keeping the framework relatively general such that it may be applied to other types of collective cellular behavior.

We first considered models of the form given by (***Equations 1 and 2***), independently of the exact shape of the advection term $a(C,\nabla C)$ or division term $r(C)$. Because of its relevance for the study of planar front propagation, we studied these models in a planar symmetry $(\rho = \rho(t,x), C = C(t,x))$ instead of a radial symme-

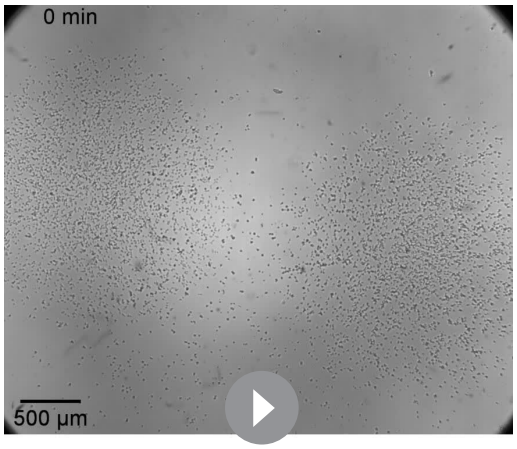

Video 7. Ring fusion during experiments (top) and as predicted by the Potts model (bottom). Note that this Potts model is a non-quantitative version and, as a result, space and time are in arbitrary units and thus not shown.
https://elifesciences.org/articles/64731#video7

a rectangle method $\int r(C(z))\rho(z)dz = \rho r_0 L/2$, where L is the length spanned by the ring and ρ is the average cell density in the ring. As there is supposedly no advection $a(C,\partial_z C)\rho = 0$ at $z = -\infty$ this yields the approximation $\sigma \approx \frac{r_0 L \rho}{2\rho(-\infty)}$. Quantitatively, we assume L to be on the order of 300µm (***Figure 1E***) and $\frac{\rho}{\rho(-\infty)}$, the ratio between cell densities in the ring and in the bulk of cells, to be on the order of 4 (***Figure 1E***). This yields an estimate of the wave speed, based solely on the shape of the cell density profile, of $\sigma \approx 0.9$ µm/min.

Mathematical analysis of the 'Go or Grow' hypothesis

The difficulty to study (***Equation 3***) analytically led us to propose a simpler version of the mean-field model that recapitulates the two key ingredients, cell division and aerotaxis, in an original way. Although it deviates from the reference Potts model in the details, it has the advantage of being analytically solvable. Cells have two distinct behaviors, depending on the O_2 concentration. Below a certain threshold C_0 cells move preferentially upward the oxygen gradient (go), with constant advection speed a_0, but they cannot divide. Above the same threshold they divide (grow) and move randomly without directional bias. This model may be considered as a strong simplification of (***Equation 1***), here restricted to the one-dimensional space, where:

$$a(C,\partial_x C) = a(C)sign(\partial_x C), \text{ with } a(C) = \begin{cases} 0, \text{ if } C>C_0 \\ a_0, \text{ if } C<C_0 \end{cases} \text{ and } r(C) = \begin{cases} r_0, \text{ if } C>C_0 \\ 0, \text{ if } C<C_0 \end{cases}. \quad (5)$$

The coupling between (***Equations 1 and 2***) then goes merely through the location of the oxygen threshold C_0. This elementary 'Go or Grow' model was meant to 1- demonstrate that its simple ingredients suffice to trigger a collective motion and 2- determine the relative contributions of cell division and aerotaxis on the speed of the ring in a general framework.

Interestingly enough, in this case (***Equation 3***) admits explicit traveling wave solutions (see more details in the Materials and methods section). Moreover, an explicit formula for the wave speed was obtained (***Figure 6C*** and Materials and methods for a detailed derivation):

$$\sigma = \begin{cases} a_0 + \frac{r_0 D}{a_0}, if\ a_0 \geq \sqrt{r_0 D} \\ 2\sqrt{r_0 D}, if\ a_0 \leq \sqrt{r_0 D} \end{cases} \quad (6)$$

To the best of our knowledge, this analytical formula is new and captures basic features of a wave under a single self-generated gradient. It is remarkable that Formula (***Equation 6***) does not depend on the dynamics of oxygen consumption and diffusion. Furthermore, Formula (***Equation 6***) presents a dichotomy according to the relative size of aerotaxis strength a_0 and the quantity $\sqrt{r_0 D}$: in the case of small-bias (*i.e.* $a_0 \leq \sqrt{r_0 D}$), the wave speed σ is independent of aerotaxis and coincides with the so-called Fisher's wave speed $2\sqrt{r_0 D}$. This speed is related to the Fisher-KPP equation (***Aronson and Weinberger, 1975***; ***Fisher, 1937***; ***Kolmogorov et al., 1937***), which describes front propagation under the combined effects of diffusion and growth (without advection). However, in the case of large-bias (*i.e.*, $a_0 > \sqrt{r_0 D}$), aerotaxis is strong enough to contribute to the speed and the wave speed increases $\sigma > 2\sqrt{r_0 D}$.

Based on these observations, we propose the fraction $\varphi = 2\sqrt{r_0 D}/\sigma$ as a measure of the relative contribution of cell division and diffusion to the overall wave speed. Indeed, when aerotaxis is absent (or as in the small-bias case not contributing to the wave speed), the value of φ is 1 and the wave is driven by cell division and unbiased random motion, that is, a reaction-diffusion wave. In the large-bias case, $1/\varphi$ describes how much faster the wave travels, compared to if it were only driven by diffusion and division. We illustrated the behavior of φ with a heatmap (***Figure 6D***) as a function of the parameters a_0 and $\ln(2)/r_0$ (the doubling time of the cell population), the diffusion coefficient being fixed to its experimental value D=30 µm^2/min.

We confront this reasoning with the experimental data: as a rough approximation with $a_0 = 1$ µm/min in experiments, assuming a doubling time of 8 hr for *Dd* cells, $r_0 = ln2/480$ min^{-1}, we are clearly in the case of large bias ($\sqrt{r_0 D} = 0.2$ µm/min) and (***Equation 4***) yields $\sigma = 1.04$ µm/min while the fraction $\varphi = 40\%$. The wave travels 2.5 times faster than a wave merely driven by cell division, showing that in this case the dominant ingredient to set the wave speed is aerotaxis. Still, our results can similarly be applied to other systems in which this balance could be different. Finally, note that the

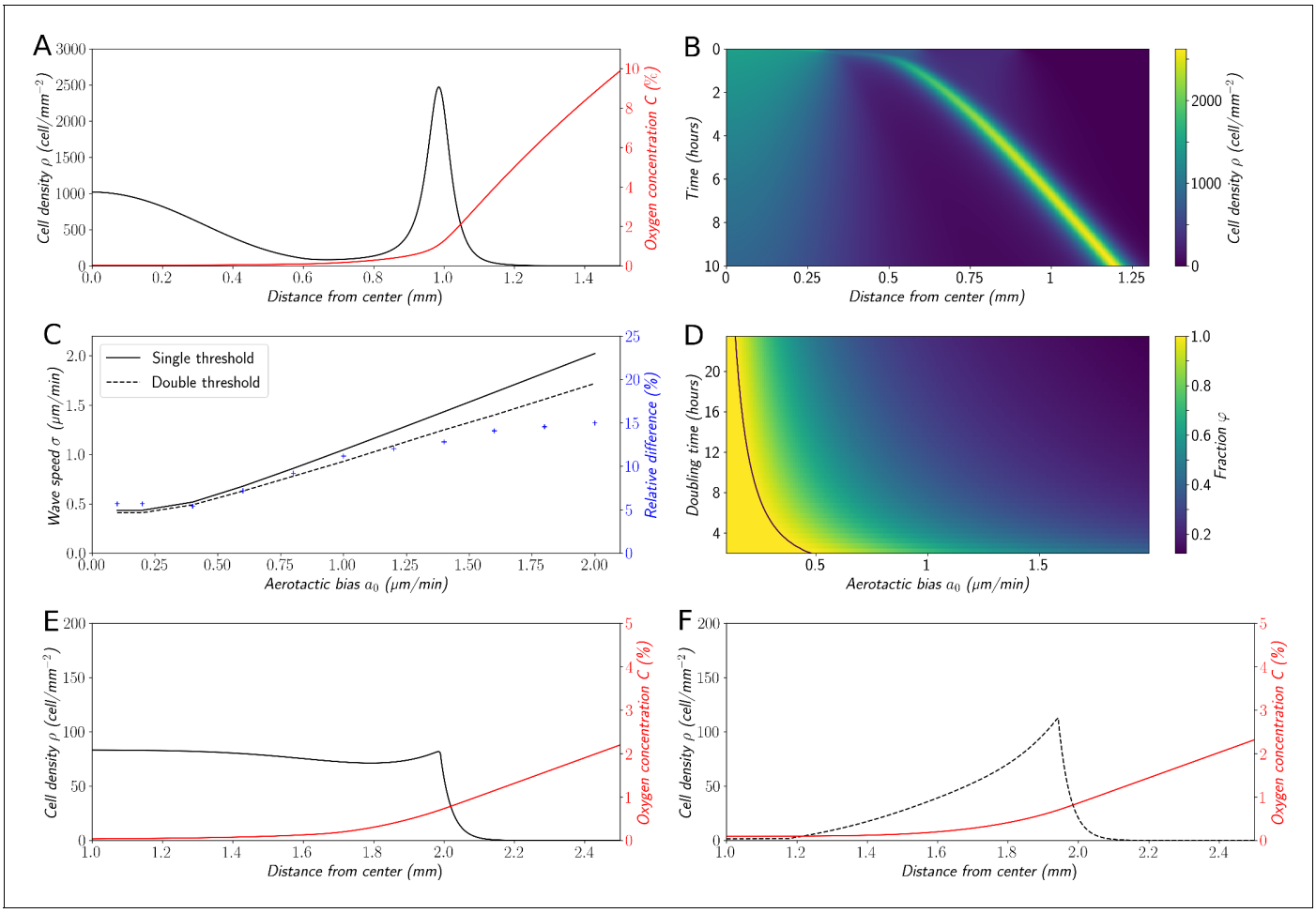

Figure 6. Variations on the 'Go or Grow' hypothesis. (**A**) Cell density and O_2 concentration profiles for the mean-field model (***Equations 1 and 2***). (**B**) Corresponding kymograph of cell density (colorbar in cells/mm^2) as a function of time and distance to the center. (**C**) Comparison of wave speeds for the elementary 'Go or Grow' model, given by Formula ***Equation 6***, and the 'Go or Grow' model with a second threshold, obtained by numerical simulation (solid and dotted lines respectively). The relative difference between the speeds of the two models is represented by crosses. (**D**) Heatmap of $\varphi = 2\sqrt{r_0 D}/\sigma$ as a measure of the relative contribution of cell division to the overall wave speed σ in the space parameter $\ln(2)/r_0$ and a_0 for the 'Go or Grow' model (***Equation 5***), where σ is given by Formula ***Equation 6***. The curve $a_0 = \sqrt{r_0 D}$ is depicted in black. (**E**) Cell density and O_2 concentration profiles for the 'Go or Grow' model with $a_0 = 1\,\mu m/min, r_0 = ln2/480 min^{-1}$ and $C_0 = 0.7\%$. (**F**) Cell density and O_2 concentration profiles for the 'Go or Grow' model with two thresholds: cells undergo aerotaxis with a constant advection speed $a_0 = 1 \mu m/min$ when the O_2 concentration is in the range (C_0', C_0) with $C_0 = 0.7\%$, $C_0' = 0.1\%$. In both cases, thresholds coincide with the cusps in the profiles.

The online version of this article includes the following source data and figure supplement(s) for figure 6:

Source data 1. Zip file containing raw data for ***Figure 6*** and associated Python code for simulations.

Figure supplement 1. Structural variations of (***Equation 1***).

Figure supplement 1—source data 1. Zip file containing raw data for ***Figure 6—figure supplement 1*** and associated Python code for simulations.

density profile of the model (***Figure 6E***) does not present a sharp front peak as in experiments (***Figure 1D,E***), Potts simulations (***Figure 3B,C***) or in the mean field model (***Figure 6A,B***). We will show below that it can be slightly modified to change the profile of the fronts while keeping the analytical results relevant thus describing a whole class of systems (***Figure 6E*** and ***Figure 6—figure supplement 1***).

Inside dynamics of the wave front

The wave speed of the elementary 'Go or Grow' model coincides with Fisher's speed, that is $\sigma = 2\sqrt{r_0 D}$, in the regime of small bias ($a_0 \leqslant \sqrt{r_0 D}$). This is the signature of a *pulled wave*,

meaning that the propagation is driven by the division and motion of cells at the edge of the front, with negligible contribution from the bulk, and little diversity in the expanding population. In contrast, when the bias is large ($a_0 > \sqrt{r_0 D}$) then the wave speed in (**Equation 6**) is greater than Fisher's speed. This is the signature of a *pushed wave*, meaning that there is a significant contribution from the bulk to the net propagation, with an expanding population maintaining diversity across expansion, see **Birzu et al., 2018**; **Stokes, 1976** for insights about the dichotomy between pulled and pushed waves. In particular, it was conjectured that the ratio $\varphi = 2\sqrt{r_0 D}/\sigma$ proposed above controls the transitions between different regimes of diversity loss in a wide class of reaction-diffusion models (**Birzu et al., 2018**; **Birzu et al., 2019**).

In order to explore this dichotomy between pulled and pushed waves, we used the framework of neutral labeling (**Roques et al., 2012**) in the context of PDE models. We colored fractions of the density profile during wave propagation to mimic labeling of cells with two colors. Then, we followed numerically the dynamics of these fractions, and quantified the mixing of the two colors. Our results were in perfect agreement with (**Roques et al., 2012**), extending their results beyond classical reaction-diffusion equations to equations which also include advection (see Materials and methods). In the case of large bias (**Figure 7A–C**), the wave is pushed and the profile is a perfect mixture of blue and yellow cells at long times. Contrarily, the wave is pulled in the regime of small bias: only cells that were already initially in the front, here colored in blue (**Figure 7B–D**), are conserved in the front, whilst yellow cells at the back cannot catch up with the front.

In the absence of associated experimental data, we explored the cellular Potts model with such neutral labeling. The results were in agreement with the PDE simulations (**Figure 7—figure supplement 1**) showing a clear, rapid mixing of the two cell populations under the propagation of a pushed wave in the regime of experimental parameter values.

Robustness of the conclusions to structural variations of the model

We voluntarily defined our elementary 'Go or Grow model' as a rough simplification of our original mean-field model in order to keep it solvable and extract a general formula for the front speed and an analysis of the relative contribution of diffusion/division and aerotaxis in that respect. However, many experimental systems will not conform to the hypothesis underlying this model (in particular the shapes of the aerotactic response and cell division modulation). In order to investigate whether the conclusions drawn from the elementary 'Go or Grow' model extend to more general situations, we decided to submit it to structural variations and check if the results obtained above still held. First, we made the hypothesis of a second oxygen threshold $C_0' < C_0$, below which cells are not sensitive to gradients any longer (**Figure 6F**). In the general case, we were not able to do a thorough analysis of this model, but through numerical exploration we found that the propagation speed remained close to the value given by formula (**Equation 6**) (at most 15% of relative difference in a relevant range of parameters, **Figure 6C**). Intuitively, the main contribution to the collective speed is the strong bias inside the high-density area at intermediate levels of O_2, whereas cells at levels below the second threshold C_0', where the dynamics of both models diverge, do not contribute much to the collective speed. We also noticed that cell density profiles (**Figure 6F**) were much closer to experimental observations and results obtained through the cellular Potts model or the original mean-field approach. Moreover, the wave speed is no longer independent of the oxygen dynamics. In the Materials and methods section, we pushed further the analysis with a specific form of oxygen consumption and developed a specific case of such a 'Go or Grow' model with a second threshold, where we were able to conduct its complete analysis. **Figure 7—figure supplement 2** shows that the conclusions concerning the contribution of growth to the wave speed are robust. Finally, we show on this modified 'Go or Grow' model that our conclusions regarding how the behavior can switch from a pulled to a pushed wave remain true as well (**Figure 7—figure supplement 3**) demonstrating that our results can be generalized to a variety of different systems showing the propagation of a front in response to a single self-generated gradient.

To go beyond this first variation with two oxygen thresholds, we also investigated the influence of the shape of the aerotactic response such as linear or logarithmic gradient sensitivity. **Figure 6—figure supplement 1** shows the qualitative outcomes of these different models. This numerical exploration indicates that a wide combination of the two key ingredients, aerotaxis and cell division, can drive the propagation of a stable wave with various density profiles. Cell division at the edge

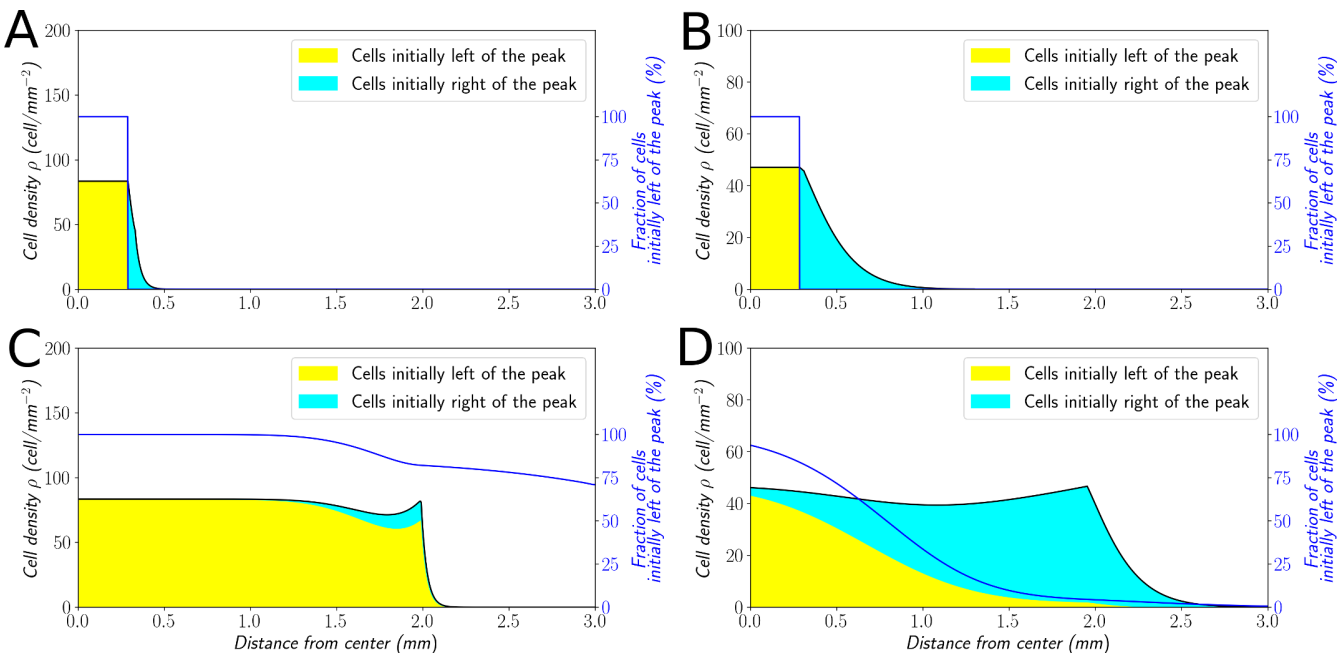

Figure 7. Classification of the expansion type in the 'Go or Grow' model. Cells initially on the left-hand side or right-hand side of the peak get labeled differently (**A** and **B**). The labeling is neutral and does not change the dynamics of the cells. We let evolve the two colored population for some time and observe the mixing of the colors (**C** and **D**). (**A** and **C**) With $a_0 = 1m \cdot min^{-1}$, the wave is pushed wave and after some time the front undergoes a spatially uniform mixing. (**B** and **D**) With $a_0 = 0.1\,\mu m \cdot min^{-1}$, the wave is pulled and only the fraction initially in the front is conserved in the front. $r_0 = ln2/480min^{-1}$ and $C_0 = 0.7\%$ for all conditions.

The online version of this article includes the following source data and figure supplement(s) for figure 7:

Source data 1. Zip file containing raw data for ***Figure 7*** and associated Python code for simulations.

Figure supplement 1. Mixing in Potts models.

Figure supplement 1—source data 1. Raw data for ***Figure 7—figure supplement 1***.

Figure supplement 2. Heatmap of $\varphi = 2\sqrt{r_0 D}/\sigma$ as a measure of the relative contribution of cell division to the overall wave speed σ in the space parameter $1/r_0$ and a_0 for the 'Go or Grow' model with a second threshold, under the specific condition that O_2 consumption term be $b(C) = b_0$ and that O_2 concentration may be negative (see Materials and methods).

Figure supplement 2—source data 1. Zip file containing raw data for ***Figure 7—figure supplement 2*** and associated Python code for simulations.

Figure supplement 3. Classification of the expansion type in the 'Go or Grow' model with a second-threshold.

Figure supplement 3—source data 1. Zip file containing raw data for ***Figure 7—figure supplement 3*** and associated Python code for simulations.

yields a net flux of cells, backward in the moving frame, that sustains the wave propagation in the long term, but may have a relatively small contribution to the wave speed.

Discussion

Overall, our results demonstrate the ability of Dd cells to respond to hypoxia through both aerotactic and aerokinetic responses. Both of these behaviors could be very important to help Dd cells to navigate complex hypoxic environments they encounter in the soil. In addition, our results are a confirmation of the ability of self-generated gradients to serve as very robust, long-lasting directional cues in environmental navigation, a property which has recently emerged in a variety of systems (***Cremer et al., 2019***; ***Tweedy and Insall, 2020***). Finally, our work goes beyond theses results as it demonstrates that oxygen can play the role of the attractant in self-generated gradients therefore potentially extending the physiological relevance of the use of such cues in collective migration.

In addition, although our experimental results were obtained on simple, 2d experiments, our findings can generalize to more complex cases. The fact that the dense front of cells follows a constant oxygen concentration (***Figure 3E***, ***Figure 4E***) provides a hint that any situation in which cell density

is locally high enough to trigger hypoxic conditions will also lead to a similar behavior. Then, depending on the dimensionality of the system, its architecture and the position of possible oxygen sources, we hypothesize that a similar front will develop and follow isoconcentration lines. Indeed, the original experiments of Adler (**Adler, 1966**) and more recent developments (**Cremer et al., 2019**; **Fu et al., 2018**; **Saragosti et al., 2011**) on bacteria demonstrated that similar ingredients as the ones presented here can lead to front propagation in both 1d and 2d situations. Similarly, using an under agarose assay, it was demonstrated that self-generated gradients of degraded folate induce a group migration of cells in bands (in 1D) or rings (in 2D spots) up to 4 mm (**Tweedy and Insall, 2020**). Beyond the dimensionality of the system, it was also shown that self-generated gradients allow cells to solve mazes by locally degrading an attractant that has a source at the exit of the maze (**Tweedy et al., 2020**). Our results are in total agreement with these past examples. To further show the generality of the underlying principles, we ran some 3D Potts simulations using a qualitative version of our model. Briefly, we show that in three dimensions, if oxygen is provided on all sides, a spherical front of cells starts moving outwards (**Video 8**). However, if we assumed that the bottom of the space was completely deprived of oxygen (i.e. a symmetry breaking situation that can be encountered in various physiological situations), this front was migrating upwards only in a half-spherical shape (**Video 8**). Our 2d results can therefore be extended to any other situations and they show that the key to proper steering are high enough cell densities and the creation of robust self-generated gradients.

While aerotaxis is well established for bacteria, its role is often invoked in multicellular organisms to explain various processes in development or cancer progression but very few *in vitro* studies were conducted to prove it is an efficient and operating mechanism or to understand the molecular mechanisms at play during aerotaxis. Deygas et al. showed that confined epithelial colonies may trigger a self-generated O_2 gradient and an aerotactic indirect response through a secondary ROS self-generated gradient (**Deygas et al., 2018**). Gilkes et al. showed that hypoxia enhances MDA-MB231 breast cancer cell motility through an increased activity of HIFs (**Gilkes et al., 2014**). HIFs activate transcription of the Rho family member RHOA and Rho kinase 1 (ROCK1) genes, leading to cytoskeletal changes, focal adhesion formation and actomyosin contractions that underlie the invasive cancer cell phenotype. This study suggests a role for aerotaxis in tumor escape, but it only demonstrates aerokinesis as O_2 gradients were not imposed to probe a directed migration toward O_2. Using a microfluidic device, the same cancer cell line was submitted to various oxygen levels as well as oxygen gradients (**Koens et al., 2020**) but the observed aerotactic response was not clear.

By contrast, the experimental results presented here with *Dd* show a strong response to hypoxia. Within 15 min, cells exhibit an aerokinetic and aerotactic response when exposed to externally imposed O_2 gradients (**Figure 2**). Self-generated O_2 gradients are produced within 20 min (**Figure 3** and **Figure 1—figure supplement 2**). But this cellular response is within the equilibration time of the oxygen distribution (**Figure 2—figure supplement 6**). Hence we can consider the cellular response as almost instantaneous with *Dd*. The difference with previously studied cells is probably due to the extreme plasticity of the rapidly moving amoeboid cells (*Dd*) and their almost adhesion independent migration mechanism (**Friedl et al., 2001**) while mesenchymal cancer cells move slower by coordinating cytoskeleton forces and focal adhesion (**Palecek et al., 1997**).

The quick response of *Dd* in directed migration assays has been largely exploited to decipher the molecular mechanisms at play during chemotaxis (**Nakajima et al., 2014**). The molecular mechanisms used for O_2 sensing and its transduction into cellular response are for the

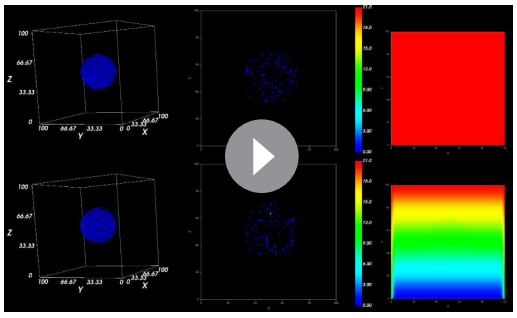

Video 8. 3D Potts simulations. Top : with oxygen sources on all sides. Bottom: with oxygen sources on all sides except on the bottom. The left column shows the behavior of the whole cell assembly in 3D (original cells are in blue, cells created during the process are shown in green). The middle column is an xz slice of the cell behavior to show that the 3d structures are indeed spheres or pseudo-spheres. The right column is the same slice as in the middle but showing oxygen profiles as a colormap.
https://elifesciences.org/articles/64731#video8

moment unknown but we can expect that the O_2 molecular sensors modulate cytoskeleton organization, particularly localized actin polymerization/depolymerization through some of the molecular components involved in classical chemotaxis toward folate or cAMP (**Pan et al., 2016**; **van Haastert et al., 2017**). However, new and unexpected mechanisms cannot be excluded.

The finding that migrating cells can influence the direction of their own migration by building chemoattractant gradients is not new. Several species of bacteria can move preferentially toward oxygen or nutrient as reported by **Adler, 1966**. However, this mechanism was only recently reported in eukaryotes (**Stuelten, 2017**): melanoma cells that break down lysophosphatidic acid (LPA) and generate a LPA gradient in the vicinity of the tumor (**Muinonen-Martin et al., 2014**), *Dd* colonies that generate folate gradients (**Tweedy et al., 2016**) or for the migration of the zebrafish lateral line primordium through a self-generated chemokine gradient (**Donà et al., 2013**; **Venkiteswaran et al., 2013**). The dispersal of melanoma cells is particularly instructive. The stroma surrounding the tumor acts as a source of LPA. The tumor cells act as a sink for LPA. As long as LPA is present in the environment a steady wave of migrating melanoma cells propagates away from the initial tumor over long distances and long time periods.

The self-generated LPA (melanoma) and folate (*Dd*) gradients were modeled with a simple numerical model that was able to predict the steady wave. In particular, it predicted an invasive front where cells are exposed to a steep chemoattractant gradient, followed by a 'trailing end' where the gradient is shallow and fewer cells migrate with poor directionality (**Tweedy and Insall, 2020**). It also predicted that the wave may have a less marked front, and/or a smaller speed, or even vanishes if the cell density was too low due to insufficient chemoattractant removal. All these features are surprisingly similar to our experimental measurements of cell density and O_2 profiles (**Figure 1E**, **Figure 3C**). The atmospheric O_2 that diffuses through the culture medium and eventually the plastic surfaces is the chemoattractant. The O_2 consumption triggers hypoxia that in turn generate an aerotactic response toward O_2 in a very narrow range of O_2 concentrations (0–1.5%) (**Figure 3C**). The exact value of the lower O_2 threshold value will deserve future investigations. The exact nature of the cellular response at these extremely low O_2 levels, and in a very shallow gradient, also has yet to be clarified.

Our different models unveil a set of basic assumptions which are sufficient for collective motion of cells without cell-cell interactions (attractive or otherwise), in contrast with (**Sandonà et al., 1995**). Cell growth is necessary to produce a long-standing wave without any damping effect. However, it may not be the main contribution in the wave speed, depending on the relative ratio between directional motion (the bias a_0), and reaction-diffusion (the Fisher half-speed $\sqrt{r_0 D}$). In the case where the former is greater than the latter, the wave is due to the combination of growth and directional motion and it is pushed. This result differs particularly from the Fisher-KPP equation with constant advection (meaning with uniform migration and division) where the wave speed is $a_0 + 2\sqrt{r_0 D}$ and the wave is pulled. In the experiments under study, we estimate directional motion to contribute the most to the cell speed, ruling out the possibility of seeing a pulled wave driven by cell division and diffusion at the edge of the front.

In conclusion, we demonstrate the remarkable stability of collective motion driven by self-generated gradients through depletion of oxygen. Through coupled dynamics, these gradients give rise to long lasting, communication-free migrations of entire colonies of cells which are important both from ecological and developmental points of view. In the case presented here where oxygen plays the role of the depleted attractant, this could prove to be a very general mechanism as oxygen is ubiquitous and always consumed by cells.

Materials and methods

Cell preparation

The AX2 cell line was used and cultured in HL5 media (Formedium, Norfolk, UK) at 22˚C with shaking at 180 rpm for oxygenation (**Sussman, 1987**). Exponentially growing cells were harvested, counted to adjust cell density to the desired one, typically 2000 cells/µL.

Observations and analysis of self-generated aerotaxis by cell confinement (spot assay)

For the spot assay, 1 µL of cell suspension containing 1000–8000 cells (typically 2000) was carefully deposited on a dry surface using a 1 µL syringe (Hamilton, Reno, NV, USA). The dry surface was either the nunclon treated surface of Nunc six wells polystyrene plates for usual experiments (ThermoFisher Scientific, Waltham, MA, USA) or polydimethylsiloxane surface (PDMS, Sylgard 184, Dow Corning, Midland, MI, USA) for experiments on oxygen-sensing films. The drop was incubated for 5 to 7 min in humid atmosphere at 22˚C before gently adding 2 ml of HL5 medium without detaching the spotted cells forming a micro-colony. A 14 mm or 18 mm diameter round glass coverslip cleaned in ethanol, thoroughly rinsed in HL5 was kept wet and deposited on top of it. In some experiments, fluorescein FITC at 16 µM was added to the HL5 medium and confocal slices were taken, showing that confined *Dictyostelium* cells were not compressed by the coverglass but separated from it by a layer of medium of about 50 µm (***Figure 1—figure supplement 1***).

The outward spreading of the *Dictyostelium* micro-colony was observed at 22˚C in transmission with three types of microscope: (i) a TE2000-E inverted microscope (Nikon, Tokyo, Japan) equipped with motorized stage, a 4x Plan Fluor objective lens (Nikon) and a Zyla camera (Andor, Belfast, Northern Ireland) using brightfield for most of the experiments lasting 16 hr (***Figure 1A***), (ii) a binocular MZ16 (Leica, Wetzlar, Germany) equipped with a *TL3000 Ergo* transmitted light base (Leica) operated in the one-sided darkfield illumination mode and a LC/DMC camera (Leica) for experiments over days (***Figure 1B***) and finally (iii) a confocal microscope (Leica SP5) with a 10x objective lens for a few larger magnification experiments (***Figure 1C***).

For computing densities, cell positions were determined using the built-in Find Maxima plugin in ImageJ (National Institutes of Health, Bethesda, MD, USA) through a custom made routine. Data analysis and plotting was performed in Matlab (Mathworks, Natick, MA, USA). For density profiles (***Figure 1E***) and kymographs (***Figure 1D***), the center of the colony was defined as the center of mass of all cells detected at all times. Cell positions were then turned into radial coordinates and cells were counted within concentric crown regions. Densities were calculated by dividing this count by the area of each crown.

Density profiles such as the ones showed in ***Figure 1E*** were treated to automatically extract the position, width and density of a ring in various experiments and at various time points. Density profiles were first stripped of values lower than 500 cell/mm^2 in order to avoid asymmetric baselines behind and in front of the ring. Resulting profiles were then fitted in Matlab by a Gaussian function with a non-zero baseline. The non-zero baseline corresponds to density in the bulk, the maximum of the Gaussian gives ring position, its height added to the non-zero baseline gives the cell density in the ring and its width the width of the ring.

Cell tracking, diffusion coefficients, and aerotactic biases

After retrieving cells' positions with optimized ImageJ macros based on Find Maxima, the individual trajectories were reconstructed with a squared-displacement minimization algorithm (http://site.physics.georgetown.edu/matlab/). Data were analysed using in-house Matlab programs. Timelaspse microscopy experiments devoted to cell tracking in the spot assay experiments was acquired at a high frame rate (1 frame every 15 s) (***Figure 1—figure supplements 4–5***) due to the very high cell density in the ring region (up to 2000 cells/mm^2, ***Figures 1E*** and ***3C***). For the microfluidic experiments, as cells were plated at a lower density (less than 200 cells/mm^2), 1 min time intervals was used to track cell trajectories (***Figure 2C***). In order to highlight aerotactic biases, cells displacements over various time lags *dt* (*dt* up to 60 min) were projected in the radial direction for spot assays and in the gradient direction X for microfluidic experiments and eventually divided by *dt* to obtain velocity biases. Individual biases were then averaged within bins of equal distance (***Figure 2D***, ***Figure 1—figure supplement 5***, ***Figure 4—figure supplement 1***). Individual effective cell diffusion constants were measured as the square of their displacement over their entire trajectory divided by the trajectory time length and divided by 4. These measurements were then similarly averaged over bins (***Figure 1—figure supplement 4***).

Microfluidic-based oxygen gradient generator: design, fabrication, and cell injection

A schematic of the present double-layer microfluidic device is shown in ***Figure 2A***. It is made of several layers of PDMS mounted on a bottom glass coverslip. The overall diameter *D* of the microfluidic device is 27 mm and the overall thickness *H* is 4 mm. Three parallel media channels are positioned for cell culture, and two gas channels are positioned at a height H_g=0.5 mm above the media channels to allow gas exchange between the channels during cell culture. The horizontal distance between the two gas channels narrows step-by-step (2 mm, 1 mm, and 0.5 mm gaps, respectively), thus yielding to generate different gradients of oxygen concentration along the media channels simultaneously. All channels are 125 µm high and 2 mm wide, and therefore, the media and gas channels are separated by a PDMS wall of 375 µm thickness. A polycarbonate (PC) film (26 mm in diameter and 0.5 mm thickness) is embedded inside the device at a height *H*f=1 mm from the bottom coverslip to prevent oxygen diffusion from the atmosphere. The cartesian coordinate origin was set at the center of the media channel (median axis), and the *x* and *y*-directions were defined as parallel to media and gas channels respectively (***Figure 2A***). The *z*-direction was set to the vertical direction from the top of the bottom coverslip.

The manufacturing steps are as follow. The media channel and gas channels were drawn with AutoCAD (Autodesk, Mill Valley, CA, USA) and replicated in SU-8 photoresist using classical photolithography techniques. These SU8 molds were silanized to make it non-adherent and reusable. PDMS was mixed at a 10:1 ratio of base:curing agent, poured over each mold to a thickness of H_g, and cured in an oven at 60˚C for more than four hours. On top of the cured PDMS layer of the gas channels, the above-mentioned PC film with 3 mm port holes punched at the locations of the media and gas channel ports was positioned. Additional PDMS was then poured over the PC film until the total PDMS layer became 3.5 mm thick, then the PDMS layer was cured in an oven at 60˚C overnight. The PDMS layers of the media and gas channel patterns were peeled off the silicon wafers and cut into 27 mm diameter circles. The PDMS layer with the gas channel pattern was punched to form inlets and outlets 2 mm in diameter to allow the infusion of gas mixtures. The channel-patterned surface of the PDMS layer with the gas channels and the top surface of the other PDMS layer with the media channels were plasma treated (PDC-001-HP; Harrick Plasma Inc, Ithaca, NY, USA) to bond with each other. After incubating the bonded PDMS mold overnight in an oven at 60˚C, 2 mm diameter inlets were punched to allow access to the media channels, respectively. Finally, the channel-patterned side of the PDMS mold and a 35 mm-diameter glass bottom dish with or without covered by an oxygen sensing film were plasma treated and bonded each other.

Measurements of aerokinesis in homogenous environments were performed using a homemade glass-duralumin environmental chamber to perform random motility assays (***d'Alessandro et al., 2018***; ***Golé et al., 2011***).

Dictyostelium cells were seeded in the media channels at density of $2x10^6$ cells/ml, and the cell culture medium was filled in the glass bottom dish up to the height covering the PDMS mold. Cells were allowed to adhere to the bottom surface (bare glass or coverglass covered with a sensing film) for 15 min.

Gas control and injection

We used a controlled oxygen concentration for three types of experiments: (i) to calibrate oxygen sensing films (see below), (ii) to create the oxygen gradients within microfluidic devices (see below) or (iii) to insure a pure hypoxic condition (pure N_2) at the end of the spot assay experiment. The gas mixture (0% to 21% O_2 in N_2) was prepared in a gas mixer (Oko-lab 2GF-MIXER to mix compressed AIR with 100% N2 or HORIBA STEC MU-3405, Kyoto, Japan to mix pure O2 and N2) by mixing pure O_2 (or air) and pure N_2. Free sensing films for calibration (i) or for the spot assay (iii) were placed inside 6-wells plates and the multiwells were placed in an environmental chamber fitting our microscope stage (H301-K-frame, Okolab, Pozzuoli, Italia). Gas was injected at about 500 mL/min in this chamber. Eventually, multi-wells were drilled to a diameter of 25 mm and the sensing films were glued with a silicone adhesive on the plate bottom to reduce the background noise from fluorescence. For microfluidic experiments, the tubes from the mixer were connected to the gas channels and gas was injected at a controlled flowrate (between 60 and 180 mL/min) into the device.

Oxygen-sensing film preparation

Oxygen-sensing films were prepared by inserting the luminescent O_2-sensitive dye 5,10,15,20-Tetrakis-(2,3,4,5,6-pentafluorophenyl)-porphyrin-Pt(II) (PtTFPP, Por-Lab, Porphyrin-Laboratories, Scharbeutz, Germany) in a 4:1 PDMS:curing agent thin layer spin-coated on 30 mm to 35 mm rounded coverglasses. Briefly, 17 mg of PtTFPP was dissolved in 5 mL chloroform and thoroughly mixed with 2.8 mg of PDMS and 0.7 mg curing agent. The mixture was degassed in a vacuum chamber for 5 hr. About 0.5 mL to 1 mL of this solution was spread on the coverglass and spin-coated for 2 min at 500 rpm with a final speed of 2000 rpm during 10 s to flatten the edge bead. Chloroform was allowed to evaporate overnight while the polymer cured at 60˚C. The final PtTFPP sensor film had a dye concentration of 4 mmol/L and was 25 µm thick. This thickness was measured using a ContourGT-K 3D Optical microscope (Bruker, Billerica, MA, USA) after removing a piece of film with a surgical blade. Sensing films were stored in dark. They were used to measure the oxygen concentration in self-generated O_2 gradients (spot assay) and for microfluidic experiments with controlled O_2 gradients.

Fluorescence microscopy for oxygen measurements

Fluorescence images of O_2-sensing films (either for film calibration or for in situ oxygen measurements in the spot assay or in microfluidic devices) were taken with two inverted epifluorescence microscopes: (i) a TE2000-E inverted microscope (Nikon) equipped with motorized stage, a 4x Plan Fluor objective lens (Nikon), a X-Cite Series 120PC illumination lamp, a TRITC bandpass filter cube and a Zyla camera (Andor) (***Figure 3Aii***, ***Figure 2—figure supplement 3***), (ii) a IX83 inverted microscope (Olympus, Tokyo, Japan) equipped with a motorized stage, a UPlanSApo 4x objective lens (Olympus), a U-HGLGPS lamp (Olympus), a RFP bandpass filter and a Zyla camera (Andor). This second microscope was used for mosaic imaging, in order to scan the whole dimension of the three media channels (about 1 cm in length) thanks to the dedicated imaging software cellSens (Olympus) (***Figure 2—figure supplement 1***).

Oxygen-sensing film calibration

Calibration was carried out with the sensing films in air, in water or in HL5 culture medium. We applied gas concentration ramps with steps of 5 min for calibration in air (time to exchange fully the gas composition of the chamber and tubes, as O_2 almost instantaneously diffuses within the 25 µm thick sensing film) and with much longer steps (i.e. 2–4 hr) for calibrations in liquid. There is indeed an additional diffusion time in the PDMS intermediate layer of our microfluidic devices or in the medium height of a Petri dish: typically, a few minutes for a 0.5-mm-thick PDMS layer and 1h30 for a 2.7-mm-thick liquid layer in a dish.

Timelapse fluorescence images we recorded and signal intensity I was measured in ROIs of typically 64x64 pixels in various positions of the image, especially along a line scanning the middle of the image (***Figure 2—figure supplement 1B***, ***Figure 2—figure supplement 3A***). The response of the sensing film in the presence of oxygen can be modeled by a linear Stern-Volmer relationship:

$$\frac{I_0 - B_g}{I(C) - B_g} = 1 + KC$$

where C is the oxygen concentration expressed as a percentage of oxygen in the injected gas phase (nearly 21% for atmospheric conditions), I_0 is the reference intensity in the absence of oxygen, B_g is the background intensity independent from the oxygen sensitive signal of the PtTFPP molecules and K is the Stern-Volmer constant used as an indicator of the sensing film sensitivity.

Notice that the background is usually not included in the Stern-Volmer relationship but a representative background image (O_2 independent) is subtracted prior to intensity measurements (***Nock et al., 2008***; ***Thomas et al., 2009***). This O_2-independent background value can be deduced from the fluorescence of a plain PDMS film prepared in the same conditions than the sensing film but devoid of PtTFPP molecules (i.e. a standard) (***Thomas et al., 2009***). We tested that procedure that is basically working but we choose to include the background as a fitting parameter because illumination conditions may change between the sample and the standard (especially the focus plane that affects the focused height of autofluorescent medium above the surface). The slight changes in thickness and PtTFPP composition of sensing films at the large spatial scales we are interested here (3–6 mm wide images, ***Figure 2—figure supplement 1A–D***, ***Figure 2—figure supplement 3A–C***)

are another source of heterogeneity especially for the K value. For those reasons, we apply the Stern-Volmer relation with K and B_g as a fitting parameters in many different small regions of interest (ROI) of the surface. For each ROI, we found that the measured intensities follow perfectly the Stern–Volmer relation (i.e. C linearly increases with the Stern-Volmer parameter $(I_0\text{-}B_g)/(I(C)\text{-}B_g)-1$, ***Figure 2—figure supplement 2B***) and that K and B_g are clearly uncorrelated, in particular B_g depends on the illumination pattern but not K.

The illumination pattern is clearly visible on fluorescence images at 21% O_2. For instance, the large field of view of ***Figure 2—figure supplement 1B*** reconstituted by the multi-area module of the microscope displays an up and down landscape in the 21% intensity (***Figure 2—figure supplement 2C***) due illumination changes in the periphery of each overlapped area but also due to the slightly different fluorescence in the gap region of the microfluidic device and especially at its interfaces. The single large field of view of ***Figure 2—figure supplement 3A*** taken with our second microscope setup displays a dome shaped pattern with 20% intensity difference between the center and borders (***Figure 2—figure supplement 3D***). The background value B_g is very correlated with the 21% signal variations in both imaging configurations (***Figure 2—figure supplement 2C***, ***Figure 2—figure supplement 3D***) and we can for each experiment calibrate a linear relationship between between B_g and $I(21\%)$ (***Figure 2—figure supplement 2D***, ***Figure 2—figure supplement 3F***).

As already stated, the background is due to the autofluorescence of the various media (PDMS layer and coverglass for the sensing film, bottom plastic dish if any, and surrounding fluid). For ***Figure 2—figure supplement 1***, the microfluidic device was filled with pure water and for ***Figure 2—figure supplement 3***, the calibration was performed in the autofluorescent HL5 medium before spotting the cells. Sometimes the sensing film was placed in a non-drilled well and in that case the strong autofluorescence of the plastic bottom of the plate becomes a major source of background (not shown). Finally, B_g also includes the read noise RN of the camera which is a constant independent of the light output or exposure time. For ***Figure 2—figure supplement 2***, we measured RN=108 A.U. and hence a light background $B_g^* = B_g\text{-}RN$=15 A.U. which is half the 'true oxygen dependent signal' at 21% O_2, $I(21\%)\text{-}RN$=30 A.U. The maximum deviation of B_g from the linear fit in ***Figure 2—figure supplement 5D*** is about 1.5 A.U. Hence a relative error 1.5/15=10% for B_g^* will be taken in the following. For ***Figure 2—figure supplement 3***, we measured RN=100 A.U. and at the top of the bell curve, B_g^*=1400–100=1300 A.U. while $I(21\%)^*$=1600–100=1500 A.U. (***Figure 2—figure supplement 3D***). Hence, the background is nearly 87% of the signal due to the HL5 autofluorescence. Nevertheless, the maximum relative deviation from the linear fit is smaller at about 25/1300 ≈ 2% of B_g^*. All these values will be used for the error analysis of the oxygen profiles below.

For uncovered (free) sensing films the sensibility K ranges between 3 and 5 $\%^{-1}$ and is very constant, weakly dependent on the illumination pattern (***Figure 2—figure supplement 2D*** and blue points in ***Figure 2—figure supplement 3E***). When films are covered with a coverglass, the fluorescence under hypoxic conditions (0%) increases significantly on the covered region (***Figure 2—figure supplement 3C***) but not at 21% (***Figure 2—figure supplement 3B***). As a results, K, which is proportional to this ratio, increases significantly (***Figure 2—figure supplement 3E***) but not B_g and I(21%) (***Figure 2—figure supplement 3D***) confirming that K and B_g are independent. This increase in K is probably due to a local temperature increase: the coverglass adsorbs more heat from the microscope illumination light and this heat is difficult to evacuate due to the confinement. In principle, for the spot assay experiment, it would be necessary to perform an independent calibration with the Stern-Volmer relation in the covered situation. However, this is difficult due to the very long time required to equilibrate the oxygen level under the confinement far from the coverglass boundary (this is why we started the Stern-Volmer fit at ROI_7 in ***Figure 2—figure supplement 3B,D,E***). A too long procedure causes other problems such as medium evaporation, stage or focus drift... To avoid that, we decided to apply the protocol described in the image analysis pipeline of ***Figure 2—figure supplement 4***. First, we perform a gas calibration ramp and do a Stern-Volmer analysis in various points of an uncovered sensing film (the subscript U is for uncovered) where I_{0U} is reliable in order to get the linear background relation $B_{gU}=\alpha\ I(21\%)_U+\beta$ and to measure the measure the ratio $R=I_{0U}/I(21\%)_U$. Reliable means here any point if gas mixture is applied uniformly when calibrating in a dish or just underneath the gas channel in microfluidic devices. Second, we choose the reference fluorescence image $I(21\%)$ immediately before starting any experiment (i.e. just after covering the spot, or just before applying the gradient in the gas channels). From that image, we build a B_g image as $\alpha\ I$

(21%)+β (as B_g is the same for uncovered and covered case) and eventually we build a reconstituted I_0 image as *R I(21%)*. Finally, we subtract and divide images with the 'Image calculator' of ImageJ (i.e. pixel by pixel) following the Stern-Volmer model and hence get a *K*-value image map and subsequently an oxygen map (***Figure 2—figure supplement 4C–D***). This enables to correct non-homogeneous illumination conditions or non-homogeneous sensing film properties as well to quickly estimate error bars on the oxygen map from the estimated errors on B_g, *I(21%)* and I_0 detailed below.

We already discussed the error on the background. In principle, *I(21%)* is a reference image (hence error free), however as an experiment (especially the spot assay) may run overnight we need somewhere to evaluate drift in the absolute intensity for instance by running an overnight timelapse experiment with a sensing film under ambient gas conditions. This error is added on *I(21%)* and was estimated as 2% of the true fluorescence signal corrected from read noise *I(21%)-RN*. Error on I_0 could be much larger. As the intensity *I(C)* is strongly nonlinearly increasing with the oxygen concentration *C*, if we measure an intensity I_0* corresponding to a residual small oxygen level C_0*, we need to correct the true I_0 value using the relation $I_0 - B_g \approx I_0 \approx I_0\left(1 + KC_0\right)$. Due to oxygen leakage along tubes and within our environmental chamber, when applying 100% N_2, we measured a residual $C_0 \approx 0.15$ O_2 in a culture medium dish using a bare fiber oxygen sensor coupled to its commercial oxymeter (Firesting, Pyroscience, Aachen, Germany). Hence with a typical *K*=5 value, we obtain a very large discrepancy between the measured fluorescence I_0* and the ideal one: $I_0 \approx 1.75 I_0$, but finally this discrepancy is not really dramatic on the measured error again due to the non-linearity.

The effect of these different error sources on the measured oxygen map is presented in ***Figure 2—figure supplement 1E*** and ***Figure 2—figure supplement 3H*** for a typical microfluidic and spot experiments. Even if we make a 1.75 error on I_0, this has little effect on the profiles except in the very hypoxic region when C<0.25% where the error exceed 50%. But even in the region around C=1%, the error is less than 10%. The error on *I(21%)* on the other hand has a significant effect on the high oxygen regions but less on the hypoxic regions. Finally, the background error is relatively visible in the intermediate oxygen concentration region (very visible on the side of the spot in ***Figure 2—figure supplement 3H***, but also to some extend around the median axis at C~10% in the microfluidic experiment, ***Figure 2—figure supplement 1E***). Finally, we defined error bars with *(max-min)/2* values of the calculated *C* when exploring the estimated errors discussed above. In the 0.5–1.5% region were we observe most of the interesting aerotactic behaviors with *Dictyostelium* cells, the precision on the oxygen concentration $\Delta C/C$ is less than 0.3. For the purpose of this paper, we can conclude that aerotaxis and aerokinesis occurs undoubtedly between *C*=0% and *C*=2% (***Figure 2***).

Numerical simulation of oxygen tension. Oxygen tension inside the device was computed using commercial finite element software (COMSOL Multiphysics 5.5; COMSOL, Inc, Burlington, MA, USA). The gas flow in the individual channels were simulated by solving the Navier-Stokes equations coupled with mass continuity for an incompressible fluid:

$$\rho_G(\boldsymbol{u}\cdot\nabla)\boldsymbol{u} = \mu_G\Delta\boldsymbol{u} - \nabla\boldsymbol{p},$$
$$\rho_G\nabla\cdot\boldsymbol{u} = 0,$$

where u is the velocity vector, *p* is the pressure, and ρ_G and μ_G are the gas density and viscosity (taken as 1 kg/m^3 and 10^{-5} Pa.s, respectively). The spatial and temporal distribution of oxygen inside the device was then calculated by solving the convection-diffusion equation:

$$\frac{\partial \boldsymbol{c}}{\partial \boldsymbol{t}} = \boldsymbol{D}\boldsymbol{c} - \boldsymbol{u}\cdot\nabla\boldsymbol{c},$$

where *c* is the oxygen concentration, *D* is the diffusion coefficient of oxygen, and *T* is the time.

The device was assumed to be in an atmosphere containing 21% O_2. Medium at 21% O_2 concentration was supplied to media channels. Gases containing 0% and 21% O_2 were respectively supplied to the left-hand and right-hand side gas channels at 30 ml/min to generate an oxygen gradient. Zero pressure and convection flux conditions were set at the outlets of the gas channels, and a no-slip condition was applied on the channel walls for fluid flow analysis. Boundary conditions for oxygen concentration were set according to Henry's law. Oxygen concentration at the interfaces between the PDMS and gas phase (atmosphere and gas mixture in the gas channel) was set

correspondingly to the product of the solubility coefficient of oxygen in PDMS and the partial pressure of oxygen. At the interfaces between PDMS and media or gel, a partition condition was applied, which balanced the mass flux of oxygen to satisfy continuity of partial pressure of oxygen:

$$\frac{c_{PDMS}}{S_{PDMS}} = \frac{c_{channel}}{S_{channel}},$$

where c_{PDMS} and S_{PDMS} are the oxygen concentration and the solubility of oxygen in the PDMS, respectively, and $c_{channel}$ and $S_{channel}$ are those in the media and gel channels. Moreover, oxygen consumption by cells was considered by setting an outward flux of oxygen of $6x10^{-8}$ [mole/(m^2.s)] on the bottom of the media channels (calculated as $b\rho^*$ where $b=1.2.10^{-16}$ mole/(cell.s) is the oxygen molar consumption per *Dd* cell per unit of time (***Torija et al., 2006***) and ρ^*=500 cell/mm^2 is the highest density used in the device).

The diffusion constants of oxygen in the various media were taken to be 2.10^{-9}, $4.1.10^{-9}$ and 2.10^{-12} m^2/s for culture medium, PDMS and PC, respectively. Oxygen solubility at 1atm were taken to be 219 (close to the measured value, see below), 1666 and 1666 µM for culture medium, PDMS and PC, respectively (PDMS and the PC values were assumed to be the same since they are reportedly within the same range ***Merkel et al., 2000***; ***Moon et al., 2009***). The computational models consisted of approximately 1,135,000 computational elements. The initial condition of oxygen concentration in each material was set to 21% O_2 everywhere (219 µM).

Potts models

Potts model simulations were run using CompuCell3D (***Swat et al., 2012***) with a mix of prebuilt modules and home-made Python steppables in particular to implement the modulation of aerotactic strength by local oxygen levels. Most parameters were fitted to experimental measurements and both time and length scales were also adapted to achieve quantitative simulations. In all simulations, we used Compucell's Volume module which applies to all cells a Hamiltonian of the form:

$$H_{volume} = \lambda_v (V - V_{cell})$$

where V is the volume of a cell and V_{cell} a target volume set to 2 pixels. This already set the length scale of our simulations to 1pixel = 10µm. λ_v was set to 800. These values were adapted to reproduce the cell speeds observed in the microfluidic experiments. To achieve this relationship, we also decided to fix that one step of the simulation (Monte Carlo Step) was meant to represent 0.1s.

Aerotaxis was modeled using CompuCell's built-in chemotaxis plugin. This leads to a new term in the Hamiltonian of the form

$$H_{chemotaxis} = \lambda_{aero} \Delta C$$

where ΔC is the difference in oxygen concentration C between the source and target pixels of a flip and λ_{aero} is the aerotactic strength. Key to our model is thus the fact that we made λ_{aero} different for each cell and dependent on the local oxygen concentration. This modulation was fitted to the microfluidic experiments and set, in the general model as:

$$\lambda_{aero}(C) = \frac{800}{1 + e^{\frac{C-0.7}{0.2}}}$$

where C is the oxygen concertation at the center of mass of a cell. ***Figure 5*** shows variations on that relationship which are:

$$\lambda_{aero}(C) = \frac{1225}{1 + e^{\frac{C-0.7}{1.5}}}$$

Based on experimental observations, we also made the effective temperature of the model different for each cell and dependent on local oxygen concentrations. This allowed us to reproduce the aerokinetic effect and the modulation of the temperature was fitted to reproduce the cell diffusion constants measured in the microfluidics experiment. The main model thus uses the following relationship for temperature T

$$T(C) = 85 + \frac{105}{1 + e^{\frac{C-0.7}{1}}}$$

Figure 5 and ***Figure 5—figure supplement 1*** show variations on this relationship, which is simply replaced by a constant value of T (115, 135 or 155).

Another key aspect of the models is the oxygen field, which is implemented using CompuCell's DiffusionSolverFE module. In the case of the microfluidics experiments, the oxygen field was made to be constant (no diffusion, no consumption by cells) and fitted on experimental measurements of this gradient shown in ***Figure 2B***. The oxygen concentrations were expressed in % giving 0 and 21 as natural boundaries. The actual oxygen profile varied in the x direction only as:

$$C(x) = \frac{21.38}{1 + e^{0.031*(x-200)}}$$

where *x* is the position in pixels in the simulation which was run on a 400 by 800 *xy* grid.

For spot assays, oxygen was allowed to diffuse freely. In our time and length units, the diffusion constant of oxygen in liquids (2.10^3 $\mu m^2.s^{-1}$) is two $pixel^2$ $step^{-1}$.

In terms of consumption, we took the oxygen consumption by Dicty cells to be $1.2.10^{-16}$ mole/(cell.s) (***Torija et al., 2006***) and we measured the oxygen solubility in HL5 medium as 250 µM (measurement with a bare fiber sensor plugged to a a Firesting oximeter, Pyroscience, Germany). Taking the measured vertical confinement of 50 µm (***Figure 1—figure supplement 1***), the amount of oxygen available, at maximum, above a single pixel of the simulation is $1.25.10^{-15}$ moles, which we define, in arbitrary units, to be 21. We can then turn the consumption of a single cell into a consumption per pixel given that the typical size of a cell is two pixels and per time step, each representing 0.1 s. We end up with a consumption, in our arbitrary units of 0.1 $pixel^{-1}$ $step^{-1}$ which is only applied to pixels occupied by a cell. Of note, in case an occupied pixel had a remaining oxygen level of less than this values, then consumption was set at this oxygen level so that all oxygen was consumed. The last ingredient in oxygen dynamics is the leak of oxygen coming from the bottom of the multiwall plate. Assuming complete hypoxia on the cells' side, this would lead to a net flux of oxygen of *DC/e* where D is the oxygen diffusion constant in polystyrene, C is the oxygen concentration on the outside and e is the thickness of the polystyrene bottom. This leads to a flux by unit surface, in our Potts units of 0.001 $pixel^{-1}.step^{-1}$. We therefore implement a source of oxygen for all pixels in the simulation, whether they are occupied by a cell or not, of the form:

$$secretion(C) = 0.001\frac{21 - C}{C}$$

where C is the local oxygen concentration at the considered pixel.

This was sufficient to faithfully reproduce the formation time of the rings. Finally, the spot simulations were run on a 500 by 500 pixels grid and we imposed boundary conditions to the oxygen field as a constant concentration of 21, the borders acting as a source of oxygen just like the edges of the coverslip in the experiments.

Cell division was also set to experimental observations. Given a doubling time of 8 hr, we implemented random divisions at each time point, each cell having a 1/ (8h * 3600 s/h * 10step/s) = 3.10^{-6} chance of dividing. However, cell division was turned off at low oxygen concentrations (<0.7%). In ***Figure 5***, a simulation is shown were this probability was set to 0 for all cells in all conditions.

In terms of initial conditions, the microfluidic simulations were started from a homogenous cell density, each cell being initialized on a grid: two pixels per cells and a six pixel gap to the next neighbor in all directions. For the spot simulations, cells were seeded in three circular, concentric regions of decreasing density. The first region was set to be 30 pixels (300 µm) in radius with a gap of 1 pixel between each cell, the second one spanned the radii between 30 and 60 pixels with a gap of two pixels between each cell and the last one spanned between 60 and 90 pixels with a gap of 3 pixels. This lead to an initial colony with a radius of 900 µm and between 1900 and 2000 cells, both very similar to experiments.

Mean-field model, Go or Grow model and simulations

Both diffusion equations (***Equations 1 and 2***) were discretized through a time-backward space-centered difference scheme with an upwind discretization for the advection operator. In the case of the mean-field model, we were considering (***Equations 1 and 2***) in a radial symmetry, which lead to the following discretization for ρ:

$$\frac{\rho_i^{n+\frac{1}{2}}-\rho_i^{n-\frac{1}{2}}}{\Delta t}-D\frac{\left(R_i+\frac{\Delta x}{2}\right)\left(\rho_{i+1}^{n+\frac{1}{2}}-\rho_i^{n+\frac{1}{2}}\right)-\left(R_i-\frac{\Delta x}{2}\right)\left(\rho_i^{n+\frac{1}{2}}-\rho_{i-1}^{n+\frac{1}{2}}\right)}{R_i\Delta x^2}$$
$$+\frac{1}{R_i\Delta x}\cdot\left\{\begin{array}{c} cR_ia_i^n\rho_i^{n+\frac{1}{2}}-R_{i-1}a_{i-1}^n\rho_{i-1}^{n+\frac{1}{2}}\ if\ C_i^n\geq C_{i-1}^n \\ R_ia_i^n\rho_i^{n+\frac{1}{2}}-R_{i+1}a_{i+1}^n\rho_{i+1}^{n+\frac{1}{2}}\ if\ C_i^n<C_{i-1}^n \end{array}\right\}=r_i^n\rho_i^{n+\frac{1}{2}}$$

, where $a_i^n=\lambda\left(C_i^n\right)\frac{C_i^n-C_{i-1}^n}{\Delta x}$, $r_i^n=r\left(C_i^n\right)$ and R_i the distance from the center.

In the case of the Go or grow model with its planar symmetry, the discretization for ρ was:

$\frac{\rho_i^{n+\frac{1}{2}}-\rho_i^{n-\frac{1}{2}}}{\Delta t}-D\frac{\rho_{i-1}^{n+\frac{1}{2}}-2\rho_i^{n+\frac{1}{2}}+\rho_{i+1}^{n+\frac{1}{2}}}{\Delta x^2}+\frac{1}{\Delta x}\cdot\left\{\begin{array}{c} a_i^n\rho_i^{n+\frac{1}{2}}-a_{i-1}^n\rho_{i-1}^{n+\frac{1}{2}}\ if\ C_i^n\geq C_{i-1}^n \\ a_i^n\rho_i^{n+\frac{1}{2}}-a_{i+1}^n\rho_{i+1}^{n+\frac{1}{2}}\ if\ C_i^n<C_{i-1}^n \end{array}\right\}=r_i^n\rho_i^{n+\frac{1}{2}}$, with $a_i^n=a\left(C_i^n\right)$.

Concerning the equation on Oxygen concentration ***Equation 2***, the consumption term $-b(C)\rho$ was expressed in two different manners: either $b(C)=b_0$ and a non-negativity constraint was added on the Oxygen concentration, just as it was the case in the cellular Potts model, or $b(C)=min\left(b_0,b_0\frac{C}{C_0'}\right)$ which leads to an oxygen consumption that goes to zero in the region of very low concentration $C<C_0'$ and therefore ensures non-negativity for C under a sufficiently small time step Δt. Both expressions led to qualitatively similar results, but we opted for the latter in all the simulations presented here. Finally, the discretization scheme for C in the planar symmetry was:

$\frac{C_i^{n+1}-C_i^n}{\Delta t}-D_{oxy}\frac{C_{i-1}^{n+1}-2C_i^{n+1}+C_{i+1}^{n+1}}{\Delta x^2}=-b_i^n\rho_i^{n+\frac{1}{2}}$, with $b_i^n=b\left(C_i^n\right)$. For the radial symmetry:

$$\frac{C_i^{n+1}-C_i^n}{\Delta t}-D\frac{\left(R_i+\frac{\Delta x}{2}\right)\left(C_{i+1}^{n+1}-C_i^{n+1}\right)-\left(R_i-\frac{\Delta x}{2}\right)\left(C_i^{n+1}-C_{i-1}^{n+1}\right)}{R_i\Delta x^2}=-b_i^n\rho_i^{n+\frac{1}{2}}$$

The schemes were coded in Python language. All simulations of (***Equations 1 and 2***) shown in this article were carried out with a mesh size $\Delta t=0.02min$ and $\Delta x=1\mu m$. The values used for the constants are: $D=30\mu m^2\cdot min^{-1}$ (effective cellular diffusion constant), $C_0=0.7\%O_2$ (threshold for cell division), $C_0'=0.1\%O_2$ (lower threshold in the two threshold 'Go or Grow' model, below which cells stop aerotaxis), $D_{oxy}=1.2\cdot10^5\mu m^2\cdot min^{-1}$ (oxygen diffusion constant in medium), $r_0=ln2/480min^{-1}$ (rate of cell division) and $b_0=0.01\%O_2min^{-1}cell^{-1}$ (using the equivalence 1.25.10^{-15} moles = 21 %O_2 discussed above in Potts model section).

The scheme on C was supplemented with the boundary condition $C(L)=21\%O_2$. We have chosen $L=9mm$ for the Go or grow model to match experimental conditions. For the mean-field model, we have chosen $L=2.5mm$ in order to match the cellular Potts model for which size was a concern for computation time.

In the mean-field model, the initial condition for ρ was taken the same as in the cellular Potts model. For the other simulations, initial conditions for ρ and C were chosen such that they were already close to the expected stationary profile.

We measured the speed of the wave σ, once the wave profile was qualitatively stable, by considering the evolution of the point $\bar{x}(t)$ such that $C(t,\bar{x}(t))=C_0$.

Mathematical analysis of the 'Go or Grow' model

We present below a preliminary analysis of the 'Go or Grow' model. A more detailed mathematical investigation of this model will be carried out in a separate article.

1.The 'Go or Grow' model admits explicit traveling wave solutions.

We recall that $z=x-\sigma t$ is the spatial variable in the moving frame at (unknown) speed $\sigma>0$. We seek a pair of stationary profiles, resp. the density $\rho(z)$ and the oxygen concentration $C(z)$. We assume that $C(z)$ is an increasing function. By translation invariance, we set without loss of generality that $C(0)=C_0$, so that ***Equation 3*** becomes:

$$\begin{cases} -\sigma\frac{\partial\rho}{\partial z} = D\frac{\partial^2\rho}{\partial z^2} - a_0\frac{\partial\rho}{\partial z},\ if\ z<0 \\ -\sigma\frac{\partial\rho}{\partial z} = D\frac{\partial^2\rho}{\partial z^2} + r_0\rho,\ if\ z>0 \end{cases} \tag{7}$$

Furthermore, the function $\rho(z)$ must satisfy at $z=0$ the following relation (i.e. the continuity of the flux) :

$$\sigma\frac{\partial\rho}{\partial z}(0^+) - \sigma\frac{\partial\rho}{\partial z}(0^-) = -\frac{a_0}{D}\rho(0) \tag{8}$$

Thus the equation becomes a second order differential equation with piecewise constant coefficients on each half-line, that can be solved explicitly.

For $z<0$, the solution is of the form $A + Be^{\frac{a_0-\sigma}{D}z}$. From ***Equation 4*** we observe that $\sigma \geq a_0$ equivalently $\frac{a_0-\sigma}{D} \leq 0$ and as ρ is bounded, it implies that $B=0$.

For $z>0$, we look at the roots of the characteristic polynomial $P(\mu) = D\mu^2 + \sigma\mu + r_0$. We note that to yield a nonnegative solution, we need $\sigma^2 \geq 4r_0D$.

If $\sigma = 2\sqrt{r_0D}$, then the solution is of the form $(Cz+D)e^{-\sqrt{\frac{r_0}{D}}z}$ and with relation ***Equation 8***, we obtain $\rho(z) = A\left(\frac{\sqrt{Dr_0}-a_0}{D}z + 1\right)e^{-\sqrt{\frac{r_0}{D}}z}$ and observe that in this case, we necessarily have $a_0 \leq \sqrt{r_0D}$.

If $\sigma>2\sqrt{r_0D}$, the solution is of the form $A'e^{-z} + B'e^{\mu_+ z}$, with $_\pm = \frac{-\sigma\pm\sqrt{\sigma^2-4r_0D}}{2D}$. By arguments exposed in ***Van Saarloos, 2003***, solutions with initial datum localized cannot decrease exponentially at a rate $\mu> -\sqrt{\frac{r_0}{D}}$, where $-\sqrt{\frac{r_0}{D}}$ corresponds to the exponential decay parameter when $\sigma = 2\sqrt{r_0D}$. This leads to $B'=0$, as $\mu_+> -\sqrt{\frac{r_0}{D}}$. Then $A=A'$, but in order to satisfy the C^1-discontinuity jump relation ***Equation 7***, it must be that :

$$\mu_- = \frac{-a_0}{D} \tag{9}$$

Equation 9 can be solved algebraically for σ, which yields $\sigma = a_0 + \frac{Dr_0}{a_0}$. Furthermore, we can rewrite ***Equation 9*** as follows $(2a_0-\sigma) = \sqrt{\sigma^2-4r_0D}$, multiplying by $2a_0+\sigma$, we find that $\left(4a_0^2-\sigma^2\right) = (2a_0+\sigma)\sqrt{\sigma^2-4r_0D}>0$, which leads to $a_0^2>\frac{\sigma^2}{4}>r_0D$.

Thus, we have disclosed all possible profiles. In the case $a_0 \leq \sqrt{r_0D}$ the profile travels at speed $\sigma = 2\sqrt{r_0D}$, whilst for $a_0>\sqrt{r_0D}$ the profile travels at speed $\sigma = a_0 + \frac{r_0D}{a_0}$.

One needs to verify that each of these profiles admits an associated oxygen profile that satisfies the condition $C(0) = C_0$, but the preceding profiles were defined up to the multiplicative constant A, by linearity of ***Equation 7***. The differential equation on C becomes with $\tilde{\rho}$ the solution given above for $A=1$:

$$-\sigma\frac{\partial C}{\partial z} = D_{oxy}\frac{\partial^2}{\partial z^2} - b\left(A\tilde{\rho}\right)C \tag{10}$$

One concludes by checking that by monotonicity there exists a unique constant A such that the solution to the differential ***Equation 10*** equation satisfies $C(0) = C_0$.

2. The wave is pushed in the case $a_0>\sqrt{r_0D}$.

A neutral fraction v^k is defined as satisfying the following linear equation in the moving frame $z = x - \sigma t$:

$$\frac{\partial v^k}{\partial t} + Lv^k := \frac{\partial v^k}{\partial t} - \sigma\frac{\partial v^k}{\partial z} - D\frac{\partial^2 v^k}{\partial z^2} + \frac{\partial}{\partial z}\left(a(z)v^k\right) - r(z)v^k = 0, \tag{11}$$

with $v^k(0,z) = v_0^k(z)$ where we identify $a(z) = a(C(z))$ and $r(z) = r(C(z))$ for the sake of clarity. This corresponds biologically to staining the cells given by the initial distribution v_0^k at time $t=0$ with a neutral label (***Roques et al., 2012***).

Defining $U(z) := \frac{(\sigma-a(z))}{D}z$, then we note that $Lf = -D\frac{\partial}{\partial z}\left(e^{-U}\frac{\partial}{\partial z}\left(e^{U}f\right)\right) - r(z)f$. This leads to setting $w := e^{\frac{U}{2}}v^k$ that satisfies the parabolic equation $\frac{\partial w}{\partial t} + \tilde{L}w = 0$,

with $\tilde{L}g := -De^{\frac{U}{2}}\frac{\partial}{\partial z}\left(e^{-U}\frac{\partial}{\partial z}\left(e^{\frac{U}{2}}g\right)\right) - r(z)g = -D\frac{\partial^2 g}{\partial z^2} + \left(\frac{U'^2}{4} - r(z) - \frac{a_0}{2}\delta\right)g$. The operator $\tilde{L}$ is self-adjoint in $L^2(R, dz)$ on the appropriate domain. Then by setting $\gamma := min\left(inf\left\{\frac{U'^2}{4} - r(z)\right\}, \left(\frac{r_0 D}{a_0}\right)^2\right) > 0$, one can first show that every element of the spectrum of $\lambda \in \sigma\left(\tilde{L}\right)$ such that $\lambda < \gamma$ is an eigenvalue of $\tilde{L}$. Second, one shows that the only eigenvalue λ of $\tilde{L}$ such that $\lambda < \gamma$ is $\lambda = 0$. Finally by standard theory of self-adjoint operators and semi-group theory, one obtains that $w(t) = Pw_0 + e^{-t\tilde{L}}(I - P)w_0$, where $\|e^{-t\tilde{L}}(I - P)w_0\|_{L^2(R,dz)} \leqslant e^{-\gamma t}\|w_0\|_{L^2(R,dz)}$. Translating these properties onto the neutral fraction v^k, we have that $v^k(t) \to \frac{\langle v_0^k, \rho\rangle_{L^2(R, e^U dz)}}{\langle \rho, \rho\rangle_{L^2(R, e^U dz)}}\rho$ at an exponential rate, where ρ is the traveling wave profile calculated in the previous section. Therefore, each fraction converges to a fixed proportion of the whole population. We conclude that after some time the wave becomes a perfect mix of each neutral fraction. This corresponds to the definition of a pushed wave according to ***Roques et al., 2012***.

3. The wave is pulled in the case $a_0 \leq \sqrt{r_0 D}$.

The preceding reasoning does not apply to this case and the intuition is clear, as the wave speed coincides with Fisher's $\sigma = 2\sqrt{r_0 D}$, which is typically the signature of a pulled reaction- diffusion front. In order to prove the pulled nature of the front, we consider $w^k = \frac{v^k}{\rho}$, where ρ is the corresponding wave profile. By computation, w^k then satisfies the following PDE:

$\frac{\partial w^k}{\partial t} - \beta(z)\frac{\partial w^k}{\partial z} - D\frac{\partial^2 w^k}{\partial z^2} = 0$ with $\beta(z) = \begin{cases} \frac{2\sqrt{r_0 D} - a_0}{D}, if z < 0 \\ 2\frac{\sqrt{r_0 D} - a_0}{\left(\sqrt{r_0 D} - a_0\right)z + 1}, if z \geq 0 \end{cases}$ and set η a positive solution to the differential equation $\eta' = \beta\eta$. As $\beta(z) \geq 0$ and β' bounded above, it can be shown by arguments similar to ***Roques et al., 2012***, that under the integrability condition $\int \left(w_0^k(z)\right)^2 \eta(z) dz < \infty$, the neutral fraction goes extinct, that is $\lim_{t=+\infty} \|\left(w^k\right)^2 \eta\|_\infty = 0$, which characterizes a pulled wave in the framework of neutral fractions.

Mathematical analysis of a specific 'Go or Grow' model with a second threshold

We present quickly a specific case for a 'Go or Grow' model with a second threshold, that is completely analytically solvable. We consider the advection term of the form $a(C)sign(\partial_x C)$ with $a(C) = \begin{cases} a_0, & if \quad C_0' < C < C_0 \\ 0, & otherwise \end{cases}$, the division rate $r(C) = \begin{cases} r_0, & if \quad C > C_0 \\ 0, & if \quad C < C_0 \end{cases}$ and the O_2 consumption rate per cell $b(C) = b_0$, without including the constraint that the O_2 concentration C be non-negative. Although this hypothesis seems physically non relevant, it is consistent with the fact that cells are not sensitive to O_2 concentration gradients below the threshold C_0'.

Given a traveling wave profile ρ, C and the corresponding front speed σ, we suppose $C(0) = C_0$ and we introduce the spatial gap $h > 0$ between the two thresholds, i.e. $C(-h) = C_0'$, so that (***Equation 1***) becomes:

$$\begin{cases} -\sigma\frac{\partial \rho}{\partial z} = D\frac{\partial^2 \rho}{\partial z^2}, \ if \ z < -h \\ -\sigma\frac{\partial \rho}{\partial z} = D\frac{\partial^2 \rho}{\partial z^2} - a_0\frac{\partial \rho}{\partial z}, \ if \ -h < z < 0 \\ -\sigma\frac{\partial \rho}{\partial z} = D\frac{\partial^2 \rho}{\partial z^2} + r_0\rho, \ if \ z > 0 \end{cases} \tag{12}$$

Introducing a multiplicative constant A, ρ is then of the shape:

$$\begin{cases} \rho(z) = A\left(B + Ee^{\frac{\sigma - a_0}{D}h}\right), \ if \ z < -h \\ \rho(z) = A\left(B + Ee^{\frac{-(\sigma - a_0)}{D}z}\right), \ if \ -h < z < 0 \\ \rho(z) = Ae^{-\mu z}, \ if \ z > 0 \end{cases} \tag{13}$$

With $B = \frac{\sigma - D}{\sigma - a_0}$, $E = \frac{D - a_0}{\sigma - a_0}$ and $= \frac{\sigma + \sqrt{\sigma^2 - 4Dr_0}}{2D}$. We obtain the following condition, that establishes a one-to-one correspondence between σ and h:

$$e^{\frac{\sigma-a_0}{D}h} = \frac{a_0(\sigma-\mu D)}{\sigma(a_0-\mu D)} \tag{14}$$

The equation on C becomes:

$$-\sigma\frac{\partial C}{\partial z} = D_{oxy}\frac{\partial^2}{\partial z^2} - b_0\rho \tag{15}$$

With the assumption that that C be continuously differentiable, we can solve ***Equation 15*** for C:

$$\begin{cases} C(z) = FAz + G, \ if\ z < -h \\ C(z) = HAz + IAe^{\frac{-(\sigma-a_0)}{D}z} + J + Ke^{\frac{-\sigma}{D_{oxy}}z}, \ if\ -h < z < 0 \\ C(z) = LAe^{-\mu z} + Me^{\frac{-\sigma}{D_{oxy}}z} + C_{init}, \ if\ z > 0 \end{cases}$$

With $F = \frac{b_0}{\sigma}\left(B + Ee^{\frac{\sigma-a_0}{D}h}\right)$, $G = C_0' + FAh$, $H = \frac{b_0 B}{\sigma}$, $I = \frac{b_0 D^2 E}{(\sigma-a_0)\left(D\sigma - D_{oxy}(\sigma-a_0)\right)}$, $L = \frac{b_0}{\left(D_{oxy}-\sigma\right)}$, $M = C_0 - LA - C_{init}$, $J = C_0 - IA - K$ and, by setting $\Delta = \frac{\sigma}{D}\left(H - F - I\left(\frac{\sigma-a_0}{D}\right)e^{\frac{\sigma-a_0}{D}h}\right) - \left(H + L\left(-\frac{\sigma}{D_{oxy}}\right) - I\left(\frac{\sigma-a_0}{D}\right)\right)\left(\frac{\sigma}{D_{oxy}}e^{\frac{\sigma}{D_{oxy}}h}\right)$, we have that $K = \frac{1}{\Delta}\left(H - F - I\left(\frac{\sigma-a_0}{D}\right)e^{\frac{\sigma-a_0}{D}h}\right)\frac{\sigma}{D_{oxy}}\left(C_{init} - C_0'\right)$ and $A = \frac{1}{\Delta}\left(\frac{\sigma}{D_{oxy}}e^{\frac{\sigma}{D_{oxy}}h}\right)\frac{\sigma}{D_{oxy}}\left(C_{init} - C_0'\right)$. This closes the system, but one more constraint remains, which is:

$$C_0' = -HAh + IAe^{\frac{(\sigma-a_0)}{D}h} + J + Ke^{\frac{\sigma}{D_{oxy}}h} \tag{16}$$

The front speed σ of a traveling wave must therefore satisfy the implicit ***Equation 16***. Finding a closed form for the solutions of ***Equation 16*** seems out of reach. Nevertheless, we can approximate the roots numerically, especially by noticing through numerical observation that ***Equation 16*** is monotone on the interval $\left(2\sqrt{r_0 D}, a_0 + \frac{r_0 D}{a_0}\right)$, where the root σ is located. Hence through a dichotomy search algorithm we can find the speed σ of the traveling wave with arbitrary accuracy.

Acknowledgements

We thank R Fulcrand for his expert help in microfabrication; G Torch, C Zoude, G Simon and A Piednoir for technical assistance. This study was supported by the CNRS - Mission pour les Initiatives Transverses et Interdisciplinaires – « Défi Modélisation du vivant - 2019», by the GDR ImaBio (AMI fellowship) and by the IFS LyC Collaborative Research Project 2019 (Tohoku University). S Hirose was supported by the STARMAJ Program (France-Japan: Research Internships for Master's Students, Université de Lyon) and K Funamoto by the CNRS (invited researcher position). This project has received funding from the European Research Council (ERC) under the European Union's Horizon 2020 research and innovation program (grant agreement No 639638 to V Calvez) and from Agence Nationale de la Recherche (grant 2019, ADHeC project, No ANR-19-CE45-0002-02 to JP Rieu).

Additional information

Funding

Funder	Grant reference number	Author
IFS	J19Ly11	Kenichi Funamoto Jean-Paul Rieu
Université de Lyon	STARMAJ	Satomi Hirose
European Research Council	639638	Vincent Calvez
Agence Nationale de la Recherche	ANR-19-CE45-0002-02	Jean-Paul Rieu
GDR Imabio	AMI	Christophe Anjard Jean-Paul Rieu

Centre National de la Recherche Scientifique	MITI 2019	Vincent Calvez Jean-Paul Rieu

The funders had no role in study design, data collection and interpretation, or the decision to submit the work for publication.

Author contributions

Olivier Cochet-Escartin, Conceptualization, Data curation, Formal analysis, Supervision, Investigation, Visualization, Methodology, Writing - original draft, Project administration, Writing - review and editing; Mete Demircigil, Conceptualization, Formal analysis, Investigation, Visualization, Methodology, Writing - original draft, Writing - review and editing; Satomi Hirose, Blandine Allais, Formal analysis, Investigation, Methodology; Philippe Gonzalo, Resources, Methodology, Writing - review and editing; Ivan Mikaelian, Resources, Formal analysis, Methodology; Kenichi Funamoto, Conceptualization, Resources, Formal analysis, Supervision, Investigation, Methodology, Project administration, Writing - review and editing; Christophe Anjard, Conceptualization, Resources, Formal analysis, Supervision, Investigation, Methodology, Writing - original draft, Project administration, Writing - review and editing; Vincent Calvez, Conceptualization, Supervision, Funding acquisition, Validation, Investigation, Methodology, Writing - original draft, Project administration, Writing - review and editing; Jean-Paul Rieu, Conceptualization, Data curation, Formal analysis, Supervision, Funding acquisition, Investigation, Visualization, Methodology, Writing - original draft, Project administration, Writing - review and editing

Author ORCIDs

Olivier Cochet-Escartin https://orcid.org/0000-0001-7924-702X
Satomi Hirose http://orcid.org/0000-0002-8594-8006
Philippe Gonzalo http://orcid.org/0000-0002-9763-0150
Kenichi Funamoto https://orcid.org/0000-0002-0703-0910

Decision letter and Author response

Decision letter https://doi.org/10.7554/eLife.64731.sa1
Author response https://doi.org/10.7554/eLife.64731.sa2

Additional files

Supplementary files

- Source data 1. Detailed measurements for quantities presented in the text as means ± standard deviations.
- Transparent reporting form

Data availability

All data generated or analysed during this study are included in the manuscript and supporting files.

References

Adler J. 1966. Chemotaxis in bacteria. *Science* **153**:708–716. DOI: https://doi.org/10.1126/science.153.3737.708, PMID: 4957395

Aronson DG, Weinberger HF. 1975. *Nonlinear Diffusion in Population Genetics, Combustion, and Nerve Pulse Propagation*. Berlin, Heidelberg: Springer. DOI: https://doi.org/10.1007/BFb0070595

Birzu G, Hallatschek O, Korolev KS. 2018. Fluctuations uncover a distinct class of traveling waves. *PNAS* **115**: E3645–E3654. DOI: https://doi.org/10.1073/pnas.1715737115, PMID: 29610340

Birzu G, Matin S, Hallatschek O, Korolev KS. 2019. Genetic drift in range expansions is very sensitive to density dependence in dispersal and growth. *Ecology Letters* **22**:1817–1827 . DOI: https://doi.org/10.1111/ele.13364, PMID: 31496047

Chang WL, Chang YC, Lin KT, Li HR, Pai CY, Chen JH, Su YH. 2017. Asymmetric distribution of hypoxia-inducible factor α regulates dorsoventral axis establishment in the early sea urchin embryo. *Development* **144**:2940–2950 . DOI: https://doi.org/10.1242/dev.145052, PMID: 28705895

Chen X, Ling HF, Vance D, Shields-Zhou GA, Zhu M, Poulton SW, Och LM, Jiang SY, Li D, Cremonese L, Archer C. 2015. Rise to modern levels of ocean oxygenation coincided with the cambrian radiation of animals. *Nature Communications* **6**:7142. DOI: https://doi.org/10.1038/ncomms8142, PMID: 25980960

Child CM. 1941. Formation and Reduction of Indophenol Blue in Development of an Echinoderm. *PNAS* **27**:523–528 . DOI: https://doi.org/10.1073/pnas.27.11.523, PMID: 16588496

Coffman JA, Denegre JM. 2007. Mitochondria, redox signaling and axis specification in metazoan embryos. *Developmental Biology* **308**:266–280. DOI: https://doi.org/10.1016/j.ydbio.2007.05.042, PMID: 17586486

Cotter DA, Raper KB. 1968. Properties of germinating spores of *Dictyostelium* discoideum. *Journal of bacteriology* **96**:1680–1689. DOI: https://doi.org/10.1128/jb.96.5.1680-1689.1968, PMID: 5749769

Cremer J, Honda T, Tang Y, Wong-Ng J, Vergassola M, Hwa T. 2019. Chemotaxis as a navigation strategy to boost range expansion. *Nature* **575**:658–663. DOI: https://doi.org/10.1038/s41586-019-1733-y, PMID: 31695195

Delanoë-Ayari H, Iwaya S, Maeda YT, Inose J, Rivière C, Sano M, Rieu JP. 2008. Changes in the magnitude and distribution of forces at different *Dictyostelium* developmental stages. *Cell Motility and the Cytoskeleton* **65**:314–331 . DOI: https://doi.org/10.1002/cm.20262, PMID: 18205201

Deygas M, Gadet R, Gillet G, Rimokh R, Gonzalo P, Mikaelian I. 2018. Redox regulation of EGFR steers migration of hypoxic mammary cells towards oxygen. *Nature Communications* **9**:4545. DOI: https://doi.org/10.1038/s41467-018-06988-3, PMID: 30382089

Donà E, Barry JD, Valentin G, Quirin C, Khmelinskii A, Kunze A, Durdu S, Newton LR, Fernandez-Minan A, Huber W, Knop M, Gilmour D. 2013. Directional tissue migration through a self-generated chemokine gradient. *Nature* **503**:285–289. DOI: https://doi.org/10.1038/nature12635, PMID: 24067609

d'Alessandro J, Mas L, Aubry L. 2018. Collective regulation of cell motility using an accurate density-sensing system. *Journal of the Royal Society Interface* **15**:45. DOI: https://doi.org/10.1098/rsif.2018.0006

Engelmann TW. 1881. Neue methode zur untersuchung der sauerstoffausscheidung pflanzlicher und tierischer organismen (New method for investigation of oxygen-searching plant and animal organisms). *Pflugers Arch. Gesammte Physiol* **25**:285–292.

Fisher RA. 1937. The wave of advance of advantageous genes. *Annals of Eugenics* **7**:355–369. DOI: https://doi.org/10.1111/j.1469-1809.1937.tb02153.x

Friedl P, Borgmann S, Bröcker EB. 2001. Amoeboid leukocyte crawling through extracellular matrix: lessons from the *Dictyostelium* paradigm of cell movement. *Journal of Leukocyte Biology* **70**:491–509. PMID: 11590185

Fu X, Kato S, Long J, Mattingly HH, He C, Vural DC, Zucker SW, Emonet T. 2018. Spatial self-organization resolves conflicts between individuality and collective migration. *Nature Communications* **9**:1–12. DOI: https://doi.org/10.1038/s41467-018-04539-4

Genbacev O, Zhou Y, Ludlow JW, Fisher SJ. 1997. Regulation of human placental development by oxygen tension. *Science* **277**:1669–1672. DOI: https://doi.org/10.1126/science.277.5332.1669, PMID: 9287221

Gilkes DM, Xiang L, Lee SJ, Chaturvedi P, Hubbi ME, Wirtz D, Semenza GL. 2014. Hypoxia-inducible factors mediate coordinated RhoA-ROCK1 expression and signaling in breast cancer cells. *PNAS* **111**:E384–E393. DOI: https://doi.org/10.1073/pnas.1321510111, PMID: 24324133

Golé L, Rivière C, Hayakawa Y, Rieu JP. 2011. A quorum-sensing factor in vegetative *Dictyostelium* discoideum cells revealed by quantitative migration analysis. *PLOS ONE* **6**:e26901. DOI: https://doi.org/10.1371/journal.pone.0026901, PMID: 22073217

Gregor T, Fujimoto K, Masaki N, Sawai S. 2010. The onset of collective behavior in social amoebae. *Science* **328**:1021–1025. DOI: https://doi.org/10.1126/science.1183415, PMID: 20413456

Hatzikirou H, Basanta D, Simon M, Schaller K, Deutsch A. 2012. 'Go or grow': the key to the emergence of invasion in tumour progression? *Mathematical Medicine and Biology* **29**:49–65. DOI: https://doi.org/10.1093/imamb/dqq011, PMID: 20610469

Hillen T, Painter KJ. 2009. A user's guide to PDE models for chemotaxis. *Journal of Mathematical Biology* **58**:183–217. DOI: https://doi.org/10.1007/s00285-008-0201-3

Keller EF, Segel LA. 1970. Initiation of slime mold aggregation viewed as an instability. *Journal of Theoretical Biology* **26**:399–415. DOI: https://doi.org/10.1016/0022-5193(70)90092-5, PMID: 5462335

Kelly B, Carrizo GE, Edwards-Hicks J, Sanin DE, Stanczak MA, Priesnitz C, Flachsmann LJ, Curtis JD, Mittler G, Musa Y, Becker T, Buescher JM, Pearce EL. 2021. Sulfur sequestration promotes multicellularity during nutrient limitation. *Nature* **591**:471–476. DOI: https://doi.org/10.1038/s41586-021-03270-3

Koens R, Tabata Y, Serrano JC, Aratake S, Yoshino D, Kamm RD, Funamoto K. 2020. Microfluidic platform for three-dimensional cell culture under spatiotemporal heterogeneity of oxygen tension. *APL Bioengineering* **4**:016106. DOI: https://doi.org/10.1063/1.5127069, PMID: 32161836

Kolmogorov A, Petrovskii I, Piskunov N. 1937. Etude de L'équation De La Diffusion Avec Croissance De La Quantité De Matière Et Son Application À Un Problème Biologique. *Bull. Univ. Moskow,Ser. Internat* **1**:1–25.

Lewis DM, Park KM, Tang V, Xu Y, Pak K, Eisinger-Mathason TS, Simon MC, Gerecht S. 2016. Intratumoral oxygen gradients mediate sarcoma cell invasion. *PNAS* **113**:9292–9297. DOI: https://doi.org/10.1073/pnas.1605317113, PMID: 27486245

Lyons TW, Reinhard CT, Planavsky NJ. 2014. The rise of oxygen in Earth's early ocean and atmosphere. *Nature* **506**:307–315. DOI: https://doi.org/10.1038/nature13068, PMID: 24553238

Merkel TC, Bondar VI, Nagai K, Freeman BD, Pinnau I. 2000. Gas sorption, diffusion, and permeation in poly (dimethylsiloxane). *Journal of Polymer Science Part B: Polymer Physics* **38**:415–434. DOI: https://doi.org/10.1002/(SICI)1099-0488(20000201)38:3<415::AID-POLB8>3.0.CO;2-Z

Moon SI, Monson L, Extrand CW. 2009. Outgassing of oxygen from polycarbonate. *ACS Applied Materials & Interfaces* **1**:1539–1543. DOI: https://doi.org/10.1021/am900206e, PMID: 20355958

Muinonen-Martin AJ, Susanto O, Zhang Q, Smethurst E, Faller WJ, Veltman DM, Kalna G, Lindsay C, Bennett DC, Sansom OJ, Herd R, Jones R, Machesky LM, Wakelam MJ, Knecht DA, Insall RH. 2014. Melanoma cells break down LPA to establish local gradients that drive chemotactic dispersal. *PLOS Biology* **12**:e1001966. DOI: https://doi.org/10.1371/journal.pbio.1001966, PMID: 25313567

Nakajima A, Ishihara S, Imoto D, Sawai S. 2014. Rectified directional sensing in long-range cell migration. *Nature Communications* **5**:1–14. DOI: https://doi.org/10.1038/ncomms6367, PMID: 25373620

Nock V, Blaikie RJ, David T. 2008. Patterning, integration and characterisation of polymer optical oxygen sensors for microfluidic devices. *Lab on a Chip* **8**:1300–1307. DOI: https://doi.org/10.1039/b801879k, PMID: 18651072

Palecek SP, Loftus JC, Ginsberg MH, Lauffenburger DA, Horwitz AF. 1997. Integrin-ligand binding properties govern cell migration speed through cell-substratum adhesiveness. *Nature* **385**:537–540. DOI: https://doi.org/10.1038/385537a0, PMID: 9020360

Pan M, Xu X, Chen Y, Jin T. 2016. Identification of a Chemoattractant G-Protein-Coupled Receptor for Folic Acid that Controls Both Chemotaxis and Phagocytosis. *Developmental Cell* **36**:428–439. DOI: https://doi.org/10.1016/j.devcel.2016.01.012, PMID: 26906738

Pugh CW, Ratcliffe PJ. 2017. New horizons in hypoxia signaling pathways. *Experimental Cell Research* **356**:116–121. DOI: https://doi.org/10.1016/j.yexcr.2017.03.008, PMID: 28315322

Roques L, Garnier J, Hamel F, Klein EK. 2012. Allee effect promotes diversity in traveling waves of colonization. *PNAS* **109**:8828–8833. DOI: https://doi.org/10.1073/pnas.1201695109, PMID: 22611189

Sandonà D, Gastaldello S, Rizzuto R, Bisson R. 1995. Expression of cytochrome c oxidase during growth and development of *Dictyostelium*. *Journal of Biological Chemistry* **270**:5587–5593. DOI: https://doi.org/10.1074/jbc.270.10.5587, PMID: 7890678

Saragosti J, Calvez V, Bournaveas N, Perthame B, Buguin A, Silberzan P. 2011. Directional persistence of chemotactic bacteria in a traveling concentration wave. *PNAS* **108**:16235–16240 . DOI: https://doi.org/10.1073/pnas.1101996108

Schiavo G, Bisson R. 1989. Oxygen influences the subunit structure of cytochrome c oxidase in the slime mold *Dictyostelium* discoideum. *Journal of Biological Chemistry* **264**:7129–7134 . DOI: https://doi.org/10.1016/S0021-9258(18)83211-2, PMID: 2540175

Stokes AN. 1976. On two types of moving front in quasilinear diffusion. *Mathematical Biosciences* **31**:307–315 . DOI: https://doi.org/10.1016/0025-5564(76)90087-0

Stuelten CH. 2017. Moving in and out: dispersion of cells in Self-Generated gradients. *Journal of Clinical & Cellular Immunology* **8**:507. DOI: https://doi.org/10.4172/2155-9899.1000507, PMID: 28868205

Sussman M. 1987. Cultivation and synchronous morphogenesis of *Dictyostelium* under controlled experimental conditions. *Methods in cell biology* **28**:9–29 . DOI: https://doi.org/10.1016/s0091-679x(08)61635-0, PMID: 3298997

Swat MH, Thomas GL, Belmonte JM, Shirinifard A, Hmeljak D, Glazier JA. 2012. Multi-scale modeling of tissues using CompuCell3D. *Methods in Cell Biology* **110**:325–366. DOI: https://doi.org/10.1016/B978-0-12-388403-9.00013-8, PMID: 22482955

Thomas PC, Halter M, Tona A, Raghavan SR, Plant AL, Forry SP. 2009. A noninvasive thin film sensor for monitoring oxygen tension during in vitro cell culture. *Analytical Chemistry* **81**:9239–9246 . DOI: https://doi.org/10.1021/ac9013379, PMID: 19860390

Tonon F, Giobbe GG, Zambon A, Luni C, Gagliano O, Floreani A, Grassi G, Elvassore N. 2019. In vitro metabolic zonation through oxygen gradient on a chip. *Scientific Reports* **9**:13557 . DOI: https://doi.org/10.1038/s41598-019-49412-6, PMID: 31537830

Torija P, Vicente JJ, Rodrigues TB, Robles A, Cerdán S, Sastre L, Calvo RM, Escalante R. 2006. Functional genomics in *Dictyostelium*: MidA, a new conserved protein, is required for mitochondrial function and development. *Journal of Cell Science* **119**:1154–1164 . DOI: https://doi.org/10.1242/jcs.02819, PMID: 16507593

Tweedy L, Susanto O, Insall RH. 2016. Self-generated chemotactic gradients-cells steering themselves. *Current Opinion in Cell Biology* **42**:46–51. DOI: https://doi.org/10.1016/j.ceb.2016.04.003, PMID: 27105308

Tweedy L, Thomason PA, Paschke PI, Martin K, Machesky LM, Zagnoni M, Insall RH. 2020. Seeing around corners: Cells solve mazes and respond at a distance using attractant breakdown. *Science* **369**:eaay9792 . DOI: https://doi.org/10.1126/science.aay9792

Tweedy L, Insall RH. 2020. Self-Generated gradients yield exceptionally robust steering cues. *Frontiers in Cell and Developmental Biology* **8**:133. DOI: https://doi.org/10.3389/fcell.2020.00133, PMID: 32195256

Ungerböck B, Charwat V, Ertl P, Mayr T. 2013. Microfluidic oxygen imaging using integrated optical sensor layers and a color Camera. *Lab on a Chip* **13**:1593–1601. DOI: https://doi.org/10.1039/c3lc41315b, PMID: 23443957

van Haastert PJ, Keizer-Gunnink I, Kortholt A. 2017. Coupled excitable Ras and F-actin activation mediates spontaneous pseudopod formation and directed cell movement. *Molecular Biology of the Cell* **28**:922–934 . DOI: https://doi.org/10.1091/mbc.e16-10-0733, PMID: 28148648

Van Saarloos W. 2003. Front propagation into unstable states. *Physics Reports* **386**:29–222 . DOI: https://doi.org/10.1016/j.physrep.2003.08.001

Venkiteswaran G, Lewellis SW, Wang J, Reynolds E, Nicholson C, Knaut H. 2013. Generation and dynamics of an endogenous, self-generated signaling gradient across a migrating tissue. *Cell* **155**:674–687 . DOI: https://doi.org/10.1016/j.cell.2013.09.046, PMID: 24119842

West CM, van der Wel H, Wang ZA. 2007. Prolyl 4-hydroxylase-1 mediates O2 signaling during development of *Dictyostelium*. *Development* **134**:3349–3358 . DOI: https://doi.org/10.1242/dev.000893, PMID: 17699611

Winn KM, Bourne DG, Mitchell JG. 2013. Vibrio coralliilyticus search patterns across an oxygen gradient. *PLOS ONE* **8**:e67975. DOI: https://doi.org/10.1371/journal.pone.0067975, PMID: 23874480

Xu Y, Wang ZA, Green RS, West CM. 2012. Role of the Skp1 prolyl-hydroxylation/glycosylation pathway in oxygen dependent submerged development of *Dictyostelium*. *BMC Developmental Biology* **12**:31 . DOI: https://doi.org/10.1186/1471-213X-12-31

Chapter 2

When Self-Generated Gradients interact with Expansion by Cell Division and Diffusion. Analysis of a Minimal Model.

This Chapter consists of the article [54], which has been submitted to *Journal de l'École polytechnique — Mathématiques*.

We investigate a minimal model for cell propagation involving migration along self-generated signaling gradients and cell division, which has been proposed in an earlier study. The model consists in a system of two coupled parabolic diffusion-advection-reaction equations. Because of a discontinuous advection term, the Cauchy problem should be handled with care. We first establish existence and uniqueness locally in time through the reduction of the problem to the well-posedness of an ODE, under a monotonicity condition on the signaling gradient. Then, we carry out an asymptotic analysis of the system. All positive and bounded traveling waves of the system are computed and an explicit formula for the minimal wave speed is deduced. An analysis on the inside dynamics of the wave establishes a dichotomy between pushed and pulled waves depending on the strength of the advection. We identified the minimal wave speed as the biologically relevant speed, in a weak sense, that is, the solution propagates slower, respectively faster, than the minimal wave speed, up to time extraction. Finally, we extend the study to a hyperbolic two-velocity model with persistence.

2.1 Introduction

In this paper, we are mainly concerned with the investigation of spreading properties for a one-dimensional parabolic system of two diffusion-advection-reaction equations, with $t \geq 0, x \in \mathbb{R}$,

$$\begin{cases} \partial_t \rho - \partial_{xx}\rho + \partial_x(\chi \mathrm{sign}(\partial_x N)\mathbb{1}_{N \leq N_{\mathrm{th}}}\rho) = \mathbb{1}_{N > N_{\mathrm{th}}}\rho & \text{(2.1.1a)} \\ \partial_t N - D\partial_{xx}N = -\rho N. & \text{(2.1.1b)} \end{cases}$$

Here $\rho(t,x)$ describes a cell population subject to diffusion, with a diffusion constant normalized to 1, and either growth or advection depending on its position. The switch between growth and advection is mediated by the value $N(t,x)$ of a chemical nutrient field: for a given threshold value N_{th}, if $N > N_{\text{th}}$, the population ρ is subject to growth with constant rate normalized to 1, and if $N \leq N_{\text{th}}$, the population is subject to advection with constant speed $\chi > 0$ in the direction of the gradient $\partial_x N$. This advection speed results from biases in individual cell trajectories, which are averaged at the macroscopic level. The chemical nutrient N undergoes a reaction-diffusion equation through a simple consumption term $-\rho N$, with the consumption rate per cell normalized to 1. All along the article, we work in the setting, where N is increasing in space, $\lim_{x\to-\infty} N(t,x) = 0$ and $\lim_{x\to+\infty} N(t,x) = 1 > N_{\text{th}}$, by normalizing the limit to 1. Under these conditions, the cell population propagates from left to right. Furthermore, we introduce the (unique) position of the threshold $\bar{x}(t)$, such that:

$$N(t,\bar{x}(t)) = N_{\text{th}}. \tag{2.1.2}$$

In Equation (2.1.1a), the advection term is discontinuous, but the flux should still be continous. Hence in particular at the interface $\bar{x}(t)$ the flux must be continuous. More precisely, consider a weak solution to Equation (2.1.1a), which is continuous and sufficiently regular on either side of the interface $\bar{x}(t)$. By a Rankine-Hugoniot type argument, ρ satisfies the following C^1-jump relation at the interface $\bar{x}(t)$:

$$\partial_x \rho\left(t,\bar{x}(t)^+\right) - \partial_x \rho\left(t,\bar{x}(t)^-\right) = -\chi\rho(t,\bar{x}(t)). \tag{2.1.3}$$

A typical initial datum $(\rho^0, N^0) \in L^\infty(\mathbb{R})^2$ for System (2.1.1) satisfies nonnegativity, *i.e.* $\rho^0, N^0 \geq 0$. In addition, we assume that ρ^0 satisfies the C^1-jump relation (2.1.3) and is bounded by an exponentially decreasing function at $x = +\infty$. Furthermore, $\partial_x N^0 > 0$, $\lim_{x\to-\infty} N^0(x) = 0$ and $\lim_{x\to+\infty} N^0(x) = 1 > N_{\text{th}}$.

System (2.1.1) was introduced in [48] by the author and collaborators as a minimal model for cell collective behaviour triggered by a self-generated gradient. In this study, the following emerging behavior of *Dictyostelium discoideum* cells (*Dd* cells in short) in hypoxic conditions was observed: when a colony of *Dd* cells is confined between two narrowly spaced plates, *Dd* cells form a dense ring moving outwards. After a brief transitory phase, the ring of cells moves at constant speed and constant density over the time course of the experiment (see Figure 2.1a). The authors emitted the hypothesis that the quick consumption of oxygen by *Dd* cells exposes them to hypoxia, *i.e.* lack of oxygen, and in turn induces *aerotaxis*, *i.e.* a bias in the individual trajectories of *Dd* cells towards higher oxygen concentrations, leading to a macroscopic outward motion. We refer to [23, 48] (see also [150]) for a biological discussion on the hypotheses under which the observed phenomenon may arise. The scientific approach in [48] leading to this minimal model can be described as follows: (i) Experimentally, it was observed that cells exhibit various individual behaviors accross the colony. (ii) In the model, two particular behaviors were retained as an alternative: either cell division, or migration towards oxygen. (iii) It was postulated that the transition between the two behaviors depends on a single threshold (see Figure 2.1b). Indeed, it is for instance well known that *Dd* cells do not have enough energy to divide, when oxygen is lacking. The term 'Go or Grow' was coined to describe this dichotomy, by analogy with a similar mechanism in the modeling of glioma cells [98], which nevertheless is of another nature, as it describes a density-dependent rather than an oxygen-dependent switch between diffusion and cell division.

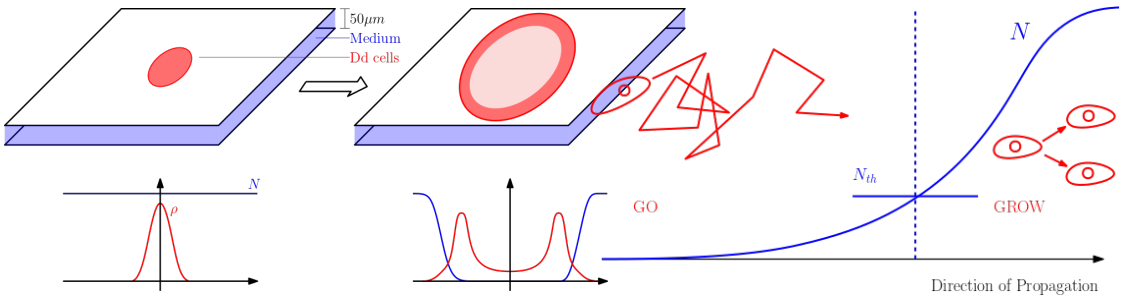

(a) (b)

Figure 2.1: (a): A schematic representation of the experiment carried out in [48]. Cells are confined between two narrowly spaced plates and quickly consume available oxygen, so that the colony experiences self-induced hypoxic conditions. This, in turn, triggers outward migration of the colony under the form of a ring expanding at constant speed over long periods of time. (b): A cartoon representation of the 'Go or Grow' hypothesis. Cells switch between two behaviors, depending on the level of oxygen. When oxygen concentration is above some threshold N_{th}, cells divide and follow Brownian trajectories (this is the 'Grow' behavior). In contrast, when oxygen concentration drops below N_{th}, cells stop dividing and follow a biased Brownian motion towards higher levels of oxygen (this is the 'Go' behavior).

The mechanism of cell division in System (2.1.1) resembles to some extent to standard reaction-diffusion models, among which the classical Fisher/Kolmogorov-Petrovsky-Piskunov [11, 72, 115] is a prototype. The F/KPP model describes in particular expansion of a cell population undergoing cell division and diffusion. However, while in standard reaction-diffusion models, growth is limited by a density-mediated mechanism (*e.g.* a quadratic saturation term in the F/KPP case), here it is limited via the dependence on the chemical nutrient N, which leads to a similar regulatory mechanism: the more cells divide, the more they consume the chemical nutrient N, the more their growth is limited.

Interestingly, this minimal model is sufficient to describe the propagation of a wave of cells, in a context of self-generated oxygen gradients. In fact, System (2.1.1) exhibits explicit traveling wave solutions and the minimal wave speed can be computed explicitly (see [48] and also Section 2.3). This gives rise to the following formula for the minimal wave speed,

$$\sigma^* = \begin{cases} \chi + \frac{1}{\chi} & \text{if } \chi > 1 \\ 2 & \text{if } \chi \leq 1 \end{cases} . \tag{2.1.4}$$

Thus, there are two different regimes: in the regime $\chi \leq 1$, which we call the *small bias* regime, the speed corresponds to the well-known F/KPP speed, $\sigma_{F/KPP} := 2$, whereas in the regime of *large bias*, $\chi > 1$, the wave speed $\chi + \frac{1}{\chi}$ is greater than $\sigma_{F/KPP}$. The threshold is reached when the advection speed χ is equal to half the F/KPP speed $\sigma_{F/KPP}$: there, the two expressions coincide.

System (2.1.1) combines two distinct propagation phenomena, one being aerotaxis of cells triggered by the self-generated gradient, and the other being expansion by division-diffusion, such as described by the F/KPP model. Biologically, it is therefore relevant to ask how these two propagation phenomena combine with each other (see [23, 48]). Since the collective propagation speed σ^* is always higher than the advection speed χ, cell division has a net positive effect on the propagation of cells. In parallel, in the regime of large bias $\chi > 1$, aerotaxis has also in turn a net positive effect on the propagation speed, compared

to mere expansion by division-diffusion, which is in agreement with the findings by [49]. In that case, we may refer to the wave as an aerotactic wave. Yet, in the regime of small bias $\chi \leq 1$, the propagation is driven by division-diffusion, and aerotaxis does not contribute to the wave speed: in that case, we refer to the propagation as a F/KPP wave.

Recently, numerous works, among which [49, 124, 179, 182], have investigated propagation of cells under self-generated gradients and shown its biological relevance as an efficient migration strategy. Notably in [49], the authors observe that the the combination of *chemotaxis* (the response to chemical gradients, which is very analogous to aerotaxis in a mathematical setting) and cell division, leads to an enhanced expansion.

Other works have investigated chemotactic waves in *Escherichia coli* bacteria (and references therein [35, 160]). These works have proposed a description at a mesoscopic scale, through a kinetic model, and at a macroscopic scale, through a parabolic model, analogous to some extent with System (2.1.1). However, the main difference is that in order to sustain the propagation of the wave, two attractants are required in [35, 160], whereas here the single attractant N is sufficient. Additionally in the case of *E. coli* cell division is negligible, while here it plays a key ingredient. We refer to [36] for a discussion on different models of propagation through self-generated signaling gradients.

In parallel, the Keller-Segel model [112, 114] has been widely used in order to give a description of cells undergoing chemotaxis. In [137], a variation on this model was proposed by adding a density-dependent growth term to the model. This Keller-Segel model with growth term has been the subject of numerous investigations in recent years, among which the works [27, 121, 137, 157, 158]. These types of models combine chemotaxis and cell division and exhibit traveling waves under some conditions on the parameters. Nevertheless, chemotactic self-aggregation (in the aformentioned studies) and aerotaxis (in the present study) lead to biases in opposite directions at the edge of expansion front. Recently, in the works [95, 99], the authors have investigated the case of *negative chemotaxis*, where the bias induced by chemotaxis is in the same direction than the propagation induced by division-diffusion and thus bears a similarity to the aerotactic advection term. In [99], the author was able to obtain bounds on the propagation speed. Since the considered model is different from ours, this result cannot be directly compared to our explicit speed Formula (2.1.4), but in the regime of small negative chemotaxis, the wave speed exactly agrees, *i.e.* $\sigma^* = 2$, and the propagation is caused by division-diffusion. In the regime of large negative chemotaxis, the wave speed increases, which is also in agreement with our findings.

Interestingly, Formula (2.1.4) coincides with the formula for the wave speed obtained in the monostable cubic reaction-diffusion equation with reaction term $f(u) = u(1-u)(1+2\chi^2 u)$ [19, 94] or the Burgers-FKPP equation of the form $\partial_t u - \partial_{xx} u + 2\chi u \partial_x u = u(1-u)$ [9]. We also mention a class of free boundary problems introduced in [20], that is linked to the large-population limit of the N-Branching Brownian Motion [52]. The authors of [20] show that the following free boundary problem for $(u, \mu_t) \in C(\mathbb{R}_+ \times \mathbb{R}) \times C(\mathbb{R}_+)$ sufficiently regular admits Formula (2.1.4) as minimal wave speed:

$$\begin{cases} \partial_t u - \partial_{xx} u = u, \text{ for } x > \mu_t \\ u(t, \mu_t) = 1 \text{ and } \partial_x u(t, \mu_t) = -\chi \end{cases}$$

In [82, 152], the authors have investigated the inside dynamics of traveling waves in reaction-diffusion equations. They have proposed a new characterization of the categorization between *pushed* and *pulled* waves. A pushed wave is subject to a significant contribution from the overall population to the net propagation, whereas a pulled wave is driven by growth and diffusion of the population at the edge of the front with negligible contribution from the overall population. In particular, it was shown in [82] that in the

monostable cubic reaction-diffusion equation with reaction term $f(u) = u(1-u)(1+2\chi^2 u)$ a transition from a pulled to a pushed nature of the wave exists at $\chi = 1$. The same dichotomy was observed at play in System (2.1.1), essentially via numerical simulations [48]: in the case of small bias $\chi \leq 1$, the traveling wave is pulled. In contrast, in the case of large bias $\chi > 1$, the traveling wave is pushed. A transition from pulled to pushed waves has recently been of interest in the works [80, 81, 148], but in these studies they are due to structural modifications of the system, *i.e.* the reaction term goes from a monostable structure to a bistable structure. However here, as well as in the case of the monostable cubic case and the Burgers-FKPP equation [9], it is a transition induced by the relative size of the parameters without changing the nature of the stable states.

Of note, the definitions of pulled and pushed waves can vary in the literature. The historical definition as proposed in [169] (see also [154, 184]) is based on the criterion whether the minimal speed σ^* is equal to the speed of the linearized front around the steady state 0 (pulled), or greater than this speed (pushed). The definition proposed in [82, 152] is based in turn on the inside dynamics of the traveling waves. In this paper, we follow the latter definition and more precisely the study of the inside dynamics of ρ, that we believe is more appropriate to the study of a system of equations, such as System (2.1.1). However, both definitions coincide in our case, since linearizing System (2.1.1) around its leading edge yields a constant chemical nutrient field $N \equiv 1$ and the linear F/KPP equation on ρ, which gives rise to a front traveling at speed $\sigma = 2$.

In this paper, we are mainly concerned with the study of the parabolic System (2.1.1), that can be viewed as a minimal model on a macroscopic scale including self-generated signaling gradients and cell division. However, following the discovery of the run and tumble motion in *E. coli* [22], it may be relevant to model collective motion of micro-organisms on a mesoscopic scale through kinetic transport equations, see for instance [6, 7, 46, 141, 171]. In particular in [35], the author has investigated the existence of traveling waves in *E. coli* populations propagating in microchannels. In *Dd* cells, persistent motion is observed as well [48]. Therefore, it is very natural to propose a kinetic model for their study, involving free transport and reorientations of cells. Hence, by analogy with the aforementioned studies, we propose the following kinetic model:

$$\begin{cases} \partial_t f(t,x,v) + v\partial_x f(t,x,v) = \lambda\left(M(v;N,\partial_x N)\rho(t,x) - f(t,x,v)\right) + r(N)\rho(t,x) & \text{(2.1.5a)} \\ \partial_t N - D\partial_{xx} N = -\rho N, & \text{(2.1.5b)} \end{cases}$$

where $v \in V$, a compact subset of $\mathbb{R}$ and $\rho(t,x) = \frac{1}{|V|}\int_V f(t,x,v)dx$. Equation (2.1.5a) describes the evolution of the mesoscopic density of cells, that undergo cell division and persistent motion: cells move with velocity v and at a constant rate λ cells reorient themselves according to the probability distribution described by the Maxwellian $M(v;N,\partial_x N)$. In addition, cells divide with rate $r(N)$, depending on the ambient oxygen level, and the new cells have a velocity that is drawn from the uniform distribution on V. In particular, we can adapt the 'Go or Grow' hypothesis to Equation (2.1.5a): for $N < N_{\text{th}}$, set cell division to zero and a fixed Maxwellian distribution with mean $\chi\text{sign}(\partial_x N)$; for $N > N_{\text{th}}$, set a fixed nonzero cell division rate and a fixed Maxwellian with zero mean.

Whilst the general study of System (2.1.5) is postponed to future investigations, we analyze in the present study the two-velocity case, which we will refer to as the two-velocity system with persistence. In fact, we consider $V = \{\pm\varepsilon^{-1}\}$, with rescaled velocity and System (2.1.5) becomes a system of two hyperbolic equations for $f^{\pm}(t,x) := f(t,x,\pm\varepsilon^{-1})$

and a parabolic equation for N, with $t \geq 0, x \in \mathbb{R}$,

$$\begin{cases} \partial_t f^+ + \varepsilon^{-1}\partial_x f^+ = \varepsilon^{-2}\left(M(+\varepsilon^{-1}; N, \partial_x N)\rho - f^+\right) + \mathbb{1}_{N>N_{\text{th}}}\rho & \text{(2.1.6a)} \\ \partial_t f^- - \varepsilon^{-1}\partial_x f^- = \varepsilon^{-2}\left(M(-\varepsilon^{-1}; N, \partial_x N)\rho - f^-\right) + \mathbb{1}_{N>N_{\text{th}}}\rho & \text{(2.1.6b)} \\ \partial_t N - D\partial_{xx} N = -\rho N, & \text{(2.1.6c)} \end{cases}$$

where $\rho := \frac{f^+ + f^-}{2}$ and,

$$M(\pm\varepsilon^{-1}; N, \partial_x N) = \begin{cases} 1 & \text{if } N > N_{\text{th}} \\ 1 \pm \varepsilon\chi & \text{if } N \leq N_{\text{th}} \text{ and } \partial_x N \geq 0 \\ 1 \mp \varepsilon\chi & \text{if } N \leq N_{\text{th}} \text{ and } \partial_x N < 0 \end{cases},$$

with $\chi < \varepsilon^{-1}$ and, up to a scale of units, $r(N) = \mathbb{1}_{N>N_{\text{th}}}$, $\lambda = \varepsilon^{-2}$ and the mean of the Maxwellian distribution equal to $\pm\chi$, when $N \leq N_{\text{th}}$.

The parabolic System (2.1.1) and the two-velocity System with persistence (2.1.6) are linked through the so-called parabolic scaling limit. Indeed, taking the limit $\varepsilon \to 0$ of Equations (2.1.6) leads, at least in a formal sense, to Equations (2.1.1). We refer to [46] for a rigorous derivation in a general chemotaxis model without cell division.

Results and Strategies of Proof

The present article contains on the one hand an analysis of the well-posedness of System (2.1.1) locally in time and on the other hand an asymptotic analysis of System (2.1.1), including: the computation of traveling wave solutions, the study of the inside dynamics of the traveling waves, as well as a weak characterization of the asymptotic behavior of the spreading speed in the Cauchy problem. We also characterize traveling wave solutions for the two-velocity System with persistence (2.1.6). All along the article we work in the setting where N is increasing in space and cells propagate from left to right. Concerning the well-posedness we give a non-optimal criterion on the initial datum N^0 under which monotonicity of N is preserved locally in time and globally in space. However, for the rest of the article, monotonicity of N is a restrictive assumption in our study.

In Section 2.2, we prove an existence and uniqueness result for the parabolic System (2.1.1) locally in time under the assumption that N is initally monotonic. Because of the discontinuity of the advection coefficients, involving the coupling with the signaling gradient, direct application of Banach's Fixed point Theorem seems not directly applicable. To circumvent this delicate issue, we use the monotonicity of N and the definition of the threshold position $\bar{x}(t)$ (see Equation (2.1.2)) and apply Banach's Fixed Point Theorem to the curve $\bar{x}(\,\cdot\,)$. Our strategy relies on an endpoint estimate of N in $W^{3,\infty}$, which is out of the range of textbook estimates (to the best of our knowledge), that we achieve by a careful handling of the singularity at the interface. This reduction to an equation on the dynamics of a curve, coupled with a PDE, is reminiscent of studies in one-dimensional free boundary problems (see, *e.g.* Chapter 3 in [67] on the Stefan problem, [117] in the context of front propagation, or [132] in the context of mutation-selection dynamics in evolutionary biology).

In Section 2.3, we exhibit all positive and bounded traveling wave solutions for Equations (2.1.1), which propagate from left to right, *i.e.* all stationary solutions in the frame $(t, z) = (t, x - \sigma t)$, with $\sigma \geq 0$. This completes the preliminary analysis performed in [48]. In that case, Equation (2.1.1a) reduces to a piecewise constant second-order differential equation. All traveling wave profiles of ρ are a concatenation of a constant profile on the

left side and an exponentially decreasing profile on the right side. In both the small and large bias regimes, there exists a minimal velocity σ^* for traveling waves, given by Formula (2.1.4). For each $\sigma \geq \sigma^*$, there exists an associated wave profile (ρ^σ, N^σ), whose exponential decay at $z = +\infty$ is slower than the decay of the profile associated to the minimal velocity σ^*, which will be a crucial observation for Section 2.5.

In Section 2.4, we investigate the inside dynamics of the traveling waves. We introduce the formalism of neutral fractions [82, 152] and extent it to System (2.1.1). The methodology consists in studying the evolution of a fraction $\nu = \frac{\rho}{\rho^\sigma}$ of the traveling wave, relative to the stationary dynamics in the moving frame prescribed by the traveling wave solution ρ^σ. This gives rise to a linear parabolic equation,

$$\partial_t \nu + L\nu = 0.$$

In the case of large bias ($\chi > 1$), the elliptic operator L is self-adjoint in a weighted L^2-space and has the following spectral properties: 0 is a simple eigenvalue, whose eigenspace is spanned by the constants, and the operator L has a spectral gap. This leads to the conclusion that every neutral fraction converges exponentially to a constant in a weighted L^2-norm, which constitues the signature of a pushed wave, according to [82, 152]. In contrast, in the regime of small bias ($\chi \leq 1$), under the condition that $\nu_0 \rho^{\sigma^*}$ is square-integrable at $z = +\infty$, the solution ν converges to 0, which is the signature of a pulled wave. To do so, we use an energy method in an L^2-setting to show uniform convergence to 0 on intervals of the form $[a, +\infty)$.

In Section 2.5, we give a weak description of the asymptotic behavior of solutions to System (2.1.1). In fact, if we define the instantaneous spreading speed to be $\dot{\tilde{x}}(t)$, we show that for initial conditions bounded above by a multiple of ρ^{σ^*} and under the technical assumption that $\dot{\tilde{x}} \in L^\infty(\mathbb{R}_+)$, we have that,

$$\liminf_{t \to +\infty} \dot{\tilde{x}}(t) \leq \sigma^*, \text{ and } \limsup_{t \to +\infty} \dot{\tilde{x}}(t) \geq \sigma^*.$$

In other words, for an inital cell profile, whose exponential decay is faster than ρ^{σ^*}, up to a time extraction, the cell profile spreads either slower or quicker than the minimal wave speed σ^*. Hence, an important conclusion of this Section is that for biologically relevant initial conditions (*e.g.* a profile, whose support is bounded above), the only reasonable candidate for convergence to a traveling wave profile, is the one associated to the minimal wave speed σ^*. However, convergence in a proper sense to the traveling wave profile remains an open problem, a major difficulty being notably the lack of a suitable comparison principle.

Finally, in Section 2.6, we compute all subsonic traveling wave solutions, *i.e.* $\sigma < \varepsilon^{-1}$, for System (2.1.6). Subsonic traveling wave solutions exist if and only if $\varepsilon^{-1} > 1$. The structure of these solutions then follows *mutatis mutandis* the structure of the solutions for the parabolic System (2.1.1). In particular we find a similar expression for the minimal wave speed,

$$\sigma^* = \frac{1}{1+\varepsilon^2} \cdot \begin{cases} \chi + \frac{1}{\chi} & \text{if } \chi \in (1, \varepsilon^{-1}) \\ 2 & \text{if } \chi \leq 1 \end{cases}. \tag{2.1.7}$$

The proof consists in solving piecewise constant linear differential equations. Furthermore, the velocity formula for $\chi \leq 1$ coincides with the velocity of traveling waves in two-velocity models with a reaction term, but without advection (see for instance [26, 93]).

2.2 Existence and Uniquess of Solutions for the Parabolic Model

In this Section, we establish existence and uniqueness locally in time for the parabolic System (2.1.1), under certain conditions. The main difficulty to prove such a result stems from the singular advection term $\partial_x \left(\chi \text{sign}(\partial_x N) \mathbb{1}_{N \leq N_{\text{th}}} \rho\right)$ in Equation (2.1.1a). Therefore, we will work in the framework, where N is increasing and $N(t, \cdot) = N_{\text{th}}$ admits a unique solution $\bar{x}(t)$. In this framework, System (2.1.1) is equivalent to the following simpler System:

$$\begin{cases} \partial_t \rho - \partial_{xx} \rho + \partial_x(\chi \mathbb{1}_{x \leq \bar{x}(t)} \rho) = \mathbb{1}_{x > \bar{x}(t)} \rho & \text{(2.2.1a)} \\ \partial_t N - D \partial_{xx} N = -\rho N & \text{(2.2.1b)} \\ N(t, \bar{x}(t)) = N_{\text{th}}. & \text{(2.2.1c)} \end{cases}$$

In order to prove existence and uniqueness of the solution $\bar{x}(t)$, it suffices to require that $\partial_x N > 0$. Nevertheless, the property that $\partial_x N(t, \cdot) > 0$ is in general not implied by the sole condition that $\partial_x N^0 > 0$. In fact, it is possible to exhibit an initial configuration (ρ^0, N^0) where N^0 is monotonic, but nearly constant, and ρ^0 is sufficiently localized, so that the concentration $N(t, x)$ is no longer monotonic after some time $t > 0$, simply because of strong depletion around a spatial location. To circumvent this issue, we will here simply study System (2.2.1) and at the end of Section, we give a simple criterion, far from being optimal, on the inital data (ρ^0, N^0) such that the property $\partial_x N > 0$ is conserved for small time. Hence the solution of System (2.2.1), (ρ, N) is in fact a solution of (2.1.1).

The strategy of proof consists in applying a fixed point mapping to the curve $t \mapsto \bar{x}(t)$, *i.e.* the unique solution to $N(t, \cdot) = N_{\text{th}}$. More precisely, the main steps consist in (i) given the curve $\bar{x}(\cdot)$, solving Equations (2.2.1a,2.2.1b). (ii) Given the solution $(\rho[\bar{x}], N[\bar{x}])$, we show existence and uniqueness of a solution to Equation $N[\bar{x}](t, \cdot) = N_{\text{th}}$, that we denote $\bar{y}(\cdot)$. We then show that the solution $\bar{y}(\cdot)$ satisfies the following ODE:

$$\begin{cases} \dot{\bar{y}}(t) = -\frac{\partial_t N[\bar{x}](t, \bar{y}(t))}{\partial_x N[\bar{x}](t, \bar{y}(t))} \\ \bar{y}(0) = \bar{x}(0) \end{cases}. \tag{2.2.2}$$

In fact, ODE (2.2.2) is equivalent to Equation $N(t, \cdot) = N_{\text{th}}$. To show well-posedness of ODE (2.2.2), we need to obtain enough regularity on N: $\partial_t N[\bar{x}]$ and $(\partial_x N[\bar{x}])^{-1}$ should be locally Lipschitz in space. But from standard parabolic theory and the fact that the time derivative is expected to have the same regularity as the double space derivative, this roughly corresponds to $\partial_{xx} N[\bar{x}]$ being locally Lipschitz in space (and $\partial_x N[\bar{x}](t, \bar{y}(t))$ uniformly bounded away from 0). Hence the required regularity of N is $W^{3,\infty}$ in space. We shall see that this regularity holds true, but it is an endpoint case. (iii) Finally, the aim is to show that the mapping $\bar{x}(\cdot) \mapsto \bar{y}(\cdot)$ is a contraction and there exists a unique solution to the Cauchy problem:

$$\begin{cases} \dot{\bar{x}}(t) = -\frac{\partial_t N[\bar{x}](t, \bar{x}(t))}{\partial_x N[\bar{x}](t, \bar{x}(t))} \\ \bar{x}(\cdot)|_{t=0} = \bar{x}(0) \end{cases}.$$

However, because of the regularity requirement on N, the mapping $\bar{x} \mapsto \bar{y}$ becomes only a contraction, as will be seen, in a space that controls also the time derivative $\dot{\bar{x}}$. This deviates from standard Picard-Lindelöf theory of integration for ODEs, where contraction in L^∞-norm is sufficient and is obtained through a local in time integration of the ODE. Furthermore, from the ODE (2.2.2) it becomes clear that $\bar{x} \mapsto \bar{y}$ is at best merely Lipschitz continuous in the $W^{1,\infty}$-norm and not a contraction. In order to circumvent this issue, we

will consider the mapping $\bar{x} \mapsto \bar{y}$ in an $W^{1,p}$-norm (with $p < \infty$) and therefore by a local in time integration of the ODE (2.2.2), the mapping $\bar{x}(\,\cdot\,) \mapsto \bar{y}(\,\cdot\,)$ becomes a contraction in that given norm.

Next, we introduce some notations and basic facts, before moving on to the statement of Theorem 2.2.1.
The evolution operator of the heat equation $e^{t\mu\partial_{xx}}$ (here $\mu = 1$ and $\mu = D$ will be of interest) on the real-line is defined as follows:

$$e^{t\mu\partial_{xx}} f(x) = \frac{1}{\sqrt{4\pi\mu t}} \int_{\mathbb{R}} e^{-\frac{(x-y)^2}{4\mu t}} f(y) dy.$$

The operator $e^{t\mu\partial_{xx}}$ satisfies the following well-known functional inequalities, as a consequence of Young's convolutional inequality. For $1 \leq p \leq q \leq \infty$:

$$\left\| e^{t\mu\partial_{xx}} f \right\|_q \leq C t^{-\frac{1}{2}\left(\frac{1}{p}-\frac{1}{q}\right)} \left\| f \right\|_p, \tag{2.2.3}$$

$$\left\| e^{t\mu\partial_{xx}} \partial_x f \right\|_q \leq C t^{-\frac{1}{2}\left(\frac{1}{p}-\frac{1}{q}+1\right)} \left\| f \right\|_p. \tag{2.2.4}$$

In addition, we consider Hölder spaces $C^{k,\alpha}(\mathbb{R})$, with $\alpha \in (0,1)$ and the norm $\| \cdot \|_{C^{k,\alpha}(\mathbb{R})} = \sum_{i=0}^{k} \left\| \partial_x^i \cdot \right\|_\infty + [\partial_x^k \cdot]_\alpha$, where $[f]_\alpha := \sup_{x,y} \frac{|f(x)-f(y)|}{|x-y|^\alpha}$. From Real Interpolation Theory with the K-method (see Chapter 1 in [126]), we know that $C^{k,\alpha}(\mathbb{R}) = \left(C^k(\mathbb{R}), C^{k+1}(\mathbb{R})\right)_{\alpha,\infty}$, where $C^k(\mathbb{R})$ is the space of functions k-times differentiable with bounded derivatives, equipped with its usual $W^{k,\infty}$-norm. This leads to the following bounds:

$$\left\| e^{t\mu\partial_{xx}} f \right\|_{C^{0,\alpha}(\mathbb{R})} \leq C t^{-\frac{\alpha}{2}} \left\| f \right\|_\infty, \tag{2.2.5}$$

$$\left\| e^{t\mu\partial_{xx}} f \right\|_{C^{1,\alpha}(\mathbb{R})} \leq C t^{-\frac{1+\alpha}{2}} \left\| f \right\|_\infty, \tag{2.2.6}$$

$$\left\| \partial_x e^{t\mu\partial_{xx}} f \right\|_\infty \leq C t^{\frac{\alpha-1}{2}} \left\| f \right\|_{C^{0,\alpha}(\mathbb{R})}, \tag{2.2.7}$$

$$\left\| \partial_{xx} e^{t\mu\partial_{xx}} f \right\|_\infty \leq C t^{\frac{\alpha}{2}-1} \left\| f \right\|_{C^{0,\alpha}(\mathbb{R})}. \tag{2.2.8}$$

Set $B(A) := B_{W^{1,p}([0,T])}(A) = \left\{ \bar{y}(\,\cdot\,) \in W^{1,p}([0,T]) \middle| \|y\|_{W^{1,p}} \leq A \right\}$, with the norm $\|y\|_{W^{1,p}} = \|y\|_p + \|\dot{y}\|_p$ and $p \in (4,\infty)$. Given a curve $\bar{x} \in B(A)$, we consider System (2.2.1) in the moving frame of reference $(t,z) = (t, x - \bar{x}(t))$, which yields:

$$\begin{cases} \partial_t \tilde{\rho} - \dot{\bar{x}}(t)\partial_z \tilde{\rho} - \partial_{zz}\tilde{\rho} + \partial_z(\chi \mathbb{1}_{z\leq 0}\tilde{\rho}) = \mathbb{1}_{z>0}\tilde{\rho} & \text{(2.2.9a)} \\ \partial_t \tilde{N} - \dot{\bar{x}}(t)\partial_z \tilde{N} - D\partial_{zz}\tilde{N} = -\tilde{\rho}\tilde{N}. & \text{(2.2.9b)} \end{cases}$$

Of note, throughout this Section $\tilde{\rho}, \tilde{N}$ denotes the solutions in the moving frame, in order to easily distinguish between for instance ρ and $\tilde{\rho}$. Without loss of generality, we also suppose that $\bar{x}(0) = 0$, so that $\tilde{\rho}^0 = \rho^0$ and $\tilde{N}^0 = N^0$. Thereafter, we will however drop the diacritical mark $\tilde{}$ and systematically designate by ρ the solution in the moving frame.

As already observed in the Introduction, continuity of the flux in Equation (2.2.9a) leads by a Rankine-Hugoniot type of argument to a C^1-jump relation (2.1.3), which in the moving frame can simply be rewritten as:

$$\partial_z \tilde{\rho}(t,0^+) - \partial_z \tilde{\rho}(t,0^-) = -\chi \tilde{\rho}(t,0).$$

In fact, it is furthermore possible to factorize $\tilde{\rho}$ under the form vU, with a function U such that the factorization precisely cancels out the C^1-jump relation at $z = 0$. For instance, we can choose $U(z) = \begin{cases} 1 & \text{if } z \leq 0 \\ e^{-\chi z} & \text{if } z > 0 \end{cases}$. Notice that U exactly satisfies the C^1-jump relation and that we obtain the following Equation on v:

$$\partial_t v - \partial_{zz} v - \beta(t,z)\partial_z v - \gamma(t,z)v = 0, \tag{2.2.10}$$

where $\beta(t,z) := \dot{\bar{x}} - \chi \mathbb{1}_{z\leq 0} - 2\chi \mathbb{1}_{z>0}$ and $\gamma(t,z) := \chi\left(\left(\chi + \frac{1}{\chi}\right) - \dot{\bar{x}}\right)\mathbb{1}_{z>0}$. Under this circumstance, v will be of higher regularity, *i.e.* $C^{1,\alpha}$. Of note, the particular choice of U is arbitrary in this Section, although as will be seen in Section 2.3, U corresponds to the traveling wave profile in the case $\chi \geq 1$. In fact, one could consider other candidates for U, but for the sake of simplicity we restrict ourselves to this particular choice.

Let us now move to the statement of a well-posedness theorem locally in time under the condition that N^0 is increasing.

Theorem 2.2.1. *Let $p \in (4,\infty)$, $\alpha \in \left(0, 1 - \frac{2}{p}\right)$ and $\alpha' \in \left(\frac{2}{p}, 1 - \frac{2}{p}\right)$. Suppose that $N^0 \in W^{3,\infty}(\mathbb{R})$ and $\frac{\rho^0}{U} \in C^{1,\alpha}(\mathbb{R})$. Additionally suppose that $\partial_x N^0 > 0$ and that $N^0(\,\cdot\,) = N_{th}$ admits a (unique) solution, for $x = 0$. For a certain $\zeta > 0$, denote $\underline{m}$ a lower bound of $\partial_x N^0$ on the interval $[-\zeta, +\zeta]$.*

Given $A > 0$ big enough (depending on $D, \chi, p, \alpha, \alpha', \left\|\frac{\rho^0}{U}\right\|_{C^{1,\alpha}}, \left\|N^0\right\|_{W^{3,\infty}}, \underline{m}, \zeta$) there exists a small enough $T > 0$, such that for any curve $\bar{x} \in B(A)$, there exists a unique solution $(\tilde{\rho}, \tilde{N})$ to System (2.2.9). Moreover, $\tilde{\rho} \in L^\infty([0,T], W^{1,\infty}(\mathbb{R}))$, $v = \frac{\tilde{\rho}}{U} \in L^\infty([0,T], C^{1,\alpha}(\mathbb{R}))$ and $\tilde{N} \in L^\infty([0,T], W^{3,\infty}(\mathbb{R}))$.

Furthermore, there exists a unique curve $\bar{x} \in B(A)$, such that the solution $(\tilde{\rho}, \tilde{N})$ to System (2.2.9) satisfies in addition the condition $\tilde{N}(t,0) = N_{th}$, or in the static frame $N(t, \bar{x}(t)) = N_{th}$, for $t \in [0,T]$. In other terms, (ρ, N) in the static frame is the unique solution to System (2.2.1).

Proof. We divide the proof of Theorem 2.2.1 into several steps:

1. a) We fix a curve $\bar{x}(\,\cdot\,) \in W^{1,p}([0,T])$ and construct the unique (mild) solution $v \in L^\infty\left([0,T], C^{1,\alpha}(\mathbb{R})\right)$ to Equation (2.2.10). Furthermore the map $\bar{x} \in B(A) \mapsto v \in L^\infty([0,T], C^{1,\alpha}(\mathbb{R}))$ is Lipschitz continuous.
   b) Given v and thus $\tilde{\rho}$, we construct the unique solution $\tilde{N} \in L^\infty\left([0,T], C^{2,\alpha'}(\mathbb{R})\right)$ to Equation (2.2.9b). Furthermore the map $\bar{x} \in B(A) \mapsto \tilde{N} \in L^\infty([0,T], C^{2,\alpha'}(\mathbb{R}))$ is Lipschitz continuous.

2. We show that $\tilde{N} \in L^\infty([0,T], W^{3,\infty}(\mathbb{R}))$. This regularity is an improvement from the more standard regularity result obtained in Step 1b) and is crucial for the rest of the proof. We carry out estimates on explicit computations and finally we refer to the Remark at the end of the proof of Theorem 2.2.1 for a brief argument to show that the obtained regularity is borderline.

3. For $t \in [0,T]$, $N(t)$ (in the static frame) admits a unique solution to the equation $N(t,\,\cdot\,) = N_{\text{th}}$ that we denote by $\bar{y}(t)$. Furthermore $\bar{y}(\,\cdot\,)$ satisfies ODE (2.2.2) and the regularity obtained on N leads to well-posedness of ODE (2.2.2).

4. For $A > 0$ big enough the map $\bar{x} \mapsto \bar{y}$ maps from $B(A)$ into itself and is furthermore a contraction. We conclude by Banach's Fixed Point Theorem and obtain

well-posedness.

Conventions. For the sake of clarity, throughout the proof we will make use of the following conventions. C will represent constants that depend on $D, \chi, p, \alpha, \alpha', \underline{m}, \zeta$. In order to simplify the presentations of the inequalities, we suppose that $A, \left\|\frac{\rho^0}{U}\right\|_{C^{1,\alpha}}, \left\|N^0\right\|_{W^{3,\infty}}, \left\|N^0\right\|_{C^{2,\alpha'}} > 1$ in order to use freely for instance the bounds $1+A \leq 2A$ or $\left\|\frac{\rho^0}{U}\right\|_{C^{1,\alpha}} \leq \left\|\frac{\rho^0}{U}\right\|^2_{C^{1,\alpha}}$. In parallel, we suppose that $T < 1$, in order to use freely bounds of the type $|t-s|^{-c} \leq |t-s|^{-d}$, for $t, s \in [0,T]$, when $0 < c < d$.

Step 1a: Existence and uniqueness of a (mild) solution v to Equation (2.2.10).
Consider the affine map $F : L^\infty\left([0,T], C^{1,\alpha}(\mathbb{R})\right) \to L^\infty\left([0,T], C^{1,\alpha}(\mathbb{R})\right)$, for $t \in [0,T]$:

$$F[u](t) = e^{t\partial_{zz}}\left(\frac{\rho^0}{U}\right) + \int_0^t e^{(t-s)\partial_{zz}}\left(\beta(s)\partial_z u(s) + \gamma(s)u(s)\right) ds. \tag{2.2.11}$$

As $\frac{\rho^0}{U} \in C^{1,\alpha}(\mathbb{R})$, we have that $e^{t\partial_{zz}}\left(\frac{\rho^0}{U}\right) \in L^\infty\left([0,T], C^{1,\alpha}(\mathbb{R})\right)$.
We will now show that the second term in (2.2.11) is in $L^\infty\left([0,T], C^{1,\alpha}(\mathbb{R})\right)$. Notice that $\beta(s,z)\partial_z u(s,z) = \partial_z\left(\beta(s,z)u(s,z)\right) + \chi u(s,0)\delta_0$. Hence by using Bounds (2.2.3,2.2.4), the fact that $\left\|e^{(t-s)\partial_{zz}}\delta_0\right\|_\infty \leq \frac{C}{\sqrt{t-s}}$ and that $|\beta| \leq C(1+|\dot{\bar{x}}(s)|)$, we have that:

$$\begin{aligned}
\left\|\int_0^t e^{(t-s)\partial_{zz}}\left(\beta(s)\partial_z u(s)\right) ds\right\|_\infty &\leq C\int_0^t\left(\frac{\left\|\beta(s)u(s)\right\|_\infty}{\sqrt{t-s}} + \frac{|u(s,0)|}{\sqrt{t-s}}\right) ds \\
&\leq C\int_0^t \frac{\left(1+|\dot{\bar{x}}(s)|\right)\left\|u(s)\right\|_\infty}{\sqrt{t-s}} ds \\
&\leq C\left\|u\right\|_\infty \int_0^t \frac{\left(1+|\dot{\bar{x}}(s)|\right)}{\sqrt{t-s}} ds \\
&\leq C\left\|u\right\|_\infty \left(1+\left\|\dot{\bar{x}}\right\|_p\right) T^{\frac{p-2}{2p}} \\
&\leq C\left\|u\right\|_\infty A T^{\frac{p-2}{2p}},
\end{aligned}$$

where we have used Hölder's inequality, $p > 2$ in order to guarantee the integrability of $s \mapsto (t-s)^{-\frac{p}{2(p-1)}}$ and the convention that $T < 1$ and $A > 1$. In a slightly easier manner, we have also that:

$$\left\|\partial_z \int_0^t e^{(t-s)\partial_{zz}}\left(\beta(s)\partial_z u(s)\right) ds\right\|_\infty \leq C\left\|\partial_z u\right\|_\infty A T^{\frac{p-2}{2p}}.$$

Finally by using Bound (2.2.6):

$$\left[\partial_z \int_0^t e^{(t-s)\partial_{zz}}\left(\beta(s)\partial_z u(s)\right) ds\right]_\alpha \leq C\left\|\partial_z u\right\|_\infty A T^{\frac{p(1-\alpha)-2}{2p}},$$

where integrability of $\left\|s \mapsto (t-s)^{-\frac{\alpha+1}{2}}\right\|_{\frac{p}{p-1}}$ is guaranteed by the condition $\alpha < 1 - \frac{2}{p}$.
This yields the bound:

$$\left\|\int_0^t e^{(t-s)\partial_{zz}}\left(\beta(s)\partial_z u(s)\right) ds\right\|_{L^\infty([0,T], C^{1,\alpha}(\mathbb{R}))} \leq C\left\|u\right\|_{L^\infty([0,T], W^{1,\infty}(\mathbb{R}))} A T^{\frac{p(1-\alpha)-2}{2p}},$$

where by the conventions, we have used that $T^{\frac{p-2}{2p}} < T^{\frac{p(1-\alpha)-2}{2p}}$. The remaining term in (2.2.11) admits a similar bound. In fact:

$$\left\| \int_0^t e^{(t-s)\partial_{zz}} \left(\gamma(s)u(s)\right) ds \right\|_{L^\infty([0,T],C^{1,\alpha}(\mathbb{R}))} \leq C \left\|u\right\|_{L^\infty([0,T]\times\mathbb{R})} AT^{\frac{p(1-\alpha)-2}{2p}}.$$

Hence F maps $L^\infty([0,T],C^{1,\alpha}(\mathbb{R}))$ into itself.

Furthermore, if we choose T small enough (depending on A), for instance such that the Lipschitz constant of F becomes $\frac{1}{2}$, then F is a contraction and by Banach's Fixed Point Theorem Equation (2.2.9a) admits a unique solution v. Furthermore, we have the bound:

$$\begin{aligned} \|v\| = \|F[v]\| \leq \|F[v]-F[0]\| + \|F[0]\| \leq \frac{\|v\|}{2} + \|F[0]\| \\ \implies \|v\|_{L^\infty([0,T],C^{1,\alpha}(\mathbb{R}))} \leq 2\left\|\frac{\rho^0}{U}\right\|_{C^{1,\alpha}(\mathbb{R})}. \end{aligned} \tag{2.2.12}$$

It remains to show that the map $\bar{x} \mapsto v$ is Lipschitz continuous. Given $\bar{x}_1, \bar{x}_2 \in B(A)$, consider the two corresponding functions $v_1, v_2 \in L^\infty([0,T],C^{1,\alpha}(\mathbb{R}))$, as well as the two corresponding maps F_1, F_2, and set $w := v_1 - v_2$:

$$\begin{aligned} w(t) &= \int_0^t e^{(t-s)\partial_{zz}} \left(\beta_1\partial_z w + (\beta_1-\beta_2)\partial_z v_2 + \gamma_1 w + (\gamma_1-\gamma_2)v_2\right) ds \\ &= \left(F_1[w] - e^{t\partial_{zz}}\left(\frac{\rho^0}{U}\right)\right) + \int_0^t e^{(t-s)\partial_{zz}} \left((\beta_1-\beta_2)\partial_z v_2 + (\gamma_1-\gamma_2)v_2\right) ds. \end{aligned}$$

First of all, by using that $e^{t\partial_{zz}}\left(\frac{\rho^0}{U}\right) = F_1[0]$ and by recalling that by the choice of T the Lipschitz constant of F_1 is $\frac{1}{2}$, we have:

$$\begin{aligned} \left\|F_1[w] - e^{t\partial_{zz}}\left(\frac{\rho^0}{U}\right)\right\|_{L^\infty([0,T],C^{1,\alpha}(\mathbb{R}))} &= \|F_1[w]-F_1[0]\|_{L^\infty([0,T],C^{1,\alpha}(\mathbb{R}))} \\ &\leq \frac{1}{2}\|w\|_{L^\infty([0,T],C^{1,\alpha}(\mathbb{R}))}. \end{aligned}$$

We have that $\beta_1 - \beta_2 = \dot{\bar{x}}_1 - \dot{\bar{x}}_2$ and $\gamma_1 - \gamma_2 = (\dot{\bar{x}}_1 - \dot{\bar{x}}_2)\chi\mathbb{1}_{z\geq 0}$, which leads for $t \in [0,T]$ to:

$$\begin{aligned} &\left\| \int_0^t e^{(t-s)\partial_{zz}} \left((\beta_1-\beta_2)\partial_z v_2 + (\gamma_1-\gamma_2)v_2\right) ds \right\|_{C^{1,\alpha}(\mathbb{R})} \\ =&\left\| \int_0^t e^{(t-s)\partial_{zz}} (\dot{\bar{x}}_1(s) - \dot{\bar{x}}_2(s))(\partial_z v_2 + \chi\mathbb{1}_{z\geq 0}v_2) ds \right\|_{C^{1,\alpha}(\mathbb{R})} \\ \leq& C\int_0^t \frac{|\dot{\bar{x}}_2(s) - \dot{\bar{x}}_1(s)|\,\|\partial_z v_2(s) + \chi\mathbb{1}_{z\geq 0}v_2(s)\|_\infty}{(t-s)^{\frac{\alpha+1}{2}}} ds \\ \leq& C\|v_2\|_{L^\infty([0,T],C^{1,\alpha}(\mathbb{R}))} \int_0^t \frac{|\dot{\bar{x}}_2(s) - \dot{\bar{x}}_1(s)|}{(t-s)^{\frac{\alpha+1}{2}}} ds \\ \leq& C\left\|\frac{\rho^0}{U}\right\|_{C^{1,\alpha}(\mathbb{R})} \|\dot{\bar{x}}_2 - \dot{\bar{x}}_1\|_p T^{\frac{p(1-\alpha)-2}{2p}}, \end{aligned}$$

where the last bound is an application of Hölder's inequality. Hence we have that:

$$\|w\|_{L^\infty([0,T],C^{1,\alpha}(\mathbb{R}))} \leq \frac{1}{2}\|w\|_{L^\infty([0,T],C^{1,\alpha}(\mathbb{R}))} + C\left\|\frac{\rho^0}{U}\right\|_{C^{1,\alpha}(\mathbb{R})} \|\dot{\bar{x}}_2 - \dot{\bar{x}}_1\|_p T^{\frac{p(1-\alpha)-2}{2p}}.$$

And finally we establish that the map $\bar{x} \mapsto v$ is Lipschitz continuous with:

$$\|w\|_{L^\infty([0,T],C^{1,\alpha}(\mathbb{R}))} \leq CT^{\frac{p(1-\alpha)-2}{2p}} \left\|\frac{\rho^0}{U}\right\|_{C^{1,\alpha}(\mathbb{R})} \|\dot{\bar{x}}_2 - \dot{\bar{x}}_1\|_p \tag{2.2.13}$$

Step 1b: Existence and uniqueness of a (mild) solution $\tilde{N}$ to Equation (2.2.9b).

Consider the map $G : L^\infty([0,T], C^{2,\alpha'}(\mathbb{R})) \to L^\infty([0,T], C^{2,\alpha'}(\mathbb{R}))$, with $\alpha' \in (\frac{2}{p}, 1-\frac{2}{p})$. For $t \in [0,T]$:

$$G[u](t) = e^{tD\partial_{zz}} N^0 + \int_0^t e^{(t-s)D\partial_{zz}} \left(\dot{\bar{x}}(s)\partial_z u(s) - v(s)Uu(s)\right) ds. \tag{2.2.14}$$

We proceed as before and treat explicitly only the following two terms:

$$\begin{aligned}
\left[\partial_{zz}\int_0^t e^{D(t-s)\partial_{zz}} v(s)Uu(s)ds\right]_{\alpha'} &\leq C\int_0^t (t-s)^{-\frac{1+\alpha'}{2}} \left\|\partial_z\left(v(s)Uu(s)\right)\right\|_\infty ds \\
&\leq C\int_0^t (t-s)^{-\frac{1+\alpha'}{2}} \left(\|\partial_z v(s)\|_\infty \|u(s)\|_\infty + \|v(s)\|_\infty \|\partial_z u(s)\|_\infty\right) ds \\
&\leq CT^{\frac{1-\alpha'}{2}} \|v\|_{L^\infty([0,T],W^{1,\infty}(\mathbb{R}))} \|u\|_{L^\infty([0,T],W^{1,\infty}(\mathbb{R}))} \\
&\leq CT^{\frac{1-\alpha'}{2}} \left\|\frac{\rho^0}{U}\right\|_{C^{1,\alpha}(\mathbb{R})} \|u\|_{L^\infty([0,T],W^{1,\infty}(\mathbb{R}))},
\end{aligned}$$

where we used the fact that $U \in W^{1,\infty}(\mathbb{R})$. And:

$$\begin{aligned}
\left[\partial_{zz}\int_0^t e^{D(t-s)\partial_{zz}} \dot{\bar{x}}(s)\partial_z u(s)ds\right]_{\alpha'} &\leq C\int_0^t (t-s)^{-\frac{1+\alpha'}{2}} |\dot{\bar{x}}(s)| \|\partial_{zz} u(s)\|_\infty ds \\
&\leq CA\|u\|_{L^\infty([0,T],W^{2,\infty}(\mathbb{R})} T^{\frac{1-\alpha'}{2}}.
\end{aligned}$$

By using Bound (2.2.12), we can choose T such that the Lipschitz constant for G becomes $\frac{1}{2}$. Therefore G is a contraction and this yields existence and uniqueness of the solution $\tilde{N}$ to Equation (2.2.9b) and $\tilde{N}$ satisfies the bound:

$$\left\|\tilde{N}\right\|_{L^\infty([0,T],C^{2,\alpha'}(\mathbb{R}))} \leq 2\left\|N^0\right\|_{C^{2,\alpha'}(\mathbb{R})} \leq 2\left\|N^0\right\|_{W^{3,\infty}}. \tag{2.2.15}$$

As before, we show that $\bar{x} \in B(A) \mapsto N \in L^\infty([0,T], C^{2,\alpha'}(\mathbb{R}))$ is Lipschitz continuous. Given $\bar{x}_1, \bar{x}_2 \in B(A)$, consider the corresponding $\tilde{N}_1, \tilde{N}_2$, as well as the two corresponding maps G_1, G_2. We recall that $w = v_1 - v_2$ and set $P := \tilde{N}_1 - \tilde{N}_2$:

$$P = G_1[P] - G_1[0] + \int_0^t e^{(t-s)D\partial_{zz}} \left((\dot{\bar{x}}_1(s) - \dot{\bar{x}}_2(s))\partial_z \tilde{N}_2(s)ds - w(s)U\tilde{N}_2(s)\right) ds.$$

By the same arguments as before, we have the following bounds:

$$\begin{aligned}
\|G_1[P] - G_1[0]\|_{L^\infty([0,T],C^{2,\alpha'}(\mathbb{R}))} &\leq \frac{1}{2}\|P\|_{L^\infty([0,T],C^{2,\alpha'}(\mathbb{R}))} \\
\left\|\int_0^t e^{(t-s)D\partial_{zz}} (\dot{\bar{x}}_1(s) - \dot{\bar{x}}_2(s))\partial_z \tilde{N}_1(s)ds\right\|_{L^\infty([0,T],C^{2,\alpha'}(\mathbb{R}))} &\leq CT^{\frac{p(1-\alpha')-2}{2p}} \left\|N^0\right\|_{C^{2,\alpha'}(\mathbb{R})} \|\dot{\bar{x}}_2 - \dot{\bar{x}}_1\|_p \\
\left\|\int_0^t e^{(t-s)\partial_{zz}} w(s)U\tilde{N}_1(s)ds\right\|_{L^\infty([0,T],C^{2,\alpha'}(\mathbb{R}))} &\leq CT^{\frac{1-\alpha'}{2}} \|w\|_{L^\infty([0,T],C^{1,\alpha}(\mathbb{R}))} \left\|N^0\right\|_{C^{2,\alpha'}(\mathbb{R})}.
\end{aligned}$$

By recalling Inequality (2.2.13) on $\|w\|_{L^\infty([0,T],C^{1,\alpha}(\mathbb{R}))}$, we obtain that the map $\bar{x} \mapsto N$ is Lipschitz continuous, with:

$$\|P\|_{L^\infty([0,T],C^{2,\alpha'}(\mathbb{R}))} \leq C\left(T^{\frac{p(1-\alpha')-2}{2p}} + T^{\frac{(1-\alpha')(p(1-\alpha)-2)}{4p}}\right)\left\|\frac{\rho^0}{U}\right\|_{C^{1,\alpha}(\mathbb{R})}\left\|N^0\right\|_{C^{2,\alpha'}(\mathbb{R})}\|\dot{\bar{x}}_2 - \dot{\bar{x}}_1\|_p\,. \tag{2.2.16}$$

Step 2: Enhanced regularity on $\tilde{N} \in L^\infty([0,T], W^{3,\infty}(\mathbb{R}))$.
First let us point out that $\tilde{N}$ satisfies Equation (2.2.9b):

$$\partial_t \tilde{N} - \partial_{zz}\tilde{N} - \dot{\bar{x}}(t)\partial_z \tilde{N} = -vU\tilde{N}.$$

Suppose that $vU\tilde{N}$ had $C^{1,\alpha''}$ regularity in space for some $\alpha'' \in (0,1)$. Then by standard Parabolic Schauder Estimates (see Chapter 8 in [116]), $\tilde{N}$ would have $C^{3,\alpha''}$ regularity in space. But because of the C^1-discontinuity of U at $z = 0$, this fails and $vU\tilde{N}$ is merely Lipschitz continuous. This constitutes the endpoint case for the Parabolic Schauder Estimates and it cannot generally be deduced that $\tilde{N}$ has $W^{3,\infty}$ regularity in space. However, in our case this result remains true, as we can single out the C^1-discontinuity of U at $z = 0$, then prove that this explicit contribution enjoys the endpoint $W^{3,\infty}$ regularity. Finally, we refer the reader to Remark 2.2 at the end of this proof, where we give an argument why any higher regularity is not to be expected.

From the preceding point, we have the following representation for $\tilde{N}$:

$$\tilde{N}(t) = e^{tD\partial_{zz}}N^0 + \int_0^t e^{(t-s)D\partial_{zz}}\left(\dot{\bar{x}}(s)\partial_z\tilde{N}(s) - v(s)U\tilde{N}(s)\right)ds. \tag{2.2.17}$$

The term $e^{tD\partial_{zz}}N^0 \in L^\infty([0,T], W^{3,\infty}(\mathbb{R}))$, as by assumption $N^0 \in W^{3,\infty}(\mathbb{R})$.
In addition, by using Bound (2.2.8):

$$\begin{aligned}\left\|\partial_{zzz}\int_0^t e^{(t-s)D\partial_{zz}}\dot{\bar{x}}(s)\partial_z\tilde{N}(s)ds\right\|_\infty &\leq \int_0^t \left\|\partial_{zz}e^{(t-s)\partial_{zz}}\dot{\bar{x}}(s)\partial_{zz}\tilde{N}(s)\right\|_\infty ds \\ &\leq CT^{\frac{p\alpha'-2}{2p}}\|\dot{\bar{x}}\|_p\left\|\tilde{N}\right\|_{L^\infty([0,T],C^{2,\alpha'}(\mathbb{R}))},\end{aligned}$$

where the integrability of $\left\|s \mapsto (t-s)^{\frac{\alpha'}{2}-1}\right\|_{\frac{p}{p-1}}$ is due to the condition $\alpha' > \frac{2}{p}$.
It remains to be shown that $\int_0^t e^{(t-s)D\partial_{zz}}\left(v(s)U\tilde{N}(s)\right)ds \in L^\infty([0,T], W^{3,\infty}(\mathbb{R}))$. In order to do so, we will decompose the term $\partial_z\left(v(s)U\tilde{N}(s)\right)$ as the sum of a $C^{0,\alpha}$ function and a discontinous function. In fact for $s \in [0,T], z \in \mathbb{R}$:

$$\partial_z\left(vU\tilde{N}\right)(s,z) = \underbrace{\partial_z\left(vU\tilde{N}\right)(s,z) - [\![\partial_z\left(vU\tilde{N}\right)(s)]\!]_{z=0}\mathbb{1}_{z\geq 0}}_{g(s,z):=} + \underbrace{[\![\partial_z\left(vU\tilde{N}\right)(s)]\!]_{z=0}}_{h(s):=}\mathbb{1}_{z\geq 0}, \tag{2.2.18}$$

where $[\![f]\!]_{z_0} = \lim_{z\to z_0^+} f(z) - \lim_{z\to z_0^-} f(z)$. Here $[\![\partial_z\left(vU\tilde{N}\right)(s)]\!]_{z=0}$ is well-defined, since $v(s), \tilde{N}(s) \in C^{1,\alpha}(\mathbb{R})$ and $U \in C^1(\mathbb{R}_+) \cap C^1(\mathbb{R}_-)$. We will conclude by treating both terms

separately and using the following bound:

$$\begin{aligned}
&\left\|\partial_{zzz}\int_0^t e^{(t-s)\partial_{zz}}\left(v(s)U\tilde{N}(s)\right)ds\right\|_\infty \\
\leq&\left\|\int_0^t \partial_{zz}e^{(t-s)\partial_{zz}}g(s)ds\right\|_\infty+\left\|\int_0^t \partial_{zz}e^{(t-s)\partial_{zz}}h(s)\mathbb{1}_{z\geq 0}ds\right\|_\infty .
\end{aligned} \tag{2.2.19}$$

Lemma 2.2.1.1. *Let $f\in L^\infty([0,T],C^{0,\alpha}(\mathbb{R}_+))\cap L^\infty([0,T],C^{0,\alpha}(\mathbb{R}_-))$, where we understand $C^{0,\alpha}(\mathbb{R}_\pm)$ as a normed space, equipped with the norm $\|\cdot\|_\infty+[\,\cdot\,]_{\alpha;\mathbb{R}_\pm}$.*

Then we have that $g:=f-[\![f]\!]_{z=0}\mathbb{1}_{z\geq 0}\in L^\infty([0,T],C^{0,\alpha}(\mathbb{R}))$ and:

$$\|g\|_{L^\infty([0,T],C^{0,\alpha}(\mathbb{R}))}\leq 2^{1-\alpha}\max\left\{\sup_{t\in[0,T]}[f(t)]_{\alpha;\mathbb{R}_+},\sup_{t\in[0,T]}[f(t)]_{\alpha;\mathbb{R}_-}\right\}+3\|f\|_\infty .$$

Proof. By construction we have that for $t\in[0,T]$, $g(t)\in C^0(\mathbb{R})$ and $\|g\|_\infty\leq 3\|f\|_\infty$, since $|[\![f]\!]_{z=0}|\leq 2\|f\|_\infty$. Let $t\in[0,T]$ and $x,y\in\mathbb{R}$ and suppose that $x<0<y$:

$$\begin{aligned}
\frac{|f(t,y)-f(t,x)|}{|y-x|^\alpha}&\leq\frac{|f(t,y)-f(t,0)|}{|y-x|^\alpha}+\frac{|f(t,0)-f(t,x)|}{|y-x|^\alpha} \\
&\leq 2\left(\frac{1}{2}\cdot\frac{|y|^\alpha}{|y-x|^\alpha}[f(t)]_{\alpha;\mathbb{R}_-}+\frac{1}{2}\cdot\frac{|x|^\alpha}{|y-x|^\alpha}[f(t)]_{\alpha;\mathbb{R}_+}\right) \\
&\leq 2\left(\frac{|y|+|x|}{2|y-x|}\right)^\alpha\max\left\{\sup_{t\in[0,T]}[f(t)]_{\alpha;\mathbb{R}_+},\sup_{t\in[0,T]}[f(t)]_{\alpha;\mathbb{R}_-}\right\} \\
&=2^{1-\alpha}\max\left\{\sup_{t\in[0,T]}[f(t)]_{\alpha;\mathbb{R}_+},\sup_{t\in[0,T]}[f(t)]_{\alpha;\mathbb{R}_-}\right\},
\end{aligned} \tag{2.2.20}$$

where we have used the concavity of $z\mapsto z^\alpha$ and the fact that $x<0<y$.

If $x,y<0$ (resp. $x,y>0$), then the left handside of (2.2.20) is simply bounded by $[f(t)]_{\alpha;\mathbb{R}_-}$ (resp. $[f(t)]_{\alpha;\mathbb{R}_+}$). □

Let $f=\partial_z\left(vU\tilde{N}\right)\in L^\infty([0,T],C^{0,\tilde{\alpha}}(\mathbb{R}_+))\cap L^\infty([0,T],C^{0,\tilde{\alpha}}(\mathbb{R}_-))$, where we have set $\tilde{\alpha}:=\min(\alpha,\alpha')$, and apply Lemma 2.2.1.1 to obtain that $g\in L^\infty([0,T],C^{0,\tilde{\alpha}}(\mathbb{R}))$. Through Bound (2.2.8), this leads to:

$$\begin{aligned}
&\left\|\int_0^t \partial_{zz}e^{(t-s)\partial_{zz}}g(s)ds\right\|_\infty \\
\leq&CT^{\frac{\tilde{\alpha}}{2}}\|g\|_{L^\infty([0,T],C^{0,\tilde{\alpha}}(\mathbb{R}))} \\
\leq&CT^{\frac{\tilde{\alpha}}{2}}\left(\max\left\{\sup_{t\in[0,T]}[\partial_z\left(vU\tilde{N}\right)(t)]_{\tilde{\alpha};\mathbb{R}_+},\sup_{t\in[0,T]}[\partial_z\left(vU\tilde{N}\right)(t)]_{\tilde{\alpha};\mathbb{R}_-}\right\}\right. \\
&\left.+\left\|\partial_z\left(vU\tilde{N}\right)\right\|_{L^\infty([0,T],C^{0,\tilde{\alpha}}(\mathbb{R}))}\right) \\
\leq&CT^{\frac{\tilde{\alpha}}{2}}\|v\|_{L^\infty([0,T],C^{1,\tilde{\alpha}}(\mathbb{R}))}\|N\|_{L^\infty([0,T],C^{1,\tilde{\alpha}}(\mathbb{R}))} \\
\leq&CT^{\frac{\tilde{\alpha}}{2}}\left\|\frac{\rho^0}{U}\right\|_{C^{1,\alpha}}\|N^0\|_{W^{3,\infty}},
\end{aligned} \tag{2.2.21}$$

where we have used that the product of $C^{1,\tilde{\alpha}}$ functions are $C^{1,\tilde{\alpha}}$.
The last term is treated differently by using explicit computations:

$$\begin{aligned}\int_0^t \partial_{zz} e^{(t-s)D\partial_{zz}} h(s) \mathbb{1}_{z\geq 0} ds &= \int_0^t \partial_z e^{(t-s)D\partial_{zz}} h(s)\delta_0 ds \\ &= -\int_0^t \frac{zh(s)}{4\pi^{\frac{1}{2}} D^{\frac{3}{2}} (t-s)^{\frac{3}{2}}} e^{-\frac{z^2}{4(t-s)}} ds \\ &= -\int_{\frac{|z|}{\sqrt{t}}}^{\infty} \frac{h\left(t-\frac{z^2}{u^2}\right)}{2\pi^{\frac{1}{2}} D^{\frac{3}{2}}} e^{-u^2} du \qquad \text{, where } u = \frac{|z|}{\sqrt{(t-s)}}.\end{aligned}$$

Hence, by the integrability of e^{-u^2}:

$$\left\| \int_0^t \partial_{zz} e^{(t-s)D\partial_{zz}} h(s) \mathbb{1}_{z\geq 0} ds \right\|_\infty \leq C \|h\|_\infty$$

But we have the following identity:

$$\begin{aligned}&h(s) \\ =&\lim_{z\to 0^+} \partial_z (vU\tilde{N})(s,z) - \lim_{z\to 0^-} \partial_z (vU\tilde{N})(s,z) \\ =&\lim_{z\to 0^+} U(z)\partial_z (v\tilde{N})(s,z) \\ &+ \lim_{z\to 0^+} (v\tilde{N})(s,z)\partial_z U(z) - \lim_{z\to 0^-} U(z)\partial_z (v\tilde{N})(s,z) - \lim_{z\to 0^-} (v\tilde{N})(s,z)\partial_z U(z) \\ =&v(s,0)\tilde{N}(s,0)[\![\partial_z U]\!]_{z=0} \\ =&-\chi v(s,0)\tilde{N}(s,0).\end{aligned}$$

Therefore:

$$\left\| \int_0^t \partial_{zz} e^{(t-s)D\partial_{zz}} h(s) \mathbb{1}_{z\geq 0} ds \right\|_\infty \leq C \|v\|_\infty \left\|\tilde{N}\right\|_\infty . \tag{2.2.22}$$

Bringing Bounds (2.2.19, 2.2.21, 2.2.22) together, we can conclude that:

$$\int_0^t e^{(t-s)D\partial_{zz}} \left(v(s) U \tilde{N}(s) \right) ds \in L^\infty([0,T], W^{3,\infty}(\mathbb{R})).$$

Thus $\tilde{N} \in L^\infty([0,T], W^{3,\infty}(\mathbb{R}))$.

Step 3: Definition of the map $\bar{x} \mapsto \bar{y}$: Existence and Uniqueness of the solution $N(t,\cdot) = N_{\text{th}}$.

We consider ρ, N again in the initial frame (t,x), where they satisfy Equations (2.2.1). Note that $\|N\|_\infty = \left\|\tilde{N}\right\|_\infty$ and $\|\rho\|_\infty \leq \|v\|_\infty$. By assumption, we have that $\partial_x N^0 > \underline{m}$ on the interval $[-\zeta, +\zeta]$. Therefore by setting $\varepsilon = \zeta \underline{m}$, we have that for $x < -\zeta, N^0(x) < N_{\text{th}} - \varepsilon$ and $x > \zeta, N^0(x) > N_{\text{th}} + \varepsilon$.

1. We start by showing that there exists $T > 0$, such that for $t \in [0,T]$ and $x \leq -\zeta$, we have that $N(t,x) < N_{\text{th}}$. Note that:

$$\begin{aligned}\left\| -\int_0^t e^{(t-s)\partial_{zz}} \rho(s) N(s) ds \right\|_\infty &\leq T \|N\|_\infty \|\rho\|_\infty \\ &\leq 4T \left\|\rho^0\right\|_{C^{1,\alpha}} \left\|N^0\right\|_{W^{3,\infty}} .\end{aligned}$$

So for $T > 0$ small enough, the right handside is smaller than $\frac{\varepsilon}{4}$.
Choose $T > 0$ small engouh, so that for $t \in (0, T]$ we have that:

$$\frac{1}{\sqrt{4\pi Dt}} \int_{\zeta}^{+\infty} e^{-\frac{x^2}{4Dt}} dx < \frac{\varepsilon}{4}.$$

From this we can deduce that for $t \in (0, T], x < -\zeta$, by recalling that $\left\|N^0\right\|_\infty = 1$, we have:

$$\begin{aligned} N(t,x) &= e^{t\partial_{xx}} N^0|_x - \int_0^t e^{(t-s)\partial_{xx}} \rho(s) N(s) ds|_x \\ &\leq \frac{1}{\sqrt{4\pi Dt}} \int_{\mathbb{R}} e^{-\frac{(x-y)^2}{4Dt}} N^0(y) dy + \left\| - \int_0^t e^{(t-s)\partial_{xx}} \rho(s) N(s) ds \right\|_\infty \\ &< \frac{N_{\text{th}} - \varepsilon}{2} + \frac{N_{\text{th}}}{2} + \frac{\left\|N^0\right\|_\infty}{\sqrt{4\pi Dt}} \int_{\zeta}^{+\infty} e^{-\frac{x^2}{4t}} dx + \frac{\varepsilon}{4} \\ &< N_{\text{th}}. \end{aligned}$$

2. By a similar reasoning, there exists $T > 0$, such that for $t \in [0, T]$ and $x \geq \zeta$, we have that $N(t, x) > N_{\text{th}}$.

3. We now show that there exists $T > 0$, such that for $t \in [0, T], x \in [-\zeta, +\zeta]$, we have that $\partial_x N(t, x) \geq \frac{m}{8}$.
The reasoning is again similar. On the one hand:

$$\left\| \partial_x \left(- \int_0^t e^{(t-s)D\partial_{xx}} \rho(s) N(s) ds \right) \right\|_\infty \leq \int_0^t \frac{C}{\sqrt{t-s}} \left\|\rho(s)\right\|_\infty \left\|N(s)\right\|_\infty ds.$$

As before we can choose $T > 0$ such that the right handside becomes smaller than $\frac{m}{8}$ (here the constant C does not depend on $\underline{m}$).
On the other hand, by choosing $T > 0$ small enough such that for every $t \in [0, T]$:

$$\frac{1}{\sqrt{4\pi Dt}} \int_0^{\zeta} e^{-\frac{y^2}{4Dt}} dy \geq \frac{1}{4}.$$

In that fashion for $x \in [-\zeta, +\zeta]$:

$$\begin{aligned} e^{tD\partial_{xx}} \partial_x N^0|_x &= \frac{1}{\sqrt{4\pi Dt}} \int_{\mathbb{R}} e^{-\frac{(x-y)^2}{4Dt}} \partial_x N^0(y) dy \\ &\geq \frac{1}{\sqrt{4\pi Dt}} \int_{-\zeta}^{\zeta} e^{-\frac{(x-y)^2}{4Dt}} \partial_x N^0(y) dy \\ &\geq \frac{m}{\sqrt{4\pi Dt}} \int_{-\zeta-x}^{\zeta-x} e^{-\frac{y^2}{4Dt}} dy \\ &\geq \frac{m}{4}, \end{aligned}$$

by noticing that either $[0, \zeta] \subset [-\zeta - x, \zeta - x]$, when $x \leq 0$, or alternatively that $[-\zeta, 0] \subset [-\zeta - x, \zeta - x]$, when $x \geq 0$. From this, we conclude that:

$$\partial_x N(t,x) = e^{tD\partial_{xx}} \partial_x N^0|_x - \partial_x \left(\int_0^t e^{(t-s)D\partial_{xx}} \rho(s) N(s) ds \right) \Big|_x \geq \frac{m}{4} - \frac{m}{8} = \frac{m}{8}.$$

4. From the considerations above, we see that there exists $T > 0$, such that for $t \in [0, T]$, the equation $N(t) = N_{\text{th}}$ has a unique solution, which we denote by $\bar{y}(t)$. We know that $\bar{y}(t) \in [-\zeta, +\zeta]$ and $\bar{y}(0) = 0$. Furthermore from the preceding analysis we know that N is differentiable and by differentiating the relation $N(t, \bar{y}(t)) = N_{\text{th}}$, $\bar{y}(t)$ satisfies an ODE:

$$\dot{\bar{y}}(t) = -\frac{\partial_t N(t, \bar{y}(t))}{\partial_x N(t, \bar{y}(t))} =: \mathcal{F}(t, \bar{y}(t)).$$

We have $N \in L^\infty([0,T], W^{3,\infty}(\mathbb{R}))$ (resp. $\rho \in L^\infty([0,T], W^{1,\infty}(\mathbb{R}))$), because $\tilde{N} \in L^\infty([0,T], W^{3,\infty}(\mathbb{R}))$ (resp. $v \in L^\infty([0,T], W^{1,\infty}(\mathbb{R}))$). But since $\partial_t N = D\partial_{xx} N - \rho N$ this leads to $\partial_t N \in L^\infty([0,T], W^{1,\infty}(\mathbb{R}))$. Additionally, since $\partial_x N(t, \bar{y}(t)) \geq \frac{m}{4}$ and $\partial_x N \in L^\infty([0,T], W^{1,\infty}(\mathbb{R}))$, we have that $(\partial_x N)^{-1} \in L^\infty([0,T], W^{1,\infty}(\mathbb{R}))$. Therefore $\mathcal{F} \in L^\infty([0,T] \times [-\zeta, \zeta])$ is uniformly in time Lipschitz continuous in the second variable. Hence the ODE is well-posed and it admits a unique solution $\bar{y} \in W^{1,\infty}([0,T])$.
We have the bound:

$$\begin{aligned}
|\dot{\bar{y}}(t)| &\leq |\partial_x N(t, \bar{y}(t))|^{-1} \left\| D\partial_{xx} N - \rho N \right\|_\infty \\
&\leq \frac{8}{\underline{m}} \left(D \left\| \partial_{xx} N \right\|_\infty + \left\| \rho \right\|_\infty \left\| N \right\|_\infty \right) \\
&\leq C \left\| N^0 \right\|_{W^{3,\infty}} \left\| \frac{\rho^0}{U} \right\|_{C^{1,\alpha'}},
\end{aligned}$$

where at the end, we have used Bounds (2.2.12,2.2.15). Hence, by the convention that $T < 1$, we have $\|\bar{y}\|_{W^{1,p}} \leq C \left\| N^0 \right\|_{W^{3,\infty}} \left\| \frac{\rho^0}{U} \right\|_{C^{1,\alpha'}}$. It therefore suffices that A is bigger than the right handside and in that case the map $\bar{x} \mapsto \bar{y}$ maps $B(A)$ into itself.

Step 4: Unique Fixed Point of the map $\bar{x} \in B(A) \mapsto \bar{y} \in B(A)$.

Given $\bar{x}_1, \bar{x}_2 \in B(A)$, consider $\bar{y}_1, \bar{y}_2 \in B(A)$. Set $\mathcal{F}_i = -\frac{\partial_t N_i}{\partial_x N_i}$, such that $\dot{\bar{y}}_i(t) = \mathcal{F}_i(t, \bar{y}_i(t)$. Note that $\bar{y}_i(t) \in [-\zeta, +\zeta]$ and that therefore $\partial_x N_i(t, \bar{y}_i(t)) > \frac{m}{8}$.

$$\begin{aligned}
|\dot{\bar{y}}_1(t) - \dot{\bar{y}}_2(t)| &= |\mathcal{F}_1(t, \bar{y}_1(t)) - \mathcal{F}_2(t, \bar{y}_2(t))| \\
&\leq |\mathcal{F}_1(t, \bar{y}_1(t)) - \mathcal{F}_1(t, \bar{y}_2(t))| + |\mathcal{F}_1(t, \bar{y}_2(t)) - \mathcal{F}_2(t, \bar{y}_2(t))| .
\end{aligned}$$

For $x \in [-\zeta, +\zeta]$, $t \in [0,T]$ and by using the lower bounded of $\partial_x N(t,x)$ from Step 3, we have that:

$$\begin{aligned}
|\partial_x \mathcal{F}_1(t,x)| &\leq \left(\sup_{x \in [-\zeta, +\zeta]} \frac{1}{\partial_x N(t,x)} \right)^2 \left\| \partial_{tx} N \partial_x N - \partial_t N \partial_{xxx} N \right\|_\infty \\
&\leq C \left\| (\partial_{xxx} N - \partial_x(\rho N)) \partial_x N - (\partial_{xx} N - \rho N) \partial_{xxx} N \right\|_\infty .
\end{aligned}$$

This latter term is bounded, in particular because of Step 2. Hence:

$$|\mathcal{F}_1(t, \bar{y}_1(t)) - \mathcal{F}_1(t, \bar{y}_2(t))| \leq C \left\| N^0 \right\|^2_{W^{3,\infty}(\mathbb{R})} \left\| \frac{\rho^0}{U} \right\|_{C^{1,\alpha}(\mathbb{R})} |\bar{y}_1(t) - \bar{y}_2(t)|. \tag{2.2.23}$$

For the second term:

$$\begin{aligned}
&|\mathcal{F}_1(t,\bar{y}_2(t)) - \mathcal{F}_2(t,\bar{y}_2(t))| \\
\leq &\frac{|\partial_t N_1(t,\bar{y}_2(t))|}{|\partial_x N_1(t,\bar{y}_2(t))||\partial_x N_2(t,\bar{y}_2(t))|}\,|\partial_x N_1(t,\bar{y}_2(t)) - \partial_x N_2(t,\bar{y}_2(t))| \\
&+ \frac{1}{|\partial_x N_2(t,\bar{y}_2(t))|}\,|\partial_t N_1(t,\bar{y}_2(t)) - \partial_t N_2(t,\bar{y}_2(t))| \\
\leq &C\left(\|\partial_{xx}N_1 - \rho_1 N_1\|_\infty \|\partial_x N_1 - \partial_x N_2\|_\infty + \|\partial_{xx}N_1 - \partial_{xx}N_2\|_\infty\right. \\
&\left.+ \|\rho_1 - \rho_2\|_\infty \|N_1\|_\infty + \|\rho_2\|_\infty \|N_1 - N_2\|\right).
\end{aligned}$$

Now take $(t,y) \in [0,T]\times\mathbb{R}$, we have:

$$\begin{aligned}
&|\partial_{xx}N_1(t,y) - \partial_{xx}N_2(t,y)| \\
=&|\partial_{zz}\tilde{N}_1(t,y-\bar{x}_1(t)) - \partial_{zz}\tilde{N}_2(t,y-\bar{x}_2(t))| \\
\leq&|\partial_{zz}\tilde{N}_1(t,y-\bar{x}_1(t)) - \partial_{zz}\tilde{N}_1(t,y-\bar{x}_2(t))| + |\partial_{zz}\tilde{N}_1(t,y-\bar{x}_2(t)) - \partial_{zz}\tilde{N}_2(t,y-\bar{x}_2(t))| \\
\leq&\left\|\partial_{zzz}\tilde{N}_1\right\|_\infty |\bar{x}_1(t) - \bar{x}_2(t)| + \left\|\partial_{zz}\tilde{N}_1 - \partial_{zz}\tilde{N}_2\right\|_\infty.
\end{aligned}$$

We have similar bounds for $\|\rho_1-\rho_2\|_\infty$, $\|N_1-N_2\|_\infty$ and $\|\partial_x N_1 - \partial_x N_2\|_\infty$. Hence, by using $\|\bar{x}_1-\bar{x}_2\|_\infty \leq T^{1-\frac{1}{p}}\|\dot{\bar{x}}_1-\dot{\bar{x}}_2\|_p$ and Bounds (2.2.13,2.2.16) this leads to:

$$\begin{aligned}
&|\mathcal{F}_1(t,\bar{y}_1(t)) - \mathcal{F}_2(t,\bar{y}_2(t))| \\
\leq &C\left\|N^0\right\|^2_{W^{3,\infty}}\left\|\frac{\rho^0}{U}\right\|^2_{C^{1,\alpha}}\left(T^{1-\frac{1}{p}} + T^{\frac{p(1-\alpha')-2}{2p}} + T^{\frac{(1-\alpha')(p(1-\alpha)-2)}{4p}}\right)\|\dot{\bar{x}}_1 - \dot{\bar{x}}_2\|_p. \qquad (2.2.24)
\end{aligned}$$

Setting $K := C\left\|N^0\right\|^2_{W^{3,\infty}}\left\|\frac{\rho^0}{U}\right\|^2_{C^{1,\alpha}}$, combining Inequalities (2.2.23,2.2.24) and using the conventions, we find that:

$$|\dot{\bar{y}_1}(t) - \dot{\bar{y}_2}(t)| \leq K\left(|\bar{y}_1(t) - \bar{y}_2(t)| + \|\dot{\bar{x}}_1 - \dot{\bar{x}}_2\|_p\right).$$

By Grönwall's lemma, we obtain:

$$\|\bar{y}_1 - \bar{y}_2\|_\infty \leq \left(e^{KT} - 1\right)\|\dot{\bar{x}}_1 - \dot{\bar{x}}_2\|_p.$$

Bootstrapping the penultimate estimate, we can prove that:

$$\|\dot{\bar{y}_1} - \dot{\bar{y}_2}\|_p \leq KT^{\frac{1}{p}}e^{KT}\|\dot{\bar{x}}_1 - \dot{\bar{x}}_2\|_p.$$

By noticing that $\|\bar{y}_1-\bar{y}_2\|_p \leq T^{\frac{1}{p}}\|\bar{y}_1-\bar{y}_2\|_\infty$ and using the two last inequalities, we find that the map $\bar{x} \in B(A) \mapsto \bar{y} \in B(A)$ is a contraction in the $W^{1,p}$-norm for $T>0$ small enough. Thus, we have a unique fixed point, which concludes the proof of Theorem 2.2.1. □

Remark. *The Step 2 of the preceding proof naturally leads to the question whether $\tilde{N} \in L^\infty([0,T],C^{3,\alpha''}(\mathbb{R}))$ for $\alpha'' \in (0,1)$. In fact, by the reasoning in Step 2, this is equivalent to wondering, whether $\int_0^t \partial_{zz}e^{(t-s)D\partial_{zz}}h(s)\mathbb{1}_{z\geq 0}ds \in L^\infty([0,T],C^{0,\alpha''}(\mathbb{R}))$. But we see that if we take $h\equiv 1$ and denote $\theta>0$ the constant such that $\frac{1}{\pi^{\frac{1}{2}}}\int_0^\theta e^{-u^2}du = \frac{1}{4}$. Then, by applying the preceding computations between $(t,z) = (\min(y^2\theta^{-2},T),y)$ and $(\min(y^2\theta^{-2},T),0)$,*

we find:

$$\begin{aligned}
&\left|\left(\int_0^{\min(y^2\theta^{-2},T)} \partial_{zz} e^{(t-s)D\partial_{zz}} \mathbb{1}_{z\geq 0} ds\Big|_{z=0}\right) - \left(\int_0^{\min(y^2\theta^{-2},T)} \partial_{zz} e^{(t-s)D\partial_{zz}} \mathbb{1}_{z\geq 0} ds\Big|_{z=y}\right)\right| \\
&= 2\pi^{\frac{1}{2}} D^{\frac{3}{2}} \int_0^{\max\left(\theta, \frac{y}{\sqrt{T}}\right)} e^{-u^2} du \\
&\geq \frac{1}{8D^{\frac{3}{2}}}.
\end{aligned}$$

Since this expression is bounded below, this shows that there $C^{0,\alpha''}$ norms will be unbounded as $y \to 0$. Hence $\int_0^t \partial_{zz} e^{(t-s)D\partial_{zz}} \mathbb{1}_{z\geq 0} ds \notin L^\infty([0,T], C^{0,\alpha''}(\mathbb{R}))$. Hence the expression is unbounded and we have that $\int_0^t \partial_{zz} e^{(t-s)D\partial_{zz}} \mathbb{1}_{z\geq 0} ds \notin L^\infty([0,T], C^{0,\alpha''}(\mathbb{R}))$. This establishes that the regularity $\tilde{N} \in L^\infty([0,T], W^{3,\infty}(\mathbb{R}))$ is in fact critical.

Corollary 2.2.1.2. *Suppose that in addition to the assumptions of Theorem 2.2.1, the initial conditions (ρ^0, N^0) satisfy the following conditions:*

1. $\frac{\partial_x N^0}{N^0}, \frac{\partial_x \rho^0}{\rho^0} \in L^\infty(\mathbb{R})$,
2. $\liminf_{x\to-\infty} \frac{\partial_x N^0}{N^0} \geq \nu > 0$ *and* $\limsup_{x\to+\infty} \frac{\partial_x \rho^0}{\rho^0} \leq -\eta < 0$,
3. $1 - N^0$ *is square-integrable at* $x = +\infty$.

Then (ρ, N), the solution given by Theorem 2.2.1, satisfies the condition $\partial_x N \geq 0$ locally in time and hence (ρ, N) is in fact a solution to System (2.1.1).

Let us briefly comment on the assumptions of Corollary 2.2.1.2. The assumption on N^0 implies that N^0 increases at least exponentially at $x = -\infty$. The assumption, that $1 - N^0$ is square-integrable at $x = +\infty$, is of course more restrictive than the condition $\lim_{x\to+\infty} N^0(x) = 1$. We will see in the next Section that the traveling wave solution satisfies the property $\tilde{N}(z) = 1 + p(z)$ with p a function that is dominated by an exponentially decreasing function at $z = +\infty$, which is then square-integrable at $z = +\infty$. Concerning the assumption on ρ^0, we already know that $\tilde{\rho} = vU$ with U an exponentially decreasing function at $z = +\infty$ and v a bounded function. Hence the additional condition translates the fact that $\limsup_{x\to+\infty} \left(\frac{\partial_x v^0}{v^0}\right) \leq \chi - \eta$. Considering that we must have $\liminf_{x\to+\infty} \frac{\partial_x v^0}{v^0} \leq 0$, otherwise v^0 is not bounded, this assumption translates a restriction on the oscillations of $\frac{\partial_x v^0}{v^0}$.

Proof. 1. We start by showing that $w := \frac{\partial_z \tilde{N}}{\tilde{N}}$ is well-defined. In fact by dividing Equation (2.2.9b) by $\tilde{N}$, we obtain:

$$\frac{\partial_t \tilde{N}}{\tilde{N}} = D(\partial_z w + w^2) + \dot{\tilde{x}} w - vU.$$

Then by observing that $\partial_z \left(\frac{\partial_t \tilde{N}}{\tilde{N}}\right) = \partial_{zt} \log \tilde{N} = \partial_t \left(\frac{\partial_z \tilde{N}}{\tilde{N}}\right)$ and by differentiating the preceding Equation, w satisfies the following equation:

$$\partial_t w = D(\partial_{zz} w + \partial_z \left(w^2\right)) + \dot{\tilde{x}} \partial_z w - \partial_z \left(vU\right).$$

This leads to the following representation formula for w:

$$w(t) = e^{tD\partial_{zz}} w^0 + \int_0^t e^{(t-s)D\partial_{zz}} \left(D\partial_z \left(w^2 \right)(s) + \dot{\tilde{x}}(s)\partial_z w(s) - \partial_z \left(v(s)U \right) \right) ds.$$

By arguments similar to the ones exposed in the proof of Theorem 2.2.1, we simply must show that for $R > 0$ big enough there exists $T > 0$ such that the right handside defines a contraction from $L^\infty([0,T], B(R))$ into itself, where $B(R) = \{ f \in L^\infty(\mathbb{R}), \|f\|_\infty \leq R \}$. We merely treat the term $w \in L^\infty([0,T], B(R)) \mapsto \int_0^t e^{(t-s)D\partial_{zz}} D\partial_z \left(w^2(s) \right) ds \in L^\infty([0,T], B(R))$. Let $w_1, w_2 \in L^\infty([0,T] \times \mathbb{R})$, we have:

$$\begin{aligned}
&\left\| \int_0^t e^{(t-s)D\partial_{zz}} \left(\partial_z \left(w_1^2 \right)(s) - \partial_z \left(w_2^2 \right)(s) \right) ds \right\|_\infty \\
\leq & C \int_0^t \left\| w_1^2(s) - w_2^2(s) \right\|_\infty \frac{ds}{\sqrt{t-s}} \\
\leq & C \int_0^t \left\| w_1(s) - w_2(s) \right\|_\infty \left\| w_1(s) + w_2(s) \right\|_\infty \frac{ds}{\sqrt{t-s}} \\
\leq & CR\sqrt{T} \left\| w_1 - w_2 \right\|_\infty .
\end{aligned}$$

Hence $w = \frac{\partial_x \tilde{N}}{\tilde{N}} \in L^\infty([0,T] \times \mathbb{R})$.

Furthermore, we show that $w \in C([0,T], L^\infty(\mathbb{R}))$. The map $t \mapsto e^{tD\partial_{xx}} w_0$ is continuous and in addition by noticing, for instance, that:

$$\begin{aligned}
&\left\| \int_0^{t+h} e^{(t+h-s)D\partial_{zz}} D\partial_z \left(w^2 \right)(s) ds - \int_0^t e^{(t-s)D\partial_{zz}} D\partial_z \left(w^2 \right)(s) ds \right\|_\infty \\
= & \left\| \int_t^{t+h} e^{(t+h-s)D\partial_{zz}} D\partial_z \left(w^2 \right)(s) ds + \left(1 - e^{hD\partial_{zz}} \right) \int_0^t e^{(t-s)D\partial_{zz}} D\partial_z \left(w^2 \right)(s) ds \right\|_\infty \\
\leq & C \left\| w \right\|_\infty^2 \int_t^{t+h} \frac{ds}{\sqrt{t+h-s}} + \left\| \left(1 - e^{hD\partial_{zz}} \right) \int_0^t e^{(t-s)D\partial_{zz}} D\partial_z \left(w^2 \right)(s) ds \right\|_\infty .
\end{aligned}$$

When $h \to 0$, the first term clearly tends to 0 and so does the second term by strong continuity of the heat semi-group.

2. Next we show that $q = \frac{\partial_z v}{v}$ is well-defined. q satisfies:

$$\partial_t q = \partial_{zz} q + \partial_z (q^2) + \partial_z (\beta q) + \partial_z \gamma.$$

The proof is similar to the preceding point. However, one should notice the following fact, in order to prove that the map: $\int_0^t e^{(t-s)\partial_{zz}} \partial_z \gamma ds \in L^\infty([0,T] \times \mathbb{R})$. Indeed, by observing that $\partial_z \gamma = \chi \left(\chi + \frac{1}{\chi} - \dot{\tilde{x}}(t) \right) \delta_0$ and applying Hölder's inequality, we have that:

$$\begin{aligned}
\left\| \int_0^t e^{(t-s)\partial_{zz}} \partial_z \gamma ds \right\|_\infty &= \left\| \chi \int_0^t \frac{\chi + \frac{1}{\chi} - \dot{\tilde{x}}(s)}{\sqrt{4\pi(t-s)}} e^{-\frac{z^2}{4(t-s)}} ds \right\|_\infty \\
&\leq C \left\| \chi + \frac{1}{\chi} - \dot{\tilde{x}} \right\|_p .
\end{aligned}$$

3. We establish that $\tilde{N}$ is nondecreasing. To do so we start by noticing that since $\limsup_{z \to +\infty} \frac{\partial_z \tilde{\rho}^0}{\tilde{\rho}^0} < -\eta < 0$. There exists an $A > 0$ such that for every $z > A$, $\frac{\partial_z v^0(z)}{v^0(z)} +$

$\frac{U'(z)}{U} < -\eta$. But by continuity of $t \mapsto \frac{\partial_z v(t,\cdot)}{v(t,\cdot)}$ in $L^\infty(\mathbb{R})$, there exists $T > 0$, such that for every $t \in [0,T]$ and $z > A$, $\frac{\partial_z \tilde{\rho}(t,z)}{\tilde{\rho}(t,z)} = \frac{\partial_z v(t,z)}{v(t,z)} + \frac{U'(z)}{U} < -\frac{\eta}{2}$. In particular $\partial_z \tilde{\rho}(t,z) < 0$ for $(t,z) \in [0,T] \times [A,+\infty)$.
Now because of Condition 1 and 3, we have in fact that for $z \in (-\infty, A], w^0(z) \geq \frac{\nu}{2} > 0$ and by the same argument, we must have for $T > 0$ small enough that for $t \in [0,T], z \in (-\infty, A], w(t,z) \geq \frac{\nu}{4} > 0$.
Therefore it remains to show that on the interval $[A,+\infty)$, we also have that $\partial_z \tilde{N} \geq 0$. For $h > 0$, let $f(t,z) := \tilde{N}(t,z+h) - \tilde{N}(t,z)$ and $g(t,z) := -\tilde{\rho}(t,z+h)\tilde{N}(t,z+h) + \tilde{\rho}(t,z)\tilde{N}(t,z)$. Then we have that:

$$\partial_t f - \dot{\tilde{x}} \partial_z f - D\partial_{zz} f = g. \tag{2.2.25}$$

Furthermore for $(t,z) \in [0,T] \times (-\infty, A)$, we have that $f \geq 0$ by the preceding and for $z > A$, if $f(t,z) = \tilde{N}(t,z+h) - \tilde{N}(t,z) < 0$, then we must have that $g(t,z) = -\tilde{\rho}(t,z+h)\tilde{N}(t,z+h) + \tilde{\rho}(t,z)\tilde{N}(t,z) \geq 0$, since $\tilde{\rho}(t,z+h) \leq \tilde{\rho}(t,z)$. Therefore we have $f_- g \geq 0$, where $(\cdot)_- = -\min(0,\cdot)$.

We have that $g(t,\cdot) \in L^2(\mathbb{R})$, since $\tilde{N}$ is dominated at $z = -\infty$ by $e^{\frac{\nu z}{4}}$ and $\tilde{\rho}$ is dominated at $z = +\infty$ by $e^{-\frac{\eta z}{2}}$. Notice that $f(0,\cdot) \in L^2(\mathbb{R})$ by the assumption that $1 - N^0$ is square-integrable at $x = +\infty$. Therefore $f(t\,\cdot) \in L^2(\mathbb{R})$ as solution to Equation (2.2.25). Hence, the following computations are justified:

$$\begin{aligned}
\frac{d}{dt}\left(\frac{1}{2}\int_{\mathbb{R}} (f_-)^2\right) &= \int_{\mathbb{R}} f_- \partial_t f_- \\
&= -\int_{\mathbb{R}} f_- \partial_t f, \text{ since } f_- \partial_t (f_-) = -f_- \partial_t f \\
&= -\dot{\tilde{x}}(t) \int_{\mathbb{R}} f_- \partial_z f - D\int_{\mathbb{R}} f_- \partial_{zz} f - \int f_- g \\
&= \dot{\tilde{x}}(t) \int_{\mathbb{R}} f_- \partial_z (f_-) - D\int_{\mathbb{R}} f_- \partial_{zz} f - \int f_- g, \text{ since } f_- \partial_z (f_-) = -f_- \partial_z f \\
&\leq \frac{\dot{\tilde{x}}(t)}{2} \int_{\mathbb{R}} \partial_z ((f_-)^2) + D\int_{\mathbb{R}} (\partial_z f_-)\partial_z f, \text{ since } f_- g \geq 0 \\
&= -D\int_{\mathbb{R}} (\partial_z f_-)^2, \text{ since } \partial_z f_- \partial_z f = -(\partial_z f_-)^2 \\
&\leq 0.
\end{aligned}$$

But, by assumption $f_-(0,\cdot) \equiv 0$. Hence $f_-(t,\cdot) \equiv 0$ and $\tilde{N}(t,\cdot)$ is nondecreasing. □

2.3 Traveling Waves for the Parabolic System

In this Section, we will investigate the existence of waves for the parabolic System (2.1.1), *i.e.* solutions of the form $(\rho(t,x), N(t,x)) = (\tilde{\rho}(x-\sigma t), \tilde{N}(x-\sigma t))$, for a velocity σ to be determined. Set $z = x - \sigma t$, any traveling wave solution must satisfy the following equations:

$$\begin{cases} -\sigma\tilde{\rho}' - \tilde{\rho}' + (\chi \text{sign}(\partial_z N)\mathbb{1}_{\tilde{N} \leq N_{\text{th}}}\tilde{\rho})' = \mathbb{1}_{\tilde{N} > N_{\text{th}}}\tilde{\rho} & \text{(2.3.1a)} \\ -\sigma\tilde{N}' - D\tilde{N}'' = -\tilde{\rho}\tilde{N}. & \text{(2.3.1b)} \end{cases}$$

For the sake of concision, we will drop the diacritical $\tilde{}$. Applying the assumption that N is increasing, Equation (2.3.1a) reduces to a second-order linear ordinary differential equation with piecewise-constant coefficients. By translation invariance of the traveling

waves, we suppose that $N(0) = N_{\text{th}}$. Adding the C^1-jump relation (2.1.3), that comes from the continuity of the flux, we obtain the following problem:

$$\begin{cases} -\sigma\rho' - \rho'' + \chi\rho' = 0 & \text{for } z < 0 \\ -\sigma\rho' - \rho'' = \rho & \text{for } z > 0 \end{cases} \quad \text{and} \quad \rho'(0^+) - \rho'(0^-) = -\chi\rho(0). \tag{2.3.2}$$

We solve this problem explicitly and thus deduce all bounded and nonnegative traveling wave profiles for ρ. Moreover, there exists a minimal speed σ^*, such that for every $\sigma \in [\sigma^*, +\infty)$, there exists a unique (up to a multiplicative factor) traveling wave profile ρ^σ. In a second step, given the profile ρ^σ, we construct a corresponding traveling wave profile N^σ and the condition $N(0) = N_{\text{th}}$ will fix the multiplicative factor of ρ, thus leading to a unique traveling wave profile (ρ^σ, N^σ) for each $\sigma \geq \sigma^*$.

Let us introduce some notations, before moving on to the statement of Theorem 2.3.1. Define the Fisher/Kolmogorov–Petrovsky–Piskunov speed $\sigma_{\text{F/KPP}} := 2$. Note that $\chi + \frac{1}{\chi} \geq \sigma_{\text{F/KPP}}$, with equality if and only if $\chi = 1$. Furthermore set for $\sigma \geq 2$, $\mu_\pm(\sigma) := \frac{\sigma \pm \sqrt{\sigma^2 - 4}}{2}$. We then have the following inequality for $\sigma > \sigma_{\text{F/KPP}} = 2$:

$$0 < \mu_-(\sigma) < \mu_-\left(\sigma_{\text{F/KPP}}\right) = 1 = \mu_+\left(\sigma_{\text{F/KPP}}\right) < \mu_+(\sigma)$$

In addition, the function $\sigma \mapsto \mu_+(\sigma)$ (resp. $\sigma \mapsto \mu_-(\sigma)$) is increasing (resp. decreasing).

Theorem 2.3.1. *Under the assumption that N is increasing, there exists a minimal speed σ^*, such that there exists a bounded and nonnegative traveling wave profile $(\rho^\sigma(z), N^\sigma(z))$ if and only if $\sigma \geq \sigma^*$. Given $\sigma \geq \sigma^*$, the traveling wave profile $(\rho^\sigma(z), N^\sigma(z))$ is unique. Moreover, the exact value of σ^* is given by Formula (2.1.4) and depends on the value of χ:*

- *if $\chi > 1$, then $\sigma^* = \chi + \frac{1}{\chi}$,*
- *if $\chi \leq 1$, then $\sigma^* = \sigma_{F/KPP} = 2$*

Furthermore, the functions ρ^σ satisfy the following properties for $z \geq 0$ with $C^\sigma, D^\sigma > 0$:

- *for $\sigma > \sigma^*, \rho^\sigma(z) = A^\sigma e^{-\mu_-(\sigma)z} + B^\sigma e^{-\mu_+(\sigma)z}$*
- *for $\chi > 1$, $\sigma = \sigma^* = \chi + \frac{1}{\chi}, \rho^{\sigma^*}(z) = A^{\sigma^*} e^{-\mu_+(\sigma^*)z}$ and $\mu_+(\sigma^*) = \chi$*
- *for $\chi \leq 1, \sigma = \sigma_{F/KPP}, \rho^{\sigma_{F/KPP}}(z) = A^{\sigma_{F/KPP}}((1-\chi)z + 1)e^{-z}$*

In addition, let $\mu > 0$, with $\mu \neq \frac{\sigma}{D}$, such that $\rho(z) \leq Ce^{-\mu z}$ for a constant $C > 0$, then there exists another constant $C > 0$, such that for $z \in \mathbb{R}$:

$$|N(z) - 1| \leq C\left(e^{-\frac{\sigma}{D}z} + e^{-\mu z}\right). \tag{2.3.3}$$

Proof. Integrating Equation (2.3.2) over the whole line yields $(\sigma - \chi)\rho^\sigma(-\infty) = \int_{\mathbb{R}_+} \rho^\sigma(z)dz$ (as we will see just below, ρ^σ is integrable at $z = +\infty$). Therefore by nonnegativity of the left handside, we find that $\sigma > \chi$. Consider Equation (2.3.2) for $z < 0$. Its characteristic polynomial is $X^2 + (\sigma - \chi)X$ and has roots 0 and $\chi - \sigma$. There exist two constants $A^-, B^- \in \mathbb{R}$, such that $\rho^\sigma(z) = A^- + B^- e^{(\chi-\sigma)z}$, for $z < 0$. Since $\sigma > \chi$, the term $e^{(\chi-\sigma)z}$ is unbounded on $\mathbb{R}_-$, which leads to $B^- = 0$.
Consider Equation (2.3.2) for $z > 0$. Its characteristic polynomial is $X^2 + \sigma X + 1$ and its discriminant is $\sigma^2 - 4$. If the discriminant is negative, the roots are complex and ρ^σ would be a linear combination of two oscillating functions, which is prohibited by the nonnegativity condition. Hence $\sigma^2 \geq 4$, or, by positivity of σ, $\sigma \geq 2$.

Suppose $\sigma > 2 = \sigma_{\mathrm{F/KPP}}$, the roots of the characteristic polynomial are then $-\mu_\pm(\sigma)$ and there exist two constants $A^+, B^+ \in \mathbb{R}$ such that $\rho^\sigma(z) = A^+ e^{-\mu_+(\sigma)z} + B^+ e^{-\mu_-(\sigma)z}$. By the continuity at $z = 0$ of ρ^σ, we obtain equality $A^- = A^+ + B^+$ and by the C^1-jump relation (2.1.3), we obtain equality $-\mu_+ A^+ - \mu_- B^+ = -\chi A^-$. Thus we find that $\rho^\sigma(z) = \frac{A^-}{\sqrt{\sigma^2-4}} \left((\mu_+(\sigma) - \chi) e^{-\mu_-(\sigma)z} + (\chi - \mu_-(\sigma)) e^{-\mu_+(\sigma)z} \right)$. One checks that this expression is nonegative for all z, if and only if, $\mu_+(\sigma) \geq \chi$. In the case of small bias $\chi \leq 1$, this inequality is always verified. In the case of large bias $\chi > 1$, this inequality is verified, if and only if $\sigma \geq \chi + \frac{1}{\chi}$. This proves all cases of Theorem for $\sigma > \sigma_{\mathrm{F/KPP}}$.
Suppose $\sigma = 2 = \sigma_{\mathrm{F/KPP}}$, then there exist two constants $A^+, B^+ \in \mathbb{R}$ such that $\rho^\sigma(z) = (A^+ z + B^+) e^{-z}$. By the same arguments as above, we have $B^+ = A^-$, $A^+ = (1-\chi)A^-$ and this leads to $\rho^\sigma(z) = A^- \left((1-\chi)z + 1 \right) e^{-z}$. To satisfy the nonnegativity condition, we must have $\chi \leq 1$, which shows that $\sigma = 2 = \sigma_{\mathrm{F/KPP}}$, is the speed of a traveling wave, if and only if $\chi \leq 1$.

The behavior of ρ^σ for $z \geq 0$ is simply a reformulation of the considerations above. In particular, note that in the case of large bias and $\sigma = \sigma^*$, we have that $\mu_+(\sigma^*) = \chi$, which leads to $\rho^{\sigma^*}(z) = A^- e^{-\chi z}$, for $z \geq 0$.

It remains to show that for every wave profile ρ^σ, we have a corresponding wave profile N^σ, which satisfies the condition $N^\sigma(0) = N_{\mathrm{th}}$. To do so, notice that by linearity of the equation on ρ, the profile ρ^σ is defined up to the multiplicative constant A^-, that is yet to be determined. Denote for a given constant $A^- > 0$, $\rho^\sigma_{A^-}$ its corresponding profile. Equation (2.3.1b) with boundary condition $N(+\infty) = 1$, then has a unique solution, which we denote $N^\sigma_{A^-}$. But it is clear that the map $A^- \mapsto N^\sigma_{A^-}(0)$ is continuous and decreasing and its range is $(0, 1)$. Therefore there exists a unique A^-, such that $N^\sigma_{A^-}(0) = N_{\mathrm{th}}$ and we obtain for a fixed $\sigma \geq \sigma^*$ a unique traveling wave profile $(\rho^\sigma_{A^-}, N^\sigma_{A^-})$.

Let us finally prove Estimate (2.3.3). By integrating Equation (2.3.1b) on the interval $(z, +\infty)$ and noticing that $N(+\infty) = 1, N'(+\infty) = 0$:

$$\sigma \left(N(z) - 1 \right) + D \left(N(z) - 1 \right)' = - \int_z^{+\infty} \rho(y) N(y) dy.$$

Hence for a constant $C > 0$:

$$\left| \left(e^{\frac{\sigma}{D} z} (N(z) - 1) \right)' \right| \leq C e^{\left(\frac{\sigma}{D} - \mu \right) z}.$$

By integrating this inequality on the interval $(0, z)$ for another $C > 0$, we find:

$$|N(z) - 1| \leq C \left(e^{-\frac{\sigma}{D} z} + e^{-\mu z} \right).$$

□

Theorem 2.3.1 shows that there exist a large number of traveling waves. However, in Section 2.5 we will show that in the circumstances of a biologically relevant initial conditions, the interesting traveling wave will be that of minimal speed σ^*.

2.4 Inside Dynamics of Traveling Waves

We elaborate on the properties of the traveling waves, following the lines of [82], as well as [152] to a small extent. We establish that in the large bias case, the wave is *pushed*, and in the small bias case (or when $\sigma > \sigma^*$), the wave is *pulled*, according to the definition proposed in [82] (see the discussion in the Introduction on the ambiguity of *pushed* and

pulled waves). To do so, we are using the formalism of neutral fractions. The aim is to study the behaviour of partitions of the traveling wave profile (see [82] and [48] for the biological relevance of this decomposition).

Definition. *Define* $L := -\partial_{zz} - \beta\partial_z$, *where* $\beta(z) = \sigma - \chi \mathbb{1}_{z\leq 0} + 2\frac{\partial_z \rho^\sigma}{\rho^\sigma}$. *A neutral fraction* ν *(of the traveling wave* ρ^σ*) is a solution to the following equation:*

$$\begin{cases} \partial_t \nu + L\nu = 0 \\ \nu(0,\,\cdot\,) = \nu^0 \end{cases}. \tag{2.4.1}$$

It is clear that any constant is a neutral fraction, as stationary solutions to Equation (2.4.1). The interest in Equation (2.4.1) stems from the following observation. Suppose we have neutral fractions $(\nu_i)_{i=1}^k \geq 0$ that satisfy $\sum_{i=1}^k \nu_i^0 = 1$. It amounts to marking each part $\nu_i^0 \rho^\sigma$ of the population with neutral labels, *i.e.* that do not interfer with the dynamics. The neutral fractions $(\nu_i(t)\rho^\sigma)_{i=1}^k$ then describe the evolution over time of the distribution of these labels. Because of this interpretation, it is natural to suppose that ν^0 takes its values in $[0,1]$, but such a restriction is of no relevance for the subsequent analysis. Of note, describing ν_i or $\nu_i\rho^\sigma$ is equivalent, only the expression of the operator L changes.

2.4.1 Pushed Front Dynamics in the Large Bias Case

In this Section, we develop arguments very similar to the ones developped in the works [79] and [82] (see also [152]). The evolution of neutral fractions is characterized in the regime of large bias ($\chi > 1$) and minimal velocity ($\sigma = \sigma^*$) by Theorem 2.4.1.

Consider the operator L in the space $L^2(e^V dz)$, where $V' = \beta$. On the appropriate domain, L is self-adjoint, has 0 as eigenvalue and an exact spectral gap $\gamma := \frac{1}{4}\min\left(\sigma^2 - 4, \frac{1}{\chi^2}\right) > 0$. This leads to the following convergence result:

Theorem 2.4.1. *Suppose that* $\chi > 1$ *and that* $\sigma = \sigma^*$. *Let* ν *be a neutral fraction (2.4.1) that satisfies* $\nu^0 \in L^2(e^V dz)$. *Then we have the following convergence result:*

$$\left\|\nu(t) - \langle \nu^0 \rangle\right\|_{L^2(e^V dz)} \leq \left\|\nu^0\right\|_{L^2(e^V dz)} e^{-\gamma t}, \tag{2.4.2}$$

with $\langle \nu^0 \rangle = \frac{\int \nu^0 e^V dz}{\int e^V dz}$ *and* $\gamma := \frac{1}{4}\min\left(\sigma^2 - 4, \frac{1}{\chi^2}\right) > 0$.

Furthermore for a constant $C > 0$, *we have:*

$$\left\|(\nu(t) - \langle \nu^0 \rangle) e^{\frac{V}{2}}\right\|_\infty \leq C\left(1 + t^{-\frac{1}{2}}\right) e^{-\gamma t}. \tag{2.4.3}$$

And as a consequence ν *converges exponentially fast to a constant on compact sets* $K \subset \mathbb{R}$, *i.e.:*

$$\sup_{z\in K} |\nu(t,z) - \langle \nu^0 \rangle| \leq \frac{C\left(1 + t^{-\frac{1}{2}}\right) e^{-\gamma t}}{\inf_K e^{\frac{V}{2}}}. \tag{2.4.4}$$

Theorem 2.4.1 states that every neutral fraction converges to a constant. In other words, independently of the initial datum for the neutral fraction, the neutral fraction will after some time, uniformly on compact sets in space represent a multiple (which does depend on the initial datum) of the total population. This is in stark contrast with the case when $\sigma = \sigma_{F/KPP}$ (or when $\sigma > \sigma^*$) in Corollary 2.4.2.1, where neutral fractions will in general go extinct (unless they are part of the leading edge). In fact, in the large

bias case when $\sigma = \sigma^*$, for $z < 0, \beta(z) > 0$ and for $z > 0, \beta(z) < 0$, which shows that $1 \in L^2(e^V dz)$. But this property is not true in the small bias case when $\sigma = \sigma_{\mathrm{F/KPP}}$ (or when $\sigma > \sigma^*$), as we will see in Subsection 2.4.2.

We define L on $L^2(e^V dz)$ with domain $D(L) = H^2(e^V dz)$. Nevertheless to simplify the spectral study of L, we introduce the pullback $\mathcal{L}$ of L to the space $L^2(dz)$, that is $\mathcal{L} = e^{\frac{V}{2}} L \left(e^{-\frac{V}{2}} \cdot\right)$, with domain $D(\mathcal{L}) = \left\{ f \in H^1(dz) \middle| f' - \frac{\beta}{2} f \in H^1(dz) \right\}$. $\mathcal{L}$ is symmetric and monotone, as for $f, g \in D(\mathcal{L})$,

$$\begin{aligned}
&\langle f, \mathcal{L} g \rangle \\
=&\int_{\mathbb{R}} e^{\frac{V}{2}} f \left(- \left(e^{-\frac{V}{2}} g \right)'' - \beta \left(e^{-\frac{V}{2}} g \right)' \right) dz \\
=&\int_{\mathbb{R}} \left(\left(e^{\frac{V}{2}} f \right)' \left(e^{-\frac{V}{2}} g \right)' - \beta e^{\frac{V}{2}} f \left(e^{-\frac{V}{2}} g \right)' \right) dz \\
=&\int_{\mathbb{R}} \left(\left(f' + \frac{\beta}{2} f \right) \left(g' - \frac{\beta}{2} g \right) - \beta f \left(g' - \frac{\beta}{2} g \right) \right) dz \\
=&\int_{\mathbb{R}} \left(f' - \frac{\beta}{2} f \right) \left(g' - \frac{\beta}{2} g \right) dz \qquad (2.4.5) \\
=&\langle \mathcal{L} f, g \rangle,
\end{aligned}$$

where $\langle f | g \rangle := \int_{\mathbb{R}} f g dz$. In fact Equality (2.4.5) holds also true if $f \in D(\mathcal{L})$ and $g \in H^1(dz)$. By observing that $D(\mathcal{L}) \subset H^1(dz)$ and density of $D(\mathcal{L})$ in $H^1(dz)$, we obtain that for every $f \in H^1(dz)$:

$$\langle f, \mathcal{L} f \rangle = \int_{\mathbb{R}} \left(f' - \frac{\beta}{2} f \right)^2 dz \geq 0. \qquad (2.4.6)$$

Finally $\mathcal{L}$ has the following expressions:

$$\begin{aligned}
&\mathcal{L} f \\
=&- f'' + \frac{\beta^2}{4} f + \frac{\beta'}{2} f \qquad (2.4.7) \\
=&- \left(e^{\frac{V}{2}} \left(e^{-\frac{V}{2}} f \right)' \right)'. \qquad (2.4.8)
\end{aligned}$$

Proposition 2.4.1.1. *The operator $\mathcal{L} : D(\mathcal{L}) \to L^2(dz)$ is closed.*

Proof. Let $(f_n, \mathcal{L} f_n) \in \Gamma(\mathcal{L})$ such that $(f_n, \mathcal{L} f_n) \xrightarrow[n \to +\infty]{L^2(dz)} (f, g) \in L^2(dz) \times L^2(dz)$. We will show that $f \in D(\mathcal{L})$ and $\mathcal{L} f = g$.

1. First, we prove boundedness of (f_n) in $H^1(dz)$:

$$\int_{\mathbb{R}} \left(f_n' - \frac{\beta}{2} f_n \right)^2 dz = \langle f_n | \mathcal{L} f_n \rangle \leq \| f_n \|_2 \| \mathcal{L} f_n \|_2 .$$

The right handside is bounded and thus $f_n' - \frac{\beta}{2} f_n$ is bounded in $L^2(dz)$. But $\frac{\beta}{2} f_n$ is also bounded in $L^2(dz)$ (since $\beta \in L^\infty(\mathbb{R})$). Hence (f_n) is bounded in $H^1(dz)$

2. The boundedness of (f_n) in $H^1(dz)$ implies weak compactness of the sequences. Hence up to extraction of a subsequence, we can assume that $f_n \xrightarrow[n \to +\infty]{H^1(dz)} \ell \in H^1(dz)$. But uniqueness of the limits in $L^2(dz)$ implies $\ell = f$, which leads to $f \in H^1(dz)$.

3. We now show strong convergence in $H^1(dz)$. Denote $r_n := f - f_n$

$$\begin{aligned}
&\int_{\mathbb{R}} \left(r_n' - \frac{\beta}{2} r_n\right)^2 dz \\
&= \left\langle f' - \frac{\beta}{2} f \middle| r_n' - \frac{\beta}{2} r_n \right\rangle - \left\langle f_n' - \frac{\beta}{2} f_n \middle| r_n' - \frac{\beta}{2} r_n \right\rangle \\
&= \underbrace{\left\langle f' - \frac{\beta}{2} f \middle| r_n' - \frac{\beta}{2} r_n \right\rangle}_{\to 0 \text{ by weak convergence in } H^1(dz)} - \underbrace{\langle \mathcal{L} f_n | r_n \rangle}_{\to 0 \text{ since } r_n \to 0 \text{ in } L^2(dz) \text{ and } \mathcal{L} f_n \text{ is bounded}},
\end{aligned}$$

where we have applied (2.4.5) with $f_n \in D(\mathcal{L})$ and $r_n \in H^1(dz)$. Thus $f_n \xrightarrow[n\to+\infty]{H^1(dz)} f$.

4. We show that $f \in D(\mathcal{L})$:

$$\left(f_n' - \frac{\beta}{2} f_n\right)' = -\mathcal{L} f_n - \frac{\beta}{2} f_n' - \frac{\beta^2}{4} f_n.$$

The right handside converges in $L^2(dz)$, which establishes that $f_n' - \frac{\beta}{2} f_n \xrightarrow[n\to+\infty]{H^1(dz)} f' - \frac{\beta}{2} f \in H^1(dz)$. Therefore $f \in D(\mathcal{L})$.

5. Finally we show that $\mathcal{L} f = g$. Let $h \in D(\mathcal{L}^*)$. By definition of $D(\mathcal{L}^*)$, we have that $\langle h | \mathcal{L} f_n \rangle \xrightarrow[n\to+\infty]{} \langle h | \mathcal{L} f \rangle$. But we also know that $\langle h | \mathcal{L} f_n \rangle \xrightarrow[n\to+\infty]{} \langle h | g \rangle$. Therefore $\mathcal{L} f - g \in D(\mathcal{L}^*)^\perp$. But since $\mathcal{L}$ is a symmetric operator, we have the inclusion $D(\mathcal{L}) \subset D(\mathcal{L}^*)$ and thus $D(\mathcal{L}^*)$ is dense. Hence $\mathcal{L} f = g$.

Thus, the operator $\mathcal{L}$ is closed. □

Proposition 2.4.1.2. *The operator $\mathcal{L} : D(\mathcal{L}) \to L^2(dz)$ is self-adjoint.*

Proof. We already know that the operator $\mathcal{L}$ is symmetric. It remains to show that it shares the same domain as its adjoint.

Let $g \in D(\mathcal{L}^*)$ and $f \in C_0^\infty(\mathbb{R}) \subset D(\mathcal{L})$. By definition of $D(\mathcal{L}^*)$, we have that:

$$|\langle g | \mathcal{L} f \rangle| \leq C(g) \|f\|_{L^2(dz)}. \tag{2.4.9}$$

But since f is a test function, we can view $\mathcal{L} g$ as a distribution. Let us take $g_n \in D(\mathcal{L})$ such that $g_n \xrightarrow[n\to+\infty]{L^2(dz)} g$. Then $\mathcal{L} g_n \xrightarrow[n\to+\infty]{D'(\mathbb{R})} \mathcal{L} g$, so that $\langle \mathcal{L} g_n | f \rangle \xrightarrow[n\to+\infty]{} \langle \mathcal{L} g | u f \rangle_{L^2(dz)}$. But from the symmetry of $\mathcal{L}$, we get $\langle \mathcal{L} g_n | f \rangle = \langle g_n | \mathcal{L} f \rangle \xrightarrow[n\to+\infty]{} \langle g | \mathcal{L} f \rangle$. Hence $\langle \mathcal{L} g | f \rangle = \langle g | \mathcal{L} f \rangle$

Therefore:

$$|\langle \mathcal{L} g | f \rangle| = |\langle g | \mathcal{L} f \rangle| \leq C(g) \|f\|_2. \tag{2.4.10}$$

By Bound (2.4.10), the linear form $f \mapsto \langle \mathcal{L} g | f \rangle$ is bounded on $C_0^\infty(\mathbb{R})$ in the L^2-norm and we can extend it to the whole space $L^2(dz)$ by uniform continuity and density of $C_0^\infty(\mathbb{R})$ in $L^2(dz)$. This shows that $\mathcal{L} g \in L^2(dz)$.

Then:

$$\begin{aligned}
&\mathcal{L} g = -\left(e^{\frac{V}{2}} \left(e^{-\frac{V}{2}} g\right)'\right)' \in L^2(dz) \\
&\implies e^{\frac{V}{2}} \left(e^{-\frac{V}{2}} g\right)' \in H^1(dz) \\
&\implies g' - \frac{\beta}{2} g \in H^1(dz) \\
&\implies g \in D(\mathcal{L}).
\end{aligned}$$

Thus $D(\mathcal{L}^*) \subset D(\mathcal{L})$, which concludes the proof. □

We are now ready to show a lower bound on the essential spectrum of the operator $\mathcal{L}$.

Proposition 2.4.1.3.

$$\sigma_{ess}(\mathcal{L}) = [\gamma, +\infty),$$

with $\gamma := \frac{1}{4}\min\left(\sigma^2 - 4, \frac{1}{\chi^2}\right) > 0$

In order to prove this proposition, we require two standard lemmata, whose proof we give for the sake of completeness.

Lemma 2.4.1.4. *Let $f \in H^1(dz)$, then $f \in C^0(\mathbb{R})$ and:*

$$\|f\|_\infty^2 \leq \frac{1}{2\pi} \left\|f'\right\|_2 \|f\|_2 .$$

Proof. Let $z \in \mathbb{R}, \eta > 0$, then:

$$f(z)^2 = \left(\frac{1}{2\pi}\int_{\mathbb{R}} \hat{f}(\xi) e^{iz\xi} d\xi\right)^2 \leq \left(\frac{1}{2\pi}\int_{\mathbb{R}} \frac{\sqrt{1+\eta|\xi|^2}\left|\hat{f}(\xi)\right|}{\sqrt{1+\eta|\xi|^2}} d\xi\right)^2$$
$$\leq \frac{1}{4\pi^2}\frac{\pi}{\sqrt{\eta}}\left(\|f\|_2^2 + \eta\left\|f'\right\|_2^2\right),$$

where we have used Cauchy-Schwartz Inequality and the fact that $\int_{\mathbb{R}} \frac{d\xi}{1+\eta|\xi|^2} = \frac{\pi}{\sqrt{\eta}}$. By taking $\eta = \frac{\|f\|_2^2}{\|f'\|_2^2}$, we obtain the desired bound.

By similar computations, we also have that:

$$(f(z+h) - f(z))^2 \leq \frac{1}{4\pi}\int_{\mathbb{R}} \left(1+|\xi|^2\right)\left|\hat{f}(\xi)\right|^2 \left|e^{i(z+h)\xi} - e^{iz\xi}\right|^2 d\xi.$$

By Dominated Convergence, we have that $\lim_{h\to 0} f(z+h) = f(z)$ and hence $f \in C^0(\mathbb{R})$. □

Lemma 2.4.1.5 (Weyl's criterion)**.** *Let T be a self-adjoint operator in the Hilbert space H. The following properties are equivalent:*
(i) $\lambda \in \sigma_{ess}(T)$.
(ii) There exists a sequence $(u_n) \subset D(T)$ such that $\|u_n\|_H = 1$, (u_n) is not relatively compact and $(T-\lambda I)u_n \xrightarrow[n\to\infty]{H} 0$.

Proof. i) $\implies$ (ii):
Let $\lambda \in \sigma_{\text{ess}}(T)$, $T - \lambda I$ is not a Fredholm operator, which means that $N(T-\lambda I)$ infinite dimensional. Therefore there exists an orthonormal family $(u_n) \in N(T-\lambda I)$, which satisfies proposition (ii).

(ii) $\implies$ (i):
Suppose $\lambda \notin \sigma_{\text{ess}}(T)$, then $T - \lambda I$ is a Fredholm operator. Consider a sequence $(u_n) \subset D(T)$ such that $\|u_n\|_H = 1$ and $(T-\lambda I)u_n \xrightarrow[n\to\infty]{H} 0$. Define $v_n \in N(T-\lambda I), w_n \in N(T-\lambda I)^\perp$ such that $u_n = v_n + w_n$. We have that $w_n = A^{-1}(T-\lambda I)$ where $A = (T-\lambda I)_{|N(T-\lambda I)^\perp}$. A^{-1} is bounded and therefore $w_n \xrightarrow[n\to\infty]{H} 0$. Furthermore (v_n) is bounded, since $\|v_n\|_H \leq \|u_n\|_H = 1$ and as a bounded sequence in a finite-dimensional subspace it admits a converging subsequence. Thus (u_n) admits a converging subsequence. □

We now prove Proposition 2.4.1.3.

Proof. 1. Let $\lambda < \gamma$, we show that $\lambda \notin \sigma_{\text{ess}}(\mathcal{L})$.

By a straightforward computation, we have that $\frac{\beta^2}{4} > \lambda$. Suppose there exists a sequence $(f_n) \subset D(\mathcal{L})$ that satisfies $(\mathcal{L} - \lambda I) f_n \xrightarrow[n\to\infty]{L^2(dz)} 0$ and $\|f_n\|_2 = 1$. We will show that (f_n) has a converging subsequence.

(f_n) is bounded in $H^1(dz)$ and we may apply Equality (2.4.6):

$$\begin{aligned}\langle (\mathcal{L} - \lambda I) f_n | f_n \rangle &= \int_{\mathbb{R}} \left(\left(f_n'\right)^2 + \left(\frac{\beta^2}{4} - \lambda \right) f_n^2 \right) dz - \frac{\chi f_n(0)^2}{2} \\ &\geq \left\| f_n' \right\|_2^2 - \frac{\chi f_n(0)^2}{2} \\ &\geq \left\| f_n' \right\|_2^2 - \frac{\chi}{4\pi} \left\| f_n' \right\|_2 .\end{aligned}$$

We used the fact that by Lemma 2.4.1.4 the domain $D(\mathcal{L}) \subset C^0(\mathbb{R})$ and thus the distribution $\frac{\beta'}{2} f_n = -\frac{\chi f_n(0)}{2} \delta_0$ is well-defined as a linear function on $C^0(\mathbb{R})$. The left handside is bounded above as a converging sequence and thus the second-order polynomial in $\|f_n'\|_2$ on the right handside is also bounded above, which in turn shows that $\|f_n'\|_2$ is uniformly bounded.

By boundedness of $\|f_n'\|_2$ and Lemma 2.4.1.4, we have that $(f_n(0))$ is a bounded sequence and thus admits a converging subsequence. Up to extraction, we can suppose that $(f_n(0))$ converges.

$$\langle (\mathcal{L} - \lambda I)(f_n - f_m) | (f_n - f_m) \rangle + \frac{\chi}{2} (f_n(0) - f_m(0))^2 \geq \left\| f_n' - f_m' \right\|_2^2 + (\inf \gamma - \lambda) \left\| f_n - f_m \right\|_2^2 ,$$

since $\gamma(z) \geq \lambda$ for $z \in \mathbb{R}$. Therefore (f_n) is a Cauchy sequence in $L^2(dz)$ (in fact even in $H^1(z)$) and converges. By Lemma 2.4.1.5, we have that $\lambda \notin \sigma_{\text{ess}}(\mathcal{L})$.

2. Let $\lambda \geq \gamma$, we show that $\lambda \in \sigma_{\text{ess}}(\mathcal{L})$.

If $\gamma = \frac{1}{4} \min\left(\sigma^2 - 4, \frac{1}{\chi^2} \right) = \frac{\sigma^2 - 4}{4}$, or equivalently when $\frac{\beta^2(z)}{4} - \gamma = 0$ for $z \geq 0$, we have that for a function $f \in D(\mathcal{L})$, such that $\text{supp}(f) \subset \mathbb{R}_+ \setminus \{0\}$, $(\mathcal{L} - \lambda) f = -f'' + (\gamma - \lambda) f$. Take a smooth increasing nonnegative function $\phi : [0,1] \to [0,1]$ such that $\phi(0) = \phi'(0) = \phi'(1) = 0$ and $\phi(1) = 0$. Define the function $f_k : \mathbb{R} \to \mathbb{R}$ like so:

$$f_k : z \mapsto c_k \cdot \begin{cases} \phi(z) & \text{if } z \in [0,1] \\ \cos\left(\sqrt{\lambda - \gamma} (z-1) \right) & \text{if } z \in [1, a_k + 1] \\ \phi(a_k + 2 - z) & \text{if } z \in [a_k + 1, a_k + 2] \\ 0 & \text{else} \end{cases} ,$$

where $a_k = \frac{2k\pi}{\sqrt{\lambda - \gamma}}$, $c_k = \left(\frac{a_k}{2} + 2 \int_0^1 \phi^2(z) dz \right)^{-\frac{1}{2}}$, if $\lambda > \gamma$, or $a_k = 2^k$, $c_k = \left(a_k + 2 \int_0^1 \phi^2(z) dz \right)^{-\frac{1}{2}}$, if $\lambda = \gamma$. In all cases $f_k \in D(\mathcal{L})$, $\|f_k\|_2 = 1$ and $(\mathcal{L} - \lambda) f_k(z) = 0$ for $z \in [1, a_k + 1]$. Hence $\|(\mathcal{L} - \lambda) f_k\|_2^2 = 2 c_k^2 \int_0^1 (\phi''(z) + (\lambda - \gamma)\phi(z))^2 dz \to 0$, because clearly $\lim_{k \to +\infty} c_k = 0$. Finally, it can be easily shown that (f_k) is not relatively compact (its only possible accumulation point would be 0, but (f_k) cannot converge to 0, since $\|f_k\|_2 = 1$). Thus by Lemma 2.4.1.5, $\lambda \in \sigma_{\text{ess}}(\mathcal{L})$.

If $\gamma = \frac{1}{4} \min\left(\sigma^2 - 4, \frac{1}{\chi^2} \right) = \frac{1}{4\chi^2}$, or equivalently when $\frac{\beta^2(z)}{4} - \gamma = 0$ for $z \leq 0$, the same reasoning applies *mutatis mutandis*. □

Proposition 2.4.1.6.

$$\sigma(\mathcal{L}) \cap (-\infty, \gamma) = \{0\}$$

Furthermore, the eigenvalue 0 *is simple.*

Proof. Let $\lambda < \gamma$ be an eigenvalue for $\mathcal{L}$ in the space $L^2(dz)$.

For $z > 0$, the characteristic polynomial of the ordinary differential equation $\mathcal{L} - \lambda = 0$ is $P(\mu) = -\mu^2 + \frac{\sigma^2}{4} - 1 - \lambda$, whose roots are $\mu_\pm = \pm\frac{1}{2}\sqrt{\sigma^2 - 4(1+\lambda)}$, which is well-defined, since $\lambda < \frac{1}{4}(\sigma^2 - 4)$. This gives rise to two eigenvectors $e^{\mu_\pm z}$, but it is clear that only $e^{\mu_- z} \in L^2(\mathbb{R}_+, dz)$.

For $z < 0$, by a similar reasoning we obtain that $e^{\nu_+ z}$ is an eigenvector for $\mathcal{L}$ in the space $L^2(\mathbb{R}_-, dz)$, with $\nu_+ = \frac{1}{2}\sqrt{\frac{1}{\chi^2} - 4\lambda}$, which is well-defined, since $\lambda < \frac{1}{4\chi^2}$, .

The eigenvector associated with the eigenvalue λ is therefore of the shape:

$$f_\lambda(z) = \begin{cases} e^{\nu_+ z} & \text{if } z < 0 \\ e^{\mu_- z} & \text{if } z \geq 0 \end{cases}.$$

However we must have that $f_\lambda \in D(\mathcal{L})$ which implies that $f'_\lambda - \frac{\beta}{2} f_\lambda$ is continuous.

$$\left(f'_\lambda - \frac{\beta}{2} f_\lambda\right)(0^+) = \left(f'_\lambda - \frac{\beta}{2} f_\lambda\right)(0^-) \iff \mu_- + \frac{\sigma}{2} = \nu_+ + \frac{\sigma - \chi}{2}$$

$$\iff \chi = \sqrt{\sigma^2 - 4(1+\lambda)} + \sqrt{\frac{1}{\chi^2} - 4\lambda}$$

The right handside is a strictly decreasing function in λ and thus the equation admits at most one root. One checks that this root is $\lambda = 0$ and we already know that $\lambda = 0$ is indeed an eigenvalue with the eigenvector $e^{\frac{V}{2}}$. □

We move on with the proof of Theorem 2.4.1.

Proof. $\mathcal{L}$ is monotone and self-adjoint, therefore by Semigroup theory (see Section 7.4 in [32]), it generates the semi-group $e^{-t\mathcal{L}}$. We consider the spectral projection $\mathcal{P}$ onto the eigenspace of $\mathcal{L}$ associated with the eigenvalue 0, which is $\mathcal{P}u = \frac{1}{\int e^V dz} \int u e^{\frac{V}{2}} dz$. Let $\mathcal{A}$ be the restriction of $\mathcal{L}$ to $N(\mathcal{P})^\perp$. We have that $\inf \sigma(\mathcal{A}) = \gamma$ and for $\lambda < \gamma$, $(\mathcal{A} - \lambda I)^{-1}$ is a bounded operator. Since $\mathcal{A}$ is a closed self-adjoint operator, $\inf \sigma(\mathcal{A}) = \inf_{\|u\|_2 = 1} \langle \mathcal{A}u | u \rangle$ and therefore $\langle (A - \lambda I)u | u \rangle \geq (\gamma - \lambda) \|u\|_2^2$, which shows that $\left\|(\mathcal{A} - \lambda I)^{-1}\right\| \leq \frac{1}{\gamma - \lambda}$. From Hille-Yosida theorem in the self-adjoint case (see Section 7.4 in [32]), we then have for every $u \in N(\mathcal{P})^\perp$ (and not just $u \in D(\mathcal{A})$) that $\left\|e^{-t\mathcal{A}}u\right\|_2 \leq e^{-\gamma t} \|u\|_2$ and $\left\|\mathcal{A}e^{-t\mathcal{A}}u\right\|_2 \leq \frac{e^{-\gamma t}}{t} \|u\|_2$. By setting $w = e^{\frac{V}{2}}\nu$, we have that:

$$w(t) = \mathcal{P}w_0 + e^{-t\mathcal{A}}(I - \mathcal{P})w_0.$$

This leads to the bound:

$$\|w(t) - \mathcal{P}w_0\|_{L^2(dz)} \leq \|w_0\|_{L^2(dz)} e^{-\gamma t}.$$

Bound (2.4.2) is simply a rewritten form of this bound.

Finally, we prove Bound (2.4.3). Set $r(t) := e^{-t\mathcal{A}}(I - \mathcal{P})w_0$, then we have:

$$\int_{\mathbb{R}} \left(\partial_z r(t) - \frac{\beta}{2} r(t)\right)^2 = \langle r(t), \mathcal{A}r(t) \rangle \leq \|r(t)\|_2 \|\mathcal{A}r(t)\|_2 \leq \frac{e^{-2\gamma t}}{t} \|r(0)\|_2^2,$$

where we have used the bounds obtained from Hille-Yosida Theorem in the self-adjoint case. Therefore $\|\partial_z r(t)\|_2 \leq \left(\frac{\|\beta\|_\infty \|r(0)\|_2}{2} + \frac{\|r(0)\|_2}{\sqrt{t}}\right) e^{-\gamma t}$. By Lemma 2.4.1.4, we then have that $\|r(t)\|_\infty \leq C\left(1 + t^{-\frac{1}{2}}\right) e^{-\gamma t}$. Or equivalently:

$$\left\|(\nu(t) - \langle \nu^0 \rangle) e^{\frac{V}{2}}\right\|_\infty \leq C\left(1 + t^{-\frac{1}{2}}\right) e^{-\gamma t}.$$

□

2.4.2 Pulled Front Dynamics in the Small Bias Case

In the small bias case $\chi \leq 1$ (or when $\sigma > \sigma^*$), the inside dynamics of the wave is drastically different. In fact, we can start by observing that Theorem 2.4.1 doesn't apply to these cases. For $\sigma = \sigma_{\mathrm{F/KPP}}$, $\frac{\partial_z \rho^\sigma}{\rho^\sigma} = \frac{1-\chi}{(1-\chi)z+1} - 1$, for $z \geq 0$. Hence $1 \cdot e^{V(z)} = C((1-\chi)z+1)^2$ for a multiplicative constant $C > 0$ and $1 \notin L^2(e^V)$. Similarily, in the case $\sigma > \sigma^*$, $1 \cdot e^V$ behaves like $e^{(\sigma - 2\mu_-(\sigma))z}$, but $\sigma - 2\mu_-(\sigma) = \sqrt{\sigma^2 - 4} > 0$ and thus $1 \notin L^2(e^V dz)$. To describe the behavior in these cases, we start by stating first a general Theorem concerning Equation (2.4.1) under a condition on β:

Theorem 2.4.2. *Consider Equation:*

$$\begin{cases} \partial_t \nu - \partial_{zz}\nu - \beta(z)\partial_z \nu = 0 \\ \nu(0, \cdot) = \nu^0 \end{cases}. \tag{2.4.11}$$

Suppose that β verifies the following conditions:

- *There exists $K > 0$, such that $\beta' \leq K$ in the sense of distributions.*
- *$\int_{\mathbb{R}} \beta_-(z)dz < +\infty$, where $(\cdot)_- = -\min(0, \cdot)$.*

We recall that $V' = \beta$. Suppose that the initial datum ν^0 satisfies the following condition:

$$\int_{\mathbb{R}} \left(\nu^0(z)\right)^2 e^{V(z)} dz < +\infty. \tag{2.4.12}$$

Then the solution ν to Equation (2.4.11) satisfies the following decay property:

$$\lim_{t \to +\infty} \left\| \nu(t) e^{\frac{V}{2}} \right\|_\infty = 0. \tag{2.4.13}$$

And as a consequence ν converges uniformly to 0 on intervals of the form $[a, +\infty)$, for $a \in \mathbb{R}$, i.e.:

$$\lim_{t \to +\infty} \sup_{z \in [a, +\infty)} |\nu(t, z)| = 0. \tag{2.4.14}$$

Next, we apply Theorem 2.4.2 to establish the pulled nature of the waves in the two mentioned cases (small bias case $\chi \leq 1$, or $\sigma > \sigma^*$).

Corollary 2.4.2.1. *Suppose that $\chi \leq 1$ and that $\sigma = \sigma_{F/KPP} = 2$ and consider a neutral fraction ν of the associated wave profile that satisfies Condition (2.4.12). In particular, any function $\nu^0 \in L^\infty(\mathbb{R})$ such that $z \mapsto \left(\nu^0(z)z\right)^2$ is integrable at $z = +\infty$ satisfies Condition (2.4.12). Then $\nu(t)$ converges to 0 uniformly on intervals of the form $[a, +\infty)$, with $a \in \mathbb{R}$. The same results holds true if we suppose that $\sigma > \sigma^*$. In particular, any function $\nu^0 \in L^\infty(\mathbb{R})$ such that $z \mapsto \left(\nu^0(z)\right)^2 e^{(\sigma - 2\mu_-(\sigma))z}$ is integrable at $z = +\infty$ satisfies Condition (2.4.12).*

Proof. We recall that $\beta(z) = \sigma - \chi \mathbb{1}_{z \leq 0} + 2\frac{\partial_z \rho^\sigma}{\rho^\sigma}$.
In the case where $\chi \leq 1$ and $\sigma = 2$, we have from Theorem 2.3.1 that:

$$\rho^\sigma(z) = \begin{cases} 1 & \text{if } z \leq 0 \\ ((1-\chi)z + 1)e^{-z} & \text{if } z > 0 \end{cases},$$

which leads to:

$$\beta(z) = \begin{cases} 2 - \chi & \text{if } z \leq 0 \\ \frac{2(1-\chi)}{(1-\chi)z+1} & \text{if } z > 0 \end{cases}.$$

β' is clearly bounded everywhere except at $z = 0$, but $\beta(0^-) = 2 - \chi$ and $\beta(0^+) = 2(1 - \chi)$. This leads to β' being bounded above in the sense of distributions and $\beta \geq 0$, hence Theorem 2.4.2 applies. Furthermore, by an easy computation up to a mulitplicative constant we have that:

$$e^{V(z)} = \begin{cases} e^{(2-\chi)z} & \text{if } z \leq 0 \\ ((1-\chi)z + 1)^2 & \text{if } z > 0 \end{cases}.$$

Hence a bounded function $\nu^0 \in L^\infty(\mathbb{R})$ satisfies Condition (2.4.12), if $\left(\nu^0(z)z\right)^2$ is integrable at $z = +\infty$.

In the case where $\sigma > \sigma^*$, we have:

$$\rho^\sigma(z) = \begin{cases} 1 & \text{if } z \leq 0 \\ \frac{\mu_+ - \chi}{\sigma - \chi} e^{-\mu_- z} - \frac{\mu_- - \chi}{\sigma - \chi} e^{-\mu_+ z} & \text{if } z > 0 \end{cases},$$

where we recall that $\mu_\pm = \frac{\sigma \pm \sqrt{\sigma^2 - 4}}{2}$. This leads to:

$$\beta(z) = \begin{cases} \sigma - \chi & \text{if } z \leq 0 \\ \sigma - 2\frac{(\mu_+ - \chi)\mu_- e^{-\mu_- z} - (\mu_- - \chi)\mu_+ e^{-\mu_+ z}}{(\mu_+ - \chi)e^{-\mu_- z} - (\mu_- - \chi)e^{-\mu_+ z}} & \text{if } z > 0 \end{cases}.$$

By the same reasoning β' is bounded above. For $z \leq 0, \beta(z) \geq 0$ and $\lim_{z \to +\infty} \beta(z) = \sigma - 2\mu_- > 0$, which establishes that $\int_{\mathbb{R}} \beta_-(z)dz < +\infty$ and hence Theorem 2.4.2 applies. Finally, we have up to a multiplicative constant that:

$$e^{V(z)} = \begin{cases} e^{(\sigma-\chi)z} & \text{if } z \leq 0 \\ e^{\sigma z} \left(\rho^\sigma(z)\right)^2 & \text{if } z > 0 \end{cases}.$$

Hence a bounded function $\nu^0 \in L^\infty(\mathbb{R})$ satisfies Condition (2.4.12), if $\left(\nu^0(z)\right)^2 e^{(\sigma - 2\mu_-)z}$ is integrable at $z = +\infty$. □

Before moving on to the proof of Theorem 2.4.2, let us make some comments. Notice that Corollary 2.4.2.1 does not apply to the neutral fraction $\nu^0 \equiv 1$, which is consistent with the fact that the neutral fraction $\nu \equiv 1$ stays constant and does not converge to 0. In fact, Condition (2.4.12) or its counterparts in Corollary 2.4.2.1 may be seen as a characterization of an initial datum ν^0, that constitutes a negligible part of the leading edge of the traveling wave. If, for the sake of the argument, we were to accept this property as a definition, then Theorem 2.4.2 or Corollary 2.4.2.1 tell us that neutral fractions, which constitute a negligible part of the leading edge of the traveling wave, go extinct in the traveling wave, *i.e* they converge to 0.
Nevertheless, just like in the work [82], Theorem 2.4.2 does not give any rate of convergence, contrary to Theorem 2.4.1, and this remains an open question. Finally let us note, that unsurprisingly in the case of large bias with $\sigma = \sigma^*$, for $\beta(z)$ is bounded above by a negative constant for $z > 0$, which establishes that $\int \beta_-(z) = +\infty$ and thus Theorem 2.4.2 conversely does not apply to that case.

We now move on to the proof of Theorem 2.4.2.

Proof. Consider $L := -\partial_{zz} - \beta(z)\partial_z$ in the weighted space $L^2(e^V dz)$ with domain $D(L) = H^2(e^V dz)$. From the arguments of the proof of Theorem 2.4.1, we have that L is self-adjoint

and it furthermore satisfies the following property for $f \in D(L)$:

$$\begin{aligned}\int_{\mathbb{R}} f(Lf)e^V dz &= \int_{\mathbb{R}} f(-f'' - \beta f')e^V \partial_z \\ &= \int_{\mathbb{R}} \left(f'^2 + \beta f f' - \beta f f'\right) e^V dz \\ &= \left\|f'\right\|^2_{L^2(e^V dz)}.\end{aligned}$$

This leads to the following dissipation rate:

$$\frac{d}{dt}\left(\frac{1}{2}\left\|\nu\right\|^2_{L^2(e^V dz)}\right) = -\left\|\partial_z \nu\right\|^2_{L^2(e^V dz)}. \tag{2.4.15}$$

Furthermore:

$$\begin{aligned}&\frac{d}{dt}\left(\frac{1}{2}\left\|\partial_z\nu\right\|^2_{L^2(e^V dz)}\right) \\ &= \int_{\mathbb{R}} \partial_z(\partial_t \nu)\partial_z \nu e^V dz \\ &= -\int_{\mathbb{R}} \partial_t \nu \partial_z(e^V \partial_z \nu) dz \\ &= -\int_{\mathbb{R}} \partial_{zz}\nu\partial_z(e^V\partial_z\nu)dz - \int_{\mathbb{R}} \beta\partial_z\nu\partial_z(e^V\partial_z\nu)dz \\ &= -\left\|\partial_{zz}\nu\right\|^2_{L^2(e^V dz)} - \frac{1}{2}\int_{\mathbb{R}} \partial_z\left((\partial_z\nu)^2\right)\beta e^V dz - \int_{\mathbb{R}}(\partial_z\nu)^2\beta^2 e^V dz - \frac{1}{2}\int_{\mathbb{R}}\beta\partial_z\left((\partial_z\nu)^2\right)e^V dz \\ &= -\left\|\partial_{zz}\nu\right\|^2_{L^2(e^V dz)} - \int_{\mathbb{R}}\left(\partial_z((\partial_z\nu)^2)\beta e^V + (\partial_z\nu)^2\beta^2 e^V\right)dz \\ &= -\left\|\partial_{zz}\nu\right\|^2_{L^2(e^V dz)} - \int_{\mathbb{R}}\left(\partial_z\left((\partial_z\nu)^2\beta e^V\right) - (\partial_z\nu)^2\beta' e^V\right)dz \\ &= -\left\|\partial_{zz}\nu\right\|^2_{L^2(e^V dz)} + \int_{\mathbb{R}}(\partial_z\nu)^2\beta' e^V dz.\end{aligned}$$

For $K > 0$ such that $\beta' \leq K$, we have that:

$$\frac{d}{dt}\left(\frac{K}{2}\left\|\nu\right\|^2_{L^2(e^V dz)} + \frac{1}{2}\left\|\partial_z\nu\right\|^2_{L^2(e^V dz)}\right) = -\left\|\partial_{zz}\nu\right\|^2_{L^2(e^V dz)} + \int_{\mathbb{R}}(\partial_z\nu)^2\left(\beta' - K\right)e^V dz \leq 0.$$

Hence $\|\nu(t)\|_{L^2(e^V dz)}$ converges to a limit and so does $\|\partial_z\nu(t)\|_{L^2(e^V dz)}$. But by Equation (2.4.15), the limit of $\|\partial_z\nu(t)\|_{L^2(e^V dz)}$ can only be 0, otherwise $\|\nu(t)\|_{L^2(e^V dz)}$ could not converge.
Finally, set $c := \int_{-\infty}^{+\infty}\beta_-$ and $W(z) = \int_0^z \beta_+ - c$. If we fix the constant of integration of V such that $V(z) = \int_0^z \beta$. Then we have the following inequality:

$$V - 2c \leq W \leq V.$$

We can conclude by the following argument:

$$\begin{aligned}
e^{-2c}\left\|\nu(t)^2 e^V\right\|_\infty &\le \left\|\nu(t)^2 e^W\right\|_\infty \\
&\le \int_{\mathbb{R}} \left|\partial_z\left(\nu^2 e^W\right)\right| dz \\
&\le 2\int_{\mathbb{R}} |\nu||\partial_z\nu| e^W dz + \int_{\mathbb{R}} |\beta_+ e^W|\nu^2 dz \\
&\le 2\int_{\mathbb{R}} |\nu||\partial_z\nu| e^W dz + \int_{\mathbb{R}} \left(e^W\right)'\nu^2 dz \\
&\le 2\int_{\mathbb{R}} |\nu||\partial_z\nu| e^W dz - 2\int_{\mathbb{R}} \nu\partial_z\nu e^W dz \\
&\le 4\int_{\mathbb{R}} |\nu||\partial_z\nu| e^W dz \\
&\le 4\left\|\nu(t)\right\|_{L^2(e^W dz)}\left\|\partial_z\nu(t)\right\|_{L^2(e^W dz)} \\
&\le 4\left\|\nu(t)\right\|_{L^2(e^V dz)}\left\|\partial_z\nu(t)\right\|_{L^2(e^V dz)},
\end{aligned}$$

where at the end we have used Cauchy-Schwarz inequality, followed by the equivalence of norms. Hence $\lim_{t\to\infty}\sup_{z\in\mathbb{R}}|\nu(t,z)^2 e^V(z)| = 0$. Finally, since $\int_{\mathbb{R}}\beta_-(z)dz < +\infty$, for every $a\in\mathbb{R}$, we have that $\inf_{z\in[a,+\infty)} e^{V(z)} > 0$ and therefore $\lim_{t\to+\infty}\sup_{z\in[a,+\infty)}|\nu(t,z)| = 0$. □

2.5 Asymptotic Spreading Properties

In this Section, we work under the hypothesis that the solution (ρ, N) of System (2.1.1) is well-defined for all time, that $x\mapsto N(t,x)$ is an increasing function and we recall that $\bar{x}(t)$ is defined as the unique solution $N(t,\bar{x}(t)) = N_{\text{th}}$. As before, we consider the system in the moving frame of reference and study $(\rho(t,z), N(t,z))$ solution of System (2.2.9), droping the diacritical ˜ for the sake of concision.

The aim of the Section is to describe the asymptotic behavior of $t\mapsto\bar{x}(t)$. In fact, we will show that under some assumptions on the initial datum, we have $\liminf_{t\to+\infty}\dot{\bar{x}}(t)\le\sigma^*$ and $\limsup_{t\to+\infty}\dot{\bar{x}}(t)\ge\sigma^*$. The strategy of proof for both results is similar and is based on an argument by contradiction: if those properties were not satisfied, then this would first lead to an abnormal behavior of ρ, which in turn contradicts the equation $N(t,0) = N_{\text{th}}$. We have not been able to prove a stronger result, such as for instance $\lim_{t\to+\infty}\dot{\bar{x}}(t) = \sigma^*$ and we believe that in order to achieve such a result, one needs to study the behavior of ρ and N simultaneously, which is much more involved than our present study. One major difficulty comes from the fact that System (2.1.1) does not have a comparison principle.

2.5.1 The Spreading may not be too fast

Theorem 2.5.1. *Suppose that $\dot{\bar{x}}\in L^\infty(\mathbb{R}_+)$ and that:*

$$\frac{\rho^0}{\rho^{\sigma^*}}\in L^\infty.$$

Then:

$$\liminf_{t\to+\infty}\dot{\bar{x}}(t)\le\sigma^*.$$

Proof. 1. We argue by contradiction and start by showing that ρ converges to 0 uniformly on intervals of the form $[a,+\infty)$ for $a\in\mathbb{R}$.

Let $t_0 \geq 0, \delta > 0$, such that for $t \geq t_0, \dot{\bar{x}}(t) \geq \sigma^* + \delta$. Set $v := \frac{\rho}{\rho^{\sigma^*+\delta}}$, where $\rho^{\sigma^*+\delta}$ is the traveling wave profile for speed $\sigma^* + \delta$ (see Theorem 2.3.1). We have that v satisfies the following Equation:

$$\partial_t v - \partial_{zz} v - \beta(t,z)\partial_z v - \gamma(t,z)v = 0,$$

with $\beta(t,z) := \dot{\bar{x}}(t) - \chi \mathbb{1}_{z<0} + 2\frac{\partial_z \rho^{\sigma^*+\delta}}{\rho^{\sigma^*+\delta}}$ and $\gamma(t,z) := (\dot{\bar{x}}(t) - (\sigma^* + \delta))\frac{\partial_z \rho^{\sigma^*+\delta}}{\rho^{\sigma^*+\delta}}$. By noticing that $(t,z) \mapsto \left\| \frac{\rho^0}{\rho^{\sigma^*}} \right\|_\infty \exp\left(\left\| \frac{\partial_z \rho^{\sigma^*+\delta}}{\rho^{\sigma^*+\delta}} \right\|_\infty \int_0^{t_0} (\sigma^* + \delta - \dot{\bar{x}}(s))_+ ds \right)$ is a super-solution to $\partial_t - \partial_{zz} - \beta(t,z)\partial_z - \gamma(t,z)$, we observe that $\frac{\rho(t_0)}{\rho^{\sigma^*}} \in L^\infty$. Hence we can suppose without loss of generality that for $t \geq 0, \dot{\bar{x}}(t) \geq \sigma^* + \delta$. Therefore, we have that $\beta(t,z) \geq \sigma^* + \delta - \chi \mathbb{1}_{z<0} + 2\frac{\partial_z \rho^{\sigma^*+\delta}}{\rho^{\sigma^*+\delta}} =: \beta^{\sigma^*+\delta}(z)$ and $\gamma(t,z) \leq 0$. Moreover, by linearity we can suppose that $\left\| \frac{\rho^0}{\rho^{\sigma^*}} \right\|_\infty \leq 1$.

Since $\gamma(t,z) \leq 0$ and $v \geq 0$, we have that v is a subsolution of $\partial_t - \partial_{zz} - \beta(t,z)\partial_z$. Hence we consider the solution $\bar{v}$ of $\partial_t - \partial_{zz} - \beta(t,z)\partial_z$, such that $v \leq \bar{v}$, with initial datum $\bar{v}^0$, which we define now. Set $\eta := \frac{\mu_+(\sigma^*) - \mu_-(\sigma^*+\delta)}{2}$ and define $g(z) = \frac{e^{-\eta z}}{1+e^{-\eta z}}$. Let $K > 0$ be big enough such that:

$$\frac{\rho^0(z)}{\rho^{\sigma^*+\delta}(z)} \leq \frac{\rho^{\sigma^*}(z)}{\rho^{\sigma^*+\delta}(z)} \leq K g(z).$$

Such a constant exists, as a consequence of Theorem 2.3.1, since for $z < 0$, $\frac{\rho^{\sigma^*}(z)}{\rho^{\sigma^*+\delta}(z)} = 1$ and for $z \to +\infty$, $\frac{\rho^{\sigma^*}(z)}{\rho^{\sigma^*+\delta}(z)} = O\left(z e^{-(\mu_+(\sigma^*) - \mu_-(\sigma^*+\delta))z} \right) = O(g(z))$. Thus, we set the initial datum $\bar{v}^0(z) = K g(z)$.

Let us show that $\partial_z \bar{v} \leq 0$. By construction, $\partial_z \bar{v}^0 \leq 0$. Furthermore $\bar{v}^0 \in H^2_{\mathrm{loc}}(\mathbb{R}, dz)$ and hence by standard regularity theory, we have that $\bar{v} \in C(\mathbb{R}_+, H^2_{\mathrm{loc}}(\mathbb{R}, dz))$. Setting $w := \partial_z \bar{v}$, combining the facts that $w(0, \cdot) \in H^1(\mathbb{R}, dz)$, $w \in C(\mathbb{R}_+, H^1_{\mathrm{loc}}(\mathbb{R}))$ and that w is solution to $\partial_t w - \partial_{zz} w - \partial_z(\beta w) = 0$, shows in fact that $w \in C(\mathbb{R}_+, H^1(\mathbb{R}, dz))$. Now we can procede as in the proof of Corollay 2.2.1.2, to show that $w_+ \equiv 0$, where $(\cdot)_+ = \max(\cdot, 0)$:

$$\begin{aligned}
\frac{d}{dt}\left(\frac{1}{2} \int_{\mathbb{R}} w_+^2(t,z) \right) &= \int_{\mathbb{R}} w_+ \partial_t w_+ dz \\
&= \int_{\mathbb{R}} w_+ \partial_t w dz \\
&= \int_{\mathbb{R}} w_+ (\partial_{zz} w + \partial_z(\beta w)) dz \\
&= -\int_{\mathbb{R}} \left(\partial_z w_+ \partial_z w + \beta w \partial_z w_+ \right) dz \\
&= -\int_{\mathbb{R}} (\partial_z w_+)^2 dz - \int_{\mathbb{R}} \beta w_+ \partial_z w_+ dz \\
&\leq -\int_{\mathbb{R}} (\partial_z w_+)^2 dz + \frac{1}{2}\int_{\mathbb{R}} (\partial_z w_+)^2 dz + \frac{\|\beta\|_\infty^2}{2}\int_{\mathbb{R}} (w_+)^2 dz \\
&\leq \frac{\|\beta\|_\infty^2}{2}\int_{\mathbb{R}} (w_+)^2 dz,
\end{aligned}$$

where we have applied arithmetic and geometric means inequality $|\beta w_+ \partial_z w_+| \leq \frac{(\partial_z w_+)^2}{2} + \frac{\|\beta\|_\infty^2 (w_+)^2}{2}$. Since $w_+(0, \cdot) \equiv 0$, by Grönwall's lemma, we have that $w_+(t, \cdot) \equiv 0$. Thus $\partial_z \bar{v} \leq 0$.

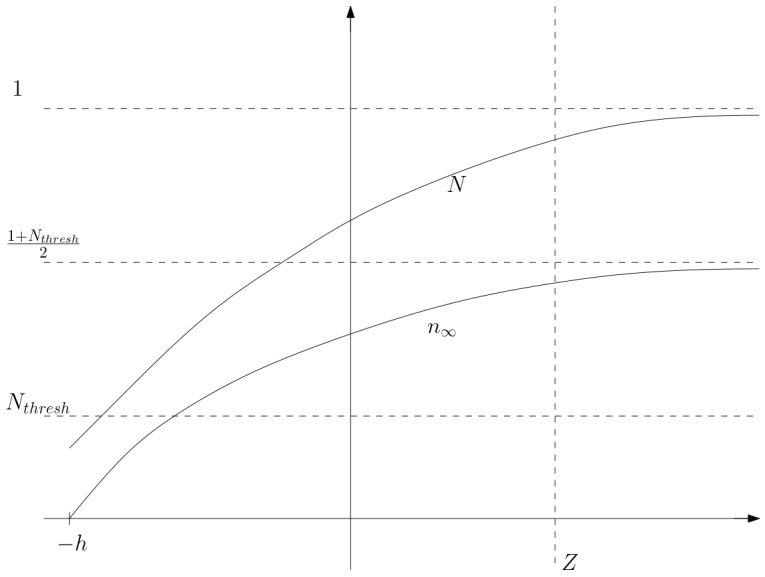

Figure 2.2: In order to prove that condition $N(t,0) = N_{\text{th}}$ cannot be satisfied, we consider solution $n(t,z)$ to Equation (2.5.1) with inital datum $n(t_1,z) = n_\infty(z)$ for $z \geq Z$ and $n(t_1,z) = 0$ for $z \in [-h, Z)$. Then $n(t) \to n_\infty$ uniformly. Furthermore N is a super-solution of Equation (2.5.1) and $N(t_1,\cdot) > n(t_1,\cdot)$, which leads to $N(t,\cdot) \geq n(t,\cdot)$ for all $t \geq t_1$. But $n(t,0) \to n_\infty(0) > N_{\text{th}}$ and thus the condition $N(t,0) = N_{\text{th}}$ is not satisfied after some time.

By the bound $\beta^{\sigma^*+\delta} \leq \beta$ and the inequality $\partial_z \bar{v} \leq 0$, we have that $\bar{v}$ is a sub-solution (and not a super-solution!) of the parabolic operator $\partial_t - \partial_{zz} - \beta^{\sigma^*+\delta}\partial_z$. But from Corollary 2.4.2.1, we know that the corresponding solution with initial datum $\bar{v}^0(z) = Kg(z)$ converges to 0 uniformly on intervals of the form $[a, +\infty)$. Hence so does $\bar{v}$ and v by the comparison principle and thus ρ converges to 0 uniformly on compact sets.

2. Let us now show that the condition $N(t,0) = N_{\text{th}}$ cannot be satisfied for time $t > 0$ sufficiently large. Let $\mu > 0$ such that $\mu < \frac{\sigma^*}{D}$ and $\mu < \mu_-(\sigma^* + \delta)$. Let $\varepsilon > 0$ be sufficiently small, such that $\frac{1+N_{\text{th}}}{2} - \frac{\varepsilon}{D\mu\left(\frac{\sigma^*}{D}-\mu\right)} > N_{\text{th}}$ and denote $B := \frac{\varepsilon}{D\mu\left(\frac{\sigma^*}{D}-\mu\right)}$. Choose $h > 0$ big enough such that $\frac{1+N_{\text{th}}}{2}\left(1 - e^{-\frac{\sigma^* h}{D}}\right) - B\left(1 - e^{-\left(\frac{\sigma^*}{D}-\mu\right)h}\right) > N_{\text{th}}$, which exists by noticing that in the limit $h \to +\infty$ the inequality is satisfied by the above.

As v converges to 0 uniformly on the set $[-h, +\infty)$, and by noticing that $\rho^{\sigma^*+\delta}(z) = o\left(e^{-\mu z}\right)$, there exists t_1, such that for $t \geq t_1$ and $z \geq -h$, we have $\rho(t,z)N(t,z) \leq \rho(t,z) \leq \varepsilon e^{-\mu z}$. Finally let $Z > 0$ be such that $N(t_1, Z) > \frac{1+N_{\text{th}}}{2}$.
We consider the parabolic equation in the domain $\Omega = (t_1, +\infty) \times (-h, +\infty)$:

$$\begin{aligned} \partial_t n - \sigma^* \partial_z n - D\partial_{zz} n + \varepsilon e^{-\mu z} = 0 \\ n(t,-h) = 0, n(t_1,\cdot) = n^{t_1}(\cdot). \end{aligned} \tag{2.5.1}$$

A stationary solution to Equation (2.5.1) is:

$$n_\infty(z) = \frac{1+N_{\text{th}}}{2} - Be^{-\mu z} + Ce^{-\frac{\sigma^*}{D}z},$$

with $C := -Be^{-\left(\frac{\sigma^*}{D}-\mu\right)h} - \frac{1+N_{\text{th}}}{2}e^{-\frac{\sigma^*}{D}h}$. Notice that $n_\infty(0) > N_{\text{th}}$, by the choices made

above.
Consider now the solution n to Equation (2.5.1) with initial datum $n(t_1, \cdot) = n_\infty \mathbb{1}_{z \geq Z}$. We will show that $n(t, \cdot) \to n_\infty$ uniformly and in particular for $z = 0$, $n(t, 0) \to n_\infty(0) > N_{\text{th}}$. Indeed set $w := n_\infty - n$, then w satisfies for $(t, z) \in \Omega$:

$$\begin{aligned} \partial_t w - \sigma^* \partial_z w - D\partial_{zz} w = 0 \\ w(t, -h) = 0, w(t_1, z) = n_\infty(z) \mathbb{1}_{z<Z}. \end{aligned}$$

It can be verified that for $(t, z) \in \Omega$, we have the following explicit expression:

$$\begin{aligned} |w(t,z)| &= \left| \frac{e^{-\frac{\sigma^{*2}}{4}t - \frac{\sigma^*}{2}z}}{\sqrt{4\pi D(t-t_1)}} \int_{-h}^{+\infty} \left(e^{-\frac{(z+h-y)^2}{4D(t-t_1)}} - e^{-\frac{(z+h+y)^2}{4D(t-t_1)}} \right) e^{\frac{\sigma^*}{2}y} n_\infty(y) \mathbb{1}_{y \leq Z} dy \right| \\ &\leq \frac{C e^{\frac{\sigma^*}{2}h} e^{-\frac{\sigma^{*2}}{4}t}}{\sqrt{(t-t_1)}} \left\| e^{\frac{\sigma^*}{2}y} n_\infty(y) \right\|_{L^1([-h,Z])}. \end{aligned}$$

Hence, $\lim_{t \to +\infty} w(t, z) = 0$ uniformly, which shows that $\lim_{t \to +\infty} n(t, z) = n_\infty(z)$ uniformly. In particular there exist $t_2 > t_1$, such that $n(t_2, 0) > N_{\text{th}}$.

In the final step, it remains to show that N is a supersolution of Equation (2.5.1). Indeed for $(t, z) \in \Omega$:

$$\begin{aligned} &\partial_t N - \sigma^* \partial_z N - D\partial_{zz} N + \varepsilon e^{-\mu z} \\ \geq &\partial_t N - \dot{\bar{x}}(t) \partial_z N - D\partial_{zz} N + \rho N \\ = &0. \end{aligned}$$

By construction $N(t_1, \cdot) \geq n(t_1, \cdot)$ and $N(\cdot, -h) > 0 = n(\cdot, -h)$. Hence we have for all $(t, z) \in \Omega, N(t, z) \geq n(t, z)$ and in particular $N(t_2, 0) \geq n(t_2, 0) > N_{\text{th}}$, which leads to a contradiction.

□

2.5.2 The Spreading may not be too slow

In this Section, we will show that $\limsup_{t \to +\infty} \dot{\bar{x}}(t) \geq \sigma^*$. The proof is based on the observation that the norm of ρ increases exponentially in a certain weighted L^1-spaces, when $\dot{\bar{x}} < \sigma^*$. In fact, as a starter, in the large bias case $\chi > 1$, take for example the weight $e^{\frac{z}{\chi}}$. By noticing that it is an eigenvalue of the dual of the elliptic operator, one sees that:

$$\frac{d}{dt} \int_{\mathbb{R}} e^{\frac{z}{\chi}} \rho(t, z) dz = \frac{\chi + \frac{1}{\chi} - \dot{\bar{x}}(t)}{\chi} \int_{\mathbb{R}} e^{\frac{z}{\chi}} \rho(t, z) dz.$$

Then if $\limsup_{t \to +\infty} \dot{\bar{x}}(t) < \sigma^*$, we have that $\int_{\mathbb{R}} e^{\frac{z}{\chi}} \rho(t, z) dz$ grows exponentially. Nevertheless, since $e^{\frac{z}{\chi}}$ is unbounded, this observation is not sufficiently instructive. Hence, instead of $e^{\frac{z}{\chi}}$ an exact eigenvalue of the dual of the elliptic operator, we consider a supersolution $e^u \in L^\infty(\mathbb{R})$ of the dual of the elliptic operator, which enables us to show that $\rho(t)$ diverges to $+\infty$ in $L^1(\mathbb{R}, e^u dz)$. Then we show that a similar statement remains true for ρ in $L^1(\mathbb{R}_+, e^u dz)$ and finally this accumulation of mass on the half-line $\mathbb{R}_+$ leads to a contradiction on the condition $N(t, 0) = N_{\text{th}}$.

Theorem 2.5.2. *Suppose that $\dot{\bar{x}} \in L^\infty(\mathbb{R}_+)$ and that $\rho^0 \in L^\infty$. Then:*

$$\limsup_{t \to +\infty} \dot{\bar{x}}(t) \geq \sigma^*.$$

Proof. Suppose by contradiction that $\limsup_{t\to+\infty} \dot{\bar{x}}(t) < \sigma^*$ ($= 2$ in the small bias case $\chi \leq 1$, $= \chi + \frac{1}{\chi}$ in the large bias case $\chi > 1$). Then there exists $\delta > 0, t_0 \geq 0$, such that for $t \geq t_0, \dot{\bar{x}}(t) \leq \sigma^* - \delta$.

1. We start by constructing a function $e^u \in L^\infty(\mathbb{R})$, such that the quantity $\int_{\mathbb{R}} e^{u(z)}\rho(t,z)dz$ tends to infinity. Given a function $u \in C^2(\mathbb{R})$, set $w(t,z) := e^{u(z)}\rho(t,z)$, then:

$$\partial_t w - \partial_{zz} w - \partial_z \left(\underbrace{\left(\dot{\bar{x}}(t) - 2u' - \chi \mathbb{1}_{z\leq 0}\right)}_{=:\beta(t,z)} w \right) - \underbrace{\left(u'^2 + u'' - \dot{\bar{x}}(t)u' + \mathbb{1}_{z>0} + \chi \mathbb{1}_{z\leq 0} u'\right)}_{=:\gamma(t,z)} w. \tag{2.5.2}$$

We now show that we can construct a function u such that γ is bounded below by a positive constant $\eta > 0$. u will be of the shape $u(z) = \mu(z)z$ with $\mu(z) = \frac{1}{\chi}$ for $z \leq 0$, $\mu(z) = -\frac{1}{\|\dot{\bar{x}}\|_\infty}$ for $z > B$, with $B > 0$, and μ will decrease slowly on the interval $[0, B]$. The key ingredients for the construction of the function u are Bounds (2.5.3,2.5.4) and Lemma 2.5.2.1.

First notice that for $t \geq t_0$ and by assuming that $2\eta < \frac{\delta}{\chi}$, we have the following Bound:

$$\left(\frac{1}{\chi}\right)^2 - \dot{\bar{x}}(t)\left(\frac{1}{\chi}\right) + \chi\left(\frac{1}{\chi}\right) = \frac{\chi + \frac{1}{\chi} - \dot{\bar{x}}(t)}{\chi} \geq \frac{\delta}{\chi}. \tag{2.5.3}$$

For the second bound we introduce the functions $g_t : \mu \in I := \left[-\frac{1}{\|\dot{\bar{x}}\|_\infty}, \frac{1}{\chi}\right] \mapsto \mu^2 - \dot{\bar{x}}(t)\mu + 1$ and show that it is uniformly in time bounded below by 2η for each $\dot{\bar{x}}(t)$. Without loss of generality we suppose that $\|\dot{\bar{x}}\|_\infty > 1$. The minimum of g_t on $\mathbb{R}$ is reached for $\mu = \frac{\dot{\bar{x}}(t)}{2}$ and its minimal value is $1 - \frac{\dot{\bar{x}}(t)^2}{4}$.

- If $\frac{\dot{\bar{x}}(t)}{2} < -\frac{1}{\|\dot{\bar{x}}\|_\infty}$, then the minimum of g_t on its domain I is $g_t\left(-\frac{1}{\|\dot{\bar{x}}\|_\infty}\right) = \frac{1}{\|\dot{\bar{x}}\|_\infty^2} - \frac{\dot{\bar{x}}}{\|\dot{\bar{x}}\|_\infty} + 1 \geq \frac{1}{\|\dot{\bar{x}}\|_\infty^2}$.
- If $\frac{\dot{\bar{x}}(t)}{2} > \frac{1}{\chi}$, then the minimum of g_t is $g_t\left(\frac{1}{\chi}\right) \geq \frac{\delta}{\chi}$.
- Else if $\frac{\dot{\bar{x}}(t)}{2} \in I$, then: (i) in the large bias case $\chi > 1$, we have that $g_t(\mu) \geq 1 - \min\left(\frac{1}{\|\dot{\bar{x}}\|_\infty^2}, \frac{1}{\chi^2}\right) > 0$. (ii) In the small bias case $\chi \leq 1$, we know that $\dot{\bar{x}}(t) \leq 2 - \delta$ and $\dot{\bar{x}}(t) \geq -\frac{2}{\|\dot{\bar{x}}\|_\infty} > -2$. Hence the minimum of g_t, which is $1 - \frac{\dot{\bar{x}}(t)^2}{2}$, is in that case positive.

Finally this leads for $\eta > 0$ small enough and for every $t \geq t_0$ to the Bound:

$$\min_{\mu\in I} g_t(\mu) \geq 2\eta. \tag{2.5.4}$$

Next, we introduce the following technical Lemma 2.5.2.1, which will be an essential ingredient for the construction of $u(z) = \mu(z)z$ with the function $z \mapsto \mu(z)$ varying slowly in the interval I, such that γ will stay bounded below by η.

Lemma 2.5.2.1. *For every $\varepsilon > 0$, there exists a nondecreasing function $\theta_\varepsilon \in W^{2,\infty}([0,1],[0,1])$ such that $\theta_\varepsilon(0) = 0$, $\theta'_\varepsilon(0) = 0$, $\theta_\varepsilon(1) = 1$ and $\theta'_\varepsilon(1) = 0$, and that:*

$$\sup_{z\in[0,1]} \theta'_\varepsilon(z)z \leq \varepsilon.$$

Let us give a quick proof of Lemma 2.5.2.1.

Proof. Consider the function $f(z) = z^\varepsilon$. Then $f'(z)z = \varepsilon z^{\varepsilon-1}$. Hence $\sup_{z\in[0,1]} f'(z)z \leq \varepsilon$. Set:

$$\theta_\varepsilon : z \mapsto \begin{cases} \varepsilon^{(\varepsilon-3)\left(1+\frac{1}{\varepsilon}\right)}\left(\varepsilon^{1+\frac{1}{\varepsilon}}(3-\varepsilon)z^2 - (2-\varepsilon)z^3\right) & \text{if } z \in \left[0, \varepsilon^{1+\frac{1}{\varepsilon}}\right) \\ f(z) & \text{if } z \in [\varepsilon^{1+\frac{1}{\varepsilon}}, 1-\varepsilon) \\ g(z) & \text{if } z \in [1-\varepsilon, 1] \end{cases},$$

where g is any concave C^1 function such that $g(1-\varepsilon) = f(1-\varepsilon)$, $g'(1-\varepsilon) = f'(1-\varepsilon)$, $g(1) = 1$ and $g'(1) = 0$. Notice that $g'(1-\varepsilon) \geq g'(1)$, hence such a concave function g exists.

First notice that by construction $\theta_\varepsilon(0) = \theta'_\varepsilon(0) = 0$, $\theta_\varepsilon\left(\left(\varepsilon^{1+\frac{1}{\varepsilon}}\right)^-\right) = f\left(\varepsilon^{1+\frac{1}{\varepsilon}}\right)$ and $\theta'_\varepsilon\left(\left(\varepsilon^{1+\frac{1}{\varepsilon}}\right)^-\right) = f'\left(\varepsilon^{1+\frac{1}{\varepsilon}}\right)$. By straightforward computations, we show that θ_ε is increasing on the interval $\left[0, \varepsilon^{1+\frac{1}{\varepsilon}}\right)$ and that $\theta'_\varepsilon(z)z$ reaches its maximum on the interval $\left[0, \varepsilon^{1+\frac{1}{\varepsilon}}\right)$ at point $z_\varepsilon := \left(\frac{2}{3}\right)^2 \frac{3-\varepsilon}{2-\varepsilon}\varepsilon^{1+\frac{1}{\varepsilon}}$, with value:

$$\begin{aligned} \theta'_\varepsilon(z_\varepsilon)z_\varepsilon &= \left(\frac{2}{3}\right)^5 \frac{(3-\varepsilon)^3}{(2-\varepsilon)^2}\varepsilon^{\varepsilon+1} \\ &\leq \left(\frac{2}{3}\right)^5 \frac{3^3}{1^2}\varepsilon^\varepsilon\varepsilon \\ &\leq \frac{32}{9}\varepsilon. \end{aligned}$$

For $z \in [1-\varepsilon, 1]$, θ_ε is increasing, as by concavity of g, we have that $g'(z) \geq g'(0) = 0$. In addition:

$$\theta'_\varepsilon(z)z = g'(z)z \leq g'(1-\varepsilon)z \leq g'(1-\varepsilon) = \frac{(1-\varepsilon)f'(1-\varepsilon)}{1-\varepsilon} \leq \frac{\varepsilon}{1-\varepsilon}.$$

Finally, by construction, we have that $\theta_\varepsilon \in W^2([0,1],[0,1])$ □

Using the function θ_ε from Lemma 2.5.2.1, for $\varepsilon > 0, B > 0$ to be determined later, we choose $u(z) = \mu(z)z$ with:

$$\mu : z \mapsto \begin{cases} \frac{1}{\chi} & \text{if } z \leq 0 \\ \frac{1}{\chi} - \theta_\varepsilon\left(\frac{z}{B}\right)\left(\frac{1}{\chi} + \frac{1}{\|\dot{\bar{x}}\|_\infty}\right) & \text{if } z \in (0, B] \\ -\frac{1}{\|\dot{\bar{x}}\|_\infty} & \text{if } z > B \end{cases}.$$

- Notice that by Bound (2.5.3), we have that for $t \geq t_0, z < 0$, $\gamma(t,z) = u'^2 + u'' - \dot{\bar{x}}(t)u' + \chi u' = \left(\frac{1}{\chi}\right)^2 - \dot{\bar{x}}(t)\left(\frac{1}{\chi}\right) + \chi\left(\frac{1}{\chi}\right) \geq \frac{\delta}{\chi} \geq 2\eta$.

- Additionally by Bound (2.5.4), we have that for $t \geq t_0, z > B$, $\gamma(t,z) = u'^2 + u'' - \dot{\bar{x}}(t)u' + 1 = g_t\left(-\frac{1}{\|\dot{\bar{x}}\|_\infty}\right) \geq 2\eta$.

- Then for $t \geq t_0, z \in (0,B)$, first notice that $\mu(z) \in I$ and we will show that for $\varepsilon > 0$ small enough and $B > 0$ big enough, we have $|\gamma(t,z) - g_t(\mu(z))| \leq \eta$.
  We have that:
  $$u'(z) = \mu(z) - \frac{z}{B}\theta'_\varepsilon\left(\frac{z}{B}\right)\left(\frac{1}{\chi} + \frac{1}{\|\dot{\bar{x}}\|_\infty}\right).$$
  But according to Lemma 2.5.2.1, $\sup_{z\in[0,B]}\theta'_\varepsilon\left(\frac{z}{B}\right)\frac{z}{B} \leq \sup_{z\in[0,1]}\theta'_\varepsilon(z)z \leq \varepsilon$. Hence for $\varepsilon > 0$ small enough the quantity $|u'(z) - \mu(z)|$ can be bounded uniformly in time by any arbitrary positive constant. Similarily:
  $$u''(z) = -\frac{1}{B}\underbrace{\left(\frac{z}{B}\theta''_\varepsilon\left(\frac{z}{B}\right)\left(\frac{1}{\chi} + \frac{1}{\|\dot{\bar{x}}\|_\infty}\right) + 2\theta'_\varepsilon\left(\frac{z}{B}\right)\left(\frac{1}{\chi} + \frac{1}{\|\dot{\bar{x}}\|_\infty}\right)\right)}_{\text{bounded by } C\left(\|\theta'_\varepsilon\|_\infty + \|\theta''_\varepsilon\|_\infty\right)}.$$
  For $B > 0$ big enough, $|u''(z)|$ can be bounded by any arbitrary positive constant. Therefore, we can pick $\varepsilon > 0$ and $B > 0$ such that $|\gamma(t,z) - g_t(\mu(z))| \leq \eta$. Then by Bound (2.5.4), we have that for $t \geq t_0, z \in (0,B)$:
  $$\gamma(t,z) \geq \eta.$$

As an intermediary conclusion, on each interval $(-\infty, 0], [0,B], [B,+\infty)$, γ is lower bounded by the positive constant $\eta > 0$.

Therefore, if we consider ω the solution to Equation for $t \geq t_0$:

$$\begin{aligned} \partial_t\omega - \partial_{zz}\omega - \partial_z(\beta(t,z)\omega) &= 0 \\ \omega(t_0,\cdot) &= e^{u(\cdot)}\rho(t_0,\cdot). \end{aligned} \tag{2.5.5}$$

Then $\omega(t,z)e^{\eta(t-t_0)}$ is a subsolution of Equation (2.5.2). Of note by the asymptotic properties of e^u, we have that $\omega(t_0,\cdot) \in L^1(\mathbb{R})$. Moreover, Equation (2.5.5) is under conservative form and hence mass is conserved. Without loss of generality, we suppose that $\int_{\mathbb{R}}\omega(t_0,z)dz = 1$ and for every $t \geq t_0$, $\int_{\mathbb{R}}\omega(t,z)dz = 1$. Hence for $t \geq t_0$:

$$\int_{\mathbb{R}} e^{u(z)}\rho(t,z)dz \geq e^{\eta(t-t_0)}$$

2. In the next step, we show that the mass of ρ in $L^1(e^u dz)$ is not exclusively concentrated on $\mathbb{R}_-$. More precisely, we show that $\liminf_{t\to\infty}\int_{t-4}^{t}\int_{\mathbb{R}_+}\omega(s,z)dzds > 0$. We start by considering the quantity:

$$I(t) = \int_{\mathbb{R}_-}\left(e^{-\frac{z}{2\chi}} - 1 + \frac{z}{2\chi}\right)\omega(t,z)dz.$$

Notice that for $z < 0$, we have $\beta(t,z) = \dot{\bar{x}}(t) - \frac{2}{\chi} - \chi = \dot{\bar{x}}(t) - \left(\chi + \frac{1}{\chi}\right) - \frac{1}{\chi} \leq \dot{\bar{x}}(t) - \sigma^* - \frac{1}{\chi} \leq -\delta - \frac{1}{\chi}$ and that this quantity is finite, since ω will be dominated by $e^{\frac{z}{\chi}}$ for $z < 0$ and so

the following series of integration by parts is justified:

$$\begin{aligned}
&\dot{I}(t)\\
=&\int_{\mathbb{R}_-}\left(e^{-\frac{z}{2\chi}}-1+\frac{z}{2\chi}\right)\left(\partial_{zz}\omega+\partial_z\left(\beta\omega\right)\right)dz\\
=&\left[\left(e^{-\frac{z}{2\chi}}-1+\frac{z}{2\chi}\right)\left(\partial_z\omega(t,z)+\beta(t,z)\omega(t,z)\right)\right]_{z=-\infty}^{z=0}\\
+&\frac{1}{2\chi}\int_{\mathbb{R}_-}\left(e^{-\frac{z}{2\chi}}-1\right)\left(\partial_z\omega+\beta\omega\right)dz\\
=&\frac{1}{4\chi^2}\int_{\mathbb{R}_-}e^{-\frac{z}{2\chi}}\omega dz+\frac{1}{2\chi}\int_{\mathbb{R}_-}\left(e^{-\frac{z}{2\chi}}-1\right)\beta\omega dz\\
=&\frac{1}{2\chi}\int_{\mathbb{R}_-}\left(\frac{1}{2\chi}+\beta\right)\left(e^{-\frac{z}{2\chi}}-1\right)\omega dz+\frac{1}{4\chi^2}\int_{\mathbb{R}_-}\omega dz\\
=&\frac{1}{2\chi}\int_{\mathbb{R}_-}\underbrace{\left(\frac{1}{2\chi}+\beta\right)}_{\leq-\delta-\frac{1}{2\chi}}\left(e^{-\frac{z}{2\chi}}-1+\frac{z}{2\chi}\right)\omega dz\\
+&\frac{1}{4\chi^2}\underbrace{\int_{\mathbb{R}_-}\omega dz}_{\leq\int_{\mathbb{R}}\omega dz}\underbrace{-\frac{1}{2\chi}\int_{\mathbb{R}_-}\left(\frac{1}{2\chi}+\beta\right)\frac{z}{2\chi}\omega dz}_{\leq 0}\\
\leq&-\frac{1}{2\chi}\left(\delta+\frac{1}{2\chi}\right)I(t)+\frac{1}{2\chi}.
\end{aligned}$$

Thus by Grönwall's Lemma, we obtain:

$$I(t)\leq I(t_0)e^{-\frac{1}{2\chi}\left(\delta+\frac{1}{2\chi}\right)(t-t_0)}+\frac{1}{4\chi^2}\leq I(t_0)+\frac{1}{4\chi^2}.$$

Furthermore $z\mapsto e^{-\frac{z}{2\chi}}-1+\frac{z}{2\chi}$ is decreasing on $\mathbb{R}_-$, hence by a Markov inequality, we obtain that:

$$\int_{-\infty}^{-h}\omega(t,z)dz\leq\frac{I(t)}{e^{\frac{h}{2\chi}}-1-\frac{h}{2\chi}}\leq\frac{8\chi^2}{h^2}\left(I(t_0)+\frac{1}{4\chi^2}\right),$$

where we haved used that $e^{\frac{h}{2\chi}}-1-\frac{h}{2\chi}\geq\frac{h^2}{8\chi^2}$. Hence, if we choose h sufficiently large then for $t\geq t_0$, we have:

$$\int_{-\infty}^{-h}\omega(t,z)dz\leq\frac{1}{2}.$$

Next, we use a parabolic Harnack inequality, such as it is stated in Theorem 1.1 in [177], to obtain the following Lemma:

Lemma 2.5.2.2. *Let $Q_1:=(-1,0)\times(-h,h)$ and $Q_2:=(-4,-2)\times(-h,h)$, then there exists a constant $C>0$, such that for every $t_2>t_0+4$, we have the following inequality:*

$$\sup_{(t_2,0)+Q_2}\omega\leq C\inf_{(t_2,0)+Q_1}\omega. \tag{2.5.6}$$

We will use Inequality (2.5.6) to establish that for every $t_2>t_1+4$:

$$\int_{t_2-4}^{t_2}\int_{\mathbb{R}_+}\omega(s,z)dzds\geq\frac{1}{1+2C}. \tag{2.5.7}$$

Either, for every $s \in (0,1)$, we have that $\int_{\mathbb{R}} \omega(t_2 - s, z)dz \geq \frac{1}{1+2C}$ and then Inequality (2.5.7) follows. Or, there exists $s \in (0,1)$, such that $\int_{\mathbb{R}} \omega(t_2 - s, z)dz < \frac{1}{1+2C}$. Then:

$$\frac{1}{1+2C} > \int_{\mathbb{R}_+} \omega(t_2 - s, z)dz \geq \int_0^h \omega(t_2 - s, z)dz \geq h \inf_{(t_2,0)+Q_1} \omega.$$

By using Inequality (2.5.6), we then have that for every $s \in (-4, -2)$:

$$\int_{-h}^0 \omega(t - s, z)dz \leq h \sup_{(t_2,0)+Q_2} \omega \leq Ch \inf_{(t_2,0)+Q_1} \omega \leq \frac{C}{1+2C}.$$

But:

$$\int_{\mathbb{R}_+} \omega(t - s, z)dz = 1 - \int_{-\infty}^{-h} \omega(t - s, z)dz - \int_{-h}^0 \omega(t - s, z)dz \geq \frac{1}{2} - \frac{C}{1+2C}.$$

Hence:

$$\int_{t_2-4}^{t_2-2} \int_{\mathbb{R}_+} \omega(s, z)dzds \geq \frac{1}{1+2C}.$$

Thus, we have established Inequality (2.5.7).

3. In the final step we show that the last result contradicts with the condition that $N(t, 0) = N_{\text{th}}$. We multiply Equation (2.2.9b) by e^u and integrate over $\mathbb{R}_+$:

$$\begin{aligned}
\frac{d}{dt}\int_{\mathbb{R}_+} e^u N dz =& \dot{\bar{x}} \int_{\mathbb{R}_+} e^u \partial_z N dz + D \int_{\mathbb{R}_+} e^u \partial_{zz} N - \int_{\mathbb{R}_+} \rho e^u N \\
=& - \dot{\bar{x}} \left(N(t, 0) + \int_{\mathbb{R}_+} N u' e^u dz \right) \\
&+ D \left(\underbrace{-\partial_z N(t, 0)}_{\leq 0} + \frac{N(t, 0)}{\chi} + \int_{\mathbb{R}_+} \left(u'' + u'^2 \right) e^u N dz \right) - \int_{\mathbb{R}_+} \rho e^u N dz \\
\leq& C(1 + \|\dot{\bar{x}}\|_\infty) \|N\|_\infty - N_{\text{th}} \int_{\mathbb{R}_+} \rho e^u dz \\
\leq& C(1 + \|\dot{\bar{x}}\|_\infty) - N_{\text{th}} \int_{\mathbb{R}_+} \omega e^{\eta(t-t_0)} dz,
\end{aligned}$$

where we have used the fact that e^u and its derivatives are integrable, N is bounded above by 1 and below by N_{th} on $\mathbb{R}_+$ and ρe^u is bounded below by $\omega e^{\eta(t-t_0)}$ (the latter being a subsolution). Finally, we integrate between $[t-4, t]$ and obtain:

$$\begin{aligned}
\int_{\mathbb{R}_+} e^u N(t, z)dz \leq& \int_{\mathbb{R}_+} e^u N(t-4, z)dz + 4C(1 + \|\dot{\bar{x}}\|_\infty) - N_{\text{th}} \int_{t-4}^t \int_{\mathbb{R}_+} e^{\eta(s-t_0)} \omega dzds \\
\leq& \int_{\mathbb{R}_+} e^u dz + C(1 + \|\dot{\bar{x}}\|_\infty) - N_{\text{th}} e^{\eta(t-4-t_0)} \int_{t-4}^t \int_{\mathbb{R}_+} \omega dz \\
\leq& C(1 + \|\dot{\bar{x}}\|_\infty) - \frac{N_{\text{th}} e^{\eta(t-4-t_0)}}{1+2C}.
\end{aligned}$$

By letting $t \to +\infty$, we have that $\int_{\mathbb{R}_+} e^u N(t, z)dz < 0$, which is a contradiction. □

2.6 Traveling Waves for a Two-Velocity System with Persistence

In this Section, we exhibit all subsonic ($\sigma < \varepsilon^{-1}$) traveling wave solutions to System (2.1.6). It is known [26] that in hyperbolic models with growth supersonic traveling wave solutions can exist, but for the sake of concision we discard them in this discussion. Furthermore by following the terminology in [26], there exist a parabolic regime $\varepsilon^{-2} > 1$ and a hyperbolic regime $\varepsilon^{-2} < 1$. Of note, the relevant quantities to compare are the tumbling rate, normalized to ε^{-2} here, and the growth rate, normalized to 1 here. Therefore we write the parabolic regime as $\varepsilon^{-2} > 1$ and not as $\varepsilon^{-1} > 1$, which is equivalent in our case. Theorem 2.6.1 notably states that subsonic traveling waves only exist in the parabolic regime, which was already observed in another model [26].

We will procede similarily than in the parabolic case (Section 2.3) and consider that $\partial_z N > 0$. In that case Equation (2.1.6) reduces in the moving frame of reference to:

$$\text{for } z < 0, \quad \begin{cases} (-\sigma + \varepsilon^{-1}) f^{+\prime} = \frac{\varepsilon^{-2}}{2} \left((1 + \varepsilon\chi) f^- - (1 - \varepsilon\chi) f^+ \right) \\ (-\sigma - \varepsilon^{-1}) f^{-\prime} = \frac{\varepsilon^{-2}}{2} \left((1 - \varepsilon\chi) f^+ - (1 + \varepsilon\chi) f^- \right) \end{cases} \tag{2.6.1a}$$

$$\text{for } z > 0, \quad \begin{cases} (-\sigma + \varepsilon^{-1}) f^{+\prime} = \frac{\varepsilon^{-2}+1}{2} f^- - \frac{\varepsilon^{-2}-1}{2} f^+ \\ (-\sigma - \varepsilon^{-1}) f^{-\prime} = \frac{\varepsilon^{-2}+1}{2} f^+ - \frac{\varepsilon^{-2}-1}{2} f^- \end{cases} \tag{2.6.1b}$$

Theorem 2.6.1. *Assume that $\partial_z N > 0$. In the parabolic regime $\varepsilon^{-2} > 1$, there exists a minimal speed $\sigma^* \in (1, \varepsilon^{-1})$, such that for any $\sigma \in [\sigma^*, \varepsilon^{-1})$, there exists a corresponding bounded and nonnegative traveling wave profile $(f^{+,\sigma}, f^{-,\sigma}, N^\sigma)$. In addition, for $\sigma \in [\sigma^*, \varepsilon^{-1})$ fixed, the traveling wave profile $(f^{+,\sigma}(z), f^{-,\sigma}(z), N^\sigma(z))$ is unique. For $\sigma \in [0, \sigma^*)$, there does not exist a traveling wave profile. The expression of σ^* is given by Formula (2.1.7) and depends on the value of χ:*

- *If $\chi \in (1, \varepsilon^{-1})$, then $\sigma^* = \frac{\chi + \frac{1}{\chi}}{1+\varepsilon^2}$. Note that in that case $\sigma^* < \varepsilon^{-1}$.*
- *If $\chi \leq 1$, then $\sigma^* = \sigma_{F/KPP} := \frac{2}{1+\varepsilon^2}$.*

In the hyperbolic regime $\varepsilon^{-2} < 1$, there does not exist any subsonic traveling wave profile, i.e a wave travaling with speed $\sigma < \varepsilon^{-1}$.

Furthermore, in the parabolic regime $\varepsilon^{-2} > 1$, for $\sigma \in [\frac{2}{1+\varepsilon^2}, \varepsilon^{-1})$, define $\mu_\pm(\sigma) := \frac{\sigma(1-\varepsilon^2) \pm \sqrt{\sigma^2(1+\varepsilon^2)^2 - 4}}{2(1-\varepsilon^2\sigma^2)}$. We then have the inequality, for $\sigma > \sigma_{F/KPP}$:

$$0 < \mu_-(\sigma) < \mu_-\left(\sigma_{F/KPP}\right) = \frac{1+\varepsilon^2}{1-\varepsilon^2} = \mu + \left(\sigma_{F/KPP}\right) < \mu + (\sigma)$$

The functions $f^{\pm,\sigma}$ have the following behavior for $z > 0$:

- *for $\sigma \in (\sigma^*, \varepsilon^{-1}), z > 0, f^{\pm,\sigma}(z) = A^\pm e^{-\mu_-(\sigma)z} + B^\pm e^{-\mu_+(\sigma)z}$;*
- *for $\chi > 1, \sigma = \sigma^* = \frac{\chi + \frac{1}{\chi}}{1+\varepsilon^2}, z > 0, f^{\pm,\sigma^*}(z) = B^\pm e^{-\mu_+(\sigma^*)z}$ and $\mu_+(\sigma^*) = \frac{\chi(1+\varepsilon^2)}{1-\varepsilon^2\chi^2}$;*
- *for $\chi < 1, z > 0, \sigma = \sigma_{F/KPP}, f^{\pm,\sigma_{F/KPP}}(z) = (A^\pm z + B^\pm) e^{-\frac{1+\varepsilon^2}{1-\varepsilon^2} z}$;*
- *for $\chi = 1, z > 0, \sigma = \sigma_{F/KPP}, f^{\pm,\sigma_{F/KPP}}(z) = B^\pm e^{-\frac{1+\varepsilon^2}{1-\varepsilon^2} z}$.*

As before note that $\frac{\chi+\frac{1}{\chi}}{1+\varepsilon^2} \geq \frac{2}{1+\varepsilon^2} = \sigma_{\mathrm{F/KPP}}$, with equality if and only if $\chi = 1$.

Proof. The proof relies on similar arguments than the proof in the parabolic case (Section 2.3). Since we are looking for subsonic solution, we suppose througout the proof that $\sigma^2 < \varepsilon^{-2}$.

Set $F(z) = \begin{pmatrix} f^+(z) \\ f^-(z) \end{pmatrix}$, $A_- = \frac{\varepsilon^{-2}}{2} \begin{pmatrix} -\frac{1-\varepsilon\chi}{\varepsilon^{-1}-\sigma} & \frac{1+\varepsilon\chi}{\varepsilon^{-1}-\sigma} \\ -\frac{1-\varepsilon\chi}{\varepsilon^{-1}+\sigma} & \frac{1+\varepsilon\chi}{\varepsilon^{-1}+\sigma} \end{pmatrix}$ and $A_+ = \frac{1}{2} \begin{pmatrix} -\frac{\varepsilon^{-2}-1}{\varepsilon^{-1}-\sigma} & \frac{\varepsilon^{-2}+1}{\varepsilon^{-1}-\sigma} \\ -\frac{\varepsilon^{-2}+1}{\varepsilon^{-1}+\sigma} & \frac{\varepsilon^{-2}-1}{\varepsilon^{-1}+\sigma} \end{pmatrix}$. Then for $z < 0, F'(z) = A_- F(z)$ and for $z > 0, F'(z) = A_+ F(z)$.

As in the parabolic case (Section 2.3), the characteristic polynomial of A_- has two roots 0 and $\frac{\varepsilon^{-2}}{2}\left(\frac{1+\varepsilon\chi}{\varepsilon^{-1}+\sigma} - \frac{1-\varepsilon\chi}{\varepsilon^{-1}-\sigma}\right)$, the later being negative, by an argument similar to the proof of Theorem 2.3.1. Therefore there exist a constant $a \in \mathbb{R}$, such that $F(z) = a \begin{pmatrix} 1+\varepsilon\chi \\ 1-\varepsilon\chi \end{pmatrix}$. The negativity of the second root also shows that there cannot exist a traveling wave profile with velocity $\sigma < \chi$.

The characteristic polynomial of A_+ is (up to a multiplicative constant) $P(X) = (\varepsilon^{-2} - \sigma^2)X^2 + \sigma(\varepsilon^{-2}-1)X + \varepsilon^{-2}$. In the hyperbolic regime $\varepsilon^{-2} < 1$, we have that $P(0) > 0$ and $P'(0) < 0$. But the leading coefficient of P is positive, hence the roots of P have positive real part, which is in contradiction with the fact that we are looking for a bounded solution. Hence in the hyperbolic regime, there do not exist any (subsonic) traveling wave solutions.

For the rest of the proof, we suppose that we are in the parabolic regime $\varepsilon^{-2} > 1$. The discriminant of the characteristic polynomial P is $\sigma^2(\varepsilon^{-2}-1)^2 - 4\varepsilon^{-2}(\varepsilon^{-2}-\sigma^2) = \sigma^2(\varepsilon^{-2}+1)^2 - 4\varepsilon^{-4}$. As in the parabolic case (Section 2.3) $\sigma = \sigma_{F/KPP}$ cancels the discriminant and we yield the condition that $\sigma \geq \sigma_{F/KPP}$, since otherwise we would have complex roots and oscillating functions.

Suppose $\sigma > \sigma_{\mathrm{F/KPP}}$, the roots of the characteristic polynomial are then $-\mu_\pm(\sigma)$. By continuity of F at $z = 0$ and elementary computations, we find that:

$$F(z) = a\frac{\mu_+(\sigma-\chi)-1}{\varepsilon^{-2}(\mu^+-\mu^-)} \begin{pmatrix} \mu_-(\sigma)(\varepsilon^{-1}+\sigma)-1 \\ \mu_-(\sigma)(\varepsilon^{-1}-\sigma)+1 \end{pmatrix} e^{-\mu_-(\sigma)z}$$
$$- a\frac{\mu_-(\sigma-\chi)-1}{\varepsilon^{-2}(\mu^+-\mu^-)} \begin{pmatrix} \mu_+(\sigma)(\varepsilon^{-1}+\sigma)-1 \\ \mu_+(\sigma)(\varepsilon^{-1}-\sigma)+1 \end{pmatrix} e^{-\mu_+(\sigma)z}.$$

First we show that the two components of the vectors are of the same sign. Indeed $(\mu_\pm(\varepsilon^{-1}+\sigma)-1)(\mu_\pm(\varepsilon^{-1}-\sigma)+1) \geq 0 \iff -\mu_\pm \leq -\frac{1}{\sigma}$. Or equivalently $-\frac{1}{\sigma}$ is bigger than the two roots of the characteristic polynomial P. But $P\left(-\frac{1}{\sigma}\right) = \frac{1}{\varepsilon^2\sigma^2} > 0$ and $P'\left(-\frac{1}{\sigma}\right) = \frac{1}{\sigma(\varepsilon^{-2}+1)}\left(\sigma^2 - \frac{2}{1+\varepsilon^2}\right) \geq \frac{1}{\sigma(\varepsilon^{-2}+1)}\left(\sigma^2 - \frac{4\varepsilon^{-4}}{(\varepsilon^{-2}+1)^2}\right) \geq 0$, where we used the fact that $\frac{4\varepsilon^{-4}}{(\varepsilon^{-2}+1)^2} \geq \frac{2}{1+\varepsilon^2}$, which is equivalent to $\varepsilon^{-2} \geq 1$. Hence the components are of the same sign, that is the positive sign, since the second component of each vector is positive.

Therefore we observe that F is positive if and only if $g(\sigma) := \mu_+(\sigma)(\sigma-\chi) - 1 \geq 0$. g is an increasing function, as $g'(\sigma) = \mu_+(\sigma) + \mu'_+(\sigma)(\sigma-\chi) > 0$ (one easily checks that $\mu'_+(\sigma) > 0$). One checks that in the case $\chi \leq 1$, $g(\sigma_{F/KPP}) \geq 0$, which establishes existence of waves for $\sigma > \sigma_{F/KPP}$, and that in the case $\chi > 1$, $g(\sigma^*) = 0$, which establishes the existence of waves for $\sigma \geq \sigma^* = \frac{\chi+\frac{1}{\chi}}{1+\varepsilon^2}$ and the nonexistence of waves for $\sigma \in (\sigma_{F/KPP}, \sigma^*)$.

Suppose $\sigma = \sigma_{\mathrm{F/KPP}}$, then one shows that for $z \geq 0$:

$$F(z) = A \begin{pmatrix} 1+\varepsilon\chi + z\frac{(1+\varepsilon^2)^2(1-\chi)}{(1-\varepsilon^2)(1-\varepsilon)} \\ 1-\varepsilon\chi + z\frac{(1+\varepsilon^2)^2(1-\chi)}{(1-\varepsilon^2)(1+\varepsilon)} \end{pmatrix} e^{-z}. \tag{2.6.2}$$

Hence F is positive if and only if $\chi \leq 1$, which establishes the criterion for existence in the last remaining case.

The decay properties follow immediately and the existence of the profile for N is treated exactly as in the parabolic case. □

Let us make some comments on Theorem 2.6.1 to show how it is linked to Theorem 2.3.1 in the limit $\varepsilon \to 0$. First of all, considering Formula (2.1.7) for σ^* given by Theorem 2.6.1, we observe that in the limit $\varepsilon \to 0$, Formula (2.1.4) given by Theorem 2.3.1 is recovered. Furthermore, the limit of all the values $\mu_\pm(\sigma^*)$ coincide and so do the shapes of the wave. For example, consider Expression (2.6.2) in the limit $\varepsilon \to 0$, we obtain for $z > 0$:

$$F(z) = A \begin{pmatrix} 1 + (1-\chi)z \\ 1 + (1-\chi)z \end{pmatrix} e^{-z}.$$

As a consequence $\rho(t, z) = A(1 + (1-\chi)z)e^{-z}$, which is exactly the form that we obtained in the proof of Theorem 2.3.1.

Acknowledgements

The author is extremely grateful to Vincent Calvez, whose insightful guidance has played a crucial role in the work presented here. The author also thanks Christophe Anjard, Olivier Cochet-Escartin and Jean-Paul Rieu for the fruitful collaboration, which has been the starting point of the present work. Finally, the author wishes to thank Jimmy Garnier, Léo Girardin and François Hamel for valuable explanations and suggestions.
This project has received funding from the European Research Council (ERC) under the European Union's Horizon 2020 research and innovation programme (grant agreement No 865711).

Chapter 3

Mathematical Modeling of Cell Collective Motion triggered by Self-generated Gradients

---

This Chapter has been published as a survey [36] in the edited volume [18]. The work has been written in collaboration with Vincent Calvez and Roxana Sublet, in particular during the internship of the latter under the joint supervision of Vincent Calvez and M. D..

Self-generated gradients have attracted a lot of attention in the recent biological literature. It is considered as a robust strategy for a group of cells to find its way during a long journey. This note is intended to discuss various scenarios for modeling traveling waves of cells that constantly deplete a chemical cue, and so create their own signaling gradient all along the way. We begin with one famous model by Keller and Segel for bacterial chemotaxis. We present the model and the construction of the traveling wave solutions. We also discuss the limitation of this approach, and review some subsequent work addressing stability issues. Next, we review two relevant extensions, which are supported by biological experiments. They both admit traveling wave solutions with an explicit value for the wave speed. We conclude by discussing some open problems and perspectives, and particularly a striking mechanism of speed determinacy occurring at the back of the wave. All the results presented in this note are illustrated by numerical simulations.

3.1 Introduction

It has been now 50 years that Evelyn F. Keller and Lee A. Segel published their article "*Traveling bands of chemotactic bacteria: A theoretical analysis*" [114], which is part of a series of works about the modeling of chemotaxis in bacteria *Esherichia coli* and amoebae *Dictyostelium discoideum* (shortnamed as Dicty in the following) [111–114]. This article described in a simple and elegant way the propagation of chemotactic waves of *E. coli* in a one-dimensional space, echoing the remarkable experiments by Adler performed in a capillary tube [5].

In the present contribution, the seminal ideas of Keller and Segel are discussed from a

modern perspective, after half a century of intense activity at the interface of mathematics and biology. Our goal is not to review exhaustively various directions of research in the modeling of chemotaxis. Our narrow objective consists in setting the focus on the notion of *self-generated gradient* (SGG), which has recently shed a new light on several biological processes, both in bacterial collective motion, and in some aspects of developmental biology [179, 181]. SGG are at the heart of the model in [114], in which cells create their own signaling gradient by consuming some nutrient, while moving collectively from one side of the domain to the other. There, collective motion results from the averaged biases in the individual trajectories, in response to nutrient heterogeneities, a process called chemotaxis. This concept of SGG can be generalized to any situation where the signal depletion and chemotaxis functions overlap within the same cells [162, 180, 181].

SGG in waves of bacteria.

The work of Keller and Segel has initiated a wealth of studies on bacterial chemotaxis. We refer to the comprehensive review of Tindall et al [174], and also the recent studies [49, 78] for new biological questions in this topic. Most of the works discussed in this note consider short time experiments, or experiments at low level of nutrients, neglecting the effect of cell division. This makes a clear distinction between SGG and reaction-diffusion waves, as the celebrated Fisher/Kolmogorov-Petrovsky-Piskunov (F/KPP) equation [12, 72, 115]. For this reason, we shall not comment further about the numerous modeling contributions following the patterns reported by Budrene and Berg [30, 33, 34] (ring expansion followed by formation of bacteria spots with remarkable symmetries). Chemotaxis has been shown to be crucial in the emergence of such patterns. However, the dynamics of ring expansion are mainly driven by growth and diffusion such as described by F/KPP, (but see [49] for a recent study where chemotaxis has been shown to enhance range expansion).

There exist many modeling contributions of chemotaxis in bacteria [100, 174], with a particular emphasis on the derivation of macroscopic models from individual rules through kinetic transport equations, see *e.g.* [7, 17, 45, 46, 71, 141, 143]. In contrast, the number of contributions about mathematical analysis of traveling waves without growth beyond [114] is relatively scarce. We refer to [102], for an (algebraic) extension of [114] with more general chemotaxis functions and uptake rates. We also refer to the series of articles by Z.A. Wang and co-authors, see [188] for a preliminary review and below for further discussion.

SGG in development and cancer.

In developmental biology, cell movement over long distances is mediated by navigating cues, including chemotactic factors [128]. It is commonly postulated that external, pre-patterned gradients, drive cellular migration. One of the key conceptual advantage of SGG is to free the developmental process from the requirement of pre-imposed long-range chemoattractant gradients. In contrast, SGG travel together with the cells, so that they can experience similar environmental conditions (chemical concentration, gradient steepness) all over the journey. This is thought to provide robustness to the developmental system [179, 180].

Recently, SGG have been shown to occur during embryogenesis, and in particular during the initiation of the posterior lateral line in zebrafish [59, 185]. More precisely, migrating cell cohorts (consisting of approximately a hundred of cells) can generate and sustain gradients of chemoattractants across their length. This experimental work is of great importance as being the first proof of the occurrence of SGG *in vivo*.

Self-generated gradients are also under investigation during cancer invasion and metastasis. This includes modeling *in silico* (see [163] and references therein), and experiments with cell cultures *in vitro* [136]. In particular, we highlight the work of [162], in which an astonishing self-guidance strategy in cancer epithelial cell populations was unravelled. In fact, cells were put in microfluidic mazes, without any pre-existing external gradients. Most of them could find their way out of the mazes by generating their own navigating cues. Experimental studies with increasingly complex mazes were also performed with Dicty cells, with quite remarkable outcomes [182].

Plan and purpose of the paper.

In Section 3.2.1 we recall the basic construction of traveling waves in the seminal article [114]. The lack of positivity of the chemical concentration is illustrated by some numerical simulations (Section 3.2.2). The issue of instability is also reviewed. Section 3.2.3 briefly presents some possible variations of the original article from the literature. It is one of the main goal of the present contribution to discuss in details two possible extensions which are biologically relevant (that is, supported by experiments). Section 3.3 contains an overview of past work where another attractant signal is added to prevent cell dispersion during propagation. This results in competing cell fluxes, with stronger advection at the back of the wave than at the edge. Section 3.4 reports on a piece of recent work including signal-dependent phenotypical switch (division/ migration). This results in a wave sustained by cell division restricted to the edge.

All mathematical results proven here are simple, namely involving explicit construction of one-dimensional traveling waves (whose respective stabilities are supported by numerical simulations of the Cauchy problems). The last construction is original, up to our knowledge, see Theorem 3.4.2. It could be of interest for experts in reaction-diffusion equations, as it exhibits a possibly new phenomenon of selection of the minimal speed at the back of the wave.

Acknowledgement.

Part of this work has been achieved during the third author's master internship at Institut Camille Jordan. The two first authors are indebted to Christophe Anjard, Olivier Cochet-Escartin and Jean-Paul Rieu for having drawn their attention to SGG beyond the case of bacterial waves. The authors are very grateful to Eitan Tadmor for his constant encouragement to write this contribution, and to a pair of anonymous reviewers for their feedbacks. reviewers This project has received financial support from the CNRS through the MITI interdisciplinary programs. This project has received funding from the European Research Council (ERC) under the European Union's Horizon 2020 research and innovation program (grant agreement No 865711).

3.2 The Keller-Segel model and variations

3.2.1 The construction of waves by Keller and Segel

In this section, we recall briefly the model and analysis in [114]. The cell density (bacteria) is denoted by $\rho(t,x)$, for time $t>0$, and position along the channel axis $x\in\mathbb{R}$, whereas

the concentration of the signaling molecule is denoted by $S(t,x)$.

$$\begin{cases} \dfrac{\partial \rho}{\partial t} + \dfrac{\partial}{\partial x}\left(-d\dfrac{\partial \rho}{\partial x} + \chi\rho \dfrac{\partial \log S}{\partial x} \right) = 0\,, \\ \dfrac{\partial S}{\partial t} = D\dfrac{\partial^2 S}{\partial x^2} - k\rho\,. \end{cases} \tag{3.2.1}$$

The equation on ρ combines unbiased (diffusive) motion with directed motion in response to the logarithmic signaling gradient (see below for further discussion about this specific choice), with intensity $\chi > 0$.

On the one hand, the equation on ρ is conservative, and the total mass of cells in the channel, which is an invariant of the system, is denoted by M, so that $M = \int_{\mathbb{R}} \rho(0,z)\,dz = \int_{\mathbb{R}} \rho(t,z)\,dz$. On the other hand, the chemical concentration decays globally in time, and the limiting value at ∞ is denoted by $S_{\rm init}$, which can be viewed as the initial, homogeneous, concentration in the channel associated with the Cauchy problem.

Noticeably, the consumption term in the equation on S, namely $-k\rho$, does not involve S itself, precluding any guarantee about the positivity of S in the long time. Nevertheless, the existence of positive traveling wave solutions $\rho(x-ct)$, $S(x-ct)$ was established in [114] by means of explicit computations, in the absence of signal diffusion $D = 0$ (for mathematical purposes), and with the condition $\chi > d$. The wave under interest has the following structure: $\rho \in L^1_+(\mathbb{R})$, with $\lim_{z\to\pm\infty} \rho(z) = 0$, and $S \in L^\infty_+(\mathbb{R})$ is increasing with $\lim_{z\to-\infty} S(z) = 0$, and $\lim_{z\to+\infty} S(z) = S_{\rm init}$, the reference value of the chemical concentration.

Theorem 3.2.1 (Keller and Segel [114]). *Assume $D = 0$, and $\chi > d$. Then, there exist a speed $c > 0$ (depending on M, k and $S_{\rm init}$, but not on χ nor on d), and a stationary solution of (3.2.1) in the moving frame $(\rho(x-ct), S(x-ct))$, such that ρ is positive and integrable, $\int_{\mathbb{R}} \rho(z)\,dz = M$, and S is increasing between the following limiting values*

$$\begin{cases} \lim_{z\to-\infty} S(z) = 0\,, \\ \lim_{z\to+\infty} S(z) = S_{\rm init}\,. \end{cases}$$

Before we recall briefly the construction of the wave solution, let us comment on the value of the wave speed c, that can be directly obtained from the second equation in (3.2.4), whatever the value of $D \geq 0$ is. Indeed, the equation in the moving frame reads

$$-c\frac{dS}{dz} = D\frac{d^2S}{dz^2} - k\rho\,.$$

By integrating this equation over the line, and using the extremal conditions at $\pm\infty$ (that can be verified *a posteriori*), we find

$$cS_{\rm init} = k\int_{\mathbb{R}} \rho(z)\,dz = kM\,. \tag{3.2.2}$$

Strikingly, the wave speed depends only on the dynamics of establishment of the gradient. In particular, it does not depend on the intensity of the chemotactic response χ. This is in contrast with several conclusions to be drawn from alternative models in the sequel (see Sections 3.3 and 3.4).

Proof. The speed c is given *a priori* by the relationship (3.2.2).

The first step in the construction of traveling wave solutions is the zero-flux condition in the moving frame $z = x - ct$, namely

$$-c\rho - d\frac{d\rho}{dz} + \chi\rho\frac{d\log S}{dz} = 0 \quad \Leftrightarrow \quad \frac{d\log\rho}{dz} = -\frac{c}{d} + \frac{\chi}{d}\frac{d\log S}{dz}$$
$$\Leftrightarrow \quad \rho(z) = a\exp\left(-\frac{c}{d}z + \frac{\chi}{d}\log S\right) ,$$

where a is a (positive) constant of integration. The second step consists in solving the following ODE (assuming $D = 0$)

$$c\frac{dS}{dz} = ka\exp\left(-\frac{c}{d}z + \frac{\chi}{d}\log S\right) \quad \Leftrightarrow \quad \left(1 - \frac{\chi}{d}\right)^{-1}\left(S_{\text{init}}^{1-\frac{\chi}{d}} - S(z)^{1-\frac{\chi}{d}}\right) = \frac{kad}{c^2}\exp\left(-\frac{c}{d}z\right) .$$

By re-arranging the terms, we obtain

$$\left(\frac{S(z)}{S_{\text{init}}}\right)^{1-\frac{\chi}{d}} = 1 + \left(\frac{\chi}{d} - 1\right)\left(\frac{kad}{c^2}S_{\text{init}}^{\frac{\chi}{d}-1}\right)\exp\left(-\frac{c}{d}z\right) .$$

Suppose that $\chi < d$, then the right-hand-side goes to $-\infty$ as $z \to -\infty$ which is a contradiction. Hence, the calculations make sense only if $\chi > d$. By translational invariance, the constant a can be chosen so as to cancel the prefactor in the right-hand-side (provided $\chi > d$), yielding the simple expression

$$\frac{S(z)}{S_{\text{init}}} = \left(1 + \exp\left(-\frac{c}{d}z\right)\right)^{\frac{d}{d-\chi}} . \tag{3.2.3}$$

The corresponding density profile is:

$$\rho(z) = a'\exp\left(-\frac{c}{d}z\right)\left(1 + \exp\left(-\frac{c}{d}z\right)\right)^{\frac{\chi}{d-\chi}} , \tag{3.2.4}$$

for some constant a', that can be determined explicitly through the conservation of mass. □

3.2.2 Positivity and stability issues

Despite its elegance, the previous construction suffers from two drawbacks. First of all, the positivity of the signal concentration S is not guaranteed in the Cauchy problem. Actually, numerical solutions soon break down because of this positivity issue. This occurs starting from a generic initial data (Figure 3.1a), and even from the traveling wave solution $(\rho(z), S(z))$ given by the expressions (3.2.3)–(3.2.4), after accumulation of numerical errors (Figure 3.1b). Nevertheless, the positivity can be manually rescued by setting $S_{n+1} = \max(S_n, \epsilon)$ for some arbitrary threshold $\epsilon \ll 1$, as suggested in [101]. In that case, the wave seems to propagate in a stable way in the long term, see Figure 3.1c.

Second, and somewhat related, is the problem of stability of the wave constructed in Section 3.2.1. Linear stability was addressed first in [153], where it was proven that the spectral problem admits no *real* positive eigenvalue. However, the linearized problem is not self-adjoint, so that this preliminary result is largely incomplete from the perspective of stability. Few years later, it was proven in [138] that the (essential) spectrum of the linear operator intersects the right half-plane, meaning that the wave is linearly unstable. The authors proved a refined instability result, when perturbations are restricted to a class of exponentially decreasing functions. Noticeably, their results cover both $D = 0$ and $D > 0$.

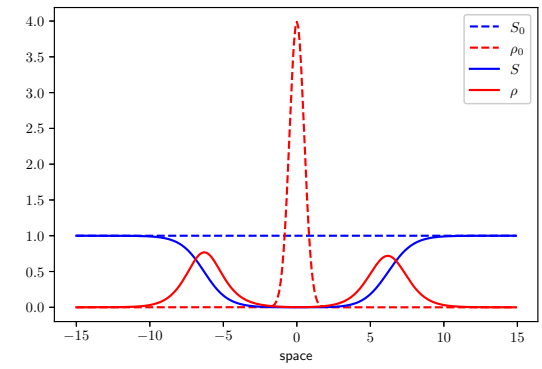

(a)

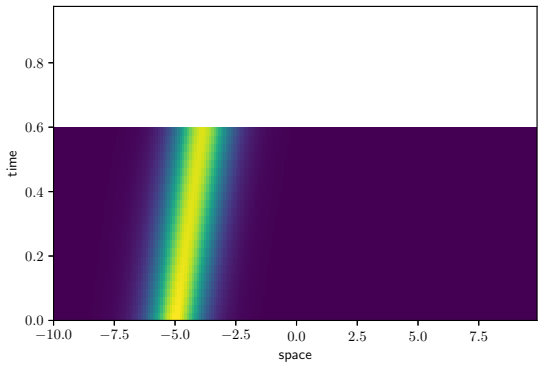

(b)

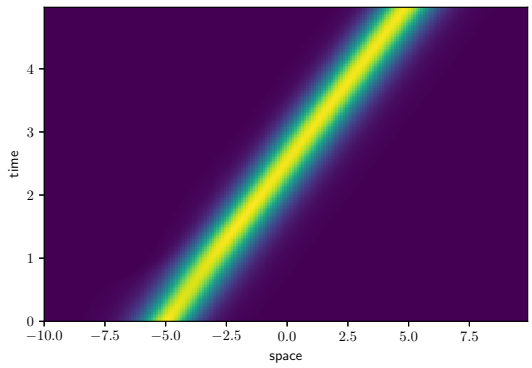

(c)

Figure 3.1: Positivity and stability issues in the numerical simulations of (3.2.1). (a) Starting from a generic initial data, the numerical scheme quickly breaks down because the signal becomes negative at some point. The initial condition is shown in dashed line, and the final state in plain line (last time before numerical breakdown). (b) Aligning the initial data on the exact density and signal profiles $(\rho(z), S(z))$ (3.2.3)–(3.2.4), yields the same conclusion. The cell density is shown in space/time. The numerical breakdown occurs at approximately $t = 0.6$. (c) The propagation of the wave can be rescued by setting manually $S_{n+1} = \max(S_n, 1E - 12)$ after each time step, as in [101]. For all the figures, the parameters are $(d = 1, \chi = 2, D = 0, k = 1)$.

This analysis has been largely extended in [50, 51] where it was proven that the wave is either transiently (convectively) unstable, that is, the spectrum is shifted in the open left half plane in a two-sided exponentially weighted function space [159], when $\chi > d$ is not too large, but it is absolutely unstable when χ is above some threshold, that is, $\frac{\chi}{d} > \beta^0_{\rm crit}(D)$, where, *e.g.* $\beta^0_{\rm crit}(0)$ is the unique real root above one of an explicit $10^{\rm th}$ order polynomial, see [50, Theorem 2.1].

Recently, it has been established the existence and nonlinear stability of stationary solutions for the problem (3.2.1) set on a half-line $\{x > 0\}$, with respectively Neumann boundary condition for ρ, and positive Dirichlet boundary condition for S at the origin [42]. The motivation comes from the study of spike solutions stabilized by a sustained amount of chemical concentration at the boundary. The stability result in [42] imposes quite stringent conditions on the decay of the initial data at $+\infty$. Nevertheless, local stability of the stationary spike does not preclude loss of positivity in the numerics when initiating the Cauchy problem with initial conditions far from equilibrium, see Figure 3.2.

Remark 3.2.2. *Many of the references mentioned above also discuss and analyze the case of a degenerate consumption rate $\frac{\partial S}{\partial t} = D\frac{\partial^2 S}{\partial x^2} - k\rho S^m$ $(m < 1)$, without changing much of the global picture.*

The case $m = 1$ differs significantly, however. It can be viewed directly on the case $D = 0$ that the logarithmic gradient of the putative wave in the moving frame, that is, $\frac{d\log S}{dz}$ cannot have a positive limit as $z \to -\infty$, simply because it satisfies the relationship $-c\frac{d\log S}{dz} = -k\rho$, the latter being integrable. Consequently, advection cannot balance diffusion at $-\infty$, preventing the existence of a traveling wave. The same conclusion holds in the case $D > 0$, for which $u = \frac{d\log S}{dz}$ is a homoclinic orbit of the following first-order equation

$$\frac{du}{dz} = -\frac{c}{D}u - u^2 + \frac{k}{D}\rho\,,$$

that leaves the origin $u = 0$ at $z = -\infty$, and gets back to the origin $u = 0$ at $z = +\infty$, see [35, Proposition 6.3].

3.2.3 Variations on the Keller-Segel model

As mentioned above, the seminal work [114] gave rise to a wealth of modeling and analysis of traveling bands of bacteria. Many extensions were proposed soon after Keller and Segel's original paper, with various sensitivity functions (other than the logarithmic sensitivity), and various consumption rates. The models have the following general form,

$$\begin{cases} \dfrac{\partial \rho}{\partial t} + \dfrac{\partial}{\partial x}\left(-d\dfrac{\partial \rho}{\partial x} + \rho\boldsymbol{\chi}\left(S, \dfrac{\partial S}{\partial x}\right)\right) = 0\,, \\ \dfrac{\partial S}{\partial t} = D\dfrac{\partial^2 S}{\partial x^2} - \mathbf{k}(S,\rho)\,. \end{cases} \tag{3.2.5}$$

where the chemotactic sensitivity $\boldsymbol{\chi}$ can be a function of both the signal concentration and its gradient (as well as the diffusion coefficient d – dependency not reported here for the sake of clarity). These variations were nicely reviewed by Tindall et al [174], and we are not going to comment them, but the contribution of Rivero et al [151]. The latter follows the approach of Stroock [171], and Alt [7]. These approaches make the connection between the individual response of bacteria to space-time environmental heterogeneities, and the macroscopic flux, hence making sense of the aforementioned averaging, by means of individual biases in the trajectories (see *e.g.* [17, 45, 46, 71, 141, 143], and more specifically [65, 161, 166, 190]

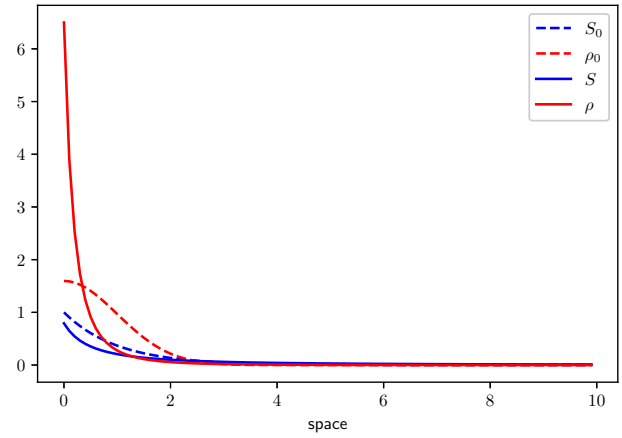

(a)

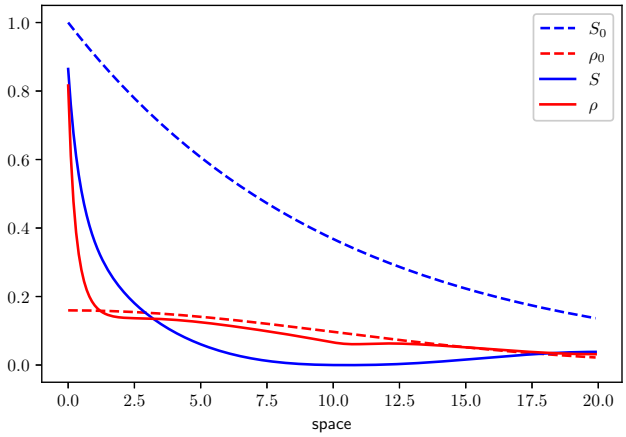

(b)

Figure 3.2: Numerical solutions of (3.2.1) with respectively Neumann boundary condition for ρ, and positive Dirichlet boundary condition for S at the origin. (a) Local stability, as established in [42] is illustrated numerically, for an initial condition chosen near the stationary state, and a relatively large diffusion of the chemical ($d = 1, \chi = 2, D = 1, k = 1$). (b) Nonetheless, the numerical solution may become nonpositive when the initial condition is far from the stationary state, and diffusion of the chemical is not too large ($d = 1, \chi = 2, D = 0.25, k = 1$). For each figure, the initial condition is shown in dashed line, and the final state in plain line (last time before numerical breakdown in (b)).

for bacterial populations). Interestingly, Rivero et al postulate a chemotactic advection speed $\boldsymbol{\chi}$ which is non-linear with respect to the chemical gradient at the macroscopic scale, namely

$$\boldsymbol{\chi}\left(S, \frac{\partial S}{\partial x}\right) = \chi \tanh\left(f(S)\frac{\partial S}{\partial x}\right), \tag{3.2.6}$$

where f is a decreasing function containing the details of signal integration by a single cell.

Up to our knowledge, none of the models in the long list of existing variations could exhibit traveling waves while preserving positivity of S and keeping the total mass $\int_{\mathbb{R}} \rho$ constant (that is, ignoring growth). The minimal requirement for ensuring positivity would essentially be that the uptake function $\mathbf{k}(S, \rho)$ is dominated by S at small concentration, typically: $\limsup_{S\to 0} \frac{\mathbf{k}(S,\rho)}{S} < \infty$. However, this intuitively leads to a shallow (logarithmic) gradient at the back of the wave, unable to guarantee the effective migration of cells left behind, see Remark 3.2.2. Cell leakage has long been identified in the biological literature, but not considered as a major issue, see for instance a discussion in [78], and also the addition of a linear growth term in [160] so that the loss of cells at the back is qualitatively compensated by cell division (for a realistic value of the division rate).

It is interesting to discuss the natural choice $-\mathbf{k}(S, \rho) = -kS\rho$ (combined with logarithmic sensivity), which has been widely studied using tools from hyperbolic equations (after performing the Hopf-Cole transformation) by Z.A. Wang and co-authors, see the review [188], and further stability results in [108, 119]. The issue of shallow gradients is overcome by the boundary conditions at infinity, ρ being uniformly positive at least on one side. Clearly, the traveling wave solutions are not integrable. This hints to the conflict of conservation of mass and chemical positivity which seem not concilable.

This leakage effect is a major mathematical issue, because most of the analytical studies build upon the existence of a wave speed and a wave profile which is stationary in the moving frame.

3.2.4 Beyond the Keller-Segel model: two scenarios for SGG

In the next two sections, we discuss two relevant modeling extensions, motivated by biological experiments, for which traveling waves exist and are expected to be stable. In the first scenario, cell leakage is circumvented by enhanced advection at the back of the wave, with an asymptotic constant value of the transport speed at $-\infty$. In the second scenario, cell leakage occurs, but it is naturally compensated by growth at the edge of the propagating front.

For each scenario, we discuss briefly the biological motivations. Then we present the explicit construction of the traveling wave solutions, together with the formula for the wave speed. When possible, we discuss the connections with some other works in the literature.

3.3 Scenario 1: strongest advection at the back

In this section, we present some study performed a decade ago, revisiting original Adler's experiment, see Figure 3.3. Inspired by massive tracking analysis, Saragosti et al [161] proposed a simple model for the propagation of chemotactic waves of bacteria, including two signals (see also [191] for an analogous approach developed independently at the same

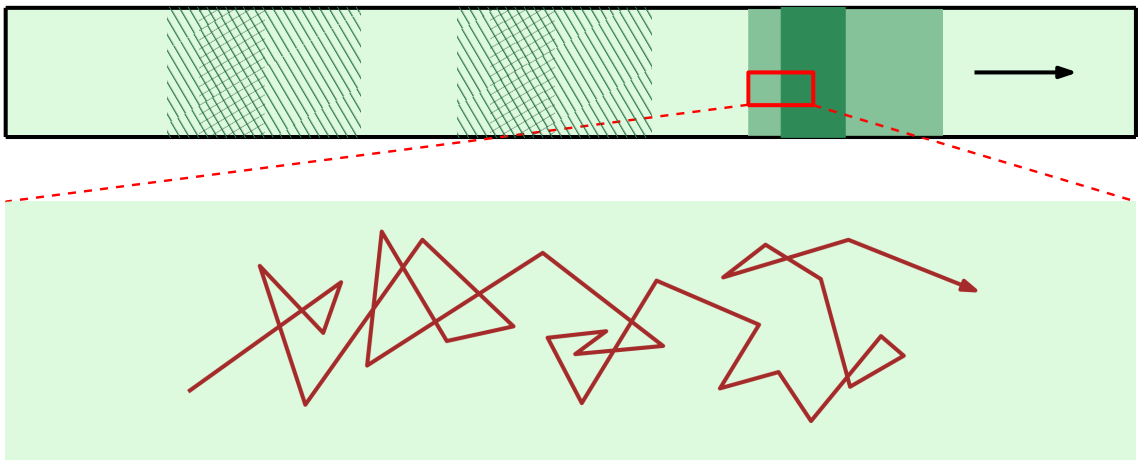

Figure 3.3: Cartoon of the experiments performed in [161] and [160]. A band of bacteria is traveling from left to right in a microfluidic channel. Videomicroscopy allows tracking individual trajectories inside the wave, revealing heterogeneous behaviors: biases are stronger at the back of the wave than at the edge.

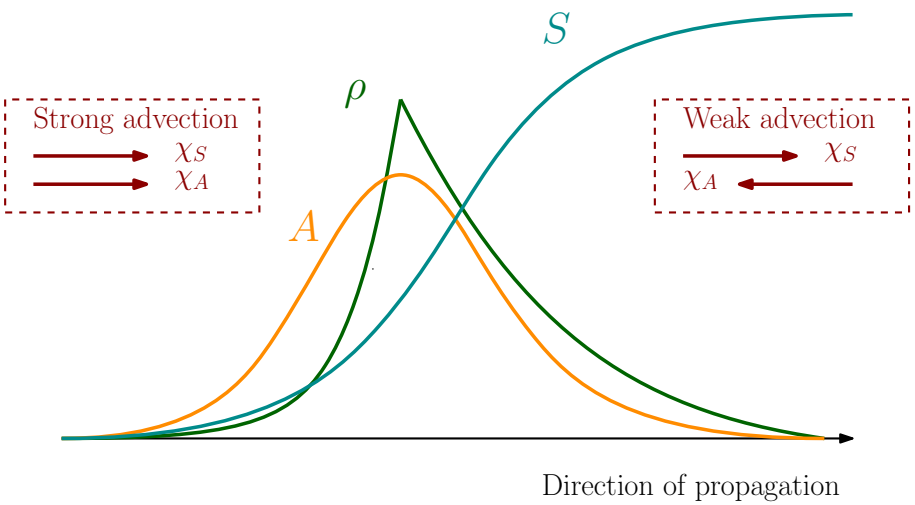

Figure 3.4: Sketch of the chemical environment viewed by the cell density in model (3.3.1). It is characterized by stronger advection at the back (the two signals have the same orientation), than at the edge (the two gradients have opposite orientations). When chemotactic speeds coincide ($\chi_S = \chi_A$), then we simply have diffusion on the right side of the peak.

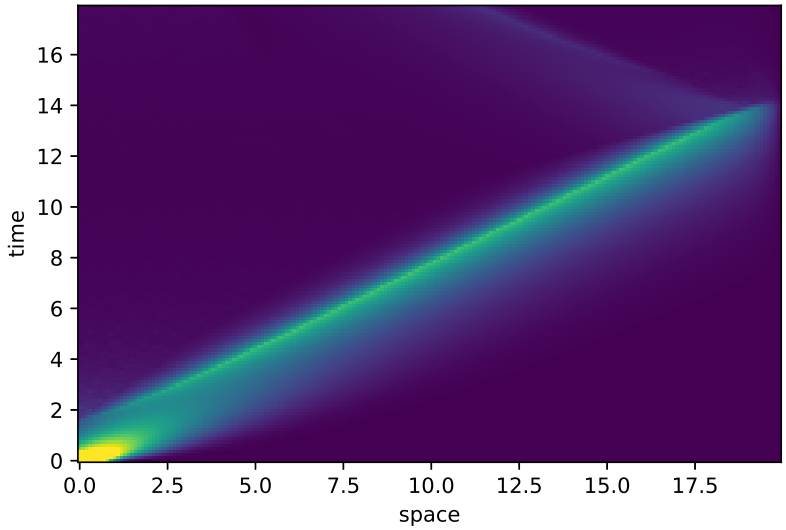

Figure 3.5: Numerical simulation of model (3.3.1) for a half-gaussian initial density of bacteria.

time). The macroscopic model is the following:

$$\begin{cases} \dfrac{\partial \rho}{\partial t} + \dfrac{\partial}{\partial x}\left(-d\dfrac{\partial \rho}{\partial x} + \rho\left(\chi_S \text{sign}\left(\dfrac{\partial S}{\partial x}\right) + \chi_A \text{sign}\left(\dfrac{\partial A}{\partial x}\right)\right)\right) = 0\,, \\ \dfrac{\partial S}{\partial t} = D_S \dfrac{\partial^2 S}{\partial x^2} - \mathbf{k}(S,\rho)\,, \\ \dfrac{\partial A}{\partial t} = D_A \dfrac{\partial^2 A}{\partial x^2} + \beta\rho - \alpha A\,. \end{cases} \tag{3.3.1}$$

As compared to (3.2.5), it is supplemented with a second chemical signal, A, which plays the role of a communication signal released by the cell population (hence, the source term $+\beta\rho$), and naturally degraded at a constant rate $\alpha > 0$. Indeed, bacteria are known to secrete amino-acids, which play the role of a chemo-attractant as part of a positive feedback loop [21, 134]

Moreover, bacteria are assumed to respond to the signal in a binary way at the macroscopic scale: the advection speed associated with each signal (S, A) can take only two values, respectively $\pm\chi_S$, $\pm\chi_A$, depending on the direction of the gradients. Then, the total advection speed is simply the sum of the two components. This was derived in [161] from a kinetic model at the mesoscopic scale, assuming a strong amplification during signal integration, see also [35] for a discussion. This can be viewed as an extremal choice of the advection speed proposed by Rivero et al [151], in the regime $f \to +\infty$ (3.2.6). The biophysical knowledge about the details of signal integration in bacteria *E. coli* have increased in the meantime [**si_pathway-based_2012**, 107, 110, 178]. Actually, the logarithmic sensing is a good approximation in a fairly large range of signal concentrations. However, we retain this simple, binary, choice for theoretical purposes.

As for the Keller-Segel model, traveling waves for (3.3.1) have the great advantage of being analytically solvable, essentially because the problem reduces to an equation with piecewise constant coefficients. Introduce again the variable $z = x - ct$ in the moving frame

at (unknown) speed c. Then, we have the following result:

Theorem 3.3.1 (Saragosti et al [161]). *There exist a speed $c > 0$, and a positive limit value $S_- < S_{\rm init}$, such that the system (3.3.1) admits a stationary solution in the moving frame $(\rho(x-ct), S(x-ct), A(x-ct))$, such that ρ is positive and integrable, $\int_{\mathbb{R}} \rho(z)\,dz = M$, A decays to zero on both sides, and S is increasing between the following limiting values*

$$\begin{cases} \lim_{z\to-\infty} S(z) = S_-\,, \\ \lim_{z\to+\infty} S(z) = S_{\rm init}\,. \end{cases}$$

Moreover, the speed $c > 0$ is determined by the following implicit relation,

$$\chi_S - c = \chi_A \frac{c}{\sqrt{c^2 + 4\alpha D_A}}\,. \tag{3.3.2}$$

Proof. Contrary to the proof of Theorem 3.2.1, the wave speed c cannot be computed by a direct argument.

As a preliminary step, we should prescribe the environmental conditions, as they are expected heuristically to be seen by the bacteria, see Figure 3.4. On the one hand, we seek an increasing profile S, hence sign $\left(\frac{dS}{dz}\right) = +1$, and the equation on the density profile ρ is decoupled from the dynamics of S. On the other hand, we assume that the communication signal A reaches a unique maximum, that can be set at $z = 0$ by translational invariance. The validation of this ansatz, *a posteriori*, will set the equation for c (3.3.2).

The equation for ρ has now piecewise constant coefficients in the moving frame,

$$-c\frac{d\rho}{dz} + \frac{d}{dz}\left(-d\frac{d\rho}{dz} + \rho\left(\chi_S + \chi_A \text{sign}\,(-z)\right)\right) = 0\,.$$

Hence, ρ is a combination of two exponential functions,

$$\rho(z) = \begin{cases} \exp\left(\lambda_- z\right) & \text{for } z < 0, \quad \lambda_- = \dfrac{-c + \chi_S + \chi_A}{d} \quad \text{(signals are aligned)}, \\ \exp\left(-\lambda_+ z\right) & \text{for } z > 0, \quad \lambda_+ = \dfrac{c - \chi_S + \chi_A}{d} \quad \text{(signals are competing)}. \end{cases}$$

Next, the attractant concentration A can be computed explicitly, by convolving the source term $\beta\rho$ with the fundamental solution of the elliptic operator $-c\frac{d}{dz} - D_A\frac{d^2}{dz^2} + \alpha$, denoted by $\mathcal{A}$, that is, $A = \beta\mathcal{A} * \rho$. Coincidentally, $\mathcal{A}$ shares the same structure as ρ, namely $\mathcal{A}(z) = a_0 \exp(\mu_- z)$ for $z < 0$ and $\mathcal{A}(z) = a_0 \exp(-\mu_+ z)$ for $z > 0$, with $\mu_\pm = \frac{1}{2D_A}\left(\pm c + \sqrt{c^2 + 4\alpha D_A}\right)$, and a_0 is a normalizing factor.

It remains to check the preliminary ansatz, that is, A changes monotonicity at $z = 0$. A straightforward computation yields

$$\frac{dA}{dz}(0) = \beta a_0 \left(-\frac{1}{1 + \lambda_-/\mu_+} + \frac{1}{1 + \lambda_+/\mu_-}\right)\,.$$

Therefore, the construction is complete, provided $\lambda_-\mu_- = \lambda_+\mu_+$, which is equivalent to (3.3.2). □

To partially conclude, let us highlight the fact that cohesion in the wave is guaranteed by the local aggregation signal A. To put things the other way around, in the absence of the driving signal S, the cells can aggregate thanks to the secretion of A, and the density reaches a stationary state (standing wave). In turn, this cohesive state can travel (with

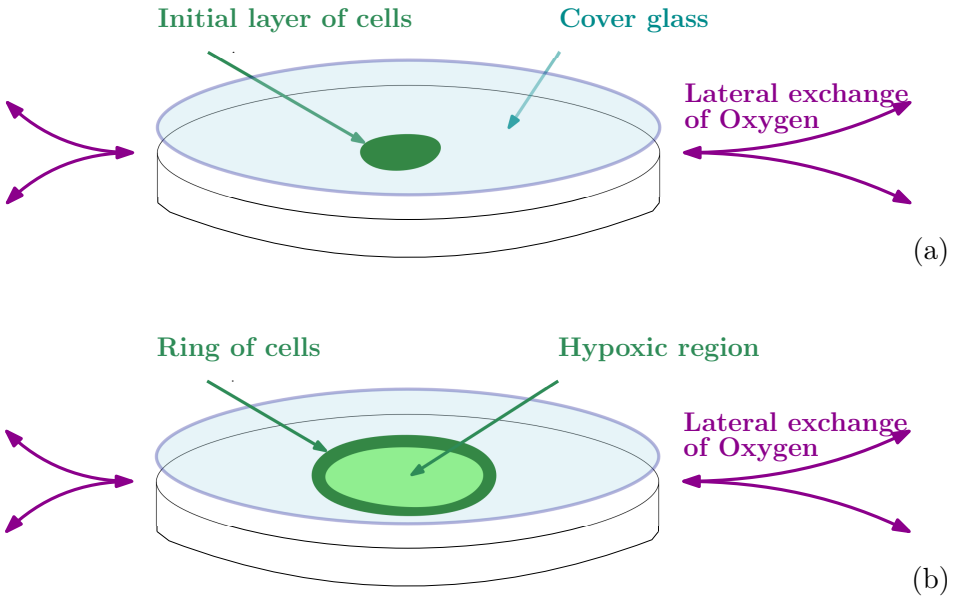

Figure 3.6: Schematic view of the experimental set-up in [48]. (a) An initial layer of Dicty cells is deposited at the center of the plate, and covered with a large glass coverslip (after [56]). This vertical confining reduces drastically the inflow of oxygen within the plate, by restricting it to lateral exchanges. (b) Soon after the beginning of the experiment, a ring of cells emerges, which is traveling over several days at constant speed with a well-preserved shape. The moving ring consumes almost all the available oxygen, so that the center of the colony is at very low concentration, below 1%.

some deformation) in the presence of the (self-generated) driving signal S. To make the link with SGG in developmental biology [59], let us point to the modeling study [170] which is devoted to the migration of cell collectives in the lateral line during development of the zebrafish. There, it is assumed that the rod of cells maintains its shape *per se* with a constant length which is a parameter of the model, see also [41] for biological evidence of cell attraction during collective motion.

3.4 Scenario 2: cell leakage compensated by growth

In this section, we present a recent model of SGG, including localized (signal-dependent) growth [48]. This work was motivated by aeroactic waves of Dicty observed in vertically confined assays, in which oxygen is consumed by the cells and is soon limited at the center of the colony, see Figure 3.6. We refer to [48] for the experimental details. The model introduced in [48] was referred to as a "go-or-grow" model, a term coined in a previous work by Hatzikirou et al [98] in the context of modeling cell invasion in brain tumors. There, the basic hypothesis was that cells could switch between two states, or phenotypes: a migrating state 'go' (with enhanced random diffusion), and a proliferating state 'grow' (with enhanced rate of division), following previous works in the same context (see *e.g.* [68]). In [98] it was assumed that hypoxia (lack of oxygen) triggers the switch in the long term dynamics of the system, by selection of the migrating phenotype, but in a global manner (oxygen supply was accounted for via the constant carrying capacity, as one parameter of the cellular automaton). Later contributions considered PDE models with density-dependent switch (see [168], as opposed to [68] where the switching rate is

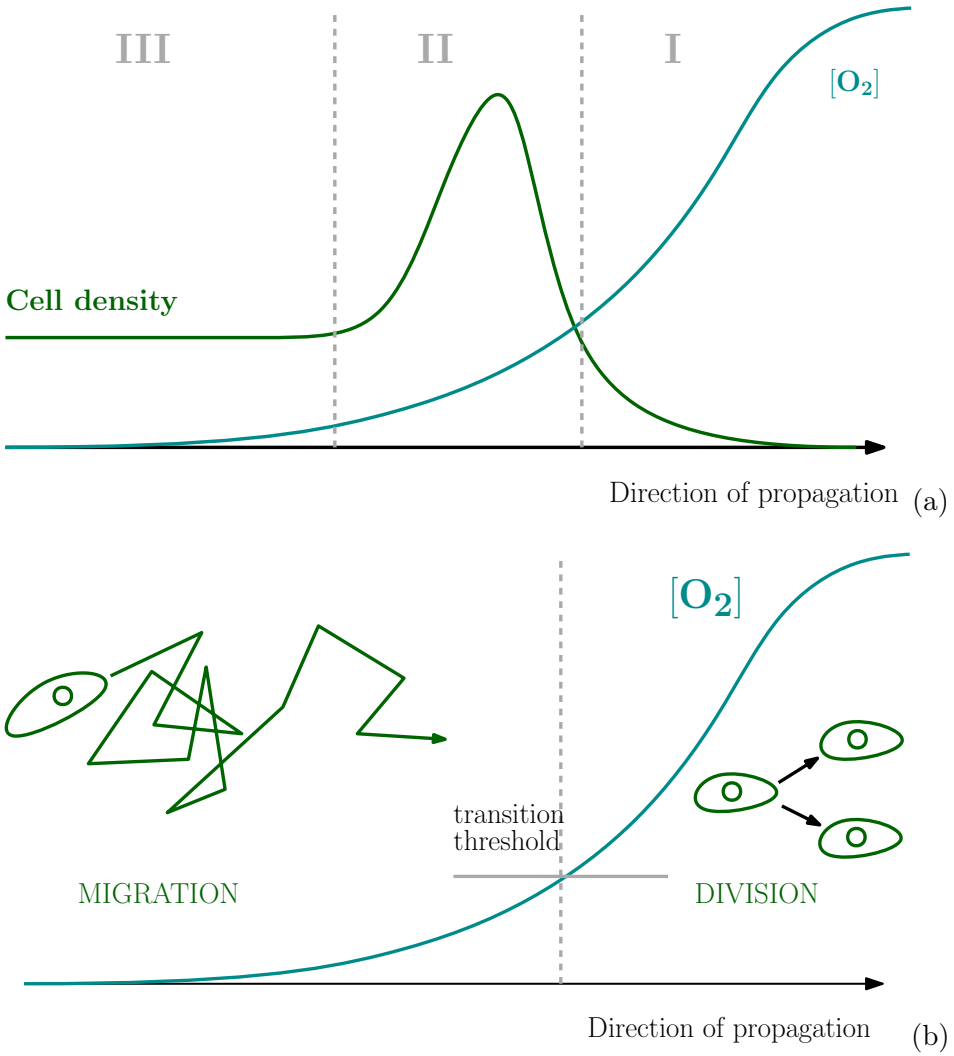

Figure 3.7: Graphical description of the 'go-or-grow' model (3.4.1). (a) Individual cell tracking in [48] shows different cell behaviours depending on the relative position with respect to the tip of the ring: (I) ahead of the moving ring, cells exhibit unbiased motion, together with division events; (II) inside the ring, cells exhibit clear directional motion (which indeed results in the formation and maintenance of the ring); (III) the trail of cells which are left behind exhibit unbiased motion, again, with more persistent trajectories (but this last observation is neglected in the model, because it was shown to have limited effect). (b) We hypothesize a single transition threshold S_0 such that cells can divide above the threshold, while they move preferentially up the gradient below the threshold, when oxygen is limited. The unbiased component of cell motion (diffusion) is common to both sides of the threshold.

not modulated, and also the experimental design of density-dependent motility in bacteria [123]).

In [48], the go-or-grow hypothesis was revisited, by studying an expanding ring of Dicty cells, with limited supply of oxygen. Figure 3.7a shows the cell density profile, as it is observed in experiments. Figure 3.7b summarizes the minimal assumption of an oxygen-dependent switch, as proposed in [48]. It was hypothesized that the transition between the proliferating state and the migrating state is modulated by the level of oxygen, with a sudden change of phenotype at some threshold S_0. Above this threshold, when oxygen is available in sufficient quantity, cells exhibit slow random (diffusive) motion and divide at some constant rate. Below this threshold, when oxygen is limited, cells stop dividing and move preferentially up the oxygen gradient. The latter hypothesis (directional motion) is different from the aforementioned go-or-grow models [68, 98, 168]. It is consistent with the observations of individual tracking within the cell population in the bulk of the wave in [48].

The following model recapitulates these assumptions,

$$\begin{cases} \dfrac{\partial \rho}{\partial t} + \dfrac{\partial}{\partial x}\left(-d\dfrac{\partial \rho}{\partial x} + \rho \boldsymbol{\chi}\left(S, \dfrac{\partial S}{\partial x}\right)\right) = \mathbf{r}(S)\rho\,, \\ \dfrac{\partial S}{\partial t} = D\dfrac{\partial^2 S}{\partial x^2} - \mathbf{k}(S,\rho)\,. \end{cases} \tag{3.4.1}$$

with the specific choice

$$\boldsymbol{\chi}\left(S, \frac{\partial S}{\partial x}\right) = \chi \text{sign}\left(\frac{\partial S}{\partial x}\right)\mathbf{1}_{S<S_0}\,, \quad \mathbf{r}(S) = r\mathbf{1}_{S>S_0}\,. \tag{3.4.2}$$

This can be viewed as another variation of (3.2.5) including growth. It can also be viewed as an extension of the celebrated F/KPP equation, with a signal-dependent growth saturation, and including advection (we refer to [40, 155, 192] and references therein for more classical synthesis of the F/KPP equation and the Keller-Segel model of cellular aggregation). Interestingly, an analogous model was proposed in [77], following a general motivation, and beginning with the statement that proliferation is necessary to sustain wave propagation. As compared with (3.4.1)–(3.4.2), in the latter work, the reproduction rate $\mathbf{r}$ is signal-dependent with a linear dependency, and there is no threshold on the chemosensitivity $\boldsymbol{\chi}$ which is simply a linear function of the gradient $\frac{\partial S}{\partial x}$. As a consequence, the wave speed cannot be calculated analytically, in constrast with (3.4.1)–(3.4.2) (see Theorem 3.4.1 below).

Before we show the construction of traveling wave solutions for (3.4.1)–(3.4.2), let us comment on the reason why such solutions can exist. The expected density profile exhibits a plateau of cells left behind the wave, see Figure 3.7a. In the vertical confining assay experiment with Dicty, this corresponds to cells that are still highly motile, but have lost the propension to move directionally. They cannot keep pace with the self-generated oxygen gradient. The increasing amount of cells which are left behind is compensated by the growth at the edge of the pulse. This localized growth term (above the oxygen threshold) creates a flux term (negative flux in the moving coordinate) which is key to the mathematical construction of the wave.

We can be more precise about the negative flux issued from cell division by looking at the traveling wave equation (3.4.1)–(3.4.2) in the moving coordinate $z = x - ct$.

$$-c\frac{d\rho}{dz} + \frac{d}{dz}\left(-d\frac{d\rho}{dz} + \rho\boldsymbol{\chi}\left(S, \frac{dS}{dz}\right)\right) = \mathbf{r}(S)\rho\,. \tag{3.4.3}$$

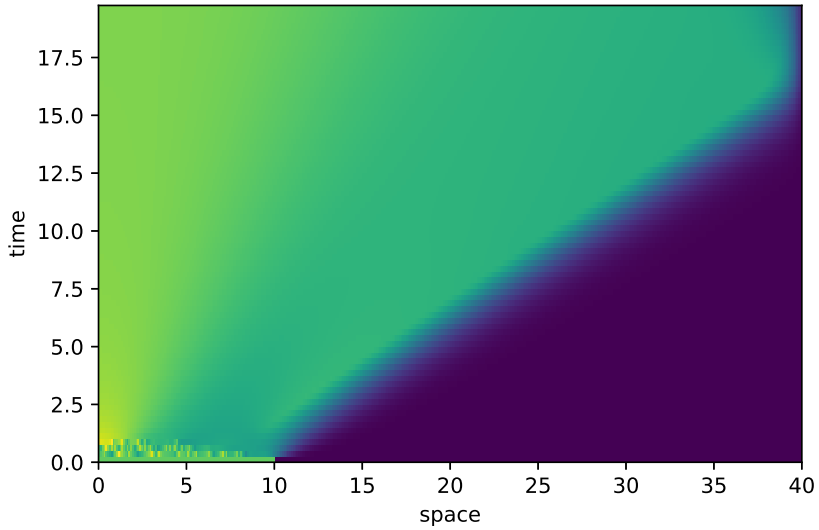

Figure 3.8: Numerical simulation of model (3.3.1) for an initial plateau of cells restricted to the interval $\{x < 10\}$.

Below the oxygen threshold, $S < S_0$, the right-hand-side vanishes, and we are left with a constant flux,

$$-c\rho - d\frac{d\rho}{dz} + \rho\boldsymbol{\chi}\left(S, \frac{dS}{dz}\right) = -J\,. \tag{3.4.4}$$

By integrating (3.4.3) on $\{S > S_0\}$, and using the continuity of the flux at the interface $\{S = S_0\}$, we find

$$J = r\int_{\{S>S_0\}} \rho(z)\,dz\,. \tag{3.4.5}$$

Note that the continuity of the flux is a pre-requisite for the well-posedness of (3.4.1)–(3.4.2), see [54] for a rigorous analysis of this problem, and unexpected mathematical subtleties.

Theorem 3.4.1 (Cochet et al [48], Demircigil [54]). *There exist a speed $c > 0$, and a positive limit value $\rho_- > 0$, such that the system (3.4.1)–(3.4.2), admits a stationary solution in the moving frame $(\rho(x-ct), S(x-ct))$, such that ρ and S have the following limiting values*

$$\begin{cases} \lim_{z\to-\infty}\rho(z) = \rho_-\,, \\ \lim_{z\to+\infty}\rho(z) = 0\,, \end{cases} \qquad \begin{cases} \lim_{z\to-\infty} S(z) = 0\,, \\ \lim_{z\to+\infty} S(z) = S_{\text{init}}\,. \end{cases}$$

Moreover, the speed is given by the following dichotomy

$$c = \begin{cases} 2\sqrt{rd} & \text{if } \chi \le \sqrt{rd}\,, \\ \chi + \dfrac{rd}{\chi} & \text{if } \chi \ge \sqrt{rd}\,. \end{cases} \tag{3.4.6}$$

Interestingly, the dichotomy in (3.4.6) depends on the relative values of the advection speed (up the gradient) χ, and half the reaction-diffusion speed of the F/KPP equation

$\sqrt{rd}$. When the aerotactic biases are small (low advection speed χ), then the wave is essentially driven by growth and diffusion. When biases are large, then the wave is mainly driven by aerotaxis. This has interesting implications in terms of maintenance of genetic diversity inside the wave (see [24, 152] for diversity dynamics among reaction-diffusion traveling waves). In fact, the so-called dichotomy between *pulled* and *pushed* waves is at play here, see [48, 54] for more details and discussion.

In contrast with the original Keller-Segel model (3.2.2), the wave speed does not depend on the features of oxygen consumption and diffusion.

Proof. As in Section 3.3, the wave speed is not given *a priori*. We seek a monotonic oxygen profile, such that $\frac{dS}{dz} > 0$. Therefore, the first equation reduces to

$$-c\frac{d\rho}{dz} - d\frac{d^2\rho}{dz^2} + \frac{d}{dz}\left\{ \begin{array}{ll} 0 & \text{if } S > S_0 \\ \chi\rho & \text{if } S < S_0 \end{array} \right\} = \left\{ \begin{array}{ll} r\rho & \text{if } S > S_0 \\ 0 & \text{if } S < S_0 \end{array} \right\}.$$

By translational invariance, we assume that $S = S_0$ occurs at $z = 0$.

For $z < 0$, we have by (3.4.4)–(3.4.5),

$$d\frac{d\rho}{dz} = J + (\chi - c)\rho\,, \quad J > 0\,. \tag{3.4.7}$$

Suppose that $c \leq \chi$. Then, $d\frac{d\rho}{dz} \geq J > 0$, which is a contradiction with the positivity of ρ. Hence, we must have $c > \chi$. The solution of (3.4.7) is unbounded unless it is constant, that is $\rho = \frac{J}{c-\chi}$, and this is the natural choice we make for the construction.

For $z > 0$ we have the standard linear problem arising in the F/KPP equation (at small density),

$$-c\frac{d\rho}{dz} - d\frac{d^2\rho}{dz^2} = r\rho\,.$$

We look for exponential solutions $\exp(-\lambda z)$. The characteristic equation, $d\lambda^2 - c\lambda + r = 0$ has real roots when $c^2 \geq 4rd$. Then, we proceed by dichotomy.

$\diamond$ The case $c = 2\sqrt{rd}$. The general solution for $z > 0$ is of the form $(a + bz)\exp(-\lambda z)$, with $\lambda = \sqrt{\frac{r}{d}}$ the double root. The constant a coincides with $\frac{J}{c-\chi}$ by continuity of the density (its value does not really matter here). Continuity of the flux at the interface $z = 0$ yields $-d(b - a\lambda) = \chi a$, hence $bd = a(\sqrt{rd} - \chi)$. Thus, the solution is admissible ($b \geq 0$) if, and only if $\chi \leq \sqrt{rd}$.

$\diamond$ The case $c > 2\sqrt{rd}$. Standard arguments in the construction of reaction-diffusion traveling waves imply to select the sharpest decay on the right side [12, 156], namely $\rho = a\exp(-\lambda z)$, with $\lambda = \frac{1}{2d}\left(c + \sqrt{c^2 - 4rd}\right)$. Continuity of the flux at the interface now writes $-d(-a\lambda) = \chi a$, which is equivalent to

$$2\chi - c = \sqrt{c^2 - 4rd} \quad \Leftrightarrow \quad \left(c = \chi + \frac{rd}{\chi}\right) \;\&\; \left(\chi > \frac{c}{2}\right).$$

It must be checked *a posteriori* that $c > 2\sqrt{rd}$, which is immediate. The last inequality constraint ensures that $\chi > \sqrt{rd}$, in contrast with the other side of the dichotomy.

Thus, the construction is complete. □

The wavefront constructed above appears to be numerically stable, driving the long-time asymptotics, see Figure 3.8. However, the very strong advection at the back of the wave creates a decreasing density profile, which is actually constant at the back of the wavefront, in contrast with the experiments showing a non-monotonic pulse (Figure 3.7). Several extensions were discussed in [48].

Logarithmic sensitivity.

Below, we discuss a natural, yet original, extension of the previous result, restoring the logarithmic gradient in the advection term. More precisely, we consider (3.4.1) again, with the following choice of functions, instead of (3.4.2)

$$\boldsymbol{\chi}\left(S, \frac{\partial S}{\partial x}\right) = \chi \log\left(\frac{\partial S}{\partial x}\right) \mathbf{1}_{S<S_0}\,, \quad \mathbf{r}(S) = r\mathbf{1}_{S>S_0}\,. \tag{3.4.8}$$

We present below a preliminary result about the existence of traveling waves, followed by heuristic arguments about the determination of the speed, and some numerical investigation.

Theorem 3.4.2. *Assume $D = 0$, and $\mathbf{k}(S, \rho) = k\rho S$ for some $k > 0$. There exists a speed $c > 0$, and a positive limit value $\rho_- > 0$, such that the system (3.4.1)–(3.4.8), admits a stationary solution in the moving frame $(\rho(x - ct), S(x - ct))$, such that ρ and S have the following limiting values*

$$\begin{cases} \lim_{z\to-\infty} \rho(z) = \rho_-\,, \\ \lim_{z\to+\infty} \rho(z) = 0\,, \end{cases} \qquad \begin{cases} \lim_{z\to-\infty} S(z) = 0\,, \\ \lim_{z\to+\infty} S(z) = S_{\rm init}\,. \end{cases}$$

Moreover, the speed is given by the following dichotomy

$$c = 2\sqrt{r \max\left\{d, \chi \log\left(\frac{S_{\rm init}}{S_0}\right)\right\}}\,. \tag{3.4.9}$$

Proof. We proceed similarly as in the proof of the previous statement. The assumption $D = 0$ enables expressing the logarithmic gradient in terms of the density:

$$-c\frac{d(\log S)}{dz} = -k\rho\,. \tag{3.4.10}$$

For $z < 0$ we have a constant (negative) flux at equilibrium in the moving frame (3.4.4),

$$-c\rho - d\frac{d\rho}{dz} + \chi\rho\frac{d(\log S)}{dz} = -J < 0\,. \tag{3.4.11}$$

Combining (3.4.10) and (3.4.11), we get the ODE satisfied by the cell density profile at the back:

$$d\frac{d\rho}{dz} = -c\rho + \frac{k\chi}{c}\rho^2 + J\,. \tag{3.4.12}$$

This ODE comes with a sign condition, for the discriminant of the right-hand-side to be non-negative (otherwise ρ cannot be positive for all $z < 0$ when $\frac{d\rho}{dz}$ is uniformly positive), that is

$$\frac{c^3}{4k\chi} \geq J\,. \tag{3.4.13}$$

This condition is complemented by the integration of (3.4.10) over $\{z > 0\}$:

$$c\log\left(\frac{S_{\rm init}}{S_0}\right) = k\int_0^{+\infty} \rho(z)\,dz = \frac{k}{r}J\,,$$

where the last identity follows from (3.4.5). This yields the constraint

$$\frac{c^3}{4r\chi} \geq c\log\left(\frac{S_{\rm init}}{S_0}\right) \quad \Leftrightarrow \quad c^2 \geq 4r\chi\log\left(\frac{S_{\rm init}}{S_0}\right)\,. \tag{3.4.14}$$

This is one part of the condition in (3.4.9). The second part comes naturally from the constraint on the characteristic equation on $\{z > 0\}$, namely $c^2 \geq 4rd$. It can be shown by simple phase plane analysis that admissible solutions exist in both cases when the inequality (3.4.9) is an equality. □

The previous analysis calls for a few comments:

1. Contrary to the former construction in Theorem 3.4.1, the latter construction does not come naturally with an equation for c. This is because there is no clear way to remove one degree of freedom on $\{z < 0\}$ under the sign condition (3.4.13). Indeed, the solution of (3.4.12) is naturally bounded for any intial condition, in opposition to (3.4.7).

2. Surprisingly, the additional restriction (3.4.14) results from conditions imposed on the solution *at the back of the wave* on $\{z < 0\}$, in opposition with the standard case, say for F/KPP and related equations, where it always come from conditions on $\{z > 0\}$ (as it is the case for the classical restriction $c^2 \geq 4rd$).

At this point, we conjecture that the minimal speed (3.4.9) giving rise to admissible solutions is selected when the Cauchy problem is initiated with localized initial data.

Claim 3.4.3. *Starting from a compactly supported initial data, the asymptotic spreading speed of solutions to* (3.4.1)–(3.4.8) *is given by* (3.4.9).

This claim is supported by numerical exploration of the system in some range of parameters, see Figure 3.9 for one typical set of paramaters. On the one hand, the claim is not surprising in the case of small bias, when $c = 2\sqrt{rd}$. In fact, this corresponds to the standard mechanism of speed determination at the edge of the front in reaction-diffusion equation with pulled waves. This was indeed confirmed in the previous model (3.4.1)–(3.4.2) [48, 54]. On the other hand, we emphasize that it does look surprising in the case of large bias, when $c = 2\sqrt{r\chi \log\left(\frac{S_{\text{init}}}{S_0}\right)}$. In the latter case, the selection of the minimal speed would come from a discriminant condition *at the back of the wave*, which would be a quite original phenomenon, up to our knowledge.

3.5 Conclusion and perspectives

We exposed the original contribution of Keller and Segel devoted to chemotactic waves of bacteria, and discussed its limitations. These limitations are mainly concerned with the possible lack of positivity of the chemical concentration in the model. A pair of extensions were described. They both resolve the positivity issue, while keeping analytical solvability of the waves thanks to the specific choice of piecewise homogeneous models. In addition, they are both supported by biological experiments, respectively with bacteria *E. coli* and Dicty cells.

To conclude, let us mention some open problems, either on the mathematical or on the modeling side.

Determinacy of the speed at the back of the wave.

The result stated in Theorem 3.4.2 appeared quite unexpectedly. If further numerical exploration with alternative schemes tends to confirm our Claim 3.4.3, we believe that

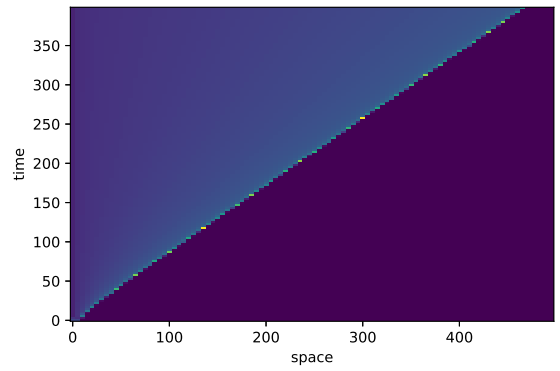

(a)

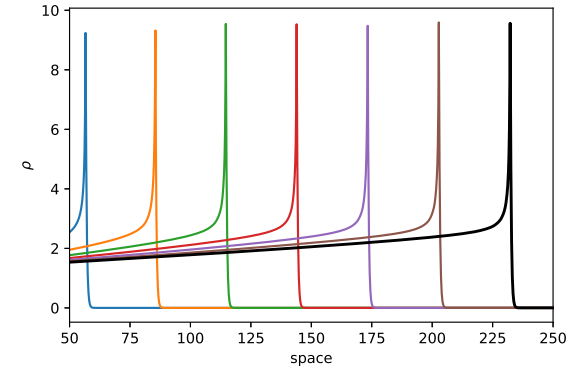

(b)

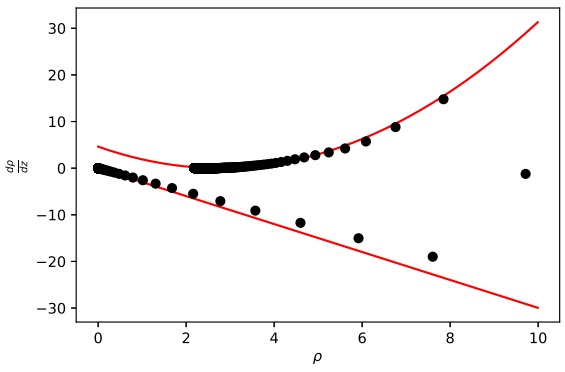

(c)

Figure 3.9: (a) Traveling wave propagation obtained after long time simulations of the Cauchy-problem (3.4.1)–(3.4.8) with parameters ($d = 1, \chi = 2, r = 1, D = 0, k = 1, S_{\text{init}} = 8, S_0 = 2$). (b) The density profile is shown at successive times in the moving frame. Note the low decay at the back of the wave, which is the signature of singular point in the ODE (3.4.12) together with the choice of J that cancels the discriminant in (3.4.13). The numerical speed is $c_{\text{num}} \approx 3.17$, close to the theoretical one, $2\sqrt{\log(4)} \approx 3.33$. (c) To better assess our Claim 3.4.3, the numerical solution is plotted in the phase plane (ρ, ρ') (black dots), against the theoretical curves, that is $\rho' = -\lambda\rho$ (for $z > 0$), and $\rho' = \frac{k\chi}{cd}\left(\rho - \frac{c^2}{2k\chi}\right)^2$ (3.4.12) (red lines). The isolated point on the right corresponds to the transition at $z = 0$, where the expected theoretical profile has a $\mathcal{C}^1$ discontinuity. We believe that the discrepancy is due to numerical errors.

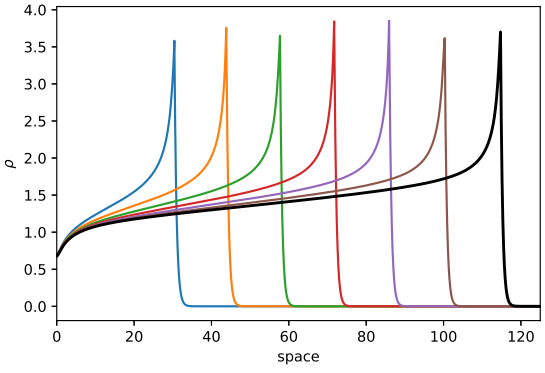

(a)

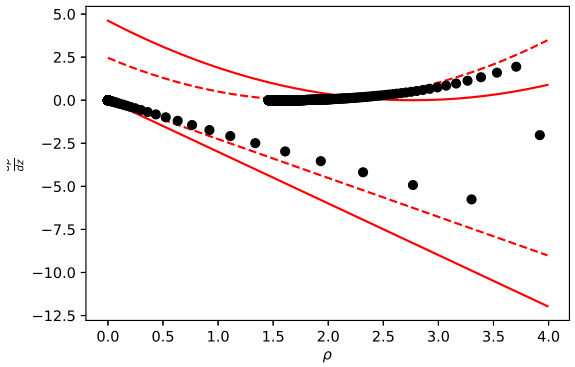

(b)

Figure 3.10: Same as in Figure 3.9, except for the diffusion coefficient of the chemical which is set to $D = 1$. (a) We observe propagation of a traveling wave in the long time asymtptotic with a reduced speed. Clearly, the wave profile differs significantly from 3.9b. (b) In particular, the solution in the phase plane does not align with the theoretical expectation available in the case $D = 0$ (red plain curves). It aligns much better with the theoretical expectation computed from the equations (3.4.10)–(3.4.14) taking the reduced numerical speed as an input (red dashed curves). We believe that the discrepancy is due to numerical errors.

understanding the mechanism of speed selection is an interesting, and possibly original problem *per se*. We stress out that this mechanism occurs at $z = -\infty$, in the sense that the sign condition on the discriminant in (3.4.12) ensures that the cell density remains positive for negative z. Alternatively speaking, we face a situation which is the mirror of the standard mechanism of speed determinacy at $z = +\infty$ in the F/KPP equation.

Traveling waves with non-zero chemical diffusion.

Figure 3.10 shows the numerical simulation of the Cauchy problem (3.4.1)–(3.4.8) with a chemical diffusion coefficient D of order one. It seems that the solution converges towards a traveling wave profile as $t \to +\infty$ with reduced speed as compared to the case without chemical diffusion (Figure 3.9). Moreover, the numerical wave plotted in the phase plane shows a similar pattern (compare Figure 3.9c and 3.10b), suggesting similar mechanisms occurring at $z = -\infty$ (in particular, a vanishing discriminant in the super-critical case $c > 2\sqrt{rd}$). However, since the relationship (3.4.10) is not satisfied with non-zero diffusion, we are lacking one equation to perform explicit computations. There exist multiple works extending the construction of waves for the original model (3.2.1) to the case of non-zero chemical diffusion. This may give some hints to address this question.

Stability.

Although stability in the Keller-Segel model (3.2.1) has drawn some attention, with a nearly complete picture by now, stability of the traveling wave solutions to the models presented in Sections 3.3 and 3.4 is almost entirely open. The first author and Hoffmann proved local non-linear stability of standing waves for (3.3.1) (without the SGG signaling S), assuming that the attractant concentration A is quasi-stationary (solving an elliptic equation at any time). They performed a change of coordinates to by-pass the discontinuity of the advection coefficient, and used higher-order energy methods to handle the singular term of the coupling.

Nevertheless, numerical investigation performed at the occasion of this work, with simple finite volume, semi-implicit, upwind schemes, argue in favor of stability of all the waves described in 3.3 and 3.4.

Spatial sorting.

Another open problem is the theoretical analysis of spatial sorting in bacteria collectives when the individuals have different chemotactic sensitivities. In [78], remarkable experiments on bacteria *E. coli*, together with a very elegant analytical argument, indicated that cells can move together despite their differences. The argument of [78] goes as follows: assume that there exist multiple types of bacteria consuming a single nutrient S, and that each type is characterized by a chemotactic sensivity χ_i ; suppose that, for each type, the chemotactic advection is of the form $\boldsymbol{\chi}_i\left(S, \frac{\partial S}{\partial x}\right) = \chi_i \frac{\partial F(S)}{\partial x}$, say the logarithmic gradient as in the original model (3.2.1) ; suppose that the solution of each type converges towards a traveling wave in the long-time, with a common speed c, so that the flux is asymptotically zero in the moving frame for each type:

$$(\forall i) \quad -c - d\frac{d}{dz}\left(\log \rho_i\right) + \chi_i \frac{d}{dz} F(S) = 0\,. \tag{3.5.1}$$

Evaluating (3.5.1) at the maximum point of the density ρ_i, say z_i^*, we would get that

$$c = \chi_i \frac{d}{dz} F(S)(z_i^*)\,. \tag{3.5.2}$$

Differentiating (3.5.1) at $z = z_i^*$, it could be deduced that

$$\frac{d^2}{dz^2} F(S)(z_i^*) = d \frac{d^2}{dz^2} (\log \rho_i)(z_i^*) \leq 0 \,. \tag{3.5.3}$$

The combination of (3.5.2) and (3.5.3) says that the peaks (z_i^*) of the densities (ρ_i) which are traveling together are restricted to the interval where $F(S)$ is concave. Moreover, they are ordered in such a way that $(\chi_i < \chi_j) \Rightarrow (z_i^* < z_j^*)$. This nice calculation indicates that different phenotypes could migrate collectively despite their differences. The intuitive reason, which can be read on (3.5.2), is that larger chemosensitivity χ_i naturally pushes the cells ahead, where they experience shallower gradients. Nonetheless, the analysis in [78] is not complete, as the existence of a stable traveling waves of different types with a common speed is taken for granted.

There exist previous theoretical works about collective migration of different phenotypes within the same chemical environment. We refer for instance to [122], which adopted the framework of the original model by Keller and Segel (3.2.1). In view of the discussion above, the stability of their theoretical outcomes is questionable. In [61], the authors extend the framework of Section 3.3, including two subpopulations with different chemotactic phenotypes. This work was supported by experimental data. However, the discussion in [78] makes it clear that the framework of [61] is not directly compatible with their findings. Actually, it is one consequence of the advection speed discontinuity in (3.3.1) that the maximum peak density is located at the sign transition, whatever the chemosensitivity coefficient is, hence violating the nice relationship (3.5.2).

Preliminary investigations suggest that the framework of Section 3.4 cannot be readily extended as well. Indeed, signal-dependent growth counter-balances the fact that more efficient chemotactic types experience shallower gradients, because they have better access to nutrient. This triggers natural selection of the more efficient type by differential growth (results not shown).

To our knowledge, there is no clear mathematical framework to handle the remarkable experiments and biological insights as shown in [78], at the present time.

Chapter 4

A Paradigm for Well-Balanced Schemes for Traveling Waves Emerging in Biological Models

---

This Chapter has been written in collaboration with Benoit Fabrèges, who has carried out the parabolic part of this Chapter. Before submitting this work to a journal, we wish to investigate if we can improve the scheme in the kinetic case.

We propose a methodology for designing well-balanced numerical schemes to investigate traveling waves in kinetic and parabolic models from mathematical biology. We combine well-balanced techniques for kinetic and parabolic models known in the literature with the so-called LeVeque-Yee formula as a dynamic estimate for the spreading speed. This latter formula is used to consider the evolution problem in a moving frame at each time step. There the equations admit stationary solutions, for which well-balanced techniques are suitable. Then, the solution is shifted back to the stationary frame in a well-balanced manner. We illustrate this methodology on two application cases: a recent kinetic model for collective movement in eukaryotic cells and the parabolic Fisher/Kolmogorov-Petrovsky-Piskunov (F/KPP) Equation. In both cases, we show that the numerical schemes capture in a consistent way simultaneously the wave speed as well as the wave profile at the leading edge. Moreover, we show that for the F/KPP Equation the scheme is able to capture to an extent the so-called Bramson shift.

4.1 Introduction

Many biological systems may give rise to spatial spreading phenomena, such as for instance the invasion of rodents [167] or the collective displacement of a population of *Escherichia coli* cells in a micro-channel [5]. Mathematical modelling of this phenomena has contributed to a better understanding of these spreading phenomena and gives also rise to a quantitative framework, which may for instance account for the spreading speed. On the mathematical side, we may cite as models, that have attracted much attention, reaction-diffusion equations (*e.g.* [11, 70, 72, 94, 115]), parabolic models of chemotaxis (*e.g.* [114,

160]) and kinetic models of chemotaxis (*e.g.* [6, 7, 35, 141]). The biological question of the spreading of a population translates then into the mathematical question of the existence of a traveling wave, *i.e.* solutions that are stationary in a moving frame of reference.

The mathematical investigation of traveling waves for biological models naturally raises the question of the numerical investigation of these traveling wave solutions. Numerically, this question is difficult, as it requires an accurate scheme over large domains in order to capture precisely the behavior of the solution over large time. Moreover the questions we may wish to address to such schemes are two-fold: (i) find the accurate spreading speed; (ii) find the accurate traveling wave profile. In fact these two questions are related, since mathematically the wave speed is intimately connected to the wave profile. In fact, as we will see notably in this article, wave profiles will often at their leading edge decrease exponentially and their exponential decay parameter can be tied to the wave speed through a dispersion relation. Hence, we wish to find numerical schemes that capture at the same time accurately a wave speed, as well as an exponential decay, which requires great precision even at very low orders of magnitude, because of the nature of exponential decays.

In this article, we will use so-called well-balanced (WB) schemes in order to investigate these questions. The notion of WB schemes has been introduced by [91] and consists roughly speaking in numerical schemes that preserve the steady state of the continuous model, *i.e.* the steady state of the numerical scheme matches the discretization of the steady state of the continuous model. Many different approaches to such schemes exist and we refer the reader for instance to [85] for a general discussion on these techniques. However in their essence, WB schemes accurately balance the flux terms and the source terms. In recent years, WB schemes have been proposed for kinetic equations of chemotaxis (see [62, 85, 88, 89] and the review [149], as well as references therein). For instance, one of the strategies consists in a Godunov scheme, where the source term is "localized" at the boundary of the cells. In order to solve the corresponding Riemann problem, one then uses the stationary solution to compute jump relations at the boundary [85]. Moreover, WB schemes have also been investigated for parabolic equations [87, 88]. In these works, the strategy consists in interpolating the function in each cell with $\mathscr{L}$-splines (see [86] for an overview on the concept of $\mathscr{L}$- splines), which correspond to the stationary solutions of the problem. The interpolation is then continous inside each cell, but at the nodes of the grid it may have C^1-discontinuities. The time integration then is computed by using the C^1 defect at each node. Of note, most referenced models are one-dimensional models, but in recent years the leap to higher dimensions has attracted interest [31, 55, 84].

Yet, in the aformentioned studies, most often the schemes were designed to describe a stationary state, not a traveling wave. We refer to the work of [37] for a WB scheme for traveling waves in kinetic models, as well as [86] for a WB scheme for a parabolic model. As mentioned above, the philosophy of WB schemes consists in balancing the fluxes and the source terms. However, in the case of a traveling wave the fluxes depend on the propagation speed. Whilst in some cases the propagation speed can be computed explicitly and thus be used in the implementation of the scheme, in most cases the propagation speed is not known *a priori*. This adds to the difficulty of designing a WB scheme for traveling waves. For instance in the work [37], the authors have proposed a numerical scheme, which is well-balanced for a wave with speed $\sigma = 0$, and have used it in order to capture traveling waves with nonzero speed. Hence, the proposed scheme is *stricto sensu* not WB for the observed traveling wave.

In the present article, in order to overcome this difficulty, we implement a strategy, which measures dynamically the spreading speed. We use an estimate of this spreading speed, which has been proposed in [118] and has recently been refered to as LeVeque-

Yee formula [131]. This formula is based on the following observation: suppose that $u(t,x) = u(x - \sigma t)$ is a traveling wave profile, which admits at $\pm\infty$ fixed limit values $u(\pm\infty)$, then u satisfies:

$$\partial_t u + \sigma \partial_x u = 0.$$

Integrating over $\mathbb{R}$ and rearranging the terms, we obtain the following identity:

$$\sigma = -\frac{\int_{\mathbb{R}} \partial_t u dx}{u(+\infty) - u(\infty)} \tag{4.1.1}$$

The LeVeque-Yee formula is then merely a discretized version of Identity (4.1.1):

$$\hat{\sigma}^n_{LY} = \frac{\Delta x}{\Delta t} \frac{\sum_i \left(u_i^{n-1} - u_i^n\right)}{u_I^n - u_0^n}, \tag{4.1.2}$$

where u is computed on a uniform Cartesian grid $(n\Delta t)_{n\in\mathbb{N}} \times (i\Delta x)_{i=0,\dots,I}$. For functions, which are not traveling waves, the right hand-side of Identity (4.1.1) is still defined and can be interpretated as an estimate of their spreading speed.

The contribution of this article consists in combining the LeVeque-Yee formula as a dynamic speed estimate with the methodology of WB schemes for kinetic or parabolic equations. The schemes, we propose in this article share the following common structure:

1. Estimate at each time step the spreading speed $\hat{\sigma}^n$ via the LeVeque-Yee Formula (4.1.2).

2. Consider over the time step the problem in the frame of reference moving at speed $\hat{\sigma}^n$ and use a WB scheme to integrate numerically the solution over the time step.

3. Given the solution integrated in time in the moving frame, shift back the solution to the stationary frame. To do so in a WB manner, interpolate in each cell the stationary solution, with the boundary conditions prescribed by the values obtained at the preceding step. Finally, compute the value of the stationary solution at the corresponding point in the stationary frame.

In order to illustrate this methodology, we apply it to two different cases: (i) a kinetic Go or Grow model [54], which has been recently introduced by one of the authors, in order to describe the emergence of aerotactic waves in eukaryotic cells (see [48]); (ii) the Fisher/Kolmogorov-Petrovsky-Piskunov equation [72, 115], which has been a prototype of traveling wave phenomena in (parabolic) reaction-diffusion equations. Next, we briefly present the two application cases.

4.1.1 Aerotactic waves in *Dictyostelium discoideum*: a Kinetic Go or Grow Model

For the first application case, we will consider a model of collective movement in *Dictyostelium discoideum* (*Dd* cells in short) at a mesoscopic scale and investigate numerically the spreading of the cell population.

In [48], one of the authors and collaborators have put into evidence the following emerging behavior of *Dd* cells in hypoxic conditions: when a colony of *Dd* cells is confined between two narrowly spaced plates, *Dd* cells form a dense ring moving outwards. After a brief transitory phase, the ring of cells moves at constant speed and constant density over the time course of the experiment (see Figure 4.1a). The authors emitted the hypothesis that the quick consumption of oxygen by *Dd* cells exposes them to hypoxia, *i.e.* lack of

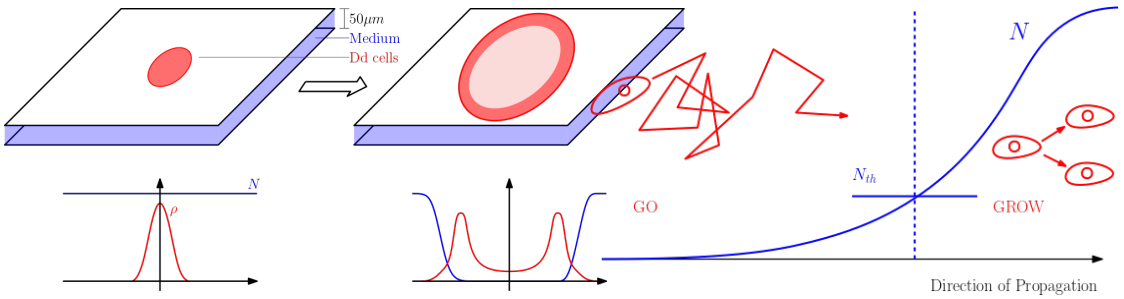

(a) (b)

Figure 4.1: (a): A schematic representation of the experiment carried out in [48]. Cells are confined between two narrowly spaced plates and quickly consume available oxygen, so that the colony experiences self-induced hypoxic conditions. This, in turn, triggers outward migration of the colony under the form of a ring expanding at constant speed over long periods of time. (b): A cartoon representation of the 'Go or Grow' hypothesis. Cells switch between two behaviors, depending on the level of oxygen. When oxygen concentration is above some threshold N_{th}, cells divide and follow Brownian trajectories (this is the 'Grow' behavior). In contrast, when oxygen concentration drops below N_{th}, cells stop dividing and follow a biased Brownian motion towards higher levels of oxygen (this is the 'Go' behavior).

oxygen, and in turn induces *aerotaxis*, *i.e.* a bias in the individual trajectories of *Dd* cells towards higher oxygen concentrations, leading to a macroscopic outward motion. In order to gain insight in this surprising collective behavior, the authors have investigated the 'Go or Grow' modeling hypothesis, whose mainspring can be motivated by the following modeling approach: (i) Experimentally, it was observed that cells exhibit various individual behaviors accross the colony. (ii) In the model, two particular behaviors were retained as an alternative: either cell division ('Grow' behavior), or migration towards oxygen ('Go' behavior). (iii) It was postulated that the transition between the two behaviors depends on a single threshold (see Figure 4.1b). Indeed, it is for instance well known that *Dd* cells do not have enough energy to divide, when oxygen is lacking. The term 'Go or Grow' was coined to describe this dichotomy, by analogy with a similar mechanism in the modeling of glioma cells [98], which nevertheless is of another nature, as it describes a density-dependent rather than an oxygen-dependent switch between diffusion and cell division.

In [54], one of the authors has proposed the extension of the 'Go or Grow' hypothesis to a modeling at a mesoscopic scale of the cell density, via a kinetic equation. This has lead to the following System:

$$\begin{cases} \partial_t f + v\partial_x f = \alpha^2 \left(M(v; N, \partial_x N)\rho - f \right) + \mathbb{1}_{N>N_{\text{th}}}\rho & \text{(4.1.3a)} \\ \partial_t N - D\partial_{xx} N = -\rho N, & \text{(4.1.3b)} \end{cases}$$

where $(t, x, v) \in \mathbb{R}_+ \times \mathbb{R} \times V$, V a compact subset of $\mathbb{R}$ (either zero- or one-dimensional), which satisfies $\frac{1}{|V|}\int_V v dv = 0$, $\alpha > 1$ and $\rho(t, x) = \frac{1}{|V|}\int_V f(t, x, v) dx$.

Equation (4.1.3a) describes the evolution of the mesoscopic cell density $f(t, x, v)$, where cells undergo division and persistent motion: cells move with velocity v and at a constant rate α^2 cells reorient themselves according to the probability distribution described by the Maxwellian $M(v; N, \partial_x N)$. The 'Go or Grow' hypothesis then translates into the fact that: (i) the cell division rate is $\mathbb{1}_{N>N_{\text{th}}}$ and cells divide if and only if $N > N_{\text{th}}$. (ii) The

Maxwellian distribution $M(v; N, \partial_x N)$ depends in the following manner on the ambient oxygen levels:

$$M(v; N, \partial_x N) = \begin{cases} M_{\text{GROW}}(v) & \text{if } N > N_{\text{th}} \\ M^+_{\text{GO}}(v) & \text{if } N \leq N_{\text{th}} \text{ and } \partial_x N \geq 0 \\ M^-_{\text{GO}}(v) & \text{if } N \leq N_{\text{th}} \text{ and } \partial_x N < 0 \end{cases}, \tag{4.1.4}$$

satisfying the properties, with $\chi \in (0, \min\{\max V, -\min V\})$:

$$\frac{1}{|V|}\int_V v M^{\pm}_{\text{GROW}}(v)dv = 0 \text{ and } \frac{1}{|V|}\int_V v M^{\pm}_{\text{GO}}(v)dv = \pm\chi. \tag{4.1.5}$$

In this article, we will be concerned with the investigation of traveling waves when $\partial_x N > 0$, *i.e.* waves that travel from left to right. Hence if we drop the diacriticals $^{\pm}$, we implicitly mean $M_{\text{GROW}} = M^+_{\text{GROW}}$. Furthermore we assume that $N(t, +\infty) = N_0 > N_{\text{th}}$. Finally, in order to simplify the notations, we introduce the "scattering operator":

$$\mathcal{C}(f; N, \partial_x N) := \alpha^2 \left(M(v; N, \partial_x N)\rho - f\right) + \mathbb{1}_{N>N_{\text{th}}}\rho \tag{4.1.6}$$

Of note, suppose that if V is of the shape αV_0 (independently of V_0 being zero- or one-dimensional) and if $\frac{1}{|V_0|}\int_{V_0} v^2 dv = 1$, then, as has been pointed out in [54], $f(t, x, v)$ converges when $\alpha \to +\infty$ in a formal sense to a function $\rho(t, x)$, which satisfies the following diffusion-advection-reaction Equation:

$$\partial_t \rho - \partial_{xx}\rho + \partial_x\left(\chi \mathbb{1}_{N<N_{\text{th}}}\rho\right) = \mathbb{1}_{N>N_{\text{th}}}\rho \tag{4.1.7}$$

Equation (4.1.7) combined with Equation (4.1.3b) on N was the main object of investigation in [54]. Hence this naturally raises the question of a numerical scheme which is asymptotic-preserving (AP) under the limit $\alpha \to +\infty$. Recently, different studies have proposed procedure for AP schemes in the context of chemotatic kinetic models (see for instance [62, 89, 149]). However, this will not be the point of view in this article and we leave the design of AP schemes for System (4.1.3) to future investigations.

4.1.2 Fisher/Kolmogorov-Petrovsky-Piskunov Equation

..

$$\partial_t u - \partial_{xx} u = u(1 - u). \tag{4.1.8}$$

Fisher/Kolmogorov-Petrovsky-Piskunov (F/KPP) Equation (4.1.8), introduced independently in [72] and [115], is a prototype of reaction-diffusion equations. It describes a population $u(t, x)$ of individuals undergoing unbiased motion, modeled through a diffusion operator, as well as competition among the population (*e.g.* for ressources) through a logistic growth term $u(1 - u)$: the higher the density u becomes, the lower the growth rate per capita $1 - u$ becomes, with a saturation when the population reaches the maximal density $u = 1$. It admits two steady stated $u = 0$ and $u = 1$: the first one is unstable, whilst the second is stable.

Interestingly, for velocity σ, Equation (4.1.8) admits nonnegative traveling wave solutions of the form:

$$u_\sigma(-\infty) = 1, u_\sigma(+\infty) = 0 \text{ and } u_\sigma(t, x) = u_\sigma(x - \sigma t) \tag{4.1.9}$$

if and only if $\sigma \geq \sigma^* = \sigma_{F/KPP} := 2$ [11, 72, 115]. These solutions are in fact invariant by translation and we will fix a specific solution by the convention that $u_\sigma(0) = \frac{1}{2}$. Hence the equation describes a linear spatial invasion of the state $u = 0$ by the state $u = 1$. Furthermore for a wide variety of initial data u^0, one can show that in a certain sense, which we will specify, u the solution of Equation (4.1.8) converges to the traveling wave with minimal velocity $\sigma^* = \sigma_{F/KPP}$. Take for example an initial datum u^0, which satisfies:

$$\liminf_{x \to -\infty} u^0(x) \geq \kappa > 0 \text{ and } \sup \text{ supp } u^0 < +\infty. \tag{4.1.10}$$

Of note these conditions may be relaxed, but for the sake of concision, we restrict our attention to this class of initial data. Then, define the position of the level set $x_c(t)$ for $c \in (0, 1)$:

$$x_c(t) = \sup\{x | u(t, x) = c\} \tag{4.1.11}$$

It has been shown in [28, 29], through a probabilistic interpretation of Equation (4.1.8) (see [96, 140] for a proof based on PDE argument), that there exists a constant x_∞ depending on the initial datum and c, such that:

$$x_c(t) = 2t - \frac{3}{2}\ln(t) + x_\infty + o(1) \text{ and } \lim_{t \to +\infty} u(t, x + x_c(t)) = u_{\sigma^*}(x). \tag{4.1.12}$$

The logarithmic shift in the asymptotic expansion of $x_c(t)$ is known as the Bramson shift. The result is in a sense very surprising, because it shows convergence to the traveling wave with speed $\sigma_{F/KPP}$ but in the frame shifted by a logarithmic correction term. As has been observed in [96], this logarithmic correction term is due to subtle interactions between the diffusion and the reaction term, when $u \sim 0$. Hence, from a numerical point of view, we can assume that capturing the Bramson shift is a very delicate task, since it requires an accurate computation of the profile of u at very low orders of magnitude. As far as we know, we are not aware of any work on a numerical scheme for Equation (4.1.8), which captures the Bramson shift.

4.1.3 Outline of the paper

In this article, we combine the LeVeque-Yee formula with the methodology of WB schemes for kinetic and parabolic equations in order to design numerical schemes that are WB for traveling waves. In Section 4.2, we consider numerical schemes for the kinetic Go or Grow model. We start by recalling an existence result for traveling waves in the two-velocity case, which comes with a wave speed formula. Then, we describe the proposed numerical scheme, which is valid for any finite set of velocities. We assess specifically this numerical scheme in the two-velocity case, where we can compare the numerical values for the propagation speed with the theoretical values. We also show numerical performances of the scheme on the eight-velocity case. The scheme's performances are compared with more standard schemes based on an operator splitting approach of the source term and the free-transport term. In Section 4.3, we propose a WB numerical scheme for F/KPP Equation (4.1.8). The scheme is compared to an operator splitting approach. Furthermore, we show that our scheme captures accurately the propagation speed and we compare the asymptotic spreading with the theoretical result (4.1.12) and in particular to the logarithmic Bramson correction to the asymptotic expansion.

4.2 A WB scheme for Traveling Waves in a Kinetic Go or Grow Model

In this Section, we briefly mention the results obtained in [54] on System (4.1.3). Then, we describe a WB numerical scheme for traveling waves in System (4.1.3) and we assess the performances of this scheme in comparison with other numerical schemes for the same system.

4.2.1 Traveling Waves for the Kinetic Go or Grow Model

Consider System (4.1.3) with velocity space $V = \{-\alpha, \alpha\}$. We will refer to it as the two-velocity case and set $f^{\pm}(t,x) = f(t,x,\pm\alpha)$. Furthermore, we consider that $\alpha > 1$, which following the terminology in [26] is refered to as the parabolic regime. In order to simplify the line of reasoning, we assume that $\partial_x N > 0$, which leads to a collective movement of the population from left to right. In [54], all nonnegative and bounded traveling wave solutions to System (4.1.3) in the parabolic regime have been exhibited.

Let us first introduce some notations. Set $\sigma_{F/KPP} := \frac{2\alpha^2}{\alpha^2+1}$ and for $\sigma \in [\sigma_{F/KPP}, \alpha)$:

$$\mu_{\pm}(\sigma) := -\frac{\sigma(\alpha^2-1) \pm \sqrt{\sigma^2(\alpha^2+1)^2 - 4\alpha^4}}{2(\alpha^2-\sigma^2)}. \tag{4.2.1}$$

We have the following inequality for $\sigma > \sigma_{F/KPP}$:

$$\mu_+(\sigma) < \mu_+\left(\sigma_{\mathrm{F/KPP}}\right) = -\frac{\alpha^2}{\alpha^2-1} = \mu_-\left(\sigma_{\mathrm{F/KPP}}\right) < \mu_-(\sigma). \tag{4.2.2}$$

In addition the function $\sigma \to \mu_+(\sigma)$ (resp. $\sigma \to \mu_-(\sigma)$) is decreasing (resp.increasing).

Theorem 4.2.1 ([54]). *In the parabolic regime $\alpha > 1$, there exists a minimal speed $\sigma^* \in (1,\alpha)$, such that for any $\sigma \in [\sigma^*, \alpha)$, there exists a corresponding bounded and nonnegative traveling wave profile $(f^{+,\sigma}, f^{-,\sigma}, N^\sigma)$. In addition, for $\sigma \in [\sigma^*, \alpha)$ fixed, the traveling wave profile $(f^{+,\sigma}(z), f^{-,\sigma}(z), N^\sigma(z))$ is unique, under the condition that $N^\sigma(0) = N_{th}$. For $\sigma \in [0, \sigma^*)$, there does not exist a nonegative traveling wave profile. The expression of σ^* is given by:*

$$\sigma^* = \begin{cases} \frac{\left(\chi+\frac{1}{\chi}\right)\alpha^2}{\alpha^2+1} & \text{if } \chi > 1 \\ \sigma_{F/KPP} = \frac{2\alpha^2}{\alpha^2+1} & \text{if } \chi \leq 1 \end{cases}. \tag{4.2.3}$$

Furthermore, the functions $f^{\pm,\sigma}$ have the following behavior for $z > 0$:

- *for $\sigma \in (\sigma^*, \alpha), z > 0, f^{\pm,\sigma}(z) = A^{\pm}e^{\mu_-(\sigma)z} + B^{\pm}e^{\mu_+(\sigma)z}$;*
- *for $\chi > 1, \sigma = \sigma^* = \frac{\left(\chi+\frac{1}{\chi}\right)\alpha^2}{\alpha^2+1}, z > 0, f^{\pm,\sigma^*}(z) = B^{\pm}e^{\mu_+(\sigma^*)z}$ and $\mu_+(\sigma^*) = -\frac{\chi(\alpha^2+1)}{\alpha^2-\chi^2}$;*
- *for $\chi < 1, z > 0, \sigma = \sigma_{F/KPP}, f^{\pm,\sigma_{F/KPP}}(z) = (A^{\pm}z + B^{\pm})e^{-\frac{\alpha^2}{\alpha^2-1}z}$;*
- *for $\chi = 1, z > 0, \sigma = \sigma_{F/KPP}, f^{\pm,\sigma_{F/KPP}}(z) = B^{\pm}e^{-\frac{\alpha^2}{\alpha^2-1}z}$.*

Of note, if we consider the proof of Theorem 4.2.1 in [54], we can in fact observe that bounded traveling waves exist for all $\sigma \in [0,\alpha)$, if one relaxes the nonnegativity condition. This observation will be useful to keep in mind, when we describe the numerical scheme.

Nevertheless, Theorem 4.2.1 deals merely with traveling wave solutions and not with the behavior of System (4.1.3) during the transitory phase. This is still an open problem, but as will be shown below, we expect the solution to System (4.1.3) to behave closely to the traveling wave of minimal wave speed. Yet, numerical investigations show that the solution behaves differently in cases $\chi > 1$ or $\chi \leq 1$. In the case $\chi > 1$, we observe that the numerical spreading speed stabilizes relatively fast, whereas in the case $\chi \leq 1$, we observe a behavior reminiscent of the Bramson shift. Therefore, in this Section we will exclusively consider the case $\chi > 1$ and postpone a detailed investigation of the $\chi \leq 1$ case.

Moreover, for a general velocity space V, a result analog to Theorem 4.2.1 is still under investigation.

4.2.2 A WB Approach for the Kinetic Go or Grow Model

We present a WB scheme for approximating numerically the solution of System (4.1.3). We consider a uniform Cartesian grid with mesh sizes $\Delta x, \Delta t > 0$. We denote $t^n := n\Delta t$, for $n \in \mathbb{N}$, $x_i = i\Delta x$, for $i \in \mathbb{Z}$ and $C_i := \left(x_{i-\frac{1}{2}}, x_{i+\frac{1}{2}}\right)$. In the numerical scheme, we will consider changes of reference of the form $(t, z) = (t, x - \sigma t)$. Hence, we introduce a parallel notation, which will be convenient for readability $z_i = i\Delta z$, with $\Delta z = \Delta x$, $\bar{C}_i := \left(z_{i-\frac{1}{2}}, z_{i+\frac{1}{2}}\right)$ as well as a staggered cell $\bar{C}_{i+\frac{1}{2}} := (z_i, z_{i+1})$. Furthermore, we suppose that:

$$V := \alpha V_0 = \alpha\{v_{-J}, v_{-J+1}, \dots, v_{-1}, v_1, \dots, v_{J-1}, v_J\},$$

with $v_j = \frac{j}{J}$ and $v_{-j} = v_j$, for $j \in \{1, \dots, J\}$. We also introduce the notation $\mathcal{J} = \{-J, \dots, -1, 1, \dots, J\}$. The assumption on V may be relaxed to any (not necessarily symmetric) finite set (as long as the uniform distribution is of mean zero on it), but for the sake of simplicity, we will restrict the study to this specific case. Finally, we we will consider $f^n_{i,j} \approx f(t^n, x_i, \alpha v_j)$.

The procedure of the numerical scheme consists first in an operator-splitting approach between Equation (4.1.3a) and Equation (4.1.3b). The steps of the scheme, which we will expand on below, can be summarized as follows:

1. We use LeVeque-Yee's formula on the profile N in order to obtain an estimate $\hat{\sigma}^n$ of the spreading speed .

2. Given $\hat{\sigma}^n$, on the time interval (t^n, t^{n+1}) we consider f in the moving frame $(t, z) = (t, x - \hat{\sigma}^n(t - t^n))$ and denote it by $\bar{f}$, which leads to Equation:

$$\partial_t \bar{f} + (v - \hat{\sigma}^n)\partial_z \bar{f} = \mathcal{C}(\bar{f}; N^n, \partial_x N^n) \tag{4.2.4}$$

   We approximate $\bar{f}$ with a WB scheme, which is in essence an adapted version of the WB scheme presented in [37]. Of note, this scheme is WB with respect to the velocity $\hat{\sigma}^n$, *i.e.* it is exact on the stationary solution of Equation (4.2.4).

3. Given $\bar{f}^{n+1}_{i,j} \approx \bar{f}(t^{n+1}, z_i, v_j)$, we procede to a shift back to the stationary frame. We observe that $f(t^{n+1}, x_i, v_j) = \bar{f}(t^{n+1}, z_i + \hat{\sigma}^n \Delta t, v_j)$ and in order to approximate this value, we consider the stationary solution of Equation (4.2.4) in the cell $\bar{C}_{i+\frac{1}{2}}$, which leads to:

$$\begin{cases} (v - \hat{\sigma}^n)\partial_z \hat{f} = \mathcal{C}(\hat{f}; N^n, \partial_x N^n) \\ \hat{f}(z_i, v) = \bar{f}^{n+1}_{i,j}, \text{ for } v_j > \hat{\sigma}^n \text{ and } \hat{f}(z_{i+1}, v_j) = \bar{f}^{n+1}_{i+1,j}, \text{ for } v_j < \hat{\sigma}^n \end{cases} \tag{4.2.5}$$

The solution $\hat{f}$ to Equation (4.2.5) is well-defined. Then, we set $f_{i,j}^{n+1} := \hat{f}(t^{n+1}, z_i + \hat{\sigma}^n \Delta t, v_j)$. Note that this procedure also constitutes a WB approach: consider a traveling wave for Equation (4.1.3a) with velocity σ and suppose that $\hat{\sigma}^n = \sigma$, then the traveling wave in the moving frame satisfies by definition Equation (4.2.5). Hence the extrapolated value for $z = z_i + \hat{\sigma}^n \Delta t$ corresponds exactly to the value of the traveling wave at the point x_i in the stationary frame.

4. Finally, we use a numerical scheme on N over the time inerval (t^n, t^{n+1}), by using in particular the values ρ_i^{n+1} obtained above.

LeVeque-Yee Formula for the Kinetic Go or Grow Model

The procedure described above relies heavily on an estimate of the propagation speed $\hat{\sigma}^n$. To estimate this speed, we use the LeVeque-Yee Formula (4.1.2), which, we recall, for a quantity u is:

$$\hat{\sigma}_{LY}^n = \frac{\Delta x}{\Delta t} \frac{\sum_i \left(u_i^{n-1} - u_i^n\right)}{u_I^n - u_0^n},$$

However, in the case of System (4.1.3), there exists two quantities f and N. This raises the question of which quantity should be used to estimate the speed. As has been observed in [131], in order for Formula (4.1.2) to be relevant, one should expect that at $\pm\infty$ the quantity u admits asymptotic states. This is the case for N, where we expect, after possibly a transitory phase that $N(t, -\infty) = 0$ and $N(t, +\infty) = N_0$. For f, there is no *a priori* asymptotic state at $x = -\infty$ and its values there may heavily depend on initial conditions. Hence we apply the LeVeque-Yee formula to N and obtain the following estimate for the propagation speed:

$$\hat{\sigma}_{LY}^n = \frac{\Delta x}{\Delta t} \frac{\sum_i \left(N_i^{n-1} - N_i^n\right)}{N_I^n - N_0^n}. \tag{4.2.6}$$

Furthermore, as will become clear below, in order for the scheme to be well-defined, one needs to ensure that $|\hat{\sigma}^n| < \max\{|V|\}$. Moreover, it will be useful for the sake of a simpler implementation to add the restriction that $\hat{\sigma}^n \geq 0$. Hence, we set:

$$\hat{\sigma}^n = \begin{cases} \hat{\sigma}_{LY}^n & \text{if } \hat{\sigma}_{LY}^n \in [0, \max\{V\}) \\ \bar{\sigma} & \text{else} \end{cases}, \tag{4.2.7}$$

where $\bar{\sigma} \in [0, \max\{V\})$ is any generic value. In practice this restriction on the speed esimtator $\hat{\sigma}^n$ will not change much, since we will be interested here in capturing traveling waves, whose speed will be in the interval $(0, \max\{V\})$.

A WB Scheme in the Moving Frame

Next, we consider the evolution of f on the interval (t^n, t^{n+1}) in the moving frame $(t, z) = (t, x - \hat{\sigma}^n(t - t^n))$, *i.e.* $\bar{f}(t, z, v) = f(t, z + \hat{\sigma}^n(t - t^n), v)$, where $\bar{f}$ solves Equation (4.2.4). Following the work in [37] (see also [85]), we procede to a localization of the scattering operator $\mathcal{C}(\bar{f})$ and concentrate the scattering events at the fixed locations $z_{i+\frac{1}{2}}$. This leads to the following approximation:

$$\begin{cases} \partial_t \bar{f} + (v_j - \hat{\sigma}^n)\partial_z \bar{f} = \Delta z \sum_{j \in \mathbb{Z}} \mathcal{C}_{i+\frac{1}{2}}(f) \delta\left(z - z_{i+\frac{1}{2}}\right) \\ \bar{f}(t^n, z, v_j) = f_{i,j}^n \text{ for } z \in C_i, \end{cases} \tag{4.2.8}$$

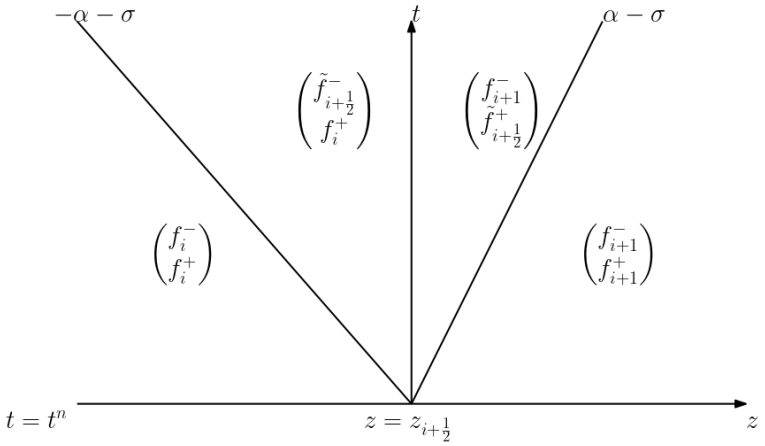

Figure 4.2: Graphic representation of the solution to the Riemann Problem (4.2.9) for $t > t^n$ and $z \in \mathbb{R}$, in the case $2J = 2$, with $V = \{-\alpha, +\alpha\}$, $\sigma > 0$. We denote $f_i^+ = f_{i,1}$ and $f_i^- = f_{i,-1}$.

where $\mathcal{C}_{i+\frac12}(\bar{f}) := \mathcal{C}(f; N^n_{i+\frac12}, \partial_x N^n_{i+\frac12})$.

A Godunov scheme.

Equation (4.2.8) lends itself to a Godunov scheme: the initial datum at time $t = t^n$ is piecewise constant and the scattering events at the boundary of the cells, *i.e.* $z = z_{i+\frac12}$, introduce jump relations. For the sake of clarity, we consider the Riemann problem with a single scattering event at $z = z_{i+\frac12}$ and the general approach will be specified below. For $t > t^n, z \in \mathbb{R}$:

$$\begin{cases} \partial_t \bar{f} + (v_j - \hat{\sigma}^n)\partial_z \bar{f} = \Delta z \mathcal{C}_{i+\frac12}(\bar{f})\delta\left(z - z_{i+\frac12}\right) \\ \bar{f}(t^n, z, v_j) = f^n_{i,j} \text{ if } z < z_{i+\frac12} \text{ and } \bar{f}(t^n, z, v_j) = f^n_{i+1,j} \text{ if } z > z_{i+\frac12}. \end{cases} \tag{4.2.9}$$

We then introduce $\tilde{f}_{i+\frac12,j}$, whose values we will specify below and define the function $\bar{f}$ for $t > t^n, z \in \mathbb{R}$ (see also Figure 4.2):

$$\bar{f}(t,z,v_j) = \begin{cases} f^n_{i,j} & \text{if } v_j < \hat{\sigma}^n \text{ and } z \le z_{i+\frac12} + (v_j - \hat{\sigma}^n)(t - t^n) \\ \tilde{f}_{i+\frac12,j} & \text{if } v_j < \hat{\sigma}^n \text{ and } z_{i+\frac12} + (v_j - \hat{\sigma}^n)(t - t^n) < z < z_{i+\frac12} \\ f^n_{i+1,j} & \text{if } v_j < \hat{\sigma}^n \text{ and } z_{i+\frac12} \le z \\ f^n_{i,j} & \text{if } v_j > \hat{\sigma}^n \text{ and } z \le z_{i+\frac12} \\ \tilde{f}_{i+\frac12,j} & \text{if } v_j > \hat{\sigma}^n \text{ and } z_{i+\frac12} < z < z_{i+\frac12} + (v_j - \hat{\sigma}^n)(t - t^n) \\ f^n_{i+1,j} & \text{if } v_j > \hat{\sigma}^n \text{ and } z_{i+\frac12} + (v_j - \hat{\sigma}^n)(t - t^n) \le z \end{cases} \tag{4.2.10}$$

One easily checks that outside of a neighborhood of $z = z_{i+\frac12}$ the function $\bar{f}$ satisfies Equation (4.2.9). Therefore it remains to define the values $\tilde{f}_{i+\frac12,j}$ in such a way that in a neighborhood of $z = z_{i+\frac12}$, the function $\bar{f}$ is also a solution in a proper sense of Equation (4.2.9). To do so, we state the procedure described in [37] and for the theoretical justifications of this procedure, we refer the reader to [85]. Consider in cell $\bar{C}_{i+\frac12}$ the

following stationary problem with prescribed boundary conditions:

$$\begin{cases} (v_j - \hat{\sigma}^n)\partial_z \tilde{f} = \mathcal{C}_{i+\frac{1}{2}}\left(\tilde{f}\right), \text{ for } z \in \bar{C}_{i+\frac{1}{2}} & (4.2.11) \\ \tilde{f}(z_i, v_j) = \bar{f}^n_{i,j} \text{ if } v_j > \hat{\sigma^n} \text{ and } \tilde{f}(z_{i+1}, v_j) = \bar{f}^n_{i+1,j} \text{ if } v_j < \hat{\sigma^n}. & (4.2.12) \end{cases}$$

This Equation admits a solution $\tilde{f}(z, v_j)$, which we use to define:

$$\tilde{f}_{i+\frac{1}{2},j} = \begin{cases} \tilde{f}(z_{i+1}, v_j) & \text{if } v_j > \hat{\sigma^n} \\ \tilde{f}(z_i, v_j) & \text{if } v_j < \hat{\sigma^n} \end{cases} \tag{4.2.13}$$

In this manner, we properly solve the Riemann Problem (4.2.9). From the Riemann Problem, via the juxtaposition of independent Riemann Problems at each interface $z = z_{i+\frac{1}{2}}$, we can then move on to the general solution of Equation (4.2.8) on the interval (t^n, t^{n+1}) under the CFL condition:

$$\max\{|V - \hat{\sigma}^n|\}\Delta t \leq \Delta z \tag{4.2.14}$$

In practice, since $\hat{\sigma}^n \in \max\{|V|\}$ (see Subsection 4.2.2), it suffices to suppose that:

$$2\max\{|V|\}\Delta t \leq \Delta z \tag{4.2.15}$$

Finally under this CFL condition, we define the Godunov scheme in the following manner:

$$\bar{f}^{n+1}_{i,j} = \begin{cases} \bar{f}^n_{i,j} - \frac{\Delta t}{\Delta z}(v - \hat{\sigma}^n)\left(\bar{f}^n_{i,j} - \tilde{f}^n_{i-\frac{1}{2},j}\right) & \text{if } v > \hat{\sigma}^n \\ \bar{f}^n_{i,j} - \frac{\Delta t}{\Delta z}(v - \hat{\sigma}^n)\left(\tilde{f}^n_{i+\frac{1}{2},j} - \bar{f}^n_{i,j}\right) & \text{if } v < \hat{\sigma}^n \end{cases} \tag{4.2.16}$$

Of note, if $\bar{f}^n$ is exactly the traveling wave solution, then the choice of $\tilde{f}^n$ (which we describe just below) will be such that $\tilde{f}^n_{i+\frac{1}{2},j} = \bar{f}^n_{i+1,j}$ if $v_j > \hat{\sigma}^n$ and $\tilde{f}^n_{i+\frac{1}{2},j} = \bar{f}^n_{i,j}$ if $v_j < \hat{\sigma}^n$. This observation with Scheme (4.2.16) shows that the traveling wave solution is going to be a stationary solution of the numerical scheme (in the moving frame).

Definition of the Scattering Matrix $S_{i+\frac{1}{2}}$.

From the preceding, the remaining question is finding the solution of Equation (4.2.11). Equation (4.2.11) is a linear equation and hence the mapping from the boundary values to the values $\tilde{f}_{i+\frac{1}{2},j}$ will be linear. In particular, we partition $V = V_+ \sqcup V_-$, such that for every $v \in V_+$, $v > \hat{\sigma}^n$ and for every $v \in V_-$, $v < \hat{\sigma}^n$. Then we wish to find the so-called scattering matrix $S_{i+\frac{1}{2}} \in M_{2J}(\mathbb{R})$, such that:

$$\left(\tilde{f}_{i+\frac{1}{2},j}\right)_j = S_{i+\frac{1}{2}} \begin{pmatrix} f_{i+1}(V_-) \\ f_i(V_+) \end{pmatrix} \tag{4.2.17}$$

In the work [37], the authors have proposed two different approaches to derive the scattering matrix $S_{i+\frac{1}{2}}$: one method is based on Case's elementary solutions (see for instance [1, 15, 44]) and the other method is based on a finite-difference approach. Here, we will only focus on the first method.

We look for a solution of Equation (4.2.11) under the form:

$$\tilde{f}(z, v_j) = \sum_{k=1}^{2K} a_k g^k(z, v_j), \tag{4.2.18}$$

where $g^k(z, v_j)$ are the so-called Case's elementary solutions, and as we will see there exists exactly $2K = 2J$ such solutions (the parameter K has been introduced for the sake of readibility). Case's elementary solutions are in separated variables under the form:

$$g^k(z, v_j) = e^{\mu_k z} F^k(v_j) \tag{4.2.19}$$

In order to find the exact expression of Case's elementary solutions (4.2.19), we solve the following spectral problem (μ, F^μ), with $\frac{1}{2J}\sum_{j\in\mathcal{J}} F^\mu(v_j) = 1$:

$$(v_j - \sigma)\mu F^\mu(v_j) = \mathcal{C}(F^\mu)(v_j) \tag{4.2.20}$$

Problem (4.2.20) depends on the shape of $\mathcal{C}$. We start by exhibiting the solutions of Problem (4.2.20) in the Grow case. Using the fact that $\rho_{F^\mu} = \frac{1}{2J}\sum_{j\in\mathcal{J}} F^\mu(v_j) = 1$, we can rewrite (4.2.20) to obtain the following expression of F^μ (as a function of μ):

$$F^\mu(v_j) = \frac{1 + \alpha^2 M_{\text{GROW}}(v_j)}{\alpha^2 + \mu(v_j - \sigma)} \tag{4.2.21}$$

In order to determine μ, we simply use the property that $\rho_{F^\mu} = 1$, which leads to the following equation:

$$\frac{1}{2J}\sum_{j\in\mathcal{J}} \frac{1 + \alpha^2 M_{\text{GROW}}(v_j)}{\alpha^2 + \mu(v_j - \sigma)} = 1 \tag{4.2.22}$$

Then any μ satisfying Equation (4.2.22) leads via Equation (4.2.21) to a solution (μ, F^μ) of Problem (4.2.20).

Similarily in the Go case, we obtain the following expression for the solutions of Problem (4.2.20):

$$\frac{1}{2J}\sum_{j\in\mathcal{J}} \frac{\alpha^2 M_{\text{GO}}(v_j)}{\alpha^2 + \mu(v_j - \sigma)} = 1 \tag{4.2.23}$$

$$F^\mu(v_j) = \frac{\alpha^2 M_{\text{GO}}(v_j)}{\alpha^2 + \mu(v_j - \sigma)} \tag{4.2.24}$$

Solving Problem (4.2.20) in the Grow case.

We are looking for the roots μ in Equation (4.2.22). We introduce the function:

$$H^\sigma : \mu \mapsto \frac{1}{2J}\sum_{j\in\mathcal{J}} \frac{1 + \alpha^2 M_{\text{GROW}}(v_j)}{\alpha^2 + \mu(v_j - \sigma)} - 1 \tag{4.2.25}$$

H^σ has $2K$ poles which can be ordered in the following manner: set $p_k := \frac{\alpha^2}{\sigma - v_k}$ and let κ be the greatest integer such that $v_\kappa < \sigma$, the poles (p_k) satisfy the following order:

$$p_{\kappa+1} < p_{\kappa+2} < \ldots < p_{2K} < 0 < p_1 < p_2 < \ldots < p_\kappa$$

It can be shown that H^σ has the following behavior (see Figure 4.3):

- On $(-\infty, p_{\kappa+1})$, H^σ is strictly decreasing from -1 to $-\infty$, and does not admit any root.

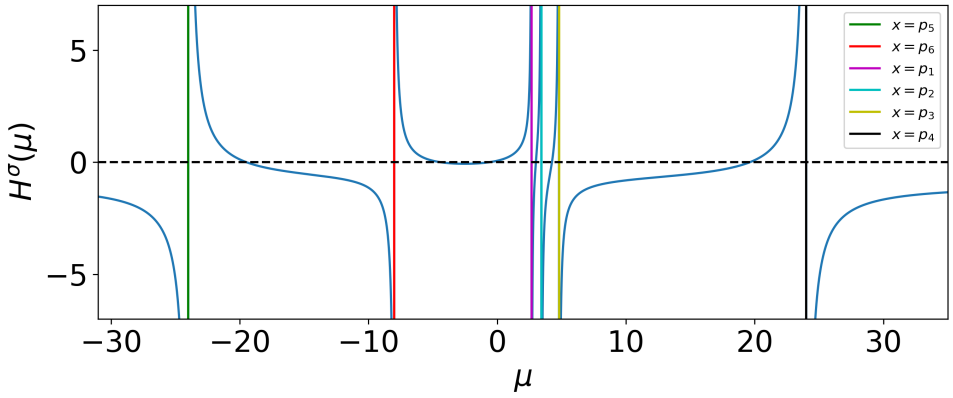

Figure 4.3: Graphic representation of $\mu \mapsto H^\sigma(\mu)$ in the Grow case, when $K = 6, V = \left\{-4, -\frac{8}{3}, -\frac{4}{3}, \frac{4}{3}, \frac{8}{3}, 4\right\}, \alpha = 4$, $M_{GROW} \equiv 1$ and $\sigma = 2$. In this case, on the interval (p_6, p_1), H^σ admits two distinct real roots. For other choices of σ, H^σ may admit a double real root on the interval (p_6, p_1), or a pair of complex-conjugated roots.

- For $k = \kappa + 1 \dots 2K - 1$, on (p_k, p_{k+1}), H^σ decreases from $+\infty$ to $-\infty$ and admits a unique root, which we denote μ_k. The root μ_k may be found numerically via a simple dichotomic search.

- On (p_{2K}, p_1), H^σ decreases and then increases and three different cases may exist on this interval:

  - H^σ admits two distinct real roots, which we denote $\mu_{2K} < \mu_1$,
  - H^σ admits a double real root and we denote it by convention $\mu_{2K} = \mu_1$,
  - H^σ doesn't admit any real root, but admits two complex-conjugated roots, which we denote $\mu_{2K} = \bar{\mu_1}$.

- For $k = 1 \dots \kappa - 1$, on (p_k, p_{k+1}), H^σ increases from $-\infty$ to $+\infty$ and admits a unique root, which we denote μ_{k+1}. This root may again be found numerically via a simple dichotomic search.

- On $(p_\kappa, +\infty)$ H^σ is strictly increasing from $-\infty$ to -1, and does not admit any root.

Hence H^σ admits exactly $2K$ roots (counted with multiplicity), which *a posteriori* justifies the claimed equality $2K = 2J$. All roots except μ_{2K}, μ_1 can be found very simply numerically. In order to compute the roots μ_{2K}, μ_1, we procede as follows:

For $P(\mu) := \Pi_{k=2}^{2K-1}(\mu - \mu_k)$ and $Q(\mu) := \Pi_{k=1}^{2K}(\mu - p_k)$, we write:

$$H^\sigma(\mu) = \frac{(a\mu^2 + b\mu + c)P(\mu)}{Q(\mu)}$$

By taking either limit $\mu \to \pm\infty$, we find that $a = -1$. Furthemore, we have that:

$$c = \frac{Q(0)H^\sigma(0)}{P(0)} = \frac{\Pi_{k=1}^{2K} p_k}{\Pi_{k=2}^{2K-1} \mu_k} H^\sigma(0)$$

And by taking the derivative and evaluating at $\mu = 0$ (which is not a root for H, as can be easily checked:

$$b = \frac{H^\sigma Q}{P}\left(\frac{H^{\sigma'}}{H^\sigma} + \frac{Q'}{Q} - \frac{P'}{P}\right)_{|\mu=0} = \gamma\left(\frac{H'(0)}{H(0)} - \sum_{k=1}^{2K}\frac{1}{p_k} + \sum_{k=2}^{2K-1}\frac{1}{\mu_k}\right)$$

Finally, we can solve the polynomial $a\mu^2 + b\mu + c$, whose roots are then μ_1, μ_{2K}.

Alternatively, in the case, where the roots μ_{2K}, μ_1 are real, one can find the unique point q, where $H^{\sigma'}$ cancels on the interval (p_{2K}, p_1), and then find via a dichotomic search the root on the interval (p_{2K}, q) and the root on the interval (q, p_1). Numerically, this approach is more precise, especially for K large. However, since the roots $\mu_2, \ldots, \mu_{2K-1}$ are found via a dichotomic search, they can be found with arbitrary precision at low computational cost. Hence the approach described above can also be arbitraily precise at low computational cost.

Solving Problem (4.2.20) in the Go case.

The Go case is treated similarily. We introduce:

$$H^\sigma : \mu \mapsto \frac{1}{2J}\sum_{j\in\mathcal{J}}\frac{\alpha^2 M_{\mathrm{GO}}(v_j)}{\alpha^2 + \mu(v_j - \sigma)} - 1 \tag{4.2.26}$$

The behavior of H^σ is the same as in the Grow case, but on the interval (p_{2K}, p_1), H^σ will always admit two real roots. In fact, one checks that $\mu = 0$ is a root for H and that $H'(0) = \sigma - \chi$. Hence either $\sigma = \chi$ and 0 is a double root, or $\sigma \neq \chi$ and another root exists on the interval (p_{2K}, p_1). Suppose that $\sigma > \chi$ (for the case $\sigma < \chi$ a similar reasoning applies), then $\mu_1 = 0$ and the remaining root μ_{2K} is negative. Finally by setting $R(\mu) = \mu - \mu_{2K}$,we yield the following relationship:

$$\frac{RP}{Q} = \frac{H^\sigma}{\mu}$$

By taking the limit $\mu \to 0$ we find that:

$$\mu_{2K} = \frac{\Pi_{k=1}^{2K} p_k}{\Pi_{k=2}^{2K-1}\mu_k} H^{\sigma'}(0).$$

Alternatively, to find the root μ_{2K}, one can find the unique point q, where $H^{\sigma'}$ cancels on the interval $(p_{2K}, 0)$, and then find via a dichotomic search the root μ_{2K} on the interval (p_{2K}, q). The same remarks than for the Grow case apply concerning the precision of this method.

The shape of g^{2K}, g^1, when the roots μ_{2K}, μ_1 are complex-conjugated or are equal.

As noted above in the Grow case, the roots μ_{2K}, μ_1 may be complex-conjugated. In that situation, F^{2K}, F^1 are also complex-conjugated. In order to avoid dealing with complex values, we may then define the functions g^{2K}, g^1 as follows:

$$\begin{aligned} g^{2K}(z, v_j) &:= e^{\mu_{2K} z} F^{2K}(v_j) + e^{\mu_1 z} F^1(v_j), \\ g^1(z, v_j) &:= i\left(e^{\mu_{2K} z} F^{2K}(v_j) - e^{\mu_1 z} F^1(v_j)\right). \end{aligned}$$

Because $F^{2K} = \overline{F^1}$ and $\mu_{2K} = \overline{\mu_1}$, g^{2K}, g^1 are real functions.

When $\mu_{2K} = \mu_1$, then one defines:

$$g^{2K}(z, v_j) := e^{\mu_{2K} z} F^{2K}(v_j),$$
$$g^1(z, v_j) := z e^{\mu_{2K} z} F^{2K}(v_j).$$

Computing the Scattering Matrix $S_{i+\frac{1}{2}}$.

Given the solutions g^k, we define the matrices $M = (m_{jk})_{jk}$ and $\tilde{M} = (\tilde{m}_{jk})_{jk}$ such that:

$$m_{jk} = \begin{cases} g^k(z_i, v_j) & \text{if } v_j < \sigma \\ g^k(z_{i+1}, v_j) & \text{if } v_j > \sigma \end{cases} \text{ and } \tilde{m}_{jk} = \begin{cases} g^k(z_{i+1}, v_j) & \text{if } v_j < \sigma \\ g^k(z_i, v_j) & \text{if } v_j > \sigma \end{cases}$$

Then one obtains the following relations:

$$\begin{pmatrix} f_{i+1}(V_-) \\ f_i(V_+) \end{pmatrix} = MA \text{ and } \left(\tilde{f}_{i+\frac{1}{2},j}\right)_j = \tilde{M}A,$$

with $A = (a_k)_k$. Finally by setting $S_{i+\frac{1}{2}} := \tilde{M}M^{-1}$, we therefore obtain:

$$\left(\tilde{f}_{i+\frac{1}{2},j}\right)_j = S_{i+\frac{1}{2}} \begin{pmatrix} f_{i+1}(V_-) \\ f_i(V_+) \end{pmatrix} \tag{4.2.27}$$

Of note, Equation (4.2.11) is translation invariant with respect to z, *i.e.* the solution of Equation (4.2.11) is the same if $z \leftarrow z + h$. This actually shows that the definition of the scattering matrix $S_{i+\frac{1}{2}}$ for each time step only depends on the fact whether at $z_{i+\frac{1}{2}}$ the scattering operator is in the Go case or the Grow case. Hence, at each time step, we just need to compute two scattering matrices (one for the Grow case and one for the Go case).

A WB Shift to the Stationary Frame

In the preceding step, we have computed $\bar{f}_{i,j}^{n+1}$, which is an approximation of f in the shifted frame $(t, z) = (t, x - \hat{\sigma}^n(t - t^n))$, *i.e.* $\bar{f}_{i,j}^{n+1} \approx \bar{f}(t^{n+1}, z_i, v_j) \approx f(t^{n+1}, x_i - \hat{\sigma}^n(t^{n+1} - t^n), v_j)$. We now wish to find a good approximation of $f(t^{n+1}, x_i, v_j)$. For this approximation, we consider the stationary state in the moving frame $(t, z) = (t, x - \hat{\sigma}^n(t - t^n))$, with prescibed boundary conditions given by $\bar{f}_{i,j}^{n+1}$:

$$\begin{cases} (v_j - \hat{\sigma}^n)\partial_z \hat{f} = \mathcal{C}_{i+\frac{1}{2}}\left(\hat{f}\right), \text{ for } z \in C^-_{i+\frac{1}{2}} \\ \hat{f}(z_i, v_j) = \bar{f}_{i,j}^n \text{ if } v_j > \hat{\sigma^n} \text{ and } \hat{f}(z_{i+1}, v_j) = \bar{f}_{i+1,j}^n \text{ if } v_j > \hat{\sigma^n} \end{cases} \tag{4.2.28}$$

We then define:

$$f_{i,j}^{n+1} = \hat{f}(z_i + \hat{\sigma}^n \Delta t, v_j) \tag{4.2.29}$$

Through this procedure, if $\hat{\sigma}^n = \sigma$ and $\bar{f}_{i,j}^{n+1}$ is a discretization of the traveling wave associated with speed σ, then $f_{i,j}^{n+1}$ will be exactly equal to the discretization shifted in space by $\sigma\Delta t$ of the same travelig wave. Hence, this procedure is well-balanced with respect to the traveling wave moving at speed σ.

In practice, to compute the values $\hat{f}(z_i, v_j)$, we use Case's elementary solutions, similarily to what we have done for the computation of the scattering matrix $S_{i+\frac{1}{2}}$. Given Case's

elementary solutions and under the condition $\hat{\sigma}^n \geq 0$, we set the matrices $N = (n_{jk})_{jk}$ and $\tilde{N} = (\tilde{n}_{jk})_{jk}$ such that:

$$n_{jk} = \begin{cases} g^k(z_i, v_j) & \text{if } v_j < \sigma \\ g^k(z_{i+1}, v_j) & \text{if } v_j > \sigma \end{cases} \quad \text{and } \tilde{m}_{jk} = g^k(z_i + \hat{\sigma}^n \Delta t, v_j)$$

Then we define $T_{i+\frac{1}{2}} := \tilde{N} N^{-1}$, which finally leads to:

$$\left(f_{i,j}^{n+1}\right)_j = T_{i+\frac{1}{2}} \begin{pmatrix} \left(\bar{f}_{i+1,j}^n\right)_{j \in \mathcal{J}_-} \\ \left(\bar{f}_{i,j}^n\right)_{j \in \mathcal{J}_+} \end{pmatrix} \tag{4.2.30}$$

Here again because of the invariance by translation, the values of $T_{\frac{1}{2}}$ depend only on whether at the point of the grid we are in the Go or Grow case.

Crank-Nicolson Scheme for N

The computation of N on the grid points (t^n, x_i) is done via a standard Crank-Nicolson scheme:

$$\frac{N_i^{n+1} - N_i^n}{\Delta t} = \frac{N_{i-1}^{n+1} - 2N_i^{n+1} + N_{i+1}^{n+1}}{2\Delta x^2} + \frac{N_{i-1}^n - 2N_i^n + N_{i+1}^n}{2\Delta x^2} - \frac{N_i^{n+1} + N_i^n}{2} \rho_i^{n+1} \tag{4.2.31}$$

This approach is not WB. One could use the methodology proposed in [87] combined with the LeVeque-Yee formula, in order to propose a WB scheme for N. However, this would be computationally more costly, as for each cell C_i, one needs to solve a different stationary problem. Furthermore, the coupling between N and f in System (4.1.3) is very weak and depends merely on $\bar{x}(t)$, the position of the threshold, *i.e.* $N(t, \bar{x}(t)) = N_{\text{th}}$. Hence, it is reasonnable to assume that using the simpler Crank-Nicolson scheme for N will not result in any substantial deterioriation of accuracy.

Computation of the Scattering Operator $\mathcal{C}_{i+\frac{1}{2}}^n$

In order to compute the scattering operator $\mathcal{C}_{i+\frac{1}{2}}^n$, we use the following approximations for $N_{i+\frac{1}{2}}^n$ and $\partial_x N_{i+\frac{1}{2}}^n$:

$$N_{i+\frac{1}{2}}^n = \frac{N_i^n + N_{i+1}^n}{2} \tag{4.2.32}$$

$$\partial_x N_{i+\frac{1}{2}}^n = \frac{N_{i+1}^n - N_i^n}{\Delta x} \tag{4.2.33}$$

4.2.3 Alternative Operator-Splitting (OS) Schemes

In order to compare the preceding WB scheme to other numerical schemes, we propose alternative schemes based on an OS of the free-transport operator and the scattering operator. We denote $g_{i,j}^{n+1}$ the value obtained via the discretization of the free-transport operator with the initial values $f_{i,j}^n$ and then $f_{i,j}^{n+1}$ is set as the value obtained via the discretization of the scattering operator. On the one hand, we use an upwind discretization of the free-transport operator, and on the other hand we use a weighted essentially non-oscillatory (WENO) method, such as proposed in [106, 125]. For the discretization of the scattering operator we use also two methods: first, an explicit Euler time integration;

second an exact integration in time, which is possible here, because of the linear nature of the scattering operator. The latter method is obviously better suited to the problem, but the Euler approach will be interesting, when comparing the numerical schemes and drawing conclusions. This leads to four numerical schemes, which we will refer to: UW-Euler, UW-Exact, WENO-Euler and WENO-Exact.

Upwind Discretization of the Free-Transport Operator

The free-transport operator is discretized on the time interval (t^n, t^{n+1}) via the standard upwind method:

$$g_{i,j}^{n+1} = f_i^n + \frac{v_j \Delta t}{\Delta x} \left(f_i^n - f_{i-1}^n \right) \text{ for } j = 1, \ldots, J \tag{4.2.34}$$

$$g_{i,j}^{n+1} = f_i^n + \frac{v_j \Delta t}{\Delta x} \left(f_{i+1}^n - f_i^n \right) \text{ for } j = -J, \ldots, -1 \tag{4.2.35}$$

WENO Discretization of the Free-Transport Operator

We use the 5th-order WENO scheme introduced in [106]. This scheme discretizes the free-transport operator in a highly accurate manner. We briefly describe the scheme and refer the reader to [165], whose notations we follow here, for further information about this scheme (see also [164]). The space derivative is discretized in the following manner:

$$\partial_x f_{i,j} = \frac{1}{\Delta x} \left(\hat{f}_{i+\frac{1}{2},j} - \hat{f}_{i-\frac{1}{2},j} \right). \tag{4.2.36}$$

The values of $\hat{f}_{i+\frac{1}{2}}$ with $j = 1, \ldots, J$ are a weighted average of three values using three different stencils:

$$\hat{f}_{i+\frac{1}{2},j} = w_1 \hat{f}^{(1)}_{i+\frac{1}{2},j} + w_2 \hat{f}^{(2)}_{i+\frac{1}{2},j} + w_3 \hat{f}^{(3)}_{i+\frac{1}{2},j}, \tag{4.2.37}$$

with:

$$\begin{aligned}
\hat{f}^{(1)}_{i+\frac{1}{2},j} &= \frac{1}{3} f_{i-2,j} - \frac{7}{6} f_{i-1,j} + \frac{11}{6} f_{i,j}, \\
\hat{f}^{(2)}_{i+\frac{1}{2},j} &= -\frac{1}{6} f_{i-1,j} + \frac{5}{6} f_{i,j} + \frac{1}{3} f_{i+1,j}, \\
\hat{f}^{(3)}_{i+\frac{1}{2},j} &= \frac{1}{3} f_{i,j} + \frac{5}{6} f_{i+1,j} - \frac{1}{6} f_{i+2,j}.
\end{aligned}$$

w_i in (4.2.37) are nonlinear weights, which are given by the following relations:

$$\begin{aligned}
w_i &= \frac{\tilde{w}_i}{\tilde{w}_1 + \tilde{w}_2 + \tilde{w}_3} \text{ and } \tilde{w}_i = \frac{\gamma_i}{(\varepsilon + \beta_i)^2} \\
\gamma_1 &= \frac{1}{10}, \gamma_2 = \frac{3}{5}, \gamma_3 = \frac{3}{10}.
\end{aligned}$$

Finally the values β_i are the so-called smoothness indicators:

$$\begin{aligned}
\beta_1 &= v_j^2 \left(\frac{13}{12} \left(f_{i-2,j} - 2 f_{i-1,j} + f_{i,j} \right)^2 + \frac{1}{4} \left(f_{i-2,j} - 4 f_{i-1,j} + 3 f_{i,j} \right)^2 \right), \\
\beta_2 &= v_j^2 \left(\frac{13}{12} \left(f_{i-1,j} - 2 f_{i,j} + f_{i+1,j} \right)^2 + \frac{1}{4} \left(f_{i-1,j} - f_{i+1,j} \right)^2 \right), \\
\beta_3 &= v_j^2 \left(\frac{13}{12} \left(f_{i,j} - 2 f_{i+1,j} + f_{i+2,j} \right)^2 + \frac{1}{4} \left(3 f_{i,j} - 4 f_{i+1,j} + f_{i+2,j} \right)^2 \right).
\end{aligned}$$

For $j = -J, \ldots, -1$, one uses exactly the same formulae to compute $\hat{f}_{i+\frac{1}{2},j}$ by replacing the list $(f_{i-2,j}, f_{i-1,j}, f_{i,j}, f_{i+1,j}, f_{i+2,j})$ with the list $(f_{i+3,j}, f_{i+2,j}, f_{i+1,j}, f_{i,j}, f_{i-1,j})$.

It turns out that the time integration plays a crucial role in this procedure and for instance an explicit Euler method is unstable with the discretization given by (4.2.36) [187]. As explained in [165], one should use a strong stability preserving (SSP) Runge-Kutta time integrator [90], which goes as follows:

$$\begin{aligned} f^{(1)} &= f^n + \Delta t L(f^n), \\ f^{(2)} &= \frac{3}{4} f^n + \frac{1}{4} f^{(1)} + \frac{1}{4} \Delta t L(f^{(1)}), \\ f^{n+1} &= \frac{1}{3} f^n + \frac{2}{3} f^{(2)} + \frac{2}{3} \Delta t L(f^{(2)}), \end{aligned}$$

where $L(f)$ is given by (4.2.36).

Explicit Euler Integration of the Scattering Operator

The explicit Euler integration in time of the scattering operator simply goes as follows:

$$f^{n+1} = g^{n+1} + \Delta t \mathcal{C}(g^{n+1}). \tag{4.2.38}$$

Exact Computation of the Scattering Operator

As a more precise alternative to the Euler integration in time, we observe that the evolution operator $e^{\Delta t \mathcal{C}}$ can be computed explicitly. In fact set:

$$E_{\text{GROW}} = e^{\Delta t \mathcal{C}_{\text{GROW}}} = \exp\left(\Delta t \left(\alpha^2 \left(\frac{1}{2J} \text{diag}((M_{\text{GROW}}(v_j))_{j \in \mathcal{J}}) J_{2J} - I_{2J}\right) + \frac{1}{2J} J_{2J}\right)\right) \tag{4.2.39}$$

$$E_{\text{GO}} = e^{\Delta t \mathcal{C}_{\text{GO}}} = \exp\left(\Delta t \alpha^2 \left(\frac{1}{2J} \text{diag}((M_{\text{GO}}(v_j))_{j \in \mathcal{J}}) J_{2J} - I_{2J}\right)\right), \tag{4.2.40}$$

where I_{2J} is the $2J \times 2J$ identity matrix and J_{2J} the $2J \times 2J$ matrix composed of ones.

Thus we obtain:

$$\left(f_{i,j}^{n+1}\right)_j = E_{\text{GROW}} \left(g_{i,j}^{n+1}\right)_j \text{ or } \left(f_{i,j}^{n+1}\right)_j = E_{\text{GO}} \left(g_{i,j}^{n+1}\right)_j, \tag{4.2.41}$$

depending on which case applies.

4.2.4 Numerical Assessements

The code for the numerical schemes in this Section can be found in [53].

Condition number for $S_{i+\frac{1}{2}}$ and $T_{i+\frac{1}{2}}$

When solving Problem (4.2.11) (resp. Problem (4.2.28)) via the matrix $S_{i+\frac{1}{2}}$ (resp. $T_{i+\frac{1}{2}}$), we face a difficulty when $\hat{\sigma}^n = v_j$ for some $j \in \mathcal{J}$, since both problems are not well-posed. In practice, because $\hat{\sigma}^n$ is a numerical estimate, the likelihood of $\hat{\sigma}^n = v_j$ is extremely low. However, this raises the question what happens when $\hat{\sigma}^n \approx v_j$. Hence, we consider the condition number of $S_{i+\frac{1}{2}}$ and $T_{i+\frac{1}{2}}$ as a function of $\sigma = \hat{s}^n$ (see Figure 4.4). We observe that when σ is close to v_j, the matrices become ill-conditioned, whereas they are

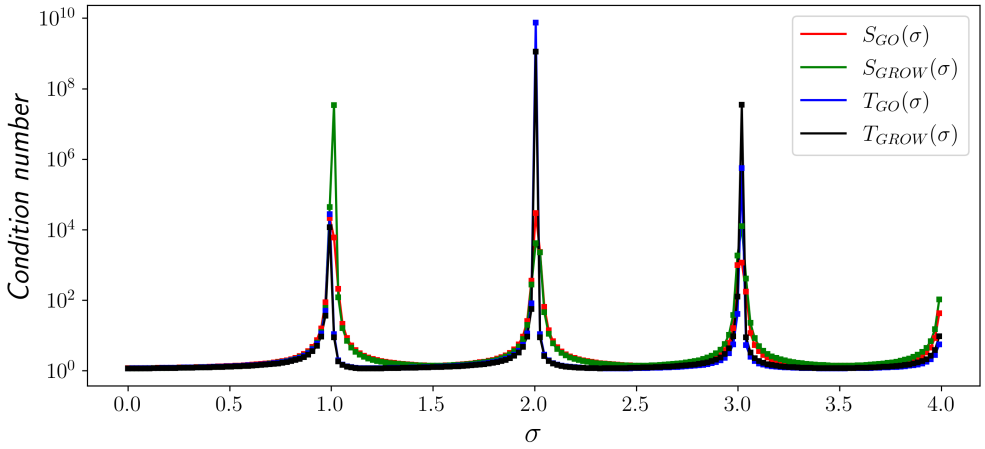

Figure 4.4: Condition numbers of $S_{GROW}(\sigma), S_{GO}(\sigma), T_{GROW}(\sigma)$ and $T_{GO}(\sigma)$ for $V = \{-4, -3, -2, -1, 1, 2, 3, 4\}$ and $\chi = 2$.

well-conditioned as soon as $|\sigma - v_j|$ is not too small for all $j \in \mathcal{J}$. Hence, one should verify this condition when using the WB scheme, at least *a posterio* (since in most cases it is difficult to estimate *a priori* the asymptotic behavior of $\hat{\sigma}^n$. In the simulations presented in this article, this condition is verified.

Comparison with OS Schemes

In this Subsection, we present preliminary numerical results, which compare the WB scheme with the other OS Schemes. These results show that the WENO-Exact scheme captures best the wave speed and the WB scheme does not perform substantially better than the other OS schemes. Similar observations are valid for the exponential decay rate. In our opinion, these results ask for a deeper analysis: in fact from Chapter 2, we know that the wave speed is set by the interface at which $N = N_{\text{th}}$. Thus, we believe that by better dealing with the dynamics at the interface, we can improve the performances of the WB scheme. This is currently under investigation. Yet, interestingly the WB scheme is the only scheme which captures in a consistent way simultaneously the numerical speed and the numerical exponential decay rate, *i.e.* $\mu_{\text{num}} \approx \mu_{\text{th}}(\sigma_{\text{num}})$ (see below for more details).

We analyze the results by considering the spreading speed and the exponential decay parameter at the leading edge of the front. The spreading speed has in all cases been measured with LeVeque-Yee Formula (4.2.6). The exponential decay parameter has been measured by computing the mean of the logarithmic derivative of ρ on the interval $[\bar{x}(t) + 2, \bar{x}(t) + 4]$, where we recall that $\bar{x}(t)$ is the position of the threshold, *i.e.* $N(t, \bar{x}(t)) = N_{\text{th}}$. This interval has been chosen, because there the logarithmic derivative is essentially constant: in particular we observe that the more points are used in the discretization of the grid, the preciser and more reliable this procedure becomes. For the initial data, we have taken profiles (f, N) close to the expected wave profiles by running the simulation once and looping the profiles. This has been done in particular, because we are interested in the asymptotic behavior of the traveling wave.

First, we have tested the aforementioned schemes in the two-velocity case with $\chi = 2$ and $V = \{-\alpha, \alpha\}$ for $\alpha = 4$ (see Figure 4.5) and $\alpha = 8$ (see Figure 4.10 in Appendix).

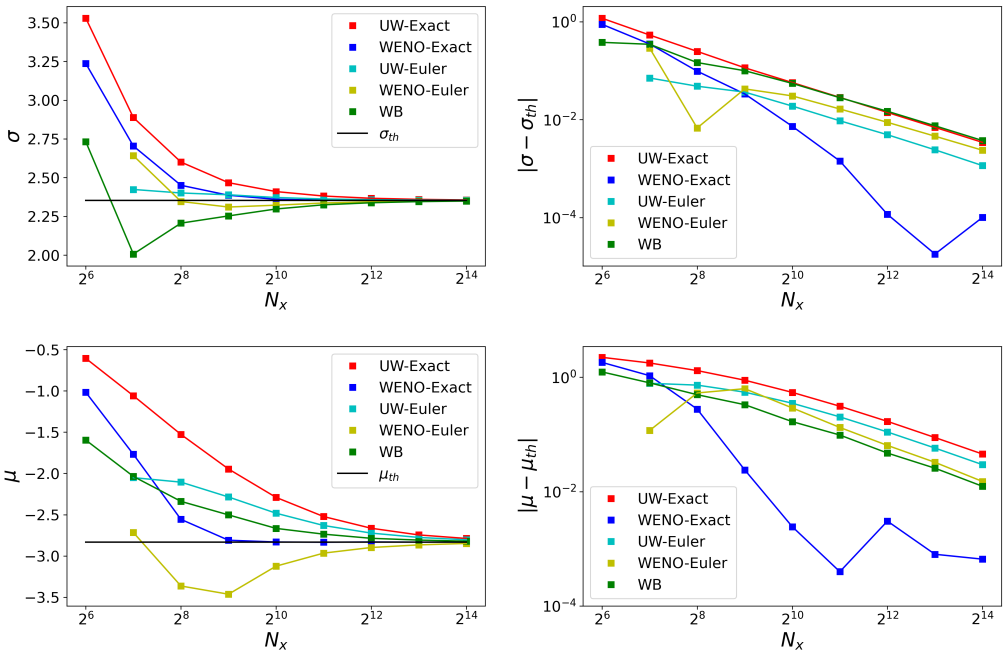

Figure 4.5: Comparison between performances of UW-Euler (cyan), UW-Exact (red), WENO-Euler (yellow), WENO-Exact (blue) and WB scheme (green) as a function of N_x, the number of points of the spatial discretization. Upper left: Plot of the numerical speed σ. Upper right: Plot of the absolute value of the numerical speed σ and the theoretical speed σ_{th} in log-scale. Lower left: Plot of the numerical exponential decay parameter μ. Lower right: Plot of the absolute value of the numerical exponential decay parameter μ and the theoretical exponential decay parameter μ_{th} in log-scale. Choice of parameters: $\boldsymbol{V = \{-4, 4\}, \alpha = 4}, \chi = 2, L = 100, dx = \frac{L}{N_x}$, $T = 15$, CFL $= 0.5$ and $\Delta t = \frac{\Delta}{2\alpha}$.

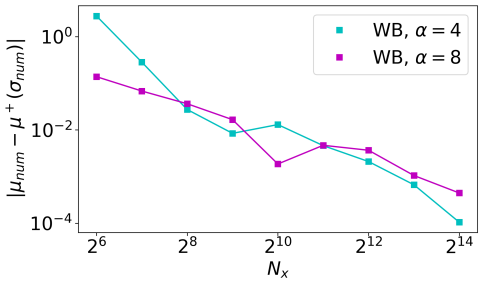

Figure 4.6: Plot in log-scale of the absolute value between μ_{num} the numerical exponential decay parameter and the $\mu_+(\sigma)$ theoretical exponential decay parameter given by Formula (4.2.1) when $\sigma = \sigma_{num}$ the numerical wave speed. Choice of parameters: $V = \{-4, 4\}, \chi = 2, L = 100, dx = \frac{L}{N_x}$, $T = 15$, CFL $= 0.5$ and $\Delta t = \frac{\Delta}{2\alpha}$.

In both cases results are comparable. Concerning the spreading speed σ, the WENO-Exact scheme performs much better than the other ones. Surpisingly, UW-Euler performs second best for the spreading speed. Moreover, we can observe that the WB and WENO-

Euler scheme underestimates the speed, whereas the other schemes overestimate the speed. Concerning the exponential decay parameter, again the WENO-Exact scheme performs much better than the other schemes. The WB scheme performs second best. In all cases except for WENO-Euler, the exponential decay parameter is overestimated. However, the WB scheme realizes the following interesting feature: the exponential decay parameter is extremely close to the decay parameter of a wave that would travel at the numerical speed (see Figure 4.6), *i.e.* which we compute via Formula (4.2.1) for μ_+. The other schemes do not satisfy this property, as can simply be seen from the fact that $\sigma \mapsto \mu_+(s)$ is decreasing, but WENO-Exact, UW-Euler and UW-Exact (resp. WENO-Euler) schemes overestimate (resp. underestimate) the speed, which leads to μ_+ smaller (resp. larger) than the theoretical value. Yet, the three schemes overestimate (resp. underestimate) the exponential decay parameter. This property might be interesting if we are interested in numerical schemes, which capture in a consistent way the speed and the exponential decay parameter simultaneously.

Finally, we have also tested the three schemes WB, WENO-Exact and UW-Exact in the eight-velocity case (see Figure 4.11 in Appendix). There, we are lacking an explicit wave formula, but it seems as if the WENO-Exact scheme converges fastest to a value for the wave speed and a value for the exponential decay rate. Thus, we use these values computed with the finest mesh as reference values. Then, similar observations as in the two-velocity case apply.

4.3 A WB Scheme for F/KPP Equation

4.3.1 A WB Approach for F/KPP Equation

In order to solve numerically F/KPP Equation (4.1.8) in a WB manner, we propose a numerical scheme, that is in its structure very similar to the numerical scheme proposed for the kinetic Go or Grow Model (4.1.3). The main differences lie in the fact, that (i) F/KPP Equation (4.1.8) is parabolic, whereas Equation (4.1.3a) is kinetic. Hence we must adapt the well-balanced approach in order to account for parabolic equations. In [87], the author has proposed exactly such an approach for parabolic operators. (ii) Contrary to what we have done for the kinetic Go or Grow Model (4.1.3) and to what has been proposed in [87], here we also investigate an implicit Euler method for time integration, besides the standard explicit Euler method for time integration. In fact, as has been pointed out in [87], for the explicit Euler method, one requires essentially a parabolic CFL condition in order to guarantee stability. For the implicit Euler method, through numerical investigation, we observe that a hyperbolic CFL condition is sufficient. Moreover, resolving the time integration implicitly comes computationally at not too high of a cost, because of the special tridiagonal structure of the problem. Of note, one could propose a similar approach for the kinetic Go or Grow Model (4.1.3), but the structure there is block tridiagonal with matrix blocks of size $2J \times 2J$, making the implementation a bit more involved, and for the kinetic model, we are not limited by a parabolic CFL condition.

We consider a nonuniform Cartesian grid $(t^n) \times (x_i)$, with $x_i = i\Delta x$, for $i \in \mathbb{Z}$ for a given Δx. Contrary to what has been done before the time points (t^n) are set dynamically, because of the lack of an *a priori* bound to satisfy a CFL condition. We set $\Delta t^n = t^{n+1} - t^n$. As before, we introduce the parallel grid with points $z_i = i\Delta z$, $\Delta z = \Delta x$, $\bar{C}_{i+\frac{1}{2}} = (z_i, z_{i+1})$ and consider $u_i^n \approx u(t^n, x_i)$.

The procedure of the numerical scheme can be summarized as follows:

1. We use LeVeque-Yee Formula (4.1.2) on the profile u in order to obtain an estimate

$\hat{\sigma}^n$ of the propagation speed.

2. Given $\hat{\sigma}^n$, on the time interval (t^n, t^{n+1}) we consider u in the moving frame $(t, z) = (t, x - \hat{\sigma}^n(t - t^n))$ and denote it by $\bar{u}$, which leads to Equation:

$$\partial_t \bar{u} - \hat{\sigma}^n \partial_z \bar{u} - \partial_{zz} \bar{u} = \bar{u}(1 - \bar{u}) \tag{4.3.1}$$

In order to deal with the nonlinear term in the right hand-side of Equation (4.3.1), we freeze the non-linear contribution to the term on each mesh $(t^n, t^{n+1}) \times \bar{C}_{i+\frac{1}{2}}$ by considering that $\bar{u}(1-\bar{u}) \approx \bar{u}\left(1 - \bar{u}^n_{i+\frac{1}{2}}\right)$, where $\bar{u}^n_{i+\frac{1}{2}} = \frac{\bar{u}^n_i + \bar{u}^n_{i+1}}{2}$. As has been noted in the Introduction (4.1.2), the dynamics of Equation (4.1.8) is predominantly set by the dynamics at the leading edge of the profile, where $u \sim 0$. There, the linearization of Equation (4.1.8) approximates extremely well the nonlinear Equation. Hence it is reasonnable to expect that this way of handling numerically the nonlinearity will not influence much the dynamics of the propagation. Thanks to the freezing of the nonlinearity, we obtain a linear problem for which we can apply the methodology of $\mathscr{L}$-spline interpolation, as proposed in [87]. Yet, as mentioned above, we propose either an explicit time integration, which leads to:

$$\begin{cases} -\hat{\sigma}^n \partial_z \bar{u} - \partial_{zz} \bar{u} = \bar{u}(1 - \bar{u}^n_{i+\frac{1}{2}}), \text{ for } z \in \bar{C}_{i+\frac{1}{2}} \\ \bar{u}(z_i) = \bar{u}^n_i \text{ and } \bar{u}(z_{i+1}) = \bar{u}^n_{i+1}, \end{cases} \tag{4.3.2}$$

or as an alternative an implicit time integration, which leads to:

$$\begin{cases} -\hat{\sigma}^n \partial_z \bar{u} - \partial_{zz} \bar{u} = \bar{u}(1 - \bar{u}^n_{i+\frac{1}{2}}), \text{ for } z \in \bar{C}_{i+\frac{1}{2}} \\ \bar{u}(z_i) = \bar{u}^{n+1}_i \text{ and } \bar{u}(z_{i+1}) = \bar{u}^{n+1}_{i+1}. \end{cases} \tag{4.3.3}$$

3. It remains to shift back to the stationary frame (t, x). Just as in the case of System (4.1.3), we use the values $\bar{u}^{n+1}_i$, which approximate $\bar{u}(t^{n+1}, z_i)$ in order to extrapolate a value for $u(t^{n+1}, x_i)$, *i.e.* $\bar{u}(t^{n+1}, z_i + \hat{\sigma}^n \Delta t^n)$. To do so we consider the stationary solution $\hat{u}$ of Equation (4.3.1) in the cell $\bar{C}_{i+\frac{1}{2}}$:

$$\begin{cases} -\hat{\sigma}^n \partial_z \hat{u} - \partial_{zz} \hat{u} = \hat{u}(1 - \bar{u}^n_{i+\frac{1}{2}}), \text{ for } z \in \bar{C}_{i+\frac{1}{2}} \\ \hat{u}(z_i) = \bar{u}^{n+1}_i \text{ and } \hat{u}(z_{i+1}) = \bar{u}^{n+1}_{i+1}, \end{cases} \tag{4.3.4}$$

with $\bar{u}^n_{i+\frac{1}{2}} = \frac{\bar{u}^n_i + \bar{u}^n_{i+1}}{2}$. Finally, we set:

$$u^{n+1}_i = \hat{u}(z_i + \hat{\sigma}^n \Delta t^n).$$

LeVeque-Yee Formula for F/KPP Equation

As before, we apply the LeVeque-Yee formula to the profile u in order to obtain an estimate for the propagation speed:

$$\hat{\sigma}^n = \frac{\Delta x}{\Delta t^{n-1}} \frac{\sum_i \left(u^{n-1}_i - u^n_i\right)}{u^n_I - u^n_0}. \tag{4.3.5}$$

The leftmost (resp. rightmost) value u^n_0 (resp. u^n_I) will in practice (possibly after a short transitory phase) be very close to the steady state 1 (resp. the steady state 0). Contrary

to the kinetic case, we do not need to set any restriction on the speed estimate $\hat{\sigma}^n$ for the computations. However, we still need to satisfy a CFL condition:

$$\hat{\sigma}^n \Delta t^n \leq \Delta x. \tag{4.3.6}$$

Therefore, we set dynamically the time points of the grid, in order to satisfy this condition without imposing a restriction on the speed estimate.

A WB Scheme in the Moving Frame

As explained above, we consider the evolution of f in the moving frame $(t, z) = (t, x - \hat{\sigma}^n \Delta t^n)$, *i.e.* $\bar{u}(t, z) = u(t, z + \hat{\sigma}^n (t - t^n))$, where $\bar{u}$ solves Equation (4.3.1). In order to approximate numerically this solution, we use the method of $\mathscr{L}$-spline interpolation proposed in [87] (except that we use an implicit in time integration).

The scheme is based either on the explicit integration in time rule:

$$\bar{u}_i^{n+1} = \bar{u}^n - \frac{\Delta t^n}{\Delta x} \left(\bar{L}^n_{i+\frac{1}{2}} - \bar{R}^n_{i-\frac{1}{2}} \right), \tag{4.3.7}$$

or on the implicit integration in time rule:

$$\bar{u}_i^{n+1} = \bar{u}^n - \frac{\Delta t^n}{\Delta x} \left(L^{n+1}_{i+\frac{1}{2}} - R^{n+1}_{i-\frac{1}{2}} \right), \tag{4.3.8}$$

where $R^{n+1}_{i-\frac{1}{2}}, L^{n+1}_{i+\frac{1}{2}}, \bar{R}^n_{i-\frac{1}{2}}, \bar{L}^n_{i+\frac{1}{2}}$ correspond to numerical fluxes at the point $z = z_i$ of two interpolated functions in $\bar{C}_{i-\frac{1}{2}}$ and $\bar{C}_{i+\frac{1}{2}}$. Numerically, we have observed that the explicit time integration is stable under the parabolic CFL condition that:

$$\Delta t^n \leq \frac{1}{2} \Delta x^2$$

The coefficient $\frac{1}{2}$ can be slightly higher, but for 0.6, we have observed instability. This empirical CFL condition is in the same spirit as an explicit CFL condition in [87]. For the implicit time integration, we have observed that under the hyperbolic CFL condition (4.3.6), the scheme remains stable.

The values $R^{n+1}_{i-\frac{1}{2}}, L^{n+1}_{i+\frac{1}{2}}, \bar{R}^n_{i-\frac{1}{2}}, \bar{L}^n_{i+\frac{1}{2}}$ are obtained by solving the linear stationary problem (4.3.3), which we recall:

$$\begin{cases} -\hat{\sigma}^n \partial_z \bar{u} - \partial_{zz} \bar{u} = \bar{u}(1 - \bar{u}^n_{i+\frac{1}{2}}), \text{ for } z \in \bar{C}_{i+\frac{1}{2}} \\ \bar{u}(z_i) = \bar{u}_i^{n+1} \text{ and } \bar{u}(z_{i+1}) = \bar{u}_{i+1}^{n+1}, \end{cases}$$

Given the solution $\hat{u}$, we then set $R^{n+1}_{i+\frac{1}{2}} := \hat{u}'(z^-_{i+1})$ and $L^{n+1}_{i+\frac{1}{2}} := \hat{u}'(z^+_i)$. Similarily for the explicit case, one can consider $\hat{u}$ solution of Equation (4.3.2) and set $\bar{R}^n_{i+\frac{1}{2}} := \hat{u}'(z^-_{i+1})$ and $\bar{L}^n_{i+\frac{1}{2}} := \hat{u}'(z^+_i)$. One can view $L^{n+1}_{i+\frac{1}{2}} - R^{n+1}_{i-\frac{1}{2}}$ as a measure of the defect of C^1-smoothness at z_i. The time integration (4.3.8) will therefore be stationary if $\hat{u}$ solves Equation (4.3.4) on the whole space, which in particular implies that it is C^1 as a solution to a second-order elliptic equation. Thus this procedure is well-balanced in the sense that the numerical scheme admits as stationary state the discretization of the continuous stationary state.

Let us now describe the implicit (linear) relation between $(L^{n+1}_{i+\frac{1}{2}}, R^{n+1}_{i+\frac{1}{2}})$ and $(\bar{u}_i^{n+1}, \bar{u}_{i+1}^{n+1})$. The same approach applies *mutatis mutandis* for the explicit case. We solve Problem

(4.3.4) with respect to $(\bar{u}_i^{n+1}, \bar{u}_{i+1}^{n+1})$. On the cell $\bar{C}_{i+\frac{1}{2}}$, it is a simple second-order differential equation with constant coefficients. We compute the roots of its characteristic polynomial:

$$\mu^2 + \hat{\sigma}^n \mu + \left(1 - \bar{u}_{i+\frac{1}{2}}^n\right) = 0 \tag{4.3.9}$$

The discriminant is $\Delta_{i+\frac{1}{2}}^n = (\hat{\sigma}^n)^2 - 4\left(1 - \bar{u}_{i+\frac{1}{2}}^n\right)$ and three cases exist:

1. Suppose $\Delta_{i+\frac{1}{2}}^n > 0$, then set $\mu_{i+\frac{1}{2},\pm}^n = \frac{-\hat{\sigma}^n \pm \sqrt{\Delta_{i+\frac{1}{2}}^n}}{2}$. Then for $z \in \bar{C}_{i+\frac{1}{2}}$, we have:

$$\hat{u}(z) = a^- e^{\mu_{i+\frac{1}{2},-}^n z} + a^+ e^{\mu_{i+\frac{1}{2},+}^n z}$$

   Therefore by setting the following matrices:

$$M = \begin{pmatrix} e^{\mu_{i+\frac{1}{2},-}^n z_i} & e^{\mu_{i+\frac{1}{2},+}^n z_i} \\ e^{\mu_{i+\frac{1}{2},-}^n z_{i+1}} & e^{\mu_{i+\frac{1}{2},+}^n z_{i+1}} \end{pmatrix} \text{ and } \tilde{M} = \begin{pmatrix} \mu_{i+\frac{1}{2},-}^n e^{\mu_{i+\frac{1}{2}}^{n-} z_i} & \mu_{i+\frac{1}{2},+}^n e^{\mu_{i+\frac{1}{2}}^{n+} z_i} \\ \mu_{i+\frac{1}{2},-}^n e^{\mu_{i+\frac{1}{2}}^{n-} z_{i+1}} & \mu_{i+\frac{1}{2},+}^n e^{\mu_{i+\frac{1}{2}}^{n+} z_{i+1}} \end{pmatrix}, \tag{4.3.10}$$

   we obtain the following two systems:

$$\begin{pmatrix} \bar{u}_i^{n+1} \\ \bar{u}_{i+1}^{n+1} \end{pmatrix} = M \begin{pmatrix} a^- \\ a^+ \end{pmatrix} \text{ and } \begin{pmatrix} L_{i+\frac{1}{2}}^{n+1} \\ R_{i+\frac{1}{2}}^{n+1} \end{pmatrix} = \tilde{M} \begin{pmatrix} a^- \\ a^+ \end{pmatrix}.$$

   Hence, finally by setting $S_{i+\frac{1}{2}} = \tilde{M} M^{-1}$, we obtain the following identity:

$$\begin{pmatrix} L_{i+\frac{1}{2}}^{n+1} \\ R_{i+\frac{1}{2}}^{n+1} \end{pmatrix} = S_{i+\frac{1}{2}} \begin{pmatrix} \bar{u}_i^{n+1} \\ \bar{u}_{i+1}^{n+1} \end{pmatrix} \tag{4.3.11}$$

2. Suppose $\Delta_{i+\frac{1}{2}}^n = 0$, then we set $\mu_{i+\frac{1}{2}}^n := -\frac{\hat{\sigma}^n}{2}$ and the solution is of the shape:

$$\hat{u}(z) = (az + b) e^{\mu_{i+\frac{1}{2}}^n z}.$$

   The definition of the matrix $S_{i+\frac{1}{2}}$ then just follows *mutatis mutandis* as precedingly.

3. In the case $\Delta_{i+\frac{1}{2}}^n < 0$, the solution $\hat{u}$ is of the shape:

$$\hat{u}(z) = \left(a \cos\left(\sqrt{-\Delta_{i+\frac{1}{2}}^n} z\right) + b \sin\left(\sqrt{-\Delta_{i+\frac{1}{2}}^n} z\right)\right) e^{-\frac{\hat{\sigma}^n z}{2}},$$

   and again the definition of the matrix $S_{i+\frac{1}{2}}$ then follows *mutatis mutandis* as precedingly.

Relation (4.3.11) can be written in explicit form, but we will not do so for the sake of concision, and combining then Relation (4.3.11) with the time integration (4.3.8), we end up with a tridiagonal system, which can easily be inverted.

A WB Shift to the Stationary Frame

In the next step, as previously we need to compute the values u_i^{n+1} (in the stationary frame) from the values $\bar{u}_i^{n+1}$ (in the moving frame $(t,z) = (t, x - \hat{\sigma}^n(t - t^n))$). As described above, this amounts to solving Equation (4.3.4), which we recall:

$$\begin{cases} -\hat{\sigma}^n \partial_z \hat{u} - \partial_{zz}\hat{u} = \hat{u}(1 - \bar{u}^n_{i+\frac{1}{2}}), \text{ for } z \in \bar{C}_{i+\frac{1}{2}} \\ \hat{u}(z_i) = \bar{u}_i^{n+1} \text{ and } \hat{u}(z_{i+1}) = \bar{u}_{i+1}^{n+1}, \end{cases}$$

and then setting:

$$u_i^{n+1} = \hat{u}(z_i + \hat{\sigma}^n \Delta t^n). \tag{4.3.12}$$

It is here that enforcing the CFL condition (4.3.6) avoids taking values from cells, which would not be direct neighbors. Equation (4.3.4) can be solved in the same manner as previously. One takes $N_{i+\frac{1}{2}} = M_{i+\frac{1}{2}}$ and for (ϕ_1, ϕ_2) the fundamental system of solutions, that we have used above:

$$\tilde{N}_{i+\frac{1}{2}} = \begin{pmatrix} \phi_1(z_i + \hat{\sigma}^n \Delta t^n) & \phi_2(z_i + \hat{\sigma}^n \Delta t^n) \end{pmatrix} \tag{4.3.13}$$

This then leads to the following 1×2 matrix:

$$T_{i+\frac{1}{2}} := \tilde{N}_{i+\frac{1}{2}} N^{-1}_{i+\frac{1}{2}},$$

and:

$$u_i^{n+1} = T_{i+\frac{1}{2}} \begin{pmatrix} \bar{u}_i^{n+1} \\ \bar{u}_{i+1}^{n+1} \end{pmatrix}. \tag{4.3.14}$$

4.3.2 Alternative Schemes

We compare the preceding WB scheme for F/KPP Equation (4.1.8) with two other numerical schemes.

OS Scheme with Crank-Nicolson Method

The first scheme is based on a OS of the heat operator and the reaction term. For the heat operator, we use the Crank-Nicolson method:

$$\frac{v_i^{n+1} - u_i^n}{\Delta t} = \frac{v_{i-1}^{n+1} - 2v_i^{n+1} + v_{i+1}^{n+1}}{2\Delta x^2} + \frac{u_{i-1}^n - 2u_i^n + u_{i+1}^n}{2\Delta x^2}. \tag{4.3.15}$$

The reaction term can be integrated exactly, which leads then to:

$$u_i^{n+1} = \frac{e^{\Delta t}}{e^{\Delta t} - 1 + \frac{1}{v_i^{n+1}}}. \tag{4.3.16}$$

WB Scheme for the "0-Wave"

The second scheme is based on the same method as the WB scheme mentioned before, but we impose that $\hat{\sigma}^n = 0$. This choice corresponds to the choice that has been investigated in [87] (and also [37] for a kinetic chemotaxis equation). As mentioned in the Introduction, this approach is only WB for a stationary state, or equivalently a traveling wave with speed 0. For the implementation of this scheme, one does not need to shift from the moving to the stationary frame, as both coincide. Or with the notations from above, we have:

$$T_{i+\frac{1}{2}} = \begin{pmatrix} 1 \\ 0 \end{pmatrix}.$$

4.3.3 Numerical Assessements

The code for the numerical schemes in this Section can be found in [66].

Condition Number for $S_{i+\frac{1}{2}}$

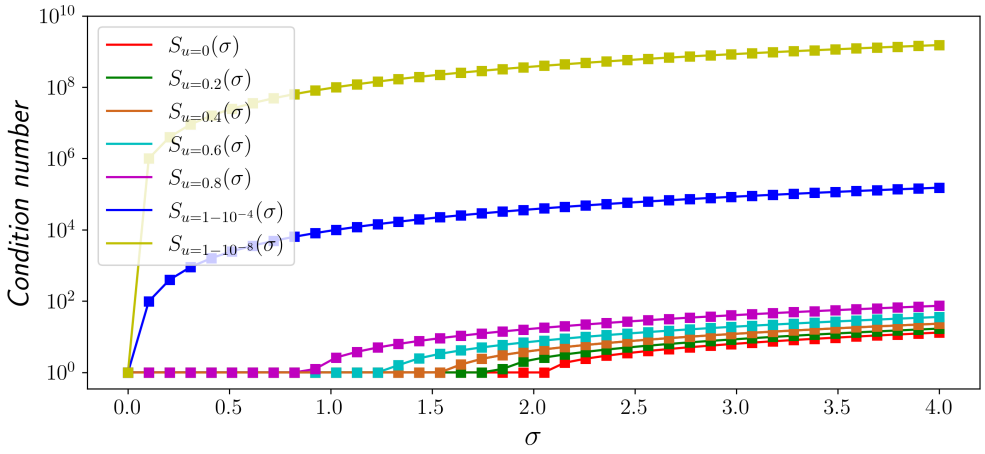

Figure 4.7: Condition numbers of $S_u(\sigma)$, where u denotes the value at which the nonlinearity is "frozen".

We consider the condition number of matrix $S_{i+\frac{1}{2}}$ (see Figure 4.7), which solves Problem (4.3.3) as a function of σ for different fixed parameters $u = \bar{u}^n_{i+\frac{1}{2}}$, *i.e.* the value at which the nonlinearity is "frozen". We observe that the matrix becomes ill-conditioned only for $u \sim 1$. In that case, one of the eigenvalues of Problem (4.3.3) $\mu \sim 0$, which explains the ill-conditioning. Yet, in practice this may not lead to a difficulty, since $u \sim 1$ corresponds to the region where the profile of the solution is a plateau. Moreover, as already mentioned, the propagation dynamics is dominantly set by the behavior at the leading edge of the profile, when $u \sim 0$. There, the matrix $S_{i+\frac{1}{2}}$ is well-conditioned for a wide range of values for σ, but in particular around the region $\sigma \sim \sigma_{F/KPP} = 2$.

The Asymptotic Propagation Speed

The F/KPP Equation (4.1.8) has an asymptotic progation speed σ of 2. We compare the ability of different schemes to capture this asymptotic velocity: the WB scheme of Section 4.3.1 in its explicit and implicit version, the OS scheme of Section 4.3.2 and the WB scheme for the "0-Wave" of Section 4.3.2 also in its explicit and implicit version.

In order to capture the asymptotic propagation speed, the F/KPP equation is solved over the time interval $[0, 1500]$. Because the expected spreading speed is $\sigma = 2$, the domain considered should be at least twice bigger: here, we take the domain $[0, 3080]$. This large domain avoids roughly speaking boundary effects, for an initial condition $u_0(x) = 1 - \frac{1}{1+e^{-3(x-40)}}$.

Figure 4.8 represents the velocity $\hat{\sigma}^n$ obtained with the LeVeque-Yee formula at the final time $t = 1500$ for the schemes considered here. With a coarse mesh, the asymptotic propagation speed obtained is far from 2 for some schemes and the spatial domain had to

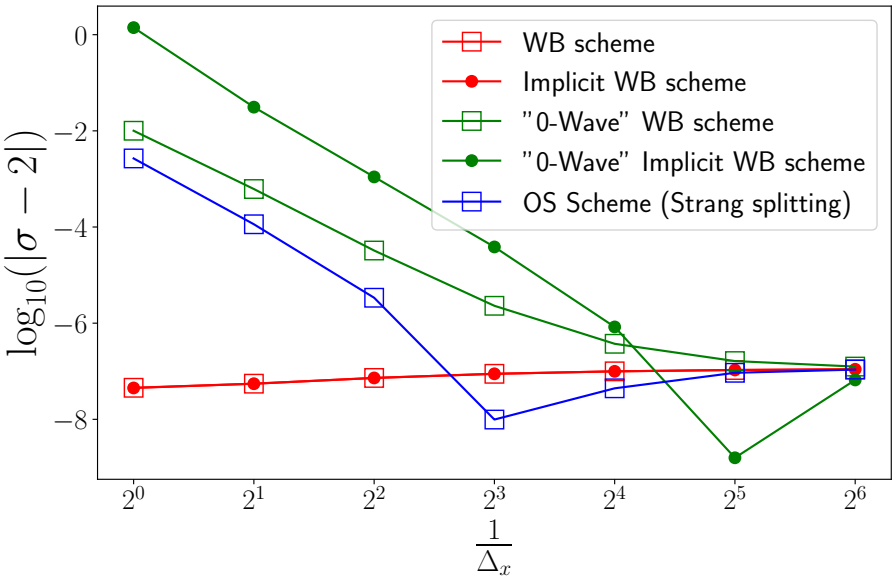

Figure 4.8: Evolution of LeVeque-Yee velocity σ for F/KPP equation at time $t = 1500$ for different schemes with respect to the space discretization size Δ_x.

be extended to $[0, 6080]$ in order to avoid boundary effects for these schemes. The same time step is chosen for all the considered schemes at each iteration. It is the one satisfying all the CFL conditions which is the parabolic one, $\Delta_t^n \leq \frac{1}{2}\Delta_x^2$, needed for the explicit WB schemes. As expected, the schemes capture the asymptotic propagation speed of 2 when the discretization is fine enough. It can be noted that the WB scheme, both in its explicit and implicit version, captures extremely well the asymptotic propagation speed even for very coarse meshes.

Capturing the Bramson Shift

We recall that the Bramson shift is the logarithmic shift that appears in the expression of the position of a level set $x_c(t)$ for $c \in (0, 1)$ given by Equation (4.1.12). In the simulations, we track the position of the level set $x_{0.5}(t)$ by linearly interpolating the solution in the mesh cell where the level set is. The coefficient $\frac{3}{2}$ of the Bramson shift is approximated by fitting $x_{0.5}(t) - 2t$ over the last half of the simulation.

We try to capture this Bramson shift by refining the discretization of the spatial domain. Using schemes that depend on a parabolic CFL condition results in a huge number of iterations in time which becomes rapidly intractable in a reasonable amount of time in practice. Moreover, the "0-Wave" implicit WB scheme and OS scheme do not capture the asymptotic propagation speed as well as the implicit WB scheme. Thus, we only fit the Bramson shift for the implicit WB scheme (see Figure 4.8). The coefficient recovered numerically seems to converge towards a value sligthly lower than 3/2. This difference could be due to the linearization of the non-linear term in the F/KPP equation.

Acknowledgements

The authors are extremely grateful to Vincent Calvez and Thierry Dumont, who have been essential to the present work.

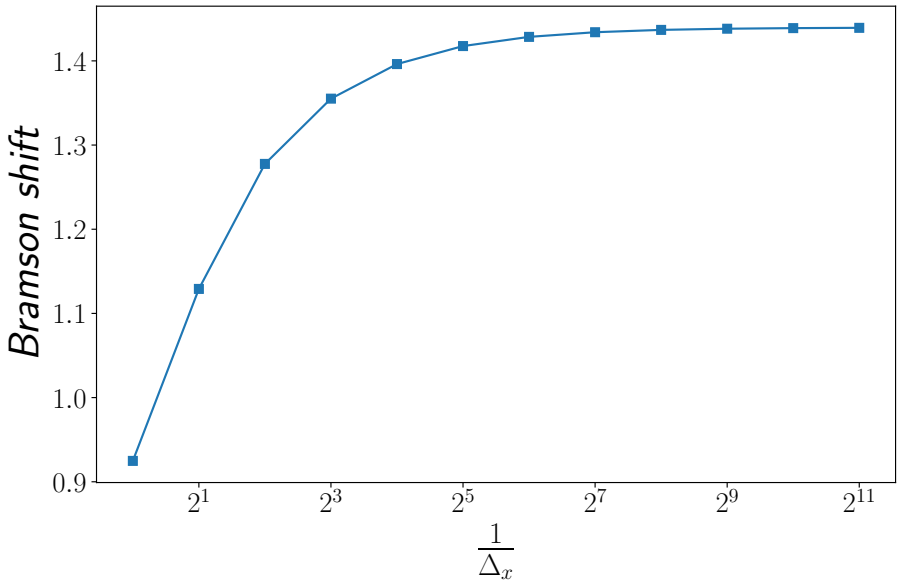

Figure 4.9: Fitting of the coefficient 3/2 of the Bramson shift with the implicit WB scheme.

This project has received funding from the European Research Council (ERC) under the European Union's Horizon 2020 research and innovation programme (grant agreement No 865711).

4.4 Appendix: Complementary Numerical Simulations

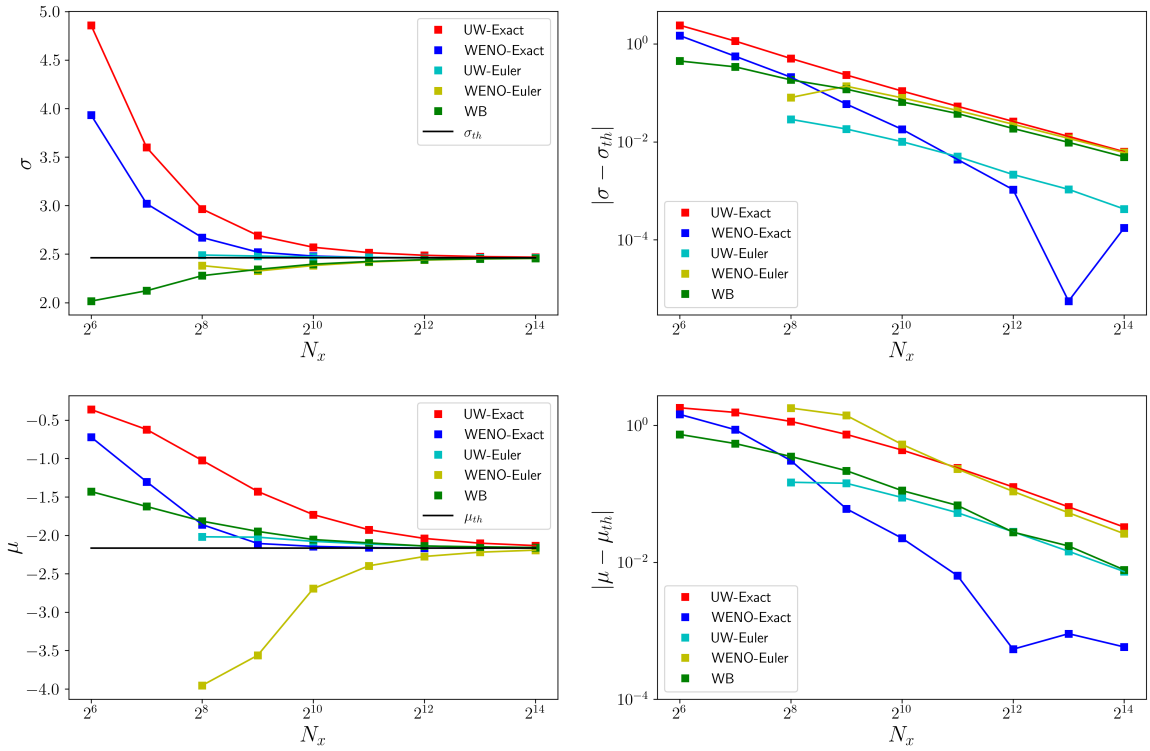

Figure 4.10: Comparison between performances of UW-Euler (cyan), UW-Exact (red), WENO-Euler (yellow), WENO-Exact (blue) and WB scheme (green) as a function of N_x, the number of points of the spatial discretization. Upper left: Plot of the numerical speed σ. Upper right: Plot of the absolute value of the numerical speed σ and the theoretical speed σ_{th} in log-scale. Lower left: Plot of the numerical exponential decay parameter μ. Lower right: Plot of the absolute value of the numerical exponential decay parameter μ and the theoretical decay parameter μ_{th} in log-scale. Choice of parameters: $\boldsymbol{V = \{-8, 8\}}, \boldsymbol{\alpha = 8}, \chi = 2, L = 100, dx = \frac{L}{N_x}$, $T = 15$, CFL $= 0.5$ and $\Delta t = \frac{\Delta}{2\alpha}$.

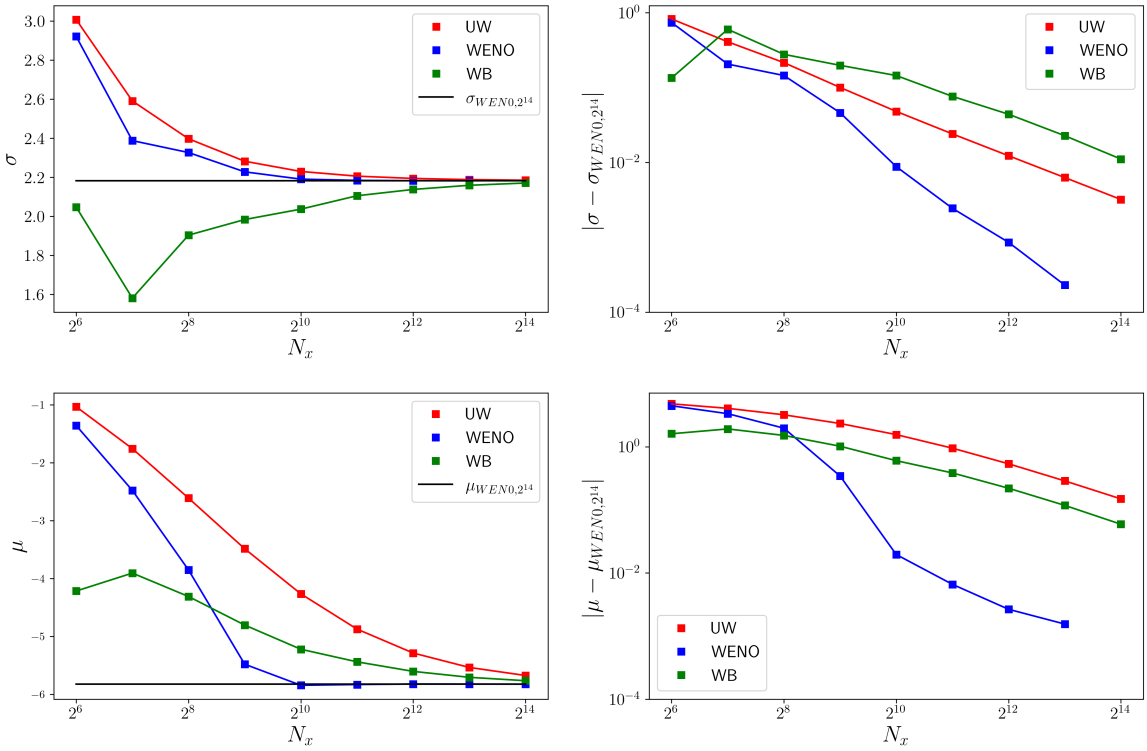

Figure 4.11: Comparison between performances of UW-Exact (red), WENO-Exact (blue) and WB scheme (green) as a function of N_x, the number of points of the spatial discretization. Upper left: Plot of the numerical speed σ. Upper right: Plot of the absolute value of the numerical speed σ and the speed $\sigma_{WENO,16384}$ obtained through WENO scheme with $N_x = 16384$ in log-scale. Lower left: Plot of the numerical exponential decay parameter μ. Lower right: Plot of the absolute value of the numerical exponential decay parameter μ and the exponential decay parameter $\mu_{WENO,16384}$ obtained through WENO scheme with $N_x = 16384$ in log-scale. Choice of parameters: $\boldsymbol{V = \{-4, -3, -2, -1, 1, 2, 3, 4\}}, \boldsymbol{\alpha = 4}, \chi = 2, L = 100, dx = \frac{L}{N_x}$, $T = 15$, CFL $= 0.5$ and $\Delta t = \frac{\Delta}{2\alpha}$.

Chapter 5

A Stochastic Individual-Based Go or Grow Model

This Chapter is a preliminary presentation of results from an ongoing collaboration with Vincent Calvez and Milica Tomašević. The presentation is voluntarily informal and nonrigorous statements are supported by numerical investigations. We propose a stochastic individual-based Go or Grow model: the first K particles (counted from right to left) are in the Grow regime, whereas the other particles are in the Go regime. The model consists then in a system of stochastic differential equations (SDE) describing Brownian motion with a drift combined with a Poissonian birth process for the first K particles. We start by giving an algorithmic description of the stochastic process. This approach is then complemented by an SDE describing the evolution of the point measure of the population. Then, we conjecture a large-population limit when $K \to +\infty$ under suitable renormalization. The limit equation is a PDE describing a Go or Grow model, with a new Go or Grow rule, compared to the Go or Grow model in Chapter 2. We give numerical evidence that in the large population limit $K \to +\infty$ the stochastic model seems to converge to the traveling waves of the PDE model. Finally, we investigate the ancestral lineage of particles, following a methodology, which has recently been proposed in [38, 74]. Numerically, we show that there exists two different regimes, which overlap with the two regimes of pulled and pushed waves from Chapter 2.

5.1 Introduction

In this Chapter, we will be interested in a stochastic individual-based Go or Grow model. This work has been trigger by the question of finding a stochastic counterpart for the parabolic Go or Grow model, which has been studied in Chapter 2, which we recall:

$$\begin{cases} \partial_t \rho - \partial_{xx}\rho + \partial_x \left(\chi \mathbb{1}_{N<N_{\text{th}}} \text{sign}(\partial_x N)\rho\right) = \mathbb{1}_{N>N_{\text{th}}}\rho & \text{(5.1.1a)} \\ \partial_t N - D\partial_{xx}N = -\rho N, & \text{(5.1.1b)} \end{cases}$$

There, recall that the rule determining the switch between the Go and the Grow behavior is controlled by the ambient oxygen level N and whether this level is below or above a

threshold value N_{th}. In order to find a stochastic counterpart, one could for instance follow the work [105, 175] by one of the authors on the parabolic-parabolic Keller-Segel model and simply replace the cell density ρ by a distribution of Dirac functions, where each Dirac function represents a single particle. Yet, the non-linear term in Equation (5.1.1b) makes it analytically much less tractable, compared to the study in [105], where ρ merely intervenes as a source term. Furthermore, the well-posedness analysis of the Cauchy problem in Chapter 2 shows that it heavily relies on an endpoint regularity estimate of N. A distribution of Dirac functions being less regular, it points to the fact that in that case the well-posedness might not be guaranteed.

In order to circumvent those difficulties, we propose a simple alternative, where the switch between the Go and the Grow behavior at position x is controlled by the number of particles, whose position is higher than x. Let $K \in \mathbb{N}^*$, the first K particles (counted from the right) are subject to the Grow regime: these particles undergo Brownian motion and will divide with rate one. The other particles are subject to the Go regime: they undergo Brownian motion with a constant drift $\chi > 0$.

This simple stochastic Go or Grow model has not been studied yet, to the best of our knowledge. But its features are reminiscent of two different well-studied classes of stochastic processes. The first class are so-called rank-based diffusion processes (see Introduction in [103] for references): a system of finite and constant number of particles interact with each other through their rank in the system, which determines their individual behavior (drift and diffusion). As an example, we mention the Atlas model proposed in [69]: N particles diffuse and the last one "pushes" the whole population, by having a positive drift. Later on, generalizations of the Atlas model have been proposed (see for instance [13, 144]). The other class are the rank-dependent branching brownian motions following the terminology [92]: there, the particles undergo Brownian motion and depending on their rank, they can divide (and possibly also die). Among this class, we mention the N-Branching Brownian Motion (N-BBM) introduced in [127] (see also [52]): N particles undergo Brownian motion and each particle divides with rate equal to one. When a particle divides the left-most particle is removed from the system. Thus, the stochastic Go or Grow model, which we will investigate in this Chapter, lies at the intersection of those two classes of models.

Outline

This Chapter documents an ungoing work and sketches only preliminary results. The discussion is voluntarily rather nonrigorous and the arguments are often illustrated with numerical simulations. In Section 5.2, we present the stochastic Go or Grow model. We start with an algorithmic construction of the stochastic process. We introduce also a specific labeling for the particles, which will be useful in Section 5.4. Then, we state the stochastic differential equation (SDE) of the model and briefly show that the trajectories of the SDE coincide with the algorithmic construction. In Section 5.3, we conjecture the limit after suitable renormalization of the stochastic process when $K \to +\infty$, which leads to a partial differential equation (PDE). This PDE admits traveling waves as solutions and we show numerically that the stochastic Go or Grow model behaves very similarily to these traveling waves. In Section 5.4, we adress the question of the ancestral distributions of a particle, when the system is close to the traveling wave state. We conjecture that the probability distribution of the ancestral distribution follows a PDE in the limit when $K \to +\infty$. According to this PDE, the qualitative behavior of the ancestral distribution differs in the case $\chi > 1$ and the case $\chi \leq 1$, which can be interpretated as an alternative

characterization of pushed and pulled traveling waves.

Notations

- $\mathcal{M}_F(\mathbb{R})$ denotes the set of finite measures on $\mathbb{R}$ endowed with the topology of weak convergence. We denote by $\mathcal{M}$ the subset of $\mathcal{M}_F$ containing finite sums of dirac measures :
$$\mathcal{M} = \left\{ \sum_{i=1}^{n} \delta_{x_i}; \quad n \in \mathbb{N}, x_1, \dots, x_n \in \mathbb{R} \right\}.$$
- $\mathcal{H} : \mathbb{R} \to \mathbb{R}$ denotes the heavy side function, *i.e.* $\mathcal{H}(x) = \mathbb{1}_{x \geq 0}$.
- Let $\mathbb{N}^* = \mathbb{N} \setminus \{0\}$. Let $H = (H^1, \dots, H^k, \dots) : \mathcal{M} \to (\mathbb{R})^{\mathbb{N}^*}$ be defined by $H(\sum_{i=1}^n \delta_{x_i}) = (x_{\sigma(1)}, \dots, x_{\sigma(n)}, 0, \dots, 0, \dots)$, where σ is a permutation such that $x_{\sigma(1)} \geq x_{\sigma(2)} \geq \cdots \geq x_{\sigma(n)}$.

5.2 The Stochastic Individual-Based Model

In this Section, we start by describing the stochastic individual-based Go or Grow model via an algorithmic construction of its trajectories. Then, we give the SDE description of the stochastic process and show briefly that the algorithmic construction corresponds to the trajectories of the SDE. Finally, we propose an alternative labeling of the particles.

5.2.1 Algorithmic Construction of the Stochastic Process

First, we will give an informal description of the dynamics of individuals who are characterized by their positions $(X_t^j)_{j \in \{1,\dots,N_t\}}$ in $\mathbb{R}$ at time t, where N_t is the total number of particles at time t. We define its associated point measure by:

$$Z_t = \sum_{j=1}^{N_t} \delta_{X_t^j} \tag{5.2.1}$$

The general Go or Grow idea goes as follows: fixing $K \geq 1$, the particle population is divided into two subgroups. The K particles that are on the far right of the real line follow the Grow behavior: they diffuse and may divide with constant rate equal to one. By division we mean that at the position of the particle, which divides, a new particle is added to the system. The rest of the particles follow the Go behavior: they diffuse, have a drift with constant advection speed $\chi > 0$ and cannot divide.

In order to give sense to the preceding description, we introduce the rank (from the right) for a particle at position X_t^i among the family $(X_t^j)_j$:

$$\text{rank}(X_t^i, Z_t) := Z_t * \mathcal{H}(X_t^i) = \langle Z_t, \mathcal{H}(\,\cdot - X_t^i) \rangle = \sum_{j=1}^{N_t} \mathcal{H}(X_t^j - X_t^i) \tag{5.2.2}$$

In the right hand-side of Equation (5.2.2), we see that each index j for which $X_t^j \geq X_t^i$ is counted once, yielding thus an integer $k \in \mathbb{N}^*$, which then means that X_t^i is the k-th highest position in the list $(X_t^j)_j$. The Go or Grow alternative then states that if $\text{rank}(X_t^i, Z_t) \leq K$ the particle X_t^i follow the Grow behavior, whereas if $\text{rank}(X_t^i, Z_t) > K$ the particle X_t^i follow the Go behavior.

For the positions between the times of division events, the particles then evolve according to the SDE:

$$dX_t^i = \chi \mathbb{1}_{\{\text{rank}(X_t^i, Z_t) > K\}} dt + \sqrt{2} dW_t^i, \tag{5.2.3}$$

where $(W^i)_{i \in \mathbb{N}^*}$ are independent standard one-dimensional Brownian motions defined on some probability space $(\Omega, \mathcal{F}, \mathbb{P})$. For a system of particles with a fixed number of particles $i \in \{1, \dots, N\}$, *i.e.* without division, the system of SDE (5.2.3) admits a unique strong solution, since the drift is bounded [186]. Furthermore, particle systems satisfying Equation (5.2.3) without division have for instance been studied in [144].

Moreover, notice that the total rate of division is equal to K, since there are K particles that divide with rate one. Hence in order to determine the times at which new particles are added to the system, one may consider an exponential clock with parameter K. Once that clock rings, one chooses uniformly a particle among the K first particles and adds a new particle with the same position to the system.

The last observation leads to a construction by induction of the sequence of division times $(T_k)_{k \geq 0}$, the number $(N_k)_{k \geq 0}$ of individuals in the population at these times (*i.e.* $N_k := N_{T_k}$ with the notations just above) and the sequence of vectors of each particle's position $(X_{T_k})_{k \geq 0}$ at these times ($X_{T_k} = (X_{T_k}^j)_{j \in \{1, \dots, N_k\}} \in \mathbb{R}^{N_k}, k \geq 0$). Let us fix the initial number of individuals $N_0 = N \in \mathbb{N}^*$ and the vector of random variables $X_0 \in \mathbb{R}^N$, which denotes the initial positions. We assume for the sake of simplicity that $N \geq K$. For each pair of consecutive division times (T_k, T_{k+1}) we denote by $X_t \in \mathbb{R}^{N_k}$ the vector of position of the individuals at time $t \in [T_k, T_{k+1})$. We introduce the following random variables independent of X_0: $(W^{j,k})_{j,k \in \mathbb{N}^*}$, which are standard independent Brownian motions; τ_k, which are independent exponential random variables with rate K (independent from the Brownian motions). For $k \geq 1$ we define the system inductively. Set $T_0 = 0$, $N_0 = N$ and assume that $(T_{k-1}, N_{k-1}, X_{k-1})$ are given for some $k \geq 1$. We let:

- $T_k = T_{k-1} + \tau_k$
- On the interval $[T_{k-1}, T_k)$ we set the number of particles to be constant and equal to N_{k-1} and their position evolve according to the SDE

$$X_t^i = X_{T_{k-1}}^i + \chi \int_{T_{k-1}}^t \mathbb{1}_{\{\text{rank}(X_t^i, Z_t) > K\}} ds + \sqrt{2} W_{t - T_{k-1}}^{i,k}, \quad t \in (T_{k-1}, T_k], 1 \leq i \leq N_{k-1}.$$

- At time T_k an individual $I_k = i$ is chosen uniformly at random among the positions $X_{T_k}^i$ of the first K particles, *i.e.* i such that $\sum_{j=1}^{N_{k-1}} \mathcal{H}(X_s^j - X_s^i) \leq K$. Let us denote its position by $X_{T_k}^i$. Then, we add the position $X_{T_k}^i$ to the vector X_{T_k} and set $N_k = N_{k-1} + 1$.

Following this procedure, the number of individuals N_t in the population at given $t \leq \sup T_k$ and the empirical measure Z_t can be recovered via:

$$N_t = \sum_{k \geq 0} N_k \ \mathbb{1}_{\{T_k \leq t < T_{k+1}\}},$$

$$Z_t = \sum_{k \geq 0} \mathbb{1}_{\{T_k \leq t < T_{k+1}\}} \sum_{j=1}^{N_k} \delta_{X_t^j}.$$

As the increments of the sequence T_k are independent exponential random variables with rate K, it is obvious that $\lim_{k \to \infty} T_k = +\infty$.

5.2.2 The SDE of the Stochastic Process

In this step, we give a description of the stochastic process $(Z_t)_{t\geq 0}$ through an SDE. Below we show that the stochastic process $(Z_t)_{t\geq 0}$ satisfying this SDE admits as trajectories the algorithmic construction above.

The stochastic process $(Z_t)_{t\geq 0}$ takes values in $\mathcal{M}$ and we fix a probability space $(\Omega, \mathcal{F}, \mathbb{P})$ such that the initial condition Z_0 is almost surely a $\mathcal{M}$-valued $\mathcal{F}_0$-measurable random variable. Let us introduce the family $\{W^i, i \in \mathbb{N}^*\}$ of independent standard one-dimensional Brownian motions defined on $(\Omega, \mathcal{F}, \mathbb{P})$ independent of Z_0 and of a Poisson point measure $\mathcal{N}(ds, di, d\theta)$ on $\mathbb{R}_+ \times \mathbb{N}^* \times [0,1]$ with intensity $ds \times \left(\sum_{j\geq 1} \delta_j(di)\right) \times d\theta$.

We notice here that the individual birth rate of a cell at the position x belonging to a population state $\nu \in \mathcal{M}$ is:

$$b(x, \nu) := \mathbb{1}_{\{\langle \nu, \mathcal{H}(\,\cdot - x)\rangle \leq K\}}. \tag{5.2.4}$$

In parallel, the individual drift of a cell at position x belonging to a population state $\nu \in \mathcal{M}$ is:

$$\chi(1 - b(x, \nu)) = \chi \mathbb{1}_{\{\langle \nu, \mathcal{H}(\,\cdot - x)\rangle > K\}}. \tag{5.2.5}$$

We may now write the the SDE satisfied by Z. For $f \in C_b^2(\mathbb{R})$ we have:

$$\begin{aligned}
\langle Z_t, f\rangle &= \langle Z_0, f\rangle + \chi \int_0^t \sum_{i=1}^{\langle Z_s^-, 1\rangle} f'(H^i(Z_s))(1 - b(H^i(Z_s), Z_s))ds \\
&+\sqrt{2}\int_0^t \sum_{i=1}^{\langle Z_s^-, 1\rangle} f'(H^i(Z_s))dW_s^i + \int_0^t \sum_{i=1}^{\langle Z_s^-, 1\rangle} f''(H^i(Z_s))ds \\
&+ \int_0^t \int_{\mathbb{N}^*} \int_0^1 \mathbb{1}_{\left\{i \leq \langle Z_{s^-}, 1\rangle\right\}} \mathbb{1}_{\left\{\theta \leq b(H^i(Z_{s^-}), Z_{s^-})\right\}} f(H^i(Z_{s^-}))\mathcal{N}(ds, di, d\theta).
\end{aligned} \tag{5.2.6}$$

$\langle Z_t, 1\rangle$ corresponds to the number of particles at time t and $H^i(Z_t)$ to the position of the i-th parrticle. *Nota bene*, index i therefore does not denote an individual particle fixed over time, contrary to what we have seen for the algorithmic construction. The first integral term corresponds to the drift term with constant drift χ, when the particle is of rank higher than K. The two middle integrals correspond to the Brownian diffusion, to which all particles are subject to. The last integral corresponds to the division of the first K cells.

We now briefly show that the trajectories of Z, which solves Equation (5.2.6), satisfy the algorithmic construction from above:

1. Suppose that the initial condition Z_0 is such that $N_0 \geq K$. We notice here that the waiting time T_1 for the first event to happen has $\mathcal{E}(K)$ distribution. Indeed,

$$\mathbb{P}(T_1 \leq t) = 1 - \mathbb{P}(T_1 > t) = 1 - \mathbb{P}(N_t = N_0).$$

   The latter in the above equation means that, putting $f = 1$, the last term did not produce any atom up to t. Hence:

$$\mathbb{P}(T_1 \leq t) = 1 - e^{-\int_0^t \int_{\mathbb{N}^*} \int_0^1 \mathbb{1}_{\left\{i \leq \langle Z_{s^-}, 1\rangle\right\}} \mathbb{1}_{\left(\theta \leq b(H^i(Z_{s^-}), Z_{s^-})\right)} ds \times \left(\sum_{j\geq 1} \delta_j(di)\right) \times d\theta}$$

$$= 1 - e^{-\int_0^t \sum_{i=1}^{\langle Z_s, 1\rangle} b(H^i(Z_{s^-}), Z_{s^-})ds}$$

. The probability that a Poisson process with rate $\lambda(ds, di, d\theta)$ produces k atoms on a set $W \subset \mathbb{R}_+ \times N^* \times [0,1]$ follows a Poisson distribution of parameter $\int_W \lambda(ds, di, d\theta)$. Noticing that for any $s \geq 0$ when $N_0 \geq k$ one has $\sum_{i=1}^{\langle Z_s, 1\rangle} b(H^i(Z_{s^-}), Z_{s^-}) = K$ gives

$$\mathbb{P}(T_1 \leq t) = 1 - e^{-Kt}.$$

2. Suppose that the initial condition is such that $N_0 < K$, then the waiting time of the first event has $\mathcal{E}(N_0)$ distribution. Similarily, the waiting time $T_2 - T_1$ of the second event has $\mathcal{E}(N_0 + 1)$ distribution, *etc...* Until we reach the $(K - N_0 + 1)$-th event, whose waiting time will have $\mathcal{E}(K)$ distribution and the same will be true for all later events.

3. Let us now show that at a division time T_k, the position of the new particle $X_{T_k}^{N_{T_k}}$ is a random variable uniformly distributed among $\left(H^i(Z_{T_k^-})\right)_{i=1,\dots,K\wedge N_{T_k^-}}$ the positions of the $K \wedge N_{T_k^-}$ first particles at time T_k^-, *i.e.* the K first particles if $N_{T_k^-}$ the number of particles at time T_k^- are higher than K, and the $N_{T_k^-}$ first particles, otherwise. We first observe that $b(H^i(Z_t), Z_t) = \mathbb{1}_{i \leq K}$ and that $\mathbb{1}_{\left(i \leq \langle Z_{t^-}, 1\rangle\right)} = \mathbb{1}_{i \leq N_t^-}$. Then, conditionally to $T_1, \dots, T_k$, the jumps of the Poisson measure $\mathcal{N}$, which we denote by $(U_j)_{j=1,\dots,k}$, are independent and follow the laws $\mathbb{1}_{i \leq K \wedge N_{T_j^-}} \frac{\sum_{j \geq 1} \delta_j(di)}{K \wedge N_{T_j^-}}$ on $\mathbb{N}^*$ (we refer the reader to the Appendix in [14]). Hence, we have:

$$\mathcal{N}(ds, di, d\theta) = \sum_{j=1}^{k} \delta_{(T_j, U_j)}.$$

Using this and Equation (5.2.6), we find that:

$$\left\langle \delta_{X_{T_k}^{N_{T_k}}}, f \right\rangle = \langle Z_{T_k} - Z_{T_k^-}, f \rangle = f\left(H^{U_k}\left(Z_{T_k^-}\right)\right),$$

which is exactly what we wanted to show, since U_k is uniformly distributed in $\{1, \dots, K \wedge N_{T_k^-}\}$.

5.2.3 Alternative Labeling of Particles

We introduce an alternative labeling of particles to the indexing in the algorithmic construction, which is often referred to as the classical Ulam-Harris-Neveu notation (see for instance [130]). This will be helpful in particular in Section 5.4, when we consider the lineages of the particles. Let:

$$\mathcal{U} = \{(j, a_1, \dots, a_l) | j \in \{1, \dots, N\}, l \in \mathbb{N}, x_i \in \{0, 1\}\} \tag{5.2.7}$$

We denote by $\mathcal{U}_t \subset \mathcal{U}$ the set of labels at time $t \geq 0$, which is definite recurisevly in the following manner:

- For time $t = 0$, the first N particles are labeled from 1 to N and $\mathcal{U}_0 = \{(j) | j \in \{1, \dots, N\}\}$.
- For time $t \in [T_k, T_{k+1})$, the labels of the particles are conserved and $\mathcal{U}_t = \mathcal{U}_{T_k}$.

- At the division time $t = T_k$, consider $(j, a_1, \dots, a_l)$ the label of the particle, which will divide. One of the resulting particles, then gets affected the label $(j, a_1, \dots, a_l, 0)$, the other one the label $(j, a_1, \dots, a_l, 1)$ and the label $(j, a_1, \dots, a_l)$ gets suppressed from the set of labels:

$$\mathcal{U}_{T_k} = \Big(\mathcal{U}_{T_k^-} \cup \{(j, a_1, \dots, a_l, 0), (j, a_1, \dots, a_l, 1)\}\Big) \setminus \{(j, a_1, \dots, a_l)\}.$$

Of note, this labeling admits the following property: for $t \geq 0$, there exists no two labels $\ell_1, \ell_2 \in \mathcal{U}_t$, such that ℓ_1 is a prefix of ℓ_2. Notice also that one could rewrite SDE (5.2.6) by the means of a Poisson point process on the set $\mathbb{R}_+ \times \mathcal{U} \times [0, 1]$.

5.3 The Large-Population Limit $K \to +\infty$

In this Section, we will be interested in the large population limit $\frac{Z_t^K}{K}$ when $K \to +\infty$, where we have specified the dependency of Z_t^K on the parameter K. We start by conjecturing the limit, whose rigorous proof is left to future investigations. Nevertheless, we summarize some directions of investigation in order to establish rigorously this limit. The limit equation is in many aspects very similar to the parabolic Go or Grow equation (5.1.1) from Chapter 2. We refer to Chapter 6, where the question of the existence and uniqueness locally in time of the solution to the limit equation is treated. Furthermore, we state a result on the structure of nonnegative traveling waves for the limit equation. This result is *mutatis mutandis* the same than what has been obtained in Chapter 2 and we do not detail its proof. In particular, this result leads to the conjecture that in the large population limit the spreading speed should converge to the spreading speed:

$$\sigma^* = \begin{cases} \chi + \frac{1}{\chi} & \text{if } \chi > 1 \\ 2 & \text{if } \chi \leq 1 \end{cases}. \tag{5.3.1}$$

Finally, we investigate this claim by studying numerically the behavior of Z_t^K. We give numerical evidence that the spreading of the K-th particle evolves linearily with speed σ^K, *i.e.*:

$$\sigma^K := \lim_{t \to +\infty} \frac{H^K(Z_t^K)}{t}, \tag{5.3.2}$$

where $H^K(Z_t^K)$ is the position of the K-particle at time t. Then, we show that in the large population limit $K \to +\infty$, we have:

$$\lim_{K \to +\infty} \sigma^K = \sigma^*. \tag{5.3.3}$$

5.3.1 The Large Population Limit: A New Go or Grow PDE

We conjecture that $\frac{Z_t^K}{K}$ converges to a function $\rho(t, x)$, which satisfies the following Equation, for $t > 0, x \in \mathbb{R}$:

$$\partial_t \rho(t, x) - \partial_{xx} \rho(t, x) + \partial_x \left(\chi \mathbb{1}_{(\rho(t) * \mathcal{H})(x) > 1} \rho(t, x)\right) = \mathbb{1}_{(\rho(t) * \mathcal{H})(x) \leq 1} \rho(t, x) \tag{5.3.4}$$

This conjecture is motivated by the following observations: the Brownian motion of the particles translates into diffusion on ρ. As already observed, the position of the first K

particles can be characterized by all the $x \in \mathbb{R}$, such that $\left\langle \frac{Z_t^K}{K}, \mathcal{H}(\cdot - x) \right\rangle \leq 1$. But we expect that:

$$\left\langle \frac{Z_t^K}{K}, \mathcal{H}(\cdot - x) \right\rangle = \left(\frac{Z_t^K}{K} * \mathcal{H} \right)(x) \xrightarrow[K \to +\infty]{} (\rho(t) * \mathcal{H})(x) = \int_x^{+\infty} \rho(t, y) dy$$

Then in the large population limit $K \to +\infty$, the particles that are subject to division, *i.e.* the particles at position x such that $\left(\frac{Z_t^K}{K} * \mathcal{H} \right)(x) \leq 1$, will translate into a division term for ρ with rate equal to one; whereas the particles that are subject to the drift, *i.e.* the particles at position x such that $\left(\frac{Z_t^K}{K} * \mathcal{H} \right)(x) > 1$, will translate into a drift with constant advection speed χ.

Equation (5.3.4) is very similar to the parabolic system (5.1.1), which was the object of Chapter 2. Nevertheless, it replaces the Go or Grow rule determined by the oxygen concentration, via the simple new Go or Grow rule: if the mass on the interval $[x, \infty)$ is higher than 1, the population at position x is subject to the Go regime, whereas if this mass is lower than 1 the population is subject to the Grow regime. Moreover, Theorem 2.3.1 from Chapter 2 applies to Equation (5.3.4) and we state it in an abbreviated version:

Theorem 5.3.1. *There exists a minimal speed σ^*, such that there exists a bounded and nonnegative traveling wave profile $\rho^\sigma(z)$, i.e. $\rho^\sigma(x - \sigma t)$ is a solution to Equation (5.3.4), if and only if $\sigma \geq \sigma^*$. Given $\sigma \geq \sigma^*$, the traveling wave profile ρ^σ is unique up to translation. Moreover, the exact value of σ^* is given by Formula (5.3.1):*

$$\sigma^* = \begin{cases} \chi + \frac{1}{\chi} & \text{if } \chi > 1 \\ 2 & \text{if } \chi \leq 1 \end{cases}.$$

As mentioned, the rigorous proof of the convergence of $\frac{Z_t^K}{K} \to \rho(t, \cdot)$ is still under investigation. But, we will briefly mention some approaches, which may be fruitful in order to establish this convergence results.

First of all, an important ingredient is the question of the existence and uniqueness of the solution to Equation (5.3.4) in order for the limit ρ to be well-defined and unique. This question will be addressed in Chapter 6, where we show that locally in time the solution ρ to Equation (5.3.4) exists and is unique. Although, we have not been able to prove existence globally in time, the uniqueness argument applies as long as the solution exists. Hence, an interesting perspective is that, if we were able to show convergence of $\frac{Z_t^K}{K}$ for all time $t \geq 0$, then this would give simultaneously the existence of ρ globally in time. Second in order to prove the convergence, we may resort to tools, such as martingale properties for $\frac{Z_t^K}{K}$, which have been used in many large population limits (see for instance [47, 76]). Another approach under consideration comes from [52], where the authors have used upper and lower barriers in order to prove the convergence of the N-BBM to a free boundary problem. Two auxiliary stochastic processes are defined, which bound above (resp. below) the positions of the particles. The authors then show that both stochastic processes converge to the same free boundary problem. Finally, the study on rank-based diffusions [109] suggest to study the convergence of $\frac{Z_t^K}{K} * \mathcal{H}$. In our case, if we consider $P := \rho * \mathcal{H}$, then P satisfies the following equation:

$$\partial_t P - \partial_{xx} P + \chi \mathbb{1}_{P>1} \partial_x P = \min\{1, P\}. \tag{5.3.5}$$

Interestingly the study of Equation (5.3.5) will be a very helpful tool in the Chapter 6, in order to establish asymptotic results on the spreading of ρ.

5.3.2 Numerical Investigations

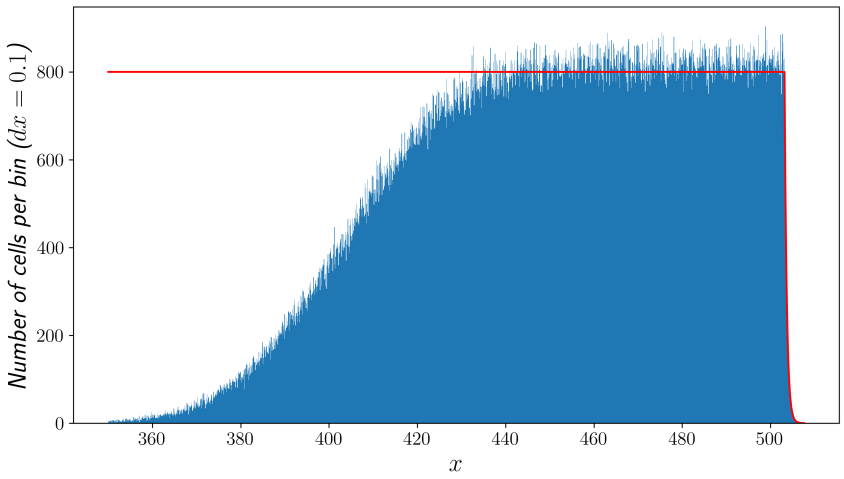

Figure 5.1: Histogram of Z_T^K for $\chi = 2, K = 4096, T = 200$ and inital datum $N = 2K$. The width of a single bin in the histogram is $dx = 0.1$. The red curve represents $y = C \begin{cases} e^{-\chi(x - H^K(Z_T^K))} & \text{if } x > H^K(Z_T^K) \\ 1 & \text{if } x \leq H^K(Z_T^K) \end{cases}$, where we recall that $H^K(Z_T^K)$ denotes the position of the K-th particle at time T and C has been chosen *a priori* with $C := K\chi dx$, which is consistent with the discretization of the histogram.

In this Subsection, we briefly present numerical investigations, which support the claim that the $\frac{Z_t^K}{K}$ converges to ρ solution to Equation (5.3.4).

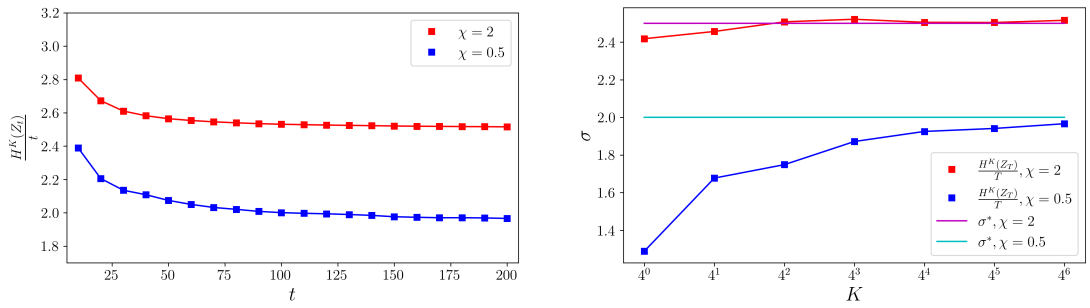

(a) (b)

Figure 5.2: (a): Graphic representation of $\frac{H^K(Z_t^K)}{t}$, where $H^K(Z_t^K)$ is the position of the K-th particle at time t, for $K = 4096$, $\chi = 2$ (red) and $\chi = \frac{1}{2}$ (blue). (b): Graphic representation of $\frac{H^K(Z_T^K)}{T}$, with $T = 200$, $\chi = 2$ (red) and $\chi = \frac{1}{2}$ (blue) as a function of K. The magenta (resp. cyan) curve represents speed $\sigma^* = \chi + \frac{1}{\chi}$ with $\chi = 2$ (resp. $\sigma^* = 2$ with $\chi = \frac{1}{2}$).

We simulate the stochastic process Z_t^K by following the algorithmic construction of Subsection 5.2.1. We set the initial datum Z_0^K as follows:

- Set $N = 2K$ the number of initial particles.

- In the case $\chi > 1$, the position of the first K particles follow an exponential law $\mathcal{E}(\chi)$. In the case $\chi \leq 1$, their position is distributed according to the law with density $\frac{\mathbb{1}_{x\geq 0}}{2-\chi}\left((1-\chi)x+1\right)e^{-x}$. In both cases, the distribution corresponds to the distribution given by the traveling wave profile ρ^{σ^*}.

- Given the distribution of the K first particles on $\mathbb{R}_+$, we wish to sample the other remaining K particles again, according to the traveling wave profile. Yet, since there are only a finite number of particles and a proper sampling of the traveling wave profile would require an infinite number of particles, we restrict the sampling of the profile to an interval of the form $[-a, +\infty)$: in the case $\chi > 1$, the remaining K particles are uniformly distributed on $\left[-\frac{1}{\chi}, 0\right]$, whereas in the case $\chi \leq 1$ the particles are uniformly distributed on $[-(2-\chi), 0]$.

In the long time behavior the distribution $\frac{Z_t^K}{K}$ is reminiscient of the traveling wave profile ρ at least in a compact set around the position of the K-th particle (see Figure 5.1). Next, we show that in both cases ($\chi > 1$ and $\chi \leq 1$), the spreading of the K-th particle evolves linearily (see Figure 5.2a), *i.e.* $\frac{H^K(Z_t^K)}{t}$ converges to a finite value, which we denote σ^K. Finally, by increasing K, we show numerically that the value σ^K seems to converge to the wave speed σ^* given by Formula (5.3.1) (see Figure 5.2b).

5.4 The Ancestral Lineage

In this Section, we wish to investigate the ancestral lineage of the particles, following a methodology, which has recently been proposed in [38, 74]. Roughly speaking, given a particle X_t^i at time t, we are interested in the positional distribution of its ancestor $Y_{s,t}^i$ at time $t-s$, for $s \geq 0$. As the mentioned studies have shown, these questions are rather delicate and in this Section, we will only discuss these questions in an informal manner and give the heuristics of the ancestral lineage distributions. We describe the approch, which stands in direct analogy with the results in [38], by leaving rigorous results to future investigations and illustrating the arguments with numerical simulations.

First, we delimit the question of the ancestral distribution to the regime of the traveling wave: as observed in the previous section, the large population limit $K \to +\infty$ gives rise to Equation (5.3.4). This equation admits a steady state, which is the traveling wave from Theorem 5.3.1. Hence, if the individual-based stochastic process $\frac{Z_t^K}{K}$ is close to the traveling wave dynamics at initial time $t = 0$, we expect the stochastic process $\frac{Z_t^K}{K}$ to remain close to the traveling wave dynamics at least for finite time $t = T < +\infty$, for K sufficiently large. Figure 5.1 hints exactly to this fact, if we ignore the part of the population, which is trailing the bulk of the propagating profile. As noted, the discrepancy for the trailing part comes from the fact that we start with a finite initial number of particles, whereas the steady dynamics woulde require an infinite number of particles. Ignoring this discrepancy, for the sake of the argument, we reason as if the stochastic process $\frac{Z_t^K}{K}$ is in its steady state. Of course, this requires a leap of faith, since we have not shown that for finite $K < +\infty$, the stochastic process $\frac{Z_t^K}{K}$ admits a steady state and we deliberately and nonrigorously equate the steady state of Equation (5.3.4) with a steady state for the stochastic process $\frac{Z_t^K}{K}$, which may or may not exist.

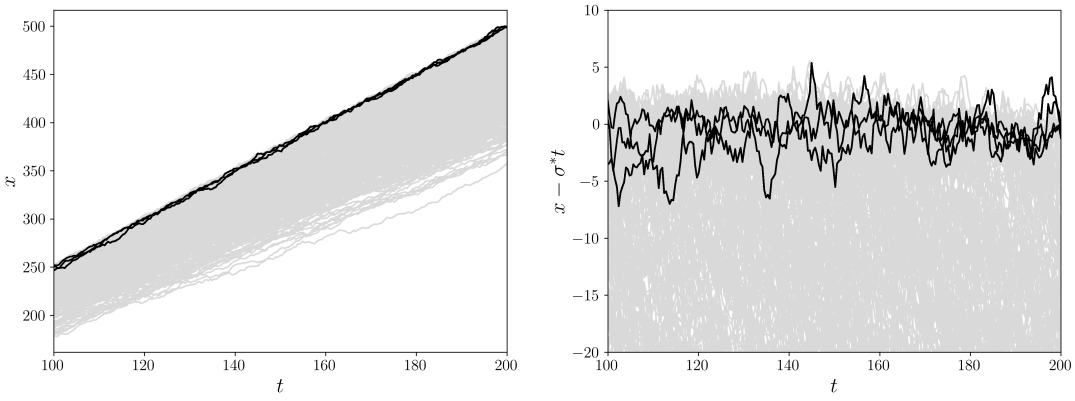

Figure 5.3: Graphical representation of the particle trajectories for $t \in [100, 200]$, with $\chi = 2, K = 256$ and initial datum $N = 2K$. The grey curves represent particle trajectories, which have been sampled uniformly among the population. The black curves represent 4 particle trajectories, which at time $T = 200$ are neighbors of the K-th particle. Of note two of these particles coalesce approximately at $t = 168$. The left graphic represents the trajectories in the frame (t, x), whereas the right graphic represents the same trajectories in the frame $(t, x - \sigma^* t)$, where $\sigma^* = \chi + \frac{1}{\chi}$.

Given a particle $X_t^{K,\ell}$, its ancestral distribution $Y_{s,t}^{K,\ell}$ is defined as follows. Consider the set $\mathcal{U}_{t-s}^K$ and find the unique label $\ell_s \in \mathcal{U}_{t-s}^K$, such that ℓ_s is a prefix of ℓ. This label is unique, since no two labels in $\mathcal{U}_{t-s}^K$ can be prefix of each other, as observed in Subsection 5.2.3, and it exists as a consequence of the algorithmic construction. Then $Y_{s,t}^{K,\ell} = X_{t-s}^{K,\ell_s}$.

We start by illustrating a typical tajectory of $Y_{s,T}^{K,\ell}$ (see Figure 5.3). This naturally leads to considering the distribution $Y_{s,T}^{K,\ell}$ in the moving frame $(t, z) = (t, x - \sigma^* t)$. Thus we define $\hat{Y}_{s,T}^{K,\ell} := Y_{s,T}^{K,\ell} - \sigma^*(T - s)$. Figure 5.4a points to the fact that in the case $\chi > 1$, $\hat{Y}_{s,T}^{K,\ell}$ admits a stationary distribution. But, what would the shape of this stationary distribution be? In order to investigate this question, we can consider the (formal) limit when $K \to +\infty$. Then, we start by observing that the (forward in time) distribution of the descendants of a particle is exactly given by the formalism of neutral fractions. From Chapter 2, recall the following definition:

Definition. *Define $L := -\partial_{zz} - \beta\partial_z$, where $\beta(z) = \sigma - \chi \mathbb{1}_{z \leq 0} + 2\frac{\partial_z \rho^\sigma}{\rho^\sigma}$. A neutral fraction ν (of the traveling wave ρ^σ) is a solution to the following equation:*

$$\begin{cases} \partial_t \nu + L\nu = 0 \\ \nu(0, \cdot) = \nu^0 \end{cases} . \tag{5.4.1}$$

Roughly speaking, if ν^0 describes a fraction of the population, which is marked by a neutral label, *i.e.* that does not interfer with the dynamics, then $\nu(t, \cdot)$ describes the fraction of the population for later time $t > 0$, which are marked by this label, *i.e.* which are descendants of the initially marked population (the neutral label being transmitted to its descent). Following this line of reasoning, the ancestral distribution $v(s, \cdot) = \tilde{v}(T - s, \cdot)$ should simply be the backward in time dynamics of Equation (5.4.1), *i.e.* for $s \geq 0$:

$$\begin{cases} \partial_s v + \mathcal{L} v = 0, \\ v(0, \cdot) = \tilde{v}(T, \cdot), \end{cases} \tag{5.4.2}$$

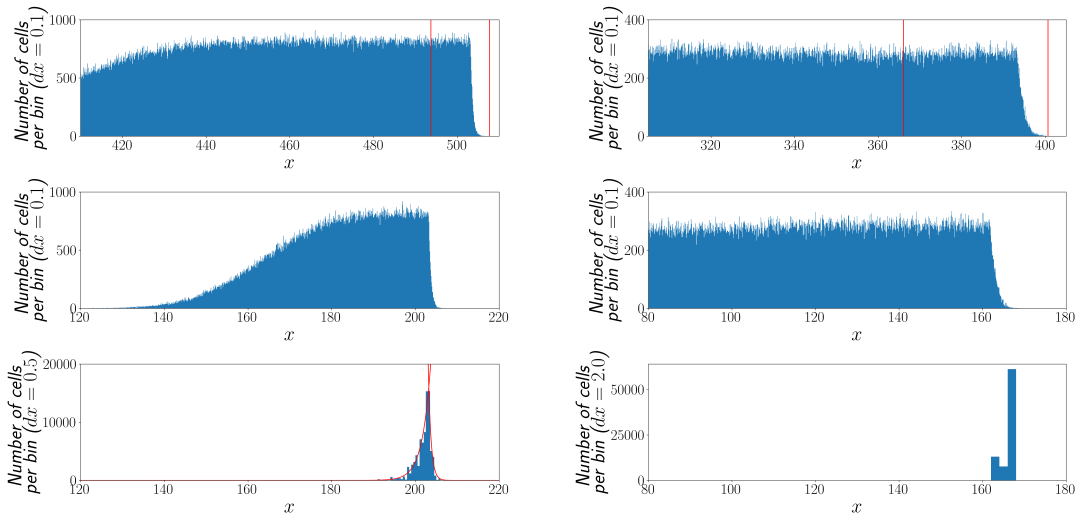

(a) (b)

Figure 5.4: Graphical representations of the ancestral distribution. The first line represents the distribution Z_T^K for $T = 200$ and $K = 4096$. The two red bars stake out the position of the first $20K$ particles at time $T = 200$. The second line represents the distribution Z_{80}^K. The third line represents the ancestral distribution at time $t = 80$, *i.e.* $s = 120$, of the first $20K$ particles at time $T = 200$ (which are between red bars in the first line). (a): The case $\chi = 2$. The red curves represent $y_1(x) = Ce^{\frac{x - H^K(Z_{80}^K)}{\chi}}$ and $y_2(x) = Ce^{-\left(\chi - \frac{1}{\chi}\right)\left(x - H^K(Z_{80}^K)\right)}$, which leads to $Cv_\infty\left(x - H^K(Z_{80}^K)\right) = \min\{y_1(x), y_2(x)\}$ (see Equation (5.4.4)). The constant C has been chosen *a posteriori* by visually fitting the curves. The distribution of the ancestors seems to be stationary in the frame $(t, x - H^K(Z_t^K))$ and to coincide with the distribution delimited by the red curves and the x-axis. The number of distinct ancestors is 937. (b): The case $\chi = \frac{1}{2}$. The ancestors of the particles all come from the leading edge. The number of distinct ancestors is 5.

where time has been reversed and $\mathcal{L} := L^* = -\partial_{zz} + \partial_z(\beta\,\cdot)$. Of note Equation (5.4.2) is under conservative form, which is consistent with the fact that a particle will have only a single ancestor at earlier time.

One of the drawbacks of this reasoning lies in the fact that it is based on the limit PDE (5.3.4). However, as observed in [38], when passing the stochastic process $\frac{Z_t^K}{K}$ to the limit $K \to +\infty$, the information of a single particle's trajectory is erased. Hence, this approach is not sufficient in order to make sense to the question of the ancestral distribution $\hat{Y}_{s,T}^{K,\ell}$ when $K \to +\infty$. Much of the work in [38] precisely consists in giving a rigorous sense to the preceding heuristics. Leaving the question of rigorous formalism to future investigations, we can continue the analogy with the work [38], where the authors have the convergence of the equivalent of $\hat{Y}_{s,T}^{K,\ell}$ to a stochastic process. Mimicking this reasoning, we can conjecture that $\hat{Y}_{s,T}^{K,\ell}$ converges to the following stochastic process, when $K \to +\infty$:

$$d\hat{Y}_s = \beta(\hat{Y}_s)ds + \sqrt{2}dW_s, \tag{5.4.3}$$

where the initial datum $\hat{Y}_0$ depends only on the position of the particles, which are sampled, and not their labels when $K \to +\infty$. In a consistent manner, Equation (5.4.2) is then simply the associated Fokker-Planck equation of the SDE (5.4.3). Hence, following this

conjecture, the trajectories in the moving frame $(t, z) = (t, x - \sigma t)$, which have been illustrated in Figure 5.3, should be close to the trajectories given by Equation (5.4.3).

Finally, Equation (5.4.2) may give an alternative point of view on the inside dynamics of the traveling waves, which have been studied in [82, 152] as well as in Chapter 2. In particular, the qualitative behavior of Equation (5.4.2) drastically differs in the pushed or pulled case.

The Pushed Case: $\chi > 1$.

A traveling wave is called pushed, when the wave is subject to a significant contribution from the overall population to the net propagation (see Chapter 2 for more details). In Chapter 2, we have proven that this is the case, when $\chi > 1$. Here, we show that in this case Equation (5.4.2) admits a stationary distribution v_∞, which is integrable. The ancestral distribution will converge exponentially fast to v_∞. Roughly speaking, if one picks a particle inside the wave, then for sufficiently large time its ancestors are distributed according to the stationary distribution v_∞. Hence, the stationary distribution v_∞ may be interpretated (see [74]) as a quantification of which parts of the wave contribute the most to the propagation.

Observe that:

$$v_\infty(z) := \exp\left(\int_0^z \beta(y)dy\right) = \exp\left(\begin{cases} \frac{z}{\chi} & \text{if } z \leq 0 \\ -\left(\chi - \frac{1}{\chi}\right) z & \text{if } z > 0 \end{cases}\right) \tag{5.4.4}$$

is a stationary solution to Equation (5.4.2). In Figure 5.4a, we have ploted v_∞ (up to a multiplicative constant and in the right frame) and it seems in fact that $\hat{Y}^{K,\ell}_{s,T}$ converges to a stationary distribution, close to v_∞ (of note, here we have taken K large and fixed).

Given the stationary solution (5.4.4), we set $f := \frac{v}{v_\infty}$. Then by a series of computations, we find that:

$$\partial_t f = \partial_{zz} f + \beta \partial_z f = -Lf, \tag{5.4.5}$$

where $L = -\partial_{zz} - \beta\partial_z$. Equation (5.4.5) has been studied in Chapter 2. We have shown that f converges exponentially fast to a constant with rate $\gamma = \frac{1}{4}\min\left\{\frac{1}{\chi^2}, \left(\chi - \frac{1}{\chi}\right)^2\right\}$. Hence the stochastic process given by Equation (5.4.3) will have a probability distribution, which converges exponentially in time $s \to +\infty$ to the stationary distribution given by v_∞.

The Pulled Case: $\chi \leq 1$.

A traveling wave is pulled, when it is driven by growth and diffusion of the population at the edge of the front with negligible contribution from the overall population. This is the case, when $\chi \leq 1$ (see Chapter 2). Contrary to the pushed case, although Equation (5.4.2) admits stationary solutions, these are not integrable. In fact:

$$v_\infty(z) := \begin{cases} e^{(2-\chi)z} & \text{if } z < 0 \\ ((1-\chi)z + 1)^2 & \text{if } z \geq 0 \end{cases}. \tag{5.4.6}$$

Hence v cannot converge to these stationary solution (recall that Equation (5.4.2) is conservative). This is illustrated numerically in Figure 5.4b, where the ancestral distribution seems to originate from the extremity of the leading edge, contrary to the case $\chi > 1$.

A precise quantitative analysis of Equation (5.4.2) is still under investigation in the case $\chi \leq 1$. Hence, we merely illustrate numerically the behavior of v, solution to Equation

(5.4.2) (see Figure 5.5). Interestingly, the behavior differs when $\chi = 1$ or $\chi < 1$. Although in both cases, v does not converge to a stationary distribution, in the case $\chi = 1$, the profile of v resembles rougly a half of a Gaussian, which is locked at $z = 0$. In the case $\chi < 1$, the profile of v resembles to a Gaussian, centered around a mean, which spreads to $z = +\infty$. Numerically, this mean spreads asymptotically like $C\sqrt{t}$. This difference can be seen heuristically from the term β: in the case $\chi = 1$, $\beta(z) = 0$ for $z \geq 0$, hence on $\mathbb{R}_+$ behaves like the heat equation on the half-line; in the case $\chi < 1$, we have $\beta(z) = \frac{2(1-\chi)}{(1-\chi)z+1}$ for $z \geq 0$, hence there is a drift towards higher positive values, which gets smaller and smaller. But in both cases ($\chi = 1$ and $\chi < 1$), the mean of the distribution given by $v(s)$ is asymptotically of order $\sqrt{t}$, which leads to the following alternative interpretation of a pulled wave: given a particle in the wave its ancestors stem from the very leading edge.

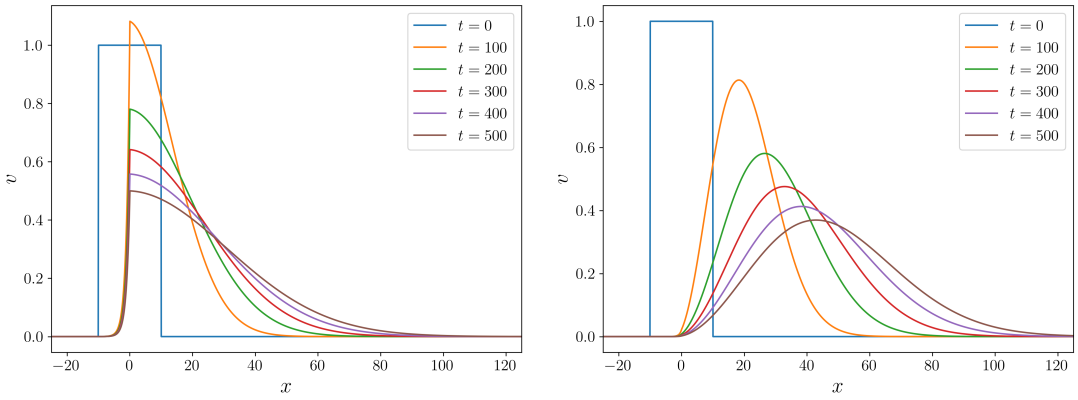

Figure 5.5: Solution v of Equation (5.4.2), with inital datum $v^0(x) = \mathbb{1}_{[-10,10]}(x)$, when $\chi = 1$ (left) and $\chi = \frac{1}{2}$ (right).

Outlook

As mentioned most of the arguments in this Chapter have been exposed in an informal and nonrigorous way. Rigorous results are still under investigation. Here, we wish to briefly stress again which questions we are currently working on. First, we look forward to prove that the large population limit of $\frac{Z_t^K}{K}$ converges to $\rho(t, \cdot)$, which satisfies Equation (5.3.4). Then, we hope to transpose the methodology on ancestral lineages proposed in [38, 74] to the model exposed here. In particular, this opens a perspective of understanding the nature of pulled and pushed waves in a different light, which has already been mentioned in [74].

Chapter 6

Alternative Go or Grow PDE Model and its Preliminary Analysis

---

This Chapter is a preliminary presentation of results from an ongoing collaboration with Christopher Henderson. We study an alternative Go or Grow PDE model (which in Chapter 5 is conjectured to be the large population limit for the stochastic Go or Grow model), where the Go or Grow regimes at position x depend on how much mass is located on the interval $[x, +\infty)$. We show an existence and uniqueness result locally in time for this alternative Go or Grow model, which is an adaptation of the equivalent result in Chapter 2. Then, we propose a conjecture of the asymptotic behavior of the spreading and give proofs for some cases of this conjecture. Finally, through an L^2-energy method, we show an asymptotic stability result for the traveling wave of minimal velocity in the case $\chi > 1$.

6.1 Introduction

In the preceding Chapter, we have conjectured that the stochastic Go or Grow model converges in the large population limit to a PDE, which can be seen as an alternative Go or Grow model:

$$\begin{cases} \partial_t \rho - \partial_{xx}\rho + \partial_x \left(\chi \mathbb{1}_{x<\bar{x}(t)}\rho\right) = \mathbb{1}_{x\geq\bar{x}(t)}\rho, & \text{(6.1.1a)} \\ \displaystyle\int_{\bar{x}(t)}^{+\infty} \rho(t,x)dx = 1. & \text{(6.1.1b)} \end{cases}$$

In a sense, this can be seen as an Equation with the constraint, given by (6.1.1b). Thus, we will sometimes refer to (6.1.1) as an Equation with constraint.

We recall the Go or Grow model, which has been the initial object of study in this manuscript (see notably Chapter 2):

$$\begin{cases} \partial_t \rho - \partial_{xx}\rho + \partial_x \left(\chi \mathbb{1}_{N<N_{\text{th}}} \text{sign}(\partial_x N)\rho\right) = \mathbb{1}_{N>N_{\text{th}}}\rho, & \text{(6.1.2a)} \\ \partial_t N - D\partial_{xx}N = -\rho N. & \text{(6.1.2b)} \end{cases}$$

Of note, if we assume that $\partial_x N > 0$ and we define $\bar{x}(t)$ the unique threshold position, such that $N(t, \bar{x}(t)) = N_{\text{th}}$, then Equation (6.1.2a) exactly reduces to Equation (6.1.1a), which is the reason, why we refer to the Equation with constraint (6.1.1) as an alternative Go

or Grow model. The difference in both models then resides only in how the curve $\bar{x}(\,\cdot\,)$, which discriminates between the Go regime ($x < \bar{x}(t)$) and the Grow regime ($x \geq \bar{x}(t)$), is defined. In a sense, the dynamics of Equation (6.1.1) is simpler, as the Go or Grow rule: the definition of $\bar{x}(t)$ can be seen as "Markovian". By this, we mean that in Equation (6.1.1), $\bar{x}(t)$ depends only on the state $\rho(t,\,\cdot\,)$. In System (6.1.2), this is not the case, as $\bar{x}(t)$ is defined through the parabolic Equation (6.1.2b). Hence, it is reasonable to expect that for Equation (6.1.1) we may overcome difficulties, which we have encountered in System (6.1.2). This Chapter pleads to an extent for this.

Interestingly, both Go or Grow models are very similar to a free boundary problem proposed in [20]:

$$\begin{cases} \partial_t u - \partial_{xx} u = u, \text{ for } x > \mu_t \\ u(t,\mu_t) = \alpha \text{ and } \partial_x u(t,\mu_t) = \beta \end{cases}, \tag{6.1.3}$$

with $\alpha, \beta \in \mathbb{R}$. In fact, if we consider $\alpha > 0$ and $\beta = -\alpha\chi$, then the traveling wave solutions of the Go or Grow models are exactly the same than the ones for the free boundary Problem (6.1.3). Furthermore the authors in [20] determine through formal computations the asymptotic behavior of μ_t, depending on χ and the initial datum u^0 (and how fast it decreases for $x \to +\infty$). The computations surprisingly depend almost only on the shape of the traveling wave profile. As mentioned, since the traveling wave solutions are the same between the Go or Grow model and this free boundary problem, inspired by the results in [20], we propose a conjecture of the asymptotic behavior of $\bar{x}(t)$ in (6.1.1):

$$x(t) = \begin{cases} 2t - \frac{3}{2}\log(t) + O(1) & \text{if } \chi < 1 \\ 2t - \frac{1}{2}\log(t) + O(1) & \text{if } \chi = 1 \\ \left(\chi + \frac{1}{\chi}\right) + O(1) & \text{if } \chi > 1 \end{cases}. \tag{6.1.4}$$

In the case $\chi < 1$, this means that we would obtain for the asymptotics a (standard) Bramson shift, which has been well studied in the case of the F/KPP Equation (see [29, 96] for instance). In the case $\chi = 1$, the asymptotics undergo a similar Bramson shift, but with a different coefficient, which has recently been observed on the Burgers-F/KPP Equation [9] and a reaction-diffusion equation with a cubic monostable reaction term [83]. The case $\chi > 1$ corresponds to the pushed case, where the result is in accordance with many results on standard reaction-diffusion equations (*e.g.* [70, 154, 169]). In this Chapter, we will expose intermediary results towards the proof of Conjecture (6.1.4).

Moreover during our investigation, we have also considered a second alternative Go or Grow model:

$$\begin{cases} \partial_t \rho - \partial_{xx}\rho + \partial_x\left(\chi \mathbb{1}_{x<\bar{x}(t)}\rho\right) = \mathbb{1}_{x\geq\bar{x}(t)}\rho, & \text{(6.1.5a)} \\ \bar{x}(t) = \sup\left\{x | \rho(t,x) = 1\right\}. & \text{(6.1.5b)} \end{cases}$$

We refer to it as the ρ-levelset Go or Grow model. This model will not be considered in this Chapter, but we briefly mention it, as it invites us to consider a link with the Burgers-F/KPP Equation, which has notably been studied in [9]. In fact, suppose that ρ is decreasing and set $\psi(s) = \mathbb{1}_{s>1}$, then we can rewrite the ρ-levelset Go or Grow model as follows:

$$\partial_t \rho - \partial_{xx}\rho + \partial_x\left(\chi\psi(\rho)\rho\right) = (1-\psi(\rho))\rho. \tag{6.1.6}$$

Now, the Burgers-F/KPP Equation is exactly Equation (6.1.6), when we use $\psi(s) := s$. Therefore one can see ρ-levelset Go or Grow model and the Burgers-FKPP Equation as part of the same class of Equations given by (6.1.6). In fact, the authors of [9] are currently investigating the class of Equation (6.1.6) with ψ convex. It seems that the equivalent of

Conjecture (6.1.4) may hold for this large class of Equations. In fact, as mentioned above, this result has already been proven for the Burgers-F/KPP Equation with $\psi(s) := s$ in [9].

Finally let us give an equivalent formulation of (6.1.1), which will be very useful in the present study. Set $P(t,x) = \int_x^{+\infty} \rho(t,y)dy$, then one shows that:

$$P_t = P_{xx} + \min\{1, P\} - \chi \mathbb{1}_{P>1} P_x. \tag{6.1.7}$$

This equation admits a comparison principle, which slightly deviates from typical comparison principles for parabolic equations (see Propositions 6.3.5 and 6.3.4). Through this comparison principle, we will be able to construct super- and subsolutions, which will lead to upper and lower bounds on $\bar{x}(t)$.

Outline

In Section 6.3, we prove existence and uniquess of the solution ρ to Equation (6.1.1) locally in time. The proof is very similar to the analogous result in Chapter 2 and is based on a fixed point theorem on the curve $\bar{x}(\,\cdot\,)$. Just as in Chapter 2, we need an enpoint regularity estimate, which we achieve by a careful handling of the singularity at the point, where $P = 1$.

In Section 6.3, we give preliminary results on the asymptotic behavior of $\bar{x}(t)$. The results are consistent with Conjecture (6.1.4). The first result is the upper bound on $\bar{x}(t) \leq \sigma^* t + C$ for any $\chi \geq 0$. This result corresponds to the upper bound for $\chi > 1$ in Conjecture (6.1.4). Then, we show that Equation (6.1.7) admits a comparison principle. This comparison principle then enables us to construct a subsolution in the case $\chi = 1$, which leads to the lower bound for $\chi = 1$ in Conjecture (6.1.4), and a supersolution in the case $\chi < 1$, which leads to the upper bound for $\chi < 1$ in Conjecture (6.1.4).

In Section 6.4, we prove asymptotic stability of the minimal traveling wave solution in a L^2-space. The proof, which is reminiscent of a line of reasoning presented in [39], is based on an energy method and uses a Poincaré inequality, which is deduced from the analysis of the spectral properties of the linearized operator.

6.2 Existence and Uniquess Result

In this Section, we establish existence and uniqueness locally in time for Equation (6.1.1), under the condition that $\bar{x}(0)$ in (6.1.1) is uniquely defined and that $\rho^0(\bar{x}(t))$ is bounded below by a positive constant. Without loss of generality, we assume that $\bar{x}(0) = 0$. The proof is an adaptation of the existence and uniqueness result in Chapter 2 for System (6.1.2) and follows the same line of reasoning. Hence, we will sketch the proof in a concise format and refer the reader to Chapter 2 for an in-depth discussion on the strategy of proof, as well as for technical details.

We start by considering Equation (6.1.1) in the moving frame $(t,z) = (t, x - \bar{x}(t))$, which leads to:

$$\begin{cases} \partial_t \tilde{\rho} - \partial_{zz}\tilde{\rho} - \dot{\bar{x}}(t)\partial_z \rho + \partial_z\left(\mathbb{1}_{z<0}\tilde{\rho}\right) = \mathbb{1}_{z\geq 0}\tilde{\rho} & \text{(6.2.1a)} \\ \displaystyle\int_0^{+\infty} \tilde{\rho}(t,z)dz = 1 & \text{(6.2.1b)} \end{cases}$$

Recall, that because of the discontinuous advection term $\partial_z\left(\mathbb{1}_{z\leq 0}\,\cdot\right)$, $\tilde{\rho}$ will have a C^1-discontinuity, which follows from a Rankine-Hugoniot type of argument:

$$\partial_z\tilde{\rho}(t,0^+) - \partial_z\tilde{\rho}(t,0^-) = -\chi\tilde{\rho}(t,0). \tag{6.2.2}$$

This naturally leads to factorize $\tilde{\rho}$ under the form $\tilde{v}U$, with a function U such that the factorization precisely cancels out the C^1-jump relation at $z = 0$. Of note, the notations are slightly different than in Chapter 2, as here $\tilde{v}$ (contrary to v in Chapter 2) denotes the factorization in the moving frame. We choose:

$$U(z) = \begin{cases} 1 & \text{if } z \leq 0 \\ e^{-\chi z} & \text{if } z > 0 \end{cases} . \tag{6.2.3}$$

This leads to the following Equation on $\tilde{v}$:

$$\partial_t \tilde{v} - \partial_{zz}\tilde{v} - \beta(t,z)\partial_z \tilde{v} - \gamma(t,z)\tilde{v} = 0, \tag{6.2.4}$$

where $\beta(t,z) := \dot{\bar{x}} - \chi \mathbb{1}_{z\leq 0} - 2\chi \mathbb{1}_{z>0}$ and $\gamma(t,z) := \chi\left(\left(\chi + \frac{1}{\chi}\right) - \dot{\bar{x}}\right)\mathbb{1}_{z>0}$. Under this circumstance, $\tilde{v}$ will be of higher regularity: in fact, first, we will show that $\tilde{v}(t) \in C^{1,\alpha}(\mathbb{R})$ for $\alpha \in (0,1)$, then we will refine this result in order to show that $\tilde{v}(t) \in W^{2,\infty}(\mathbb{R})$ (by adapting the argument of Chapter 2, we can even show that this regularity is an endpoint case and that $\tilde{v}(t) \notin C^{2,\alpha}(\mathbb{R})$ for any $\alpha \in (0,1)$). Furthermore we introduce v in the stationary frame, such that:

$$\rho(t,x) = v(t,x)e^{-\chi(x-\bar{x}(t))\mathbb{1}_{x\geq \bar{x}(t)}}. \tag{6.2.5}$$

Next, by differentiating Constraint (6.1.1b), $\bar{x}(t)$ must satisfy the following ODE:

$$\dot{\bar{x}}(t) = \frac{1 - \partial_x \rho(t, \bar{x}(t)^+)}{\rho(t,\bar{x}(t))}, \tag{6.2.6}$$

or, equivalently:

$$\dot{\bar{x}}(t) = \frac{1 - \partial_x v(t,\bar{x}(t))}{v(t,\bar{x}(t))} + \chi. \tag{6.2.7}$$

Of note, precisely because of the regularity $v(t) \in W^{2,\infty}(\mathbb{R})$, we expect the ODE (6.2.7) to be well-defined.

The strategy of proof consists in applying a fixed point mapping to the curve $t \mapsto \bar{x}(t)$. More precisely, the main steps consist in (i) given the curve $\bar{x}(\,\cdot\,)$, solving Equation (6.2.1a). (ii) Given the solution $\tilde{\rho}[\bar{x}]$ and thus $\rho[\bar{x}]$, we show that there exists a unique solution $\bar{y}(t)$ locally in time, such that:

$$\int_{\bar{y}(t)}^{+\infty} \rho[\bar{x}](t,x)dx = 1. \tag{6.2.8}$$

Differentiating this relation leads to:

$$\begin{aligned} 0 =& -\dot{\bar{y}}(t)\rho(t,\bar{y}(t)) + \int_{\bar{y}(t)}^{+\infty} \left(\partial_{xx}\rho(t,x) - \partial_x\left(\chi \mathbb{1}x < \bar{x}(t)\rho(t,x)\right) + \mathbb{1}_{x\geq\bar{x}(t)}\rho(t,x)\right)dx \\ =& -\dot{\bar{y}}(t)\rho(t,\bar{y}(t)) - \partial_x\rho(t,\bar{y}(t)^+) + \chi\mathbb{1}_{\bar{y}(t)<\bar{x}(t)}\rho(t,\bar{y}(t)) + P(t,\bar{x}(t)\vee\bar{y}(t)), \end{aligned}$$

where $P(t,x) := \int_x^{+\infty}\rho(t,y)dy$. By noticing that $\frac{\partial_x v}{v} = \frac{\partial_x \rho}{\rho} + \chi\mathbb{1}_{\,\cdot\,\geq\bar{x}(t)}$, we can rearrange terms and obtain the following ODE:

$$\begin{cases} \dot{\bar{y}}(t) = \chi - \frac{\partial_x v(t,\bar{y}(t))}{v(t,\bar{y}(t))} + \frac{P(t,\bar{x}(t)\vee\bar{y}(t))}{\rho(t,\bar{y}(t))} \\ \bar{y}(0) = 0 \end{cases} . \tag{6.2.9}$$

We will show that the ODE (6.2.9) is well-posed, which then defines a mapping $\bar{x} \mapsto \bar{y}$. (iii) We show that the mapping $\bar{x} \mapsto \bar{y}$ is a contraction on a small enough time interval, which

established by Banach's Fixed Point Theorem, the existence and uniqueness of a fixed point. For this fixed point $\bar{x}$, ODE (6.2.9) and ODE (6.2.6) coincide, which establishes a unique solution to Equation (6.1.1).

Exactly as in Chapter 2, in order to have sufficient regularity on $\tilde{v}$ given by Equation (6.2.4), we need some type of regularity on $\dot{\bar{x}}$. Yet, from ODE (6.2.9), it becomes clear that the mapping $\bar{x} \mapsto \bar{y}$ will be at most Lipschitz continous in $W^{1,\infty}$. In order to circumvent this issue, we consider the mapping $\bar{x} \mapsto \bar{y}$ in $W^{1,p}$, with $p \in (4, +\infty)$. Considering the mapping $\bar{x} \mapsto \bar{y}$ in $W^{1,p}$ leads through a time integration of Equation (6.2.9) to a contraction in $W^{1,p}$ for small enough time. Furthermore, here in this proof at a crucial point, when we show that $\tilde{v}(t) \in W^{2,\infty}(\mathbb{R})$, we need a uniform bound on $\|\dot{\bar{x}}\|_\infty$ for the curves $\bar{x}(\,\cdot\,)$ considered, contrary to what was need in the well-posedness proof in Chapter 2. Hence, we introduce the set:

$$B(A) := \left\{ \bar{y}(\,\cdot\,) \in W^{1,p}([0,T]) \middle| \|y\|_{W^{1,p}} \leq A \text{ and } \|\dot{\bar{x}}\|_\infty \leq A \right\}, \tag{6.2.10}$$

with the norm $\|y\|_{W^{1,p}} = \|y\|_p + \|\dot{y}\|_p$ and $p \in (4, \infty)$. $B(A)$ is a closed subset of $W^{1,p}([0,T])$ and thus is complete. We will then construct the mapping $\bar{x} \in B(A) \to \bar{y} \in B(A)$, which for A large enough and T small enough, will be a contraction. Finally, $B(A)$ being a complete normed space, we may apply Banach's Fixed Point Theorem.

Next, we recall bounds from Chapter 2. The evolution operator of the heat equation $e^{t\partial_{xx}}$ on the real-line is defined as follows:

$$e^{t\partial_{xx}} f(x) = \frac{1}{\sqrt{4\pi t}} \int_{\mathbb{R}} e^{-\frac{(x-y)^2}{4t}} f(y) dy. \tag{6.2.11}$$

Although, we will only briefly sketch the proof in this Section and refer the reader to Chapter 2 for more details, we recall the functional inequalities that operator $e^{t\partial_{xx}}$ satisfies and that are used in order to establish the result in this Section:

$$\left\| e^{t\partial_{xx}} f \right\|_q \leq C t^{-\frac{1}{2}\left(\frac{1}{p}-\frac{1}{q}\right)} \|f\|_p, \tag{6.2.12}$$

$$\left\| e^{t\partial_{xx}} \partial_x f \right\|_q \leq C t^{-\frac{1}{2}\left(\frac{1}{p}-\frac{1}{q}+1\right)} \|f\|_p. \tag{6.2.13}$$

$$\left\| e^{t\partial_{xx}} f \right\|_{C^{0,\alpha}(\mathbb{R})} \leq C t^{-\frac{\alpha}{2}} \|f\|_\infty, \tag{6.2.14}$$

$$\left\| e^{t\partial_{xx}} f \right\|_{C^{1,\alpha}(\mathbb{R})} \leq C t^{-\frac{1+\alpha}{2}} \|f\|_\infty, \tag{6.2.15}$$

$$\left\| \partial_x e^{t\partial_{xx}} f \right\|_\infty \leq C t^{\frac{\alpha-1}{2}} \|f\|_{C^{0,\alpha}(\mathbb{R})}, \tag{6.2.16}$$

$$\left\| \partial_{xx} e^{t\partial_{xx}} f \right\|_\infty \leq C t^{\frac{\alpha}{2}-1} \|f\|_{C^{0,\alpha}(\mathbb{R})}. \tag{6.2.17}$$

Let us now move to the statement of a well-posedness theorem locally in time under the condition that $\rho^0(\bar{x}(0))$ be bounded below a positive constant.

Theorem 6.2.1. *Let $p \in (4, \infty)$, $\alpha \in \left(\frac{2}{p}, 1 - \frac{2}{p}\right)$. Suppose that $v^0 := \frac{\rho^0}{U} \in W^{2,\infty}(\mathbb{R})$. Additionally suppose that there exists $\xi > 0$ and $\underline{m}$, such that for $x \in [-\xi, \xi]$:*

$$\rho^0(x) \geq \underline{m}. \tag{6.2.18}$$

Given $A > 0$ big enough (depending on $\chi, p, \alpha, \left\|v^0\right\|_{W^{2,\infty}}, \underline{m}, \xi$) there exists a small enough $T > 0$, such that for any curve $\bar{x} \in B(A)$, there exists a unique solution $\tilde{\rho}$ to Equation (6.2.1a). Moreover, $\tilde{\rho} \in L^\infty([0,T], W^{1,\infty}(\mathbb{R}))$ and $v = \frac{\tilde{\rho}}{U} \in L^\infty([0,T], C^{1,\alpha}(\mathbb{R}))$.

Furthermore, there exists a unique curve $\bar{x} \in B(A)$, such that the solution $\tilde{\rho}$ to System (6.2.1a) satisfies in addition Condition (6.2.1b). In other terms, $\tilde{\rho}$ is the unique solution of (6.2.1).

Proof. We now move on to the Proof of Theorem 6.2.1. We skip many of the technicalities and refer the reader to Chapter 2.

Step 1: Existence and uniqueness of a (mild) solution $\tilde{v}$ to Equation (6.2.4).

Fix $\bar{x} \in B(A)$. Consider the affine map $F : L^\infty\left([0,T], C^{1,\alpha}(\mathbb{R})\right) \to L^\infty\left([0,T], C^{1,\alpha}(\mathbb{R})\right)$, for $t \in [0,T]$:

$$F[u](t) = e^{t\partial_{zz}} v^0 + \int_0^t e^{(t-s)\partial_{zz}} \left(\beta(s)\partial_z u(s) + \gamma(s)u(s)\right) ds. \tag{6.2.19}$$

Following the proof of Chapter 2, we can show that F is a contraction for $T > 0$ small enough. Hence there exists a unique $\tilde{v} \in L^\infty\left([0,T], C^{1,\alpha}(\mathbb{R})\right)$ solution to Equation (6.2.1a), for $\bar{x}$ fixed.

Furthermore we can show by the same arguments that the mapping $\bar{x} \in B(A) \mapsto \tilde{v} \in L^\infty\left([0,T], C^{1,\alpha}(\mathbb{R})\right)$ is Lipschitz continuous.

Step 2: Enhanced regularity on $\tilde{v} \in L^\infty([0,T], W^{2,\infty}(\mathbb{R}))$.

By the preceding point, we have that:

$$\tilde{v}(t) = e^{t\partial_{zz}} v^0 + \int_0^t e^{(t-s)\partial_{zz}} \left(\beta(s)\partial_z \tilde{v}(s) + \gamma(s)\tilde{v}(s)\right) ds.$$

For the first term, we have that $e^{t\partial_{zz}} v^0 \in L^\infty([0,T], W^{2,\infty}(\mathbb{R}))$.
Then we set $f(t,z) := \beta(t,z)\partial_z \tilde{v}(t,z) + \gamma(t,z)\tilde{v}(t,z)$, $g(t,z) := f(t,z) - [\![f(t,\cdot)]\!]_{z_0} \mathbb{1}_{z \geq 0}$ and $h(t) := [\![f(t,\cdot)]\!]_{z_0}$, such that:

$$\beta(t,z)\partial_z \tilde{v}(t,z) + \gamma(t,z)\tilde{v}(t,z) = f(t,z) = g(t,z) + h(t)\mathbb{1}_{z \geq 0}.$$

By recalling that $\beta(t,z) = \dot{\bar{x}}(t) - \chi - \chi \mathbb{1}_{z \geq 0}$ and $\gamma(t,z) = \chi\left(\left(\chi + \frac{1}{\chi}\right) - \dot{\bar{x}}\right)\mathbb{1}_{z>0}$, we can show by elementary analysis arguments that for $t \in [0,T]$:

$$\|g(t)\|_{C^{0,\alpha}(\mathbb{R})} \leq C\left(1 + |\dot{\bar{x}}(t)|\right) \|\tilde{v}(t)\|_{C^{1,\alpha}(\mathbb{R})}.$$

Hence, by applying Inequality (6.2.17) and Hölder's Inequality:

$$\begin{aligned}
&\left\| \partial_{zz} \int_0^t e^{(t-s)\partial_{zz}} g(s) ds \right\|_\infty \\
\leq & C \int_0^t \left(1 + |\dot{\bar{x}}(s)|\right) (t-s)^{\frac{\alpha}{2}-1} \|\tilde{v}(s)\|_{C^{1,\alpha}(\mathbb{R})} ds \\
\leq & C \|\tilde{v}\|_{L^\infty([0,T], C^{1,\alpha}(\mathbb{R}))} \left(T^{\frac{1}{p}} + \|\dot{\bar{x}}\|_p\right) \left\| t \mapsto t^{\frac{\alpha}{2}-1} \right\|_{\frac{p}{p-1}},
\end{aligned}$$

where the $L^{\frac{p}{p-1}}$-integrability of $t \mapsto t^{\frac{\alpha}{2}-1}$ is guaranteed by the condition $\alpha > \frac{2}{p}$.

The remaining term is treated by using explicit computations:

$$\begin{aligned}
&\int_0^t \partial_{zz} e^{(t-s)\partial_{zz}} h(s) \mathbb{1}_{z\geq 0} ds \\
&= \int_0^t \partial_z e^{(t-s)\partial_{zz}} h(s) \delta_0 ds \\
&= -\int_0^t \frac{z h(s)}{\sqrt{4\pi}(t-s)^{\frac{3}{2}}} e^{-\frac{z^2}{4(t-s)}} ds \\
&= -\int_{\frac{|z|}{\sqrt{t}}}^{\infty} \frac{h\left(t-\frac{z^2}{u^2}\right)}{2\pi^{\frac{1}{2}}} e^{-u^2} du \qquad \text{, where } u = \frac{|z|}{\sqrt{(t-s)}}.
\end{aligned}$$

Hence, by the integrability of e^{-u^2}:

$$\left\| \int_0^t \partial_{zz} e^{(t-s)\partial_{zz}} h(s) \mathbb{1}_{z\geq 0} ds \right\|_\infty \leq C \|h\|_\infty$$

But we clearly have that:

$$\|h\|_\infty \leq C\left(1 + \|\dot{\bar{x}}\|_\infty\right) \leq C(1+A),$$

by the definition of $B(A)$, see (6.2.10). Of note, here it is crucial to suppose that $\|\dot{\bar{x}}\|_\infty$ can be uniformly bounded (contrary to what was needed in the proof of Chapter 2). In fact, under the mere condition that $\|\dot{\bar{x}}\|_p$ is uniformly bounded, $\int_0^t \partial_{zz} e^{(t-s)\partial_{zz}} h(s) \mathbb{1}_{z\geq 0} ds$ is not bounded in L^∞.

Finally, combining all these elements, we obtain that $\tilde{v} \in L^\infty([0,T], W^{2,\infty}(\mathbb{R}))$.

Step 3: Definition of the map $\bar{x} \mapsto \bar{y}$: Existence and Uniqueness of the solution $\int_\cdot^{+\infty} \rho(t,x)dx = 1$.

By considering ρ in the initial frame (t,x) and using the fact that ρ^0 is bounded below by $\underline{m}$ on the interval $[-\xi,\xi]$, we start by showing that for T small, we have for $x \in [-\xi,\xi]$ and $t \in [0,T]$:

$$\rho(t,x) \geq \frac{\underline{m}}{2}.$$

This can be done through elementary estimates on the heat kernel (see Chapter 2). Furthermore, using the fact that $v \in C([0,T], L^\infty(\mathbb{R}))$, which can easily be shown, we show that for $T > 0$ small enough, for $t \in [0,T]$, there exists $\bar{y}(t) \in [-\xi,\xi]$, such that:

$$\int_{\bar{y}(t)}^{+\infty} \rho[\bar{x}](t,x)dx = \int_{\bar{y}(t)}^{+\infty} v[\bar{x}](t,x) e^{-\chi(x-\bar{x}(t))\mathbb{1}_{x\geq \bar{x}(t)}} dx = 1. \tag{6.2.20}$$

From there on, by differentiating this relation, we obtain ODE (6.2.9), which we recall:

$$\begin{cases} \dot{\bar{y}}(t) = \chi - \frac{\partial_x v(t,\bar{y}(t))}{v(t,\bar{y}(t))} + \frac{P(t,\bar{x}(t)\vee\bar{y}(t))}{\rho(t,\bar{y}(t))} \\ \bar{y}(0) = 0 \end{cases}.$$

Notice that $\rho[\bar{x}](t,x) \geq \frac{\underline{m}}{2}$, $v \in L^\infty([0,T], W^{2,\infty}(\mathbb{R}))$, which is a consequence of $\tilde{v} \in L^\infty([0,T], W^{2,\infty}(\mathbb{R}))$ and $\rho \in L^\infty([0,T], W^{1,\infty}(\mathbb{R}))$, which is a consequence of Factorization (6.2.5) and $v \in L^\infty([0,T], W^{1,\infty}(\mathbb{R}))$. Finally, we have $P(t,\bar{x}(t)\vee\cdot) \in L^\infty([0,T], W^{1,\infty}_{\text{loc}}(\mathbb{R}))$, since $\partial_x P(t,\bar{x}(t)\vee x) = -\rho(t,\bar{x}(t)\vee x)$. Thus ODE (6.2.9) is well-posed. Moreover, if we

choose A big enough, then $\bar{y} \in B(A)$. Thus we have defined the mapping $\bar{x} \in B(A) \mapsto \bar{y} \in B(A)$.

Step 4: Unique Fixed Point of the map $\bar{x} \in B(A) \mapsto \bar{y} \in B(A)$.

Given $\bar{x}_1, \bar{x}_2 \in B(A)$, consider the associated $\bar{y}_1, \bar{y}_2 \in B(A)$, as well as $v_1, v_2, P_1, P_2, \rho_1, \rho_2$. Set:

$$\mathcal{F}_i(t,x) := \chi - \frac{\partial_x v_i(t,x)}{v_i(t,x)} + \frac{P_i(t, \bar{x}_i(t) \vee x)}{\rho_i(t,x)}. \tag{6.2.21}$$

We start by the following bound:

$$\begin{aligned} &|\dot{\bar{y}_1}(t) - \dot{\bar{y}_2}(t)| \\ =&|\mathcal{F}_1(t, \bar{y}_1(t)) - \mathcal{F}_2(t, \bar{y}_2(t))| \\ \leq&|\mathcal{F}_1(t, \bar{y}_1(t)) - \mathcal{F}_1(t, \bar{y}_2(t))| + |\mathcal{F}_1(t, \bar{y}_2(t)) - \mathcal{F}_2(t, \bar{y}_2(t))|. \end{aligned} \tag{6.2.22}$$

For $x \in [-\xi, \xi]$, $t \in [0,T]$, by using that $\rho_1(t,x) \geq \frac{m}{2}$ and therefore $v_1(t,x) \geq C\underline{m}$, we have that:

$$|\partial_x \mathcal{F}_1(t,x)| \leq \frac{C}{\underline{m}^2} \left(\|v_1\|^2_{L^\infty([0,T], W^{2,\infty}(\mathbb{R}))} + \|\rho_1\|^2_{L^\infty([0,T], W^{1,\infty}(\mathbb{R}))} \right).$$

Hence:

$$|\mathcal{F}_1(t, \bar{y}_1(t)) - \mathcal{F}_1(t, \bar{y}_2(t))| \leq C|\bar{y_1}(t) - \bar{y_2}(t)|. \tag{6.2.23}$$

For the second term, we observe that:

$$\begin{aligned} &|\mathcal{F}_1(t, \bar{y}_2(t)) - \mathcal{F}_2(t, \bar{y}_2(t))| \\ \leq& C \Big(\|v_1 - v_2\|_{L^\infty([0,T], W^{1,\infty}(\mathbb{R}))} + \|\rho_1 - \rho_2\|_{L^\infty([0,T], L^\infty(\mathbb{R}))} \\ &+ \|(t,x) \mapsto P_1(t, \bar{x}_1(t) \vee x) - P_2(t, \bar{x}_2(t) \vee x)\|_{L^\infty([0,T], L^\infty(\mathbb{R}))} \Big). \end{aligned}$$

Now take $(t,y) \in [0,T] \times \mathbb{R}$, we have:

$$\begin{aligned} &|\partial_x v_1(t,y) - \partial_x v_2(t,y)| \\ =&|\partial_z \tilde{v}_1(t, y - \bar{x}_1(t)) - \partial_z \tilde{v}_2(t, y - \bar{x}_2(t))| \\ \leq&|\partial_z \tilde{v}_1(t, y - \bar{x}_1(t)) - \partial_z \tilde{v}_1(t, y - \bar{x}_2(t))| + |\partial_z \tilde{v}_1(t, y - \bar{x}_2(t)) - \partial_z \tilde{v}_2(t, y - \bar{x}_2(t))| \\ \leq& \|\partial_{zz} \tilde{v}_1\|_\infty |\bar{x}_1(t) - \bar{x}_2(t)| + \|\partial_z \tilde{v}_1 - \partial_z \tilde{v}_2\|_\infty. \end{aligned}$$

Similarily:

$$\begin{aligned} &|P_1(t,y) - P_2(t,y)| \\ =&|\tilde{P}_1(t, 0 \vee (y - \bar{x}_1(t))) - \tilde{P}_2(t, 0 \vee (y - \bar{x}_2(t)))| \\ \leq&|\tilde{P}_1(t, 0 \vee (y - \bar{x}_1(t))) - \tilde{P}_1(t, 0 \vee (y - \bar{x}_2(t)))| \\ &+ |\tilde{P}_1(t, 0 \vee (y - \bar{x}_2(t))) - \tilde{P}_2(t, 0 \vee (y - \bar{x}_2(t)))| \\ \leq& \|\tilde{\rho}_1\|_\infty |\bar{x}_1(t) - \bar{x}_2(t)| + \frac{1}{\chi} \|\tilde{v}_1 - \tilde{v}_2\|_\infty, \end{aligned}$$

where the last bound follows from the observation, that:

$$\begin{aligned} &\left| \int_{0 \vee (y - \bar{x}_1(t))}^{+\infty} \tilde{\rho}_1(t,z) dz + \int_{0 \vee (y - \bar{x}_2(t))}^{+\infty} \tilde{\rho}_2(t,z) dz \right| \\ \leq& \int_0^{+\infty} e^{-\chi z} |\tilde{v}_1(t,z) - \tilde{v}_2(t,z)| dz \\ \leq& \frac{1}{\chi} \|\tilde{v}_1 - \tilde{v}_2\|_\infty. \end{aligned}$$

The remaining bounds are dealt with in a similar fashion. Finally, we have:

$$\begin{aligned}
&|\mathcal{F}_1(t,\bar{y}_2(t)) - \mathcal{F}_2(t,\bar{y}_2(t))| \\
\leq & C\left(\left(\|\tilde{v}_1\|_{L^\infty([0,T],W^{2,\infty}(\mathbb{R}))} + \|\tilde{\rho}_1\|_{L^\infty([0,T],W^{1,\infty}(\mathbb{R}))}\right)|\bar{x}_1(t)-\bar{x}_2(t)| \right. \\
&\left. + \|\tilde{v}_1 - \tilde{v}_2\|_{L^\infty([0,T],W^{1,\infty}(\mathbb{R}))} + \|\tilde{\rho}_1 - \tilde{\rho}_2\|_\infty\right) \qquad (6.2.24)
\end{aligned}$$

Let us recall that $\bar{x} \in B(A) \mapsto \tilde{v} \in L^\infty([0,T], C^{1,\alpha}(\mathbb{R}))$ is Lipschitz continuous and so is $\bar{x} \in B(A) \mapsto \tilde{\rho} \in L^\infty([0,T]\times\mathbb{R}))$. Then, by using $\|\bar{x}_1 - \bar{x}_2\|_\infty \leq T^{1-\frac{1}{p}} \|\dot{\bar{x}}_1 - \dot{\bar{x}}_2\|_p$ and bringing Bounds (6.2.22,6.2.23,6.2.24) together, we obtain:

$$|\dot{\bar{y}}_1(t) - \dot{\bar{y}}_2(t)| \leq C\left(|\bar{y}_1(t) - \bar{y}_2(t)| + \|x_1 - x_2\|_{W^{1,p}}\right)$$

By Grönwall's lemma, we obtain:

$$\|\bar{y}_1 - \bar{y}_2\|_\infty \leq \left(e^{CT} - 1\right)\|\dot{\bar{x}}_1 - \dot{\bar{x}}_2\|_{W^{1,p}}\,.$$

Bootstrapping the penultimate estimate, we can prove that:

$$\|\dot{\bar{y}}_1 - \dot{\bar{y}}_2\|_p \leq CT^{\frac{1}{p}} e^{CT}\|\dot{\bar{x}}_1 - \dot{\bar{x}}_2\|_{W^{1,p}}\,.$$

By noticing that $\|\bar{y}_1 - \bar{y}_2\|_p \leq T^{\frac{1}{p}}\|\bar{y}_1 - \bar{y}_2\|_\infty$ and using the two last inequalities, we find that the map $\bar{x} \in B(A) \mapsto \bar{y} \in B(A)$ is a contraction in the $W^{1,p}$-norm for $T > 0$ small enough. Thus, we have a unique fixed point, which concludes the proof of Theorem 6.2.1. □

6.3 Asymptotic Behavior of $\bar{x}(t)$

In this Section, we present preliminaries on the asymptotic behavior of $\bar{x}(t)$, when $t \to +\infty$. Of course, we implicitly assume that ρ, the solution to Equation (6.1.1) exists globally in time. We recall that following the discussion in the Introduction, we conjecture the following asymptotic behavior:

$$\bar{x}(t) = \begin{cases} 2t - \frac{3}{2}\log(t) + O(1) & \text{if } \chi < 1 \\ 2t - \frac{1}{2}\log(t) + O(1) & \text{if } \chi = 1 \\ \left(\chi + \frac{1}{\chi}\right) + O(1) & \text{if } \chi > 1 \end{cases}.$$

In this Section, we prove the following results, leaving the remaining questions to future investigations:

$$\begin{cases} \bar{x}(t) \leq 2t - \frac{3}{2}\log(t) + O(1) & \text{, if } \chi < 1 \\ 2t - \frac{1}{2}\log(t) + O(1) \leq \bar{x}(t) \leq 2t + O(1) & \text{, if } \chi = 1 \\ \bar{x}(t) \leq \left(\chi + \frac{1}{\chi}\right) + O(1) & \text{, if } \chi > 1 \end{cases}$$

6.3.1 A Simple Upper Bound on $\bar{x}(t)$

We start by proving a simple upper bound on $\bar{x}(t)$. This upper bound corresponds to the conjectured upper bound in the case $\chi > 1$, but not in the case $\chi \leq 1$. We consider

Equation (6.1.1) in the moving frame $(t, z) = (t, x - \bar{x}(t))$. This leads to Equation (6.2.1), which we recall:

$$\begin{cases} \partial_t \tilde{\rho} - \partial_{zz}\tilde{\rho} - \dot{\bar{x}}(t)\partial_z \rho + \partial_z \left(\mathbb{1}_{z<0} \tilde{\rho} \right) = \mathbb{1}_{z \geq 0} \tilde{\rho} \\ \displaystyle\int_0^{+\infty} \tilde{\rho}(t, z) dz = 1 \end{cases}$$

Proposition 6.3.1. *In the case $\chi > 1$, we suppose that:*

$$\int_{\mathbb{R}} \rho^0(z) e^{-\frac{z}{\chi}} < +\infty.$$

In the case $\chi \leq 1$, we suppose that:

$$\int_{\mathbb{R}} \rho^0(z) e^{-z} < +\infty.$$

Then, there exists a constant $C \geq 0$, such that:

$$\bar{x}(t) \leq \sigma^* t + C$$

Proof.

- Let us suppose that $\chi > 1$ and set:

$$I(t) := \int_{\mathbb{R}} e^{\frac{z}{\chi}} \tilde{\rho}(t, z) dz$$

Deriving I and integrating by parts, then leads to:

$$\begin{aligned} \dot{I} &= \int_{\mathbb{R}} e^{\frac{z}{\chi}} \left(\partial_{zz}\tilde{\rho} + \dot{\bar{x}}\partial_z \tilde{\rho} - \partial_z \left(\chi \mathbb{1}_{z<0} \tilde{\rho} \right) + \mathbb{1}_{z \geq 0} \tilde{\rho} \right) dz \\ &= \frac{I}{\chi^2} - \frac{\dot{\bar{x}} I}{\chi} + I \\ &= \frac{\sigma^* - \dot{\bar{x}}(t)}{\chi} I. \end{aligned}$$

Therefore, we have:

$$I(t) = I(0) \exp\left(\frac{\sigma^* t - \bar{x}(t)}{\chi} \right).$$

But, by using the Constraint (6.2.1b), we find that:

$$I(0) \exp\left(\frac{\sigma^* t - \bar{x}(t)}{\chi} \right) = I(t) = \int_{\mathbb{R}} e^{\frac{z}{\chi}} \tilde{\rho}(t, z) dz \geq \int_0^{+\infty} \tilde{\rho}(t, z) dz = 1.$$

Taking the logarithmic and rearranging the terms, we obtain:

$$\bar{x}(t) \leq \sigma^* t + \chi \ln(I(0))$$

- In the case $\chi \leq 1$, we set:

$$I(t) := \int_{\mathbb{R}} e^{z} \tilde{\rho}(t, z) dz$$

Deriving I, then leads to:

$$\dot{I} = I - \dot{\bar{x}} I + \int_{\mathbb{R}} \left(\chi \mathbb{1}_{z<0} + \mathbb{1}_{z \geq 0} \right) \tilde{\rho}(t, z) dz \leq (2 - \dot{\bar{x}}) I.$$

Hence:

$$I(t) \leq I(0) \exp\left(2t - \bar{x}(t) \right).$$

The rest of the proof goes as in the case $\chi > 1$.

□

6.3.2 A Comparison Principle for P

We recall that $P(t,x) = \int_x^{+\infty} \rho(t,y)dy$ satisfies Equation (6.1.7) in the stationary frame of reference:

$$\partial_t P = \partial_{xx} P + \min\{1, P\} - \chi \mathbb{1}_{P \geq 1} \partial_x P.$$

The Equation on P is interesting, as it encodes in a local manner, whether the density is in the Go regime (when $P > 1$) or the Grow regime (when $P \leq 1$). This will give rise to a comparison principle, which was for example lacking for System (6.1.2). Indeed, suppose P_1, P_2 two solutions of Equation (6.1.7), such that $P_1(0, \cdot) \leq P_2(0, \cdot)$, and that there exists $(t,x) \in \mathbb{R}_+ \times \mathbb{R}$, such that $P_1(t,x) = P_2(t,x)$. Suppose that $P_1(t,x) = P_2(t,x) > 1$, then both solutions are in the Go regime and locally satisfy Equation:

$$\partial_t P_i = \partial_{xx} P_i - \chi \partial_x P_i + 1,$$

which clearly satisfies a comparison principle. Similarily when the solutions are in the Grow regime. Hence, the only case, when solutions may not remain ordered, is when $P_1(t,x) = P_2(t,x) = 1$. We believe that at $P = 1$, there exists no mechanism, which guarantees that solutions remain ordered. However, if we construct a subsolution $\underline{P}$ (resp. supersolution $\overline{P}$), which has a convex (resp. concave) cusp at $\underline{P} = 1$ (resp. $\overline{P} = 1$), then because of the cusp, it is impossible that the solution P and the subsolution (resp. supersolution) touch first, where $P = 1$. This leads to the two following propositions:

Proposition 6.3.2. *Let $\underline{P}$, such that :*

1. $\underline{P}(0, \cdot) < P(0, \cdot)$
2. *For every (t,x) such that $\underline{P}(t,x) = 1$, we have:*

$$\partial_x \underline{P}(t, x^-) < \partial_x \underline{P}(t, x^+)$$

3. *$\underline{P}$ satisfies:*

$$\partial_t \underline{P} \leq \partial_{xx} \underline{P} + \min\{1, \underline{P}\} - \chi \mathbb{1}_{\underline{P} \geq 1} \partial_x \underline{P}$$

Then $\underline{P} < P$.

Proposition 6.3.3. *Let $\overline{P}$, such that :*

1. $P(0, \cdot) < \overline{P}(0, \cdot)$
2. *For every (t,x) such that $\overline{P}(t,x) = 1$, we have:*

$$\partial_x \overline{P}(t, x^-) > \partial_x \overline{P}(t, x^+)$$

3. *$\overline{P}$ satisfies:*

$$\partial_t \overline{P} \geq \partial_{xx} \overline{P} + \min\{1, \overline{P}\} - \chi \mathbb{1}_{\overline{P} \geq 1} \partial_x \overline{P}$$

Then $\overline{P} > P$.

The proof of both propositions follows from the observations just above. We briefly sketch the proof of Proposition 6.3.2. The proof of Proposition 6.3.3 follows *mutatis mutandis*.

Proof of Proposition 6.3.2. We argue by contradiction. Let $t_0 > 0$ be the first time, such that there exists $x_0 \in \mathbb{R}$, such that $\underline{P}(t_0, x_0) = P(t_0, x_0)$. Because of the remarks above, this can only happen, when $\underline{P}(t_0, x_0) = P(t_0, x_0) = 1$. But by the definition of the left and right derivatives, we have:

$$\begin{aligned} 0 \leq P(t_0, x) - \underline{P}(t_0, x) &= \left(\partial_x P(t_0, x_0) - \partial_x \underline{P}(t_0, x_0^+)\right)(x - x_0) + o((x - x_0)) \quad \text{for } x > x_0 \\ 0 \leq P(t_0, x) - \underline{P}(t_0, x) &= \left(\partial_x P(t_0, x_0) - \partial_x \underline{P}(t_0, x_0^-)\right)(x - x_0) + o((x - x_0)) \quad \text{for } x < x_0 \end{aligned}$$

But this implies that:

$$\partial_x \underline{P}(t_0, x_0^+) \leq \partial_x P(t_0, x_0) \leq \partial_x \underline{P}(t_0, x_0^-),$$

which contradicts Item 2 in Proposition 6.3.2. □

6.3.3 A Subsolution in the Case $\chi = 1$

In this Subsection we construct a subsolution for the $\chi = 1$ case, which leads to the conjectured lowerbound $\bar{x}(t) \geq 2t - \frac{\ln(t)}{2} - K$.

Proposition 6.3.4. *Suppose that:*

1. *There exists $t_0 > e^{\frac{1}{e}}$ and $A > 0$, such that for every $x \geq A$:*

$$e^{-\frac{x^2}{4t_0}} \leq P(0, x)$$

2. *There exists $B > 0$ and $\beta \in \mathbb{R}$, such that for every $x \leq -B$:*

$$-x + \alpha \leq P(0, x)$$

Then, there exists a constant $K \in \mathbb{R}$, such that:

$$\bar{x}(t) \geq 2t - \frac{\ln(t)}{2} - K$$

Proof. We start by some elementary results, which will be useful in order to construct a subsolution. Let $k \in \left(e^{\frac{1}{e}}, \sqrt{t_0}\right)$. Set $G_k(t, x) = \frac{k}{\sqrt{t}} e^{t - \frac{x^2}{4t}}$ and denote $x_k(t)$ the nonnegative solution to the Equation $G_k(t, \cdot) = 1$ for $t \geq t_0$. By elementary operations, we find that:

$$x_k(t) = \sqrt{4t^2 - \frac{t \ln(t)}{2} + \ln(k)} \tag{6.3.1}$$

$$\dot{x_k}(t) = \frac{2 - \frac{\ln(t)}{8t} - \frac{1}{8t} + \frac{\ln(k)}{4t}}{\sqrt{1 - \frac{\ln(t)}{8t^2} + \frac{\ln(k)}{4t}}} \tag{6.3.2}$$

$k > e^{\frac{1}{e}}$, implies that $\frac{1}{2\ln(k)} < e = \inf_{t \geq 1} \frac{t}{\ln(t)}$. Therefore we have that:

$$\frac{2}{\sqrt{1 - \frac{\ln(t)}{8t^2} + \frac{\ln(k)}{4t}}} < 2.$$

$k < \sqrt{t_0}$ implies that $\ln(t) \geq 2\ln(k)$ for $t \geq t_0$. Hence:

$$\frac{-\frac{\ln(t)}{8t} - \frac{1}{8t} + \frac{\ln(k)}{4t}}{\sqrt{1 - \frac{\ln(t)}{8t^2} + \frac{\ln(k)}{4t}}} < 0.$$

Thus:

$$\dot{x_k}(t) \leq 2. \tag{6.3.3}$$

Finally $k < \sqrt{t_0}$ implies also that $t\ln(t) > 2\ln(k)$ for $t \geq t_0$. Therefore, by Equation (6.3.1):

$$\frac{x_k(t)}{2t} < 1. \tag{6.3.4}$$

Let us now construct a subsolution. For $(t,x) \in \mathbb{R}_+ \times \mathbb{R}$, set:

$$\underline{P}(t,x) = \begin{cases} \frac{k}{t+t_0} e^{t+t_0-\frac{x^2}{4(t+t_0)}} & \text{if } x > x_k(t+t_0) \\ -(x - x_k(t+t_0)) + 1 & \text{if } x \leq x_k(t+t_0) \end{cases}$$

Then we have that $\underline{P}$ has a convex cusp at $x = x_k(t+t_0)$ by using (6.3.4):

$$\partial_x \underline{P}(t, \tilde{x}(t)^-) = -1 \leq -\frac{x_k(t+t_0)}{2(t+t_0)} = \partial_x \underline{P}(t, \tilde{x}(t)^+),$$

Furthermore $\underline{P}$ is a subsolution for $x > x_k(t+t_0)$ as, there it is a solution to the linearized F/KPP Equation. For $x < \tilde{x}(t)$:

$$\partial_t P - \partial_{xx} P - 1 + \partial_x P = \dot{x_k}(t) - 2 \leq 0,$$

as a consequence of (6.3.3). Therefore $\underline{P}$ is a subsolution.

If we consider a translation of $\underline{P}$, $(t,x) \mapsto \underline{P}(t, x+c)$. Then for $c > 0$ large enough, we have that $\underline{P}(0, \cdot + c) \leq P(0, \cdot)$, by the assumptions on the initial datum. Thus, we can apply the comparison principle given by Proposition 6.3.2. This then leads to:

$$\bar{x}(t) \geq x_k(t+t_0) - c \geq 2t - \frac{\ln(t)}{2} - K,$$

for a constant $K \in \mathbb{R}$. □

6.3.4 A Supersolution in the Case $\chi < 1$

In this Subsection we construct a supersolution $\overline{P}$ in the case $\chi < 1$ and show the lower bound $\bar{x}(t) \leq 2t - \frac{3}{2}\ln(t) + K$. To do se we consider Equation (6.1.7) in the frame $(t,z) = \big(t, x - 2t + \frac{3}{2}\ln(t+t_0)\big)$, which leads to:

$$\partial_t P = \partial_{zz} P + \left(2 - \frac{3}{2(t+t_0)}\right) \partial_z P - \chi \mathbb{1}_{P>1} \partial_z P + \min\{1, P\}. \tag{6.3.5}$$

The exact shape of $\overline{P}$ may seem at first rather involved. However, the reasoning is similar than in the preceding Subsection: the supersolution $\overline{P}$ is the concatenation of a supersolution of Equation (6.3.5) when $\overline{P} \leq 1$ and a linear function when $\overline{P} > 1$. We start by giving a heuristics of the shape of $\overline{P}$ in the region $\overline{P} \leq 1$, which comes from considering Equation (6.3.5) in self-similar variables. In [96], it has already been shown that considering these types of problems in self-similar variables may turn out to be very fruitful. Then, we define the supersolution $\overline{P}$ in the variables (t,z) and show that this leads to the following proposition:

Proposition 6.3.5. *Suppose that:*

1. *There exists $t_0 > 0$ and $A > 0$, such that for every $z \geq A$:*

$$P(0,z) \leq e^{-\frac{z^2}{4t_0}}$$

2. There exists $B > 0$ and $\beta > 0$, such that for every $z \leq -B$:

$$P(0, z) \leq \frac{-z}{2-\chi} + \beta \tag{6.3.6}$$

Then, there exists a constant $K \in \mathbb{R}$, such that:

$$\bar{x}(t) \leq 2t - \frac{3\ln(t)}{2} + K$$

Let us note, that the traveling wave in the proper moving frame satisfies $\rho_\infty(z) = \frac{1}{2-\chi}\left((1-\chi)z\mathbb{1}_{z\geq 0} + 1\right)e^{-z\mathbb{1}_{z\geq 0}}$ and thus for $z \leq 0$, we have $\int_z^{+\infty} \rho(t,y)dy = \frac{-z}{2-\chi} + 1$, which makes Assumption (6.3.6) reasonable. In fact, from the proof of Proposition 6.3.5, it becomes clear that we can slighlty relax Assumption (6.3.6), but for the sake of concision, we will not do so here.

Heuristics: Self-similar Variables

We start by giving a heuristics for the specific shape of the supersolution. Let us assume that the result is true and that for instance for $z \geq 0$, we have $P(z) \leq 1$. Then inspired by [96], we consider Equation (6.3.5) in self-similar variables $(\tau, \eta) = \left(\ln(t + t_0), \frac{z}{\sqrt{t+t_0}}\right)$. Set:

$$\omega(\tau, \eta) := e^{\frac{\eta^2}{8} - \frac{\tau}{2}} P\left(\frac{9}{4\varepsilon^2}\left(e^\tau - 1\right), \frac{3}{2\varepsilon}\eta e^{\frac{\tau}{2}}\right).$$

Then, we obtain for $\eta > 0$ (assuming that $P(z) \leq 1$ for $z \geq 0$):

$$\partial_\tau \omega + \mathcal{M}\omega = \varepsilon e^{-\frac{\tau}{2}}\left(\frac{\eta}{4}\omega - \partial_\eta \omega\right),$$

where $\mathcal{M} := -\partial_{\eta\eta} + \left(\frac{\eta^2}{16} - \frac{3}{4}\right)$.

Now suppose that $\omega(\eta) := \eta e^{-\frac{\eta^2}{8}}$, which is in the nullspace of $\mathcal{M}$. Then :

$$\partial_\tau \omega + \mathcal{M}\omega - \varepsilon e^{-\frac{\tau}{2}}\left(\frac{\eta}{4}\omega - \partial_\eta \omega\right) = \varepsilon e^{-\frac{\tau}{2}}\left(\frac{1}{\eta} - 4\eta\right)\omega$$

Hence ω is not a supersolution, but it may be reasonable to expect, that a small perturbation of ω becomes a supersolution. Now consider:

$$\omega(\eta) := \eta e^{R(\tau) - \left(\frac{1}{8} - \beta(\tau)\right)\eta^2}, \tag{6.3.7}$$

with $R(\tau) = -C\varepsilon e^{-\frac{\tau}{2}}$, $\beta(\tau) = \varepsilon e^{-\frac{\tau}{2}}$. Then we obtain:

$$\begin{aligned}
&\frac{1}{\omega}\left(\partial_\tau \omega + \mathcal{M}\omega + \varepsilon e^{-\frac{\tau}{2}}\left(\omega_\eta - \frac{\eta}{4}\omega\right)\right) \\
=&\dot{R} + \dot{\beta}\eta^2 + \beta\eta^2 - 4\beta - 4\beta^2\eta^2 + \varepsilon e^{-\frac{\tau}{2}}\left(\frac{1}{\eta} - \frac{\eta}{2}\right) + 2\varepsilon\beta e^{-\frac{\tau}{2}}\eta \\
\geq&\varepsilon e^{-\frac{\tau}{2}}\left(\frac{C}{2} + \frac{3}{2}\eta^2 - 4 - 4\varepsilon e^{-\frac{\tau}{2}}\eta^2 + \frac{1}{\eta} - \frac{\eta}{2}\right) \\
=&\varepsilon e^{-\frac{\tau}{2}}\left(\left(\frac{3}{2} - 4\varepsilon e^{-\frac{\tau}{2}}\right)\eta^2 + \frac{1}{\eta} - \frac{\eta}{2} - 4 + \frac{C}{2}\right) \\
=&\varepsilon e^{-\frac{\tau}{2}}\left(\frac{\eta^2}{2} + \frac{1}{\eta} - \frac{\eta}{2} - 4 + \frac{C}{2}\right) \text{ , under the condition } \varepsilon \leq \frac{1}{4}
\end{aligned}$$

But the function $\eta \mapsto \frac{\eta^2}{2} + \frac{1}{\eta} - \frac{\eta}{2} - 4$ is clearly bounded below, hence we can choose $C > 0$ big enough, so that ω becomes a supersolution.

Construction of a Supersolution

In this Subsection, we prove Proposition 6.3.5 by constructing a supersolution $\overline{P}$, whose shape for $z \geq 0$ large corresponds exactly to ω given by (6.3.7), but in standard variables.

Proof of Proposition 6.3.5. Let:

$$F(t,z) := \alpha z e^{-z} e^{-\frac{z^2}{4(t+t_0)}} e^{\frac{1}{\sqrt{t+t_0}}\left(\frac{z^2}{t+t_0}-C\right)}. \tag{6.3.8}$$

This is the equivalent in standard variables of ω given by (6.3.7). Then:

$$\begin{aligned}
\partial_t F &= \left(\frac{z^2}{4(t+t_0)^2} - \frac{3z^2}{2(t+t_0)^{\frac{5}{2}}} + \frac{C}{2(t+t_0)^{\frac{3}{2}}}\right) F \\
\partial_z F &= \left(\frac{1}{z} - 1 - \frac{z}{2(t+t_0)} + \frac{2z}{(t+t_0)^{\frac{3}{2}}}\right) F \\
\partial_{zz} F &= \left(\left(\frac{1}{z} - 1 - \frac{z}{2(t+t_0)} + \frac{2z}{(t+t_0)^{\frac{3}{2}}}\right)^2 + \left(-\frac{1}{z^2} - \frac{1}{2(t+t_0)} + \frac{2}{((t+t_0))^{\frac{3}{2}}}\right)\right) F \\
&= \left(1 + \frac{z^2}{4(t+t_0)^2} + \frac{4z^2}{(t+t_0)^3} - \frac{2}{z} - \frac{3}{2(t+t_0)} + \frac{6}{((t+t_0))^{\frac{3}{2}}}\right. \\
&\left. + \frac{z}{(t+t_0)} - \frac{4z}{(t+t_0)^{\frac{3}{2}}} - \frac{2z}{(t+t_0)^{\frac{5}{2}}}\right) F
\end{aligned}$$

Hence :

$$\begin{aligned}
&\frac{1}{F}\left(\partial_t F - \partial_{zz} F - \left(2 - \frac{3}{2(t+t_0)}\right)\partial_z F - F\right) \\
=&\frac{z^2}{2(t+t_0)^{\frac{5}{2}}}\left(1 - \frac{8}{\sqrt{t+t_0}}\right) + \frac{3}{2z(t+t_0)} - \frac{3z}{4(t+t_0)^2} + \frac{3z}{(t+t_0)^{\frac{5}{2}}} + \frac{\frac{C}{2}-6}{(t+t_0)^{\frac{3}{2}}} \\
\geq&\frac{z^2}{4(t+t_0)^{\frac{5}{2}}} - \frac{3z}{4(t+t_0)^2} + \frac{3z}{(t+t_0)^{\frac{5}{2}}} + \frac{\frac{C}{2}-6}{(t+t_0)^{\frac{3}{2}}} \text{ , under the condition that } \frac{8}{\sqrt{t_0}} \leq \frac{1}{2} \\
=&\frac{z^2}{4(t+t_0)^{\frac{5}{2}}} - \frac{3z}{4(t+t_0)^2} + \frac{3z}{(t+t_0)^{\frac{5}{2}}} + \frac{\frac{C}{2}-6}{(t+t_0)^{\frac{3}{2}}} \\
=&\frac{z}{4(t+t_0)^{\frac{5}{2}}}\left(4z - 3\sqrt{t+t_0}\right) + \frac{\frac{C}{2}-6}{(t+t_0)^{\frac{3}{2}}} \\
\geq&\frac{-\frac{9}{64} + \frac{C}{2} - 6}{(t+t_0)^{\frac{3}{2}}} \\
\geq&0 \text{ , under the condition that } C \geq \frac{393}{32}.
\end{aligned}$$

Set $G_\alpha(z) := \alpha z e^{-z}$ with $\alpha > e$, so that $G_\alpha(\,\cdot\,) = 1$ has two positive roots. Consider z_α the biggest root and by an easy asymptotic expansion, we have that $z_\alpha \sim \ln \alpha$. Let $\varepsilon > 0$, and take $t_0 > 0$ and $\alpha > 0$ big enough, such that for every $t \geq 0$, we have:

$$\left|\frac{1}{z_\alpha} - \frac{z_\alpha}{2(t+t_0)} + \frac{2z_\alpha}{(t+t_0)^{\frac{3}{2}}}\right| < \varepsilon \tag{6.3.9}$$

Take t_0 big enough, then $F(t,\cdot)=1$ also has two positive solutions and we denote $\tilde{z_\alpha}(t)$ the biggest root. Then, for t_0 big enough, we have that for all $t \geq t_0$:

$$\left|\frac{1}{z_\alpha}-\frac{1}{\tilde{z_\alpha}(t)}\right|<\frac{\varepsilon}{3}, \left|\frac{z_\alpha}{2(t+t_0)}-\frac{\tilde{z_\alpha}(t)}{2(t+t_0)}\right|<\frac{\varepsilon}{3} \text{ and } \left|\frac{2z_\alpha}{(t+t_0)^{\frac{3}{2}}}-\frac{2\tilde{z_\alpha}(t)}{(t+t_0)^{\frac{3}{2}}}\right|<\frac{\varepsilon}{3} \quad (6.3.10)$$

Finally, notice that :

$$\begin{aligned}\partial_z F(t,\tilde{z_\alpha}(t)) &= \left(\frac{1}{\tilde{z_\alpha}(t)}-1-\frac{\tilde{z_\alpha}(t)}{2(t+t_0)}+\frac{2\tilde{z_\alpha}(t)}{(t+t_0)^{\frac{3}{2}}}\right)F(t,\tilde{z_\alpha}(t)) \\ &= \frac{1}{\tilde{z_\alpha}(t)}-1-\frac{\tilde{z_\alpha}(t)}{2(t+t_0)}+\frac{2\tilde{z_\alpha}(t)}{(t+t_0)^{\frac{3}{2}}} \end{aligned} \quad (6.3.11)$$

Combining (6.3.9,6.3.10,6.3.11), we obtain:

$$|\partial_z F(t,\tilde{z_\alpha}(t))+1| \leq 2\varepsilon \quad (6.3.12)$$

Let $\varepsilon>0$ be small enough and $A \in \left(\frac{1+\varepsilon}{2-\chi}, 1-2\varepsilon\right)$. Consider for $(t,z)\in\mathbb{R}_+\times\mathbb{R}$:

$$\overline{P}(t,z)=\begin{cases} F(t,z) & \text{if } z\geq \tilde{z_\alpha}(t) \\ -A(z-\tilde{z_\alpha}(t))+1 & \text{if } z<\tilde{z_\alpha}(t)\end{cases}$$

Then, by Bound (6.3.12):

$$-\partial_z\overline{P}(t,\tilde{z_\alpha}(t)^+) \geq 1-2\varepsilon > A = -\partial_z\overline{P}(t,\tilde{z_\alpha}(t)^-)$$

Hence $\overline{P}$ has a concave cusp at $z=\tilde{z_\alpha}(t)$.
For $z<\tilde{z_\alpha}(t)$:

$$\begin{aligned}&\partial_t\overline{P}-\partial_{zz}\overline{P}-1+\left(\chi-2+\frac{3}{2(t+t_0)}\right)\partial_z\overline{P} \\ =&A\dot{\tilde{z_\alpha}}(t)+A(2-\chi)-1+\frac{3A}{2(t+t_0)} \\ \geq&A\dot{\tilde{z_\alpha}}(t)+\varepsilon+\frac{3A}{2(t+t_0)}\end{aligned}$$

But we can always choose $t_0>0$ big enough so that $\left|A\dot{\tilde{z_\alpha}}(t)+\frac{3A}{2(t+t_0)}\right|<\varepsilon$, since $\dot{z_\alpha}(t)\to 0$, when $t\to+\infty$. Thus $\overline{P}$ is a supersolution.

Finally, as in the case of Proposition 6.3.4, we consider a translation of $\overline{P}$, $(t,x)\mapsto\overline{P}(t,x-c)$. Then for $c>0$ large enough, we have that $\overline{P}(0,\cdot-c)\geq P(0,\cdot)$ by the Assumptions of Proposition 6.3.5. Thus, we can apply the comparison principle given by Proposition 6.3.3. This then leads to:

$$\bar{x}(t)\leq 2t-\frac{3\ln(t)}{2}+K,$$

for a constant $K\in\mathbb{R}$. □

6.4 Asymptotic Stability of the Traveling Wave in the Case $\chi > 1$

In this Section, we will prove that the traveling wave with minimal velocity $\sigma^* = \chi + \frac{1}{\chi}$ in the case $\chi > 1$ is asymptotically stable. The proof is largely inspired by a similar result in [39] for a model of chemotactic clustering in *E. coli*. The strategy of proof can be summarized as follows: we consider the linearization of the problem around the stationary state given by the traveling wave. In a certain L^2-setting, the evolution operator e^{-tL} of the linearized problem leads to an exponential convergence of the nonlinear problem to the nullspace of L under a small perturbation condition. In addition, the nonlinear problem satisfies a conservation law. This conservation law then selects a unique element in the nullspace of L, which corresponds to the traveling wave. Although the line of reasoning is an adaptation of the proof in [39], we stress that the proof here is less involved, as there, the authors have used an improved Poincaré inequality in a weighted L^2-space, whereas here a more standard Poincaré inequality is sufficient.

We consider the following Equation with constraint, which has already been introduced earlier, see (6.2.1), but dropping the diacritical $\tilde{}$:

$$\begin{cases} \partial_t \rho - \partial_{zz}\rho - \dot{\bar{x}}(t)\partial_z \rho + \partial_z\left(\mathbb{1}_{z<0}\rho\right) = \mathbb{1}_{z\geq 0}\rho & \text{(6.4.1a)} \\ \displaystyle\int_0^{+\infty} \rho(t,z)dz = 1. & \text{(6.4.1b)} \end{cases}$$

Equation (6.4.1) has the unknowns $(\rho, \dot{\bar{x}})$, where $\dot{\bar{x}}(\,\cdot\,)$ can roughly be seen as a Lagrange multiplier associated with Constraint (6.4.1b).

$(\rho_\infty(z), \sigma^*) = \left(\chi e^{-\chi z \mathbb{1}_{z\geq 0}}, \chi + \frac{1}{\chi}\right)$ is a stationary solution to Equation (6.4.1). Consider $v = \frac{\rho}{\rho_\infty}$, then:

$$\partial_t v + Lv + \dot{\varepsilon}(t)\partial_z v = 0, \tag{6.4.2}$$

with $Lf = -f'' - \beta f'$, $\beta(z) = \sigma^* - \chi - \chi \mathbb{1}_{z\geq 0}$, and $\dot{\varepsilon}(t) = \sigma^* - \dot{\bar{x}}(t)$. Next, we introduce the space $L^2(e^V dz)$, where $V' = \beta$:

$$V(z) = \begin{cases} -\left(\chi - \frac{1}{\chi}\right) z & \text{if } z > 0 \\ \frac{z}{\chi} & \text{if } z \leq 0 \end{cases} \tag{6.4.3}$$

For $f, g \in L^2(e^V dz)$, we use the following notations in this Section:

$$\|f\| := \sqrt{\int_{\mathbb{R}} f^2(z) e^{V(z)} dz} \text{ and } \langle f, g\rangle := \int_{\mathbb{R}} f(z) g(z) e^{V(z)} dz. \tag{6.4.4}$$

From Chapter 2, we know that the operator L is self-adjoint in the space $L^2(e^V dz)$ and we have:

$$\langle f, Lg\rangle = \langle f', g'\rangle.$$

Furthermore, 1 is the simple eigenvector associated with the eigenvalue 0 of L and L has a spectral gap $\gamma = \left(\frac{\min\left(\frac{1}{\chi}, \chi - \frac{1}{\chi}\right)}{2}\right)^2$. From this, we obtain a Poincaré inequality in the space $L^2(e^V dz)$.

Proposition 6.4.1. *Given $f \in H^1(e^V dz)$:*

$$\left\| f - \left\langle f, \frac{1}{\|1\|} \right\rangle \frac{1}{\|1\|} \right\| \leq \frac{1}{\sqrt{\gamma}} \|f'\|$$

Next, we define the perturbation from equilibrium $u := v - v_\infty = v - 1$ and we notice that u satisfies the following conservation law, as a consequence of (6.4.1b):

$$\langle u(t), e^{-(\sigma-\chi)z} \mathbb{1}_{z\geq 0} \rangle = \int_0^{+\infty} u(t,z) e^{-\chi z} dz = 0 \tag{6.4.5}$$

Notice that this can be rewritten under the following form by integration by parts:

$$\begin{aligned} 0 &= \int_0^{+\infty} u(t,z) e^{-\chi z} dz \\ &= -\int_0^{+\infty} (u(t,z)e^{-\chi z})' z dz \\ &= -\int_0^{+\infty} (u'(t,z) - \chi u(t,z)) z e^{-\chi z} dz \\ &= -\langle u'(t) - \chi u(t), z e^{-(\sigma-\chi)z} \mathbb{1}_{z\geq 0} \rangle \end{aligned} \tag{6.4.6}$$

Of note, we can obtain a second conservation law,as a consequence of the first, which is that:

$$M = \int_{\mathbb{R}} u(t,z) e^{-\chi z \mathbb{1}_{z\geq 0}} dz$$

However this conservation law will not be used here.

The aim is to show that $u(t) \to 0$. To do so we introduce the following quantities :

$$\begin{aligned} E(t) &:= \frac{1}{2} \|u\|^2 = \frac{1}{2} \int_{\mathbb{R}} u(t,z)^2 e^{V(z)} dz, \\ F(t) &:= \frac{1}{2} \|\partial_z u\|^2 = \frac{1}{2} \|w\|^2 = \frac{1}{2} \int_{\mathbb{R}} w(t,z)^2 e^{V(z)} dz, \\ G(t) &:= \frac{1}{2} \|\partial_{zz} u\|^2 = \frac{1}{2} \|\partial_z w\|^2 = \frac{1}{2} \int_{\mathbb{R}} (\partial_z w(t,z))^2 e^{V(z)} dz, \end{aligned}$$

where $w := \partial_z u$. Furthermore, we introduce two parameters θ, ϕ, such that:

$$\cos(\theta) := \frac{\langle 1, e^{-(\sigma-\chi)z} \mathbb{1}_{z\geq 0} \rangle}{\|1\| \left\| e^{-(\sigma-\chi)z} \mathbb{1}_{z\geq 0} \right\|}, \tag{6.4.7}$$

$$\cos(\phi) := \frac{\langle 1, z e^{-(\sigma-\chi)z} \mathbb{1}_{z\geq 0} \rangle}{\|1\| \left\| z e^{-(\sigma-\chi)z} \mathbb{1}_{z\geq 0} \right\|}. \tag{6.4.8}$$

It is clear that $\cos(\theta), \cos(\phi) > 0$ as positive multiples of integrals of positive functions.

Next, we introduce a Proposition on the dissipation rate for F:

Proposition 6.4.2. *We have the following dissipation rate for F:*

$$\dot{F} = -2G - \chi w(t,0)^2 - \varepsilon \langle w, \partial_z w \rangle$$

Proof.

$$\begin{aligned}
\dot{F} &= \int_{\mathbb{R}} w\partial_t w e^V dz \\
&= \int_{\mathbb{R}} w\partial_z\partial_t u e^V dz \\
&= \int_{\mathbb{R}} w\partial_z \left(-Lu - \dot{\varepsilon}(t)\partial_z u\right) e^V dz \\
&= \int_{\mathbb{R}} w \left(\partial_{zz} w + \partial_z(\beta w)\right) e^V dz - \dot{\varepsilon}\langle w, \partial_z w\rangle \\
&= \int_{\mathbb{R}} w \left(-Lw + \partial_z(\beta) w\right) e^V dz - \dot{\varepsilon}\langle w, \partial_z w\rangle \\
&= -\int_{\mathbb{R}} wLwe^V dz - \chi w(t,0)^2 - \dot{\varepsilon}\langle w, \partial_z w\rangle \\
&= -\int_{\mathbb{R}} (\partial_z w)' e^V dz - \chi w(t,0)^2 - \dot{\varepsilon}\langle w, \partial_z w\rangle \\
&= -2G - \chi w(t,0)^2 - \dot{\varepsilon}\langle w, \partial_z w\rangle
\end{aligned}$$

□

We now state the asymptotic stability result, which is the main results of this Section:

Theorem 6.4.3. *Let $\delta < \chi$, then there exist constants $C(\delta) > 0$, $C_1, C_2 > 0$ (given by Lemmata[1] 6.4.3.1, 6.4.3.4 and 6.4.3.5), such that for every $\eta < 2\gamma\cos^2(\phi)$, if:*

$$\sqrt{F(0)} < \min\left\{ \frac{\delta}{C_1}, \frac{1 - \frac{\eta}{2\cos^2(\phi)}}{C(\delta)\left(\frac{C_1}{\cos(\phi)\sqrt{\gamma}} + C_2\right)} \right\} \tag{6.4.9}$$

Then, we have:

$$\|u(t)\|^2 \leq \frac{2F(0)}{\gamma\cos^2(\theta)} e^{-\eta t} \tag{6.4.10}$$

Before moving on to the proof of the Theorem 6.4.3, we introduce a series of Lemmata, whose proofs are postponed to the end of the Section.

Lemma 6.4.3.1. *Let $\delta < \chi$, then there exists a constant $C(\delta) > 0$, such that whenever $|u(t,0)| \leq \delta$, we have:*

$$|\dot{\varepsilon}(t)| \leq C(\delta)\left(|u(t,0)| + |w(t,0)|\right)$$

Of note, in Lemma 6.4.3.1, no restrictions are needed on $|w(t,0)|$, which is a key point, since without this property, the present strategy of proof is bound to fail.

Lemma 6.4.3.2. *Suppose that $\langle f, e^{-(\sigma-\chi)z}\mathbb{1}_{z\geq 0}\rangle = 0$, then:*

$$\cos(\theta)\|f\| \leq \left\| f - \langle f, \frac{1}{\|1\|}\rangle \frac{1}{\|1\|} \right\|,$$

where $\cos(\theta) > 0$ is given by (6.4.7).

Lemma 6.4.3.3. *Suppose that $\langle f' - \chi f, ze^{-(\sigma-\chi)z}\mathbb{1}_{z\geq 0}\rangle = 0$, then :*

$$\cos(\phi)\left\|f'\right\| \leq \left\| f' - \langle f', \frac{1}{\|1\|}\rangle \frac{1}{\|1\|} \right\|,$$

where $\cos(\phi) > 0$ is given by (6.4.8).

[1] See just below.

Lemma 6.4.3.4. *We have that:*

$$|u(t,0)| \leq C_1\sqrt{F(t)}$$

Lemma 6.4.3.5. *We have that:*

$$|w(t,0)| \leq C_2\sqrt{G(t)}$$

Proof of Theorem 6.4.3. We start by showing that under Condition (6.4.9), $\dot{F} \leq 0$. In fact first by Lemma 6.4.3.4 observe that, as long as $\sqrt{F(t)} < \frac{\delta}{C_1}$, we have that:

$$|u(t,0)| \leq C_1\sqrt{F(t)} < \delta.$$

Suppose by contradiction that there exists a time $t_0 > 0$, such that $\sqrt{F(t_0)} = \frac{\delta}{C_1}$. Then for all $t \in [0, t_0]$, we have that:

$$\begin{aligned}
&\dot{F}(t) \\
\leq& -2G + |\dot{\varepsilon}(t)\langle w, \partial_z w\rangle| \text{ , by Proposition 6.4.2} \\
\leq& -2G + C(\delta)\left(|u(t,0)| + |w(t,0)|\right)\|w\|\,\|\partial_z w\| \text{ , by Lemma 6.4.3.1} \\
\leq& -2G + 2C(\delta)\left(C_1\sqrt{F} + C_2\sqrt{G}\right)\sqrt{FG} \text{ , by Lemmata 6.4.3.4 and 6.4.3.5} \\
\leq& -2G + 2C(\delta)\left(\frac{C_1}{\cos(\phi)\sqrt{\gamma}} + C_2\right)\sqrt{F}G \text{ , by Lemma 6.4.3.3 and Proposition 6.4.1} \\
\leq& -2G(t)\left(1 - C(\delta)\left(\frac{C_1}{\cos(\phi)\sqrt{\gamma}} + C_2\right)\sqrt{F(t)}\right)
\end{aligned}$$

But, because of Conditon (6.4.9), this shows that $\dot{F}(0) \leq 0$, which then implies further that $\dot{F}(t) \leq 0$. Hence $F(\,\cdot\,)$ is nonincreasing on the interval $[0, t_0]$, which contradicts the definition of t_0. Thus, for all time $t \geq 0$, we have $\sqrt{F(t)} < \frac{\delta}{C_1}$ and moreover that $\dot{F} \leq 0$. This leads to the following decay rate:

$$\dot{F} \leq -2G\left(1 - C(\delta)\left(\frac{C_1}{\cos(\phi)\sqrt{\gamma}} + C_2\right)\sqrt{F(0)}\right),$$

by Condition (6.4.9). Using now Lemma (6.4.3.3) in combination with Proposition (6.4.1), we obtain:

$$\begin{aligned}
&\dot{F} \\
\leq& -2\gamma\cos^2(\phi)F\left(1 - C(\delta)\left(\frac{C_1}{\cos(\phi)\sqrt{\gamma}} + C_2\right)\sqrt{F(0)}\right) \\
\leq& -\eta F
\end{aligned}$$

Hence, by Grönwall's Inequality:

$$F(t) \leq F(0)e^{-\eta t}$$

Finally by Lemma 6.4.3.2 and Proposition 6.4.1, we have:

$$\|u(t)\|^2 \leq \frac{\|w(t)\|^2}{\gamma\cos^2(\phi)} \leq \frac{2F(0)}{\gamma\cos^2(\theta)}e^{-\eta t}$$

□

Let us conclude this Section by given quick proofs of Lemmata 6.4.3.1-6.4.3.5.

Proof of Lemma 6.4.3.1.

$$\dot{\varepsilon} = \frac{1}{\chi} - \frac{1 - \partial_z u(t,0)}{\chi + u(t,0)}$$

It suffices to note that when $\partial_z u(t,0) = u(t,0) = 0$, we have $\dot{\varepsilon} = 0$ and that $\dot{\varepsilon}$ is Lipschitz in those two quantities as long as $\chi + u(t,0)$ is bounded away from 0. □

Proof of Lemma 6.4.3.2. In order to prove the Lemma, we first show the following property in Hilbert spaces. For $\|p\| = \|q\| = 1$, we have that:

$$\sup_{\|g\|=1, \langle g,q\rangle = 0} \langle g, p\rangle = \sqrt{1 - \langle p, q\rangle^2} \tag{6.4.11}$$

Consider (p, r), an orthonormal basis of $\mathrm{span}(p, q)$. Then $g = ap + br + g_\perp$, where $g_\perp \perp \mathrm{span}(p, q)$, $a^2 + b^2 + \|g_\perp\|^2 = 1$ and $0 = a\langle p, q\rangle + b\langle r, q\rangle$. We have $\langle g, p\rangle = a$. In order to maximize a, one need to chose $g_\perp = 0$ and hence $a^2 + b^2 = 1$. From this we obtain $a^2\left(1 + \frac{\langle p,q\rangle^2}{\langle r,q\rangle^2}\right) = 1$. This leads to $a^2 = \frac{\langle r,q\rangle^2}{\langle r,q\rangle^2 + \langle p,q\rangle^2} = \langle r, q\rangle^2$, since $q \in \mathrm{span}(p, r)$. Finally by an easy computation, we have $|\langle r, q\rangle| = \sqrt{1 - \langle p, q\rangle^2}$.

To conclude the proof of Lemma 6.4.3.2, we apply Result (6.4.11) with $p = \frac{f}{\|f\|}, q = \frac{1}{\|1\|}$ and we lower bound the sup by choosing a specific $g = \frac{e^{-(\sigma-\chi)z}\mathbb{1}_{z\geq 0}}{\left\|e^{-(\sigma-\chi)z}\mathbb{1}_{z\geq 0}\right\|}$:

$$\begin{aligned}
&\left\| f - \left\langle f, \frac{1}{\|1\|}\right\rangle \frac{1}{\|1\|}\right\|^2 \\
&= \|f\|^2 \left(1 - \left\langle \frac{f}{\|f\|}, \frac{1}{\|1\|}\right\rangle^2\right) \\
&\geq \|f\|^2 \left\langle \frac{e^{-(\sigma-\chi)z}\mathbb{1}_{z\geq 0}}{\left\|e^{-(\sigma-\chi)z}\mathbb{1}_{z\geq 0}\right\|}, \frac{1}{\|1\|}\right\rangle^2 \\
&= \cos(\theta)^2 \|f\|^2,
\end{aligned}$$

where $\cos(\theta)$ was already defined by (6.4.7). □

Proof of Lemma 6.4.3.3. In order to prove the Lemma, pick f such that $\langle f' - \chi f, ze^{-(\sigma-\chi)z}\mathbb{1}_{z\geq 0}\rangle = 0$. Define $h := f - c$, with $c := \frac{\langle f, ze^{-(\sigma-\chi)z}\mathbb{1}_{z\geq 0}\rangle}{\langle 1, ze^{-(\sigma-\chi)z}\mathbb{1}_{z\geq 0}\rangle}$. One then has that $\langle h', ze^{-(\sigma-\chi)z}\mathbb{1}_{z\geq 0}\rangle = 0$. But then we have $f' = h'$, so $\|f'\| = \|h'\|$ and $\langle f', 1\rangle = \langle h', 1\rangle$. Hence:

$$\begin{aligned}
&\sup_{\|f'\|=1, \langle f' - \chi f, ze^{-(\sigma-\chi)z}\mathbb{1}_{z\geq 0}\rangle = 0} \left\langle f', \frac{1}{\|1\|}\right\rangle \\
=&\sup_{\|g'\|=1, \langle g', ze^{-(\sigma-\chi)z}\mathbb{1}_{z\geq 0}\rangle = 0} \left\langle g', \frac{1}{\|1\|}\right\rangle \\
=&\sqrt{1 - \cos^2(\phi)}
\end{aligned}$$

The rest of the proof is *mutatis mutandis* the same as the proof of Lemma 6.4.3.2. □

Proof of Lemma 6.4.3.4. We have that:

$$\begin{aligned}
\int_{\mathbb{R}} u'\beta e^V &= -\int_{\mathbb{R}} u(\beta e^V)' \\
&= -\int_{\mathbb{R}} (u\beta' + u\beta^2)e^V \\
&= \chi u(t,0) - \int_{\mathbb{R}} u\beta^2 e^V
\end{aligned}$$

Hence :

$$\chi|u(t,0)| \leq \left\|u'\right\| \|\beta\| + \|u\| \left\|\beta^2\right\| \leq C(\sqrt{F} + \sqrt{E}) \leq C\sqrt{F}$$

The last inequality is an application of Proposition 6.4.1 in combination with Lemma 6.4.3.2. □

Proof of Lemma 6.4.3.5. Same proof as Lemma 6.4.3.4, but at the end we use Proposition 6.4.1 in combination with Lemma 6.4.3.3. □

Outlook

As mentioned the results exposed in this Chapter are preliminary and the questions raised here are still under investigation. First, we believe that the special structure of the alternative Go or Grow model (6.1.1) may lead to a proof of existence globally in time. In particular the "Markovian" aspect of the Go or Grow rule here, *i.e.* $\int_{\bar{x}(t)}^{+\infty} \rho(t,x)dx = 1$, may turn out to be fruitful. Moreover, Equation (6.1.7) on P can also be a helpful tool. Then, we wish to continue investigating Conjecture (6.1.4). The lower bound for $\chi < 1$ may likely be obtained by constructing a suitable subsolution. We believe that the main difficulty lies in the upper bound for $\chi = 1$, since this case was also the difficult part in the study [9] on Burgers-F/KPP Equation. Finally, an interesting perspective to this investigation is that the proofs for the alternative Go or Grow model (6.1.1) may apply to the free boundary problem (6.1.3) proposed in [20], where the asymptotics have been obtained through formal computations. We are not aware of any rigorous proofs of the asymptotics for the free boundary problem (6.1.3). In addition, the techniques may turn out to be applicable to a wider class of Equations, such as equations of type (6.1.6) for a wide array of possible functions $\psi(\,\cdot\,)$, but this remains hypothetical to this point.

Appendix A

Figures and Figure Supplements: Hypoxia triggers Collective Aerotactic Migration in *Dictyostelium discoideum*

This Section contains the figures and figure supplements of Chapter 1.

RESEARCH ARTICLE

Figures and figure supplements

Hypoxia triggers collective aerotactic migration in *Dictyostelium discoideum*

Olivier Cochet-Escartin *et al*

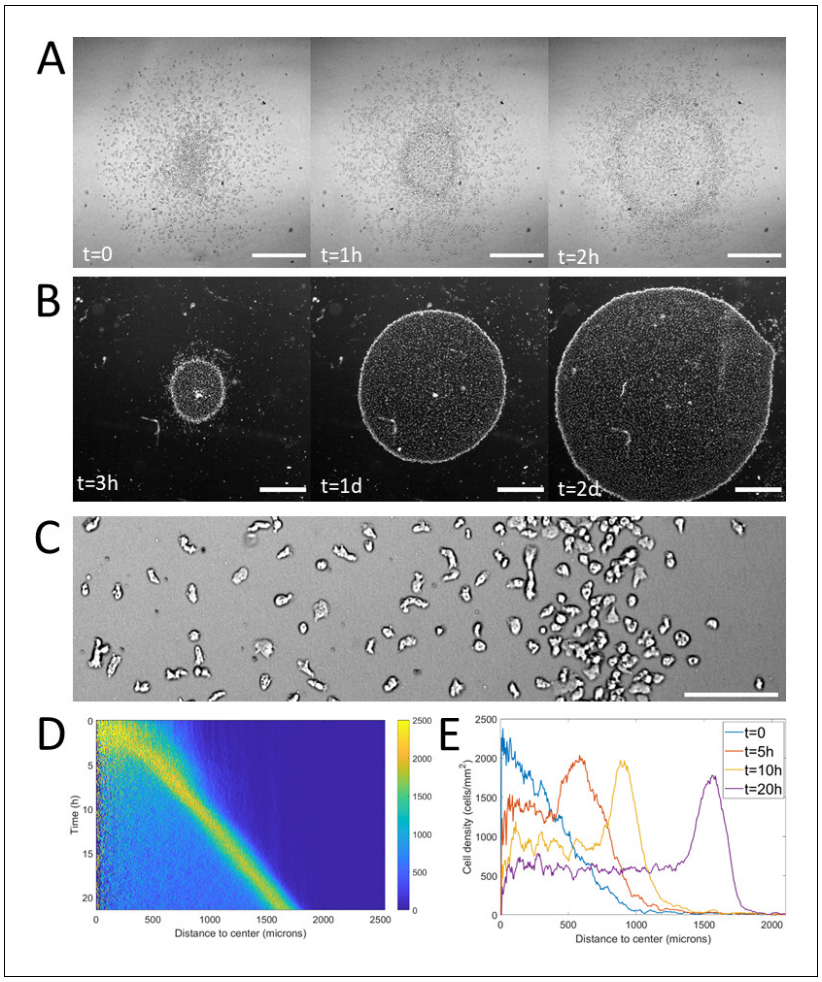

Figure 1. Formation and dynamics of a dense ring of cells after vertical confinement. (**A**) Snapshots of early formation, scale bars: 500 µm. (**B**) Snapshots at longer times imaged under a binocular, scale bars: 1 mm. (**C**) Close up on a ring (band with a higher density on the right hand side) already formed moving rightward and showing different cellular shapes in the ring and behind it, scale bar: 100 µm. (**D**) Kymograph of cell density over 20 hr showing the formation and migration of the highly dense ring. (**E**) Cell density profiles in the radial direction at selected time points.

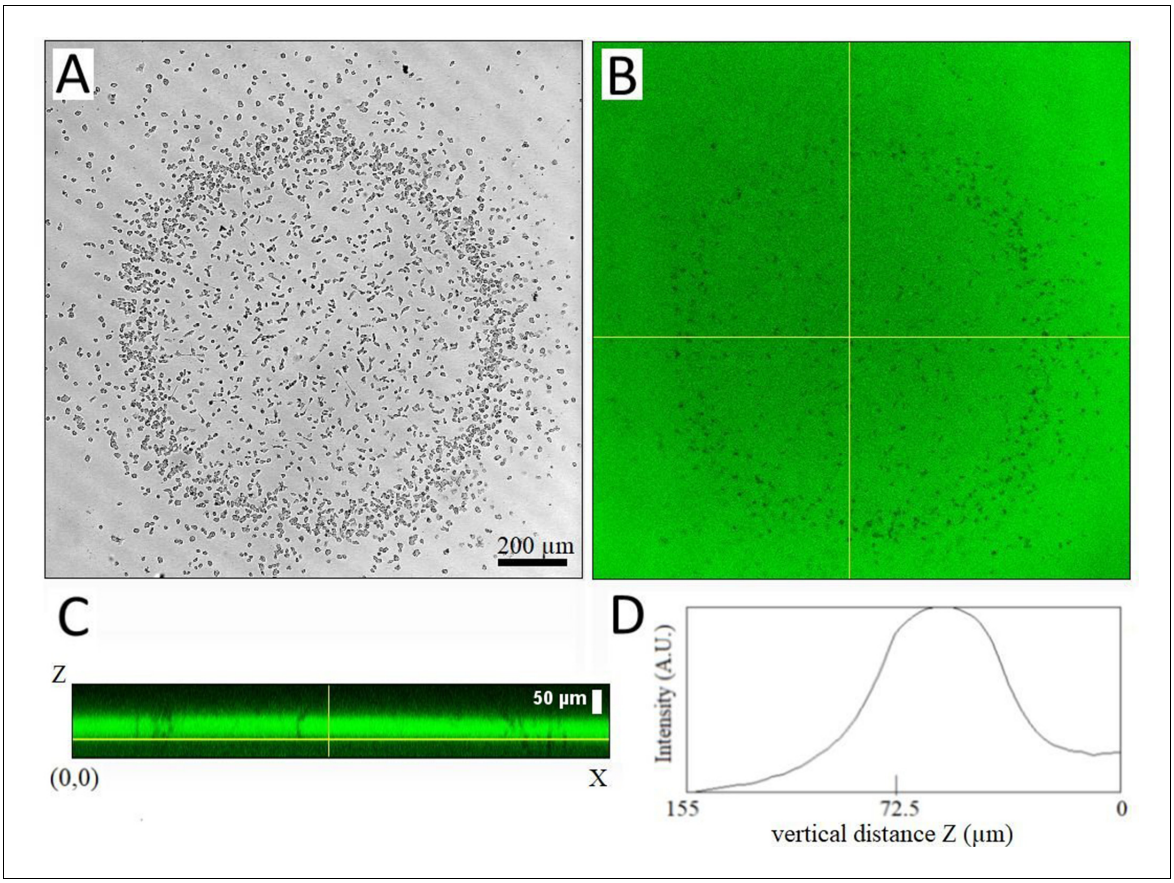

Figure 1—figure supplement 1. Measurement of the confinement height 105 min after covering a cell colony with ~1000 cells plated on plastic with a coverglass using. (**A-B**) Confocal transmission and fluorescence XY images (slice 37) of a Z-stack from inside the plastic bottom of the well to the coverglass; (**C**) Side view XZ along the horizontal line in B. (**D**) Vertical intensity profile along Z (averaged over X). The Full width at half maximum (FWHM) is about 50 µm. Z-stacks were taken with a confocal microscope at 2.57 µm/slice using a 10x objective with a very small pinhole size (0.25 Airy), the fluorescence is due to fluorescein FITC added at 16 µM in HL5 medium.

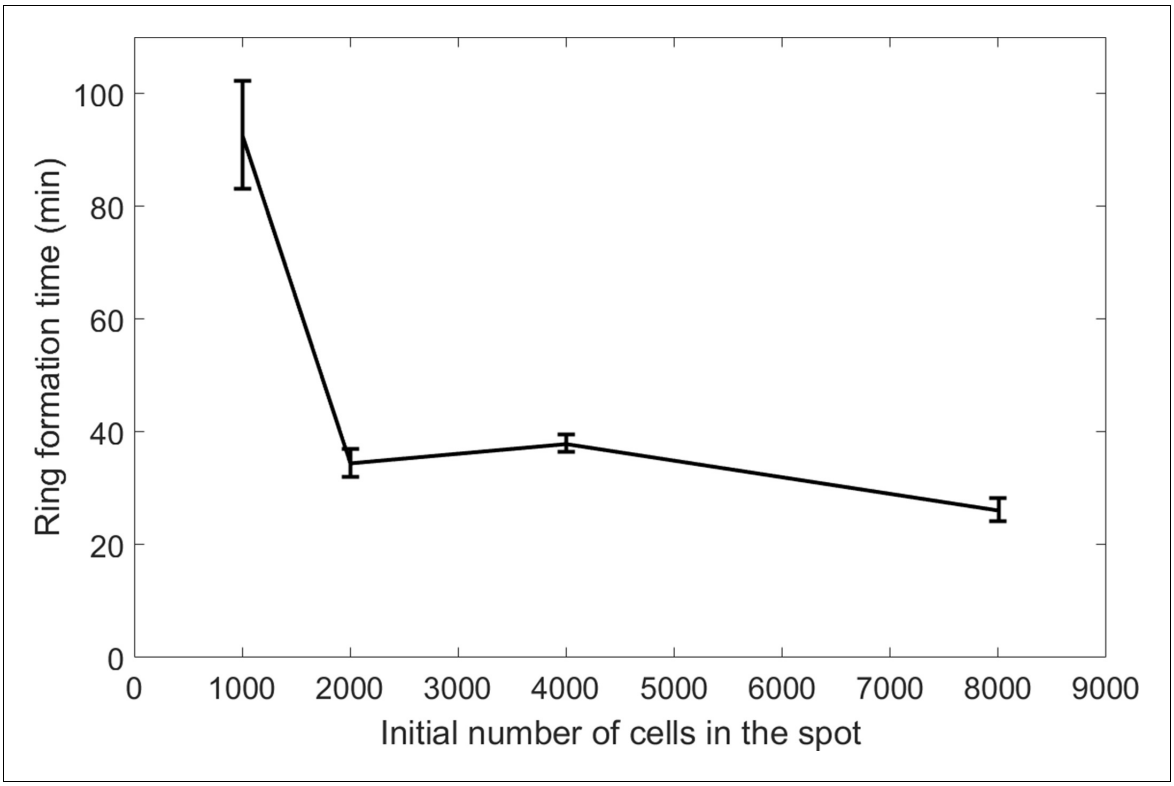

Figure 1—figure supplement 2. Ring formation time decreases with cell number. Error bars represent std of n ≥ 4 independent experiments.

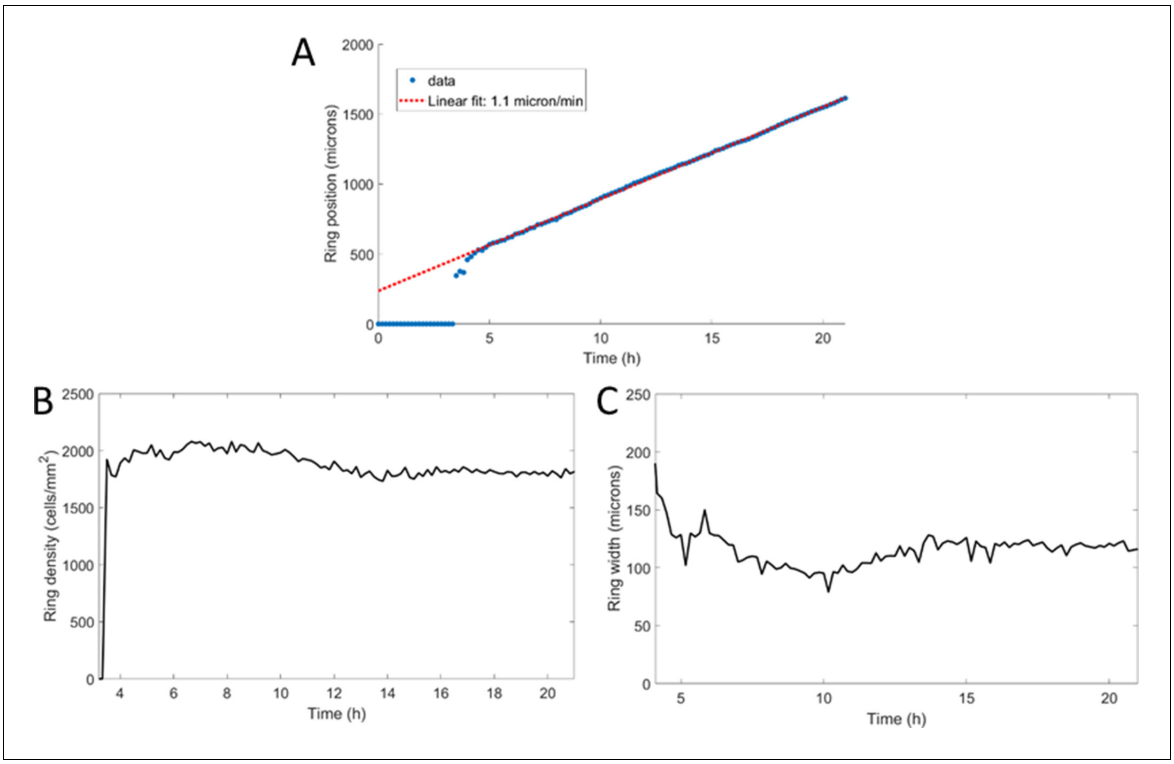

Figure 1—figure supplement 3. Morphological properties of a propagating ring. (**A**) Position of the ring as a function of time with a linear fit yielding a speed of 1.1 µm/min. (**B**) Cell density within the ring as a function of time, starting after ring formation. (**C**) Ring width at half height as a function of time, after ring formation.

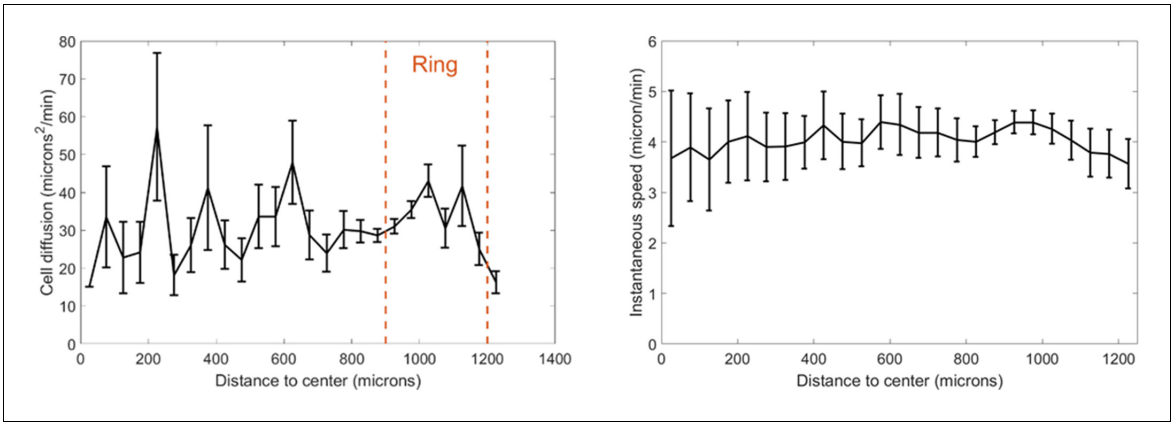

Figure 1—figure supplement 4. Effective cell diffusion constant and instantaneous speeds as a function of distance to the center. Cell diffusion is defined as the squared of the migrated distance during a trajectory divided by 4 t with t the duration of that trajectory. Cells were tracked between t=9h and t=10h and orange dashed line represent the position of the ring at these times. Each point is the mean±std of cells within the given distance bin, n=2746 cells total.

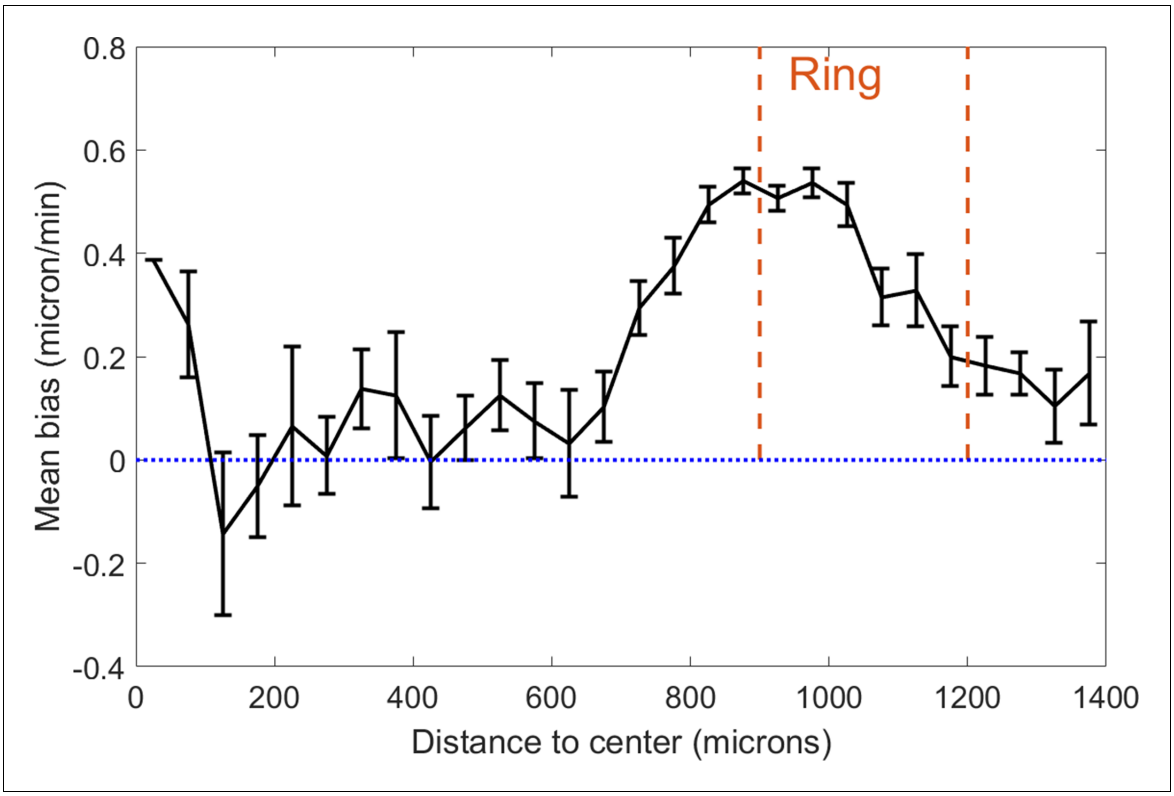

Figure 1—figure supplement 5. Cell velocity bias in the spot assay as a function of distance to the center. This bias is defined as the projected speed in the radial direction. Each point is the mean±std of cells within the given distance bin, n=2211 cells total. Cells were tracked between t=9h and t=11h and orange dashed lines represent the positions occupied by the ring at these times. Dotted blue line is a guide for the eye representing a 0 bias, that is non-oriented motion.

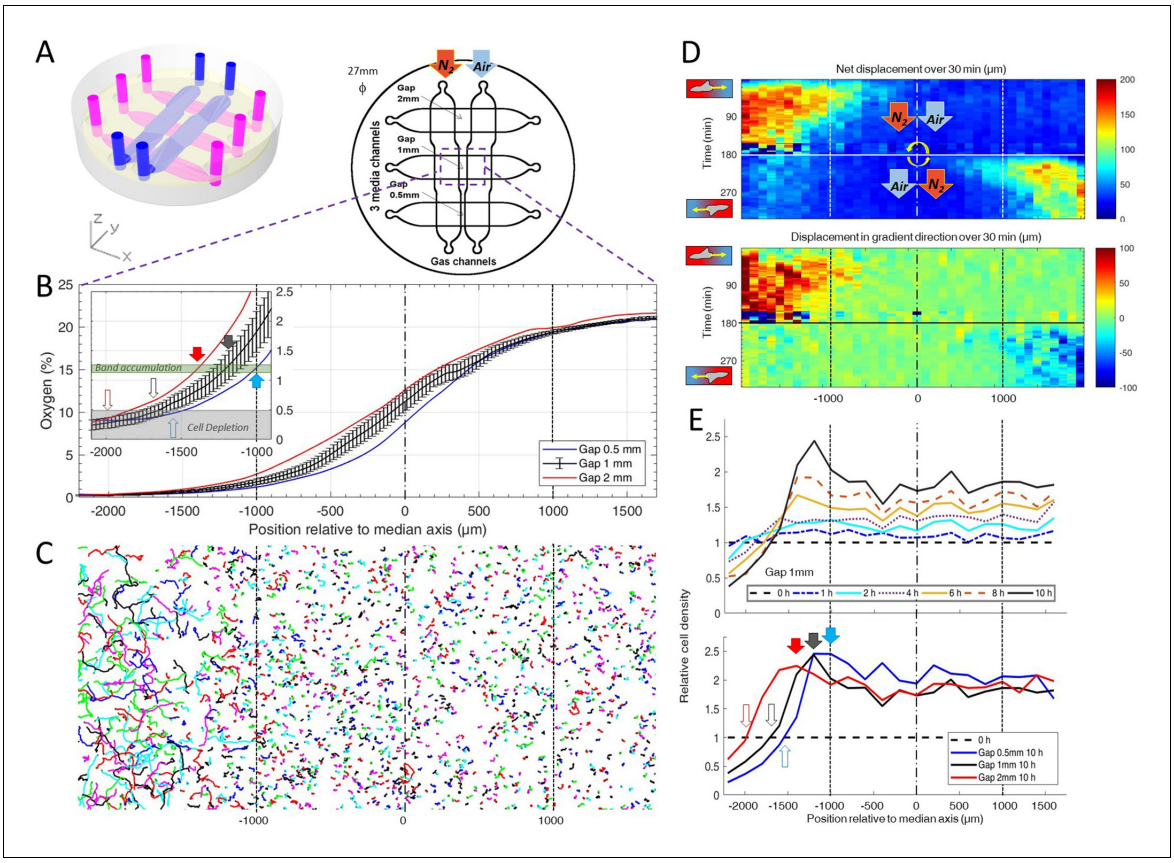

Figure 2. *Dictyostelium* single cells are attracted by an external O_2 gradient when O_2 level drops below 2%. (**A**) Schemes of the new double-layer PDMS microfluidic device allowing the control of the O_2 gradient by the separation distance (gap) between two gas channels located 0.5 mm above the three media channels and filled with pure nitrogen, and air (21% O_2). (**B**) Measured O_2 concentration profiles 30 min after N_2-Air injection to the left and right channels respectively (0–21% gradient) as a function of the position along the media channel for the three gaps. Error bars (see Methods) are reported only for gap 1 mm for clarity. The inset shows the 0–2.5% region under the nitrogen gas channel (arrows, see E). (**C**) Trajectories lasting 1 hr between 3 hr and 4 hr after establishment of a 0–21% gradient. Cells are fast and directed toward the air side in the region beyond the −1000 µm limit (O_2<2%). (**D**) Cell net displacement over 30 min (end to end distance, top kymograph) and 30 min displacement projected along gradient direction (bottom kymograph). Cells are fast and directed toward O_2, where O_2<2%, within 15 min after 0–21% gradient establishment at t=0. At t=180 min, the gradient is reversed to 21–0% by permuting gas entries. Cells within 15 min again respond in the 0–2% region. (**E**) Relative cell density histogram (normalized to t=0 cell density) as a function of the position along media channel. Top panel: long term cell depletion for positions beyond −1600 µm (O_2<0.5%, see inset of B) and resulting accumulation at about −1200 µm for gap 1 mm channel. The overall relative cell density increase is due to cell divisions. Bottom panel: cell depletion and accumulation at 10 hr for the three gaps. The empty and filled arrows pointing the limit of the depletion region, and max cell accumulation respectively are reported in the inset of B.

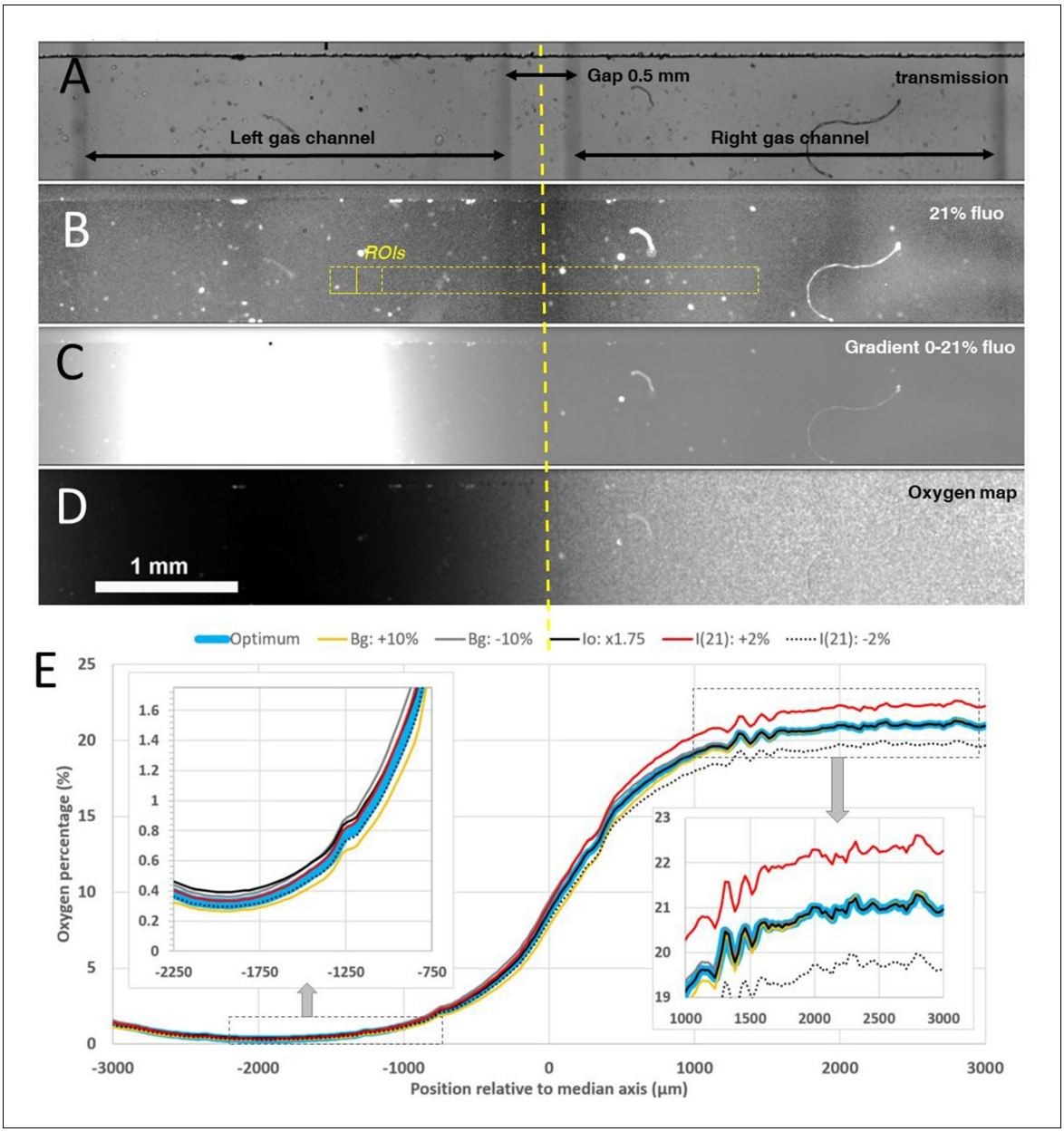

Figure 2—figure supplement 1. Oxygen profile measurements inside the microfluidic gradient generator device with a sensing film mounted on the bottom of the media channel. (**A-B**) Transmission and homogeneous 21% O_2 level fluorescence images of the media channel with gap 0.5 mm between the two gas channels. (**C**) Raw fluorescence image in presence of 0–21% gradient established by injecting pure N2 in the left gas channel and air in the right one (image was taken 30 min after the beginning of the gas injection). (**D-E**) Corresponding calculated O_2 map and O_2 profile. In D colors correspond to slight changes within the experimental uncertainty of the parameters used for the calculation (see text), insets correspond to the hypoxic (~0%) and normoxic (~21%) sides of the profile.

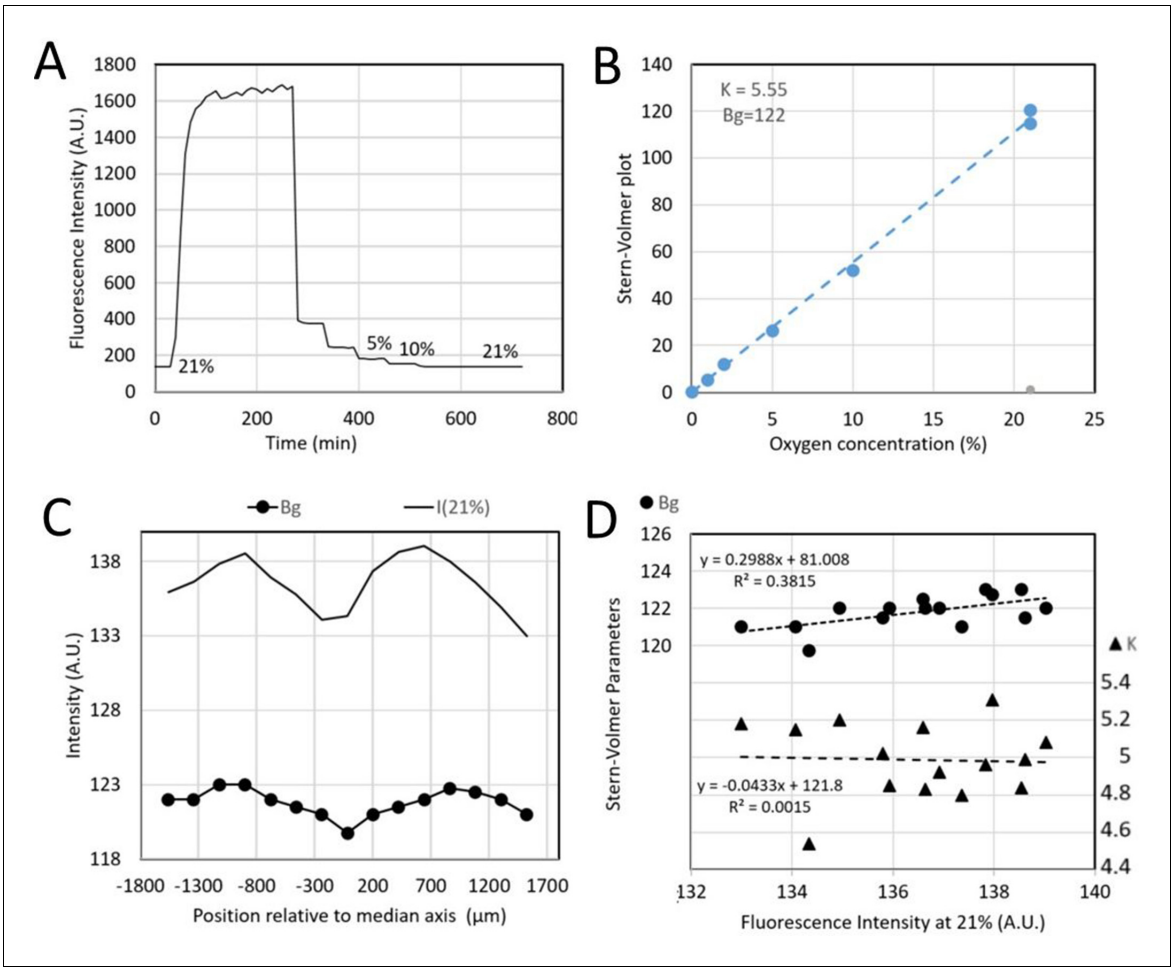

Figure 2—figure supplement 2. Typical calibration data of sensing films mounted on a microfluidic device. (**A**) Fluorescence intensity changes when applying an oxygen concentration ramp with the concentration in each gas channel. (**B**) Corresponding Stern-Volmer plot (see text). (**C**) Measured intensity at 21% O_2 level (solid line) and fitted background B_g (bullets) for different ROI locations depicted in yellow in ***Figure 2—figure supplement 1B***. (**D**) Fitted B_g (bullets) and Stern-Volmer sensitivity parameter K (triangles) as a function of 21% O_2 level intensity.

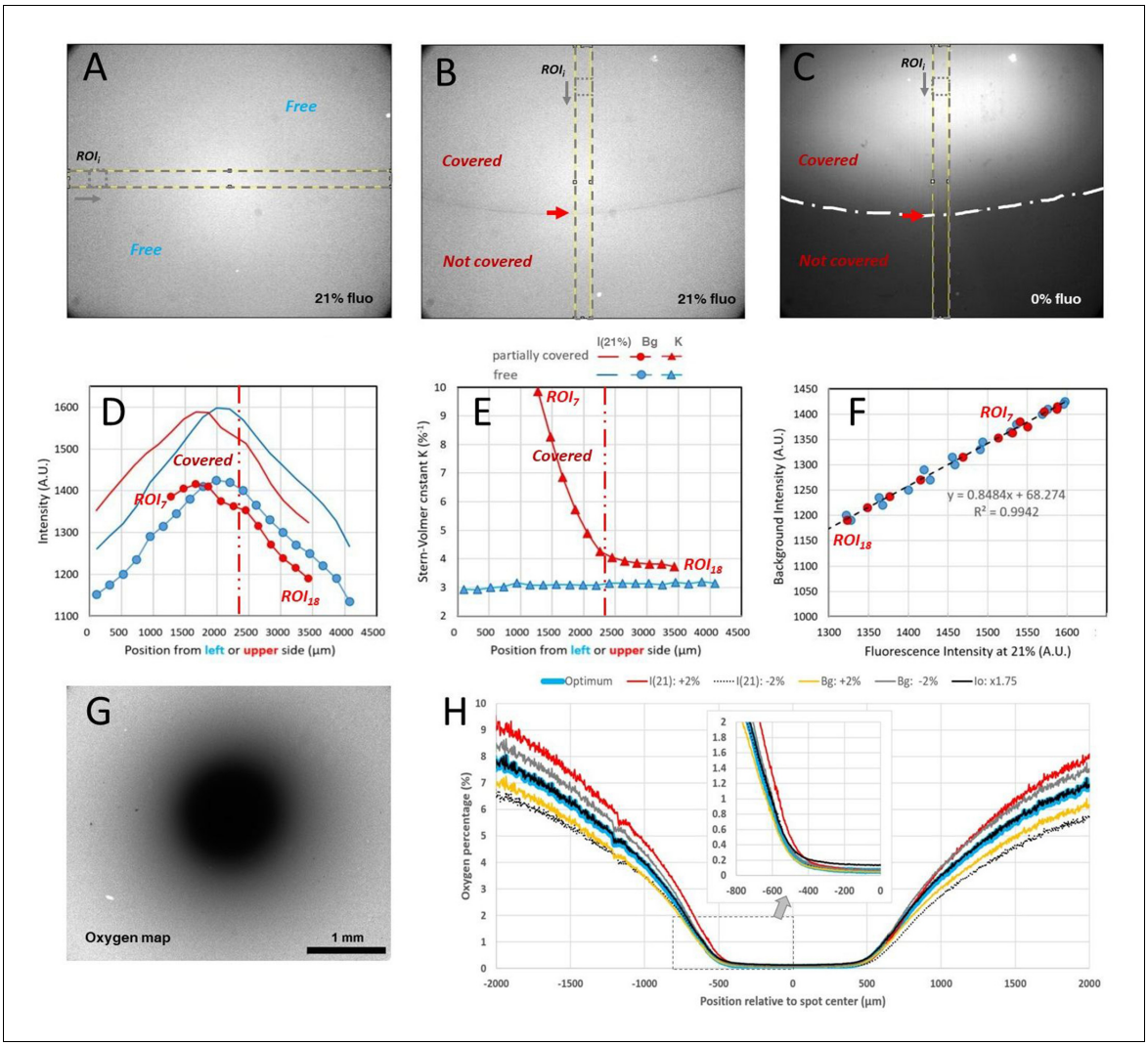

Figure 2—figure supplement 3. Typical calibration data and oxygen profile measurement with covered sensing films for the spot assay. (**A**) Homogeneous 21% O_2 level fluorescence image of an uncovered sensing film. (**B**) Homogeneous 21% O_2 level fluorescence image of sensing film partially covered by a plain coverglass simulating the border of the spot assay (the red arrow indicates the glass boundary also depicted as a long dotted line in C. (**C**) Fluorescence intensity when pure N_2 was flushed for 80 min (same region as in B) with the partial coverage of the sensing film). (**D**) Measured intensity at 21% O_2 level (solid line) and fitted background B_g (bullets) for different ROI positions depicted in yellow in A for uncovered film (blue color) and in B for partially covered film (red color). (**E**) Fitted B_g (bullets) and Stern-Volmer sensitivity parameter K (triangle) along the ROI positions for the uncovered (blue color) and partially covered situation (red color). (**F**) Fitted B_g plotted as a function of the 21% O_2 level intensity for the uncovered and covered situations. (**G-H**) Calculated O_2 map of *a Dictyostelium* spot covered and corresponding profile along a median horizontal line. Colors correspond to slight changes within the experimental uncertainty of the parameters used for the calculation, insets correspond to the hypoxic (~0–2%) left side of the profile.

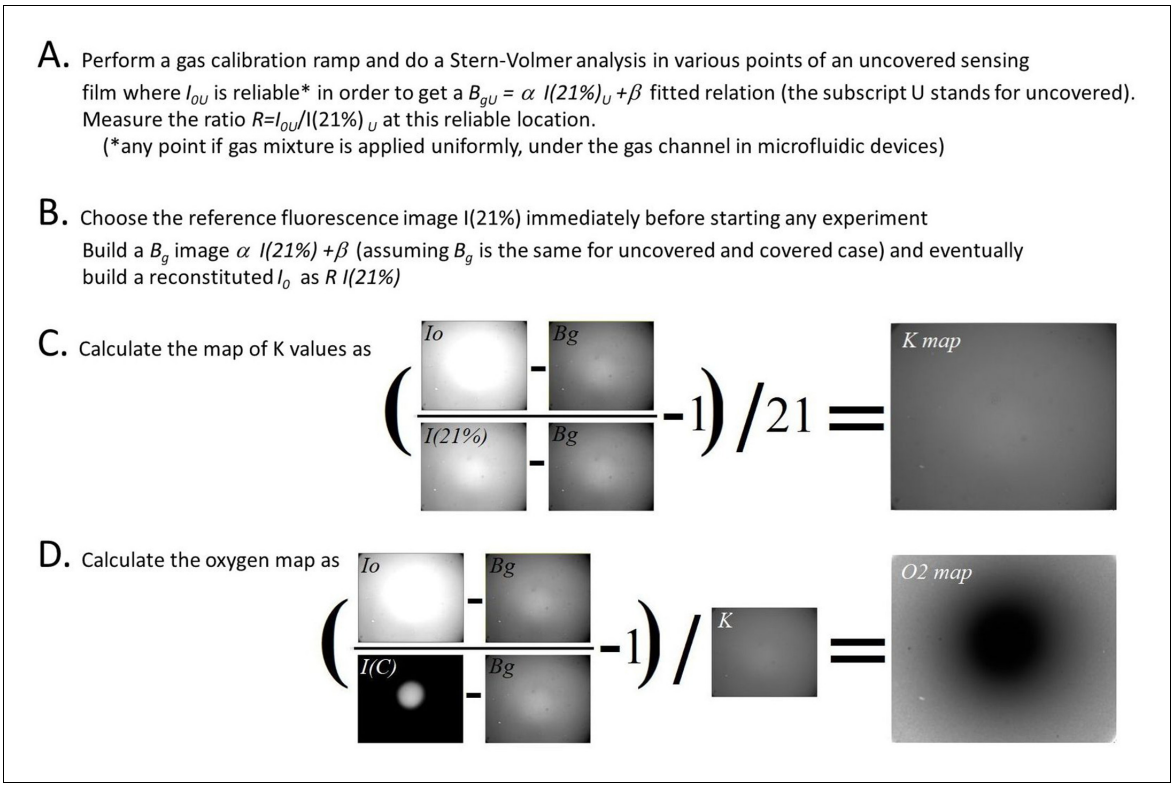

Figure 2—figure supplement 4. Image analysis pipeline to quantify oxygen map from O_2 sensitive sensing films. Images correspond to an hypoxic circular zone created by a confined *Dictyostelium* spot.

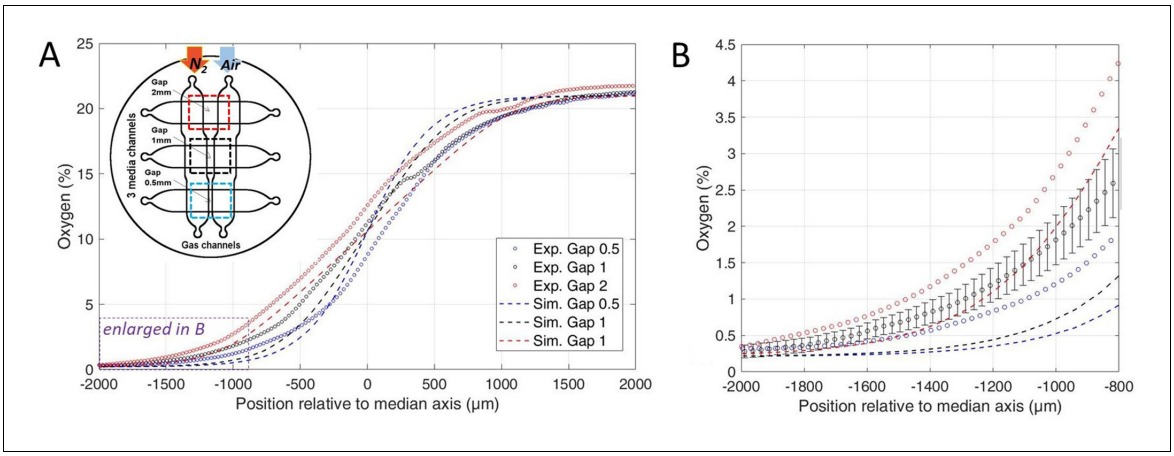

Figure 2—figure supplement 5. Numerical simulations of oxygen profiles. (**A**) Comparison of the measured stationary oxygen profile in the microfluidic device (circles) and simulated ones (dotted lines) for the three gaps. Oxygen is measured thanks to the sensing film. The inset shows the gas injection conditions in the device: pure N_2 and air are flushed in left and right gas channel, respectively. (**B**) Enlarged oxygen profile in the hypoxic side. The estimated error bar on experimental measurements (showed for clarity on gap 1 mm data only) is explained in Materials and methods. Simulations are made with Comsol and explained in Methods.

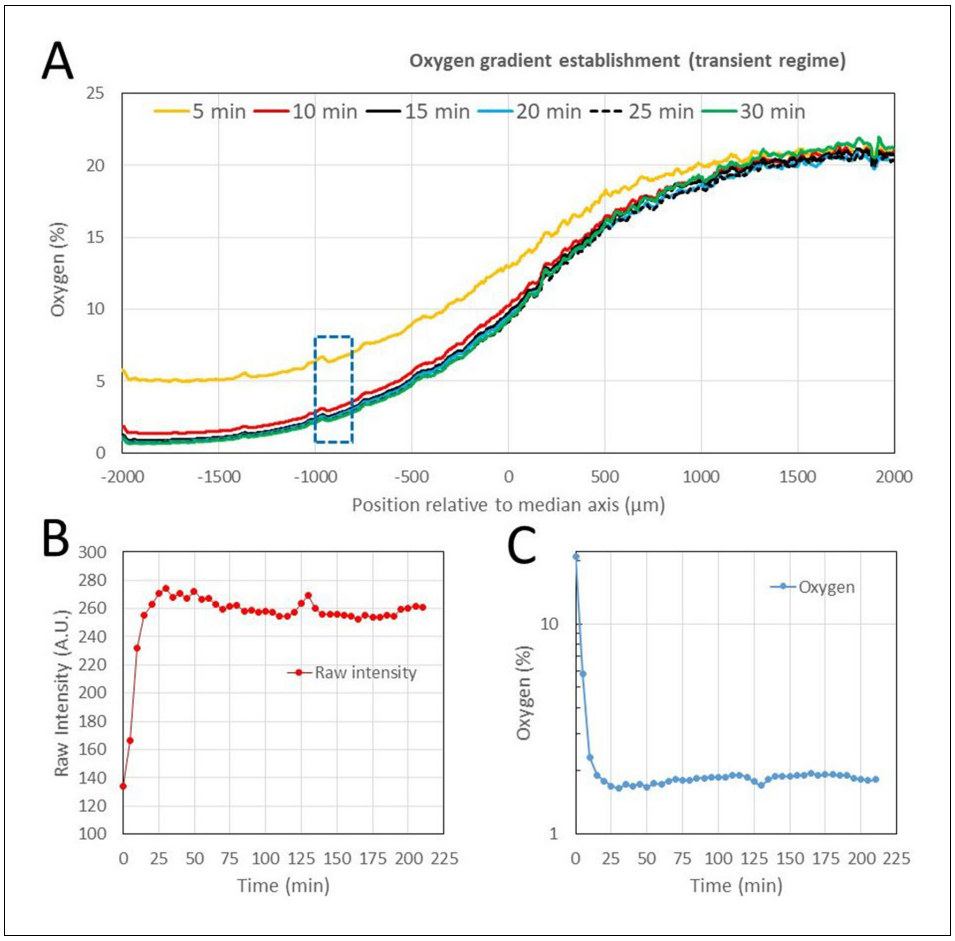

Figure 2—figure supplement 6. Experimental oxygen gradient establishment in the microfluidic device (gap 0.5 mm). Pure N_2 and air are flushed at time 0 in left and right gas channel, respectively. (**A**) Oxygen profile measured using the sensing films at 5 min time interval. (**B-C**) Raw intensity and measured oxygen in the ROI between −1000 µm and −800 µm from the device median axis in the region where the oxygen is about 1.5% (dotted region in A). Within 15 min, each signal reached 95% of its equilibrium value.

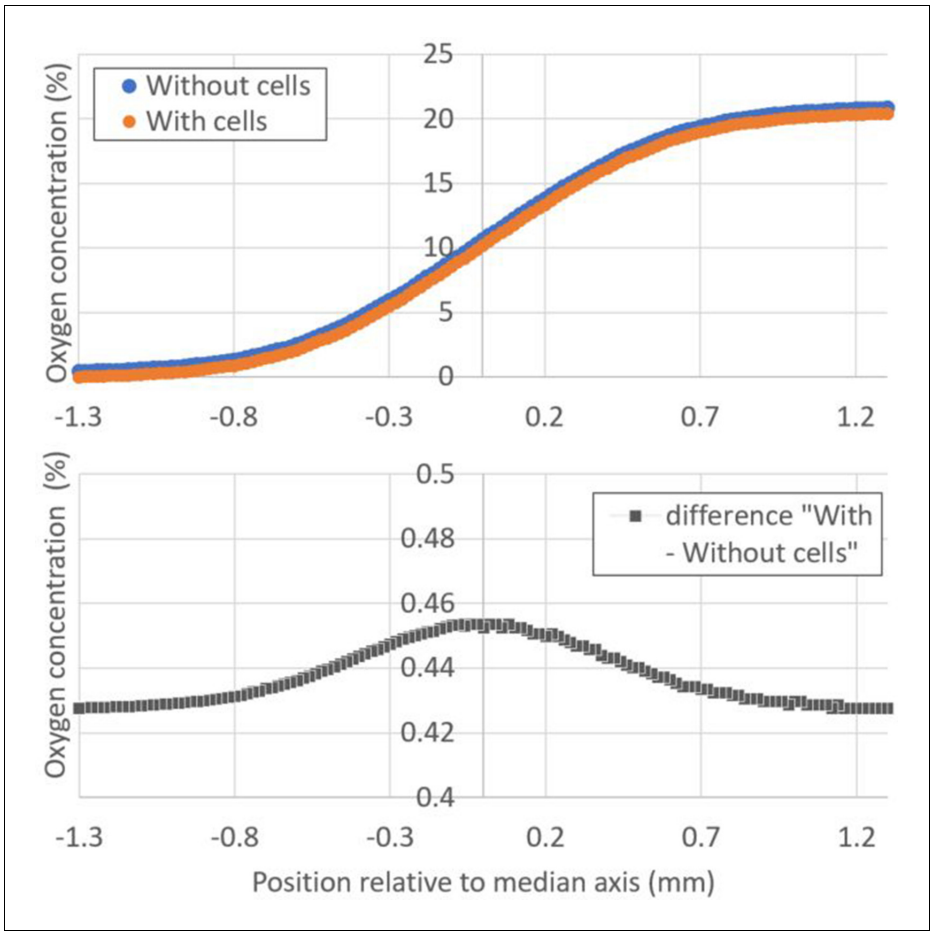

Figure 2—figure supplement 7. Influence of plated cells on the steady oxygen tension in the microfluidic device (Computational results). (**A**) Absolute value of the oxygen concentration as a function of the position relative to the median axis of the device for the gap 1 mm channel in presence (orange markers) or absence of cells (blue markers). Nitrogen is supplied on the left gas channel and 21% O_2 is supplied on the right channel. Cells density was taken as 500 cells/mm^2, which is the upper experimental limit. (**B**) Corresponding difference between the two simulated situations (presence and absence of cells). In the region of interest where cells exhibit a strong aerotactic response (i.e., around 1% O_2 or −1 mm from the median axis), this difference is around 0.43% O_2 which is comparable to the error bar on O_2 measurements using sensing films (***Figure 2B***). The rate of oxygen consumption by *Dd* cells was taken as $1.2.10^{-16}$ mol.cell^{-1}.s^{-1}.

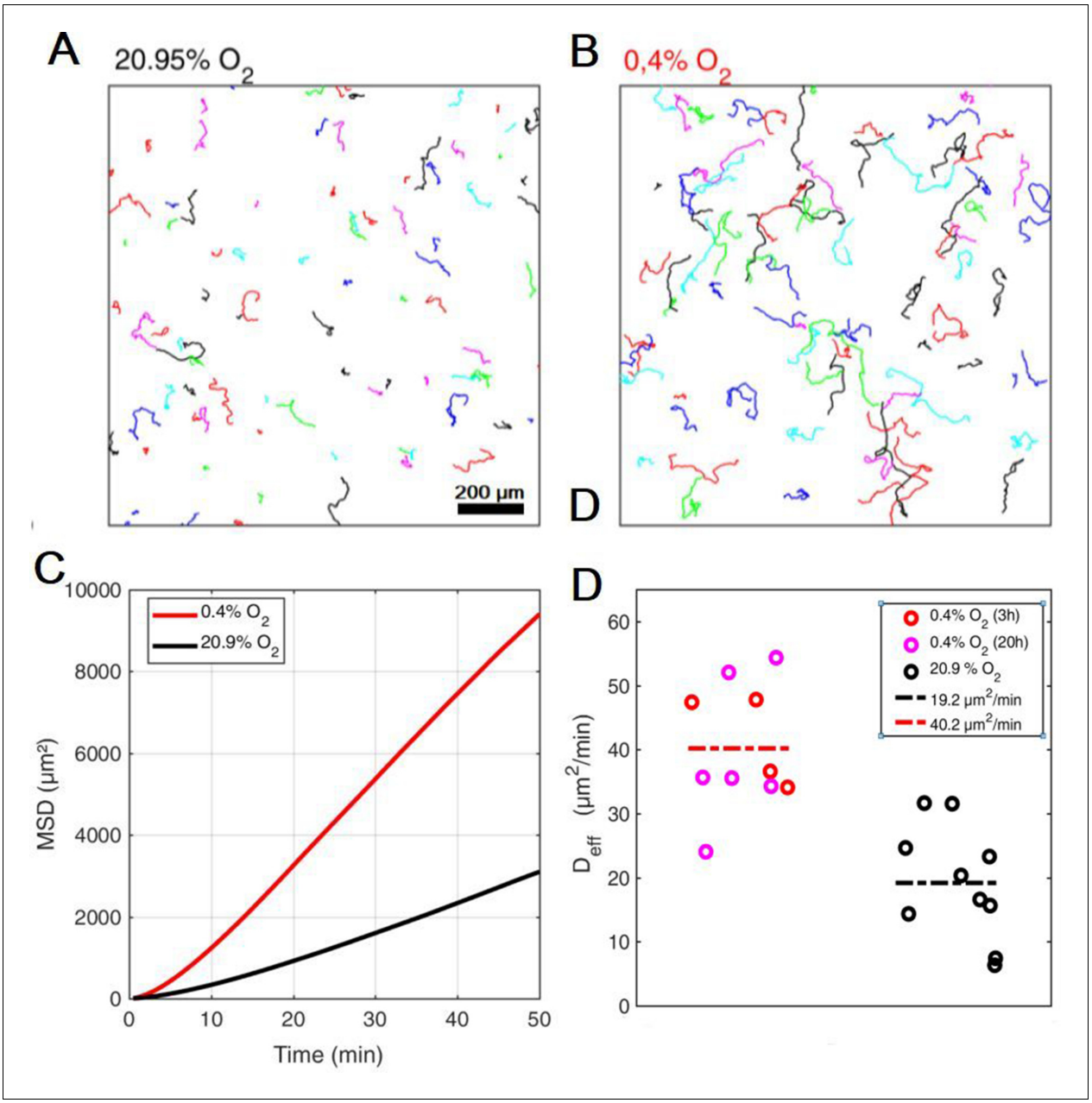

Figure 2—figure supplement 8. Aerokinesis of *Dd* cells in homogenous environments. (**A-B**) Representative cell trajectories over 1 hr in either atmospheric, C=20.95% (**A**) or hypoxic, C=0.4% (**B**) conditions. (**C**) Quantification of cell motility as mean square displacements in both conditions. (**D**) Effective diffusion constants in both conditions, also shown after 3 and 20 hr in hypoxic conditions. Dashed lines represent the mean in each conditions over 10 fields of view stemming from five independent experiments in each case.

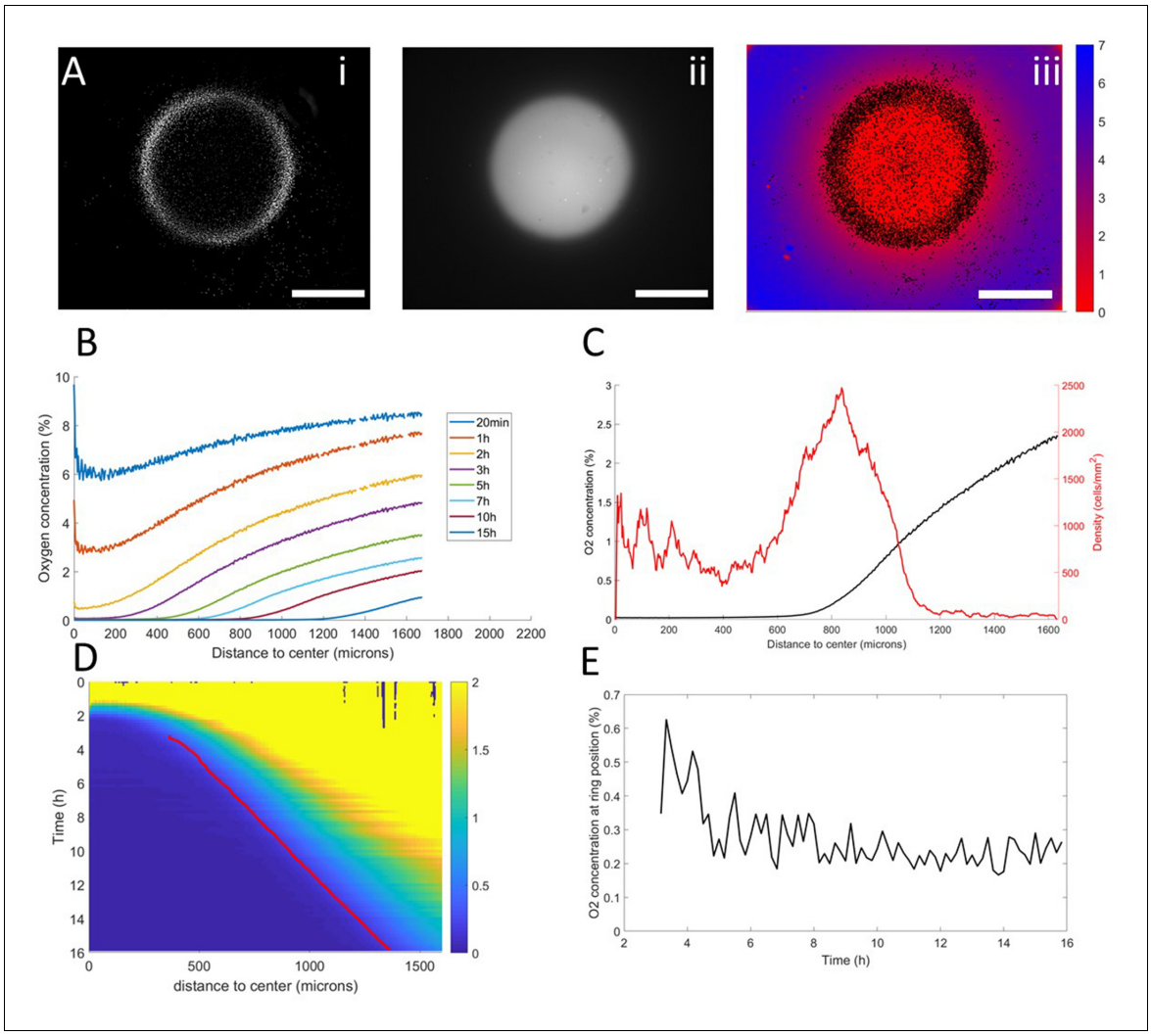

Figure 3. Interplay between ring dynamics and O_2 profiles. (**A**) (i) Treated image showing cell distribution at t=10h, (ii) raw fluorescent signal indicative of strong O_2 depletion, (iii) reconstructed image showing the center of mass of all detected cells and quantitative O_2 profiles (colorbar, in % of O_2), scale bars: 1 mm. (**B**) O_2 profiles averaged over all angles and shown at different times. (**C**) Radial profile of cell density and O_2 concentration at t=10h showing the position of the ring relative to the O_2 profile. (**D**) Kymograph of O_2 concentration (colorbar in %) with the position of the ring represented as a red line. The colormap is limited to the 0–2% range for readability but earlier time points show concentrations higher than the 2% limit. (**E**) O_2 concentration as measured at the position of the ring as a function of time showing that the ring is indeed following a constant concentration after a transitory period.

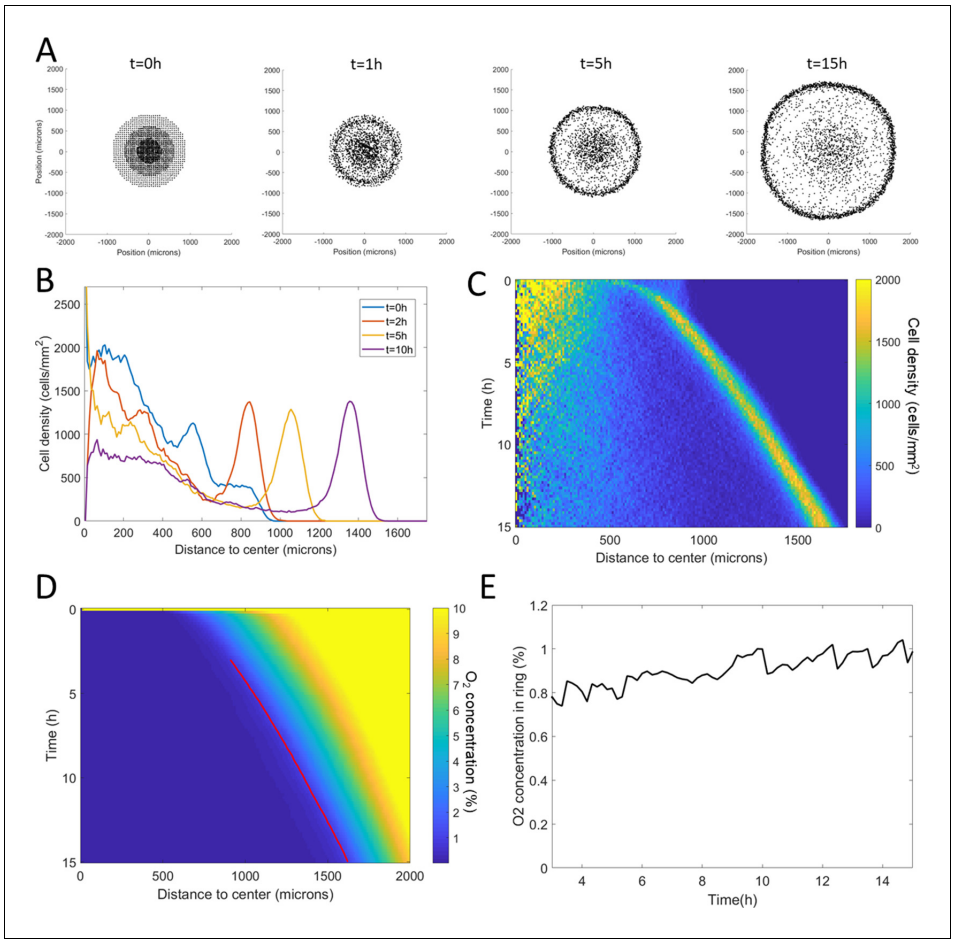

Figure 4. Minimal Potts model of ring formation and migration. (**A**) Snapshots of a simulated colony of cells showing the formation of highly dense ring of cells. (**B**) Cell density profiles averaged over all angles for four different times. (**C**) Corresponding kymograph of cell density (colorbar in cells/mm^2) as a function of time and distance to the center. Quantification in terms of microns and hours is described in the Materials and methods section. (**D**) Kymograph of O_2 concentration (colorbar in %) with the position of the ring represented as a red line. The colormap is limited to the 0–10% range for readability but earlier time points show concentrations higher than the 10% limit. (**E**) O_2 concentration at the ring position as a function of time showing that, here too, the ring follows a constant O_2 concentration.

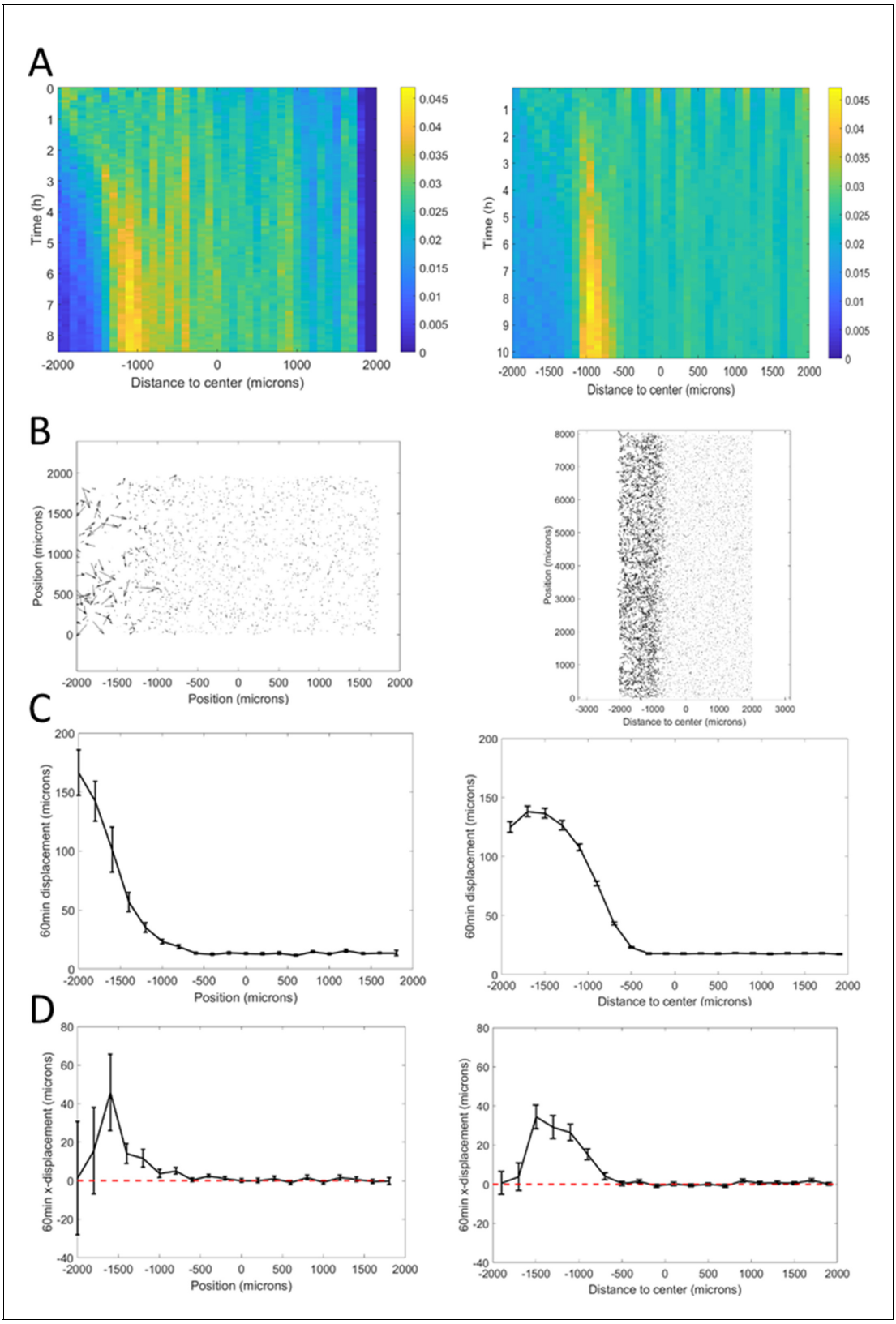

Figure 4—figure supplement 1. Adjusting Potts model (right) to microfluidic experiments (left). (**A**) Density kemographs showing cell accumulation in a low oxygen region. Colorbar represents the fraction of all cells within a bin in distance. (**B**) Vectorial displacements displayed by cells over 1 hr. Higher

Figure 4—figure supplement 1 continued on next page

Figure 4—figure supplement 1 continued

activity at low oxygen concentrations, on the left, is clearly visible in both cases. (**C**) Quantification of cell activity as the norm of the displacements over 1 hr at different positions in the central channel. (**D**) Quantification of cell bias as the displacement of the cells in the x-direction over 1 hr. In C and (**D**), each point is the mean ± std of cells within the given distance bin, n=3392 cells total for experiments (left) and n=7520 cells total for simulations (right).

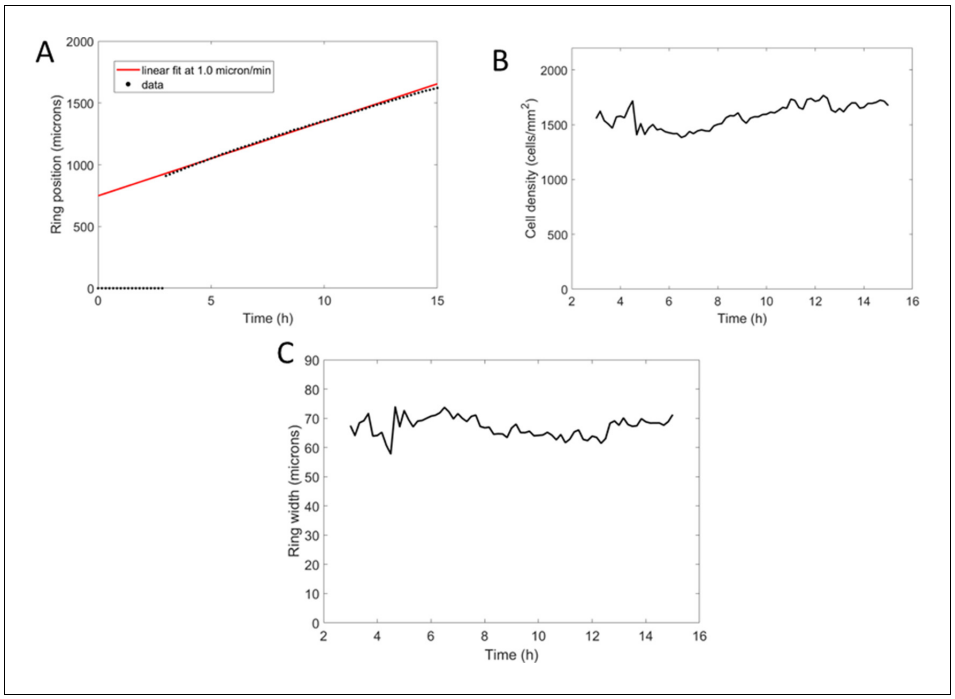

Figure 4—figure supplement 2. Potts model ring features with parameters adjusted from the microfluidic experiments (***Figure 4—figure supplement 1***). (**A**) Position of the ring as a function of time along with a linear fit yielding a speed of 1.1 μm/min. (**B**) Cell density within the ring as a function of time, after its formation. (**C**) Width of the ring as a function of time.

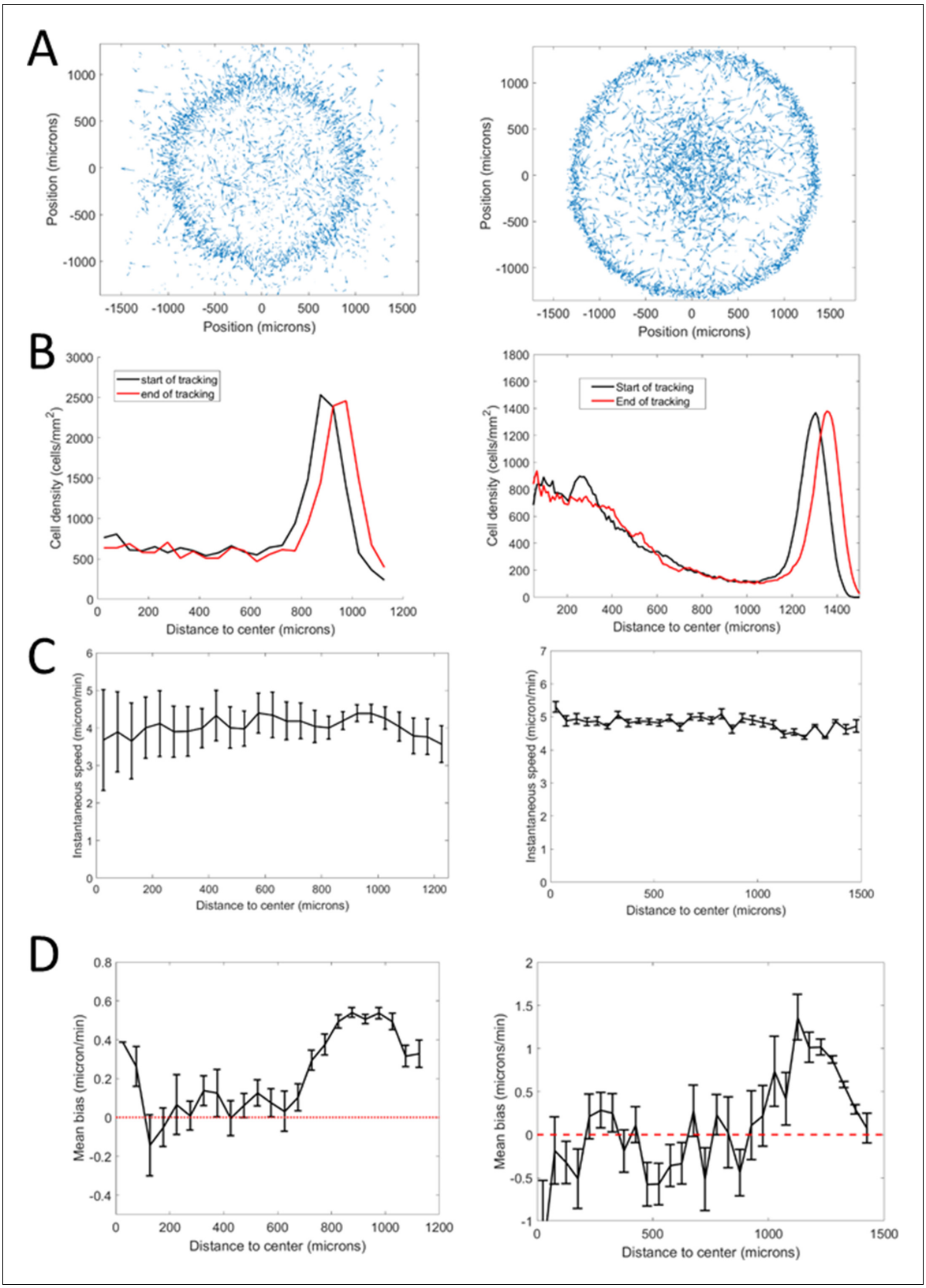
A
Position (microns)
Position (microns)
Position (microns)
Position (microns)
B
start of tracking
end of tracking
Cell density (cells/mm2)
Distance to center (microns)
Start of tracking
End of tracking
Cell density (cells/mm2)
Distance to center (microns)
C
Instantaneous speed (micron/min)
Distance to center (microns)
Instantaneous speed (micron/min)
Distance to center (microns)
D
Mean bias (micron/min)
Distance to center (microns)
Mean bias (microns/min)
Distance to center (microns)

Figure 4—figure supplement 3. Comparison of cell behavior in spot experiments (left) and Potts models (right). (**A**) Sample vectorial displacements over 1 hr. (**B**) Cell density profiles at the beginning (black) and end (red) of the time window used for cell tracking. This indicates ring position for other plots. (**C**) Quantification of cell velocities as a function of position. (**D**) Mean bias in the radial direction measured as the norm of the projected velocity in that direction. In (**C**) and (**D**), each point is the mean±std of cells within the given distance bin, n=4715 cells total for experiments (left) and n=5670 cells total for simulations (right).

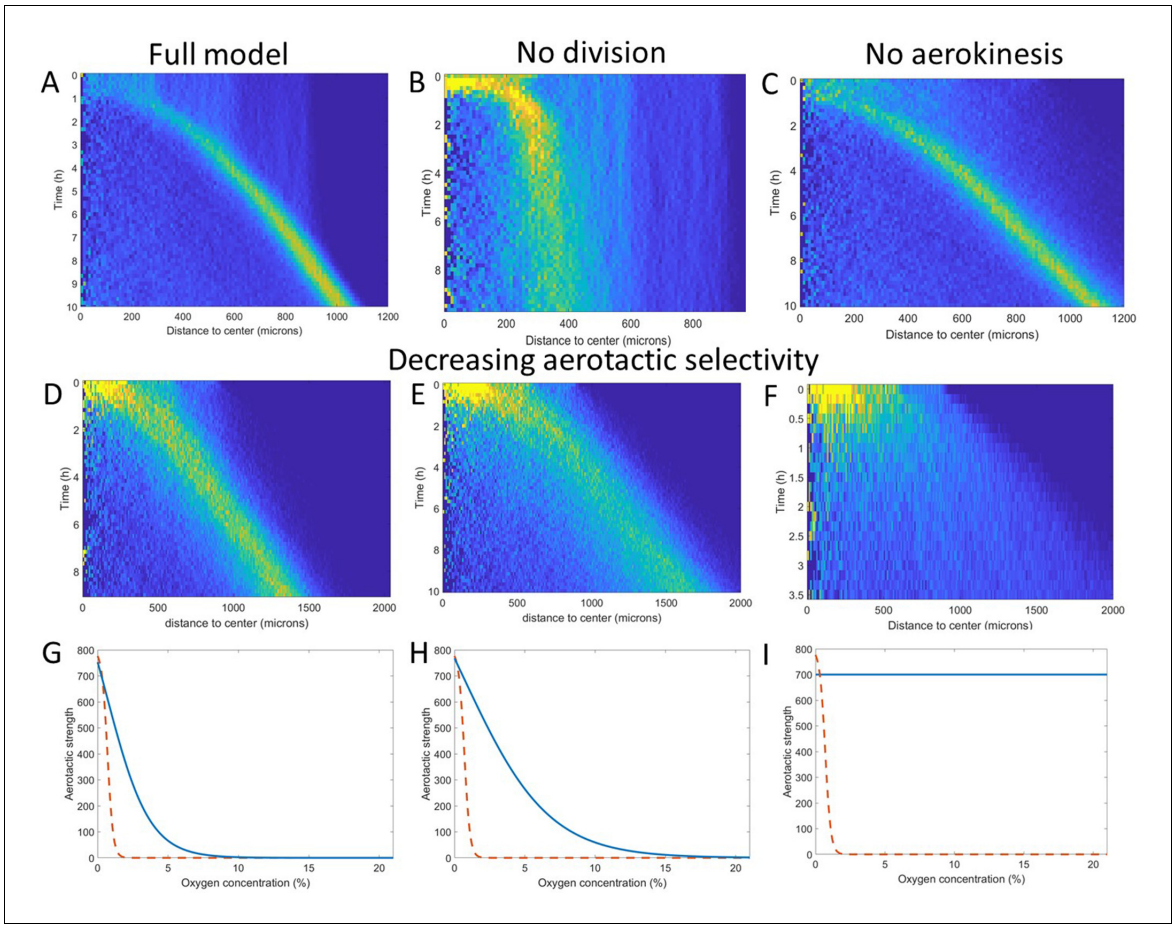

Figure 5. Key ingredients of the Potts model by density kymograph (DK) evaluation. (**A**) DK for the full model with reduced oxygen consumption as a basis for comparison. (**B**) DK in the absence of cell division, note the difference in length scale showing a clear limitation of motion in that case. (**C**) DK in the absence of aerokinesis (cell activity is not modulated by local oxygen concentrations). (**D**) DK with a modulation of aerotactic strength as shown in (**G**), note the wider ring. (**E**) DK with a modulation of aerotactic strength as shown in (**H**). (**F**) DK with a modulation of aerotactic strength as shown in (**I**), no ring appears and cells quickly migrate outwards as shown by the difference in time scales. (**G–I**) Three different aerotactic modulations, in blue, compared to the one used in the full model, shown in (**A**), drawn here as a red dashed line.

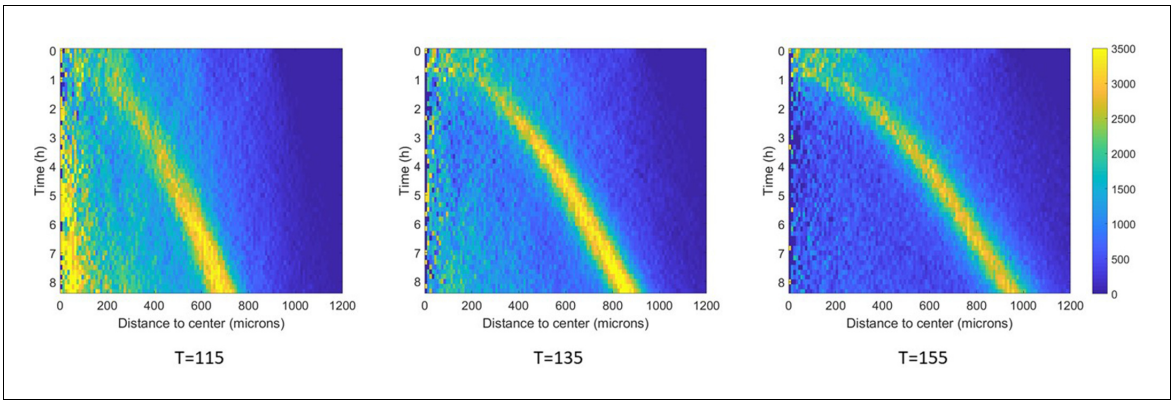

Figure 5—figure supplement 1. Effect of temperature on ring migration in Potts models. Density kemographs (all similarly scaled) of the full model, deprived of aerokinesis, at three different temperatures. Colorbar represents cell density in cells/mm^2. As temperature increases, fewer cells are left behind the ring and the ring moves at faster velocities.

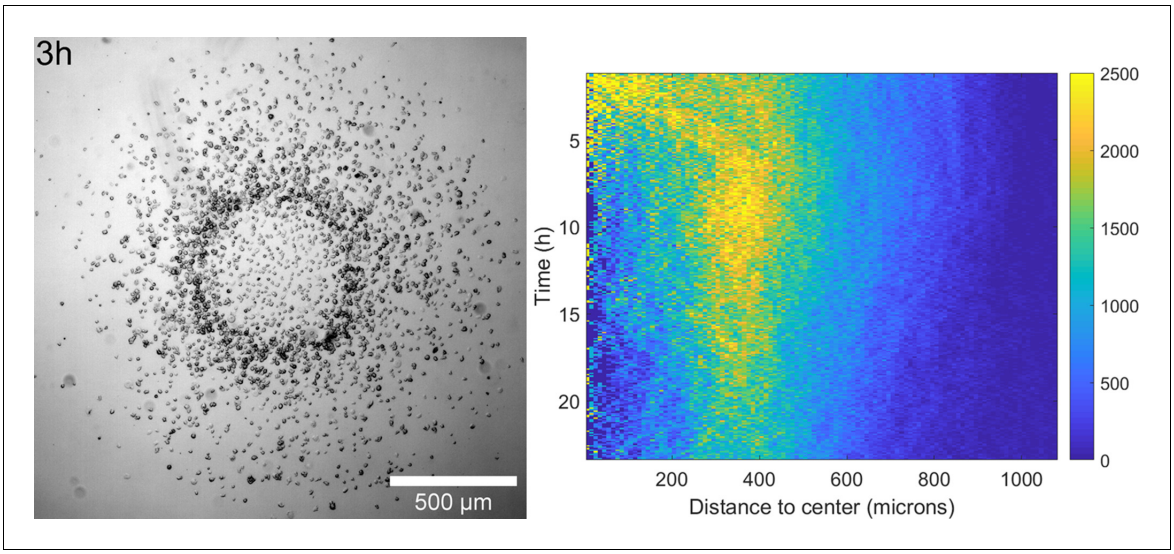

Figure 5—figure supplement 2. Ring formation in a phosphate buffer. Left: Snapshot of a spot assay in phosphate buffer at t=3h clearly showing the formation and migration of a dense ring of cells. Right: corresponding density kemograph (cell densities in cells/mm^2) showing clear similarities with the predictions of ***Figure 5B***.

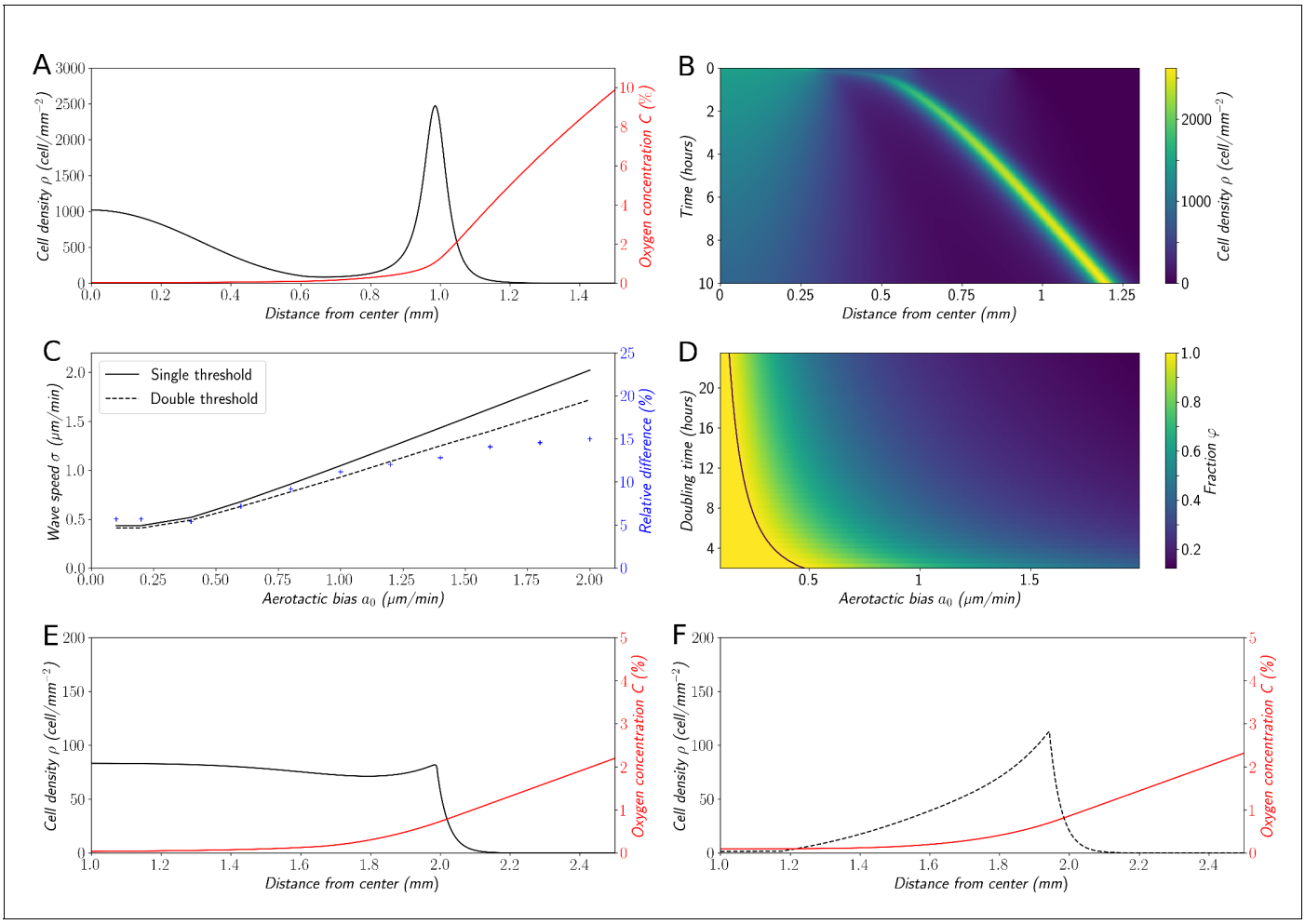

Figure 6. Variations on the 'Go or Grow' hypothesis. (**A**) Cell density and O_2 concentration profiles for the mean-field model (***Equations 1 and 2***). (**B**) Corresponding kymograph of cell density (colorbar in cells/mm^2) as a function of time and distance to the center. (**C**) Comparison of wave speeds for the elementary 'Go or Grow' model, given by Formula ***Equation 6***, and the 'Go or Grow' model with a second threshold, obtained by numerical simulation (solid and dotted lines respectively). The relative difference between the speeds of the two models is represented by crosses. (**D**) Heatmap of $\varphi = 2\sqrt{r_0 D}/\sigma$ as a measure of the relative contribution of cell division to the overall wave speed σ in the space parameter $\ln(2)/r_0$ and a_0 for the 'Go or Grow' model (***Equation 5***), where σ is given by Formula ***Equation 6***. The curve $a_0 = \sqrt{r_0 D}$ is depicted in black. (**E**) Cell density and O_2 concentration profiles for the 'Go or Grow' model with $a_0 = 1\,\mu m/min, r_0 = ln2/480 min^{-1}$ and $C_0 = 0.7\%$. (**F**) Cell density and O_2 concentration profiles for the 'Go or Grow' model with two thresholds: cells undergo aerotaxis with a constant advection speed $a_0 = 1\mu m/min$ when the O_2 concentration is in the range (C_0', C_0) with $C_0 = 0.7\%$, $C_0' = 0.1\%$. In both cases, thresholds coincide with the cusps in the profiles.

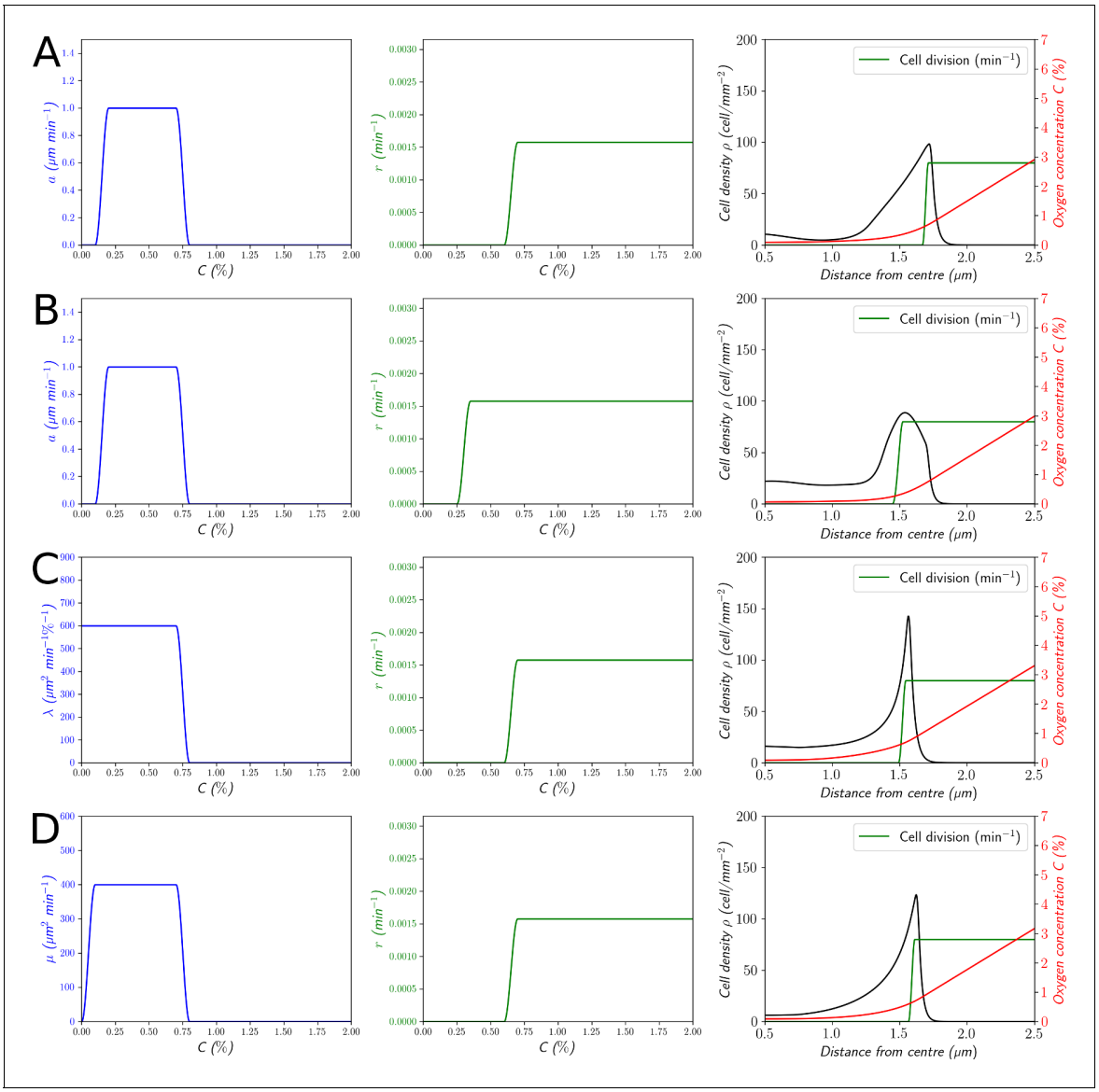

Figure 6—figure supplement 1. Structural variations of (***Equation 1***). (**A** and **B**) The left column represents $\mathrm{a}(\mathrm{C})$. (**C**) The left column corresponds to a linear gradient sensing mechanism with $\mathrm{a}(\mathrm{C},\partial_{\mathrm{x}}\mathrm{C})=\lambda(\mathrm{C})\partial_{\mathrm{x}}\mathrm{C}$. (**D**) The left column corresponds to a logarithmic gradient sensing mechanism with $\mathrm{a}(\mathrm{C},\partial_{\mathrm{x}}\mathrm{C})=\mu(\mathrm{C})\partial_{\mathrm{x}}\mathrm{C}/\mathrm{C}$. For (**C** and **D**), the multiplicative factors of $\lambda(\mathrm{C})$ and $\mu(\mathrm{C})$ have been chosen such that the speed of the front $\sigma\approx 1\mathrm{m}\cdot\mathrm{min}^{-1}$. The middle column represents the cell division rate $\mathrm{r}(\mathrm{C})$. The right column represents the corresponding cell density and O_2 concentration profiles. The green curve represents the cell division rate as a function of the position. (**A**) $\sigma=1.04\mathrm{m}\cdot\mathrm{min}^{-1}$, (**B**) $\sigma=1.20\mathrm{m}\cdot\mathrm{min}^{-1}$, (**C**) $\sigma=0.97\mathrm{m}\cdot\mathrm{min}^{-1}$, (**D**) $\sigma=1.03\mathrm{m}\cdot\mathrm{min}^{-1}$.

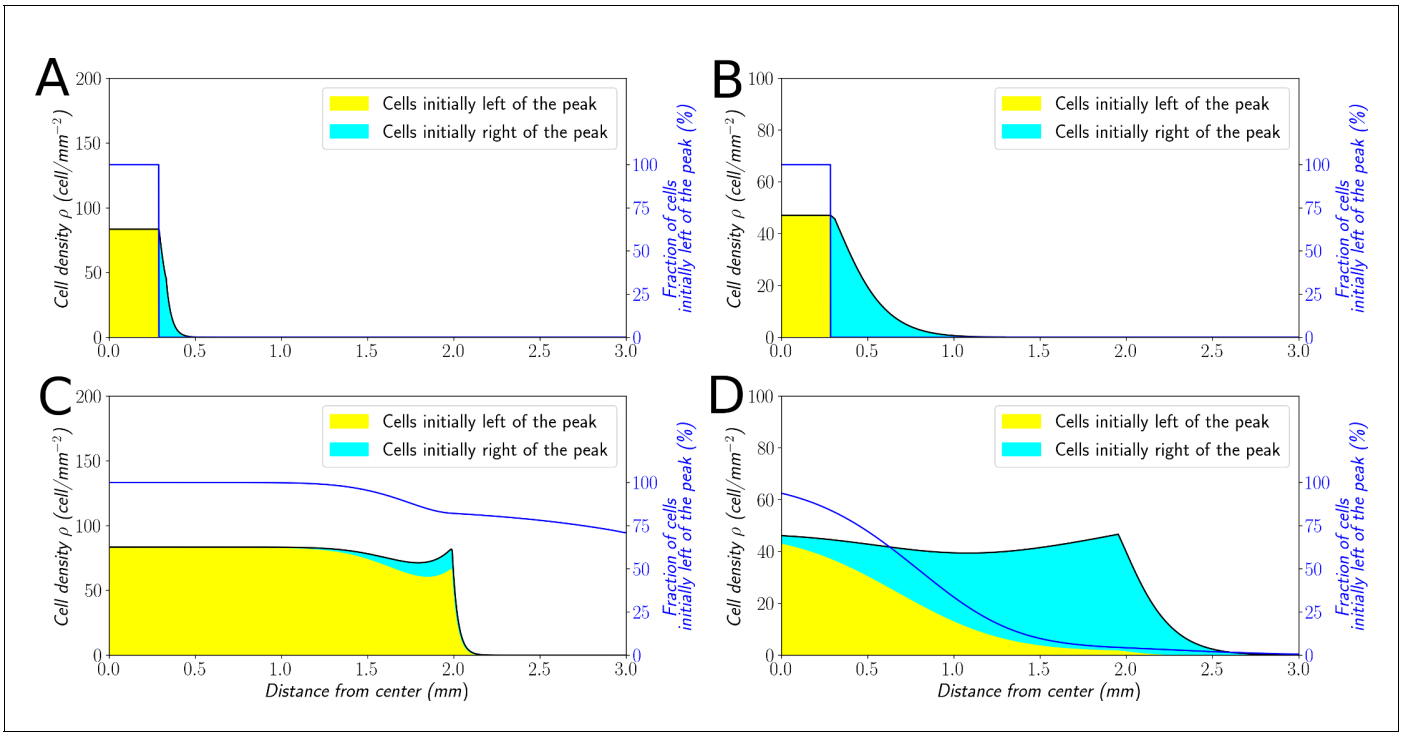

Figure 7. Classification of the expansion type in the 'Go or Grow' model. Cells initially on the left-hand side or right-hand side of the peak get labeled differently (**A** and **B**). The labeling is neutral and does not change the dynamics of the cells. We let evolve the two colored population for some time and observe the mixing of the colors (**C** and **D**). (**A** and **C**) With $a_0 = 1m \cdot min^{-1}$, the wave is pushed wave and after some time the front undergoes a spatially uniform mixing. (**B** and **D**) With $a_0 = 0.1\,\mu m \cdot min^{-1}$, the wave is pulled and only the fraction initially in the front is conserved in the front. $r_0 = ln2/480min^{-1}$ and $C_0 = 0.7\%$ for all conditions.

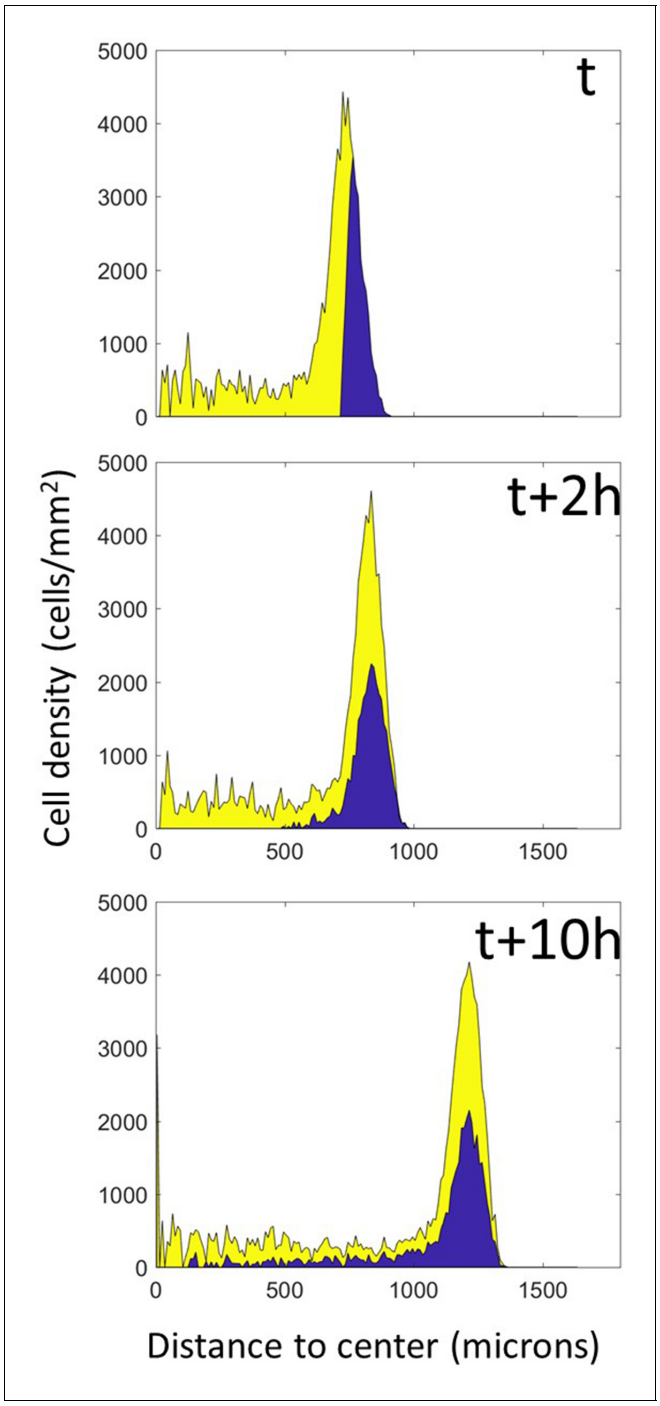

Figure 7—figure supplement 1. Mixing in Potts models. A simulation of the full model was stopped at an arbitrary time and cells were colored according to their position at this time. The simulation was then restarted from this time point and left to run for the equivalent of 10 hr, at which point complete mixing of both populations is clearly visible.

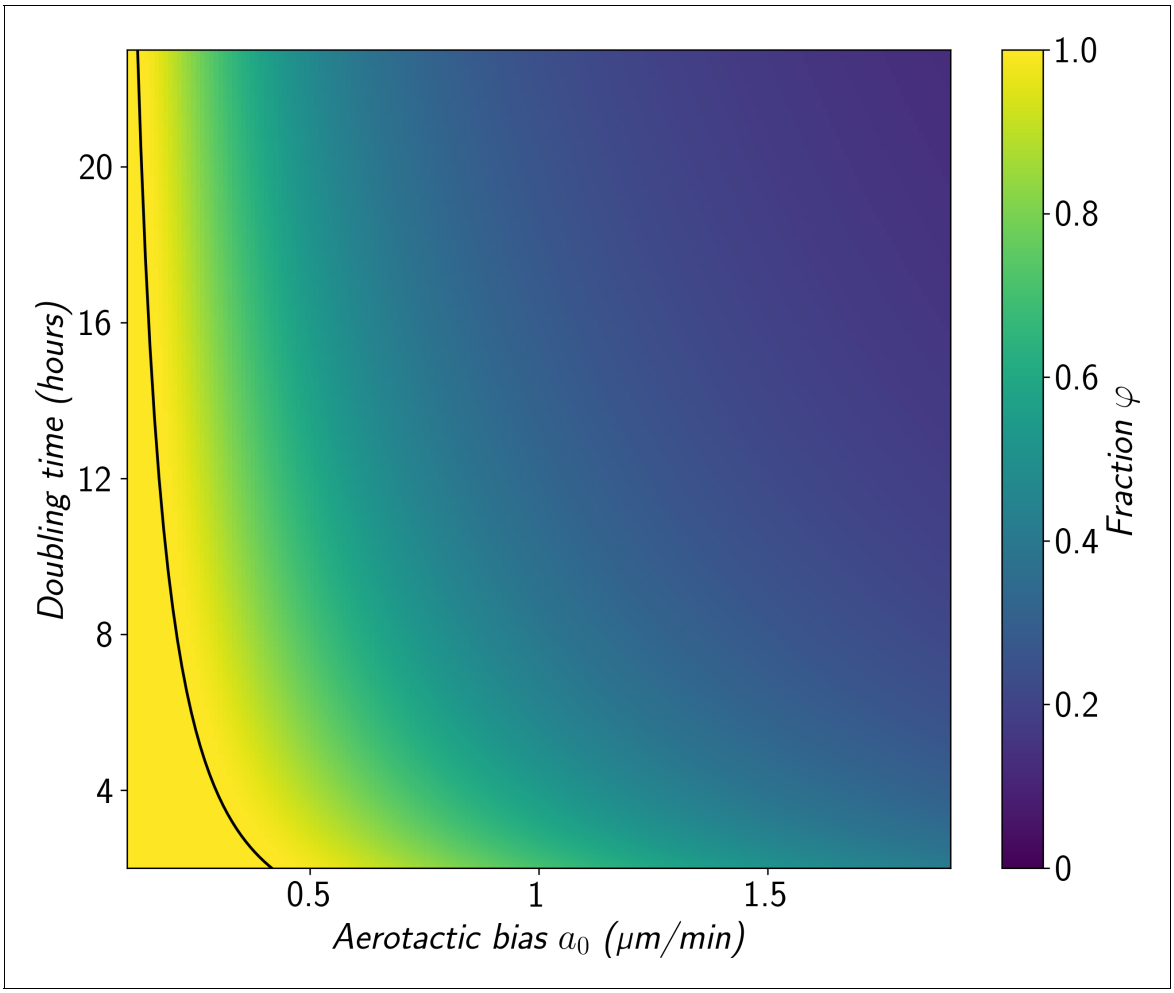

Figure 7—figure supplement 2. Heatmap of $\varphi = 2\sqrt{r_0 D}/\sigma$ as a measure of the relative contribution of cell division to the overall wave speed σ in the space parameter $1/r_0$ and a_0 for the 'Go or Grow' model with a second threshold, under the specific condition that O_2 consumption term be $b(C) = b_0$ and that O_2 concentration may be negative (see Materials and methods). The curve $a_0 = \sqrt{r_0 D}$ is depicted in black.

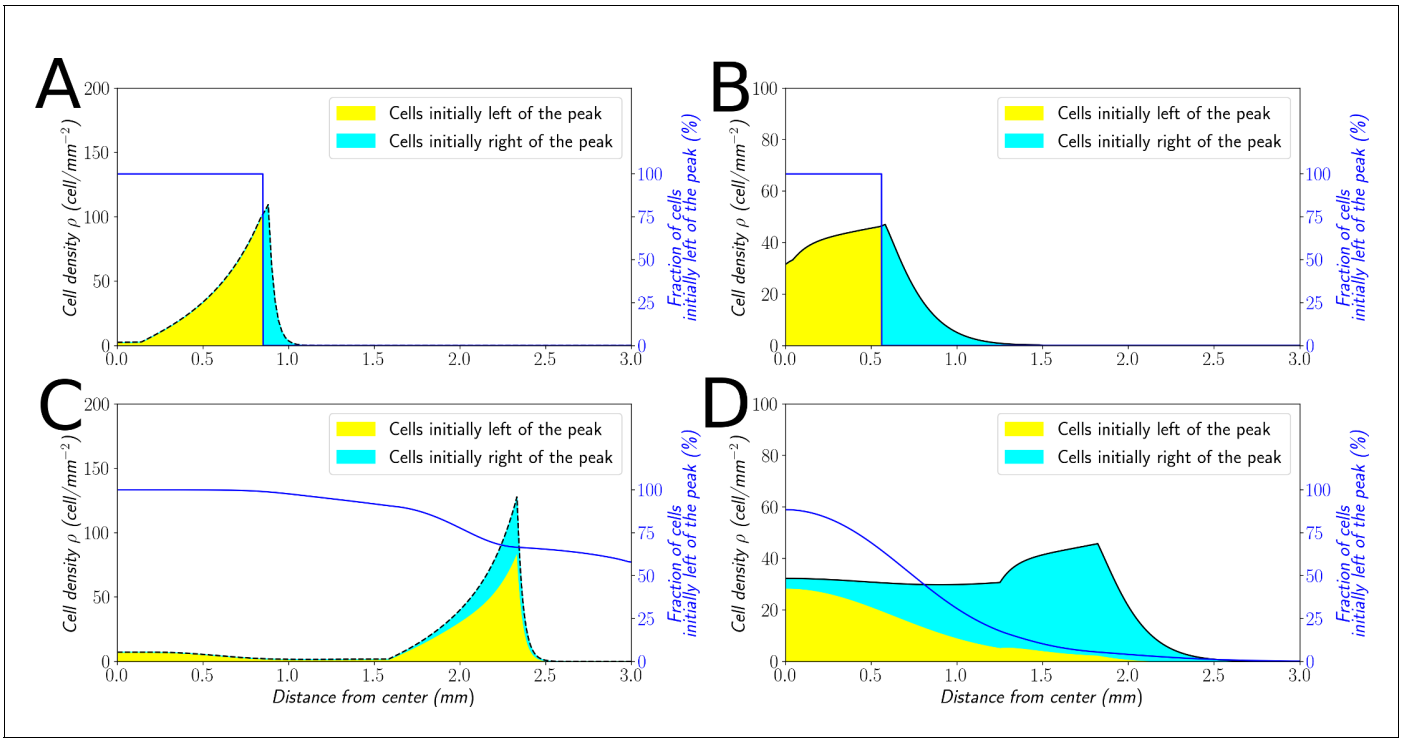

Figure 7—figure supplement 3. Classification of the expansion type in the 'Go or Grow' model with a second-threshold. Cells initially on the left-hand side or right-hand side of the peak get labeled differently (**A** and **B**). The labeling is neutral and does not change the dynamics of the cells. We let evolve the two colored population for some time and observe the mixing of the colors (**C** and **D**). (**A** and **C**) With $a_0 = 1\mathrm{m} \cdot \mathrm{min}^{-1}$, the wave is pushed and after some time the front undergoes a spatially uniform mixing. (**B** and **D**) With $a_0 = 0.1\,\mu\mathrm{m} \cdot \mathrm{min}^{-1}$, the wave is pulled and only the fraction initially in the front is conserved in the front.

Appendix B

Commentary: The Dynamics of Aerotaxis in a Simple Eukaryotic Model

---

This Section contains a commentary, published in [150], to the work in [23], which considers a very similar experiment to the one presented in Chapter 1, but where the conclusions of the authors differ slightly from the ones in Chapter 1.

frontiers in Cell and Developmental Biology

GENERAL COMMENTARY
published: 02 March 2022
doi: 10.3389/fcell.2022.844812

Commentary: The Dynamics of Aerotaxis in a Simple Eukaryotic Model

Jean-Paul Rieu[1]*, *Olivier Cochet-Escartin*[1], *Christophe Anjard*[1], *Mete Demircigil*[2] and *Vincent Calvez*[2]

[1]Institut Lumière Matière, UMR5306, Université Lyon 1-CNRS, Université de Lyon, Villeurbanne, France, [2]Institut Camille Jordan, UMR5208, Université Lyon 1-CNRS, Université de Lyon, Villeurbanne, France

Keywords: Self-generated gradients, Aerotaxis, Collective migration, Oxygen sensing, Dictyostelium discoideum

A Commentary on

The Dynamics of Aerotaxis in a Simple Eukaryotic Model

by Biondo, M., Panuzzo, C., Ali, S. M., Bozzaro, S., Osella, M., Bracco, E., and Pergolizzi, B. (2021). Front. Cell Dev. Biol. 9:720623. doi: 10.3389/fcell.2021.720623

OPEN ACCESS

Edited by:
Verena Ruprecht, Centre for Genomic Regulation (CRG), Spain

Reviewed by:
Jean Clairambault, Institut National de Recherche en Informatique et en Automatique (INRIA), France

***Correspondence:**
Jean-Paul Rieu
jean-paul.rieu@univ-lyon1.fr

Specialty section:
This article was submitted to Molecular and Cellular Pathology, a section of the journal Frontiers in Cell and Developmental Biology

Received: *28 December 2021*
Accepted: *20 January 2022*
Published: *02 March 2022*

Citation:
Rieu J-P, Cochet-Escartin O, Anjard C, Demircigil M and Calvez V (2022) Commentary: The Dynamics of Aerotaxis in a Simple Eukaryotic Model. Front. Cell Dev. Biol. 10:844812. doi: 10.3389/fcell.2022.844812

We read with interest the article by Biondo et al. (2021) in Frontiers in Cell and Developmental Biology, "*The Dynamics of Aerotaxis in a Simple Eukaryotic Model*." Reproducing the confinement assay we published in eLife earlier this year (Cochet-Escartin et al., 2021) with the same cell line, they found the same emergent behavior, i.e., the propagation of a ring of cells, which they named corona, from a dense, confined colony through the self-generation of oxygen gradients by cell consumption. The authors claimed that cell division plays no role in the phenomenon, whereas in our study, we insisted on its important role.

This message is wrong. In this commentary, we first clarify that ring formation is independent on cell division but that ring propagation over long times depends on it. Second, we discuss the possible experimental biases that may have led the authors to this conclusion.

Cell division is not necessary for ring formation but is necessary for its sustained propagation. Biondo et al. observed exactly the same collective phenotype as us for the confined colony in a starving buffer that prevents cell division. A ring forms internally, but as soon as it reaches the colony edge (at ~6 h), it stops and cells aggregate (compare Movie 3 of Biondio et al. with our movie M6 and Figure 5; Supplementary Figure 2, Cochet-Escartin et al.). In contrast, in a nutrient medium, the ring propagates far away from the initial colony for days (see **Figure 1A** below). Biondo et al. neither commented on this fundamental difference between the two conditions nor on our model that demonstrates that cell division is necessary to maintain ring propagation even if it contributes little to the expansion speed (Figures 5A,B and Eq. 6, Cochet-Escartin et al.). Independently of any model, a simple mass balance equation for the total cell number N with NB cells in the bulk region (core) and NR cells in the ring region invalidates Biondo's assertion that division plays no role:

$$N(t) = N_B(t) + N_R(t) = \rho_B \pi (R(t) - L)^2 + \rho_R 2\pi R(t) L \quad (1)$$

Using the experimental observations (Figures 1D,E, Supplementary Figure S3B in Cochet-Escartin et al., **Figures 1B–D** below) that the ring width L and density ρ_R and bulk density ρ_B are constant, and that the ring radius R is expanding at constant speed $R(t) = R_0 + \sigma t$, we predict that $N_B(t)$ increases faster with time (i.e., as $R^2 \sim t^2$) than $N_R(t)$ (i.e., as $LR \sim t$). Experimentally, up to 30 h, $N_B(t)$ increases faster than linearly with time while N_R increases linearly (**Figure 1C**). Initially $N_B/N_R = 1$, but after 24 h, $N_B/N_R = 1.8$, and after 47 h, $N_B/N_R = 2.8$ (**Figure 1C**). Hence, N_B largely contributes to the overall cell number increase $N(t)$. By comparison, Biondo et al. assume a constant $N_R(t)$, and they do not consider bulk cells at all.

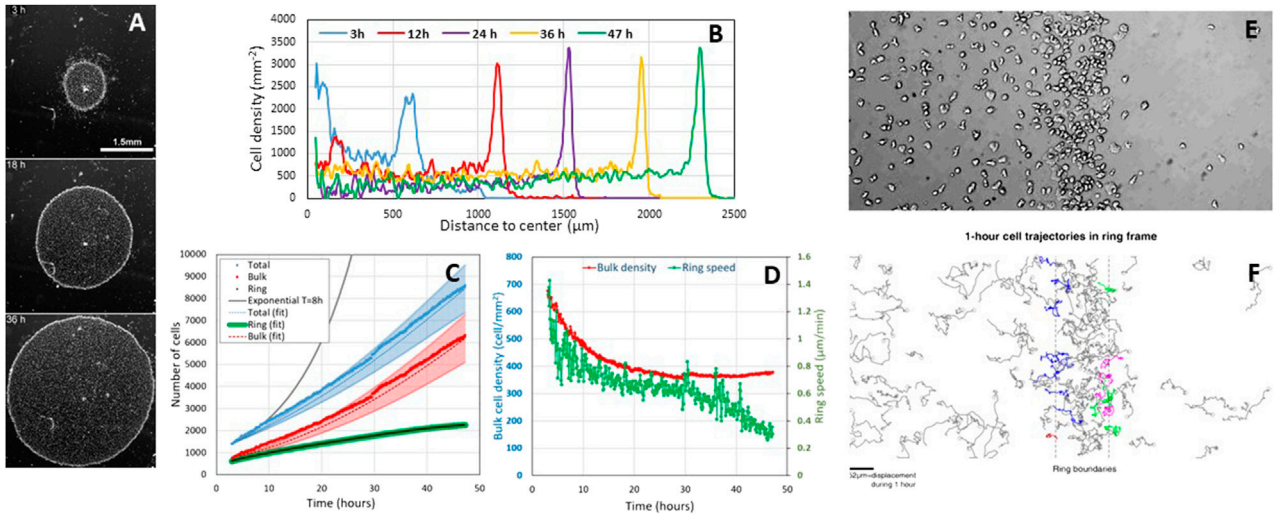

FIGURE 1 | Cell proliferation during the aerotactic expansion of a small confined colony of vegetative *Dictyostelium* cells with an initial number of cell $N(0\ \text{h}) = 1{,}000$ and an initial radius $R(0\ \text{h}) = 600\ \mu\text{m}$. **(A)** Snapshots at 3, 18, and 36 h showing the propagation of an external dense ring of cells mowing outwardly. Scale bar, 1.5 mm. **(B)** Corresponding stationary radial density profiles. **(C)** Measurements of the number of ring and bulk cells as well as the sum of the two subpopulations (total). The ring cells were estimated by measuring their density per unit length and multiplying by the perimeter. The bulk and total cell numbers have been fitted by **Eqs 1**, **2** (dotted lines) with $\varphi_{R\to B} = 12$ cells/mm/h and error bars correspond to a 20% error on $\varphi_{R\to B}$. **(D)** Ring speed and bulk cell density measurements over time. **(E,F)** Close view of the ring region to estimate the cell exchanges between the ring and the bulk. **(F)** Cell trajectories lasting 1 h in the ring frame. Ring borders are depicted by the dashed line. Blue, red, green, and purple trajectories correspond to trajectories that escape the ring toward the bulk, reach the ring from the bulk, reach the ring from the front, and escape the ring from the front, respectively. Overall, the net flux of cell from ring to front is zero; the net flux of cell from ring to bulk is approximately $\varphi_{R\to B} = 12$ cells/mm/h.

Cell divisions hold in the ring. Our confined colony grows slower than exponentially (see solid black line with a typical 8 h doubling time (d'Alessandro et al., 2016) in **Figure 1C**), but it grows (i.e., $N(47\ \text{h})/N(0\ \text{h}) = 8.5$). In Cochet-Escartin et al., we propose a go-or-grow model where aerotaxis holds at low O_2 and cell division at high O_2. The threshold is around 1% O_2 as estimated by direct aerotaxis investigations using microfluidic devices (Cochet-Escartin et al.) and from literature values for cell division in hypoxic conditions (Schiavo and Bisson, 1989; West et al., 2007). Such value corresponds to the O_2 level measured in the ring (Cochet-Escartin et al.). Hence, divisions occur mostly in the ring, but ring cells are constantly transferred to the bulk to maintain a constant ρ_B while R is increasing. This transfer occurs in our models (see Figure 7 of Cochet-Escartin et al.), but perhaps it was not sufficiently supported by data. In **Figures 1E,F**, we present manually tracked trajectories in the ring frame. A few ones displayed with a green or purple color enter or escape the outward ring position, canceling any ring-to-front flux. Far more trajectories are directed backward (i.e., ring to bulk, in blue). Interestingly, the measured flux of such a cell transfer, $\varphi_{R\to B} = 12$ cells/mm/h, explains fairly well the bulk cell number increase using the following equation:

$$dN_B = 2\pi R \phi_{R\to B} dt \tag{2}$$

The fit is displayed in **Figure 1C**.

Biondo et al. may have caught a transient regime only. Biondo et al. measured 3% and 5% O_2 in the bulk and ring regions, respectively (Supplementary Figure S1). Above 2% O_2, aerotaxis should not hold (Cochet-Escartin et al.); the division rate is fairly the same as in normoxic conditions (Schiavo and Bisson, 1989; West et al., 2007). A possible reason for this discrepancy is that O_2 is overestimated. Their measurements were performed with a commercial sensing film that is not compatible with transmission microscopy, contrary to the technology we developed in Cochet-Escartin et al. They may have a different confinement on plastic (their usual experimental condition) than on the sensing film. A loose (resp. tight) confinement may generate a higher (resp. lower) O_2 value under the colony. They also made colonies with a huge amount of cells (50,000 instead of 1,000 and 2,000 in our case). As the self-generated O_2 field depends on the consumption of every cell, we expect a huge degree of hypoxia. Finally, they never reached a stationary expansion regime due to the large initial excess of inner cells. That excess density slowly decreases with time as visible on their kymograph. We have actually simulated a moderate bulk cell excess in our work (Figure 4 of Cochet-Escartin et al.) which is also transiently visible at 3 h in **Figure 1B**. Such an inner cell mass transfer has to be taken into account to establish a correct mass balance equation, and the only $L(t)R(t)$ quantity tested by Biondo et al. is clearly not sufficient to draw a conclusion on cell divisions.

AUTHOR CONTRIBUTIONS

All authors listed have made a substantial, direct and intellectual contribution to the work, and approved it for publication.

FUNDING

This study was supported by the CNRS - Mission pour les Initiatives Transverses et Interdisciplinaires' "Défis Modélisation du vivant - 2019", by the European Research Council (ERC) under the European Union's Horizon 2020 research and innovation program (grant agreement No 865711 to VC) and by the International Human Frontier Science Program Organization, Grant Number RGP0051/2021 (to J-PR).

REFERENCES

Biondo, M., Panuzzo, C., Ali, S. M., Bozzaro, S., Osella, M., Bracco, E., et al. (2021). The Dynamics of Aerotaxis in a Simple Eukaryotic Model. *Front. Cel Dev. Biol.* 9, 720623. doi:10.3389/fcell.2021.720623

Cochet-Escartin, O., Demircigil, M., Hirose, S., Allais, B., Gonzalo, P., Mikaelian, I., et al. (20212021). Hypoxia Triggers Collective Aerotactic Migration in *Dictyostelium discoideum*. *eLife* 10, e64731. doi:10.7554/eLife.64731

d'Alessandro, J., Mas, L., Aubry, L., Rieu, J. P., Rivière, C., and Anjard, C. (2018). Collective Regulation of Cell Motility Using an Accurate Density-Sensing System. *J. R. Soc. Interf.* 15, 45. doi:10.1098/rsif.2018.0006

Schiavo, G., and Bisson, R. (1989). Oxygen Influences the Subunit Structure of Cytochrome C Oxidase in the Slime Mold *Dictyostelium discoideum*. *J. Biol. Chem.* 264, 7129–7134. doi:10.1016/s0021-9258(18)83211-2

West, C. M., van der Wel, H., and Wang, Z. A. (2007). Prolyl 4-hydroxylase-1 Mediates O2 Signaling during Development ofDictyostelium. *Development* 134, 3349–3358. doi:10.1242/dev.000893

Conflict of Interest: The authors declare that the research was conducted in the absence of any commercial or financial relationships that could be construed as a potential conflict of interest.

Bibliography

[1] R. E. Aamodt and K. M. Case. "Useful Identities for Half-Space Problems in Linear Transport Theory". *Annals of Physics* 21 (1963).

[2] J. Adler. "Chemotaxis: Old and New". *Botanica Acta* 101 (1988).

[3] J. Adler, G. L. Hazelbauer, and M. M. Dahl. "Chemotaxis toward Sugars in Escherichia Coli". *Journal of Bacteriology* 115 (1973).

[4] J. Adler. "Chemoreceptors in Bacteria". *Science (New York, N.Y.)* 166 (1969).

[5] J. Adler. "Chemotaxis in Bacteria". *Science (New York, N.Y.)* 153 (1966).

[6] W. Alt. "Orientation of Cells Migrating in a Chemotactic Gradient". *Biological Growth and Spread*. Ed. by W. Jäger, H. Rost, and P. Tautu. Berlin, Heidelberg: Springer Berlin Heidelberg, 1980.

[7] W. Alt. "Biased Random Walk Models for Chemotaxis and Related Diffusion Approximations". *Journal of Mathematical Biology* 9 (1980).

[8] D. Amadori and L. Gosse. *Error Estimates for Well-Balanced Schemes on Simple Balance Laws: One-dimensional Position-Dependent Models*. Springer, 2015.

[9] J. An, C. Henderson, and L. Ryzhik. "Pushed, Pulled and Pushmi-Pullyu Fronts of the Burgers-FKPP Equation". *arXiv:2108.07861 [math]* (2021).

[10] J. P. Armitage. "Chapter 5 Three Hundred Years of Bacterial Motility". *Foundations of Modern Biochemistry*. Ed. by M. G. Ord and L. A. Stocken. Vol. 3. Further Milestone In Biochemistry. JAI, 1997.

[11] D. G. Aronson and H. F. Weinberger. "Nonlinear Diffusion in Population Genetics, Combustion, and Nerve Pulse Propagation". *Partial Differential Equations and Related Topics*. Ed. by J. A. Goldstein. Berlin, Heidelberg: Springer Berlin Heidelberg, 1975.

[12] D. G. Aronson and H. F. Weinberger. "Multidimensional nonlinear diffusion arising in population genetics". *Advances in Mathematics* 30 (1978).

[13] A. D. Banner, R. Fernholz, and I. Karatzas. "Atlas Models of Equity Markets". *The Annals of Applied Probability* 15 (2005).

[14] V. Bansaye and S. Méléard. "Some Stochastic Models for Structured Populations : Scaling Limits and Long Time Behavior". *arXiv:1506.04165 [math]* (2017).

[15] L. Barichello and C. Siewert. "A Discrete-Ordinates Solution for a Non-Grey Model with Complete Frequency Redistribution". *Journal of Quantitative Spectroscopy & Radiative Transfer* 62 (1999).

[16] N. Barkai and S. Leibler. "Robustness in Simple Biochemical Networks". *Nature* 387 (1997).

[17] N. Bellomo, A. Bellouquid, Y. Tao, and M. Winkler. "Toward a mathematical theory of Keller–Segel models of pattern formation in biological tissues". *Mathematical Models and Methods in Applied Sciences* 25 (2015).

[18] N. Bellomo, J. A. Carrillo, and E. Tadmor, eds. *Active Particles, Volume 3: Advances in Theory, Models, and Applications*. Modeling and Simulation in Science, Engineering and Technology. Cham: Springer International Publishing, 2022.

[19] E. Ben-Jacob, H. Brand, G. Dee, L. Kramer, and J. S. Langer. "Pattern Propagation in Nonlinear Dissipative Systems". *Physica D: Nonlinear Phenomena* 14 (1985).

[20] J. Berestycki, É. Brunet, and B. Derrida. "Exact Solution and Precise Asymptotics of a Fisher–KPP Type Front". *Journal of Physics A: Mathematical and Theoretical* 51 (2018).

[21] H. C. Berg. *E. coli in motion*. Springer, 2004.

[22] H. C. Berg and D. A. Brown. "Chemotaxis in Escherichia Coli Analysed by Three-dimensional Tracking". *Nature* 239 (1972).

[23] M. Biondo, C. Panuzzo, S. M. Ali, S. Bozzaro, M. Osella, E. Bracco, and B. Pergolizzi. "The Dynamics of Aerotaxis in a Simple Eukaryotic Model". *Frontiers in Cell and Developmental Biology* 9 (2021).

[24] G. Birzu, O. Hallatschek, and K. S. Korolev. "Fluctuations uncover a distinct class of traveling waves". *Proceedings of the National Academy of Sciences* 115 (2018).

[25] A. Blanchet, J. Dolbeault, and B. Perthame. "Two-Dimensional Keller-Segel Model: Optimal Critical Mass and Qualitative Properties of the Solutions." *Electronic Journal of Differential Equations (EJDE)[electronic only]* 2006 (2006).

[26] E. Bouin, V. Calvez, and G. Nadin. "Hyperbolic Traveling Waves Driven by Growth". *Mathematical Models and Methods in Applied Sciences* 24 (2014).

[27] J. J. Bramburger. "Exact Minimum Speed of Traveling Waves in a Keller–Segel Model". *Applied Mathematics Letters* 111 (2021).

[28] M. Bramson. *Convergence of Solutions of the Kolmogorov Equation to Travelling Waves*. Vol. 44. Memoirs of the American Mathematical Society. American Mathematical Society, 1983.

[29] M. D. Bramson. "Maximal displacement of branching brownian motion". *Communications on Pure and Applied Mathematics* 31 (1978).

[30] M. P. Brenner, L. S. Levitov, and E. O. Budrene. "Physical Mechanisms for Chemotactic Pattern Formation by Bacteria". *Biophysical Journal* 74 (1998).

[31] G. Bretti and L. Gosse. "Diffusive Limit of a Two-Dimensional Well-Balanced Approximation to a Kinetic Model of Chemotaxis". *Partial Differential Equations and Applications* 2 (2021).

[32] H. Brezis and H. Brézis. *Functional Analysis, Sobolev Spaces and Partial Differential Equations*. Vol. 2. Springer, 2011.

[33] E. O. Budrene and H. C. Berg. "Complex Patterns Formed by Motile Cells of Escherichia Coli". *Nature* 349 (1991).

[34] E. O. Budrene and H. C. Berg. "Dynamics of Formation of Symmetrical Patterns by Chemotactic Bacteria". *Nature* 376 (1995).

[35] V. Calvez. "Chemotactic Waves of Bacteria at the Mesoscale". *Journal of the European Mathematical Society* 22 (2019).

[36] V. Calvez, M. Demircigil, and R. Sublet. “Mathematical Modeling of Cell Collective Motion Triggered by Self-Generated Gradients”. *Active Particles, Volume 3: Advances in Theory, Models, and Applications*. Ed. by N. Bellomo, J. A. Carrillo, and E. Tadmor. Cham: Springer International Publishing, 2022.

[37] V. Calvez, L. Gosse, and M. Twarogowska. “Travelling Chemotactic Aggregates at Mesoscopic Scale and BiStability”. *SIAM Journal on Applied Mathematics* 77 (2017).

[38] V. Calvez, B. Henry, S. Méléard, and V. C. Tran. *Dynamics of Lineages in Adaptation to a Gradual Environmental Change*. 2021.

[39] V. Calvez and F. Hoffmann. “Nonlinear Stability of Chemotactic Clustering with Discontinuous Advection”. *arXiv:2009.11048 [math]* (2020).

[40] V. Calvez, B. Perthame, and S. Yasuda. “Traveling wave and aggregation in a flux-limited Keller-Segel model”. *Kinetic & Related Models* 11 (2018).

[41] C. Carmona-Fontaine, E. Theveneau, A. Tzekou, M. Tada, M. Woods, K. M. Page, M. Parsons, J. D. Lambris, and R. Mayor. “Complement Fragment C3a Controls Mutual Cell Attraction during Collective Cell Migration”. *Developmental Cell* 21 (2011).

[42] J. A. Carrillo, J. Li, and Z.-A. Wang. “Boundary spike-layer solutions of the singular Keller–Segel system: existence and stability”. *Proceedings of the London Mathematical Society* 122 (2021).

[43] P. Cattiaux and L. Pédèches. “The 2-D Stochastic Keller-Segel Particle Model : Existence and Uniqueness”. 2016.

[44] C. Cercignani. “Elementary Solutions of the Linearized Gas-Dynamics Boltzmann Equation and Their Application to the Slip-Flow Problem”. *Annals of Physics* 20 (1962).

[45] F. Chalub, Y. Dolak-Struss, P. Markowich, D. Oelz, C. Schmeiser, and A. Soreff. “Model hierarchies for cell aggregation by chemotaxis”. *Mathematical Models and Methods in Applied Sciences* 16 (2006).

[46] F. A. C. C. Chalub, P. A. Markowich, B. Perthame, and C. Schmeiser. “Kinetic Models for Chemotaxis and Their Drift-Diffusion Limits”. *Monatshefte für Mathematik* 142 (2004).

[47] N. Champagnat and S. Méléard. “Invasion and Adaptive Evolution for Individual-Based Spatially Structured Populations”. *Journal of Mathematical Biology* 55 (2007).

[48] O. Cochet-Escartin, M. Demircigil, S. Hirose, B. Allais, P. Gonzalo, I. Mikaelian, K. Funamoto, C. Anjard, V. Calvez, and J.-P. Rieu. “Hypoxia Triggers Collective Aerotactic Migration in Dictyostelium Discoideum”. *eLife* 10 (2021). Ed. by T. Piotrowski, N. Barkai, R. M. Merks, and R. Insall.

[49] J. Cremer, T. Honda, Y. Tang, J. Wong-Ng, M. Vergassola, and T. Hwa. “Chemotaxis as a Navigation Strategy to Boost Range Expansion”. *Nature* 575 (2019).

[50] P. N. Davis, P. van Heijster, and R. Marangell. “Spectral stability of travelling wave solutions in a Keller–Segel model”. *Applied Numerical Mathematics*. Nonlinear Waves: Computation and Theory-X. 141 (2019).

[51] P. N. Davis, P. v. Heijster, and R. Marangell. “Absolute instabilities of travelling wave solutions in a Keller–Segel model”. *Nonlinearity* 30 (2017).

[52] A. De Masi, P. A. Ferrari, E. Presutti, and N. Soprano-Loto. “Hydrodynamics of the N-BBM Process”. *Stochastic Dynamics Out of Equilibrium*. Ed. by G. Giacomin, S. Olla, E. Saada, H. Spohn, and G. Stoltz. Springer Proceedings in Mathematics & Statistics. Cham: Springer International Publishing, 2019.

[53] M. Demircigil. *WB Scheme for Kinetic Go or Grow Model*. `https://plmlab.math.cnrs.fr/mete.demircigil/well-balanced-kinetic-go-or-grow-scheme`.

[54] M. Demircigil. “When Self-Generated Gradients Interact with Expansion by Cell Division and Diffusion. Analysis of a Minimal Model”. 2022.

[55] B. Després and C. Buet. *The Structure of Well-Balanced Schemes for Friedrichs Systems with Linear Relaxation*. 2014.

[56] M. Deygas, R. Gadet, G. Gillet, R. Rimokh, P. Gonzalo, and I. Mikaelian. “Redox Regulation of EGFR Steers Migration of Hypoxic Mammary Cells towards Oxygen”. *Nature Communications* 9 (2018).

[57] Y. Dolak and C. Schmeiser. “Kinetic Models for Chemotaxis: Hydrodynamic Limits and Spatio-Temporal Mechanisms”. *Journal of Mathematical Biology* 51 (2005).

[58] J. Dolbeault and B. Perthame. “Optimal Critical Mass in the Two Dimensional Keller–Segel Model in R2”. *Comptes Rendus Mathematique* 339 (2004).

[59] E. Donà, J. D. Barry, G. Valentin, C. Quirin, A. Khmelinskii, A. Kunze, S. Durdu, L. R. Newton, A. Fernandez-Minan, W. Huber, M. Knop, and D. Gilmour. “Directional Tissue Migration through a Self-Generated Chemokine Gradient”. *Nature* 503 (2013).

[60] K. W. Doolittle, I. Reddy, and J. G. McNally. “3D Analysis of Cell Movement during Normal and Myosin-II-Null Cell Morphogenesis in Dictyostelium”. *Developmental Biology* 167 (1995).

[61] C. Emako, C. Gayrard, A. Buguin, L. N. d. Almeida, and N. Vauchelet. “Traveling Pulses for a Two-Species Chemotaxis Model”. *PLOS Comput Biol* 12 (2016).

[62] C. Emako and M. Tang. “Well-Balanced and Asymptotic Preserving Schemes for Kinetic Models”. *arXiv:1603.03171 [math]* (2016).

[63] T. W. Engelmann. “Neue Methode Zur Untersuchung Der Sauerstoffausscheidung Pflanzlicher Und Thierischer Organismen”. *Archiv für die gesamte Physiologie des Menschen und der Tiere* 25 (1881).

[64] T. Engelmann. “Backterium Photometricum. Ein Beitrag Zur Vergleichenden. Physiolodie Des Licht-Und Farbensinnes”. *Pflugers Arch Gesamte Physiol Menschen Tierre* 42 (1883).

[65] R. Erban and H. G. Othmer. “From Individual to Collective Behavior in Bacterial Chemotaxis”. *SIAM Journal on Applied Mathematics* 65 (2004).

[66] B. Fabrèges. *WB Scheme for F/KPP Equation*. `https://plmlab.math.cnrs.fr/fabreges/reaction_diffusion_schemes`.

[67] A. Fasano. “Mathematical Models of Some Diffusive Processes with Free Boundaries”. *SIMAI e-Lecture Notes* 1 (2008).

[68] S. Fedotov and A. Iomin. “Migration and proliferation dichotomy in tumor cell invasion”. *Physical Review Letters* 98 (2007).

[69] E. R. Fernholz. “Stochastic Portfolio Theory”. *Stochastic Portfolio Theory*. Springer, 2002.

[70] P. C. Fife and J. B. McLeod. “The Approach of Solutions of Nonlinear Diffusion Equations to Travelling Front Solutions”. *Archive for Rational Mechanics and Analysis* 65 (1977).

[71] F. Filbet, P. Laurençot, and B. Perthame. “Derivation of Hyperbolic Models for Chemosensitive Movement”. *Journal of Mathematical Biology* 50 (2005).

[72] R. A. Fisher. “The Wave of Advance of Advantageous Genes”. *Annals of eugenics* 7 (1937).

[73] H. Z. Ford, A. Manhart, and J. R. Chubb. *Signalling Centre Vortices Coordinate Collective Behaviour in Social Amoebae*. 2022.

[74] R. Forien, J. Garnier, and F. Patout. “Ancestral Lineages in Mutation-Selection Equilibria with Moving Optimum”. 2021.

[75] N. Fournier and B. Jourdain. “Stochastic Particle Approximation of the Keller-Segel Equation and Two-Dimensional Generalization of Bessel Processes”. *Annals of Applied Probability* 27 (2017).

[76] N. Fournier and S. Méléard. “A Microscopic Probabilistic Description of a Locally Regulated Population and Macroscopic Approximations”. *Annals of Applied Probability* 14 (2004).

[77] B. Franz, C. Xue, K. J. Painter, and R. Erban. “Travelling Waves in Hybrid Chemotaxis Models”. *Bulletin of Mathematical Biology* 76 (2013).

[78] X. Fu, S. Kato, J. Long, H. H. Mattingly, C. He, D. C. Vural, S. W. Zucker, and T. Emonet. “Spatial self-organization resolves conflicts between individuality and collective migration”. *Nature Communications* 9 (2018).

[79] T. Gallay. “Ondes Progressives Dans Les Systèmes de Réaction-Diffusion”. Cours École d’Été de l’Institut Fourier, 2005.

[80] S. R. Gandhi, K. S. Korolev, and J. Gore. “Cooperation Mitigates Diversity Loss in a Spatially Expanding Microbial Population”. *Proceedings of the National Academy of Sciences* 116 (2019).

[81] S. R. Gandhi, E. A. Yurtsev, K. S. Korolev, and J. Gore. “Range Expansions Transition from Pulled to Pushed Waves as Growth Becomes More Cooperative in an Experimental Microbial Population”. *Proceedings of the National Academy of Sciences* 113 (2016).

[82] J. Garnier, T. Giletti, F. Hamel, and L. Roques. “Inside Dynamics of Pulled and Pushed Fronts”. *Journal de Mathématiques Pures et Appliquées* 98 (2012).

[83] T. Giletti. “Monostable Pulled Fronts and Logarithmic Drifts”. 2021.

[84] L. Gosse. “A Two-Dimensional Version of the Godunov Scheme for Scalar Balance Laws”. *SIAM Journal on Numerical Analysis* 52 (2014).

[85] L. Gosse. *Computing Qualitatively Correct Approximations of Balance Laws*. Vol. 2. Springer, 2013.

[86] L. Gosse. “L-Splines and Viscosity Limits for Well-Balanced Schemes Acting on Linear Parabolic Equations”. *Acta Applicandae Mathematicae* 153 (2018).

[87] L. Gosse. “Viscous Equations Treated with $\mathcal{L}$-Splines and Steklov-Poincaré Operator in Two Dimensions”. *Innovative Algorithms and Analysis*. Ed. by L. Gosse and R. Natalini. Cham: Springer International Publishing, 2017.

[88] L. Gosse and N. Vauchelet. "Numerical High-Field Limits in Two-Stream Kinetic Models and 1D Aggregation Equations". *SIAM Journal on Scientific Computing* (2016).

[89] L. Gosse and N. Vauchelet. "Some Examples of Kinetic Scheme Whose Diffusion Limit Is Il'in's Exponential-Fitting". *Numerische Mathematik* 141 (2019).

[90] S. Gottlieb, C.-W. Shu, and E. Tadmor. "High Order Time Discretization Methods with the Strong Stability Property" (2001).

[91] J. M. Greenberg and A. Y. Leroux. "A Well-Balanced Scheme for the Numerical Processing of Source Terms in Hyperbolic Equations". *SIAM Journal on Numerical Analysis* 33 (1996).

[92] P. Groisman and N. Soprano-Loto. "Rank Dependent Branching-Selection Particle Systems". *Electronic Journal of Probability* 26 (2021).

[93] K. P. Hadeler. "Hyperbolic Travelling Fronts". *Proceedings of the Edinburgh Mathematical Society* 31 (1988).

[94] K. P. Hadeler and F. Rothe. "Travelling Fronts in Nonlinear Diffusion Equations". *Journal of Mathematical Biology* 2 (1975).

[95] F. Hamel and C. Henderson. "Propagation in a Fisher-KPP Equation with Non-Local Advection". *Journal of Functional Analysis* 278 (2020).

[96] F. Hamel, J. Nolen, J.-M. Roquejoffre, and L. Ryzhik. "A Short Proof of the Logarithmic Bramson Correction in Fisher-KPP Equations". *Networks & Heterogeneous Media* 8 (2013).

[97] J. Haškovec and C. Schmeiser. "Convergence of a Stochastic Particle Approximation for Measure Solutions of the 2D Keller-Segel System". *Communications in Partial Differential Equations* 36 (2011).

[98] H. Hatzikirou, D. Basanta, M. Simon, K. Schaller, and A. Deutsch. "'Go or Grow': The Key to the Emergence of Invasion in Tumour Progression?" *Mathematical medicine and biology: a journal of the IMA* 29 (2012).

[99] C. Henderson. "Slow and Fast Minimal Speed Traveling Waves of the FKPP Equation with Chemotaxis". *arXiv:2102.06065 [math]* (2021).

[100] T. Hillen and K. J. Painter. "A user's guide to PDE models for chemotaxis". *Journal of Mathematical Biology* 58 (2009).

[101] M. Hilpert. "Lattice-Boltzmann model for bacterial chemotaxis". *Journal of Mathematical Biology* 51 (2005).

[102] D. Horstmann and A. Stevens. "A Constructive Approach to Traveling Waves inChemotaxis". *Journal of Nonlinear Science* 14 (2004).

[103] T. Ichiba, S. Pal, and M. Shkolnikov. "Convergence Rates for Rank-Based Models with Applications to Portfolio Theory". *Probability Theory and Related Fields* 156 (2013).

[104] R. Insall. "The Interaction between Pseudopods and Extracellular Signalling during Chemotaxis and Directed Migration". *Current Opinion in Cell Biology.* Cell Adhesion and Migration 25 (2013).

[105] J.-F. Jabir, D. Talay, and M. Tomašević. "Mean-Field Limit of a Particle Approximation of the One-Dimensional Parabolic-Parabolic Keller-Segel Model without Smoothing". *Electronic Communications in Probability* 23 (2018).

[106] G.-S. Jiang and C.-W. Shu. "Efficient Implementation of Weighted ENO Schemes". *Journal of Computational Physics* 126 (1996).

[107] L. Jiang, Q. Ouyang, and Y. Tu. "Quantitative Modeling of Escherichia coli Chemotactic Motion in Environments Varying in Space and Time". *PLOS Comput Biol* 6 (2010).

[108] H.-Y. Jin, J. Li, and Z.-A. Wang. "Asymptotic stability of traveling waves of a chemotaxis model with singular sensitivity". *Journal of Differential Equations* 255 (2013).

[109] B. Jourdain and J. Reygner. "Propagation of Chaos for Rank-Based Interacting Diffusions and Long Time Behaviour of a Scalar Quasilinear Parabolic Equation". *Stochastic partial differential equations: analysis and computations* (2013).

[110] Y. V. Kalinin, L. Jiang, Y. Tu, and M. Wu. "Logarithmic Sensing in Escherichia Coli Bacterial Chemotaxis". *Biophysical Journal* 96 (2009).

[111] E. F. Keller and L. A. Segel. "Conflict between Positive and Negative Feedback as an Explanation for the Initiation of Aggregation in Slime Mould Amoebae". *Nature* 227 (1970).

[112] E. F. Keller and L. A. Segel. "Initiation of Slime Mold Aggregation Viewed as an Instability". *Journal of Theoretical Biology* 26 (1970).

[113] E. F. Keller and L. A. Segel. "Model for chemotaxis". *Journal of Theoretical Biology* 30 (1971).

[114] E. F. Keller and L. A. Segel. "Traveling Bands of Chemotactic Bacteria: A Theoretical Analysis". *Journal of Theoretical Biology* 30 (1971).

[115] A. Kolmogorov, I. Petrovsky, and N. Piskunov. "Etude de l Équation de La Diffusion Avec Croissance de La Quantité de Matière et Son Application à Un Problème Biologique, Bjul. Moskowskogo Gos". 1 (1937).

[116] N. Krylov. *Lectures on Elliptic and Parabolic Equations in Hölder Spaces*. Vol. 12. Graduate Studies in Mathematics. American Mathematical Society, 1996.

[117] J. Lee. "A Free Boundary Problem in Biological Selection Models". *arXiv:1707.01232 [math, q-bio]* (2017).

[118] R. J. Leveque and H. C. Yee. "A Study of Numerical Methods for Hyperbolic Conservation Laws with Stiff Source Terms". *Journal of Computational Physics* 86 (1990).

[119] J. Li, T. Li, and Z.-A. Wang. "Stability of traveling waves of the Keller–Segel system with logarithmic sensitivity". *Mathematical Models and Methods in Applied Sciences* 24 (2014).

[120] L. Li, S. F. Nørrelykke, and E. C. Cox. "Persistent Cell Motion in the Absence of External Signals: A Search Strategy for Eukaryotic Cells". *PLOS ONE* 3 (2008).

[121] T. Li and J. Park. "Traveling Waves in a Chemotaxis Model with Logistic Growth". *Discrete & Continuous Dynamical Systems - B* 24 (2019).

[122] T.-C. Lin, Z.-A. Wang, ,Institute of Applied Mathematical Sciences, NCTS Taipei Office, National Taiwan University, Taipei 106, and ,Department of Applied Mathematics, The Hong Kong Polytechnic University, Hung Hom, Kowloon, Hong Kong. "Development of traveling waves in an interacting two-species chemotaxis model". *Discrete & Continuous Dynamical Systems - A* 34 (2014).

[123] C. Liu et al. “Sequential Establishment of Stripe Patterns in an Expanding Cell Population”. *Science* 334 (2011).

[124] W. Liu, J. Cremer, D. Li, T. Hwa, and C. Liu. “An Evolutionarily Stable Strategy to Colonize Spatially Extended Habitats”. *Nature* 575 (2019).

[125] X.-D. Liu, S. Osher, and T. Chan. “Weighted Essentially Non-oscillatory Schemes”. *Journal of Computational Physics* 115 (1994).

[126] A. Lunardi. *Interpolation Theory*. Vol. 9. Edizioni della normale, 2009.

[127] P. Maillard. “Speed and Fluctuations of N-particle Branching Brownian Motion with Spatial Selection”. *Probability Theory and Related Fields* 166 (2016).

[128] R. Majumdar, M. Sixt, and C. A. Parent. “New paradigms in the establishment and maintenance of gradients during directed cell migration”. *Current Opinion in Cell Biology*. Cell adhesion and migration 30 (2014).

[129] D. Malchow, D. F. Lusche, C. Schlatterer, A. De Lozanne, and A. Müller-Taubenberger. “The Contractile Vacuole in Ca2+-Regulation in Dictyostelium: Its Essential Function for cAMP-induced Ca2+-Influx”. *BMC Developmental Biology* 6 (2006).

[130] A. Marguet. “Uniform Sampling in a Structured Branching Population”. *Bernoulli* 25 (2019).

[131] C. Mascia, P. Moschetta, and C. Simeoni. “Phase Transitions of Biological Phenotypes by Means of a Prototypical PDE Model”. *Communications in Applied and Industrial Mathematics* 11 (2020).

[132] S. Mirrahimi and J.-M. Roquejoffre. “Uniqueness in a Class of Hamilton–Jacobi Equations with Constraints”. *Comptes Rendus Mathematique* 353 (2015).

[133] T. J. Mitchison and L. P. Cramer. “Actin-Based Cell Motility and Cell Locomotion”. *Cell* 84 (1996).

[134] N. Mittal, E. O. Budrene, M. P. Brenner, and A. v. Oudenaarden. “Motility of Escherichia coli cells in clusters formed by chemotactic aggregation”. *Proceedings of the National Academy of Sciences* 100 (2003).

[135] K. Moissoglu, R. Majumdar, and C. A. Parent. “Cell Migration: Sinking in a Gradient”. *Current Biology* 24 (2014).

[136] A. J. Muinonen-Martin et al. “Melanoma Cells Break Down LPA to Establish Local Gradients That Drive Chemotactic Dispersal”. *PLOS Biology* 12 (2014).

[137] G. Nadin, B. Perthame, and L. Ryzhik. “Traveling Waves for the Keller–Segel System with Fisher Birth Terms”. *Interfaces and Free Boundaries* 10 (2008).

[138] T. Nagai and T. Ikeda. “Traveling waves in a chemotactic model”. *Journal of Mathematical Biology* 30 (1991).

[139] M. P. Neilson, D. M. Veltman, P. J. M. van Haastert, S. D. Webb, J. A. Mackenzie, and R. H. Insall. “Chemotaxis: A Feedback-Based Computational Model Robustly Predicts Multiple Aspects of Real Cell Behaviour”. *PLOS Biology* 9 (2011).

[140] J. Nolen, J.-M. Roquejoffre, and L. Ryzhik. “Convergence to a Single Wave in the Fisher-KPP Equation”. *Chinese Annals of Mathematics, Series B* 38 (2017).

[141] H. G. Othmer, S. R. Dunbar, and W. Alt. “Models of Dispersal in Biological Systems”. *Journal of Mathematical Biology* 26 (1988).

[142] H. G. Othmer and T. Hillen. “The Diffusion Limit of Transport Equations Derived from Velocity-Jump Processes”. *SIAM Journal on Applied Mathematics* 61 (2000).

[143] H. G. Othmer and T. Hillen. "The Diffusion Limit of Transport Equations II: Chemotaxis Equations". *SIAM Journal on Applied Mathematics* 62 (2002).

[144] S. Pal and J. Pitman. "One-Dimensional Brownian Particle Systems with Rank-Dependent Drifts". *The Annals of Applied Probability* 18 (2008).

[145] C. S. Patlak. "Random Walk with Persistence and External Bias". *The bulletin of mathematical biophysics* 15 (1953).

[146] W. Pfeffer. *Locomotorische Richtungsbewegungen Durch Chemische Reize:(Aus Den" Untersuchungen Aus Dem Botanischen Institut Zu Tübingen Bd. I. p. 363-482).* W. Engelmann, 1884.

[147] W. Pfeffer. *Über Chemotaktische Bewegung von Bakterien, Flagellaten Und Volvocineen: (Aus Den" Untersuchungen Aus Dem Botanischen Institut Zu Tübingen Bd. II. p. 582-661).* 1888.

[148] A. R. Pluess. "Pursuing Glacier Retreat: Genetic Structure of a Rapidly Expanding Larix Decidua Population". *Molecular Ecology* 20 (2011).

[149] M. Ribot. "A Survey on Well-Balanced and Asymptotic Preserving Schemes for Hyperbolic Models for Chemotaxis". *ESAIM: Proceedings and Surveys* 61 (2018).

[150] J.-P. Rieu, O. Cochet-Escartin, C. Anjard, M. Demircigil, and V. Calvez. "Commentary: The Dynamics of Aerotaxis in a Simple Eukaryotic Model". *Frontiers in Cell and Developmental Biology* 10 (2022).

[151] M. A. Rivero, R. T. Tranquillo, H. M. Buettner, and D. A. Lauffenburger. "Transport models for chemotactic cell populations based on individual cell behavior". *Chemical Engineering Science* 44 (1989).

[152] L. Roques, J. Garnier, F. Hamel, and E. K. Klein. "Allee Effect Promotes Diversity in Traveling Waves of Colonization". *Proceedings of the National Academy of Sciences* 109 (2012).

[153] G. Rosen and S. Baloga. "On the stability of steadily propagating bands of chemotactic bacteria". *Mathematical Biosciences* 24 (1975).

[154] F. Rothe. "Convergence to Pushed Fronts". *Rocky Mountain Journal of Mathematics* 11 (1981).

[155] L. Ryzhik, B. Perthame, and G. Nadin. "Traveling waves for the Keller–Segel system with Fisher birth terms". *Interfaces and Free Boundaries* 10 (2008).

[156] W. van Saarloos. "Front propagation into unstable states". *Physics Reports* 386 (2003).

[157] R. B. Salako and W. Shen. "Existence of Traveling Wave Solutions to Parabolic-Elliptic-Elliptic Chemotaxis Systems with Logistic Source". *Discrete & Continuous Dynamical Systems - S* 13 (2020).

[158] R. B. Salako and W. Shen. "Spreading Speeds and Traveling Waves of a Parabolic-Elliptic Chemotaxis System with Logistic Source on $\mathbb{R}^N$". *Discrete & Continuous Dynamical Systems* 37 (2017).

[159] B. Sandstede. "Chapter 18 - Stability of Travelling Waves". *Handbook of Dynamical Systems*. Ed. by B. Fiedler. Vol. 2. Handbook of Dynamical Systems. Elsevier Science, 2002.

[160] J. Saragosti, V. Calvez, N. Bournaveas, B. Perthame, A. Buguin, and P. Silberzan. "Directional Persistence of Chemotactic Bacteria in a Traveling Concentration Wave". *Proceedings of the National Academy of Sciences* 108 (2011).

[161] J. Saragosti, V. Calvez, N. Bournaveas, A. Buguin, P. Silberzan, and B. Perthame. "Mathematical Description of Bacterial Traveling Pulses". *PLoS Computational Biology* 6 (2010). Ed. by C. V. Rao.

[162] C. Scherber, A. J. Aranyosi, B. Kulemann, S. P. Thayer, M. Toner, O. Iliopoulos, and D. Irimia. "Epithelial Cell Guidance by Self-Generated EGF Gradients". *Integrative Biology: Quantitative Biosciences from Nano to Macro* 4 (2012).

[163] N. Sfakianakis, A. Madzvamuse, and M. A. J. Chaplain. "A Hybrid Multiscale Model for Cancer Invasion of the Extracellular Matrix". *Multiscale Modeling & Simulation* 18 (2020).

[164] C.-W. Shu. "Essentially Non-Oscillatory and Weighted Essentially Non-Oscillatory Schemes". *Acta Numerica* 29 (2020).

[165] C.-W. Shu. "High-Order Finite Difference and Finite Volume WENO Schemes and Discontinuous Galerkin Methods for CFD". *International Journal of Computational Fluid Dynamics* 17 (2003).

[166] G. Si, M. Tang, and X. Yang. "A Pathway-Based Mean-Field Model for E. coli Chemotaxis: Mathematical Derivation and Its Hyperbolic and Parabolic Limits". *Multiscale Modeling & Simulation* 12 (2014).

[167] J. G. Skellam. "Random Dispersal in Theoretical Populations". *Bulletin of Mathematical Biology* 53 (1991).

[168] T. L. Stepien, E. M. Rutter, and Y. Kuang. "Traveling Waves of a Go-or-Grow Model of Glioma Growth". *SIAM Journal on Applied Mathematics* 78 (2018).

[169] A. N. Stokes. "On Two Types of Moving Front in Quasilinear Diffusion". *Mathematical Biosciences* 31 (1976).

[170] S. J. Streichan, G. Valentin, D. Gilmour, and L. Hufnagel. "Collective cell migration guided by dynamically maintained gradients". *Phys. Biol.* (2011).

[171] D. W. Stroock. "Some Stochastic Processes Which Arise from a Model of the Motion of a Bacterium". *Zeitschrift für Wahrscheinlichkeitstheorie und Verwandte Gebiete* 28 (1974).

[172] C. H. Stuelten. "Moving in and Out: Dispersion of Cells in Self-Generated Gradients". *Journal of Clinical & Cellular Immunology* 8 (2017).

[173] B. L. Taylor, I. B. Zhulin, and M. S. Johnson. "Aerotaxis and Other Energy-Sensing Behavior in Bacteria". *Annual Reviews in Microbiology* 53 (1999).

[174] M. J. Tindall, P. K. Maini, S. L. Porter, and J. P. Armitage. "Overview of Mathematical Approaches Used to Model Bacterial Chemotaxis II: Bacterial Populations". *Bulletin of Mathematical Biology* 70 (2008).

[175] M. Tomasevic. "A New McKean-Vlasov Stochastic Interpretation of the Parabolic-Parabolic Keller-Segel Model: The Two-Dimensional Case". *Annals of Applied Probability* 31 (2021).

[176] M. Tomasevic and D. Talay. "A New McKean-Vlasov Stochastic Interpretation of the Parabolic-Parabolic Keller-Segel Model: The One-Dimensional Case". *Bernoulli. Official Journal of the Bernoulli Society for Mathematical Statistics and Probability* 26 (2020).

[177] N. S. Trudinger. "Pointwise Estimates and Quasilinear Parabolic Equations". *Communications on Pure and Applied Mathematics* 21 (1968).

[178] Y. Tu, T. S. Shimizu, and H. C. Berg. "Modeling the chemotactic response of Escherichia coli to time-varying stimuli". *Proceedings of the National Academy of Sciences* 105 (2008).

[179] L. Tweedy and R. H. Insall. "Self-Generated Gradients Yield Exceptionally Robust Steering Cues". *Frontiers in Cell and Developmental Biology* 8 (2020).

[180] L. Tweedy, D. A. Knecht, G. M. Mackay, and R. H. Insall. "Self-Generated Chemoattractant Gradients: Attractant Depletion Extends the Range and Robustness of Chemotaxis". *PLOS Biology* 14 (2016).

[181] L. Tweedy, O. Susanto, and R. H. Insall. "Self-Generated Chemotactic Gradients—Cells Steering Themselves". *Current Opinion in Cell Biology*. Cell Dynamics 42 (2016).

[182] L. Tweedy, P. A. Thomason, P. I. Paschke, K. Martin, L. M. Machesky, M. Zagnoni, and R. H. Insall. "Seeing around Corners: Cells Solve Mazes and Respond at a Distance Using Attractant Breakdown". *Science (New York, N.Y.)* 369 (2020).

[183] K. Uchiyama. "Brownian First Exit from and Sojourn over One Sided Moving Boundary and Application". *Zeitschrift für Wahrscheinlichkeitstheorie und Verwandte Gebiete* 54 (1980).

[184] W. Van Saarloos. "Front Propagation into Unstable States". *Physics reports* 386 (2003).

[185] G. Venkiteswaran, S. W. Lewellis, J. Wang, E. Reynolds, C. Nicholson, and H. Knaut. "Generation and Dynamics of an Endogenous, Self-Generated Signaling Gradient across a Migrating Tissue". *Cell* 155 (2013).

[186] A. Y. Veretennikov. "On strong solutions and explicit formulas for solutions of stochastic integral equations". *Matematicheskii Sbornik* 153 (1980).

[187] R. Wang and R. J. Spiteri. "Linear Instability of the Fifth-Order WENO Method". *SIAM Journal on Numerical Analysis* (2007).

[188] Z.-A. Wang. "Mathematics of traveling waves in chemotaxis –Review paper–". *Discrete and Continuous Dynamical Systems - Series B* 18 (2012).

[189] C. J. Weijer. "Dictyostelium Morphogenesis". *Current Opinion in Genetics & Development* 14 (2004).

[190] C. Xue. "Macroscopic equations for bacterial chemotaxis: integration of detailed biochemistry of cell signaling". *Journal of Mathematical Biology* 70 (2015).

[191] C. Xue, H. J. Hwang, K. J. Painter, and R. Erban. "Travelling Waves in Hyperbolic Chemotaxis Equations". *Bulletin of Mathematical Biology* 73 (2011).

[192] Y. Zeng and K. Zhao. "On the logarithmic Keller-Segel-Fisher/KPP system". *Discrete & Continuous Dynamical Systems* 39 (2019).

Collective movement in *Dictyostelium discoideum* and other species. Modeling, analysis and simulations.

Abstract: This thesis is concerned with the modeling of collective cell movement and the analysis of spreading phenomena arising in these models. The starting point of the thesis is the mathematical modeling of an experiment, where a colony of *Dictyostelium discoideum* is able to escape hypoxia through a remarkable collective behavior. It is shown that oxygen consumption leads to self-generated oxygen gradients, which serve as directional cues and trigger a collective movement towards higher oxygen regions. This movement is sustained over large scales by the perpetual consumption of oxygen by the cells. Through an elementary PDE model, the so-called Go or Grow model, we show that the combination of cell division and aerotaxis plays a key role in this collective behavior. In particular, this approach leads to an explicit formula for the propagation speed.
We carry out a thorough mathematical analysis of the Go or Grow model, including a result of existence and uniqueness locally in time of the model, an analysis of the inside dynamics of the propagating population, as well as a weak characterization of the asymptotic spreading behavior.
Following the aforementioned investigation, we address the question under which circumstance a cell population may propagate, by generating their own signaling gradients. We do a survey on existing results in the literature and discuss various modeling scenarios, which lead to this type of propagation phenomena.
Then, we propose an approach to design well-balanced numerical schemes for traveling waves in kinetic and parabolic models. The approach combines an estimate of the instantaneous spreading speed with techniques taken from the literature to design well-balanced schemes.
Finally, we study a stochastic individual-based Go or Grow model, which is based on a simple Go or Grow rule. We conjecture the large population limit, which can be seen as an alternative Go or Grow model, and investigate numerically the ancestral lineages of particles. This leads to an alternative viewpoint on the inside dynamics. The alternative Go or Grow model is analyzed and we give preliminary results estimating the asymptotic behavior of the spreading.

Keywords: Mathematical Biology, Chemotaxis, Modeling, Propagation Phenomena, Parabolic Equations, Kinetic Equations, Well-Balanced Schemes, Stochastic Processes.